

AD-A282 810



VOLUME 32

# Diagnostic Techniques for Semiconductor Materials Processing

DTIC  
ELECTE  
1994

1994  
Coleman  
W. Lang  
Loma  
N. S. rear  
Larrabee

It has been approved  
release and sale; its  
unlimited.

**Diagnostic Techniques for  
Semiconductor Materials Processing**

519px

**94-23529**



**94 7 25 191**

DTIC QUALITY INSPECTED 5

## Diagnostic Techniques for Semiconductor Materials Processing

Symposium held November 29–December 2, 1993, Boston, Massachusetts, U.S.A.

EDITORS:

**O.J. Glembocki**

Naval Research Laboratory  
Washington, DC, U.S.A.

**S.W. Pang**

University of Michigan  
Ann Arbor, Michigan, U.S.A.

**F.H. Pollak**

Brooklyn College of CUNY  
Brooklyn, New York, U.S.A.

**G.M. Crean**

National Microelectronics Research Centre  
Cork, Ireland

**G. Larrabee**

Booz, Allen & Hamilton  
Dallas, Texas, U.S.A.

|                                      |   |
|--------------------------------------|---|
| Accession For                        |   |
| NTIS                                 | CRA&I <input checked="" type="checkbox"/> |
| DTIC                                 | TAB <input type="checkbox"/>              |
| Unannounced <input type="checkbox"/> |   |
| Justification .....                  |   |
| By .....                             |   |
| Distribution /                       |   |
| Availability Codes                   |   |
| Dist                                 | Avail and/or<br>Special                   |
| A-1                                  |   |



MATERIALS RESEARCH SOCIETY  
Pittsburgh, Pennsylvania

Publication of this proceedings was supported by the Office of Naval Research, Contract #94413--0012. Opinions, findings, conclusions, or recommendations expressed herein do not necessarily reflect the views of the U.S. government.

Single article reprints from this publication are available through University Microfilms Inc., 300 North Zeeb Road, Ann Arbor, Michigan 48106

CODEN: MRSPDH

Copyright 1994 by Materials Research Society.  
All rights reserved.

This book has been registered with Copyright Clearance Center, Inc. For further information, please contact the Copyright Clearance Center, Salem, Massachusetts.

Published by:

Materials Research Society  
9800 McKnight Road  
Pittsburgh, Pennsylvania 15237  
Telephone (412) 367-3003  
Fax (412) 367-4373

Library of Congress Cataloging in Publication Data

Diagnostic techniques for semiconductor materials processing:  
Symposium K held November 29-December 2, 1993, Boston, Massachusetts,  
USA / editors, O.J. Glembocki, S.W. Pang, F.H. Pollak, G.M. Crean,  
G. Larrabee

p. cm.—(Materials Research Society symposium proceedings; v. 324.)  
Papers presented at the symposium on "Diagnostic Techniques for Semiconductor Materials Processing," held as part of the 1993 Fall Meeting of the Materials Research Society in Boston, MA.

Includes bibliographical references and index.

ISBN 1-55899-223-5

I. Semiconductors--Testing--Congresses. I. Glembocki, O.J. II. Pang, S.W. III. Pollak, F.H. IV. Crean, G.M. V. Larrabee, G. VI. Materials Research Society. Meeting (1993: Boston, Mass.). Symposium K VII. Series: Materials Research Society symposium proceedings; v. 324.

TK7871.85.D497 1994  
621.3815'2'0287--dc20

94-20397  
CIP

Manufactured in the United States of America



## Contents

|  |      |
|--|------|
| PREFACE .....  | xiii |
| ACKNOWLEDGMENTS .....                                  | xv   |
| MATERIALS RESEARCH SOCIETY SYMPOSIUM PROCEEDINGS ..... | xvi  |

### PART I: REFLECTANCE DIFFERENCE SPECTROSCOPY AND ELLIPSOMETRY

|   |    |
|---|----|
| *REAL-TIME SURFACE AND NEAR-SURFACE OPTICAL<br>DIAGNOSTICS FOR EPITAXIAL GROWTH .....   | 3  |
| D.E. Aspnes   |    |
| *IN SITU AND EX SITU APPLICATIONS OF SPECTROSCOPIC<br>ELLIPSOMETRY .....  | 15 |
| John A. Woollam, Blaine Johs, William A. McGahan,<br>Paul G. Snyder, Jeffrey Hale, and Huade Walter Yao   |    |
| IN-SITU MULTILAYER FILM GROWTH CHARACTERIZATION BY<br>BREWSTER ANGLE REFLECTANCE DIFFERENTIAL SPECTROSCOPY .....  | 27 |
| N. Dietz, D.J. Stephens, G. Lucovsky, and K.J. Bachmann   |    |
| SIMULTANEOUS REAL TIME SPECTROSCOPIC ELLIPSOMETRY<br>AND REFLECTANCE FOR MONITORING SEMICONDUCTOR AND<br>THIN FILM PREPARATION .....                              | 33 |
| Ilsin An, Hien V. Nguyen, A.R. Heyd, and R.W. Collins   |    |
| SPECTROSCOPIC ELLIPSOMETRY CHARACTERISATION OF<br>THIN FILM POLYSILICON .....   | 39 |
| S. Lynch, L. Spinelli, M. Sherlock, J. Barrett, and<br>G.M. Crean   |    |
| CHARACTERIZATION OF POLYCRYSTALLINE SILICON MULTILAYERS<br>WITH THIN NITRIDE/OXIDE FILMS USING SPECTROSCOPIC<br>ELLIPSOMETRY .....                                | 47 |
| L.M. Asinovsky  |    |
| IN-SITU DUAL-WAVELENGTH ELLIPSOMETRY AND LIGHT<br>SCATTERING MONITORING OF Si/Si <sub>1-x</sub> Ge <sub>x</sub> HETEROSTRUCTURES<br>AND MULTI-QUANTUM WELLS ..... | 53 |
| C. Pickering, D.A.O. Hope, W.H. Leong, D.J. Robbins, and<br>R. Greef  |    |
| REFLECTANCE ANISOTROPY AND SPECTROSCOPIC ELLIPSOMETRY<br>CHARACTERISATION OF WET SILICON WAFER CLEANING .....   | 59 |
| J.T. Beechinor, P.V. Kelly, and G.M. Crean  |    |
| PROCESS MONITORING FOR FABRICATION OF MERCURIC IODIDE<br>ROOM TEMPERATURE RADIATION DETECTORS .....   | 65 |
| J.M. Van Scyoc, T.E. Schlesinger, H. Yao, R.B. James,<br>M. Natarajan, X.J. Bao, J.S. Iwanczyk, B.E. Patt, and<br>L. van den Berg                                 |    |

\*Invited Paper

## PART II: REFLECTANCE AND LIGHT SCATTERING SPECTROSCOPIES

|  |     |
|--|-----|
| *CHARACTERIZATION OF ELECTRONIC MATERIALS BY OPTICAL<br>REFLECTANCE SPECTROSCOPY AND DIGITAL SIGNAL PROCESSING .....     | 75  |
| Pieter L. Swart  |     |
| INFRARED AND ULTRAVIOLET ANALYSIS OF DUAL-ION<br>IMPLANTED GaAs .....  | 87  |
| Beatrys M. Lacquet, Gustavo E. Aizenberg, and Pieter L. Swart  |     |
| DETERMINATION OF BPSG THIN-FILM PROPERTIES USING<br>IR REFLECTION SPECTROSCOPY OF PRODUCT WAFERS .....                   | 93  |
| Thomas M. Niemczyk, James E. Franke, Lizhong Zhang,<br>David M. Haaland, and Kenneth J. Radigan                          |     |
| SPECTRAL REFLECTANCE AS AN IN SITU MONITOR FOR MOCVD .....   | 99  |
| W.G. Breiland and K.P. Killeen   |     |
| REAL TIME PROCESS MONITORING WITH MULTIWAVE-LENGTH<br>PYROMETRIC INTERFEROMETRY (PI) .....                               | 105 |
| F.G. Böbel, A. Wowchak, P.P. Chow, J. Van Hove, and L.A. Chow  |     |
| CHARACTERIZATION OF QUANTUM WELL STRUCTURES USING<br>MICROSCOPE-SPECTROPHOTOMETRY .....                                  | 111 |
| Rachel M. Geatches, Karen J. Reeson, Alan J. Criddle, and<br>Roger P. Webb   |     |
| LIGHT SCATTERING MEASUREMENTS OF SURFACE ROUGHNESS IN<br>MOLECULAR BEAM EPITAXY GROWTH OF GaAs .....                     | 119 |
| C. Lavoie, M.K. Nissen, S. Eisebitt, S.R. Johnson,<br>J.A. Mackenzie, and T. Tiedje                                      |     |
| REAL-TIME IN SITU MONITORING OF DEFECT EVOLUTION AT<br>WIDEGAP II-VI/GaAs HETEROINTERFACES DURING EPITAXIAL GROWTH ..... | 125 |
| C.M. Rouleau and R.M. Park   |     |
| THE UTILITY OF LASER LIGHT SCATTERING IN ASSESSING THE<br>MIXABILITY OF REAGENTS FOR CHEMICAL VAPOR DEPOSITION .....     | 133 |
| Bin Ni, Gene P. Reck, and James W. Proscia   |     |

## PART III: PHOTOREFLECTANCE AND PHOTOLUMINESCENCE SPECTROSCOPIES

|   |     |
|---|-----|
| *CONTACTLESS ELECTROMODULATION CHARACTERIZATION OF<br>COMPOUND SEMICONDUCTOR SURFACES AND DEVICE STRUCTURES ..... | 141 |
| J.M. Woodall  |     |
| PHOTOREFLECTANCE CHARACTERIZATION OF ETCH-INDUCED<br>DAMAGE IN DRY ETCHED GaAs .....                              | 153 |
| O.J. Glembocki, J.A. Tuchman, K.K. Ko, S.W. Pang,<br>A. Giordana, and C.E. Stutz                                  |     |
| IN-SITU DIAGNOSTICS OF PLASMA-INDUCED DAMAGE ON<br>GaAs BY PHOTOREFLECTANCE SPECTROSCOPY .....                    | 161 |
| Hideo Nakanishi and Kazumi Wada   |     |
| PHOTOREFLECTANCE CHARACTERISATION OF REACTIVE ION<br>ETCHED SILICON .....   | 167 |
| M. Murtagh, J.T. Beechinor, P.A.F. Herbert, P.V. Kelly,<br>G.M. Crean, and C. Jeynes                              |     |

\*Invited Paper

|  |     |
|--|-----|
| LAYERED SEMICONDUCTOR PHOTOREFLECTANCE DIAGNOSTICS .....   | 175 |
| Konstantin O. Boltar and Valery A. Fedirko   |     |
| OPTICAL CHARACTERIZATION OF InGaAs/InP QUANTUM WIRES AND DOTS .....  | 181 |
| S.Q. Gu, E. Reuter, Q. Xu, H. Chang, R. Panepucci, I. Adesida, S.G. Bishop, C. Caneau, and R. Bhat   |     |
| PHOTOREFLECTANCE STUDY OF MODULATION-DOPED GaAs/GaAlAs QUANTUM DOTS FABRICATED BY REACTIVE-ION ETCHING .....   | 187 |
| P.D. Wang, C.M. Sotomayor Torres, M.C. Holland, H. Qiang, F.H. Pollak, and G. Gumbs  |     |
| RAMAN AND PHOTOLUMINESCENCE CHARACTERIZATION OF FIB PATTERNED AlGaAs/GaAs MULTIPLE QUANTUM WELLS .....   | 193 |
| Ahn Goo Choo, Xuelong Cao, Spirit Tlali, Howard E. Jackson, Peter Chen, Andrew J. Steckl, and Joseph T. Boyd   |     |
| INFLUENCE OF GROWTH CONDITIONS ON THE MODULATION MECHANISM OF PHOTOREFLECTANCE SPECTRA OF SINGLE InGaAs/InAlAs QUANTUM WELLS .....   | 199 |
| Y. Baltagi, C. Bru, T. Benyattou, M.A. Garcia-Perez, G. Guillot, M. Gendry, J.L. Leclercq, V. Drouot, and G. Hollinger   |     |
| CHARACTERIZATION OF PSEUDOMORPHIC HEMT STRUCTURES BY MODULATION SPECTROSCOPY .....   | 205 |
| A. Dimoulas, K. Zekentes, and M. Androulidaki  |     |
| PHOTOLUMINESCENCE CHARACTERIZATION OF InP-BASED HEMT STRUCTURES .....  | 211 |
| Henry T. Hendriks, Steven K. Brierley, William E. Hoke, and Noren Pan  |     |
| PHOTOREFLECTANCE CHARACTERIZATION OF InGaAs/GaAs SUPERLATTICES GROWN ON [111]-ORIENTED SUBSTRATES .....  | 217 |
| R.G. Rodrigues, K. Yang, L.J. Schowalter, and J.M. Borrego   |     |
| PHOTOREFLECTANCE CHARACTERIZATION OF InGaAs LATTICE MATCHED TO InP .....   | 225 |
| V. Bellani, M. Amiotti, M. Geddo, G. Guizzetti, and G. Landgren  |     |
| <br><b>PART IV: INFRARED AND RAMAN SPECTROSCOPIES</b>  |     |
| ROOM TEMPERATURE MEASUREMENT OF PHOTOLUMINESCENCE SPECTRA OF SEMICONDUCTORS USING AN FT-RAMAN SPECTROPHOTOMETER .....  | 233 |
| J.D. Webb, D.J. Dunlavy, T. Ciszek, R.K. Ahrenkiel, M.W. Wanlass, R. Noufi, and S.M. Vernon  |     |
| FIBER OPTICS-BASED FOURIER TRANSFORM INFRARED SPECTROSCOPY FOR IN-SITU CONCENTRATION MONITORING IN OMCVD .....   | 241 |
| Sateria Salim, K.F. Jensen, and R.D. Driver  |     |
| APPLICATION OF FTIR SPECTROSCOPY TO THE CHARACTERIZATION OF AS-DEPOSITED AND CHEMICAL MECHANICAL POLISHED (CMP) ELECTRON CYCLOTRON RESONANCE (ECR) PLASMA BASED SiO <sub>2</sub> FILMS ..... | 249 |
| Mukesh Desai, Ron Carpio, Rahul Jairath, Matt Stell, and Robert Tolles   |     |

|  |     |
|--|-----|
| CHARACTERIZATION OF POLYSILICON FILMS BY RAMAN SPECTROSCOPY AND TRANSMISSION ELECTRON MICROSCOPY: A COMPARATIVE STUDY .....                        | 255 |
| David R. Tallant, Thomas J. Headley, John W. Medernach, and Franz Geyling  |     |
| PHOTOLUMINESCENCE STUDY OF HYDROGEN-RELATED DEFECTS IN SILICON .....   | 261 |
| A. Henry, B. Monemar, J.L. Lindström, Y. Zhang, and J.W. Corbett   |     |
| RAMAN SCATTERING CHARACTERIZATION OF ULTRATHIN FILMS OF $\beta$ -SiC .....   | 267 |
| Ahn Goo Choo, Spirit Tlali, Howard E. Jackson, J.P. Li, and Andrew J. Steckl   |     |
| CHARACTERIZATION OF Cd <sub>1-x</sub> Zn <sub>x</sub> Te ALLOYS USING INFRARED REFLECTIVITY AND RAMAN SCATTERING SPECTROSCOPY .....                | 273 |
| D.N. Talwar, Z.C. Feng, and P. Becla   |     |
| OPTICAL CHARACTERIZATION OF AlInP/GaAs HETEROSTRUCTURES .....  | 279 |
| F.G. Johnson, G.E. Kohnke, and G.W. Wicks  |     |
| CHARACTERIZATION OF INTERFACIAL STRUCTURE OF InGaAs/InP SHORT PERIOD SUPERLATTICES BY RAMAN SCATTERING AND HIGH RESOLUTION X-RAY DIFFRACTION ..... | 285 |
| Teruo Mozume   |     |
| <br><b>PART V: IN-SITU DIAGNOSTICS</b>   |     |
| IN-PROCESS DIAGNOSTIC SYSTEM FOR SEMICONDUCTOR MATERIALS USING UHV WAFER TRANSFER CHAMBER .....  | 293 |
| F. Uchida, M. Matsui, H. Kakibayashi, M. Kouguchi, A. Mutoh, and H. Nagano   |     |
| DEVELOPING A METHOD FOR WIDE-CONTROL OF THE SELF-BIAS AND ITS ADOPTION TO ION-DAMAGE CONTROL .....   | 299 |
| Takeo Ohte, Makoto Goto, and Minoru Sugawara   |     |
| RELATING PHOTORESIST ETCH CHARACTERISTICS TO LANGMUIR PROBE MEASUREMENTS IN AN ELECTRON CYCLOTRON RESONANCE SOURCE .....                           | 305 |
| K.T. Sung, W.H. Juan, S.W. Pang, and M. Dahimene   |     |
| SURFACE REACTIVITY OF SILICON AND GERMANIUM IN CF <sub>4</sub> -O <sub>2</sub> REACTIVE ION ETCHING .....  | 311 |
| Christophe Cardinaud, A. Campo, and G. Turban  |     |
| REAL-TIME THERMO-MECHANICAL PROPERTY EVALUATION OF THIN FILMS .....  | 317 |
| John A. Rogers and K.A. Nelson   |     |
| HYDROCARBON ECR REACTIVE ION ETCHING OF III-V SEMICONDUCTORS WITH SIMS PLASMA PROBE DIAGNOSTICS .....  | 323 |
| Douglas L. Melville, J.G. Simmons, and D.A. Thompson   |     |
| IN-SITU MONITORING BY MASS SPECTROMETRY FOR GaAs ETCHED WITH AN ELECTRON CYCLOTRON RESONANCE SOURCE .....  | 329 |
| D.J. Kahaian and S.W. Pang   |     |

|   |     |
|---|-----|
| AlGaAs MICROELECTRONIC DEVICE PROCESSING USING AN<br>As CAPPING LAYER .....   | 335 |
| J.K. Grepstad, H. Husby, R.W. Bernstein, and B.-O. Fimland  |     |
| OPTICAL EMISSION END-POINT DETECTION FOR VIA HOLE<br>ETCHING IN InP AND GaAs POWER DEVICE STRUCTURES .....          | 341 |
| S.J. Pearton, F. Ren, C.R. Abernathy, and C. Constantine  |     |
| REACTIVE SPUTTERING IN OXIDIZING/REDUCING ATMOSPHERES .....   | 347 |
| J.D. Klein, A. Yen, and S.L. Clauson  |     |
| IN SITU SUBSTRATE TEMPERATURE MEASUREMENT DURING MBE<br>BY BAND-EDGE REFLECTION SPECTROSCOPY .....                  | 353 |
| J.A. Roth, T.J. de Lyon, and M.E. Adel  |     |
| SINGLE PHOTON LASER IONIZATION AS AN IN-SITU<br>DIAGNOSTIC FOR MBE GROWTH .....                                     | 359 |
| April L. Alstrin, Adina K. Kunz, Paul G. Strupp, and<br>Stephen R. Leone  |     |
| REAL-TIME MONITORING AND CONTROL OF SILICON EPITAXY<br>USING EMISSION FOURIER TRANSFORM INFRARED SPECTROSCOPY ..... | 365 |
| Z.H. Zhou, H. Kim, and Rafael Reif  |     |

#### PART VI: EX-SITU PROCESS DIAGNOSTICS

|   |     |
|---|-----|
| DEEP-LEVEL TRANSIENT SPECTROSCOPY STUDIES OF<br>CZOCHELSKI-GROWN n-TYPE SILICON .....   | 373 |
| Yutaka Tokuda, Isao Katoh, Masayuki Katayama, and<br>Tadasi Hattori   |     |
| RELATIONSHIP BETWEEN MINORITY CARRIER PARAMETERS AND<br>SOLAR CELL CHARACTERISTICS OF ELECTROMAGNETIC CAST<br>POLYCRYSTALLINE SILICON .....                     | 379 |
| Eiichi Suzuki, Kyojiro Kaneko, and Toru Nunoi   |     |
| TRAPPING OF MOLECULAR HYDROGEN IN POROUS SILICON AND<br>AT Si/SiO <sub>2</sub> INTERFACES AND A POSSIBLE REINTERPRETATION<br>OF THE P <sub>b</sub> CENTER ..... | 385 |
| Peter Stallinga, T. Gregorkiewicz, and C.A.J. Ammerlaan   |     |
| STUDY OF SILICON SURFACE ROUGHNESS BY ATOMIC FORCE<br>MICROSCOPY .....  | 391 |
| Andrew G. Gilicinski, Rebecca M. Rynders, Scott E. Beck,<br>Yale E. Strausser, James R. Stets, Brian S. Felker, and<br>David A. Bohling                         |     |
| THE EFFECT OF POLYSILICON DEPOSITION AND DOPING<br>PROCESSES ON DOUBLE-POLY CAPACITORS—ELECTRICAL AND<br>AFM EVALUATION .....                                   | 397 |
| W.M. Paulson, L.H. Breaux, R.I. Hegde, and P.J. Tobin   |     |
| DETERMINATION OF HYDROGEN IN SEMICONDUCTORS AND<br>RELATED MATERIALS BY COLD NEUTRON CAPTURE PROMPT<br>GAMMA-RAY ACTIVATION ANALYSIS .....                      | 403 |
| Rick L. Paul and Richard M. Lindstrom   |     |
| THE PERFORMANCE STUDY OF ION IMPLANTER BASED MEDIUM<br>ENERGY ION SPECTROSCOPY WITH SOLID STATE DETECTOR .....  | 409 |
| Z.J. Radzinski, S. Yokoyama, I. Ishibashi, and M. Hirose  |     |

|  |     |
|--|-----|
| LOW COHERENCE INTERFEROMETRY FOR NON-INVASIVE<br>SEMICONDUCTOR MONITORING .....  | 415 |
| Chris M. Lawson and Robert R. Michael  |     |
| EVALUATION OF DRY ETCHING INDUCED DAMAGE OF GaInAs<br>USING TRANSMISSION LINES AND SCHOTTKY DIODES .....   | 421 |
| S. Thomas III and S.W. Pang  |     |
| STUDY OF ZENER DIODES BY SEM-DVC .....   | 427 |
| S. Mil'shtein, D. Kharas, and S. Iatrou  |     |
| CHARACTERIZATION OF CADMIUM ZINC TELLURIUM OBTAINED<br>BY MODIFIED-BRIDGMAN TECHNIQUE .....  | 433 |
| D.R. Acosta and F. Rabago  |     |
| SURFACE PHOTOVOLTAGE MEASUREMENT OF MINORITY CARRIER<br>DIFFUSION LENGTHS EXCEEDING WAFER THICKNESS: APPLICATION<br>TO IRON MONITORING WITH PART PER QUADRILLION SENSITIVITY ..... | 439 |
| A.M. Kontkiewicz, J. Lagowski, M. Dexter, and P. Edelman   |     |
| CHARACTERIZATION OF REACTIVE ION ETCH DAMAGE IN GaAs<br>BY TRIPLE CRYSTAL X-RAY DIFFRACTION .....  | 445 |
| Victor S. Wang, Richard J. Matyi, and Karen J. Nordheden   |     |
| NEW ALGORITHMS FOR RAPID FULL-WAFER MAPPING BY HIGH<br>RESOLUTION DOUBLE AXIS X-RAY DIFFRACTION .....  | 451 |
| N. Loxley, S. Cockerton, L.M. Cooke, T. Gray, B.K. Tanner,<br>and D.K. Bowen   |     |
| USE OF SYNCHROTRON WHITE BEAM X-RAY TOPOGRAPHY TO<br>CHARACTERIZE IR DETECTOR MANUFACTURING PROCESSES .....  | 457 |
| M. Dudley, Jun Wu, D.J. Larson, Jr., and D. DiMarzio   |     |

#### PART VII: DRY ETCHING AND PATTERNING

|   |     |
|---|-----|
| ULTRA-SMOOTH DRY ETCHING OF GaAs USING A HYDROGEN<br>PLASMA PRETREATMENT .....  | 465 |
| R.J. Shul, Kent D. Choquette, A.J. Howard, D.J. Rieger,<br>C.A. DiRubio, R.S. Freund, and R.C. Wetzel   |     |
| SIMULATION OF DRY ETCHING PROCESSES FOR III-V<br>COMPOUNDS TECHNOLOGY APPLICATIONS .....  | 471 |
| K. Ketata, S. Koumetz, M. Ketata, and R. Debrie   |     |
| REACTIVE ION ETCHING OF GaN THIN FILMS .....  | 477 |
| Michael Manfra, Stuart Berkowitz, Richard Molnar,<br>Anna Clark, T.D. Moustakas, and W.J. Skocpol   |     |
| EFFECTS OF HALOGEN-CONTAINING GAS PLASMA AND RAPID<br>THERMAL ANNEAL TREATMENT ON THE REACTIVE ION ETCHED<br>SILICON .....  | 481 |
| Kwang-Ho Kwon, Bo-Woo Kim, Hyung-Ho Park, Jin-Yeong Kang,<br>and Gun-Yung Yeom  |     |
| REACTIVE-ION-ETCHING OF 100nm LINEWIDTH TUNGSTEN<br>FEATURES USING SF <sub>6</sub> /H <sub>2</sub> AND A Cr-LIFTOFF MASK .....  | 487 |
| Loretta M. Shirey, Kelly W. Foster, William Chu, John Kosakowski,<br>Kee Woo Rhee, Charles Eddy, Jr., Doewon Park, I. Peter Isaacson,<br>Daniel McCarthy, Christie R.K. Marrian, Martin C. Peckerar,<br>and Elizabeth A. Dobisz |     |

|  |     |
|--|-----|
| A NEW ENVIRONMENTALLY STABLE POSITIVE TONE<br>CHEMICALLY AMPLIFIED RESIST SYSTEM — KRS ..... | 493 |
| Wu-Song Huang, Ramee Kwong, Ahmad Katmani, Mahoud Khojasteh,<br>and Kim Y. Lee               |     |
| AUTHOR INDEX .....   | 499 |
| SUBJECT INDEX .....  | 503 |

## Preface

These proceedings are the refereed papers presented at the symposium on "Diagnostic Techniques for Semiconductor Materials Processing" that was held as part of the 1993 Fall Meeting of the Materials Research Society in Boston, MA. The symposium focused on various aspects of process diagnostics and device processing. Diagnostic techniques which were considered fell into two classes: invasive and non invasive. Optical characterization techniques were the most widely applied characterization tools used in both materials and process monitoring. Techniques such as reflectance difference, ellipsometry, reflectance, absorption, light scattering, photoreflectance, Raman scattering and thermal wave modulated reflectance were shown to be powerful probes of various materials properties. The materials properties that were probed included surface stoichiometry and morphology, etch damage, Fermi level pinning position and thin film properties such as thickness, alloy content, and interfacial roughness. Real time diagnostics such as ellipsometry and reflectance difference were shown to be sensitive tools of materials properties during processing. These techniques show promise of sophisticated feedback control of materials growth. In the area of process diagnostics many techniques such as Langmuir probe, optical emission, mass spectrometry, IR reflection and absorption were shown to be powerful tools of various process parameters including reactive species concentrations, reaction products, and residual gases in chamber.

The symposium brought together participants from academic, industry, and government laboratories. There is great interest in the development of diagnostic techniques for device fabrication. The application of diagnostic tools utilized in research to manufacturing environments was an underlying theme in the papers presented. As the research interest in this area grows, further and more exciting developments are expected in integrating processing and process diagnostics. The quality of the papers presented and the interest and discussions that were simulated indicated that process diagnostics will continue to be an active research and development area for semiconductor processing.

O.J. Glembocki  
S.W. Pang  
F.H. Pollak  
G.M. Crean  
G. Larrabee

May 1994



## Acknowledgments

We would like to thank all the contributors and participants for a successful and stimulating symposium. We also like to acknowledge our session chairs who kept the discussions lively and the sessions on schedule. We especially like to thank the reviewers who provided careful reviews of the papers at the meeting to allow rapid publication of the proceedings. We also like to express our appreciation to our invited speakers who provided excellent reviews and set the tone for the various sessions. They are:

D.E. Aspnes  
J.E. Butler  
R.A. Gottscho  
E.A. Irene  
G.S. Oehrlein  
P.L. Swart  
J.M. Woodall  
J.A. Woollam

We are indebted to the following sponsors who provided generous financial support for this symposium:

ASTeX (Applied Science and Technology)  
Digital Instruments, Inc.  
MKS Instruments, Inc.  
Naval Research Laboratory  
The Office of Naval Research

---

MATERIALS RESEARCH SOCIETY SYMPOSIUM PROCEEDINGS

---

- Volume 297—Amorphous Silicon Technology—1993, E.A. Schiff, M.J. Thompson, P.G. LeComber, A. Madan, K. Tanaka, 1993, ISBN: 1-55899-193-X
- Volume 298—Silicon-Based Optoelectronic Materials, R.T. Collins, M.A. Tischler, G. Abstreiter, M.L. Thewalt, 1993, ISBN: 1-55899-194-8
- Volume 299—Infrared Detectors—Materials, Processing, and Devices, A. Appelbaum, L.R. Dawson, 1993, ISBN: 1-55899-195-6
- Volume 300—III-V Electronic and Photonic Device Fabrication and Performance, K.S. Jones, S.J. Pearton, H. Kanber, 1993, ISBN: 1-55899-196-4
- Volume 301—Rare-Earth Doped Semiconductors, G.S. Pomrenke, P.B. Klein, D.W. Langer, 1993, ISBN: 1-55899-197-2
- Volume 302—Semiconductors for Room-Temperature Radiation Detector Applications, R.B. James, P. Siffert, T.E. Schlesinger, L. Franks, 1993, ISBN: 1-55899-198-0
- Volume 303—Rapid Thermal and Integrated Processing II, J.C. Gelpey, J.K. Elliott, J.J. Wortman, A. Ajmera, 1993, ISBN: 1-55899-199-9
- Volume 304—Polymer/Inorganic Interfaces, R.L. Opila, A.W. Czanderna, F.J. Boerio, 1993, ISBN: 1-55899-200-6
- Volume 305—High-Performance Polymers and Polymer Matrix Composites, R.K. Eby, R.C. Evers, D. Wilson, M.A. Meador, 1993, ISBN: 1-55899-201-4
- Volume 306—Materials Aspects of X-Ray Lithography, G.K. Celler, J.R. Maldonado, 1993, ISBN: 1-55899-202-2
- Volume 307—Applications of Synchrotron Radiation Techniques to Materials Science, D.L. Perry, R. Stockbauer, N. Shinn, K. D'Amico, L. Terminello, 1993, ISBN: 1-55899-203-0
- Volume 308—Thin Films—Stresses and Mechanical Properties IV, P.H. Townsend, J. Sanchez, C-Y. Li, T.P. Weihs, 1993, ISBN: 1-55899-204-9
- Volume 309—Materials Reliability in Microelectronics III, K. Rodbell, B. Filter, P. Ho, H. Frost, 1993, ISBN: 1-55899-205-7
- Volume 310—Ferroelectric Thin Films III, E.R. Myers, B.A. Tuttle, S.B. Desu, P.K. Larsen, 1993, ISBN: 1-55899-206-5
- Volume 311—Phase Transformations in Thin Films—Thermodynamics and Kinetics, M. Atzmon, J.M.E. Harper, A.L. Greer, M.R. Libera, 1993, ISBN: 1-55899-207-3
- Volume 312—Common Themes and Mechanisms of Epitaxial Growth, P. Fuoss, J. Tsao, D.W. Kisker, A. Zangwill, T.F. Kuech, 1993, ISBN: 1-55899-208-1
- Volume 313—Magnetic Ultrathin Films, Multilayers and Surfaces/Magnetic Interfaces—Physics and Characterization (2 Volume Set), C. Chappert, R.F.C. Farrow, B.T. Jonker, R. Clarke, P. Grünberg, K.M. Krishnan, S. Tsunashima/E.E. Marinero, T. Egami, C. Rau, S.A. Chambers, 1993, ISBN: 1-55899-211-1
- Volume 314—Joining and Adhesion of Advanced Inorganic Materials, A.H. Carim, D.S. Schwartz, R.S. Silberglitt, R.E. Loehman, 1993, ISBN: 1-55899-212-X
- Volume 315—Surface Chemical Cleaning and Passivation for Semiconductor Processing, G.S. Higashi, E.A. Irene, T. Ohmi, 1993, ISBN: 1-55899-213-8

---

## MATERIALS RESEARCH SOCIETY SYMPOSIUM PROCEEDINGS

---

- Volume 316—Materials Synthesis and Processing Using Ion Beams, R.J. Culbertson, K.S. Jones, O.W. Holland, K. Maex, 1994, ISBN: 1-55899-215-4
- Volume 317—Mechanisms of Thin Film Evolution, S.M. Yalisove, C.V. Thompson, D.J. Eaglesham, 1994, ISBN: 1-55899-216-2
- Volume 318—Interface Control of Electrical, Chemical, and Mechanical Properties, S.P. Murarka, T. Ohmi, K. Rose, T. Seidel, 1994, ISBN: 1-55899-217-0
- Volume 319—Defect-Interface Interactions, E.P. Kvam, A.H. King, M.J. Mills, T.D. Sands, V. Vitek, 1994, ISBN: 1-55899-218-9
- Volume 320—Silicides, Germanides, and Their Interfaces, R.W. Fathauer, L. Schowalter, S. Mantl, K.N. Tu, 1994, ISBN: 1-55899-219-7
- Volume 321—Crystallization and Related Phenomena in Amorphous Materials, M. Libera, T.E. Haynes, P. Cebe, J. Dickinson, 1994, ISBN: 1-55899-220-0
- Volume 322—High-Temperature Silicides and Refractory Alloys, B.P. Bewlay, J.J. Petrovic, C.L. Briant, A.K. Vasudevan, H.A. Lipsitt, 1994, ISBN: 1-55899-221-9
- Volume 323—Electronic Packaging Materials Science VII, R. Pollak, P. Børgesen, H. Yamada, K.F. Jensen, 1994, ISBN: 1-55899-222-7
- Volume 324—Diagnostic Techniques for Semiconductor Materials Processing, O.J. Glembocki, F.H. Pollak, S.W. Pang, G. Larrabee, G.M. Crean, 1994, ISBN: 1-55899-223-5
- Volume 325—Physics and Applications of Defects in Advanced Semiconductors, M.O. Manasreh, M. Lannoo, H.J. von Bardeleben, E.L. Hu, G.S. Pomrenke, D.N. Talwar, 1994, ISBN: 1-55899-224-3
- Volume 326—Growth, Processing, and Characterization of Semiconductor Heterostructures, G. Gumbs, S. Luryi, B. Weiss, G.W. Wicks, 1994, ISBN: 1-55899-225-1
- Volume 327—Covalent Ceramics II: Non-Oxides, A.R. Barron, G.S. Fischman, M.A. Fury, A.F. Hepp, 1994, ISBN: 1-55899-226-X
- Volume 328—Electrical, Optical, and Magnetic Properties of Organic Solid State Materials, A.F. Garito, A. K-Y. Jen, C. Y-C. Lee, L.R. Dalton, 1994, ISBN: 1-55899-227-8
- Volume 329—New Materials for Advanced Solid State Lasers, B.H.T. Chai, T.Y. Fan, S.A. Payne, A. Cassanho, T.H. Allik, 1994, ISBN: 1-55899-228-6
- Volume 330—Biomolecular Materials By Design, H. Bayley, D. Kaplan, M. Navia, 1994, ISBN: 1-55899-229-4
- Volume 331—Biomaterials for Drug and Cell Delivery, A.G. Mikos, R. Murphy, H. Bernstein, N.A. Peppas, 1994, ISBN: 1-55899-230-8
- Volume 332—Determining Nanoscale Physical Properties of Materials by Microscopy and Spectroscopy, M. Sarikaya, M. Isaacson, H.K. Wickramasighe, 1994, ISBN: 1-55899-231-6
- Volume 333—Scientific Basis for Nuclear Waste Management XVII, A. Barkatt, R. Van Konynenburg, 1994, ISBN: 1-55899-232-4
- Volume 334—Gas-Phase and Surface Chemistry in Electronic Materials Processing, T.J. Mountziaris, P.R. Westmoreland, F.T.J. Smith, G.R. Paz-Pujalt, 1994, ISBN: 1-55899-233-2
- Volume 335—Metal-Organic Chemical Vapor Deposition of Electronic Ceramics, S.B. Desu, D.B. Beach, B.W. Wessels, S. Gokoglu, 1994, ISBN: 1-55899-234-0

*Prior Materials Research Society Symposium Proceedings  
available by contacting Materials Research Society*

---

PART I

---

**Reflectance Difference  
Spectroscopy and Ellipsometry**

## REAL-TIME SURFACE AND NEAR-SURFACE OPTICAL DIAGNOSTICS FOR EPITAXIAL GROWTH

D. E. ASPNES

Department of Physics, NCSU, Raleigh, NC 27695-8202 USA

### ABSTRACT

Various optical diagnostics are being developed to meet new challenges in semiconductor epitaxy. New data-analysis algorithms allow near-surface alloy compositions and interface properties to be obtained by kinetic ellipsometry (KE) without any knowledge of the underlying sample structure. New information about growth is being obtained by surface-oriented probes such as laser light scattering (LLS), surface photoabsorption (SPA), and reflectance-difference (-anisotropy) spectroscopy (RDS/RAS). Examples are provided and likely directions of further progress discussed.

### OVERVIEW

The technology of epitaxial growth is facing increasingly difficult challenges. New materials such as wide bandgap semiconductors and epitaxial metals, more complex device structures such as vertical cavity surface-emitting lasers, increasingly stringent tolerances on layer compositions and thicknesses, emphasis on selective-area epitaxies for growing quantum structures, the general trend away from simple physical to complex chemical deposition methods, and the need to maintain satisfactory yields despite increasing economic pressures are relentlessly moving the field toward obtaining accurate information about the sample during growth. While the ultimate goal is closed-loop feedback control, the more modest and currently achievable target of real-time monitoring will already allow conditions to be modified on-line to meet composition and thickness specifications, and will provide records by which causes of downstream failures of complex devices can be identified and eliminated.

To meet these challenges attention is being directed toward epioptics, the optical study of surfaces and near-surface regions, to use a term recently proposed by McGilp.<sup>1</sup> Near IR—visible—near UV surface-diagnostic techniques now in relatively common use include laser light scattering (LLS),<sup>2-4</sup> second-harmonic generation (SHG)<sup>5</sup> and its generalization, sum-frequency generation,<sup>6</sup> IR absorption spectroscopy (IRAS),<sup>7</sup> surface differential reflectance (SDR) in its normal incidence<sup>8</sup> and p-polarized Brewster-angle (surface photoabsorption (SPA))<sup>3,9-12</sup> forms, the ellipsometric equivalent of SDR,<sup>13</sup> and reflectance-difference (reflectance-anisotropy) spectroscopy (RDS/RAS).<sup>14-24</sup>

These approaches achieve surface sensitivity, and in some cases specificity, by using spectral dependence to identify or symmetry to enhance the surface contributions to the overall optical signal. In LLS the measured property is the diffusive scattering that occurs if the surface becomes rough. SHG deals with second-harmonic light that is generated when an intense photon beam interacts with the sample. In RDS the measured property is the sample anisotropy. SHG and RDS are surface specific because the surface has a different symmetry from that of the bulk. IRAS achieves surface specificity because IRAS data are obtained in spectral regions

where the substrate is transparent. Both SDR and SPA deal quantitatively with the changes that occur in reflectance when surface conditions are changed, although SPA achieves higher sensitivity through the use of p-polarized light at pseudo-Brewster incidence. SHG, RDS, and IRAS are true surface spectroscopies because they can obtain information about surfaces under steady-state conditions, although most early and much recent RDS data were obtained in the SDR mode. The current sensitivities of SDR, SPA, and RDS are now significantly better than 0.01 monolayer (ML). Although not an optical probe in the usual sense, X-ray diffraction is now providing real-time information from another perspective.<sup>25</sup>

While surface information is necessary for understanding basic mechanisms, the important parameters for control purposes are actually bulk properties, specifically layer thickness and composition. Because neither is directly related to surface conditions, these quantities must be determined by bulk-oriented probes such as spectroreflectometry (SR)<sup>26</sup> and spectroellipsometry (SE),<sup>27-35</sup> which return information integrated over the penetration depth of light. SR determines the scalar reflectances  $R_s = |r_s|^2$ ,  $R_p = |r_p|^2$ , or  $R = |r_n|^2$ , where  $r_s$ ,  $r_p$ , and  $r_n$  are the complex reflectances for s-polarized, p-polarized, and normally incident light, respectively. SE determines the complex reflectance ratio  $\rho = r_p/r_s$ . This is often expressed as a pseudo-dielectric function  $\langle \epsilon \rangle = \langle \epsilon_1 \rangle + i\langle \epsilon_2 \rangle$ , which is defined as the dielectric function of the hypothetical uniform substrate that would give the observed value of  $\rho$ . Although both reflectometry and ellipsometry require optical access to the sample, problems concerning window deposits and strain can be eliminated with proper design.<sup>36</sup>

Reflectometry has long been used by the optical-coatings industry for real-time characterization of thicknesses and average compositions of depositing films.<sup>37</sup> However, much of semiconductor technology is based on samples consisting of many layers some of which may be only a few Å thick and some of which may have graded compositions. For these systems neither reflectometry nor Fresnel analysis is adequate. Ellipsometry and minimal-data analysis approaches must be used.

Minimal-data or virtual-interface (VI) algorithms are a new development that has significantly advanced analytic capabilities by providing a means of determining *near-surface* properties of depositing materials from optical data without any knowledge whatever of the underlying sample structure.<sup>28,38</sup> This eliminates the two major weaknesses of Fresnel analysis, error propagation and instability. The implications are substantial, because it is now possible to analyze arbitrarily thin layers, which is precisely what is needed for closed-loop feedback control. As an example of the power of this approach, the Bellcore group used VI analysis of KE data to grow  $\text{Al}_x\text{Ga}_{1-x}\text{As}$  quantum structures with continuously graded compositions where the composition  $x$  was regulated to within several percent by analysis of the running outermost 3 Å of depositing material.<sup>30</sup>

The epioptics field is expanding so rapidly that a complete summary is not available, although more comprehensive reviews have been written.<sup>39</sup> To provide a perspective for further discussion I divide the parameters associated with epitaxy into three categories: primary, secondary, and tertiary. The primary properties are layer thickness and composition, especially near-surface composition, because if these cannot be grown to specification there is no point in continuing. Secondary properties are sample characteristics that are determined by surface conditions, such as doping levels, interface widths, and spontaneous bulk ordering of

alloys. Tertiary properties are those associated with the growth environment itself, such as sample temperature, chamber pressure, types and fluences of reactants, etc. Although tertiary parameters have received the most attention, the nonlinearity of chemical processes, the extreme example of which is atomic layer epitaxy (ALE),<sup>40</sup> ensures that growth control would not be a solved problem even if all tertiary parameters were known exactly. This will become even more relevant when nonlinearities are exploited specifically, for example using ALE to achieve uniformity over multiple wafers in a production reactor. Also, when thickness and composition are controlled directly small drifts in growth conditions can be compensated as they occur. Accordingly, primary and secondary properties are the appropriate focus here.

## INTERFACES; NEAR-SURFACE COMPOSITION

Because the determining the thickness and composition of evolving layers from kinetic data is a different problem from that of determining layer thicknesses and compositions of fabricated samples, it is not surprising that alternative analytic approaches exist. VI analysis represents an interesting case, because the determination of the properties of an outer layer independent of any knowledge of underlying structure seems to defy conventional wisdom.

The essentials of VI analysis can be understood with the help of Fig. 1, which shows a theoretical  $\langle \epsilon \rangle$  trajectory for the sequential deposition of InAs and InP on an InP substrate that already contains a buried dielectric discontinuity from a previously deposited InAs layer. The trajectory consists of a piecewise combination of approximately exponential spirals each of which would converge on the dielectric function  $\epsilon_0$  of the overlayer if deposition were to continue until the film was optically thick. If the dielectric responses of the materials involved are not too different, any given  $\langle \epsilon \rangle$  spiral can be defined to good accuracy by any point on it and its focus. (For  $r_s$  and  $r_p$ , spirals are exactly definable in this way with no restrictions on the dielectric responses.) Consequently, if the identity of the depositing material is known information about deeper layers is not needed. In the application indicated in Fig. 1, the thickness of the buried InAs layer can be determined by the offset between the two spirals formed by deposition of InP. This approach has been used recently to quantitatively analyze the amount of As exchanged with P on (001) InP upon exposure to As.<sup>32</sup>

The method by which  $\epsilon_0$  (and therefore composition) of the outermost layer can be determined by VI analysis is more subtle, but can be understood by recognizing that at any given wavelength the substrate can communicate with the surface through only the transmitted and back-reflected modes. In a reflectance or ellipsometric measurement where only ratios are important, this means that for any wavelength the entire history of the sample is summarized in a single complex parameter, which can be viewed as the reflectance  $r_v$  of a virtual interface  $v$  within the material. If the deposition rate is known,  $\epsilon_0$  and  $r_v$  can both be determined exactly from  $r_s$  or  $r_p$  if either are known at the start and finish of layer deposition.<sup>38</sup> In the limit of zero thickness, or more generally for data acquired continuously during deposition, this condition reduces to a knowledge of the value and thickness derivative of  $r_s$  or  $r_p$ . For  $p$  or  $\langle \epsilon \rangle$  the analysis is not exact, since  $r_s$  and  $r_p$  generally involve different values of  $r_v$ . However, if one assumes that the values of  $r_v$  for both  $r_s$  and  $r_p$  arise from the same virtual substrate, an approximate analytic solution can be obtained.<sup>38</sup> For epitaxy the virtual substrate approximation (VSA) is accurate to better than 0.1%.

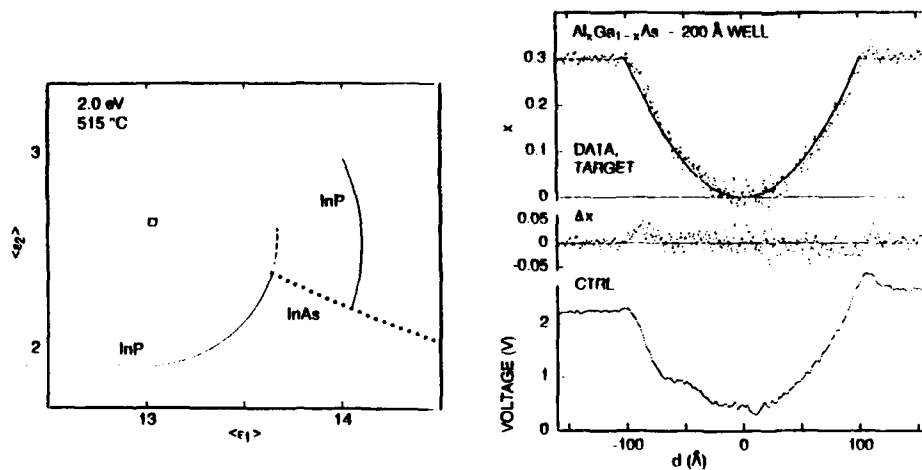


Fig. 1. Calculated  $\langle \epsilon \rangle$  trajectory for sequential deposition of InAs and InP on an InP substrate containing a buried dielectric discontinuity.

Fig. 2. Compositional data for a 200-Å-wide parabolic quantum well grown by closed-loop feedback control. Top: data and target values; middle: difference; bottom: control voltage (after ref. 30).

The VI method is structurally quite different from the Fresnel approach, which makes use of only the most recent values of  $r_s$ ,  $r_p$ , or  $\rho$  together with sample properties determined from previous iterations. The weakness of Fresnel analysis is its feed-forward character, or use of previously established sample parameters, which makes it extremely sensitive to cumulative error.

An example of an application of VI analysis is given in Fig. 2, which shows real-time data pertaining to the growth of a 200-Å-wide  $\text{Al}_x\text{Ga}_{1-x}\text{As}$  parabolic quantum well where the compositions shown at the top were determined from a VSA analysis of  $\langle \epsilon \rangle$  data acquired at 0.65 s intervals.<sup>30</sup> The target composition is the solid curve. Discrepancies relative to target values, shown in the middle, were corrected automatically by having the computer adjust the flow of the Al-containing species, triisobutyl aluminum (TIBAl), to the growth surface. The control voltage is shown at the bottom. The results are noteworthy not only because they are the first (and so far only) example of closed-loop feedback control of epitaxy, but also because  $x$  was determined by analysis of the running outermost 3 Å of depositing material.<sup>30</sup>

More generally, if the VSA is valid but neither composition nor deposition rate are known, five parameters must be determined. This requires the second derivative (curvature) to be established as well, which usually requires measurements over some 10s of Å. In fact, without knowing the convergence point of a spiral it is not possible to determine its scale and therefore  $\epsilon_0$ , because the magnitude of the first derivative is needed in the VI calculation. If the VSA is not valid then all 7 parameters must be determined by curve fitting, as has also recently



been noted by Urban and Tabet.<sup>41</sup>

### III. SURFACE ANALYSIS

The development of all optical surface-analysis probes has taken a common path, which begins with kinetic studies at a single wavelength, progresses to spectral kinetic measurements, then (if the technique permits) advances to detailed spectral analyses of surfaces under steady-state conditions. LLS is in stage 1, SPA is now moving into stage 2, and RDS/RAS is in stage 3. As the sensitivity of SHG and Raman scattering is still improving and samples at growth temperature are not sufficiently transparent to allow conventional multiple-internal-reflection IRAS, I discuss only the first three.

#### A. LLS

While LLS has long been used as a means of visually assessing surface morphology during molecular beam epitaxy (MBE) growth, recent applications are more quantitative. Pidduck et al. used LLS to investigate step flow in Si CVD.<sup>2</sup> Horikoshi et al. used LLS to detect the onset of Ga droplet formation in GaAs homoepitaxy, thereby identifying when saturation coverage had been achieved.<sup>3</sup>

Celii et al. recently used LLS to determine the critical thickness of  $\text{In}_x\text{Ga}_{1-x}\text{As}$  layers grown on GaAs, taking advantage of the connection between surface roughness and misfit dislocations.<sup>4</sup> The Celii et al. data are shown in Fig. 3. The sample consisted of a superlattice of 46 Å layers of  $\text{In}_{0.16}\text{Ga}_{0.84}$  interleaved with 170 Å thick layers of GaAs on a GaAs substrate. Growth proceeded pseudomorphically up to the sixth layer, when the surface began to roughen as shown by the increase of scattered light. Roughness continued to increase during subsequent growth. TEM micrographs showed that the associated dislocations were forming ridges 8-10 Å high in the (110) direction. A similar anisotropy in the relaxation of InP films deposited on GaAs on Si was studied by Acher et al. using RDS.<sup>15</sup>

#### B. SPA

Another experimentally simple approach that has seen widespread application is SPA. Most work has involved single-wavelength kinetic studies, but spectral data has recently been reported.<sup>11-12</sup> Not surprisingly, spectral information increases diagnostic power substantially.

A kinetics application illustrating control possibilities for ALE is shown in Fig. 4.<sup>10</sup> This figure shows the SPA response of an  $\text{AsH}_3$ -saturated (001) GaAs surface that is exposed to trimethylgallium (TMG) at different temperatures during OMCVD at approximately 4-6 kPa pressure. The 470 °C data exhibit a well-defined plateau, indicating self-limiting growth. Differences of substrate temperatures of only 20 °C are difficult to measure on an absolute scale but are clearly seen here. This allows ALE conditions to be established precisely. Kobayashi et al. also demonstrated a correlation between the change in SPA signal during  $\text{H}_2$  purging and the sheet hole density, showing a connection between surface conditions and dopant incorporation. This was interpreted as being due to attached methyl groups.<sup>10</sup>

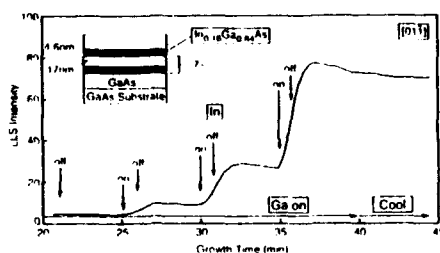


Fig. 3. LSS data for the  $\text{In}_{0.16}\text{Ga}_{0.84}\text{As}$  superlattice shown in the inset. Misfit dislocations generated when the critical thickness is reached at the onset of the sixth InGaAs layer cause increased scattering (after ref. 4).

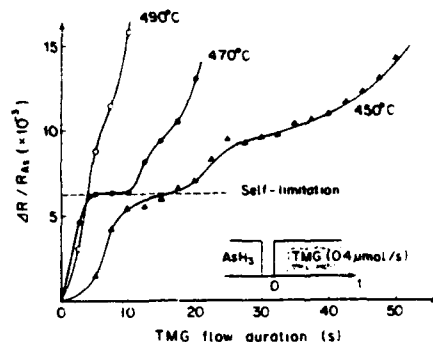


Fig. 4. SPA data obtained by exposing an  $\text{AsH}_3$ -stabilized (001) GaAs surface to TMG during OMCVD at several substrate temperatures as indicated (after ref. 10).

An example of an SPA application involving spectral measurements is given in Fig. 5.<sup>12</sup> These data were obtained by exposing a  $\text{AsH}_3$ -stabilized (100) GaAs substrate in an OMCVD growth environment to GaCl and triethylgallium (TEG). The TEG was used to generate a reference spectrum for a Ga-terminated surface. Because the GaCl-exposed surface exhibits essentially the same spectral response for both (011) (shown) and (011) orientations of the plane of incidence, the data indicate that the GaCl- and TEG-exposed surfaces are equivalent, possibly even identical, and that the GaCl-exposed surface is also terminated with Ga.

### C. RDS/RAS

RDS/RAS is now an established technique for obtaining information about the electronic structure of growth surfaces and kinetic information concerning surface-reactant interactions. Because RDS can analyze surfaces under steady-state conditions it avoids the "which-surface" ambiguity inherent in methods such as SPA that can pm;u acquire data by modifying the surface. Recent attention has focused on the optical equivalent of RHEED oscillations,<sup>19,21</sup> extension to phosphide-containing species,<sup>22</sup> application to interfaces such as Si-SiO<sub>2</sub>,<sup>24</sup> improvement of theoretical treatments,<sup>42,43</sup> and the determination of mechanisms of ALE growth.<sup>18</sup>

The most thoroughly investigated surface to date is (001) GaAs, which was studied under a wide range of conditions by Kamiya et al.<sup>16,17</sup> Using RD data taken on surfaces prepared by MBE and independently characterized by RHEED, Kamiya et al. demonstrated that (001) GaAs surfaces in UHV and in atmospheric pressure (AP)  $\text{H}_2$  were virtually identical, and identified reconstructions that occur on (001) GaAs surfaces under OMCVD growth conditions. The UHV — AP  $\text{H}_2$  comparison data are shown in Fig. 6.<sup>16</sup> The striking similarity shows that the surfaces are very similar, possibly identical, in the two environments. Theoretical calculations

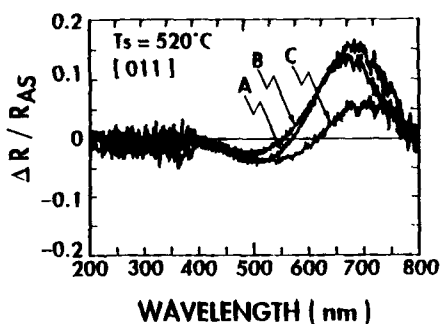


Fig. 5. SPA spectra obtained by exposing an  $\text{AsH}_3$ -stabilized (100) GaAs surface to GaCl and TEG during OMCVD (after ref. 12).

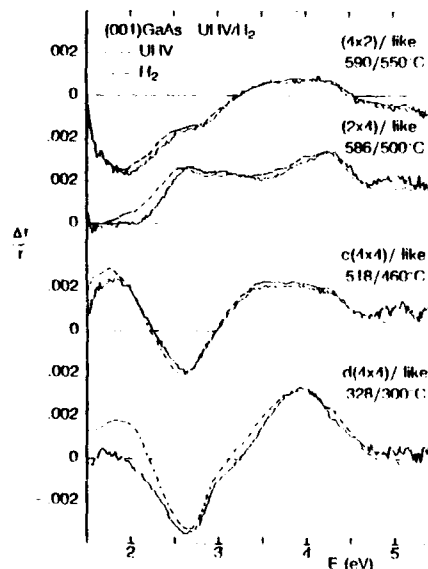


Fig. 6. RD spectra for (001) GaAs surfaces prepared in UHV by MBE (dashed curves) and in  $\text{AP H}_2$  by OMCVD (solid lines) (after ref. 16).

identified the structures near 1.9 and 2.6 eV with transitions involving Ga-Ga and As-As surface dimers, respectively, so these features can be used to track the relative surface concentrations of these surface species.<sup>44</sup> The OMCVD region of the As-pressure/sample temperature phase diagram was found to be an extension of the MBE region, providing further evidence of the essential similarity of (001) GaAs in the two environments and also showing that under typical OMCVD growth conditions the (001) GaAs surface is  $c(4 \times 4)$ -like, that is, terminated by 2 outer layers of As instead 1 as in MBE. The work also showed that these higher As coverages were a consequence of the vastly higher As partial pressures encountered in OMCVD, which at any given temperature push the equilibrium point to higher As coverages. Recent data obtained during growth have confirmed these conclusions.<sup>22,23</sup>

Another process of considerable current interest is ALE. The absence of real-time data has produced many models but no clear consensus concerning basic mechanisms. To investigate this process, the Belcore group took advantage of the cyclic nature of the process to synthesize RD spectra at 150 ms intervals over a 40 s cycle consisting of a 10 s exposure to  $\text{AsH}_3$  in  $\text{H}_2$ , a 4 s exposure to  $\text{H}_2$ , a 7 s exposure to TMG in  $\text{H}_2$ , and a 19 s exposure to  $\text{H}_2$ .<sup>18</sup> The data, shown in Fig. 7, reveal that  $\text{AsH}_3$  exposure produces as expected a  $c(4 \times 4)$  reconstruction (spectra 3 and 36), and that this termination is hardly perturbed by initial exposure to TMG (spectrum 39). This observation alone eliminates essentially all previous models of ALE, which

view the process as one where the (001) GaAs surface switches between single-layer coverages of As and Ga with the latter possibly terminated by methyl radicals. Continuing TMG exposure produces a change that is nearly linear in time, consistent with an excluded-volume mechanism. However, although spectrum 81 at the end of the TMG phase is similar that of the (2×4) reconstruction of Fig. 6, its details do not correspond to any reconstruction previously observed. One possibility is that the surface is terminated by methyl radical. Another is that TMG forces a reconstruction that is metastable and cannot be reached without the presence of TMG. Further work is needed to resolve the issue.

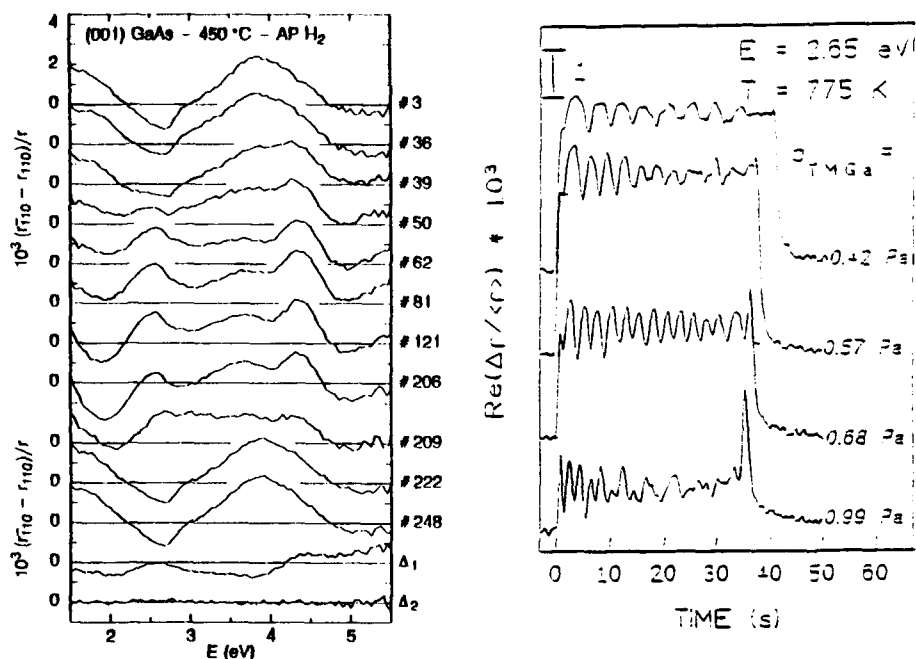


Fig. 7. RD spectra of (001) GaAs at different times during an ALE cycle. AsH<sub>3</sub> flow was terminated at spectrum 36. TMG was initiated at spectrum 39 and terminated at spectrum 81. AsH<sub>3</sub> flow was resumed at spectrum 206 (after ref. 18).

Fig. 8. RD oscillations observed during OMCVD growth on (001) GaAs at H<sub>2</sub> and AsH<sub>3</sub> pressures of 100 mbar and 70 Pa, respectively, and a sample temperature of 502 °C. TMG pressures are as indicated (after ref. 21).

Probably the most interesting recent development is the systematic observation of relatively large oscillations during OMCVD that correspond to oscillations seen with RHEED in MBE.<sup>45</sup> An example is given in Fig. 8.<sup>21</sup> Conditions that maximize this effect have now been established for both low<sup>19</sup> and high<sup>21</sup> reactor pressures. The oscillations shown in Fig. 8 were obtained at the photon energy of 2.65 eV, at which the contribution of surface As dimers is a

maximum. As in RHEED, each oscillation accurately represents growth of 1 ML of material. The mechanism giving rise to these oscillations is not understood, although it is clearly a cooperative phenomenon involving oscillating As-As surface coverage probably between partial single and double layers. Similar oscillations have been observed with tertiarybutylarsine (TBAs).<sup>21</sup> Deppert et al. have used these oscillations to measure growth-rate nonlinearities at the onset of growth by low pressure OMCVD.<sup>19</sup>

In recent analytic work, Hingerl et al. derived relations for connecting measured SPA anisotropies to RD spectra, allowing RD databases to be used in the interpretation of SPA results.<sup>46</sup> These results open the possibility of more detailed analyses through a combination of SPA and RDS.

Although not pertaining directly to epitaxial growth, Wormeester et al. recently used ellipsometry to determine the RD response of surface states on the  $(2 \times 1)$  reconstruction of (001) Ge.<sup>20</sup> Work on (001) surfaces of Si and Ge is important because results involving simpler materials may stimulate further theoretical analysis of surface induced optical anisotropy effects. Because optical anisotropies are so small, their accurate calculation represents a formidable theoretical challenge.<sup>42-44</sup> However, Morris and Matthai have recently used an *ab initio* pseudopotential approach to obtain the first accurate calculation of an RD spectrum of a reconstruction on (001) GaAs, specifically the  $(2 \times 4)$ .<sup>43</sup>

#### IV. FUTURE DIRECTIONS

Real-time optical characterization will clearly become increasingly important not only as a result of further refinements but also with respect to applications to new materials systems. Rapid data acquisition will be required for controlling growth of multinary systems. Parallel and serial versions of rapid-scan ellipsometers have been developed and their capabilities explored by Collins et al.<sup>29,35</sup> and Duncan et al.<sup>33</sup> The use of optical multichannel detection with SPA and RDS will allow surface reconstructions in OMCVD to be assessed at a glance, as is now done with RHEED in MBE. Since VI analysis is exact, it has made the development of normal-incidence complex reflectometry as an alternative to SE for the real-time analysis of very thin films much more attractive. Although the technological obstacles are formidable, an added advantage is that most deposition stations already provide normal-incidence optical access to the sample.

Growth chambers must also evolve to meet the specific needs of optical measurements. Requirements not only include optical access to the sample through transparent, strain-free, and deposition-free windows, but also the development of runout-corrected and vibration-free sample mounts and manipulators as recently discussed by Maracas et al.<sup>34</sup> Although samples are often rotated for uniformity during growth, this may prove to be an advantage because ellipsometric data obtained with rotating samples will contain an RD-like component that can be analyzed for surface coverages using standard RD databases.<sup>46</sup>

The near-term future should also see substantial advances in capabilities and applications of SHG, SFG, IRAS, and Raman scattering. To achieve a detailed understanding of growth mechanisms these approaches must be developed, because the analytic capability of visible-near UV linear optical techniques to determine surface chemistry is limited. However,

nonlinear and IR interactions with surface species are weak, making this a genuine challenge, but new high intensity sources such as free-electron lasers may make such measurements feasible. Approaches dealing with lateral inhomogeneity by the use of small spot sizes,<sup>27</sup> imaging,<sup>47</sup> or direct analysis<sup>48</sup> also need to be developed to deal with the increasingly important phenomenon of selective-area epitaxy.

## V. ACKNOWLEDGMENT

It is a pleasure to acknowledge the contributions of my collaborators in the growth-control and RDS work discussed in Secs. II and III: I. Kamiya, H. Tanaka, R. Bhat, M. J. S. P. Brasil, L. T. Florez, S. Gregory, J. P. Harbison, R. E. Nahory, M. A. A. Pudensi, W. E. Quinn, S. A. Schwarz, and M. C. Tamargo. The experimental work described in Secs. II and III was done when all authors were at Bellcore, where I. Kamiya and K. Hingerl were supported by ONR Contract N-00014-90-J-1267.

## REFERENCES

1. J. F. McGilp, *J. Phys.: Condens. Matter* **2**, 7985 (1990).
2. A. J. Pidduck, D. J. Robbins, A. G. Cullis, D. B. Gasson, and J. L. Glasper, *J. Electrochem. Soc.* **136**, 3083 (1989); A. J. Pidduck, D. J. Robbins, D. B. Gasson, C. Pickering, and J. L. Glasper, *J. Electrochem. Soc.* **136**, 3088 (1989); C. Pickering, *Thin Solid Films* **206**, 275 (1991); C. M. Rouleau and R. M. Park, *J. Vac. Sci. Technol.* **A11**, 1792 (1993).
3. Y. Horikoshi, H. Yamaguchi, F. Briones, and M. Kawashima, *J. Crystal Growth* **105**, 326 (1990).
4. F. G. Celii, E. A. Beam III, L. A. Files-Sesler, H.-Y. Liu, and Y. C. Kao, *Appl. Phys. Lett.* **62**, 2705 (1993).
5. T. Stehlin, M. Feller, P. Guyot-Sionnest, and Y. R. Shen, *Optics Lett.* **13**, 389 (1988); M. E. Pemble, D. S. Buhaenko, S. M. Francis, P. A. Goulding, and J. T. Allen, *J. Crystal Growth* **107**, 37 (1991); P. V. Kelly, J. D. O'Mahoney, J. F. McGilp, and Th. Rasing, *Appl. Surface Sci.* **56-58**, 453 (1992).
6. R. Superfine, P. Guyot-Sionnest, J. H. Hunt, C. T. Kao, and Y. R. Shen, *Surface Sci.* **200**, L445 (1988); Y. R. Shen, *Nature* **337**, 519 (1989).
7. Y. J. Chabal, G. S. Higashi, K. Raghavachari, and V. A. Burrows, *J. Vac. Sci. Technol.* **A7**, 2104 (1989); P. E. Gees and R. F. Hicks, *J. Vac. Sci. Technol.* **A10**, 892 (1992).
8. S. Selci, F. Ciccacci, G. Chiarotti, P. Chiaradia, and A. Cricenti, *J. Vac. Sci. Technol.* **A5**, 327 (1987); D. Eres and J. W. Sharp, *Appl. Phys. Lett.* **60**, 2764 (1992).
9. Y. Horikoshi, M. Kawashima, and N. Kobayashi, *J. Crystal Growth* **111**, 200 (1991); A. Usui, *Thin Solid Films* **225**, 53 (1993).
10. N. Kobayashi and Y. Kobayashi, *Thin Solid Films* **225**, 32 (1993).
11. N. Kobayashi and Y. Horikoshi, *J. Appl. Phys. Jpn.* **29**, L702 (1990); K. Nishi, A. Usui, and H. Sakaki, *Appl. Phys. Lett.* **61**, 31 (1992).

12. K. Nishi, A. Usui, and H. Sakaki, *Thin Solid Films* **225**, 47 (1993).
13. D. Gautard, J. L. Laport, M. Cadoret, and C. Pariset, *J. Cryst. Growth* **71**, 125 (1985); M. Gendry, J. Durand, M. Erman, J. B. Theeten, L. Nevot, and B. Pardo, *Appl. Surface Sci.* **44**, 309 (1990); S. Andrieu and F. Arnaud d'Avitaya, *J. Cryst. Growth* **112**, 146 (1991).
14. D. E. Aspnes, J. P. Harbison, A. A. Studna, and L. T. Florez, *Phys. Rev. Lett.* **59**, 1687 (1987); G. Paulsson, K. Deppert, S. Jeppesen, J. Jönsson, L. Samuelson, and P. Schmidt, *J. Cryst. Growth* **111**, 115 (1991); B. A. Joyce, J. Zhang, T. Shitara, J. H. Neave, A. Taylor, S. Armstrong, M. E. Pemble, and C. T. Foxon, *J. Cryst. Growth* **115**, 338 (1991); V. L. Berkovits, V. N. Bessolov, T. N. L'vova, E. B. Novikov, V. I. Safarov, R. V. Khasieva, and B. V. Tsarenkov, *J. Appl. Phys.* **70**, 3707 (1991).
15. O. Acher, S. M. Koch, F. Omnes, M. Defour, M. Razeghi, and B. Drévillon, *J. Appl. Phys.* **68**, 3564 (1990).
16. I. Kamiya, D. E. Aspnes, H. Tanaka, L. T. Florez, J. P. Harbison, and R. Bhat, *Phys. Rev. Lett.* **68**, 627 (1992).
17. I. Kamiya, D. E. Aspnes, L. T. Florez, and J. P. Harbison, *Phys. Rev.* **B46**, 15894 (1992).
18. D. E. Aspnes, I. Kamiya, H. Tanaka, and R. Bhat, *J. Vac. Sci. Technol.* **B10**, 1725 (1992).
19. K. Deppert, J. Jönsson, and L. Samuelson, *Thin Solid Films* **224**, 133 (1993).
20. H. Wormeester, D. J. Wentink, P. L. de Boeij, C. M. J. Wijers, and A. van Silfhout, *Phys. Rev.* **B47**, 12664 (1993).
21. F. Reinhardt, W. Richter, K. Ploska, P. Kurpas, and K. C. Rose, *Appl. Phys. Lett.* (in press).
22. N. Esser, M. Köpp, P. Haier, A. Kelnberger, and W. Richter, *J. Vac. Sci. Technol.* **B11**, 1481 (1993); V. Wagner, D. Drews, M. v. d. Emde, N. Esser, D. R. T. Zahn, J. Geurt, and W. Richter, *Appl. Phys. Lett.* (in press).
23. I. Kamiya, H. Tanaka, D. E. Aspnes, M. Koza, and R. Bhat, *Appl. Phys. Lett.* (in press).
24. T. Yasuda, D. E. Aspnes, D. R. Lee, C. H. Bjorkman, and G. Lucovsky, *J. Vac. Sci. Technol.* (in press).
25. D. W. Kisker, P. H. Fuoss, K. L. Tokuda, G. Renaud, S. Brennan, and J. L. Kahn, *Appl. Phys. Lett.* **56**, 2025 (1990); P. H. Fuoss, D. W. Kisker, F. J. Lamelas, G. B. Stephenson, P. Imperatori, and S. Brennan, *Phys. Rev. Lett.* **69**, 2791 (1992).
26. H. Sankur, W. Southwell, and R. Hall, *J. Electron. Mater.* **20**, 1099 (1991); K. Bacher, B. Pezeshki, S. M. Lord, and J. S. Harris, Jr., *Appl. Phys. Lett.* **61**, 1387 (1992); S. A. Chalmers and K. P. Killeen, *Appl. Phys. Lett.* **62**, 1182 (1993).
27. M. Erman and J. B. Theeten, *J. Appl. Phys.* **60**, 859 (1986).
28. D. E. Aspnes, W. E. Quinn, and S. Gregory, *Appl. Phys. Lett.* **56**, 2569 (1990).
29. Y.-T. Kim, R. W. Collins, and K. Vedam, *Surface Sci.* **233**, 341 (1990); I. An, Y. M. Li, H. V. Nguyen, and R. W. Collins, *Rev. Sci. Instrum.* **63**, 3842 (1992).

30. D. E. Aspnes, W. E. Quinn, M. C. Tamargo, M. A. A. Pudensi, S. A. Schwarz, M. J. S. P. Brasil, R. E. Nahory, and S. Gregory, *Appl. Phys. Lett.* **60**, 1244 (1992).
31. B. Johs, J. L. Edwards, K. T. Shiralagi, R. Droopad, K. Y. Choi, G. N. Maracas, D. Meyer, G. T. Cooney, and J. A. Woollam, *Proc. Mater. Res. Soc.* **222**, 75 (1992).
32. M. C. Tamargo, M. J. S. P. Brasil, R. E. Nahory, D. E. Aspnes, B. Philips, D. M. Hwang, S. A. Schwarz, and W. E. Quinn, *Mater. Res. Soc. Symp. Proc.* **263**, 267 (1992).
33. W. M. Duncan and S. A. Henck, *Appl. Surface Sci.* **63**, 9 (1993); S. A. Henck, W. M. Duncan, L. M. Lowenstein, and S. W. Butler, *J. Vac. Sci. Technol.* **A11**, 1179 (1993).
34. G. N. Maracas, J. L. Edwards, K. Shiralagi, K. Y. Choi, R. Droopad, B. Johs, and J. A. Woollam, *J. Vac. Sci. Technol.* **A10**, 1832 (1992); G. N. Maracas, J. L. Edwards, D. S. Gerber, and R. Droopad, *Appl. Surface Sci.* **63**, 1 (1993).
35. H. V. Nguyen, I. An, and R. W. Collins, *Phys. Rev.* **B47**, 3947 (1993).
36. A. A. Studna, D. E. Aspnes, L. T. Florez, B. J. Wilkens, and R. E. Ryan, *J. Vac. Sci. Technol.* **A7**, 3291 (1989).
37. H. A. Macleod, *Opt. Acta* **19**, 1 (1972); E. Pelletier, *Proc. SPIE* **401**, 74 (1983); R. Herrmann and A. Zöllner, *Proc. SPIE* **401**, 83 (1983); C. J. van der Laan, *Appl. Opt.* **25**, 753 (1986).
38. D. E. Aspnes, *J. Opt. Soc. Am.* **A10**, 974 (1993).
39. C. Pickering, in *Handbook of Crystal Growth*, vol. III (in press); W. Richter, *Proc. Roy. Soc.* (in press); D. E. Aspnes, *Surface Science* (in press).
40. S. M. Bedair, B. T. McDermott, Y. Ide, N. H. Karam, H. Hashemi, M. A. Tischler, M. Timmons, J. C. L. Tarn, and N. El-Masry, *J. Cryst. Growth* **93**, 182 (1988).
41. F. K. Urban III and M. F. Tabet, *J. Vac. Sci. Technol.* **A11**, 976 (1993).
42. C. M. J. Wijers and G. P. M. Poppe, *Phys. Rev.* **B46**, 7605 (1992); C. M. J. Wijers, G. P. M. Poppe, P. L. de Boeij, H. G. Bekker, and D. J. Wentink, *Thin Solid Films* (in press).
43. S. J. Morris and C. C. Matthai, *J. Vac. Sci. Technol.* (submitted).
44. Y. C. Chang and D. E. Aspnes, *Phys. Rev.* **B41**, 12002 (1990); Y. C. Chang, S. F. Ren, and D. E. Aspnes, *J. Vac. Sci. Technol.* **A10**, 1856 (1992).
45. B. A. Joyce, P. J. Dobson, J. H. Neave, K. Woodbridge, J. Zhang, P. K. Larsen, and B. Bölger, *Surface Sci.* **186**, 423 (1986).
46. K. Hingerl, D. E. Aspnes, I. Kamiya, and L. T. Florez, *Appl. Phys. Lett.* **63**, 885 (1993).
47. D. Beaglehole, *Rev. Sci. Instrum.* **59**, 2557 (1988).
48. M. Haverlag and G. S. Oehrlein, *J. Vac. Sci. Technol.* **B10**, 2412 (1992).



## *In situ* and *Ex situ* Applications of Spectroscopic Ellipsometry

John A. Woollam<sup>\*,†</sup>, Blaine Johs<sup>†</sup>, William A. McGahan<sup>†</sup>, Paul G. Snyder,<sup>\*</sup> Jeffrey Hale,<sup>\*</sup> and Huade Walter Yao<sup>\*</sup>, Center for Microelectronic and Optical Materials Research, and Department of Electrical Engineering, University of Nebraska, Lincoln, NE 68588-0511<sup>\*</sup>, and JA Woollam Co., Inc., 650 J Street, Lincoln, NE 68508<sup>†</sup>.

### Abstract

We briefly review the optics of ellipsometry, followed by discussions of a series of example applications of the technique including single films on a substrate; multilayer stacks common to silicon integrated circuit fabrication; flat panel display materials, and *in situ* semiconductor growth and deposition control.

### Ellipsometric Fundamentals

There are several common optical configurations for ellipsometers, including use of retardation modulators, and rotating polarizers.<sup>1</sup> The configuration shown in Figure 1 has a fixed polarizer, sample, and rotating polarizer (analyzer).<sup>2,3</sup> A monochromatic, linearly polarized, collimated light beam is incident on the material of interest at an oblique angle of incidence. Typically this angle is 65° to 75° measured from the sample normal. Figure 2 shows why it is highly advantageous to have both spectroscopic and variable angle capability. The sensitivity for accurate measurement of an unknown material parameter such as layer thickness or alloy fraction is highly dependent on both angle of incidence and wavelength.

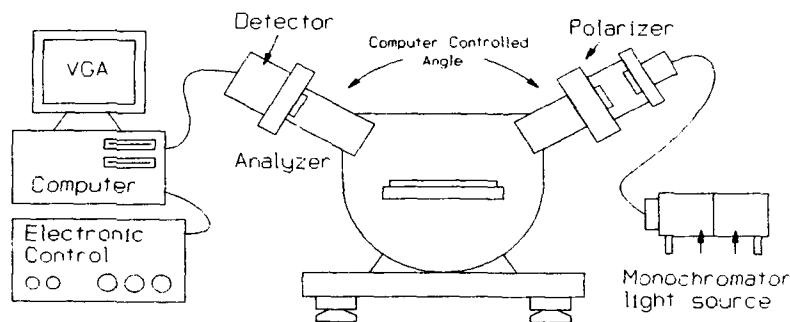


**Figure 1:** Variable angle of incidence spectroscopic ellipsometer.

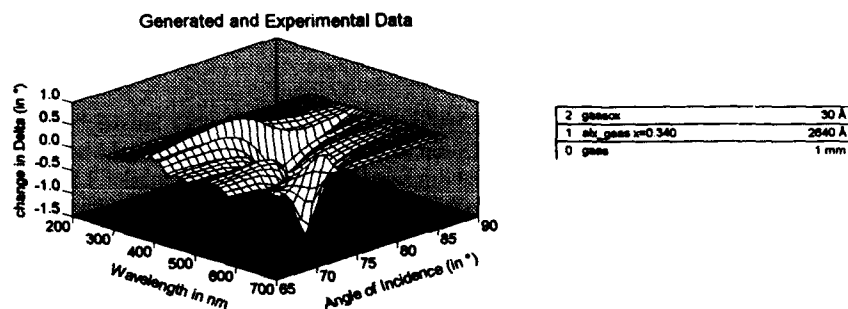


**Figure 2:** Change in calculated delta for a 1.0 % change in the AlGaAs alloy fraction for the sample shown. Note the strong dependence of the sensitivity on both wavelength and angle of incidence.

Ellipsometers measure a complex number  $\rho = \tan\psi \exp(j\Delta)$  and data are often expressed in terms of  $\psi$  and  $\Delta$  (or  $\tan\psi$  and  $\cos\Delta$ ).  $\rho = r_p/r_s$  where  $r_p$  and  $r_s$  are the complex Fresnel reflection coefficients derived from solving Maxwell's equations of electrodynamics at the interface between two optically distinguishable media.<sup>1</sup> The Fresnel coefficients are functions of the angle of incidence, the complex optical index of refraction of the materials in the sample, and the layer thicknesses in multilayer materials.

Because the Fresnel coefficients for multilayered media contain a large number of algebraic terms the desired optical constants and layer thicknesses can not be solved for directly from the measured  $\rho$  as a function of angle and wavelength.<sup>1</sup> Instead, a model for the physical structure needs to be constructed, based on best estimates of the nature and dimensions of the actual sample. That model is the basis for calculating predicted  $\psi$  and  $\Delta$  spectra. Next, experimental  $\psi$  and  $\Delta$  data are acquired, and a comparison between experimental and calculated  $\psi$  and  $\Delta$  is made. We use a biased estimator for this comparison, given as

$$BE = \sum_{i=1}^{N-1} \frac{(\psi^C - \psi^M)^2}{\sigma_i^2} + \frac{(\Delta^C - \Delta^M)^2}{\sigma_i^2}$$

where C and M signify calculated and measured respectively, and  $\sigma_i$  are the standard deviations of the measurements.<sup>4</sup>

The set of parameters is next found which minimizes the biased estimator, using the Levinberg-Marquardt algorithm in a regression analysis<sup>5</sup>. The resulting set of parameters is then examined to determine the physical realism of the values. For example, if a layer thickness was known to be near 15nm and the regression resulted in a value of 250nm then the reasonableness of the originally assumed model must be re-examined. That is, the technique is model dependent. Luckily there are a huge number of examples

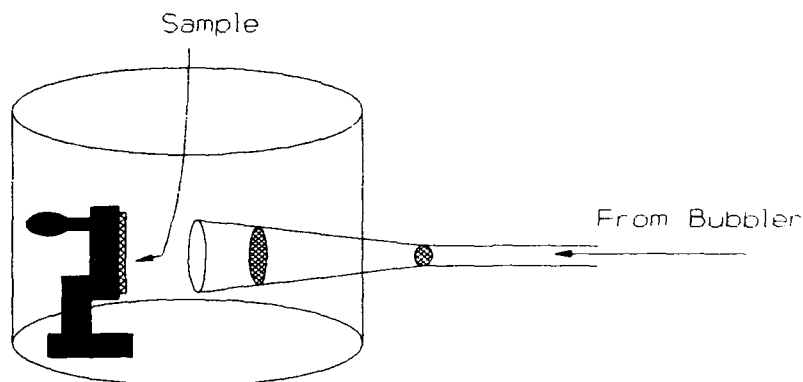
where the results are reasonable, and parameter values found to be in excellent agreement with the same parameters obtained from other techniques<sup>6</sup>. These methods include cross sectional transmission electron microscopy and Rutherford Backscattering, for example.<sup>7</sup>

The advantages of ellipsometric materials analysis are that it is non-destructive, rapid, non-invasive (even photoresists are not "exposed" by the light beam), and that it works in a variety of ambients including air, vacuum, and even under liquids. Additionally ellipsometry is submonolayer sensitive.

#### Examples

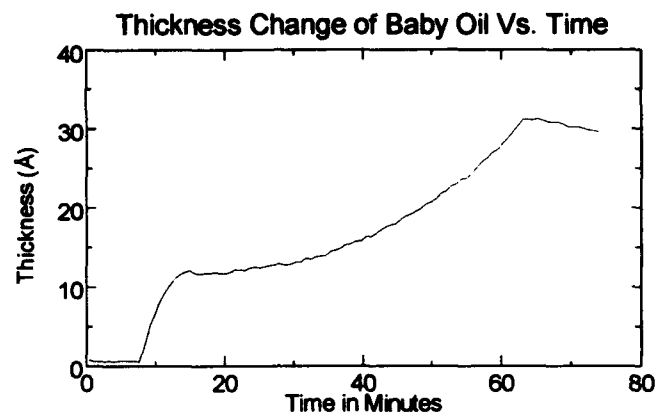
##### A. Transparent Thin Films.

To illustrate the monolayer sensitivity of spectroscopic ellipsometry, Figure 3 shows an "environmental chamber" in which dry, high purity air is passed through a "baby oil" bubbler to deposit an extremely thin film of oil on an iridium metal substrate. Iridium will be used as the mirror surface by NASA on its X-ray telescope to be launched in 1999. Mirror contamination detection is a concern. The baby oil experiments were preliminary, to demonstrate the high sensitivity of ellipsometry to hydrocarbon contamination.



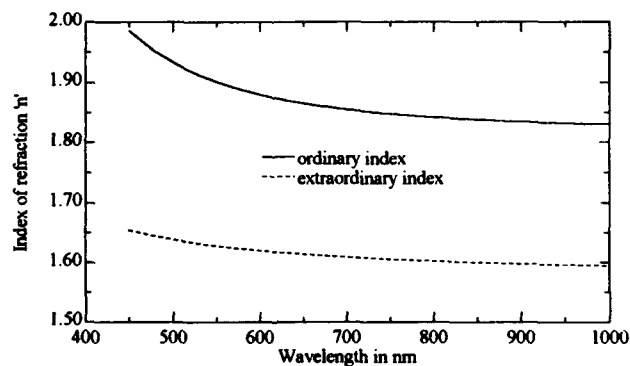
**Figure 3:** Environmental chamber for contamination studies with VASE.

Figure 4 shows the change in thickness vs time during baby oil condensation. Notice that the changes in thickness are at a rate of about 0.05 nm per minute with a noise level of less than an atomic monolayer.



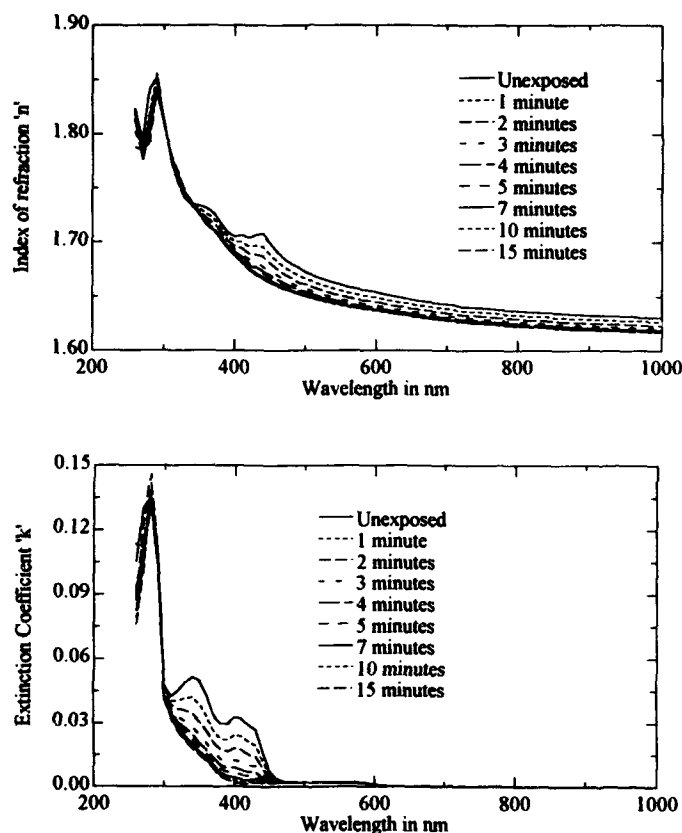
**Figure 4:** Dynamic VASE data for baby oil contamination of a surface.

Figure 5 shows the ordinary and extraordinary branches of the index of refraction determined ellipsometrically of a polyimide film 957 nm thick on a silicon wafer. Thus the dispersion relations of both isotropic and anisotropic optical thin films can be determined by ellipsometry.



**Figure 5:** Ordinary and extraordinary indices of refraction of a 957 nm polymer film, from analysis of VASE data.

Another interesting experiment is shown in figure 6 where the index and extinction coefficient of a photoresist are shown before, during and after exposure to light. The ellipsometer used for these measurements had the monochromator ahead of the sample (rotating analyzer ellipsometer) and thus minimally exposed the photoresist during measurement. Thus the dynamics of photochemical reactions can be studied.



**Figure 6:** Photoresist optical constants as a function of UV light exposure, as obtained from analysis of VASE data. Note the bleaching of the absorption peaks below ~460 nm.

A final note in this section is that the index of refraction and thickness of very thin films are often correlated variables<sup>8</sup>. Thus neither can be uniquely determined when both are unknown. The thicker the film the generally lower is the correlation of these parameters. Thus ellipsometry can determine both  $n$  and thickness for films thicker than a

few tens of nm. Separation of  $n$  and  $k$  is not possible by normal incidence reflectance measurements for films of any thickness. Another way to decorrelate  $n$ ,  $k$ , and the film thickness is to combine ellipsometry with optical transmission<sup>9</sup>. In this way film thickness, optical constants, and vertical index grading profiles can often be determined uniquely. This is illustrated in figure 7 where the index of indium tin oxide (ITO) vs depth is plotted. Additionally ellipsometry plus transmission permits measurement of the dispersion of the index of refraction and extinction coefficient, as seen in figure 8. Note the basic optical bandgap absorption starting near 300 nm ( $\sim 4\text{eV}$ ), as well as the Drude edge optical absorption in the near infrared. The Drude edge is determined by the number of free carriers and the effective mass of these carriers and is thus related to the electrical conductivity. Thus ellipsometry provides a quick non-destructive optical measurement of the electrical conductivity of these transparent conductors.

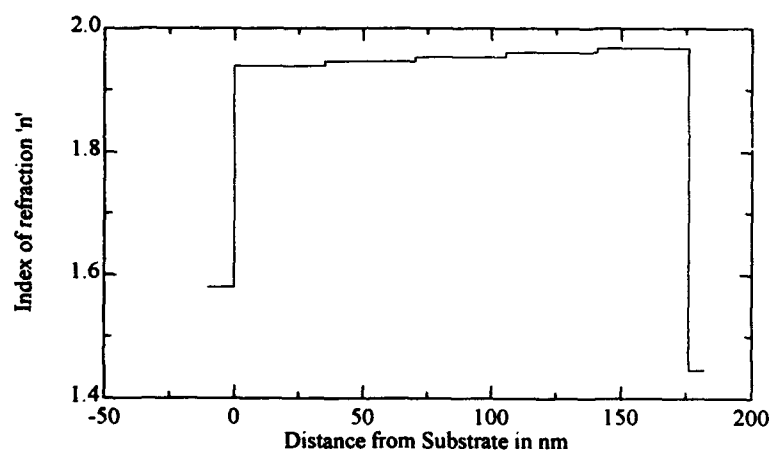


**Figure 7:** Depth profile of the index of refraction at 500 nm of an indium tin oxide (ITO) film on BK7 glass, obtained from simultaneous analysis of VASE and transmission data.

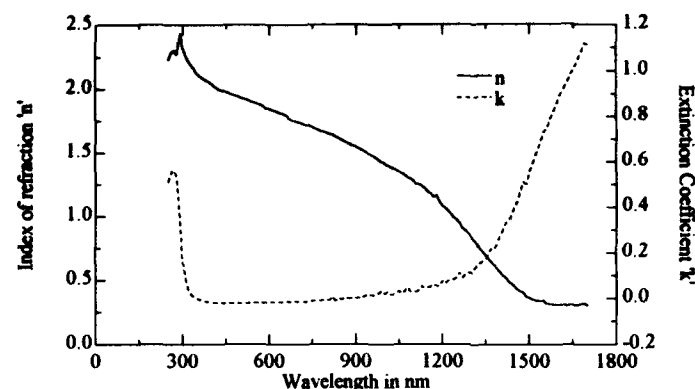


**Figure 8:** Optical constants of indium tin oxide (ITO) obtained from analysis of VASE and transmission data for an ITO film on BK7 glass.

#### B. Films for Semiconductor Circuits.

There are numerous materials used in integrated circuit manufacture for which ellipsometry is highly effective as an analytical tool<sup>7, 10, 11</sup>. These include: 1) Natural and thermal oxide thicknesses; 2) Poly-silicon microstructure including amorphous silicon fraction along with layer thickness and surface roughness. 3) Metallization including titanium and titanium nitride. Figure 9 shows a comparison of ellipsometrically determined thicknesses for a semiconductor structure with thicknesses determined by calibrated cross sectional transmission electron microscopy. Excellent agreement is found<sup>7</sup>. Note that ellipsometry non-destructively determined five layer thicknesses and the void fraction in the poly-si layer, a total of six variables.

| Layer thickness (nm)           | VASE      | XTEM      |
|--------------------------------|-----------|-----------|
| Silicon dioxide (native)       | 5.4 nm    | 5.0 nm    |
| Silicon Nitride                | 15.2 nm   | 16.0 nm   |
| Silicon Dioxide                | 33.1 nm   | 33.0 nm   |
| Poly-Si: 96% c-Si,<br>4% voids | 323.4 nm  | 320.0 nm  |
| Silicon Dioxide                | 31.6 nm   | 30.9 nm   |
| Silicon                        | Substrate | Substrate |

**Figure 9:** Comparison of ellipsometrically determined thicknesses for a semiconductor structure with thicknesses determined by calibrated cross sectional transmission electron microscopy.

### C. Patterned Flat Panel Display Structures.

Figure 10 shows the index of refraction dispersion of a ZnS:Mn electroluminescent layer in a stack consisting of  $\text{SiO}_x\text{N}_y/\text{ZnS:Mn}/\text{SiO}_x\text{N}_y/\text{Patterned ITO/glass}$ . Along with the index of refraction, the Cauchy coefficients representing dispersion in the  $\text{SiO}_x\text{N}_y$  layers (and thus the x-value) as well as the thicknesses of the four layers were determined. Thus spectroscopic ellipsometry can be very effectively used for diagnostics on commercially important flat-panel display multilayer materials. Mapping of properties over the area of the panel can also be done.

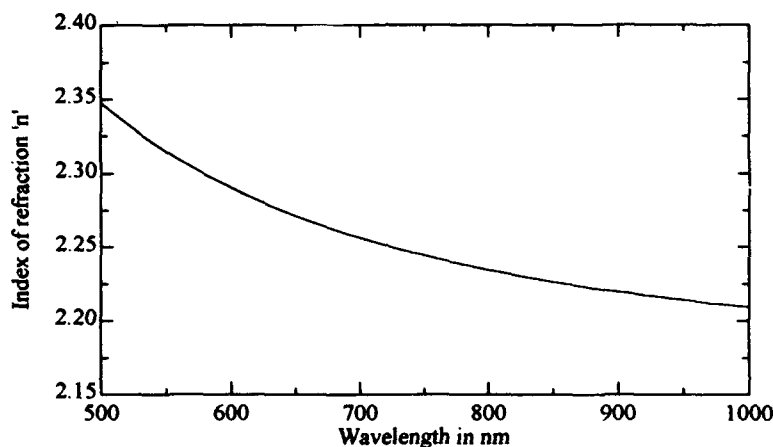


Figure 10: ZnS:Mn Index of refraction, from VASE analysis of patterned four layer sample containing a one micron ZnS:Mn film.

### D. Control of Superlattice Growth by Molecular Beam Epitaxy (MBE).

A final example of applications of spectroscopic ellipsometry is the monitoring and control of depositions. Shown in figure 11 is an ellipsometer that takes data simultaneously at 44 wavelengths in a fraction of a second. Examples of its use include MBE and metal organic chemical vapor deposition (MOCVD) crystal growth, electron cyclotron resonance (ECR) etching and deposition, and sputtering. In all of these, monolayer sensitivity (and in some cases control of the deposition) have been demonstrated. Figure 12 shows the  $\psi$  parameter acquired at 44 visible wavelengths vs time during growth of a four period superlattice of AlAs/GaAs. As the growth took 600 seconds and data were acquired twice per second, there were 52,800 data points acquired! The user can select out those most important for determining the desired physical parameters, which in the case shown was layer thickness. Thickness control was implemented using the ellipsometrically determined thickness vs time to open and close



shutters during the deposition. The nominal thicknesses of 1.50 nm (AlAs) and 20.0 nm (GaAs) were achieved with 90 percent confidence limits of 0.1 nm (AlAs) and 0.45 nm (GaAs) being typical.

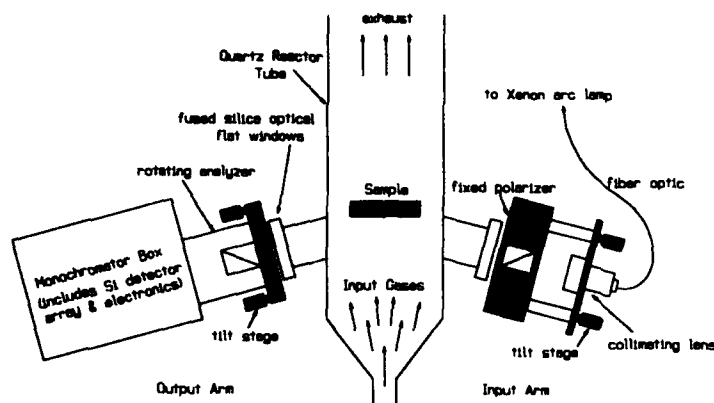


Figure 11: 44 Wavelength ellipsometer.

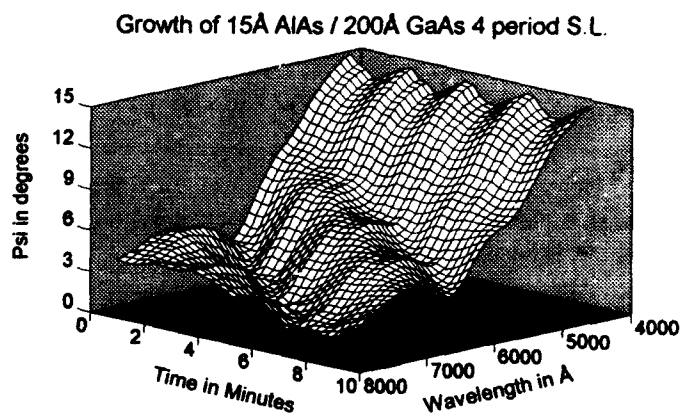


Figure 12: Spectral VASE data as a function of time, acquired during MBE growth of AlAs/GaAs superlattice, four periods.

### Conclusions

Applications of spectroscopic ellipsometry have advanced rapidly in the past several years due to the ever increasing speed of computers, and due to the parallel development of data analysis software and new approaches to problem solving. In this brief review we have chosen to illustrate the power of ellipsometry in solving various materials problems of industrial importance such as hydrocarbon contamination of surfaces, photoresists, integrated circuit materials, flat panel display multilayer structures, and *in situ* real time process control. In addition to these commercial applications there are numerous impressive advances being made in the more fundamental science aspects using spectroscopic ellipsometry<sup>6</sup>.

### Acknowledgments

The Authors would like to thank Professor George Maracas, Mr. Yale Strausser, Mr. Gerry Cooney, Mr. Duane Meyer, and Professor Mark Schattenburg for their participation in parts of the work reported. Support was received from Intel Corporation, the US Army Night Vision Laboratory, the Advanced Research Projects Agency, and other corporate sponsors.

### References

1. R.M.A. Azzam and N.M. Bashara, Ellipsometry and Polarized Light, North Holland Press, Amsterdam, 1977.
2. P. S. Hauge and F. H. Dill, IBM J. Res. Devel., **17**, 472, (1973).
3. D.E. Aspnes and A. A. Studna, Appl. Optics, **14**, 220, (1975).
4. G.E. Jellison, Jr., Thin Solid Films, **234**, 416, (1993).
5. W. H. Press, B. P. Flannery, S. A. Teukolsky, and W. T. Vetterling, Numerical Recipes, Cambridge University Press, 1986.
6. Proceedings of First International Conference on Spectroscopic Ellipsometry, edited by A. C. Boccara, C. Pickering, and J. Rivory, Elsevier Sequoia, Amsterdam, 1993.
7. Y.M. Xiong, P.G. Snyder, J.A. Woollam, and E. R. Krosche, J. Vac. Sci. Techn., **A10**, 950, (1992).
8. G. H. Bu-Abbud, N.M. Bashara, and J.A. Woollam, Thin Solid Films, **138**, 27, (1986).

9. W. A. McGahan, B. Johs, and J. A. Woollam, thin solid Films, 234, 443 (1993)
10. E. A. Irene, Thin solid Films, 233, 96 (1993).
11. B. Johs, J. L. Edwards, K. T. Shiralagi, R. Droopad, K. Y. Choi, G. N. Maracas, D. Meyer, G. T. Cooney, and J. A. Woollam, Mat. Res. Soc. Symp. Proc., 222, 75 (1991).
12. B. Johs, D. Doerr, S. Pittal, I. B. Bhat, S. Dakshinamurthy, Thin Solid Films, 233, 293 (1993).
13. S. Nafis, N. J. Ianno, P. G. Snyder, W. A. McGahan, B. Johs, and J. A. Woollam, Thin Solid Films, 233, 253 (1993).

## In-situ Multilayer Film Growth Characterization by Brewster Angle Reflectance Differential Spectroscopy

N. Dietz, D.J. Stephens, G. Lucovsky and K.J. Bachmann  
North Carolina State University, Raleigh, NC 27695

### ABSTRACT

Brewster Angle Reflectance Differential Spectroscopy (BARDS) has been proposed as an optical method for real-time characterization of the growth of thin films. BARDS is based on changes in the reflectivity,  $R_p$ , of parallel (p)-polarized light incident at, or near, the Brewster angle of the substrate material. Changes in  $R$  are sufficiently large to monitor layer growth, and to determine the thickness and the optical constants of the deposited film. In this paper we extend the method to multilayer film deposition. The derivative properties of  $R$  are correlated with differences in the optical constants of the two materials, and with the sharpness of their interface. We present spectra for  $\text{SiO}_2/\text{Si}_3\text{N}_4/\text{SiO}_2/\text{Si}$ , demonstrating some of these aspects of this new and effective approach to in-situ monitoring.

### I. INTRODUCTION

During the last decade, with increasing use of thin film deposition techniques, the need for in-situ growth monitoring has resulted in the development of various characterization methods. Due to the nondestructive character and the real-time application, optical probe techniques such as reflectance-difference spectroscopy (RDS)<sup>1,2</sup>, surface photo-absorption (SPA)<sup>3</sup>, dynamic optical reflectivity (DOR)<sup>4</sup> and Brewster angle reflectance spectroscopy (BAPS)<sup>5</sup> have been developed for in-situ characterization of the growth of thin films. For a transparent substrate a well defined Brewster angle exists where the reflection coefficient,  $r_p$ , of the component of the incident light polarized parallel to the plane of incidence, vanishes. For an absorbing substrate, the Brewster angle law has to be modified from the condition  $R_p = 0$  to a reflectance minima condition  $dR_p/d\phi = 0$ . This definition of the Brewster angle is then also called the pseudo-Brewster or first Brewster angle. It has been shown that the Brewster angle law can be generally formulated as a function of the complex optical functions  $\epsilon = \epsilon_1 + i\epsilon_2$ , which apply to transparent as well as absorbing media<sup>6</sup>.

Compared to transparent media, the influence of the absorbing media on the Brewster angle can be expressed as a shift in the angle  $\phi_B$  at which  $dR_p/d\phi = 0$  and in an offset, i.e.  $R_p|_{\phi_B} \geq 0$ . The reflectivity  $R_p|_{\phi_B}$  lies in the order of  $10^{-6}$  -  $10^{-4}$  for weakly absorbing media and increases up to  $10^{-2}$  for strong absorbing media, such as metals. Assuming the growth of a film with a certain optical dielectric function  $\epsilon = \epsilon_1 + i\epsilon_2$  on a substrate, the reflected light from the surface can be initially split in two contributions. First, a large contribution related to the bulk properties of the substrate and second, a small contribution due to the growing film. Setting the angle of incidence at the Brewster angle  $\phi_B$  of the substrate, its bulk contribution is set to zero, which allows highly sensitive detection of the initial layer growth. Changes in the growth conditions, such as a variation in the growth rate, density fluctuations or changes in the optical function  $\epsilon$  during the growth results in a change of the slope in the monitored reflectance spectrum or in a discontinuity in the derivative reflectance spectrum, respectively.

### II. MODEL CONSIDERATION

In the modeling of the changes in the reflectance for multilayer film growth, homogeneous isotropic substrates and films are assumed. For monochromatic light which is parallel polarized to the plane of incidence, no perpendicular reflectance components,  $r_s$ , have to be considered as, only the parallel reflectance components,  $r_p$ , contribute to the reflectance amplitude. For brevity, the index  $p$  will be dropped in the following text.

Assuming an 'n' layer system; ambient / film 1 / ... / film n / substrate (see Fig. 1), the reflection coefficient from the (n-1)<sup>th</sup> to the n<sup>st</sup> layer,  $r_{(n-1)n}$ , is given by:

$$r_{(n-1)n} = \frac{\epsilon_{f_n} \sqrt{\epsilon_{f(n-1)} - \epsilon_a \sin^2 \phi_0} - \epsilon_{f(n-1)} \sqrt{\epsilon_{f_n} - \epsilon_a \sin^2 \phi_0}}{\epsilon_{f_n} \sqrt{\epsilon_{f(n-1)} - \epsilon_a \sin^2 \phi_0} + \epsilon_{f(n-1)} \sqrt{\epsilon_{f_n} - \epsilon_a \sin^2 \phi_0}}, \quad (1a)$$

and reflection coefficient from the n<sup>th</sup> layer to the substrate,  $r_{ns}$ , is given by

$$r_{ns} = \frac{\epsilon_s \sqrt{\epsilon_{f_n} - \epsilon_a \sin^2 \phi_0} - \epsilon_{f_n} \sqrt{\epsilon_s - \epsilon_a \sin^2 \phi_0}}{\epsilon_s \sqrt{\epsilon_{f_n} - \epsilon_a \sin^2 \phi_0} + \epsilon_{f_n} \sqrt{\epsilon_s - \epsilon_a \sin^2 \phi_0}}. \quad (1b)$$

The phase factor  $\Phi_n$  for the n<sup>th</sup> layer can be described by:

$$\Phi_n = \frac{2\pi d_{f_n}}{\lambda} \sqrt{\epsilon_{f_n} - \epsilon_a \sin^2 \phi_0}. \quad (2)$$

The thickness of the n<sup>th</sup> film is  $d_{f_n}$ ,  $\phi_0$  is the angle of incidence and  $\epsilon_a$  and  $\epsilon_s$  are the complex dielectric functions of the ambient and the substrate, respectively. The complex dielectric functions of the (n-1)<sup>th</sup> and n<sup>th</sup> films are indexed by  $\epsilon_{f(n-1)}$  and  $\epsilon_{f_n}$ , respectively. Figure 1 shows the reflected and transmitted waves for a 2 layer ( ambient - film 1 - film 2 - substrate ) system for a p-polarized light beam.

The reflectance amplitude  $rr_n$  can be calculated from a 'n' - 2x2 matrix multiplication

$$\begin{bmatrix} M_{11} & M_{12} \\ M_{21} & M_{22} \end{bmatrix} = \begin{bmatrix} 1 & r_{a1} \\ r_{a1} & 1 \end{bmatrix} \begin{bmatrix} 1 & r_{12} \\ r_{12} e^{-2j\phi_1} & e^{-2j\phi_1} \end{bmatrix} \begin{bmatrix} 1 & r_{23} \\ r_{23} e^{-2j\phi_2} & e^{-2j\phi_2} \end{bmatrix} \dots \begin{bmatrix} 1 & r_{(n-1)n} \\ r_{(n-1)n} e^{-2j\phi_n} & e^{-2j\phi_n} \end{bmatrix}$$

with  $rr_n = \frac{M_{21}}{M_{11}}$ . (3)

Figure 2 shows the calculated change in the reflectivity for a SiO<sub>2</sub>-Si<sub>3</sub>N<sub>4</sub>-SiO<sub>2</sub> multilayer system grown on a Si substrate. The angle of incidence is chosen at 70 degrees. The chosen wavelength is 670 nm. The derivative spectrum of the reflectivity versus film thickness is also shown. This clearly reveals a discontinuity at the interface of each layer. The changes in the slope can be used to characterize the different dielectric functions for each film.

### III. EXPERIMENT

The experimental arrangement is schematically shown in Fig. 3. A laser diode with  $\lambda=670\text{nm}$  and 6.5mW power is used as light source. The parallel light beam is split into a reference and a signal channel. The signal beam is polarized parallel to the plane of incidence, using a Glan-Thompson polarizer, P, with an extinction ratio smaller than  $10^{-6}$ . The polarized light is focused onto the sample held at an angle of 70 degrees, which is close to the Brewster angle,  $\phi_B$ , of the silicon substrate. The reflected intensity is detected by a photomultiplier tube, PMT, and processed using a preamplifier and lock-in amplifier technique. The laser intensity is monitored at the reference channel to correct light intensity fluctuations.

Thin films of SiO<sub>2</sub> and Si<sub>3</sub>N<sub>4</sub> were deposited on a n-Si (100) substrate using remote plasma enhanced CVD processing described elsewhere<sup>7</sup>. The flow rates for SiO<sub>2</sub> deposition were 300 sccm He flow, 15 sccm oxygen flow and 7.5 to 25 sccm SiH<sub>4</sub>/Ar (10% SiH<sub>4</sub> diluted in Argon) for growth rates of 50 Å/min to 200 Å/min, respectively. The flow rates for Si<sub>3</sub>N<sub>4</sub> deposition were 300 sccm He flow, 25 sccm SiH<sub>4</sub>/Ar flow and 10 to 20 sccm NH<sub>3</sub> flow introduced through a ring 5 cm above the substrate. Substrate temperature and process pressure were maintained at 300 °C and 300 mtorr, respectively. The plasma was created by RF excitation at 13.56 MHz with a RF power of 400 W.

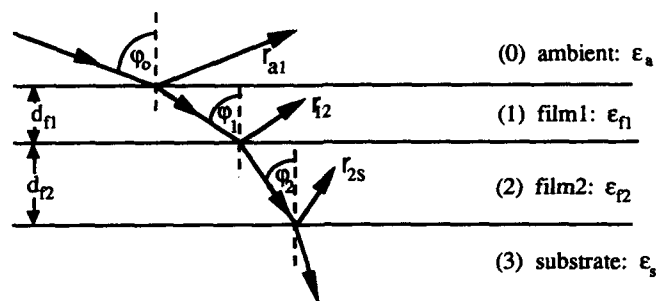


Fig. 1: Reflection of a plane wave (p-polarized to the plane of incidence) by a two layer-film structure between (0) ambient and (3) substrate.  $\phi_0$  is the angle of incidence;  $\phi_1$  and  $\phi_2$  are the angles of refraction;  $r_{a1}$ ,  $r_{12}$  and  $r_{2s}$  are the reflection coefficients for the interfaces.

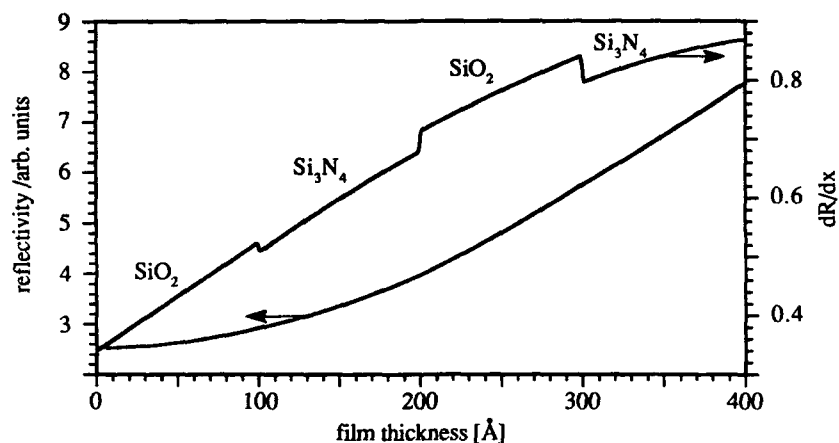


Fig. 2: Calculated changes in the reflectivity for  $\text{SiO}_2$ - $\text{Si}_3\text{N}_4$ - $\text{SiO}_2$  multilayer deposition, on top of a Si substrate.

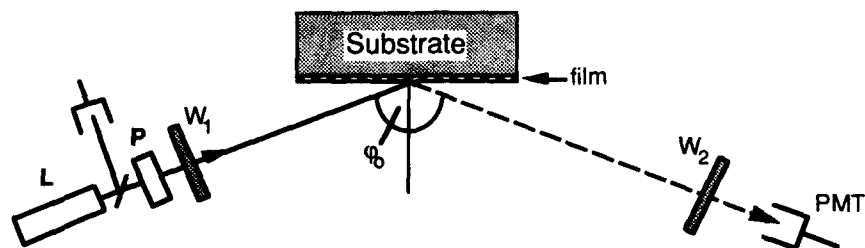


Fig. 3: Schematic diagram of the experimental setup; L: Laser; P: Glan Thompson polarizer; PMT: photo multiplier tube;  $W_1$  and  $W_2$  are the optical ports into the growth chamber.

#### IV. RESULTS AND DISCUSSION

The changes of the real-time monitored reflected intensity during the  $\text{SiO}_2$  growth is shown in fig. 4 for two different processing conditions. The  $\text{SiO}_2$  films are deposited at  $300^\circ\text{C}$  with a growth rate of  $\sim 100\text{\AA}/\text{min}$ . Spectrum (b) in Fig. 4 shows the changes in the reflected intensity for  $\text{SiO}_2$  growth starting with a hydrogen terminated Si (100) surface and Fig. 4 (a) shows the changes in the reflected intensity starting with a preoxidized Si surface. The preoxidation process involved a 60 sec He-oxygen plasma without  $\text{SiH}_4$  flow at  $300^\circ\text{C}$ , which oxidized the Si surface, resulting in a uniform  $\text{SiO}_2$  layer of about  $6\text{\AA}$ . The  $\text{SiO}_2$  deposition parameters are identical for both spectra. The observed changes in the reflected intensity differ in the observed slope as well as the monitored intensity maxima.

To reveal the film thickness, the growth rate and the optical constants of the deposited  $\text{SiO}_2$  layer, spectrum 4(a) is compared with a theoretical spectrum, calculated using eqs. (1) to (4) assuming one layer ( $\text{SiO}_2$ ), ambient,  $\epsilon_a = 1$ , and Si substrate,  $\epsilon_s = (15.20, 0.15)$ . Figure 5 shows the experimental spectrum (as a function of thickness) compared with the theoretical spectrum for a  $\text{SiO}_2$  layer. Best agreement is observed assuming a dielectric function of  $\epsilon_f = (2.14, 0.01)$  with a calculated growth rate of  $85\text{\AA}/\text{min}$  for the grown  $\text{SiO}_2$  film, however, two discrepancies can be seen. First, the local minima of the experimental spectra are broadened and second, a large difference in the resolved peak maxima compared to the theoretical model can be observed. The broadened minima can be explained as a result of beam divergence, substrate surface roughness and depolarization effects in the optical ports of the growth chamber. The discrepancy in the intensity maxima is explained by the interaction of the laser beam with the RF-plasma, which is due to absorption of the laser light by excited hydrogen in the RF-plasma. This interaction results in a significantly lower detected intensity during the deposition process. Therefore, a calculation of the absolute reflectivity cannot be performed. Choosing a laser wavelength outside the absorption region eliminates this difficulty and permits the evaluation of possible additional sources of distortions of the experimental reflectance curve in future.

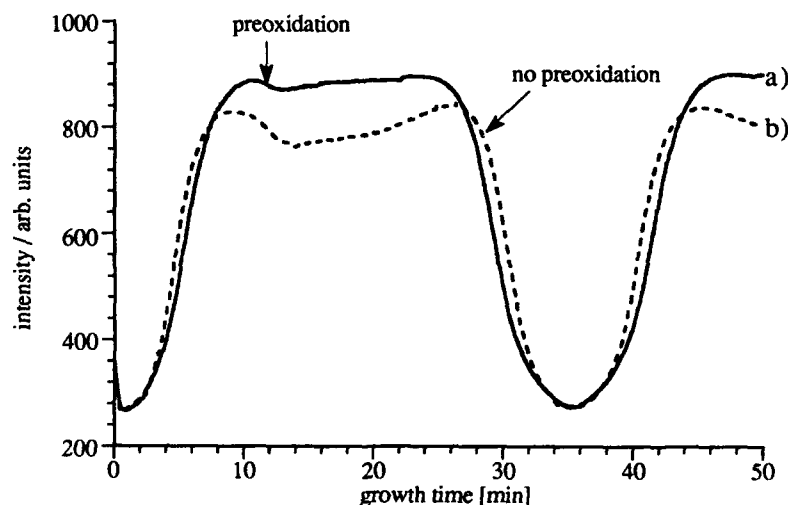


Fig. 4: Real-time monitoring of the reflected intensity during  $\text{SiO}_2$  deposition, with and without preoxidation step.

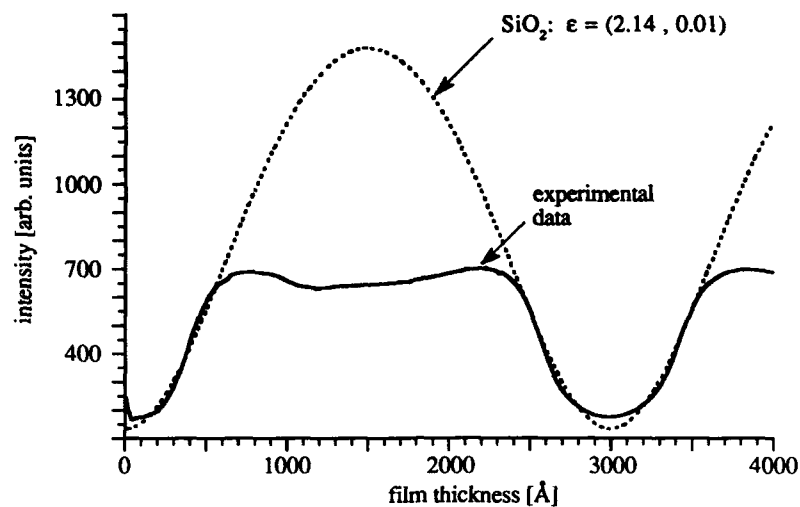


Fig. 5: Fitting of the experimental data (fulline) for the growth of SiO<sub>2</sub> on Si by a theoretical curve (dashed line) with a dielectric function (2.14, 0.01) at 670 nm.

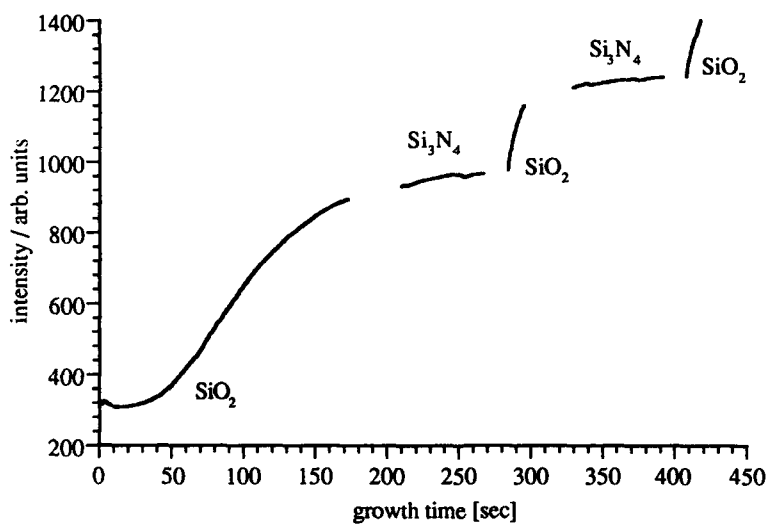


Fig. 6: Monitored changes in the reflected intensity during a SiO<sub>2</sub> - Si<sub>3</sub>N<sub>4</sub> multilayer deposition.



Figure 6 shows the changes in the reflected intensity during a multilayer SiO<sub>2</sub> - Si<sub>3</sub>N<sub>4</sub> growth starting with a H-terminated Si (100) surface. The SiO<sub>2</sub> was deposited with a growth rate of about 200 Å/min and the Si<sub>3</sub>N<sub>4</sub> was deposited with a growth rate of about 55 Å/min. Due to the interaction between the laser light and the applied plasma during the deposition process, a drop in the intensity occurred while switching the deposition from the SiO<sub>2</sub> process to the Si<sub>3</sub>N<sub>4</sub> process. This resulted in a drop in the intensity of the reflected light. After 10 to 30 sec the process was stabilized. The observed changes in the slope of the reflected intensity versus time curve upon switching between SiO<sub>2</sub> and Si<sub>3</sub>N<sub>4</sub> deposition are related to the differences in the growth rates and the dielectric functions of the deposited SiO<sub>2</sub> and Si<sub>3</sub>N<sub>4</sub> films. If the growth rate for each deposition process is known, the intensity spectrum as a function of time can be converted into a film thickness scaling and the revealed changes in the slopes can be related to the optical constants for each film.

## V. CONCLUSION

BARDS allows the real-time monitoring of multilayer film growth. Theoretical calculations show that differences in the dielectric functions for each film result in a discontinuity in the differential spectrum. First results for SiO<sub>2</sub> and Si<sub>3</sub>N<sub>4</sub> film depositions show that the information obtained by BARS can be used to obtain the film thickness, the growth rate and optical constants of the deposited film. Results on multilayer SiO<sub>2</sub> - Si<sub>3</sub>N<sub>4</sub> film deposition display changes in the slope of the monitored reflected intensity versus time curve upon switching between SiO<sub>2</sub> and Si<sub>3</sub>N<sub>4</sub> deposition, which are related to the differences in the growth rates and optical constants of the deposited layers.

## ACKNOWLEDGMENT

The authors would like to thank C.G. Parker for RPECVD processing. This research is supported by the NSF grant CDR 8721505.

## REFERENCES

- 1 D.E. Aspnes, W.E. Quinn, M.C. Tamargo, M.A.A. Pudensi, S.A. Schwarz, M.J.S.P. Brasil, R.E. Nahory, and S. Gregory, *Appl. Phys. Lett.* **60**(10), 1244-6 (1992).
- 2 D.E. Aspnes, J.P. Harbison, A.A. Studna, and L.T. Florez, *Appl. Phys. Lett.* **52**(12), 957-9 (1988).
- 3 N. Kobayashi, T. Makimoto, Y. Yamauchi, and Y. Horikoshi, *J. Cryst. Growth* **107**(1-4), 62-7 (1991).
- 4 J.V. Armstrong, T. Farrell, T.B. Joyce, P. Kightley, T.J. Bullough, and P.J. Goodhew, *J. Crystal Growth* **120**, 84-87 (1992).
- 5 N. Dietz and H.J. Lewerenz, *Appl. Surf. Sci.* **69**, 350-354 (1993).
- 6 H.J. Lewerenz, N. Dietz, *J. Appl. Phys.* **73** (10), 4975-87 (1993).
- 7 C.G. Parker, C. Silvestre, M. Watkins, R.T. Kuehn and J.R. Hauser, *Proceedings of UGIM Symposium*, May 1993.

## SIMULTANEOUS REAL TIME SPECTROSCOPIC ELLIPSOMETRY AND REFLECTANCE FOR MONITORING SEMICONDUCTOR AND THIN FILM PREPARATION

Ilsin An, Hien V. Nguyen, A. R. Heyd\*, and R. W. Collins  
Materials Research Laboratory and Department of Physics, The Pennsylvania State University,  
University Park, PA 16802. \* At present: NASA Lewis Research Ctr., Cleveland, OH 44135.

### ABSTRACT

This paper describes an expansion of the capabilities of real time spectroscopic ellipsometry (SE) that results from simultaneous measurement of a reflectance spectrum  $R_A$  along with the two spectra in the ellipsometric angles  $(\psi, \Delta)$ .  $R_A$  provides information complementary to  $(\psi, \Delta)$ , but until now has not been exploited in real time spectroscopic applications. Earlier, we have developed a novel rotating-polarizer multichannel ellipsometer for real time studies of thin film growth that utilizes a photodiode array (PDA) detector for high-speed acquisition of  $(\psi, \Delta)$  spectra. Employing this instrument with a 12.5 Hz polarizer rotation rate, three-parameter (3-p) data sets  $\{\psi(h\nu, t), \Delta(h\nu, t), R_A(h\nu, t); 1.4 \leq h\nu \leq 4.5 \text{ eV}\}$  can now be obtained with a time resolution as short as 40 ms during film growth. A resilient new analysis approach based on mathematical inversion and least-squares fitting is described to interpret the 3-p data set. The 3-p approach has been successful in characterizing plasma-enhanced chemical vapor deposition (PECVD) of amorphous semiconductors, and provides the film dielectric functions and thicknesses independently at each time during film growth.  $R_A(h\nu)$  exhibits deviations from the spectrum predicted in successful modeling of  $(\psi, \Delta)$  spectra alone. These deviations result from diffuse light scattering by particulates in the plasma. We show how additional information can be extracted from the spectral dependence of the scattering loss.

### INTRODUCTION AND OVERVIEW

Recently real time spectroscopic ellipsometry (SE) has been developed and applied to better understand the processes of thin film nucleation, coalescence, and bulk growth in adverse deposition environments [1]. The goal of this measurement is to deduce the optical properties of one or more layers that make up the evolving thin film. From the optical properties, we can learn about the microstructure of the film (e.g., bond-packing density) and its electronic characteristics (e.g., optical gaps, critical point energies). Because the optical properties of the film evolve with thickness in the early stages of growth, data analysis here often requires solving the classical problem in SE at each measurement time [2]. Specifically, one may need to determine spectra in the real and imaginary parts of the dielectric function ( $\epsilon_1, \epsilon_2$ ), as well as the film thickness  $d$ , from a single pair of spectra in the ellipsometry angles  $(\psi, \Delta)$ .

In this paper, we report a more general approach to solving the classical ellipsometry problem designed for real time applications. This approach relies on deducing a third spectrum, the reflectance  $R_A$ , from measurements obtained during thin film deposition.  $R_A$  can be acquired simultaneously with  $(\psi, \Delta)$  in the same multichannel rotating polarizer ellipsometer, and this measurement represents a natural, yet powerful, extension of the multichannel measurement described in detail in earlier publications [3]. In order to utilize  $R_A$  in solving the classical problem in SE, we establish the correct film thickness as that value yielding the best agreement between measured and calculated  $R_A$  spectra. In performing such analyses, however, we have found that the discrepancies in the measured  $R_A$  spectra from the calculated results can provide important and unique insights into plasma processes and film properties. Thus, the importance of the three-parameter (3-p) optical spectroscopy lies not only in its ability to assist in analyzing the layered structure of the film, but also in characterizing such processes as light scattering from plasma particulates or larger scale structure on the film surface.

### EXPERIMENTAL DETAILS

In this study, we employed a multichannel ellipsometer [3] consisting of (i) a collimated Xe source, (ii) a quartz Rochon polarizer assembly with an angular frequency of  $\omega_0 = 2\pi(12.5)$  rad/s, (iii) a high vacuum reactor with optical access at a  $70^\circ$  incidence angle, (iv) a fixed calcite Glan-Taylor analyzer, (v) a prism spectrograph, and (vi) a 1024-pixel Si PDA. The detector elements were grouped by eight; thus, 128 spectral points were collected from 1.4 to 4.5 eV.

The array is read out four times per optical cycle, clocked by an encoder mounted on the polarizer motor shaft. The irradiance at pixel group  $k$  of the detector ( $k=1, \dots, 128$ ) is [1]:

$$I(h\nu_k) = I_0(h\nu_k) [1 + \alpha(h\nu_k) \cos 2(\omega_0 t - P_{Sk}) + \beta(h\nu_k) \sin 2(\omega_0 t - P_{Sk})]. \quad (1)$$

The coefficients  $\{I_0, \alpha, \beta\}$  are functions of the photon energy  $h\nu_k$ , associated with pixel group  $k$ . The phase angle,  $P_{Sk}$ , is determined in calibration [4] and accounts for the fact that at  $t=0$ , defined by the trigger pulse of the encoder, the polarizer is oriented at  $-P_{Sk}$ . Because of the delay between reading out one pixel group and the next,  $P_{Sk} = P_{S0} + (k-1)\delta P$ , where  $\delta P = 0.16^\circ$ .

The photodiode array is an integrating detector; thus the raw spectra obtained in the four read-outs of the array can be expressed as integrals,  $S_j(h\nu_k)$  over the four quadrants ( $j=1, \dots, 4$ ) of the optical cycle. Accuracy and precision are enhanced by averaging the  $S_j(h\nu_k)$  values obtained over an even number of optical cycles, yielding  $\langle S_j(h\nu_k) \rangle$ .  $\{I_0, \alpha, \beta\}$  in Eq. (1) can be deduced from the average integrals, thusly:

$$I_{0k} = (1/\pi) (\langle S_{1k} \rangle + \langle S_{2k} \rangle + \langle S_{3k} \rangle + \langle S_{4k} \rangle) \quad (2a)$$

$$\alpha_k = (1/2I_{0k}) (\langle S_{1k} \rangle - \langle S_{2k} \rangle - \langle S_{3k} \rangle + \langle S_{4k} \rangle) \quad (2b)$$

$$\beta_k = (1/2I_{0k}) (\langle S_{1k} \rangle + \langle S_{2k} \rangle - \langle S_{3k} \rangle - \langle S_{4k} \rangle). \quad (2c)$$

From  $\alpha_k$  and  $\beta_k$  of Eqs. (2b-c), the two ellipsometric angles  $\psi_k$  and  $\Delta_k$  can be calculated [1]:

$$\cos \Delta_k = \beta_k / (1 - \alpha_k^2)^{1/2} \quad (3a)$$

$$\tan \psi_k = [(1 + \alpha_k) / (1 - \alpha_k)]^{1/2} \tan A, \quad (3b)$$

where  $\tan \psi_k \exp(i\Delta_k) = r_{pk}/r_{sk}$ . In these equations,  $A$  is the analyzer angle, and  $r_p$  ( $r_s$ ) are the complex amplitude reflection coefficients for  $p$  ( $s$ ) polarized waves, which depend on  $h\nu_k$ .

In order to utilize the dc Fourier component  $I_{0k}$  in Eq. (2a), we start with the expression,  $I_{0k} = I_{00k} R_{Ak}$ , where  $R_{Ak} = \{r_{pk}^2 \cos^2 A + r_{sk}^2 \sin^2 A\}$ . Here,  $R_{Ak}$  is the reflectance of the sample for incident light that is linearly polarized, having its plane of vibration tilted at an angle  $A$  with respect to the  $p$ -direction.  $I_{00k}$  represents the sample-independent spectral response of the optical system. Thus,  $I_{00k}$  can be determined from known optical properties and structure of the starting substrate. In summary, then, the spectrum in  $R_A$  is obtained from

$$R_{Ak} = \{I_{0k}/I_{0k,sub}\} \{r_{p,sub,k}^2 \cos^2 A + r_{s,sub,k}^2 \sin^2 A\}. \quad (4)$$

Equations (3a-b) and Eq. (4) form the theoretical basis of the 3-p technique and connect the measured parameters  $\{I_0, \alpha, \beta\}$  to the processed data  $\{(\psi, \Delta), R_A\}$ . The processed data in turn are related to the film properties  $\{(\epsilon_1, \epsilon_2), d\}$ , namely the dielectric function and thickness, through the Fresnel coefficients, given below Eq. (3b) and in Eq. (4).

Thin films of hydrogenated amorphous silicon (a-Si:H) were prepared by rf PECVD from pure  $\text{SiH}_4$  gas at a pressure of 0.2 Torr. The substrates were Si wafers, overdeposited with dc magnetron-sputtered Cr. The Cr was prepared under conditions optimized for a high density and ultrasmooth surface. The substrates were mounted onto the grounded electrode and heated to  $250^\circ\text{C}$ . For film growth, rf power levels from 2 W to 20 W, were applied to the opposing electrode, yielding power fluxes at the substrate from 0.052 to 0.52  $\text{W}/\text{cm}^2$ . Each triplet of spectra in  $\{(\psi, \Delta), R_A\}$  was computed from a set of average waveform integrals,  $\langle S_j \rangle$  ( $j=1, \dots, 4$ ), acquired in 160 ms during film growth. Thus, the averaging was performed over 4 optical cycles. The repetition time for successive sets of raw spectra was also 160 ms. For operation at 2 W and 20 W, with deposition rates of 80  $\text{\AA}/\text{min}$  and 530  $\text{\AA}/\text{min}$ , this results in a measurement of  $\{(\psi, \Delta), R_A\}$  every 0.2  $\text{\AA}$  and 1.4  $\text{\AA}$ , respectively.

## RESULTS AND DISCUSSION

Figure 1 shows the evolution of the parameters  $\{(\langle \epsilon_1 \rangle, \langle \epsilon_2 \rangle), \delta R_A/R_{A,sub}\}$  obtained during a-Si:H growth onto the Cr substrate at the rf plasma power of 20 W. The real and imaginary parts of the pseudo-dielectric functions of the sample,  $\{(\langle \epsilon_1 \rangle, \langle \epsilon_2 \rangle)\}$ , in Fig. 1 are calculated directly from  $(\psi, \Delta)$  using Fresnel's equations for a single interface [1]. For the lower surface in Fig. 1,  $\delta R_A = R_A - R_{A,sub}$ ; thus,  $\delta R_A/R_{A,sub} = [I_0(t) - I_0(0)]/I_0(0)$ . Here  $I_0(t)$  and  $I_0(0)$  correspond to the dc component spectra for the film measured at time  $t$  during growth and for the substrate measured prior to film growth, respectively. The goal in analyzing these

data is to extract the true dielectric functions and the thicknesses for the one or more layers that describe the a-Si:H film structure, as well as their time evolution.

One analysis procedure that has been applied successfully to solve this problem from a microstructural standpoint has been described earlier [3], but the description will not be repeated here. It relies solely on the real time ( $\psi, \Delta$ ) [or ( $\langle \epsilon_1 \rangle, \langle \epsilon_2 \rangle$ )] spectra and employs a two-layer model for the film. The near-substrate layer is assumed to be a high density a-Si:H material with a thickness-independent dielectric function. The overlying surface layer is assumed to be a low density a-Si:H, consisting of a physical mixture of the underlying dense material and free space (or void), with a dielectric function determined from the Bruggeman effective medium theory [5]. In the analysis of the real time ( $\psi, \Delta$ ) spectra, using linear regression methods, the time evolution of the two layer thicknesses and the relative void volume fraction in the surface layer are extracted, in addition to the dielectric function of the underlying layer.

Figure 2 provides the two thicknesses extracted in this analysis for the deposition of Fig. 1. As described earlier, the observed behavior is consistent with a sequence of nuclei formation and coalescence, followed by bulk film growth. In the nucleation regime in Fig. 2, the underlying layer thickness is less than a monolayer (2.5 Å). In this regime, the surface layer simulates the clusters of atoms that increase in thickness and make contact at  $t \sim 1.75$  s. Cluster contact occurs at a surface layer thickness of 23.5 Å, when the underlying layer reaches one monolayer. From this point onward, the bulk layer increases in thickness, and the surface layer simulates nucleation-generated surface microstructure that smoothens (by  $\sim 5$  Å) in a coalescence process. This analysis has been presented in order to demonstrate the time scale of the growth processes, and to compare the results of this analysis with those of alternative methods.

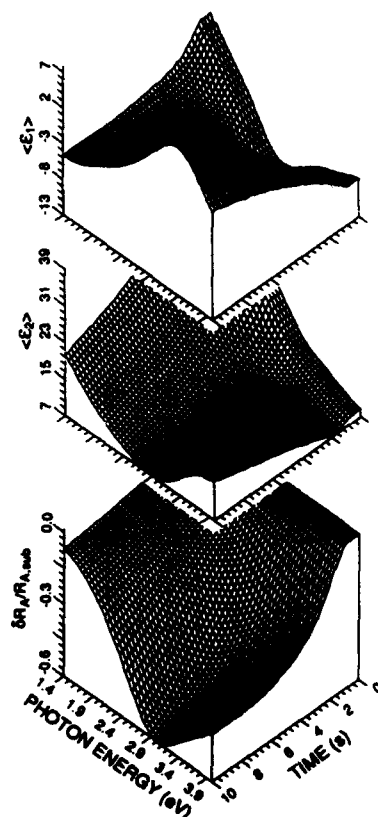
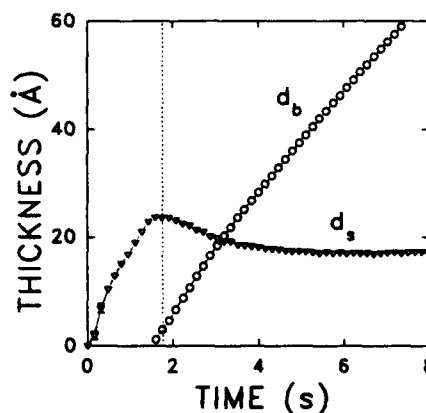


Fig. 1 (left) Three 3-dimensional surfaces, including the real and imaginary parts of the pseudo-dielectric function (upper surfaces), and the relative change in the reflectance, collected during 10 s of a-Si:H PECVD onto a magnetron-sputtered Cr substrate film. The acquisition and repetition times were 160 ms, yielding 64 triplets of spectra.

Fig. 2 (bottom) Surface and bulk layer thicknesses ( $d_s$  and  $d_b$ , respectively) obtained in a linear regression analysis best fit to the two experimental pseudo-dielectric functions (upper surfaces) of Fig. 1. Note that clusters in the initial stage of growth make contact at a time of 1.75 s, when the first bulk-like monolayer forms ( $d_b = 2.5$  Å).



The analysis of Fig. 2 has one drawback in that the dielectric function of the nucleating a-Si:H film is simulated as a physical mixture of bulk material and void according to the predictions of the effective medium theory [5]. This approach neglects possible size effects on the optical properties or possible differences in the structure or composition of the material in isolated particle form. Thus, techniques that provide the dielectric function and thickness of the film independently from each successive real time pair or triplet of spectra are of interest.

Next we will describe a new analysis approach for solving this problem within the framework of a single layer model. This approach relies on all three parameters in Fig. 1, namely  $\{(\epsilon_1, \epsilon_2), \delta R_A/R_{A,sub}\}$ , and the outcome is  $\{(\epsilon_1, \epsilon_2), d\}$  for the film at a specific time in the nucleation process (i.e., when the film consists of a single layer). In the first step, one selects a particular set of spectra of interest collected in the nucleation process (see Fig. 2). A guess is then made for the thickness of the film at this time. Once a thickness value is available, then the  $(\psi, \Delta)$  spectra can be inverted to provide a trial dielectric function for the film. From the trial thickness and dielectric function, and the known optical characteristics of the substrate, a predicted reflectance spectrum can be calculated. The calculated and experimental reflectance spectra,  $R_{Ack}$  and  $R_{Ak}$ , respectively, are compared and an average error is calculated, namely  $\sigma_R = (1/N) \sum_k |R_{Ack} - R_{Ak}| / R_{Ack}$ , where  $N$  is the total number of spectral points. The above steps are repeated for a range of initial thickness guesses. In the absence of errors in  $R_{Ak}$ , the correct thickness value is the one that minimizes  $\sigma_R$ .

Figure 3 demonstrates the application of this approach to the a-Si:H deposition of Figs. 1 and 2. Here, the three spectra collected at  $t=1.6$  s just prior to coalescence have been selected for analysis, and a well-defined minimum in  $\sigma_R$  is observed at 22 Å. The dielectric function corresponding to this thickness is presented in Fig. 4. In Fig. 3, the summation to determine the error is restricted to the energy range below 3.0 eV (see discussion below).

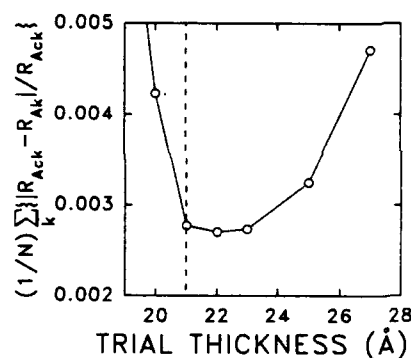


Fig. 3 A schematic of the procedure used to determine the dielectric function and thickness of ultrathin a-Si:H from the 3-p data set of Fig. 1, during nucleation (at  $t=1.6$  s, see Fig. 2). In this figure, a measure of the average deviation between the calculated and experimental reflectance spectra is plotted versus a trial choice for the film thickness. The correct thickness value is the one that minimizes the deviation (22 Å in this case). The broken line shows the thickness obtained in a two-parameter analysis that relies solely on the pseudo-dielectric function of Fig. 1. In this latter analysis, the correct thickness is chosen to ensure that  $\epsilon_2 \rightarrow 0$  at the lowest photon energies.

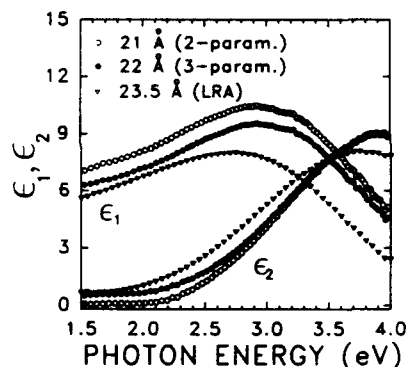


Fig. 4 Dielectric functions for ultrathin a-Si:H obtained in three different analyses. In one case (open points), the thickness was deduced from ellipsometric data alone by ensuring that  $\epsilon_2 \rightarrow 0$  at the lowest photon energy. In the second case (solid points), all three optical parameters were employed, and the thickness was chosen to provide the best overall agreement between the experimental and calculated reflectance spectra. In the third case (triangles), the linear regression analysis approach of Fig. 2 was utilized in which the dielectric function was simulated assuming a mixture of bulk a-Si:H and void.

In order to assess the validity of the solution identified in Fig. 3, we also performed an alternative analysis that relies on the  $(\psi, \Delta)$  [or  $(\langle \epsilon_1 \rangle, \langle \epsilon_2 \rangle)$ ] spectra alone. In this alternative analysis, the film thickness is chosen to ensure that  $\epsilon_2$  vanishes below the a-Si:H band gap. This approach leads to a film thickness of 21 Å, in good agreement with the 3-p solution of Fig. 3. The dielectric function for the a-Si:H, deduced using this thickness is also included in Fig. 4. The two results in Fig. 4 for film thickness solutions of 21 and 22 Å reveal that a  $\pm 0.5$  Å range of thickness leads to a possible range in  $\epsilon_1$  of  $\pm 0.45$  throughout the normal-dispersion regime. Such relatively large variations for small differences in film thickness are characteristic of attempts to extract the dielectric functions of ultrathin films. In spite of this, the overall shape of  $\epsilon$  is not altered by differences in the thickness solution on the Å scale.

Finally, we note that the thickness obtained in the analysis of Fig. 2 is 23.5 Å. The larger discrepancy between this value and the other two is easily understood. The best fit dielectric function in the linear regression analysis, calculated assuming a mixture of bulk a-Si:H and void (48 vol.%), reveals significant deviations in overall shape from those obtained in the other analyses, as shown in Fig. 4. The 0.25 eV higher peak energies in both  $\epsilon_1$  and  $\epsilon_2$ , obtained by the inversions with  $d=21-22$  Å, represent the correct result and appear to be related, not to size effects, but to excess H in the nucleating layer (in comparison with bulk material). Excess H here has also been observed by infrared measurements of PECVD a-Si:H [6]. The higher peak energies in  $\epsilon_1$  and  $\epsilon_2$  cannot be simulated assuming a mixture of bulk material and void; however, the assumption does lead to the proper thickness, within a monolayer (2.5 Å).

The new 3-p analysis as demonstrated in Figs. 3 and 4 provides an advantage over the other two methods, since it requires no assumptions regarding the form of the dielectric function of the film. A number of authors have also performed 3-p measurements either at a single photon energy in real time or spectroscopically on static thin films [7-10]. In order to obtain the properties of single films on known substrates, these authors have often focused on mathematical inversion to extract  $(\epsilon_1, \epsilon_2, d)$  for the film from  $(\psi, \Delta, R_A)$ . Here, we recognize the lower precision and accuracy of the reflectance, and the possible artifacts involved in its measurement due to non-specular light scattering (see next paragraph). As a result, we use this parameter solely to establish a criterion for the proper thickness; the dielectric function is then obtained by inversion of the higher precision  $(\psi, \Delta)$  spectra. It is possible that systematic errors in  $R_A$ , however, may lead to an incorrect thickness and hence a distorted dielectric function. One advantage of the spectroscopic approach is the ability to select the spectral range of analysis to minimize systematic errors, as long as one understands their origin.

The presence of systematic errors in  $R_A$  is clear from the relatively large magnitude of the average error in Fig. 3 for the best fit thickness of 22 Å. The minimum value of  $\sigma_R=0.0025$  in Fig. 3 is larger than would be expected on the basis of random errors alone. The availability of a continuous, reasonably-accurate, two-parameter  $(\psi, \Delta)$  analysis for this deposition (see Figs. 2 and 4) allows us to understand the origin of the systematic errors in  $R_A$ . Namely, they allow us to calculate the predicted reflectance of the structure  $R_{Ac}$ , based on the deduced thickness (Fig. 2) and optical properties (Fig. 4) of the film. Thus, in the main part of Fig. 5 we plot  $L(t) = [I_{0c}(t) - I_{0e}(t)] / [(I_{00} + I_{0c}(t))/2]$ , a measure of the difference between the calculated (c) and experimental (e) reflectance spectra, for the deposition of Figs. 1 and 2 at selected times in the nucleation regime (lines). Positive values over the full range show that the calculated reflectance is as much as 2.5% higher than the measured reflectance. This would be consistent with a loss mechanism in the experiment due to non-specular light scattering from the beam.

The observed reflectance  $R_A$  was found to increase abruptly to values close to the predicted reflectance  $R_{Ac}$  upon extinguishing the plasma. This demonstrated that the scattering arises from particulates in the plasma. In fact, the loss function  $L(t)$  is defined to be proportional to the total integrated scattering, assuming  $L(t) \ll 1$ . The inset of Fig. 5 shows that the scattering loss by plasma particulates obeys a  $\lambda^{-4}$  dependence, where  $\lambda$  is the wavelength of light. Thus, the loss is consistent with Rayleigh scattering from particles much smaller than  $\lambda$ . Such scattering does not influence the  $(\psi, \Delta)$  spectra as demonstrated by the polarization-independence of the scattering loss, measured in transmission through the plasma.

Now the limitations of the 3-p analysis of Figs. 3 and 4 can be understood in greater detail. The parameter  $R_A$  decreases as a function of time during the growth of a-Si:H on Cr due to the higher reflectance of the metal compared to the semiconductor; thus  $\delta R_A / R_{A,sub} < 0$  in Fig. 1. As a result, any loss of reflected light due to scattering by particles in the plasma will simulate an increase in thickness, providing that the dielectric function is fixed in the analysis. It is for this reason that the analysis in Fig. 2 was confined to photon energies of 3.0 eV and lower where the scattering due to particulates in the plasma is minimized.

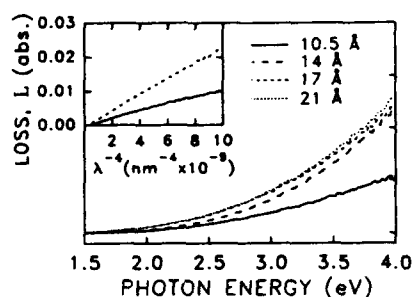


Fig. 5 Scattering loss  $L$  calculated according to Eq. (4) and plotted as a function of photon energy for the a-Si:H deposition of Fig. 1. The results were obtained at different film thicknesses in the nucleation process. The loss in this case is due to light scattering from particles in the plasma. The inset shows selected data plotted versus  $\lambda^{-4}$ , where  $\lambda$  is the wavelength of the light.

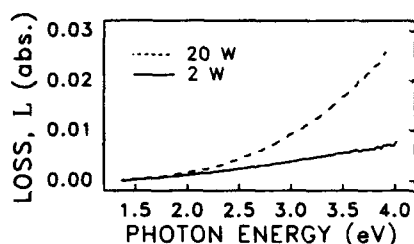


Fig. 6 Scattering loss  $L$  from Eq. (4) plotted as a function of photon energy for two different a-Si:H depositions with rf power fluxes of 0.052 (solid line) and 0.52 mW/cm<sup>2</sup> (broken line). These results were obtained at thicknesses of  $22 \pm 1$  Å, just prior to coalescence.

In spite of the apparent difficulties that the light scattering places on the interpretation of the 3-p data set, useful information on plasma particulates can be obtained concurrently with ellipsometric information. For example, Fig. 6 shows the difference between the calculated and experimental reflectance spectra at the same stage in the deposition process ( $22 \pm 1$  Å) for two films of a-Si:H prepared at power levels of 2 W and 20 W. Because the magnitude of the variations in Fig. 6 scale with the integrated scattering loss, the trends there are consistent with common experience; namely, that the concentration of plasma particulates is minimized under low plasma power conditions. Obviously, plasma particulates are undesirable in the preparation of thin film materials [11], particularly in a-Si:H which is used in a wide variety of electronic applications. The magnitude of the scattering loss allows one to assess the problem and choose a plasma configuration and preparation conditions that minimize its occurrence.

#### ACKNOWLEDGMENTS

This work was supported by the National Science Foundation under grant no. DMR-9217169 and by NREL under subcontract No. XG-1-10063-10.

#### REFERENCES

- [1] R.W. Collins, *Rev. Sci. Instrum.* **61**, 2029 (1990).
- [2] D.E. Aspnes, in *Optical Properties of Solids: New Developments*, edited by B.O. Seraphin (North-Holland, Amsterdam, 1976) Chapt. 15, p. 799.
- [3] I. An, Y.M. Li, H.V. Nguyen, and R.W. Collins, *Rev. Sci. Instrum.* **63**, 3842 (1992).
- [4] I. An, Y. Cong, N.V. Nguyen, and B.S. Pudliner, *Thin Solid Films* **206**, 300 (1991).
- [5] D.E. Aspnes, J.B. Theeten, and F. Hottier, *Phys. Rev. B* **20**, 3292 (1979).
- [6] Y. Toyoshima, K. Arai, A. Matsuda, and K. Tanaka, *Appl. Phys. Lett.* **57**, 1028 (1990).
- [7] D.K. Burge and H.E. Bennett, *J. Opt. Soc. Am.* **54**, 1428 (1964).
- [8] W.-K. Paik and J. O'M. Bockris, *Surf. Sci.* **28**, 60 (1971).
- [9] B.D. Cahan, *Surf. Sci.* **56**, 354 (1976).
- [10] A. Hamnett, S. Higgins, P. Fisk, and W. Albery, *Electroanal. Chem.* **270**, 479 (1989).
- [11] S. Veprék *et al.*, *Mater. Res. Soc. Symp. Proc.* **297**, 13 (1993).

## SPECTROSCOPIC ELLIPSOMETRY CHARACTERISATION OF THIN FILM POLYSILICON

S. LYNCH, L. SPINELLI, M. SHERLOCK, J. BARRETT AND G.M. CREAN,  
National Microelectronics Research Centre, Lee Maltings, Prospect Row, Cork, Ireland.

### ABSTRACT

Phase modulated Spectroscopic Ellipsometry (SE), in the spectral range from 1.5eV to 4.6eV, was employed to characterise thin film polysilicon (poly-Si) deposited by Low Pressure Chemical Vapour Deposition (LPCVD) on SiO<sub>2</sub>/Si(100) substrates as a function of process parameters. The LPCVD deposition temperature was varied from 550°C to 620°C for silane pressures ranging from 100mTorr to 230mTorr. A variation in poly-Si microstructure was observed as a function of film depth. The influence of deposition conditions on poly-Si surface morphology was quantified using both atomic force microscopy (AFM) and SE. An increase in the measured Raman TO phonon amplitude was observed for the 620°C sample set as a function of increasing LPCVD process pressure.

### INTRODUCTION

Polycrystalline silicon (poly-Si) is widely used in microelectronic and photovoltaic applications [1,2]. The microstructural properties of this material are highly process dependent. A variation in microstructure can have a significant effect on the resultant material properties and impact process integration. Therefore, on-line fabrication process control of deposited thin film poly-Si is essential.

To-date, a large volume of data has been published on the optical characterisation of poly-Si [3-9]. These studies have highlighted the significant variation in optical response observed as a function of growth technique, in particular for atmospheric and low pressure chemical vapour deposition (LPCVD). Recently, the optical properties of fine-grain and large-grain poly-Si have been measured using spectroscopic ellipsometry (SE) [7]. However, a lack of experimental data exists detailing the variation in optical response as a function of deposition process parameters. In this work, the optical response of thin-film LPCVD poly-Si is investigated as a function of both process temperature and pressure using a phase modulated SE technique.

### EXPERIMENTAL

LPCVD deposition of poly-Si was performed in a THERMCO diffusion furnace. The poly-Si layers, of target thickness 2000Å, were deposited onto thermal silicon dioxide (layer thickness 850Å) on single crystal CZ n-type 2-4 Ωcm Si(100) substrates. The LPCVD deposition temperature was varied from 550°C to 620°C for silane pressures ranging from 100mTorr to 230mTorr with the experimental matrix detailed in table I.

SE analysis was performed in the energy range 1.5eV (826nm) to 4.6eV (270nm) using a Jobin-Yvon phase modulated ellipsometer at a measurement interval of 0.02eV. The beam spot size was approximately 5x2mm at an angle of incidence of 68°.

Atomic force microscopy (AFM) was used to characterise the surface morphology of the LPCVD poly-Si thin films as a function of deposition conditions. Image acquisition was performed using a Park Scientific AutoProbe AFM (Model AP-100). The analysis area for each micrograph was 4μm<sup>2</sup>. Raman spectra were recorded using a Jobin Yvon micro-Raman spectrometer at a 457.9nm laser line. The calculated laser intensity at the sample surface was 2mW cm<sup>-2</sup>.



**Table I :** LPCVD poly-Si deposition parameters along with AFM surface roughness measurements

| Sample No. | Deposition Temperature (°C) | Deposition Pressure (mTorr) | SiH <sub>4</sub> Flow (scmm) | Deposition Rate (Å/min) | Surface Roughness (Å) |
|------------|-----------------------------|-----------------------------|------------------------------|-------------------------|-----------------------|
| A          | 620                         | 100                         | 32                           | 60                      | 176                   |
| B          | 620                         | 150                         | 70                           | 84                      | 203                   |
| C          | 620                         | 200                         | 41                           | 67                      | 95                    |
| D          | 620                         | 230                         | 70                           | 84                      | 127                   |
| E          | 580                         | 100                         | 38                           | 24                      |                       |
| F          | 580                         | 150                         | 79                           | 32                      | 34                    |
| G          | 580                         | 230                         | 79                           | 32                      |                       |
| H          | 550                         | 100                         | 41                           | 12                      |                       |
| I          | 550                         | 150                         | 82                           | 15                      | 11                    |
| J          | 550                         | 200                         | 54                           | 13                      |                       |
| K          | 550                         | 230                         | 82                           | 15                      |                       |

## RESULTS AND DISCUSSION

The measured imaginary part of the pseudodielectric functions for the 230 mTorr series of LPCVD samples, plotted from 2.6eV to 4.6eV, are presented in figure 1. Significant differences are observed in the optical properties of the three samples reflecting the complex microstructure of the poly-Si thin films as a function of LPCVD deposition conditions.

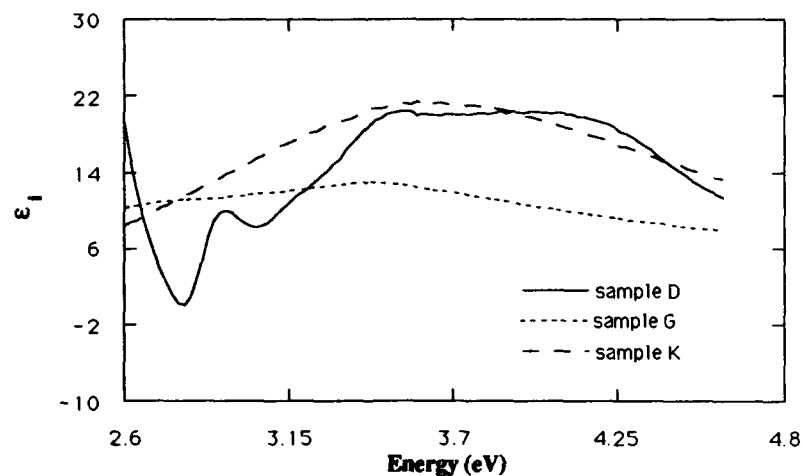


**Figure 1:** Measured imaginary parts of the pseudodielectric function spectra for samples D, G and K over the spectral range 2.6eV to 4.6eV.

The measured SE spectra were analysed using the three layered optical model detailed in figure 2. The dielectric function data employed for the poly-Si layers was fine grain poly-Si [7] for depositions at 620°C and amorphous-Si (a-Si) [10] for deposition temperatures below this. A fine grain poly-Si dielectric function was used as the transition temperature from a-Si to crystalline poly-Si occurs between 580°C to 600°C [11]. The Bruggeman effective medium approximation was employed to model inhomogeneous layers [12]. The goodness of fit between the experimental and best fit simulated SE spectra is given by the value of  $\chi^2$  from a least squares fitting routine.

Calculated  $\chi^2$  values ranged from 15.5 to 19.1, 7.5 to 16.3 and 8.4 to 9.4 for the 620°C, 580°C and 550°C sample sets respectively. The reason for poor spectral fitting can be observed from the calculated best fit simulated SE spectrum presented in figure 3. While the interference oscillations are well modelled, the fit is poor in the UV spectral region, i.e. the near surface of the poly-Si layer.

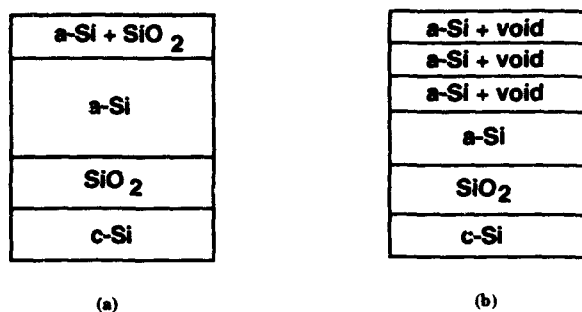


**Figure 2:** Three and five layered SE optical models, on c-Si substrates, for samples deposited at 550°C and 580°C. For deposition at 620°C, a-Si was replaced by crystalline fine grain poly Si in the models.

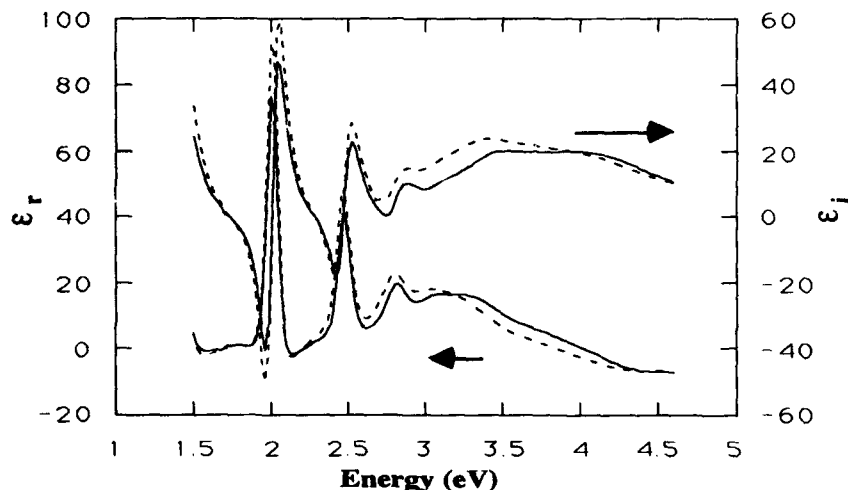


**Figure 3:** Experimental (solid lines) and best fit, employing a three layer optical model, (dashed lines) pseudodielectric function spectra for sample B.

It was clear from the  $\chi^2$  values obtained from best fits to a three layer structure that a more complex microstructural model was required. A model incorporating surface roughness and a graded refractive index for the thin film poly-Si layer was therefore elaborated. The optimum layered structure is shown in figure 2(b). The experimental and best fit simulated (five layered model) SE spectra for samples B and J are presented in figures 4 and 5.

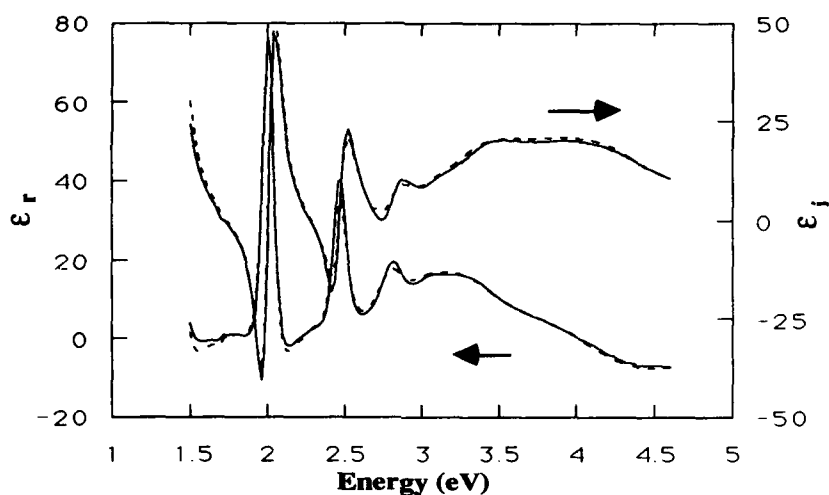


**Figure 4:** Experimental (solid lines) and best fit, employing a five layer optical model, (dashed lines) pseudodielectric function spectra for sample B.

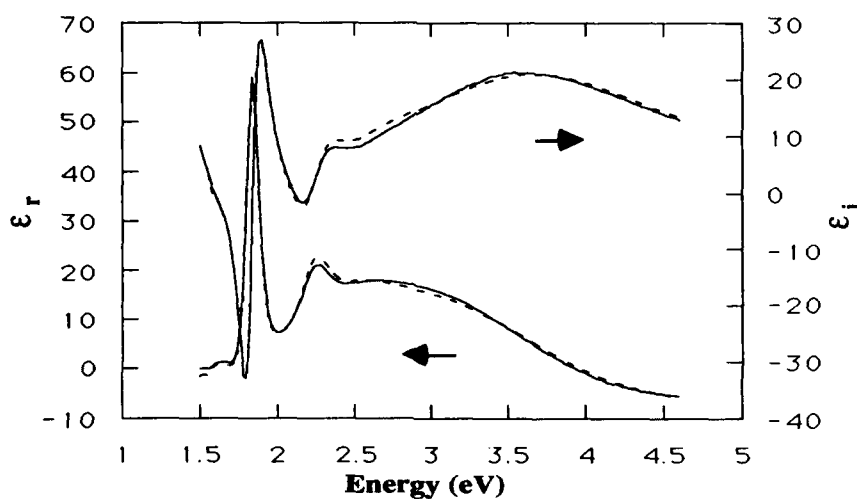


**Figure 5:** Experimental (solid lines) and best fit, employing a five layer optical model, (dashed lines) pseudodielectric function spectra for sample J.

It is evident, from figures 4 and 5, that the fits in the UV spectral region are now in good agreement with the experimental data. The extracted best fit material parameters for the complete LPCVD sample matrix are tabulated in table II. Two distinct observations can be made from table II; firstly that the five layer model proposed in figure 2(b) has significantly improved  $\chi^2$  values and secondly that the near surface region of the poly-Si structure (15% to 20% of layer thickness) is less dense than the underlying poly-Si irrespective of process temperature as reflected in the best fit parameters for layers 3, 4 and 5. The values of  $\chi^2$  obtained are all close to 1 reflecting the improvement in fit observed in figures 4 and 5. This variation in microstructure, calculated from an effective optical response, is consistent with previous optical data [8,9] and maybe ascribed to competitive poly-Si grain growth [5].

**Table II:** Extracted SE parameters for five layer optical models. The second component in the layers was void. For samples A to D, a-Si was replaced by fine grain poly-Si.

| Sample | Layer 1<br>Thickness (Å)<br>SiO <sub>2</sub> | Layer 2<br>Thickness (Å)<br>Percentage a-Si | Layer 3<br>Thickness (Å)<br>Percentage a-Si | Layer 4<br>Thickness (Å)<br>Percentage a-Si | Layer 5<br>Thickness (Å)<br>Percentage a-Si | $\chi^2$ |
|--------|--|---|---|---|---|----------|
| A      | 848  | 1762, 100                                   | 176, 97                                     | 50, 80                                      | 80, 76                                      | 4.1      |
| B      | 859  | 1763, 100                                   | 190, 90                                     | 71, 80                                      | 34, 60                                      | 1.5      |
| C      | 846  | 1712, 100                                   | 190, 93                                     | 85, 89                                      | 72, 72                                      | 2.7      |
| D      | 846  | 1679, 100                                   | 257, 90                                     | 15, 80                                      | 72, 70                                      | 2.0      |
| E      | 845  | 1708, 100                                   | 237, 93                                     | 82, 85                                      | 21, 70                                      | 2.0      |
| F      | 846  | 1378, 90                                    | 165, 86                                     | 179, 88                                     | 17, 56                                      | 2.6      |
| G      | 853  | 1543, 100                                   | 337, 95                                     | 76, 76                                      | 93, 57                                      | 1.0      |
| H      | 849  | 1800, 100                                   | 308, 90                                     | 52, 81                                      | 23, 72                                      | 0.7      |
| I      | 850  | 1730, 100                                   | 347, 92                                     | 70, 82                                      | 21, 73                                      | 0.6      |
| J      | 848  | 1531, 100                                   | 426, 90                                     | 95, 82                                      | 16, 69                                      | 0.5      |
| K      | 848  | 1568, 100                                   | 395, 90                                     | 83, 82                                      | 18, 69                                      | 0.5      |

The AFM results presented in table I show surface roughness as a function of LPCVD poly-Si deposition conditions. It is observed that the measured surface roughness is process temperature dependent. Figure 6 shows the AFM images of the surface morphology of samples B and I. The difference between the two samples is striking. The AFM micrograph of the surface of the 550°C poly-Si film is smooth with large grains whereas the 620°C poly-Si film has a rough surface with small needle-like grains and complicated surface morphology. No direct relationship was found between the degree of film roughness and deposition pressure for poly-Si films deposited at 620°C.

Analysis of the best-fit material parameters for layer five, extracted from the measured SE spectra, shows that the extracted SE data is consistent with the AFM results. In particular, it details that as the process temperature decreases the surface of the poly-Si layers become smoother. Thin film LPCVD poly-Si layers deposited at 620°C show a variation in poly-Si content from 60% to 76% with large variations in layer thickness (34Å to 80Å). The intermediate deposition temperature films have lower percentages of poly-Si in layer five, 56% to 70%, and lower layer thicknesses. Deposition at 550°C is characterised by a high percentage of poly-Si, 69% to 73%, with layer thickness less than 23Å i.e. smooth surfaces. It should be noted that the difference between the two optical models (five and three layer) was less than 5% for poly-Si layer thickness determination. Comparison with mechanical profilometry measurements showed a maximum difference of 4% in poly-Si layer thickness for the five layer models.

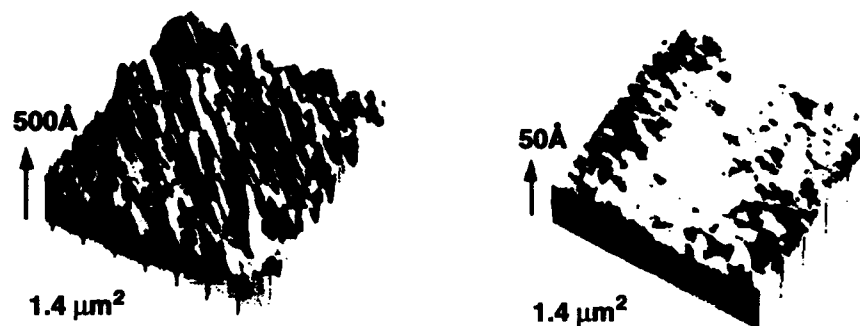


**Figure 6:** AFM micrographs of the surfaces of samples B and I over  $1.4 \mu\text{m}^2$ .

The relationship between deposition pressure and calculated  $\chi^2$  values for the different deposition temperatures is presented in figure 7. The variation in  $\chi^2$  values for the LPCVD depositions at  $550^\circ\text{C}$  is small (0.5 to 0.7) indicating that the optical properties of the amorphous poly-Si deposited at  $550^\circ\text{C}$  are not process pressure dependent in the range 100mTorr to 230mTorr. A similar response is observed for the  $580^\circ\text{C}$  series. However,  $\chi^2$  values vary considerably, from 1.5 to 4.1, for poly-Si deposition at  $620^\circ\text{C}$ . One may therefore conclude that the dielectric function of crystalline poly-Si deposited at  $620^\circ\text{C}$  is process pressure dependent.

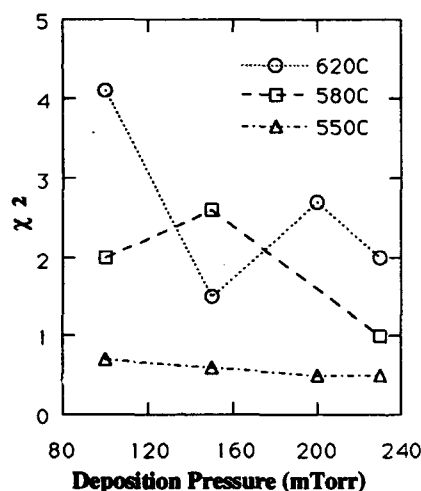


**Figure 7:** Relationship between deposition pressure and  $\chi^2$  values for the five layered optical models for deposition temperatures  $550^\circ\text{C}$ ,  $580^\circ\text{C}$  and  $620^\circ\text{C}$ .

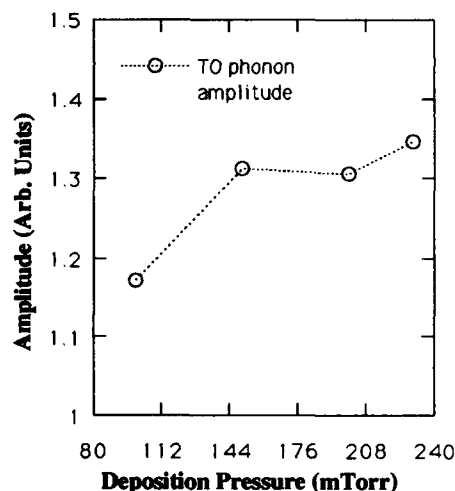


**Figure 8:** Raman TO phonon amplitude as a function of process pressure for the LPCVD depositions at  $620^\circ\text{C}$ .

In order to further elucidate the physical mechanism responsible for this variation in calculated  $\chi^2$  values as a function of deposition pressure Raman spectroscopy was employed. The TO phonon amplitude as a function of deposition pressure at  $620^\circ\text{C}$  is shown in figure 8. An increase in TO phonon amplitude as a function of increasing process pressure is observed.

This is consistent with an increase in the integrated crystalline quality of the LPCVD poly-Si thin films [4]. It should be noted that no direct relationship was found between the degree of film roughness and deposition pressure and that this parameter will also have an influence on the dielectric function response.

## CONCLUSIONS

In this study SE, AFM and Raman spectroscopy were employed to characterise thin film poly-Si layers as a function of both LPCVD deposition pressure and temperature. A five layer optical model was found necessary to accurately reflect the microstructure of the LPCVD poly-Si thin films. A continuous variation in the optical properties consistent with a variation in poly-Si film microstructure was observed. The influence of deposition conditions on film morphology was quantified using AFM analysis and results were found to be in good agreement with material parameters extracted from SE analysis. Raman spectroscopy revealed an increase in TO phonon amplitude as a function of deposition pressure for films deposited at 620°C indicating significant variation in microstructure. This was reflected in the observed process pressure dependent dielectric function of the 620°C deposited films obtained using SE.

## ACKNOWLEDGEMENTS

The authors would like to thank G.E. Jellison for supplying the optical properties of fine grain crystalline polysilicon.

## REFERENCES

- [1] F. Faggin and T. Klein, *Solid State Electron.*, **13**, 1125 (1970).
- [2] *Physics of Semiconductor Devices*, S.M. Sze, J. Wiley & Sons (1981).
- [3] T.I. Kamins, *J. Electrochem. Soc.*, **127**, 686 (1980).
- [4] G. Harbeke, L. Kraushauer, E.F. Stegmeier A.E. Widmer, H.F. Kappert and G. Neugebauer, *J. Electrochem. Soc.*, **131**, 675 (1984).
- [5] C. Khul, H. Scholtterer and F. Schwidetsky, *J. Electrochem. Soc.*, **121**, 1496 (1974).
- [6] B.G. Bagley, D.E. Aspnes, A.C. Adams and C.J. Mogab, *Appl. Phys. Lett.*, **38**, 56 (1981).
- [7] G.E. Jellison, M.F. Chisholm and S.M. Gorbatkin, *Appl. Phys. Lett.*, (1993).
- [8] G.E. Jellison, M. Keefer and L. Thorquist, *Proceedings MRS Fall Meeting* (1992).
- [9] L.M. Asinovsky, *Thin Solid Films*, **233**, 210 (1993).
- [10] *Handbook of Optical Constants of Solids*, ed. E.D. Palik, Academic Press, New York, (1985).
- [11] *VLSI Technology*, S.M. Sze, J. Wiley & Sons (1991).
- [12] D.A.G. Bruggeman, *Ann. Phys. (Leipzig)* **24**, 636 (1936).

## CHARACTERIZATION OF POLYCRYSTALLINE SILICON MULTILAYERS WITH THIN NITRIDE/OXIDE FILMS USING SPECTROSCOPIC ELLIPSOMETRY

L.M. ASINOVSKY, Rudolph Research, Flanders, NJ 07836

### ABSTRACT

Spectroscopic ellipsometry has been used to characterize oxide/poly-Si/oxide with thin nitride/oxide layer. Films were deposited on Si substrate using low-pressure chemical vapor deposition (LPCVD) techniques. The measurements were taken at angles of incidence of 65 and 70 degrees in the wavelength range from 300 to 800 nm. The analysis of the data using effective medium and two-dimensional Lorentz oscillator approximations identified complete recrystallization of the poly-Si after annealing and its transformation to  $\mu$ -c-Si. Three wafers taken at the sequential stages of the manufacturing process were studied. Although parameters of the thin nitride/oxide layers are strongly correlated, reasonable estimates of the thicknesses were found. The results were consistent with the measured Auger electron spectroscopy (AES) profiles.

### Introduction.

$\text{SiO}_2/\text{Si}_3\text{N}_4/\text{SiO}_2$  (ONO) structure is widely used in the manufacturing of the memory devices as a dielectric insulator and surface passivation material. One of the common application is the use of the ONO on top of the  $\text{SiO}_2$ /polySi/ $\text{SiO}_2$  (OPO) structure deposited on the Si substrate.

In order to characterize the properties of the ONO, it is important accurately determine thicknesses and structure (purity of the material) of the sublayers. Precise determination of these parameters is very difficult and several methods, using single-wavelength ellipsometry of etch-beveled surface [1] or IR ellipsometry [2], were developed. However, the former method is destructive and the latter is difficult to implement for OPO-ONO structure.

The spectroscopic ellipsometry is increasingly used for characterization of the challenging thin film structures and its application to the OPO-ONO structure has been recently reported [3]. Polysilicon was represented using Effective-Medium-Approximation (EMA) and the measurement were made only on complete OPO-ONO wafer. The discrepancy of the EMA representation can therefore result in additional errors of the ONO parameters determination.

In this work a set of three witness wafers, taken at the sequential stages of the OPO-ONO manufacturing process was measured using spectroscopic ellipsometry. Polysilicon optical constants were represented using harmonic oscillator model, which yields better fit to the model than EMA. This allowed more accurate estimate of the ONO parameters. The results were found consistent with the Auger measurements.

### Measurement and data reduction.

P-type Czochralski {100} silicon 16-25  $\Omega$  cm wafers were used as substrates. Wafers were thermally oxidized, poly-Si was LPCVD deposited at  $\sim 650^\circ\text{C}$ , phosphorus ion-doped ( $\sim 10^{18}$  i/cm<sup>3</sup>) and annealed for 2 hours at  $\sim 1000^\circ\text{C}$  to improve stoichiometry. Silicon dioxide and  $\text{Si}_3\text{N}_4$  were subsequently deposited with Plasma-Enhanced CVD (PECVD).

Rapid thermal oxidation (RTO) in dry oxygen was used to reoxidized surface of the  $\text{Si}_3\text{N}_4$ . A set of three samples (witnesses), taken at the sequential stages of the technological process, were measured at room temperature and atmosphere (fig.2). Spectra were taken at two angle of incidence (75 and 60 deg.) in the range of 300 to 800 nm in 5 nm intervals (100 points). Rudolph Research S2000 Spectroscopic Ellipsometer was used for measuring and modeling of the data. Auger Electron Spectroscopy depth profiling was done for the sample #3 with 1  $\mu\text{m}$ , 3keV measuring electron beam in the 1x1mm area, sputtered by 140  $\mu\text{A}/\text{cm}^2$ , 2keV electron beam.

Spectroscopic ellipsometry provides  $\cos \Delta$ ,  $\tan \Psi$  spectra, where  $\Delta$  and  $\Psi$  are ellipsometric angles that describe reflection of the polarized light from the samples. The physical parameters of the sample are found by modeling of  $\Delta, \Psi$  spectra and comparing it to the measured one. The best fit to the experimental data is achieved by minimizing  $\chi^2(p_1, \dots, p_m)$  merit function with Marquardt-Levenberg linear regression algorithm, where  $p_1, \dots, p_m$  are physical parameters to be found[4]:

$$\chi^2 = \frac{1}{2N} \sum_j \left[ W_1 \left( \frac{\Psi_{\text{calc}}(p_1 \dots p_m) - \Psi_{\text{exp}}}{\sigma_{\tan \Psi}} \right)^2 + W_2 \left( \frac{\Delta_{\text{calc}}(p_1 \dots p_m) - \Delta_{\text{exp}}}{\sigma_{\Delta}} \right)^2 \right]$$

where  $N$  - number of points in the measured spectrum,  $W_1, W_2$  - weight coefficients,  $\sigma_{\Delta}$  and  $\sigma_{\Psi}$  are standard deviations of the respective measured values. Standard deviations ( $\delta p_i$ ) of the parameters  $p_i$  are determined from the covariance matrix  $C$ :  $\delta p_i = \sqrt{C_{ii}}$ , where  $C_{ij} = H_{ij}^{-1} = \left( \frac{1}{2} \frac{\partial^2 \chi^2}{\partial p_i \partial p_j} \right)^{-1}$ . Fit error (FE) is used to compare the quality of the fit:  $\text{FE} = \chi(\sigma_{\Delta} \rightarrow 1, \sigma_{\Psi} \rightarrow 1)$ .

Several approaches are used to represent optical properties of the materials. Standard reference spectra [5] is used for Si substrate and  $\text{SiO}_2$  thermal oxide. Bruggeman EMA is used to represent optical response of the polysilicon and oxynitride. The effective refractive index  $n_E$  in this approximation can be obtained from the following equation:

$$\sum_i f_i \frac{n_i^2 - n_E^2}{n_i^2 + 2n_E^2} = 0; \quad \sum_i f_i = 1;$$

where  $f_i, n_i$  are volume fractions and refractive indices of the constituents, respectively.

Harmonic (2D-Lorentz) Oscillators approximation (HOA) [7][9] is used to represent optical constants spectrum of the polysilicon ( $\mu\text{c-Si}$ ):

$$\epsilon(E) = 1 + \sum_{\alpha=1}^n A_{\alpha} \left\{ \frac{1}{E + E_{\alpha} + i\Gamma_{\alpha}} - \frac{1}{E - E_{\alpha} + i\Gamma_{\alpha}} \right\}$$

where  $\epsilon = \epsilon_1 + i\epsilon_2$  is a dielectric function,  $n=4$ ,  $A_{\alpha} = |A_{\alpha}|e^{i\phi_{\alpha}}$ ,  $E_{\alpha}$  and  $\Gamma_{\alpha}$  are amplitude, energy and dumping coefficient of the  $\alpha$ -th oscillator,  $E$  is energy(wavelength) in eV.

## Analysis of the results and discussion

The modeling of the samples #1, #2, #3 was done sequentially; the film stack found from the sample #1 was assumed unaltered and used in further analysis of samples #2 and #3. The general pattern of the  $\Delta, \Psi$  spectra (fig. 3) behavior is set by the OPO structure. Addition of the relatively thin layers of Si nitride and oxide on the top, causes almost parallel shift in vertical direction of the UV shoulder (where poly-Si is opaque) and small change in the wavelength position of the interference peaks. This observation emphasizes the importance of accurate description of the underlying OPO structure and receiving of the good fit to the measured data.



Poly-Si was first modeled using Bruggeman EMA with c-Si, a-Si, SiO<sub>2</sub> as a constituents of the composite mixture. The modeling procedure for this type of application is described in details elsewhere [6] and was followed. The layer was represented by two films to reflect the presence of the roughness interface. The thicknesses of all layers and constituents volume fractions of the poly-Si films were iterated. The results of the best fit ( fig. 1 ) suggest that poly-Si layer was almost completely recrystallized during annealing with small concentration (6%) of the a-Si and virtually no SiO<sub>2</sub> or void network in the interface layer. However, distinctive discrepancies of the fit in the UV and IR ends of the spectrum indicate that these results must be taken very cautiously and can serve only as a raw estimate of the real structure. The behavior of the spectrum calls for the increase of the 'amorphization' in the top part of the poly-Si - to smoothen the 365 nm peak without increase in the absorption , unavoidably brought in by the a-Si, as it can only worsen the fit in the NIR. The most plausible, explanation of this behavior is that EMA can not correctly represent optical properties of the recrystallized poly-Si ( $\mu$ c-Si) . One of the main reasons is broadening of the interband transition peaks due to disordering and finite crystallite size [7][8]. As a result the effect of the micro-crystallinity is most significant in the vicinity of these critical points (CPs) - in our case 2D CP at 365 nm, which arises from the transition along the  $\Gamma$ -L axis of the Brillouin zone.

It is appropriate, therefore, to apply Harmonic Oscillator (HO) representation of the dielectric function. The model parameters of sample#1 found in EMA were used with the top poly-Si film represented by HO. The thicknesses of all films and parameters of the oscillators were allowed to adjust .Excellent fit was achieved in the UV shoulder, but no improvement in the IR part of the spectrum . Thicknesses of the layers almost did not change (fig.1), but optical constants spectrum , modeled with HO , assumed characteristic for  $\mu$ c-Si shape (fig.3). It is interesting to notice, that the optical constants spectrum received in HO approximation has exactly the same behavior as previously reported spectrum[6] derived by direct iteration on optical constants during simultaneous modeling of data taken at two AOI on a similar sample.

It is conceivable that long-range order was not completely restored during recrystallization process, which causes some deviation from the c-Si .To check what kind of correction of the optical constants spectrum can bring about the improvement in the fit in the NIR range, the HO approximation was also applied to the third layer . All parameters of the filmstack were allowed to adjust to achieve the best fit . Discrepancy in the NIR disappear but, remarkably, the optical constants spectra generated using HO approximation was practically undistinguishable from reference spectrum. The only difference was the decrease on 0.01 in absorption coefficient vs. the reference spectrum.

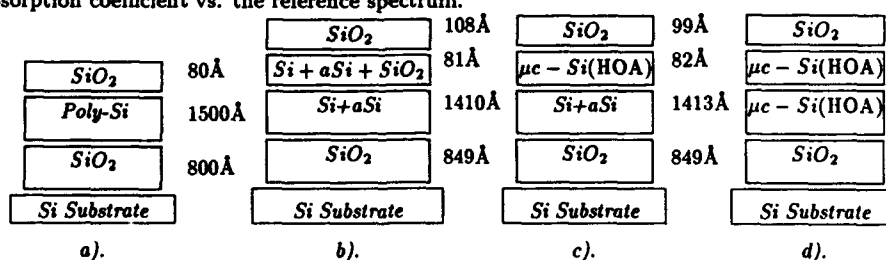


fig.1 Models of the sample#1 : a). Nominal filmstack ; b). model#1 ( EMA representation): film#2- c-Si, film#3- 0.94 c-Si + 0.06 aSi; FE=1.78,  $\chi^2=54.6$  ; c). model#2 (Combined EMA and HOA) FE=3.6,  $\chi^2=43$  ; d).model#3 (HOA): parameters of HO - in Table 2, FE=3.08,  $\chi^2=2.1$ .

Table I: Parameters of the oscillators in HOA of sample#1(model#3)

| $\mu\text{c-Si(HOA)}$ Film#2 |         |         |          |              | $\mu\text{c-Si(HOA)}$ Film#3 |         |               |              |
|------------------------------|---------|---------|----------|--------------|------------------------------|---------|---------------|--------------|
| #                            | E (eV)  | A       | $\Gamma$ | $\Phi$ (rad) | E (eV)                       | A       | $\Gamma$ (eV) | $\Phi$ (rad) |
| 1                            | 3.3943  | 2.6459  | 0.169    | -0.5836      | 3.3574                       | 2.5808  | 0.1024        | -0.9606      |
| 2                            | 3.6469  | 9.7382  | 0.4854   | -0.5315      | 3.3968                       | 8.9092  | 0.5437        | -0.534       |
| 3                            | 4.2592  | 6.4137  | 0.1797   | 0.1292       | 4.3382                       | 6.4845  | 0.01          | 0.0875       |
| 4                            | 10.3197 | 17.3454 | 3.3609   | 0.9647       | 8.6315                       | 23.1005 | 2.6473        | 0.7126       |

|   |   |  |  |   |   |
|---|---|--|--|---|---|
| <div>SiO<sub>2</sub></div> <div><math>\mu\text{c-Si(HOA)}</math></div> <div><math>\mu\text{c-Si(HOA)}</math></div> <div>SiO<sub>2</sub></div> <div>Si Substrate</div> | <div>101<math>\pm</math> 0.7Å</div> <div>90<math>\pm</math> 0.7Å</div> <div>1405<math>\pm</math>3Å</div> <div>849<math>\pm</math>1Å</div> | <div>Si<sub>3</sub>N<sub>4</sub>+SiO<sub>2</sub></div> <div>SiO<sub>2</sub></div> <div><math>\mu\text{c-Si(HOA)}</math></div> <div><math>\mu\text{c-Si(HOA)}</math></div> <div>SiO<sub>2</sub></div> <div>Si Substrate</div> | <div>142<math>\pm</math>0.4Å</div> <div>101Å</div> <div>90Å</div> <div>1405Å</div> <div>849Å</div> | <div>SiO<sub>2</sub></div> <div>Si<sub>3</sub>N<sub>4</sub></div> <div>SiO<sub>2</sub></div> <div><math>\mu\text{c-Si(HOA)}</math></div> <div><math>\mu\text{c-Si(HOA)}</math></div> <div>SiO<sub>2</sub></div> <div>Si Substrate</div> | <div>59.4<math>\pm</math>5Å</div> <div>48.6<math>\pm</math>5Å</div> <div>135<math>\pm</math>10Å</div> <div>90Å</div> <div>1405Å</div> <div>849Å</div> |
|   |   |  |  |   |   |
|   |   |  |  |   |   |
|   |   |  |  |   |   |
|   |   |  |  |   |   |
| Sample #1   |   | Sample#2   |  | Sample#3  |   |

fig.2 . Results of the modeling Samples #1- #3.

$\pm$  - indicates 90% confidence interval for thickness value, which was iterated during the modeling. Sample#1 :  $\chi^2=2.1$ , FE=3.08 (HO parameters are in Table 1). Sample#2:  $\chi^2=4.2$ , FE=0.5, Silicon Nitride EMA:  $0.842 \pm 0.002 \text{ Si}_3\text{N}_4 + 0.158 \text{ SiO}_2$ . Sample#3:  $\chi^2=23$ , FE=0.85.

Modeling of the sample#2 was done using results of the sample#1. Best fit was achieved by iteration on thickness and constituents volume fractions of silicon nitride using EMA representation (fig.2). Sample#3 was received by oxidation (RTO) of sample#2. First modeling was done in the assumption that oxidation affected only two top layers and underlying structure did not changed. Thickness and volume fractions of silicon nitride (in EMA) and thickness of the top SiO<sub>2</sub> were used as adjustable parameter. No reasonable fit was achieved. The growth of the oxide at the inner surface of the nitride layer reported by T.S.Chao et al [1] can be a possible explanation. During the oxidation optical thickness is practically invariant. This fact and the thickness of the layers makes the problem very ambiguous and dependant upon initial values. Correlation of the parameters result in significant uncertainty of the thickness values (fig.2), which neither further UV, nor reflectivity measurements can improve [10] . However, correct selection of the initial approximation gives a good estimate of the thickness of the films even with crude model of sharp interfaces. Auger profile measurement gave consistent results for the thicknesses of the films, indicated presence of  $\sim 5\%$  of SiO<sub>2</sub> in the Nitride layer and  $\sim 5\text{\AA}$  interface layer between nitride and oxide; this is within margin of error due to correlation of the parameters in ellipsometric measurement.

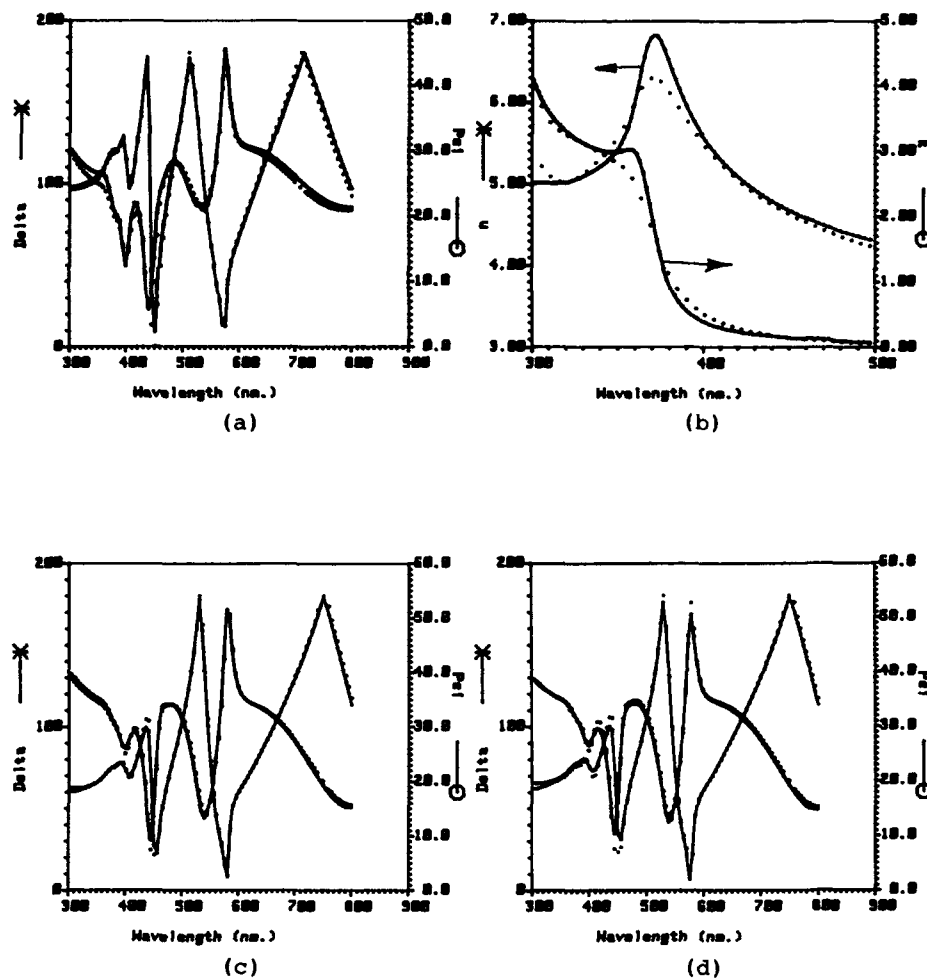


Fig.3 Best fit results . a). Sample #1, Model 1 (EMA representation); b).  $n, k$  of the  $\mu c - Si$  calculated in HOA compared to reference  $c-Si$  spectrum c). Sample #2; d). Sample #3. Dotted line - measured data (for b - HOA calculated  $n, k$ ), — (solid line) calculated spectra (for d - reference spectra).

## Conclusion

Spectroscopic ellipsometry has been used to characterize oxide/ poly-Si/oxide/nitride/oxide (OPONO) structure on the Si substrate. Analysis of the data taken at AOI 75° and 65° deg. in 300-800 nm spectral range identified complete recrystallization of the poly-Si after annealing and suggested its transformation to the  $\mu$ c-Si. Modeling of the results using Bruggeman EMA and HOA, showed that Harmonic Oscillators representation significantly improves the fit and yields results consistent with the that received by direct iteration of optical constants in modeling of Multiple Angle of Incidence data.

Finally, accurate representation of the underlying OPO structure and analysis of the samples taken at the sequential stages of the technological process allowed to estimate thickness of the ONO sublayers.

## REFERENCES

1. T.C. Chao, C.L. Lee, T.F. Lei J. Appl.Phys.**73**, 1732, (1993).
2. M. Wiedner, A.Roseler Physica Status Solidi (a) **130**,115 (1992).
3. P.G. Snyder,Y.M. Xiong,J.A. Woollam et al. Surf. Interface Anal. **18**, 113(1992).
4. W.H.Press,B.P.Flannery,W.T.Vetterling'Numerical Recipes',Cambridge Univ.Press, 1986.
5. Reference  $n,k$  spectra was taken from D.E.Aspnes, A.A.Studna,E.Kinsborn, Phys.Rev B **29**, 768 (1978) and Handbook of Optical Constants of Solids, ed. by E.D.Palik (Academic Press ,NY, 1985)
6. L.M. Asinovsky Thin Solid Films **233**, 210 (1993).
7. V.I. Gavrilenko et al. Phys. Stat. Sol. **155**,723(1989).
8. S.Boultadakis, S.Logothetidis, S.Ves J.Appl.Phys. **72**, 3648 (1992); *ibid* **73**, 914 (1993).
9. F.Terry J. Appl. Phys. **70**, 409 (1991).
10. L.M. Asinovsky, to be published elsewhere.

## IN-SITU DUAL-WAVELENGTH ELLIPSOMETRY AND LIGHT SCATTERING MONITORING OF Si/Si<sub>1-x</sub>Ge<sub>x</sub> HETEROSTRUCTURES AND MULTI-QUANTUM WELLS

C. PICKERING\*, D.A.O. HOPE\*, W.Y. LEONG\*, D.J. ROBBINS\* AND R. GREEF†  
\* Defence Research Agency, St Andrews Road, Malvern, Worcs WR14 3PS, UK.  
† Dept of Chemistry, University of Southampton, Southampton, SO9 5NH, UK.

### ABSTRACT

In-situ dual-wavelength ellipsometry and laser light scattering have been used to monitor growth of Si/Si<sub>1-x</sub>Ge<sub>x</sub> heterojunction bipolar transistor and multi-quantum well (MQW) structures. The growth rate of B-doped Si<sub>0.8</sub>Ge<sub>0.2</sub> has been shown to be linear, but that of As-doped Si is non-linear, decreasing with time. Refractive index data have been obtained at the growth temperature for  $x = 0.15, 0.20, 0.25$ . Interface regions ~ 6-20Å thickness have been detected at hetero-interfaces and during interrupted alloy growth. Period-to-period repeatability of MQW structures has been shown to be  $\pm 1\text{ML}$ .

### INTRODUCTION

As the complexity of device structures increases it is becoming more important to produce multilayer structures to a precise specification. Si<sub>1-x</sub>Ge<sub>x</sub> alloys are under investigation for applications in heterojunction bipolar transistors (HBT) and MQW far-IR detectors. These structures require growth of very thin, strained layers with well controlled constant, or graded, composition and dopant profiles. Achievement of the ultimate performance of such devices may require in-situ process control. This paper reports real-time monitoring of low-pressure vapour phase epitaxial (LPVPE) growth of both HBT and MQW structures using in-situ dual-wavelength ellipsometry (DWE) and laser light scattering (LLS). We have previously used these techniques to optimise the growth of high quality homoepitaxial Si layers<sup>1,2</sup> and preliminary results on Si<sub>1-x</sub>Ge<sub>x</sub>/Si heterostructures have been reported recently<sup>2,3</sup>.

### EXPERIMENTAL

The epitaxial layers were grown on Si(001) substrates by LPVPE in a UHV-background stainless steel reactor described previously<sup>4</sup>, growth temperatures being in the range 610-750°C. GeH<sub>4</sub> and SiH<sub>4</sub> in ratios of 0.05-0.08:1 were used, together with H<sub>2</sub> at total pressures of ~15Pa, to produce alloy layers with  $0.15 \leq x \leq 0.25$ . B<sub>2</sub>H<sub>6</sub> and AsH<sub>3</sub> were used for p- and n-type doping, respectively. Heterostructures were usually grown by using a 10-20s growth interrupt at each interface to establish correct gas ratios before switching into the growth chamber, total gas pressure being maintained by balance H<sub>2</sub> during the interrupt.

In-situ DWE measurements were made using the 364nm (3.41eV) and 488nm (2.54eV) lines from an Ar<sup>+</sup> laser at 70° angle of incidence, together with a rotating-analyzer system as described previously<sup>1,2</sup>. LLS measurements were made using the 488nm line from the same source beam, the scattered intensity (I) being monitored normal to the wafer<sup>1,2</sup>.  $\Delta\psi$  (phase difference-amplitude ratio) data at the two wavelengths were recorded once per second and I was sampled once every 2s. The  $\Delta\psi$  data were converted, after correction for window effects, into pseudo-refractive index,  $\langle n \rangle = \langle n \rangle + i\langle k \rangle$ , or pseudo-dielectric function,  $\langle \epsilon \rangle = \langle \epsilon_1 \rangle + i\langle \epsilon_2 \rangle$ , data<sup>1</sup>. The data were fitted using a regression analysis package<sup>5</sup> which allows fitting of optical constants, layer thicknesses and growth rates, based on ideal abrupt interfaces and the Fresnel reflectance relations.

## RESULTS AND DISCUSSION

The two wavelengths used in DWE were chosen to have a high and low penetration depth ( $\sim 1\mu\text{m}$  at  $\lambda=488\text{nm}$ ,  $\sim 0.01\mu\text{m}$  at  $\lambda=364\text{nm}$ ) to provide complementary information. Thus, the visible wavelength provides a real-time measurement of growth rate for relatively thick layers, while the UV wavelength gives a real-time indication of composition and microscopic surface roughness. In addition, LLS gives information on surface morphology, being sensitive to surface roughness with lateral spatial wavelengths  $\geq \lambda/2$ .  $\text{Si}_{1-x}\text{Ge}_x$  has a tendency to grow on Si with an undulating surface to minimise the elastic strain energy due to the lattice mismatch<sup>6</sup>. LLS and DWE have shown<sup>1-3</sup> that the delay before onset of this surface roughness decreases and its rate of development increases as the growth temperature or Ge content increases. A composition/growth temperature/thickness regime has been identified for the growth of smooth, fully strained alloy layers. Thus,  $\text{Si}_{0.8}\text{Ge}_{0.2}$  grown at  $750^\circ\text{C}$  shows rapid roughening (detected after  $\sim 80\text{\AA}$ ) while at  $610^\circ\text{C}$  layers remain smooth until thicknesses  $\sim 1500\text{\AA}$  have been deposited<sup>1-3</sup>. For  $x \sim 0.15$ , thicker layers can be deposited even at  $700^\circ\text{C}$ , without roughening.

Figure 1 shows DWE traces ( $\Delta$  only) obtained during growth of the p-type base and n-type emitter regions of a HBT structure. The lower penetration depth of  $\lambda=364\text{nm}$  is evident since  $\Delta$  rapidly reaches a constant value representative of  $\bar{n}$  for bulk  $\text{Si}_{0.8}\text{Ge}_{0.2}$  while interference fringes continue for the other wavelength. This can be seen more clearly in figure 2 which shows extended growth of  $\text{Si}_{0.8}\text{Ge}_{0.2}$  at  $610^\circ\text{C}$ . In the fit to these data,  $\bar{n}$  is allowed to be different at each wavelength but is kept constant as a function of time, except for a  $\sim 10\text{\AA}$  anomalous interface region which will be discussed in more detail later. Further constraints on the fit parameters are imposed by the requirement that the growth rate is the same at each wavelength. Thus, the data for the bulk of the layer are very well fitted by a model assuming growth of a layer with constant  $\bar{n}$  at a constant rate of  $1.05(\pm 0.01)\text{\AA/s}$ . No change in growth rate as a function of time was detected for undoped or B-doped  $\text{Si}_{0.8}\text{Ge}_{0.2}$ . However, as can be seen in figure 1, the fringe separation for As-doped Si increases with time, indicating a decreasing growth rate<sup>3</sup>. Growth of undoped Si produces a regular set of fringes (not shown), giving a constant growth rate of  $7.65(\pm 0.02)\text{\AA/s}$  at  $700^\circ\text{C}$ . Growth of Si:As with  $\text{AsH}_3/\text{SiH}_4$  ratios of  $3.8 \times 10^{-6}$  commenced at the same rate but this decreased gradually to  $\sim 2.5\text{\AA/s}$  after about 25min. This is believed to be due to As surface segregation and these results will be discussed elsewhere.

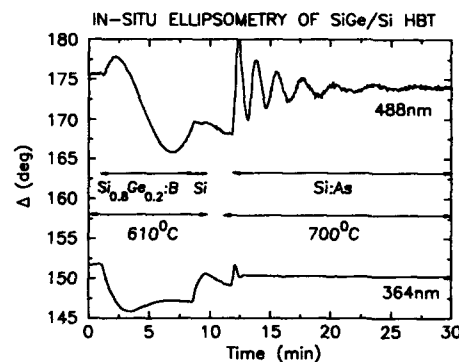


Figure 1. DWE traces ( $\Delta$  only) for growth of HBT structure.

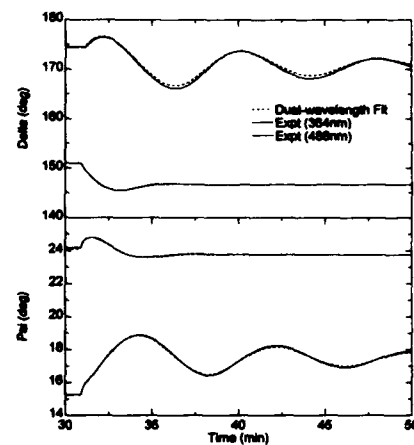


Figure 2. DWE traces for  $\text{Si}_{0.8}\text{Ge}_{0.2}$  growth on Si at  $610^\circ\text{C}$ . Top and bottom traces are for  $\lambda = 488\text{nm}$ .

The anomalous initial growth region mentioned earlier can be seen more clearly in figure 3 which shows results from  $\sim 100\text{\AA}$  growth of  $\text{Si}_{0.8}\text{Ge}_{0.2}$  (A-B) followed by Si growth. A distinct change can be seen, particularly at  $\lambda=488\text{nm}$ , after about 10s alloy growth. The fits which deviate markedly from the data are obtained from models assuming growth of a single uniform alloy layer followed by a single uniform Si layer. The fits which agree well with the data include an interface layer with different optical constants to the bulk and are shown in more detail for  $\lambda=364\text{nm}$  in figure 4. For this model, the optical constants, growth rate and thickness of an interface layer at each heterojunction have also been fitted. Typically, the layer at the interface of  $\text{Si}_{0.8}\text{Ge}_{0.2}$  on Si is  $\sim 10\text{\AA}$  thick while that at the Si on  $\text{Si}_{0.8}\text{Ge}_{0.2}$  interface is  $\sim 20\text{\AA}$ , both having growth rates between the bulk Si and  $\text{Si}_{0.8}\text{Ge}_{0.2}$  rates. In other words, there is a time-dependent build-up of the growth rate of  $\text{Si}_{0.8}\text{Ge}_{0.2}$  on Si, and an initial enhancement of that of Si on  $\text{Si}_{0.8}\text{Ge}_{0.2}$ , in agreement with the conclusions from molecular-beam epitaxy (MBE) growth studies based on Ge surface segregation. Because of high parameter correlations for these very thin layers there are large confidence limits on the optical constants. Real-time spectroscopic ellipsometry measurements now in progress should provide more information on the optical constants of these interface layers.

Further information on interface regions has been obtained by studying interrupted  $\text{Si}_{1-x}\text{Ge}_x$  alloy growth. Figure 5 shows data taken during growth of  $\text{Si}_{0.85}\text{Ge}_{0.15}$  at  $700^\circ\text{C}$ , in the form of  $\langle\epsilon_1\rangle$ - $\langle\epsilon_2\rangle$  trajectories. The fit shown from A to E is calculated for growth of a uniform alloy layer on Si. A repeated part of this deposition is also shown which was interrupted after  $\sim 60\text{\AA}$  of growth at point B. During the interrupt only  $\text{H}_2$  is in the growth chamber and no movement of the locus point (B) was observed. On resumption of the growth, the point moved to lower  $\langle\epsilon_2\rangle$  values at constant  $\langle\epsilon_1\rangle$ , which is equivalent to the beginning of a movement back to the Si point. After  $\sim 10\text{\AA}$  of growth the trajectory resumes its alloy-growth direction to point C. A further interrupt at C cause a similar Si-like growth on resumption (C-D), as shown by comparison with the trajectory obtained during Si cap growth (D-A) which returns to the starting point. Figure 6 shows results of a similar growth run at  $610^\circ\text{C}$  interrupted at B and D. The anomalous interface regions after resumption of growth (B-C and D-E) have been fitted here by  $12\text{-}13\text{\AA}$  of a layer with the same optical constants as the Si substrate, before continuation of the alloy layer growth (C-D and E-F). These data therefore indicate that a Si-like region is grown first on resumption of the growth. Confirmation of a reduced Ge content can be seen in secondary ion mass spectroscopy (SIMS) profiles through interrupted regions. Comparison of

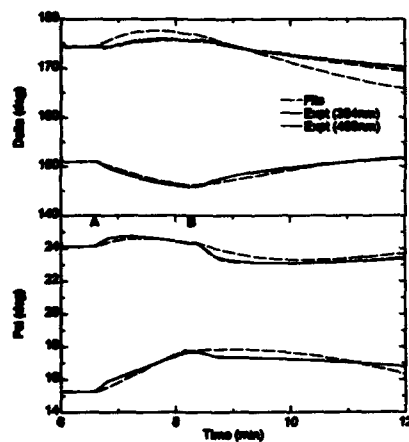


Figure 3. DWE traces for  $\text{Si}_{0.8}\text{Ge}_{0.2}$  growth (from A) on Si at  $610^\circ\text{C}$  followed by 10s delay (B) and Si growth. Top and bottom traces are for  $\lambda = 488\text{nm}$ .

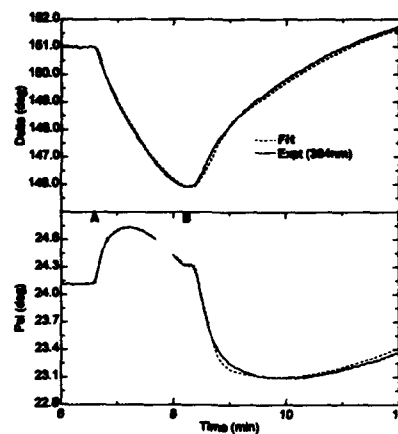


Figure 4.  $\Delta$ ,  $\psi$  traces at  $\lambda = 364\text{ nm}$  as in figure 3.

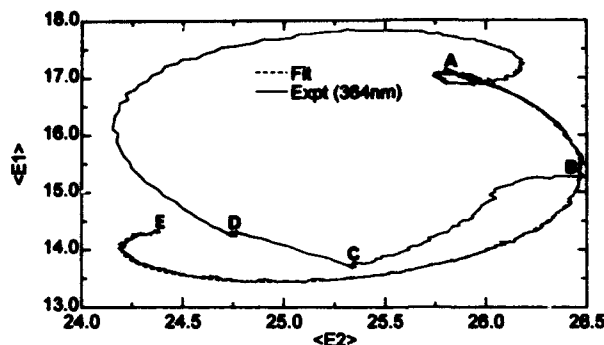


Figure 5.  $\langle \epsilon_1 \rangle$  -  $\langle \epsilon_2 \rangle$  traces for  $\text{Si}_{0.85}\text{Ge}_{0.15}$  growth (A-E and A-D) on Si at 700°C. Growth run A-D was interrupted at B and C for 10s. Si cap growth is from D-A.

figures 5 and 6 shows that this 'homo-interface' effect is reduced only slightly (by ~25%) by increasing the growth temperature from 610°C to 700°C. However, at the higher temperature, the anomalous hetero-interface (SiGe on Si) effects, possibly related to Ge segregation, have virtually disappeared, in agreement with the MBE results, which also indicated a strong temperature dependence<sup>7</sup>. Thus, the homo-interface effect may have a different origin and may be related to the different H-terminated surface environments of the Si and alloy surfaces. Further experiments are in progress to obtain a clearer understanding of this phenomenon.

Before ellipsometry can be applied for process control, a database is required of  $\bar{n}$  at the growth temperature as a function of composition for several wavelengths. Figure 7 shows data obtained during a sequential deposition of  $\text{Si}_{1-x}\text{Ge}_x$  with  $x=0.15$  (from A), 0.20 (from B), 0.25, each composition being grown to be optically thick at  $\lambda=364\text{nm}$ . The results are shown in terms of  $\langle \bar{n} \rangle$  which is equivalent to  $\bar{n}$  at the optically thick constant values. For the highest  $x$ , roughening can be seen after ~4.5min growth as indicated by the deviation of  $\langle \bar{n} \rangle$  from the fit, due to the formation of the undulations as discussed earlier<sup>3</sup>. The values of  $\bar{n}$  decrease monotonically from 5.05 (Si) to 4.74 ( $x=0.15$ ), 4.62 ( $x=0.20$ ) and 4.52 ( $x=0.25$ ). These values are close to those expected from interpolation between results obtained by Humlicek and Garriga<sup>8</sup> at ~530°C. The excellent fits shown in figure 7 again indicate that after the initial interface region the growth is accurately modelled by growth of a uniform layer with constant growth rate. The growth rate can be seen from the raw data to decrease with increasing  $x$ , the fits giving

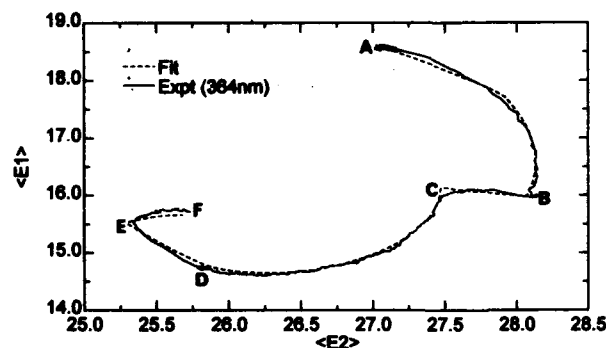


Figure 6.  $\langle \epsilon_1 \rangle$  -  $\langle \epsilon_2 \rangle$  traces for  $\text{Si}_{0.85}\text{Ge}_{0.15}$  growth on Si at 610°C. Growth was interrupted at B and D for 10s.



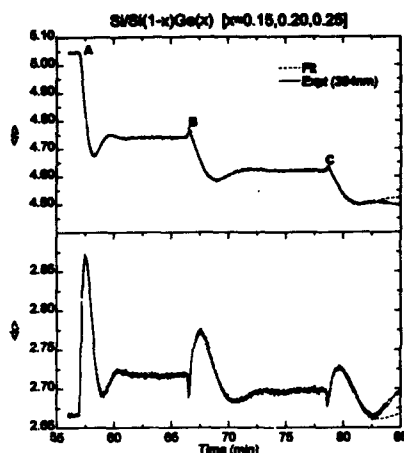


Figure 7.  $\Delta n, \Delta k$  traces for sequential deposition at 610°C of  $\text{Si}_{0.85}\text{Ge}_{0.15}$  (from A),  $\text{Si}_{0.8}\text{Ge}_{0.2}$  (from B), and  $\text{Si}_{0.75}\text{Ge}_{0.25}$ .

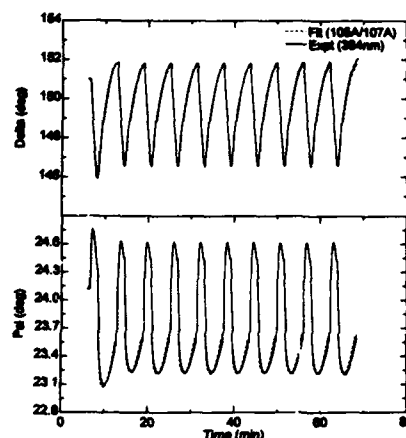


Figure 8.  $\Delta\psi$  traces for growth of 10-period  $\text{Si}_{0.8}\text{Ge}_{0.2}/\text{Si}$  MQW (nominally 100/100Å).

values of 2.1 Å/s ( $x=0.15$ ), 1.1 Å/s ( $x=0.20$ ) and 0.95 Å/s ( $x=0.25$ ). Anomalous interface regions can again be clearly seen at the alloy interfaces (B and C), which can be fitted with ~6 Å thick layers with Si-like optical constants as in the interrupted growth fits discussed earlier.

DWE has also been used to study the reproducibility of MQW structures. Figure 8 shows data obtained during growth of a 10-period  $\text{Si}_{0.8}\text{Ge}_{0.2}/\text{Si}$  MQW with nominal well and barrier thicknesses of 100 Å. The more rapid decrease of  $\Delta$  during well growth compared to the increase during barrier growth reflects the faster growth rate of the alloy. The fit shown was obtained

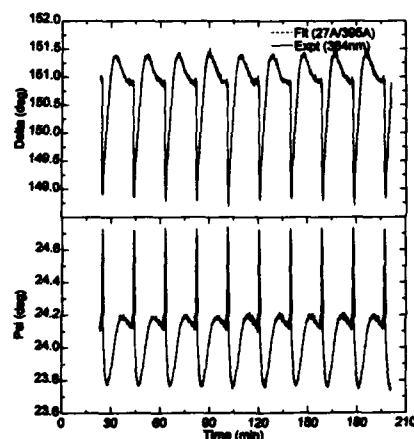


Figure 9.  $\Delta\psi$  traces for growth of 10-period  $\text{Si}_{0.8}\text{Ge}_{0.2}/\text{Si}$  MQW (nominally 30/400Å).

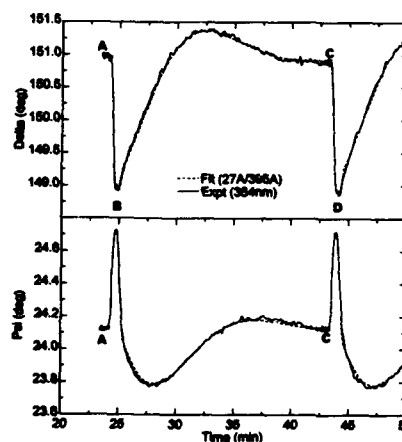


Figure 10.  $\Delta\psi$  traces from figure 9 of first two  $\text{Si}_{0.8}\text{Ge}_{0.2}$  wells (A-B and C-D) and Si barrier (B-C).

from the complete data set but with each period assumed to be identical, ie only one set of  $\bar{n}$ , growth rates and thicknesses was allowed to vary. The excellent fit obtained with this assumption is an indication of the repeatability from period to period, only slight deviations being visible towards the end of the growth. The differences in  $\Delta$  and  $\psi$  values from the first period compared to the rest are also predicted well by the model and are due to penetration of the light into the substrate. After the first three layers the substrate is no longer 'seen' and the trace settles down into a regular pattern.

Figure 9 shows DWE traces obtained during a 10-period MQW structure with nominally 30Å well and 400Å barrier thicknesses as required for far-IR detector structures. Again, an excellent fit can be seen assuming identical periods. The variability in the lower value of  $\Delta$  at the end of each well growth gives an indication of the reproducibility of well thickness. Variations within  $\pm 1\text{\AA}$  would produce the observed variation, assuming the composition is unchanged. Figure 10 shows an expanded fit to the first two wells and their separating barrier, showing the excellent fit quality. Fits to the first two wells gave well and barrier thicknesses of 27Å and 395Å respectively, while fits to the last two wells gave 27Å and 390Å. Thus, the repeatability of the wells is within  $\pm 1\text{\AA}$  and of the barriers is within  $\pm 3\text{\AA}$ .

## CONCLUSIONS

In-situ optical monitoring has been used to study growth of  $\text{Si}_{1-x}\text{Ge}_x$ , HBT and MQW structures. B-doped  $\text{Si}_{0.8}\text{Ge}_{0.2}$  has been shown to have a constant growth rate but a decreasing rate was observed for As-doped Si. Anomalous interface regions have been detected by DWE at  $\text{Si}_{0.8}\text{Ge}_{0.2}$ /Si hetero-interfaces and during interrupted alloy growth. The repeatability of MQW structures has been shown to be  $\pm 1\text{ML}$ .

## ACKNOWLEDGEMENTS

The authors would like to thank J. L. Glasper for SIMS measurements. This work is supported in part by ESPRIT Project 6135 "MIDAS".

## REFERENCES

1. C. Pickering, in *Handbook of Crystal Growth 3B*, edited by D. T. J. Hurle (North Holland, Amsterdam, 1994) (in press).
2. C. Pickering, *Thin Solid Films*, **206**, 275 (1991).
3. C. Pickering, R. T. Carline, D. J. Robbins, W. Y. Leong, D. E. Gray and R. Greef, *Thin Solid Films*, **223**, 126 (1993).
4. D. J. Robbins, J. L. Glasper, A. G. Cullis and W. Y. Leong, *J. Appl. Phys.*, **69**, 3719 (1991).
5. J. A. Woollam Co., 650 J St., Lincoln, NE 68508, USA.
6. A. J. Pidduck, D. J. Robbins, A. G. Cullis, W. Y. Leong and A. D. Pitt, *Thin Solid Films*, **222**, 98 (1993).
7. N. Ohtani, S. M. Mokler, M. H. Xie, J. Zhang and B. A. Joyce, *Surf. Sci.*, **284**, 305 (1993).
8. J. L. Glasper (unpublished work).
9. J. Humlicek and M. Garriga, *Appl. Phys. A*, (1993) (in press).

## REFLECTANCE ANISOTROPY AND SPECTROSCOPIC ELLIPSOMETRY CHARACTERISATION OF WET SILICON WAFER CLEANING

J. T. BEECHINOR, P.V. KELLY AND G.M. CREAN

National Microelectronics Research Centre, Lee Maltings, Prospect Row, Cork, Ireland.

### ABSTRACT

Silicon surfaces cleaned using standard wet chemical processes used in silicon device fabrication have been characterised by two optical techniques, spectroscopic ellipsometry (SE) and reflectance anisotropy spectrometry (RAS). Standard peroxide-based Si(100) wafer cleans were studied by SE. It is demonstrated that the residual film on the Si surface is critically dependent on both the sequence and type of cleaning steps performed. The sensitivity of RAS performed on-line under an air ambient to HF etched Si(110) and 4° off axis Si(100) surfaces is evaluated in comparison with kinetic SE data.

### INTRODUCTION

Silicon surface preparation prior to fabrication process steps such as film growth or oxidation will be one of the most critical challenges for deep submicron CMOS ULSI technology. Increasing attention will therefore focus on Si-surface chemistry and passivation. In particular the issue of characterisation of native and chemical oxides must be addressed. For example, the absence or presence of an  $\text{SiO}_x$  layer on a Si surface will significantly impact the adsorption of specific metallic contaminants [1]. However tighter control of surface quality will require the development of surface sensitive non-contact monitoring techniques.

Epioptic probes [2] offer significant potential for non-contact, surface sensitive characterisation tools applicable to on-line monitoring of both wet and dry wafer cleaning processes. This work focusses on the evaluation of the sensitivity of two such epioptic techniques, spectroscopic ellipsometry (SE) and reflectance anisotropy (RA), to wet cleaned silicon surfaces.

### EXPERIMENTAL

Single crystal CZ grown n-type Si(100), Si(100) cut 4° off axis towards [110], and Si(110) wafers were employed in this study. Table I describes the cleaning steps investigated in this study. The RCA cleans [3] were carried out using an FSI MERCURY acid spray processor. The HF-based cleans were carried out using immersion baths.

SE measurements were obtained using a phase modulated variable angle spectroscopic ellipsometer having a spot size of 2x5 mm on the sample surface. SE spectra were measured at an angle of incidence of 75° in the photon energy range from 2.0 eV to 4.5 eV in intervals of 0.02 eV, and expressed as a complex dielectric function  $\epsilon_r$  are  $\epsilon_i$  [4.]

RAS measurements were made using a phase modulated RA spectrometer [5] having a spot size of 12 mm diameter normally incident on the sample surface. RA spectra were measured in the photon energy range of 3.0 eV to 4.5 eV at an interval of 0.02 eV.

Table I. Wet cleaning processes for silicon wafers.

| Process                          | Description  |
|----------------------------------|--|
| SC1 clean step                   | H <sub>2</sub> O <sub>2</sub> :H <sub>2</sub> O 1:5 (30 s)<br>H <sub>2</sub> O <sub>2</sub> :H <sub>2</sub> O:NH <sub>4</sub> OH 1:10:1 (90 s)<br>H <sub>2</sub> O <sub>2</sub> :H <sub>2</sub> O 1:5 (30 s) |
| SC2 clean step                   | H <sub>2</sub> O <sub>2</sub> :H <sub>2</sub> O:HCl 1:5:1 (90 s)   |
| Standard RCA clean Spray         | SC1+100:1H <sub>2</sub> O:HF(120 s)+DI rinse+SC2   |
| RCA "HF last" clean Spray        | SC1+SC2+100:1H <sub>2</sub> O:HF(120 s)(+DI rinse)   |
| RCA "HF last" clean Spray/HF dip | SC1+SC2+10:1H <sub>2</sub> O:HF(30 s)  |
| DI rinse                         | Deionised water rinse  |
| HF etch                          | 7:1 H <sub>2</sub> O:HF etch (30,60 90 or 120 s)   |
| BHF etch                         | 4:1 or 7:1 Buffered HF etch (60 s)   |

## RESULTS AND DISCUSSION

The measured pseudo-dielectric function ( $\epsilon_i$ ) spectra for native oxide covered, standard RCA cleaned and "HF-last" RCA cleaned Si(100) wafers are shown in Figure 1. Spray cleaning was employed to process batches of three wafers in each case. SE measurements were also made on a further batch of Si(100) wafers, where the HF-last dip was performed by immersion without a final DI rinse. It is observed that the  $E_2$  Si peak in  $\epsilon_i$ , which is particularly sensitive to surface film thickness, increases in amplitude from the native oxide covered surface, to the standard RCA cleaned surface, to the "HF-last" process while the  $E_1$  Si peak height is reduced by the HF-last process

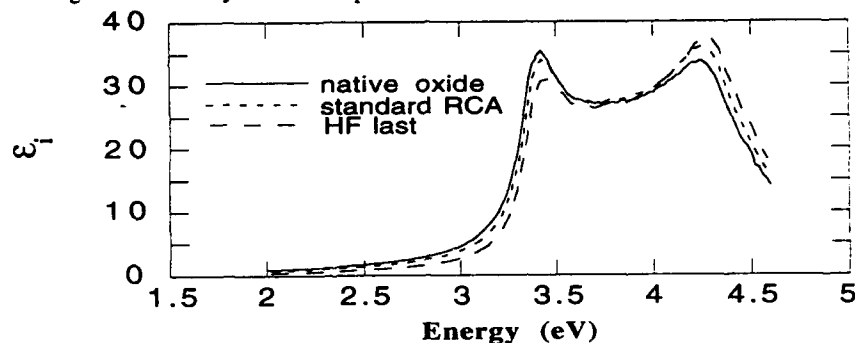


Figure 1. The imaginary part of the pseudo-dielectric function  $\epsilon_i$  of native oxide covered Si(100), standard RCA cleaned Si(100) and HF-last cleaned Si(100) with final rinse.

The measured SE spectra were analysed using two distinct optical models. Model A assumed the surface film as a thin layer of SiO<sub>2</sub> on Si, using reference dielectric function data for Si(100) [6], yielding an effective oxide thickness as a parameter. However, this model did not take into account the observed dependence of the refractive index of thin silicon oxide on film thickness [7]. A native or chemical silicon oxide modelled by a film of SiO<sub>2</sub> and a-Si has been shown to be a more accurate representation [8]. In this present work, this model has been expanded to a three-component homogeneous layer on c-Si(100), model B, where the layer is composed of SiO<sub>2</sub> as major component, with a silicon suboxide (SiO) and c-Si as minor components, to represent the increased refractive index and the effect of interfacial roughness, respectively. The layer dielectric function was calculated by the Bruggeman effective medium approximation (EMA) [9]. Fitting of SE data to optical models was performed using a least-squares Marquardt algorithm.

Table II. Best fit extracted material parameters for SE spectra of RCA cleaned wafers

| Model | Process :             | Native Oxide | Standard RCA clean | RCA/HF-last with final rinse | RCA/HF-last without final rinse |
|-------|-----------------------|--------------|--------------------|------------------------------|---------------------------------|
| A     | SiO <sub>2</sub> d(Å) | 20.28        | 15.97              | 9.64                         | 11.00                           |
|       | Si(100)               |              |                    |                              |                                 |
|       | $\chi^2$              | 1.63         | 1.74               | 2.30                         | 2.32                            |
| B     | Layer 1 d(Å)          | 15.42        | 12.86              | 7.17                         | 8.47                            |
|       | Composition:          |              |                    |                              |                                 |
|       | SiO <sub>2</sub> %    | 70.47        | 78.75              | 53.53                        | 54.38                           |
|       | SiO %                 | 14.77        | 11.46              | 9.60                         | 10.11                           |
|       | Si(100) %             | 14.76        | 9.79               | 36.87                        | 35.51                           |
|       | Si(100)               |              |                    |                              |                                 |
|       | $\chi^2$              | 1.51         | 1.67               | 2.18                         | 2.08                            |

The extracted best fit material parameters for the RCA clean matrix are presented in table II. Three general observations may be made. Firstly, the effective oxide thickness after a HF-last process is consistently smaller than for the standard RCA process. Secondly, model B provides a consistently better fit than model A, indicating that the higher refractive index layer used to model the native oxide or residual film is a more accurate representation of the thin oxide. In addition model B also shows that the chemical oxide produced by the standard RCA process is of higher quality than the native oxide insofar as its best fit silicon dioxide content is higher. Thirdly, a poorer fit is obtained for the residual film after a HF-last clean, than after a standard RCA process.

The residual film thicknesses for the HF-last RCA cleaned wafers suggest that a simple chemical termination of the silicon surface is not obtained. Omission of the final DI rinse in the case of 10:1 HF dipped wafers produced similar residual film thicknesses to the spray clean. The clearest conclusion from these results is the marked difference in the composition of the residual film after the HF-last process. Neither model attempts to represent the hydrogen passivation of the surface which occurs at least to some degree for HF-last RCA processes, nor do they explicitly address interfacial roughness.

The second part of this study focussed on the HF etch step in the absence of an RCA treatment. Figure 2(a) shows the SE measured dielectric function for a Si(100) wafer before, immediately after a 7:1HF etch for 30 s following a DI rinse and 40 minutes after this etch, as compared with the bare Si(100) reference dielectric function. Using model A or B above, an effective oxide thickness significantly less than the equivalent of a monolayer is obtained. The calculated spectra from either model differ negligibly due to the small film thickness, indicating a chemical termination of the bare silicon surface. It is also observed from Figure 2(a) and Table II, that the height of the E<sub>2</sub> peak is correlated to effective oxide thickness, the highest value being for the reference data from bare Si(100) [6]. In contrast, the increase in the E<sub>1</sub> peak appears uncorrelated to either the nature of the residual film or its thickness. The presence of the film is sufficient to increase the E<sub>1</sub> peak significantly above its value for the bare wafer.

Figure 2(b) shows the differential  $\epsilon_i$  (HF etched)- $\epsilon_i$  (oxidised) SE spectra as a function of time after the etch, highlighting the kinetic sensitivity of SE. It is observed that the differential SE spectrum is remarkably stable over a period of 50 minutes after the etch, indicating that excellent passivation is achieved with the 7:1 HF etch. This passivation is gradually lost after a further 2 hours in an air ambient.

Figure 3 plots the kinetics of re-oxidation via the effective oxide thickness measured using model B to fit successive SE spectra, measured at four minute intervals, and shows the gradual deterioration of the passivation. Figure 3 also illustrates the different effective oxide thicknesses and kinetics of re-oxidation on Si(100) substrates cut 4° off-axis towards [011] after 7:1HF etches of 30 s, 60 s and 90 s duration. While the native oxide on the off-axis substrates is thicker than for the on-axis wafers, larger effective oxide thicknesses and faster re-oxidation kinetics are deduced from SE measurements on the off-axis Si(100) substrates.

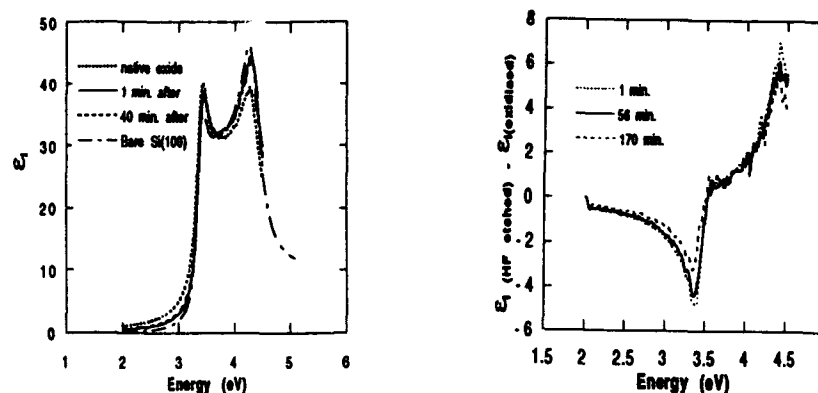


Figure 2. (a) The imaginary part of the dielectric function  $\epsilon_2$ , measured by SE from Si(100) before, immediately after, and 40 minutes after a 7:1HF etch, compared to the bare Si(100) reference data from ref. [6]. (b) Difference in SE  $\epsilon_2$  spectra of etched and unetched Si(100).

The existence of a weak reflectance anisotropy centred on 3.45 eV has been reported [10] for HF-etched Si(100) substrates cut 4.5° and 6° off-axis towards [011] measured under UHV and H<sub>2</sub>-ambient MOVPE conditions, where the hydrogen termination of the surface has been confirmed. In this work, the reflectance anisotropy between the Si [011] and  $\bar{0}\bar{1}1$  axes of the 90 s 7:1 HF etch sample was measured under an air ambient 5 minutes after removal of the wafer from HF. No feature at 3.45 eV was distinguishable above the noise level. The effect of 5 minutes exposure to an air ambient on this feature after HF etching is as yet unquantified. However, the SE results indicate that the passivation is not as good as for the on-axis Si(100) surface after this time.

Early work on RAS revealed marked differences between the native oxidised and buffered HF etched Si(110) surfaces [11], which possess an inherent anisotropy and consequently large RA signal due to their 2-fold rotational symmetry. Figure 4 details the increase in effective oxide thickness on Si(110), extracted from SE spectra using model A with a Si(110) substrate reference file, as a function of time after a 60 s 7:1 HF etch for 60 s following a DI rinse. Figure 5 shows the difference in the Si(110) RA spectra measured before and after this etch. A negative peak around 3.3 eV is observed for the HF etched wafer, consistent with the literature [11]. This peak decreases slowly over the first hour after etching as the effective oxide thickness measured by SE increases. A DI rinse performed after 7:1 HF etching does not significantly alter the passivation as observed by SE (Figure 4) or the evolution of the peak in the differential RA spectrum with time after etching, as shown in Figure 6.

The influence of 7:1 HF, 7:1 BHF, and 4:1 BHF etches on the passivation of the Si(110) surface is compared in Figure 4. The BHF etch clearly produces an inferior passivation layer and rapid re-oxidation of the surface. However, the characteristic RA feature at 3.3 eV which appears after etching was observed to persist for 24 hours in the case of both 4:1 and 7:1

BHF etches, as demonstrated in figure 7. It is concluded therefore that the origin of this RA feature is not related to passivation. This RA feature decreases in amplitude over 20 hours, consistent with the literature, but apparently unrelated to re-oxidation.

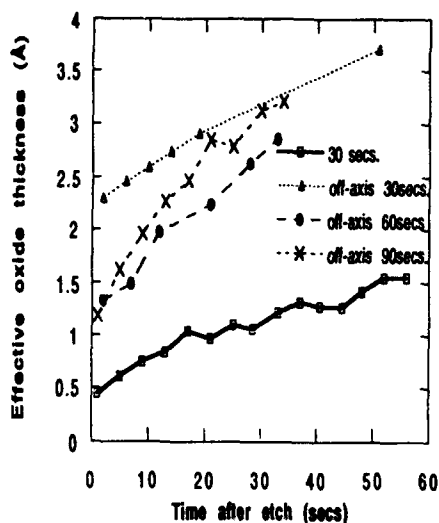


Figure 3. Increase in effective oxide thickness with time after HF etching of Si(100) and 4° off-axis Si(100)

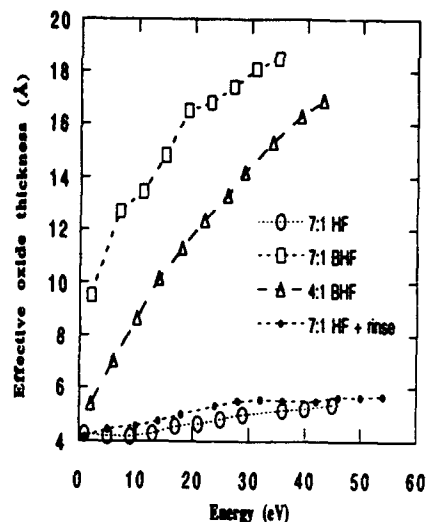


Figure 4. Effective oxide thickness as a function of time after etching oxidised Si(110) for 60 s, with 7:1 HF, 7:1 HF and rinse, 7:1 BHF, and 4:1 BHF solutions.

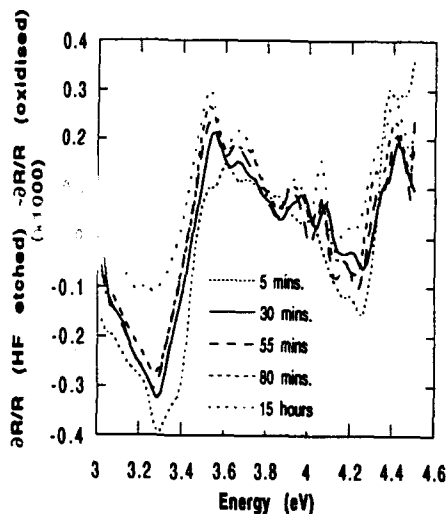


Figure 5. Differential spectra RA(etched) - RA(oxidised) as a function of time after a 7:1 HF etch. The RA signal is defined as:

$$\frac{\Delta R}{R} = \text{Re} \left[ \frac{2(r_{110} - r_{001})}{(r_{110} + r_{001})} \right]$$

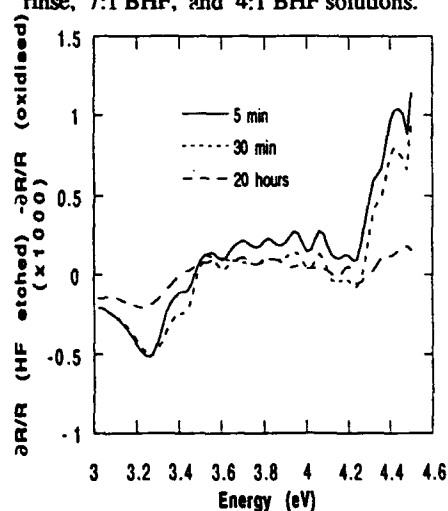


Figure 6. Differential spectra RA(etched) - RA(oxidised) as a function of time after a 7:1 HF etch and final DI rinse

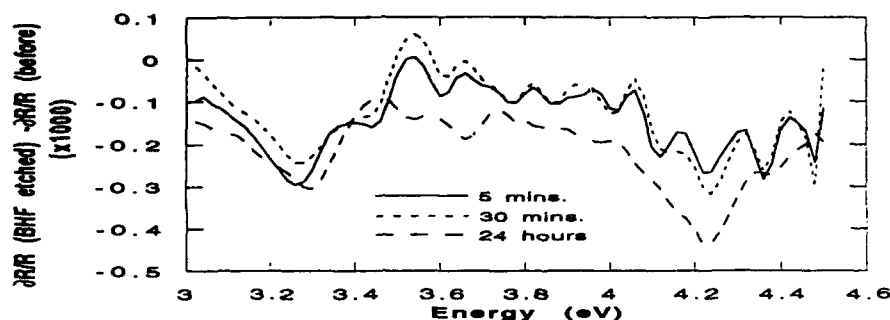


Figure 7. Differential spectra RA(etched) - RA(oxidised) as a function of time after a 4:1 BHF etch.

## CONCLUSIONS

This work has demonstrated the sensitivity of SE spectra to native and chemically oxidised Si(100) wafers and has provided further evidence of the need to model such ultra-thin oxides using higher refractive index values than are found in thick oxides. The contrasting effects of standard and HF-last RCA cleans have been demonstrated. The influence of surface orientation on HF etching of oxidised silicon wafers has been demonstrated using SE.

It is shown using SE that buffered HF produces a substantially inferior passivation on Si(110) which re-oxidises rapidly by comparison with the HF etched surface. Comparison of the kinetics of the RA and SE features which appear after BHF etching indicate that they decay on markedly different timescales, and suggests that their origins are different, although their spectral positions are similar. Further investigation of HF and BHF etch induced RA and SE features is required to establish their origins, and their relationship to the quality of the silicon surface produced by wet etches, so that they may be applied in on-line epioptic monitoring tools.

## ACKNOWLEDGEMENTS

This work was funded by the Commission of the European Communities (CEC), under the ESPRIT Research Programme, within Basic Research Action 6878, Epioptics Applied to Semiconductor Interfaces (EASI).

## REFERENCES

1. E. Morato, T. Yoshimi and Y. Shimanuki, *Electrochem. Soc. Ext. Abstr.* **89-1** (1989) 352
2. J.F. McGilp, *J. Phys. Condens. Matter* **2** (1990) 7985
3. W.Kern and D. Puotinen, *RCA Rev.* **31** (1970) 187
4. R.M.A. Azzam and N.M. Bashara, "Ellipsometry and Polarised Light", 1977.
5. D.E. Aspnes, J.P. Harbison, A.A. Studna and L.T. Florez, *Appl. Phys. Lett* **52** (1988) 957
6. G.E. Jellison Jr., *Opt. Mater.* **1** (1992) 41
7. E.A. Taft and L. Cordes, *J. Electrochem. Soc.* **126** (1979) 131
8. E.A. Irene, *Thin Solid Films* **233/234** (1993) 96
9. D.A. M. Bruggemann, *Ann. Phys. Lpz.*, **24** (1935), 636.
10. A.B. Müller, F. Reinhardt, U. Resch, W. Richter, K.C. Rose and U. Rossow, *Thin Solid Films*, **233/234** (1993) 19
11. D.E. Aspnes and A.A. Studna, *Phys. Rev. Lett.* **54** (1985) 1956



## PROCESS MONITORING FOR FABRICATION OF MERCURIC IODIDE ROOM TEMPERATURE RADIATION DETECTORS

J. M. Van Scyoc<sup>1</sup>, T. E. Schlesinger<sup>1</sup>, H. Yao<sup>2</sup>, R. B. James<sup>3</sup>, M. Natarajan<sup>4</sup>, X. J. Bao<sup>4</sup>,  
J. S. Iwanczyk<sup>5</sup>, B. E. Patt<sup>5</sup>, and L. van den Berg<sup>6</sup>

<sup>1</sup> Carnegie Mellon University, Department of Electrical and Computer Engineering, Pittsburgh, PA 15213

<sup>2</sup> University of Nebraska, Center for Microelectronic and Optical Materials Research, and Department of Electrical Engineering, Lincoln, NE 68588

<sup>3</sup> Sandia National Laboratories, Advanced Materials Research Division, Livermore, CA 94550

<sup>4</sup> TN Technologies, Inc., Round Rock, TX 78680

<sup>5</sup> Xsirus, Inc., Camarillo, CA 93012

<sup>6</sup> EG&G Energy Measurements, Goleta, CA 93116

### ABSTRACT

In the fabrication of mercuric iodide room temperature radiation detectors, as in any semiconductor process, the quality of the final device can be very sensitive to the details of the processing steps. Each processing step can either reduce the intrinsic defects and those extrinsic defects introduced by earlier steps, or it can introduce new defects. In mercuric iodide these defects can act as trapping and recombination centers, thereby degrading immediate device performance or leading to long-term reliability problems. With careful study and monitoring of each step, the process can be modified to improve the end product. In this work we used several techniques to study processing steps and their effects. Photoluminescence spectroscopy and photoionization revealed defects introduced during processing. One critical step is the formation of electrical contacts, as both the material choice and deposition method have an impact. Four point probe sheet resistance methods were used to characterize the loss of material from the contact as it reacted with or moved into the bulk semiconductor. Ellipsometry was used to characterize the intrinsic optical functions of the material, and to study the effects of surface aging on these functions. Results from this work provide suggestions for the modification and monitoring of the detector fabrication process.

### INTRODUCTION

Many diverse applications currently utilize, or could possibly utilize, nuclear radiation detection and spectroscopy. One major field currently of interest is the close monitoring of nuclear materials, for the verification of non-proliferation treaties, or the tracking of unauthorized, concealed materials. Environmental monitoring and remediation is another large field that is in its early stages. Concealed weapons and contraband detection, nuclear medicine and imaging, industrial process gauging, and basic science also have a need for such measurements. For all of these applications a compact, portable, low-maintenance instrument would be extremely useful. However, traditional detectors, such as high purity germanium (HPGe) or lithium-drifted silicon (Si(Li)), require cooling well below room temperature, necessitating a bulky apparatus that is fragile and that requires continued attention.

The semiconductor red mercuric iodide ( $\alpha$ -HgI<sub>2</sub>) has several properties that make it an ideal material for room temperature use, therefore allowing the production of the desired portable instruments [1-5]. In particular, the high atomic number of the elements ( $Z_{\text{Hg}}=80$  and  $Z_{\text{I}}=53$ ) means that the material has a high stopping power for photon energies into the MeV range, the relatively low electron-hole pair creation energy of 4.2eV at room temperature allows a large response per incident photon, and the large bandgap of 2.13eV at 300K results in a high intrinsic resistivity ( $10^{14}\Omega\cdot\text{cm}$ ), and low dark currents ( $10^{-12}\text{A}$ ). These properties result in a material suitable for some of the highest resolution and sensitivity room temperature radiation detectors [6].

The detector device structure used is usually quite simple, with thin ( $\sim 250\text{\AA}$ ) palladium contacts deposited on the large faces of a  $\text{HgI}_2$  slab around  $1\text{cm} \times 1\text{cm} \times 1\text{mm}$ . The charge created by the incident photons and separated by an applied bias is then measured by means of a system composed of a charge-sensitive preamplifier, a spectroscopic amplifier, and a multi-channel analyzer. These sensors are generally applied to the spectroscopic examination of x-ray and  $\gamma$ -ray emissions. Figure 1 shows an example spectrum collected with a small ( $5\text{mm} \times 5\text{mm} \times 0.5\text{mm}$ )  $\text{HgI}_2$  detector whose design was optimized for x-rays.

Although mercuric iodide has great potential in theory, there are many practical problems that currently limit the actual device performance achieved [7]. One primary problem is that not all charge that is generated by incoming photons is collected at the contacts. This incomplete charge collection effect is demonstrated by the left-side tailing of the  $59.5\text{keV}$  peak in the spectrum of Figure 1, as the "lost" charge results in a lower pulse height than is expected. This leads to a loss of resolution by the broadening of peaks, and a loss of sensitivity as there are fewer counts at the location of the photopeak. Another problem is the long term unreliability and instability of some detectors. The spectral quality from such a detector will degrade over time, with peak height and sharpness decreasing. Third, the material is very sensitive to mechanical handling, and can be easily damaged. Finally, all of these factors lead to a low final yield of high quality detectors, which means that the unit cost is prohibitive for many of the potential applications where a compact, hand-held spectrometer would be useful.

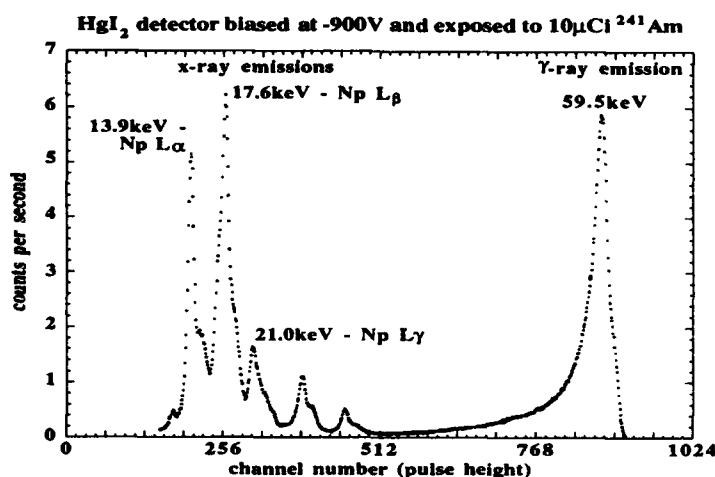


Figure 1. Example x-ray/ $\gamma$ -ray spectrum from a room temperature  $\text{HgI}_2$  detector.

The underlying cause of all of these problems, of course, is the material properties. The largest limitations are related to charge traps and recombination centers. These centers trap charges and may release them at unpredictable times, potentially over the scale from sub-seconds to years, and lead to the observed degradation of performance. One source of these traps is impurities that are present in the material, either from the start, or introduced during processing. Other sources include intrinsic defects in the crystal structure from growth or processing. The other prime material problems are physical and chemical in nature. Red mercuric iodide has a tetragonal unit cell, and forms a layered structure. These layers are connected at iodine planes only by weak van der Waal bonds, and thus the material is easily delaminated. Overall, the material is simply soft, and plastic deformation can occur under a sample's own weight, if not properly supported. The material is also very sensitive to heating, as at around  $125^\circ\text{C}$  the red tetragonal  $\alpha\text{-HgI}_2$  phase

undergoes an phase transition to the yellow orthorhombic  $\beta$ - $\text{HgI}_2$  phase, which has inferior detector properties. Finally, mercuric iodide is strongly reactive with many agents, and the mercury and iodine have sufficient vapor pressures that the surfaces of an unencapsulated sample will degrade within hours.

All of these complications lead to the situation that mercuric iodide crystal growth and device fabrication are non-trivial. Extreme care is required in the entire fabrication and handling process. Therefore, processing diagnostics are useful to identify problems and point toward solutions. Off-line procedures allow further time to fully study the process and allow for recommendations of large-scale changes. On-line diagnostics allow for the rapid detection of problems arising during actual fabrication, and allow for adjustments to compensate. This paper discusses measurements that were primarily developed as cases of the former, but some of which are applicable (with some simplifications) for on-line diagnostics.

## EXPERIMENTS AND RESULTS

### Photoluminescence

Photoluminescence (PL) has been shown to be a good technique for the detection and identification of defect states in many materials. In mercuric iodide, much work has been done to determine and understand the rich spectra found in most samples.

PL involves exciting a sample optically with above bandgap illumination, and collecting and measuring the resulting luminescence spectrum as the excited electrons return to lower energy states. Generally mercuric iodide PL is done using an argon ion laser (4880Å line) in CW mode, with a power of 20mW, and the sample is cooled in liquid helium to around 4.2K. The resultant peaks in the spectrum relate to the band edge and the defect states, or phonon replicas of these. With these parameters, the excitation penetrates only a few micrometers, so the spectra relates to the near-surface layers. In  $\text{HgI}_2$  PL there are two regions of interest, the near band edge region of 5290 to 5410Å, and the deep level region of 5400 to 8500Å. From the extensive characterization that has been done previously, correlations between relative peak intensities and locations, and associated process steps have been found for items such as impurities, sample aging, vacuum exposure, stoichiometry changes, and contact materials [8-13].

The technique is non-destructive, except for the required thermal cycling and extra material handling required. It can therefore be done on samples in the middle of processing, although a simplified version would be required for real-time online measurements.

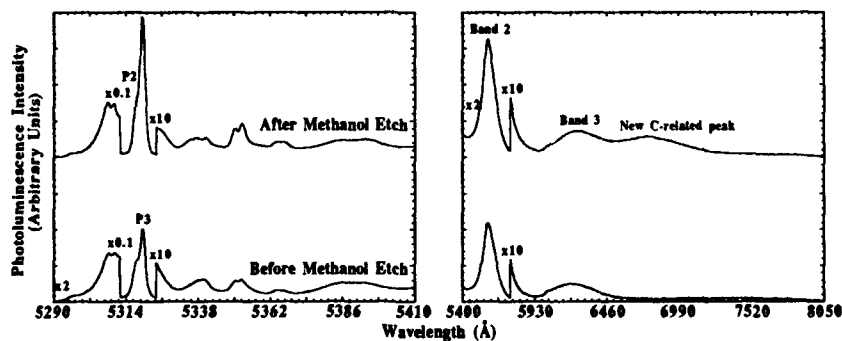


Figure 2. Photoluminescence spectrum before and after methanol etching of a  $\text{HgI}_2$  crystal sample, showing the introduction of an impurity-related defect state at  $\sim 6700\text{\AA}$ .

One example of a processing problem revealed by PL is shown in Figure 2. These PL spectra are from a sample immediately before and after a methanol etch. This work was done primarily as a test of alternative etchants, as the current usual etchant of choice is 10% by weight of potassium iodide in deionized water solution; however, in fabrication the sample could also be exposed to solvents such as methanol during cleaning and rinsing steps. The spectra here show that even though a high purity semiconductor grade methanol was used, a new defect level appears after the etch. In particular, this level appears to be a C-related impurity defect. It has been shown in other work that such defects severely degrade the resultant detector performance because of charge trapping effects.

#### Photoionization / Photoresponse

Another method that is useful for studying traps in mercuric iodide is photoionization (PI). In this newly developed technique a temperature controlled sample is illuminated with photons of increasing energy and the photocurrent, or photoresponse, is measured. The resultant peaks in the spectrum as a function of wavelength, for below bandgap excitation, relate to the trap levels. Varying the temperature gives further detailed information regarding these traps.

Figure 3 shows an example of a PI spectrum. The sample here is a piece of mercuric iodide that was intentionally doped with copper to a concentration on the order of 10ppm before the application of the palladium electrodes. The peak at around 2.05eV is seen only in the Cu-doped samples, and therefore it most likely relates to a trap introduced by the presence of this impurity.

Another parameter that can be obtained from this measurement is the barrier height of the metal/semiconductor interface. Extrapolating the linear portion of the square root of the response per incident photon to its zero-response value gives the barrier height, and the direction of the current gives the type of barrier (hole/electron).

This technique can be considered non-destructive when applied to partially fabricated detectors, as the contacts applied for the detector can be used for the PI/PR measurement. Again, the issues are merely those of thermal cycling and materials handling, and the limitations of the time and equipment needed for a measurement on-line.

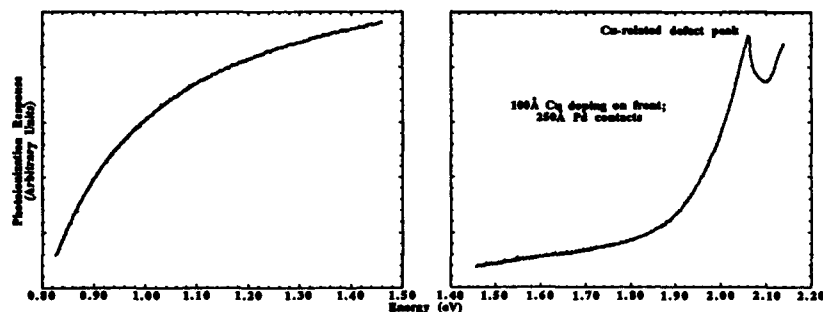


Figure 3. Photoionization spectrum of a Cu-doped Pd-contacted HgI<sub>2</sub> sample at 300K.

#### Four-point Probe Sheet Resistance

One area of the mercuric iodide detector fabrication that has not been fully studied is the choice of contact material and deposition method. Given the reactive nature of mercuric iodide, it is likely that any materials brought into contact for use as an electrode is going to change the substrate and be changed itself. Besides the formation of new products by reaction, mobile species from the

contact can move into the bulk of the mercuric iodide, thereby introducing further charge trapping centers.

A simple technique that can be used to characterize the quality of the contact and its interface with the mercuric iodide is the four-point probe sheet resistance measurement [13]. Four tungsten carbide tips in a linear arrangement are brought into contact with the sample and a known current is injected through the outer two. The voltage measured between the inner two probes is directly related to the resistance of the sample film, which is related to the effective thickness of the conductive film. Monitoring this resistance versus time reveals changes in the contact film.

Copper contacts showed an exponentially increasing resistance, as expected, since copper is known to diffuse rapidly into mercuric iodide. Figure 4 shows the more unexpected results. Palladium and the refractory metal tungsten are generally considered relatively stable on mercuric iodide. However, it appears that these materials move into and/or react with the mercuric iodide, as the resistance does increase. Both do form a reaction barrier, though, as the resistance eventually stabilizes, leading to the apparently stable contact that is generally assumed. Pd does this rapidly, and this is why the contacts have been generally thought to be stable. The W change is somewhat slower, but still stabilizes within a few days.

The technique is a somewhat destructive technique, as the probing mechanically damages the extremely soft mercuric iodide. In fact, in order to obtain stable resistance readings, relatively thick films (~1000Å), and very careful probe tip application are required. Otherwise, the tips simply poke through the film and measure the very high resistance of the bulk mercuric iodide.

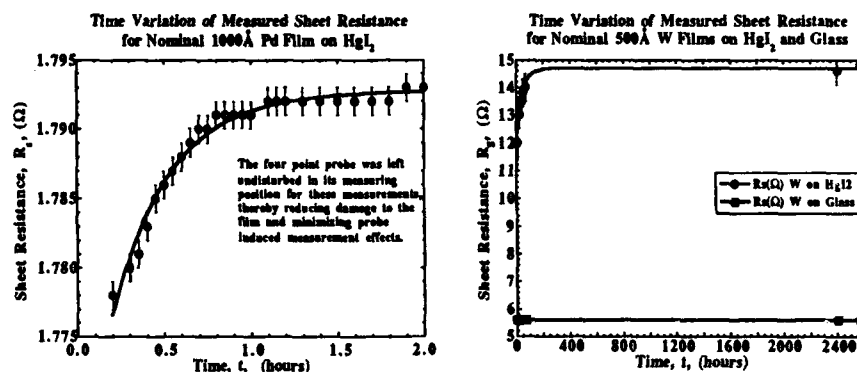


Figure 4. Four-point probe sheet resistance measurements of Pd and W contacts on HgI<sub>2</sub>.

#### Variable Angle Spectroscopic Ellipsometry (VASE)

One final technique was employed to study the optical functions of bare mercuric iodide. Variable angle spectroscopic ellipsometry (VASE) can give detailed information about the dielectric functions of the material [14]. Since the HgI<sub>2</sub> structure is anisotropic, separate functions are required for the c-axis and a,b-axes.

Ellipsometry in general determines the ratio of complex reflectance  $r_p$  to  $r_s$ , with  $r_p$  and  $r_s$  the reflection coefficients of light polarized parallel to and perpendicular to the plane of incidence, respectively. This complex ratio is traditionally determined as an amplitude and an angle.

$$\rho = r_p / r_s = \tan(\psi) * \exp(i*\Delta)$$

with  $\Delta$  and  $\psi$  the calculated values. The pseudo-dielectric and optical constants are obtained from these values by further calculations. Using variable angles of incidence and wavelengths, one can obtain further data which gives greater information about the optical functions of the sample.

Once these functions are characterized for bare, unadulterated mercuric iodide, they can be used

to study the effects of certain processing steps. One inevitable processing step is aging. Mercuric iodide left exposed to air (or even in other ambients) exhibits a large change in the surface. This surface degradation is known as aging. This phenomenon is possibly related to the sublimation of material from the surface, since the vapor pressure of the mercury and iodine are rather high at room temperature. Figure 5 shows the optical functions for an aging sample. These spectra show that there is indeed a change in the optical characteristics related to aging. It is believed that this change is caused by an increase in the amount of "voids" present in the near surface region, which fits with the picture of material subliming away.

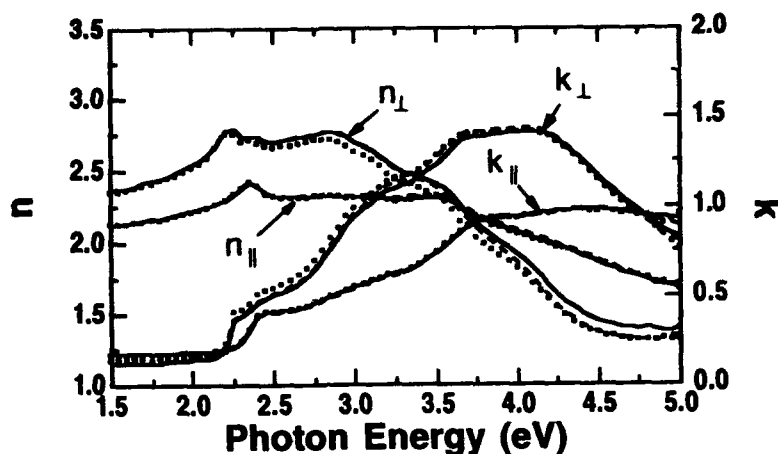


Figure 5.  $\text{HgI}_2$  surface aging effects, characterized by the VASE measurements, via the changes of anisotropic refractive indices. The solid lines represent measurements right after the 10% KI etching, and the dashed and dotted lines are results, from the same sample, measured ~20 hours and ~548 hours after the etching, respectively.

#### Fabrication Modifications

These measurements all lead to the conclusion that certain processing steps can be improved. These measurements show where in the process sequence defects are introduced. Particular changes that are suggested include the use of high purity starting materials and processing chemicals, the proper choice of contact material, and the minimization of material aging. Also, some of these methods, the PL, PI, and VASE, in particular, can be simplified enough to incorporate into real-time online diagnostic tools. With these tools, acute or chronic changes in the amount of defects present in a detector under production could be detected, and conditions changed before too much material, time, and effort is wasted. This could potentially increase yield enough to lower the per unit cost to a point where other applications of detectors become feasible.

#### **SUMMARY AND CONCLUSIONS**

Various measurements, including photoluminescence, photoionization, four-point probe sheet resistance, and variable angle spectroscopic ellipsometry have been conducted on mercuric iodide samples subjected to the processing steps required for room temperature x-ray and  $\gamma$ -ray spectroscopic detector fabrication. These measurements highlight the effects of different steps and show correlations between the presence of defects and detector problems. These measurements, therefore, suggest changes required in the processing steps. Finally, some of these techniques can be incorporated into online fabrication diagnostics to more rapidly correct yield problems.

## ACKNOWLEDGEMENTS

This work was supported by the U. S. Department of Energy. One of us (T. E. S.) would like to acknowledge the support of the National Science Foundation through the Presidential Young Investigator Program.

## REFERENCES

1. W. R. Willig, Nucl. Instrum. Methods **96**, 615 (1971).
2. H. L. Malm, IEEE Trans. Nucl. Sci. NS-**19**, 263 (1972).
3. J. P. Ponpon, R. Stuck, and P. Siffert, Nucl. Instrum. Methods **119**, 297 (1974).
4. J. H. Howes and J. Watling, Mat. Res. Soc. Symp. Proc. **16**, 207 (1983).
5. H. L. Malm, T. W. Raudoff, M. Martina, and K. R. Zanio, IEEE Trans. Nucl. Sci. NS-**20**, 500 (1973).
6. R. C. Whited and M. Schieber, Nucl. Instrum. Methods **162**, 119 (1979).
7. N. L. Skinner, C. Ortale, M. M. Schieber, and L. van den Berg, Nucl. Instrum. Meth. Phys. Res. A**283**, 119 (1989).
8. X. J. Bao, T. E. Schlesinger, R. B. James, R. H. Stulen, C. Ortale, and A. Y. Cheng, J. Appl. Phys. **68**, 86 (1990).
9. R. B. James, X. J. Bao, T. E. Schlesinger, J. M. Markakis, A. Y. Cheng, and C. Ortale, J. Appl. Phys. **66**, 2578 (1989).
10. X. J. Bao, T. E. Schlesinger, R. B. James, G. L. Gentry, A. Y. Cheng, and C. Ortale, J. Appl. Phys. **69**, 4247 (1991).
11. X. J. Bao, T. E. Schlesinger, R. B. James, R. H. Stulen, C. Ortale, and L. van den Berg, J. Appl. Phys. **67**, 7265 (1990).
12. R. B. James, X. J. Bao, T. E. Schlesinger, C. Ortale, and A. Y. Cheng, J. Appl. Phys. **67**, 2571 (1990).
13. J. M. Van Scyoc, T. E. Schlesinger, R. B. James, A. Y. Cheng, C. Ortale, and L. van den Berg, Mat. Res. Soc. Symp. Proc. **302**, 115 (1993).
14. H. Yao and B. Johs, Mat. Res. Soc. Symp. Proc. **302**, 341 (1993).

---

## PART II

---

### **Reflectance and Light Scattering Spectroscopies**



## CHARACTERIZATION OF ELECTRONIC MATERIALS BY OPTICAL REFLECTANCE SPECTROSCOPY AND DIGITAL SIGNAL PROCESSING

PIETER L. SWART

Sensors Sources and Signal Processing Research Group, Faculty of Engineering, Rand Afrikaans University, PO Box 524, Auckland Park 2006, South Africa

### ABSTRACT

Ion implantation, diffusion, epitaxy, oxidation and ion exchange are common processing steps which alter the refractive index of dielectric media. These changes can be probed non-destructively by optical methods such as infrared and ultraviolet-visible spectroscopy, and related to material structure. An overview is given of the bilinear transform of reflectance and its use in conjunction with Fourier spectral analysis for thickness and refractive index estimation. Closed-form solutions are presently available for the bilinear transformed reflectance of heteroepitaxial multilayer structures, and for materials containing graded refractive index profiles. Salient features such as positions of interfaces and refractive index steps in multilayer media; depth and width of buried inhomogeneous layers; and width of a transition region between layers of constant refractive index can be determined directly. Under certain restrictive assumptions the bilinear transformed reflectance is shown to be invertible, which allows one to determine the complete refractive index profile. Examples are presented which illustrate the determination of thickness and refractive index of individual layers in multilayered structures. Specific examples include silicon-on-insulator, and III-V heteroepitaxial structures such as InP/InGaAs/InP. Analysis of the reflectance of medium to high energy implanted Si or GaAs allows determination of mean damage depth and standard deviation. The invertibility of the bilinear transformed reflectance is illustrated by estimating the refractive index profile of nitrogen implanted silicon.

### INTRODUCTION

Device architectural degrees of freedom include planar dimensions, layer composition and doping levels, as well as layer thickness. With the rapid progress in epitaxy of compound semiconductors, complex multilayer structures can be grown to high degrees of perfection. Ternary and quaternary III-V compounds, involving several layers ranging in thickness from tens of nanometers to several micrometers, find application in microwave active devices and opto-electronic components. Device processing steps such as ion-implantation and thermal treatment could also result in crystal damage or perturbation of carrier profiles and interface gradients between different layers. Consequently, there exists a need for a rapid, non-destructive technique for the determination of the individual layer thicknesses and refractive indices, as well as the depth and profiles of implanted ions and lattice damage.

As a result of its inherent non-destructive nature, optically based methods abound. Reflectance techniques such as spectroscopic ellipsometry, infrared and UV-VIS reflectance spectroscopy, differential reflectance, electro- and photorelectance, and inelastic light scattering techniques such as Raman spectroscopy and photoluminescence are employed to determine composition, structure, strain, defects, impurity levels, interface and surface roughness, barrier heights, electric field strengths, thickness, carrier density, carrier velocity, position of carrier concentration peaks, transition layers, etc.[1-8]

Spectroscopic ellipsometry has proved itself as a very sensitive and accurate technique for determination of thickness and composition of thin heteroepitaxial layers during or after the growth process. However, it suffers from the following drawbacks if multilayers are to be analyzed[4]:

- the required multi-parameter least-squares curve fit may lead to spurious solutions
- *a-priori* knowledge of the number of layers, layer thickness and optical constants is required.

This paper presents a review of an optical technique based on Fourier spectral analysis of the bilinear transformed infrared reflectance. It was initially developed for silicon-on-insulator[5] and later refined for multilayer heteroepitaxial material[6] and inhomogeneous layers [9,10]. It is a truly multilayer method, since there is no upper limit to the number of layers which can be resolved, and the maximum thickness is only limited by the coherence length of the light source. The minimum layer thickness which can be resolved is material dependent, but it generally lies between 100 nm and 200 nm. It therefore forms an ideal complement to spectroscopic ellipsometry.

## THEORY AND SIMULATIONS

**Homogeneous multilayer structure:** The optical reflectance pattern of multilayer media is rich in information, but until recently it has been a rather daunting task to extract structure parameters from it. Without an underlying theory, its Fourier spectrum seemed to be just as difficult to interpret. Consider a layered structure consisting of an infinitely thick substrate with refractive index  $n_s$  and  $m$  layers, thickness  $d_1, d_2, \dots, d_m$  and refractive index  $n_1, n_2, \dots, n_m$ , respectively. The layers are numbered consecutively from the surface. Monochromatic light with wavenumber  $w$  incident from air, suffers multiple reflections and refractions at the interfaces. In principle the resulting reflectance for normal incidence may be calculated by either the matrix method[11] or by means of the theory of graphs[12]. We will outline a derivation based on the matrix technique[11]. Each individual layer ( $j$ ) can be modelled by means of a  $2 \times 2$  characteristic matrix  $M_j$  which contains sine and cosine terms of the phase thickness  $\theta_j$ , where

$$\theta_j = 2\pi w n_j d_j \quad (1)$$

where  $n_j$  is the refractive index (lossless film), and  $d_j$  the thickness of the  $j$ 'th layer.  $w = 1/\lambda$  is the wavenumber. The assembly of  $m$  layers is characterized by the matrix product of all individual characteristic matrices, leading to a matrix  $A$ . This is used to calculate an effective refractive index  $n_e$  [6]. The total reflectance is given by

$$R^{(m)}(w) = \left| \frac{(1 - n_e)}{(1 + n_e)} \right|^2 \quad (2)$$

Both the numerator and denominator of  $R^{(m)}(w)$  contain sums of products of sines and cosines of the phase thickness of the various layers. This implies that the Fourier spectrum of reflectance of the multilayer contains an infinite number of Fourier terms, which makes it impractical for obtaining thickness and other parameters. However, if the reflectance is first bilinearly transformed [13], the discrete frequency components present in the denominator are totally removed, leaving only a well defined number in the numerator [13]. This transform is defined by:

$$B^{(m)}(w) = \frac{1 + R(w)}{1 - R(w)} = \frac{1}{2n_s} [(A_{11}^{(m)})^2 + (A_{21}^{(m)})^2] + \frac{n_s}{2} [(A_{22}^{(m)})^2 + (A_{12}^{(m)})^2] \quad (3)$$

where  $A_{kl}^{(m)}(k, l = 1, 2)$  are the elements of the matrix  $A$ .

It can be shown that the number of Fourier components is given by[6]:

$$N = 0.5[3^m + 1] \quad (4)$$

For example,  $N = 5; 14; 41$  for  $m = 2; 3; 4$ , respectively.

**Homogeneous multilayer structure with small refractive index steps:** If the steps in refractive index

between the various layers are small (less than say 20%), only first order interference effects have to be taken into consideration. Under these conditions, which is typical for III-V and II-VI semiconductors, the expression for bilinear transformed reflectance becomes particularly simple, and the number of discrete frequency components in its Fourier spectrum is reduced to  $m$ , where  $m$  is the number of layers[6].

$$B^{(m)}(w) = B_0^{(m)} + \frac{n_s - \frac{1}{n_s}}{2} \sum_{i=1}^m \left( \frac{n_{i+1} - n_i}{n_s} \right) \cos \left( 2 \sum_{j=1}^i \theta_j \right) \quad (5)$$

This expression pertains to a layered structure where the layers are numbered from the surface, and with  $n_{m+1} = n_s$ , the substrate refractive index.

It can be seen from eq.(5) that the Fourier spectrum of  $B^{(m)}(w)$  in this instance consists of a series of  $m$  delta functions convoluted with the Fourier transform of the data window. These spectral peaks appear in the same sequence as the interfaces with the surface at zero frequency, and each of the lines corresponding to a different interface. With relatively small changes in refractive index between layers, the spectrum is an almost scaled cross-sectional representation of the layered medium. The amplitudes of the spectral lines are proportional to the steps in refractive index between the layers. The technique of thickness estimation is illustrated by simulated reflectance data of a 5-layer AlGaAs-GaAs structure, shown schematically in Fig. 1(a). The data are simulated in the wavelength range 0.9 to 2.25  $\mu\text{m}$  below the direct band edge. The refractive index of  $\text{Al}_x\text{Ga}_{1-x}\text{As}$  is a function of the mole fraction  $x$  of AlAs in the alloy, as well as the optical wavelength. Expressions for  $n(x, \lambda)$  were obtained from the model presented by Adachi[14]. We neglected the type and doping dependence of the GaAs and AlGaAs in the simulation. This will not affect the peak positions significantly; only the amplitudes.

The layer parameters, starting from the front surface, are:  $x_1 = 0.3$ ;  $d_1 = 4 \mu\text{m}$ ;  $x_2 = 0.02$ ;  $d_2 = 0.8 \mu\text{m}$ ;  $x_3 = 0.2$ ;  $d_3 = 0.8 \mu\text{m}$ ;  $x_4 = 0.1$ ;  $d_4 = 1.3 \mu\text{m}$ ;  $x_5 = 0.3$ ;  $d_5 = 15 \mu\text{m}$ . These values were used to calculate the reflectance as a function of inverse wavelength[6]. The reflectance curve, shown in Fig. 1(b), was bilinear transformed over the inverse wavelength range  $4450 \text{ cm}^{-1}$  to  $11250 \text{ cm}^{-1}$ . The data record was corrected for dispersion, high-pass filtered, zero padded and Fourier transformed by the fast Fourier transform (FFT) algorithm. The resulting Fourier power spectrum is presented in Fig. 1(c). Because the maximum step in refractive index is less than 6% for  $x_{\text{max}} = 0.3$ , the Fourier spectrum may be converted directly to an approximate cross sectional view of the multilayer structure. The spectral peaks occur only at positions corresponding to the interfaces, with the amplitude of the power spectral lines directly proportional to the square of the difference in fractional change in the refractive indices of adjacent layers.

The minimum thickness which can be resolved is determined by the resolution of the Fourier transform, which in turn depends on the length of the data record. If at least one period of a signal is required in order to determine its Fourier spectrum, then:

$$d_{\text{min}} = \frac{1}{2n(w_{\text{max}} - w_{\text{min}})} \quad (6)$$

where  $(w_{\text{max}} - w_{\text{min}}) =$  available wavenumber range. For example, if  $n = 3.5$ , and  $(w_{\text{max}} - w_{\text{min}}) = 10^4 \text{ cm}^{-1}$ ,  $d_{\text{min}} = 0.14 \mu\text{m}$ .  $w_{\text{max}}$  is limited by dispersion and absorption, while  $w_{\text{min}}$  could be restricted by free carrier effects. The deleterious effects of dispersion may be reduced by means of a non-linear deformation of the wavenumber axis[15].

**Buried inhomogeneous refractive index profiles:** Many processes involved in the fabrication of electronic devices modify the dielectric properties of the materials, either by alteration of the crystalline structure of semiconductors by ion-implantation, or by electrical charges produced

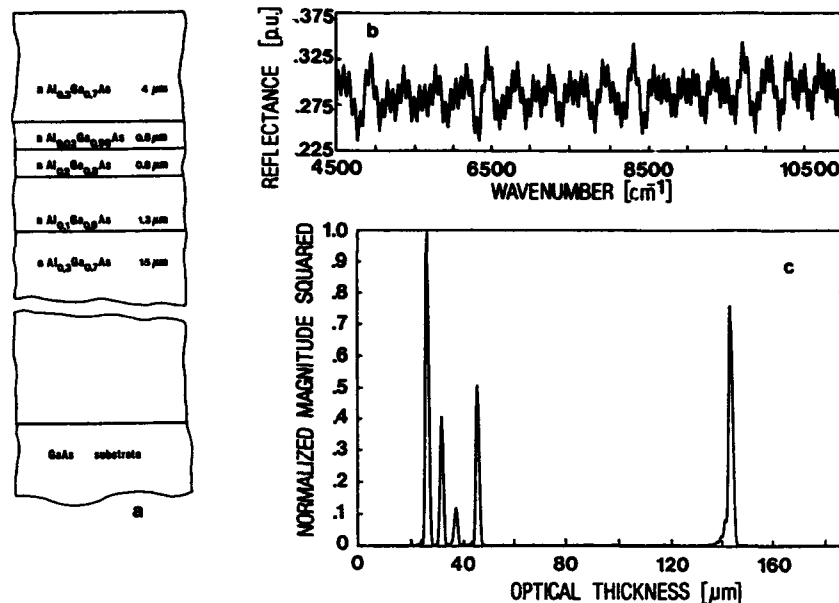


Fig. 1(a) 5 layer AlGaAs-GaAs structure; (b) Simulated reflectance; (c) Fourier spectrum of the transformed reflectance versus optical thickness  $2nd$ .

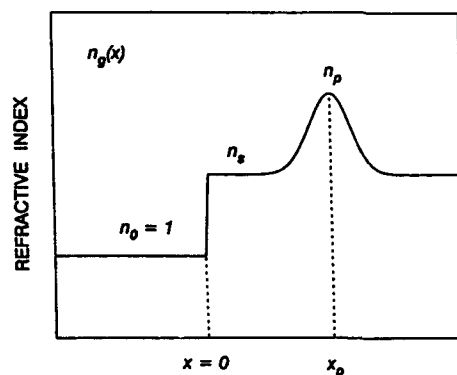


Fig. 2 A buried gaussian refractive index profile.

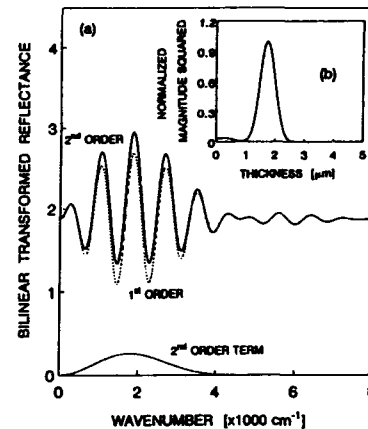


Fig. 3(a) Calculated bilinear transformed reflectance of silicon containing a buried layer with a gaussian refractive index profile with  $n_p > n_s$ . First and second order term are shown ( $n_s = 3.45$ ;  $n_p = 4.8$ ;  $x_p = 1.7 \mu\text{m}$ ;  $\sigma = 0.1 \mu\text{m}$ ). (b) Fourier power spectrum of the bilinear transformed reflectance. The peak is located at  $x = x_p = 1.75 \mu\text{m}$ .

by activation of dopants after annealing [16,17]. These dielectric modifications can be used to evaluate the different manufacturing processes. In fact, several measurement methods are based on the analysis of reflectance measurements, simulations and least-square fits [16-19]. However, the interpretation of results may get complicated when increasing the complexity of the media. Semiconductors possessing graded refractive index profiles are typical examples, as shown in Fig. 2. We have developed analytical solutions for reflectance, bilinear transformed reflectance and transmittance of these materials. Our formulas include first and second order effects, but in some situations a first order approximation is adequate for facilitating the necessary computations.

The bilinear transformed reflectance for a medium with a graded refractive index was calculated by dividing a hypothetical profile in homogeneous differential layers and treating the system as a layered structure [20,21]. Considering that the thickness ' $\Delta x$ ' of every layer tends to zero; that the refractive index ' $n$ ' is a function of the depth ' $x$ '; and neglecting terms of order higher than two, the bilinear transformed reflectance can be expressed as:

$$B(w) = \frac{1+r_{01}^2}{1-r_{01}^2} - \frac{2r_{01}}{1-r_{01}^2} \rho_1(w) + \frac{1+r_{01}^2}{1-r_{01}^2} \rho_2(w) \quad (7)$$

where  $r_{01}$  is the reflectivity coefficient between air and the surface of the material, and the functions  $\rho_1$  and  $\rho_2$ , accounting for the first and second order effects, respectively, are:

$$\rho_1(w) = \int_0^{\infty} \frac{1}{n(x)} \frac{dn(x)}{dx} \cos \left[ 4\pi w \int_0^x n(\xi) d\xi \right] dx \quad (8)$$

$$\rho_2(w) = \int_0^{\infty} \frac{1}{n(x)} \frac{dn(x)}{dx} \int_x^{\infty} \frac{1}{n(\xi)} \frac{dn(\xi)}{d\xi} \cos \left[ 4\pi w \int_x^{\xi} n(\beta) d\beta \right] d\xi dx \quad (9)$$

If the refractive index change is not very large,  $\rho_2(w)$  can be neglected. In this instance calculations using numerical methods are very time efficient compared to the matrix method. With this simplification some cases can be solved analytically, e.g. a gaussian refractive index profile with a standard deviation  $\sigma$ , where the refractive indices at the substrate and at the peak are  $n_s$  and  $n_p$ , respectively, and the depth from the surface to the peak is  $x_p$ . It can be shown that for  $|n_p - n_s| \ll n_s$ , eq.(7) can be approximated by:

$$B(w) = B_0 + Kw \exp \left[ -\frac{(4\pi\sigma n_p w)^2}{2} \right] \sin(4\pi n_p x_p w) \quad (10)$$

where  $K$  is a constant dependent on  $\sigma$ ,  $n_p$  and  $n_s$ . Eq.(10) represents a sinusoid modulated by a Rayleigh function, with frequency ' $2n_p x_p$ ' proportional to the position of the peak of the gaussian. From eq.(10) we obtain that the maximum of the envelope occurs at  $w_p = (4\pi\sigma n_p)^{-1}$ . This last observation may be used for estimating  $\sigma$  from reflectance measurements.

In order to illustrate the validity of this theory, simulations were performed by means of eq.(7) as well as by the matrix formulation [11]. The case of a buried gaussian refractive index profile is analyzed. Figure 3(a) shows the bilinear transformed reflectance calculated with eqs.(3) and (7) for this type of profile where  $\sigma = 0.1 \mu\text{m}$ ,  $x_p = 1.7 \mu\text{m}$ ,  $n_s = 3.45$  and  $n_p = 4.8$ . The first order approximation as well as the second order term are shown in Fig. 3(a). Note that frequency information ( $2n_p x_p$ ) is produced by first order effects. Fourier spectral analysis

of the bilinear transformed reflectance (Fig. 3(b)) presents one peak centred at  $1.75 \mu\text{m}$ , this value being very close to that used for  $x_0$ .

For moderate refractive index changes, e.g.  $n_p = 3.8$ ,  $\rho_2$  was negligible for the whole wavenumber range used, and simulations by means of eq.(7) were more than 25 times faster than those performed by the matrix method. The position of the maximum of the envelope did not change significantly when changing  $n_p$  between 3.6 and 3.8, allowing one to determine  $\sigma$  in a direct way, as it was explained in the theory.

A closed-form solution may also be obtained for the bilinear transformed reflectance of a gaussian-shaped transition layer between a surface layer of constant refractive index and the bulk. Although it is usually assumed that sharp interfaces exist between epitaxial layers and substrates in either homo- or heteroepitaxial structures, high temperature processing induces diffusion of mobile atomic species. The resulting graded refractive index profile between layers possessing constant refractive indices may affect the optical properties significantly. Suppose this transition region can be represented by a half-gaussian:

$$n(x) = n_a + u(x-d_a)(n_s - n_a) \left[ \exp \left[ -\frac{(x-d_a)^2}{2\sigma^2} \right] - 1 \right] \quad (11)$$

where  $n_a$  is the refractive index of the layer,  $d_a$  is the distance between the surface and the start of the transition region, and  $u(x)$  is the unit step function. An approximate solution for the first order expression of the bilinear transformed reflectance is given for this profile by:

$$B(w) = B_0 - \frac{(n_a^2 - 1)(n_s - n_a)}{2n_a^2} [G(y) \cos \theta_a - H(y) \sin \theta_a] \quad (12)$$

where

$$\begin{aligned} B_0 &= \frac{n_a^2 + 1}{2n_a} & y &= 4\pi\sigma n_s w & \theta_a &= 4\pi n_a d_a w \\ G(y) &= [1.75 \exp(-y^2/2) - 0.75] \exp(-y^2/6.5) \\ H(y) &= \sqrt{\pi/2} y \exp(-y^2/2) \end{aligned} \quad (13)$$

The simulated reflectance of a material containing such a layer is presented in Fig. 4. The following parameters were employed:  $n_s = 3.87$ ;  $n_a = 3.45$ ;  $x_d = 1 \mu\text{m}$ ;  $\sigma = 0.05$  and  $0.1 \mu\text{m}$ , respectively. We note from Fig. 4(a) and (b) that the amplitude of the reflectance diminishes with increasing wavenumber, as well as  $\sigma$ . The Fourier transforms of the bilinear transformed reflectance of results presented in Figs. 4(a) and (b) are shown as inserts. Note that the spectral peaks are situated at  $x = 1.05 \mu\text{m}$  and  $x = 1.06 \mu\text{m}$ , respectively. This is a few percent larger than  $x_0$  because of the finite extent of the transition region.

**Profiling:** The refractive index profile in processed electronic and photonic material is of considerable interest. It may be directly related to device performance, such as in optical waveguides, or indirectly when it is useful for quality control of processing steps. Ion implantation, diffusion, epitaxy, oxidation and ion exchange are common processing steps which to a greater or lesser extent alter the refractive index of dielectric media. For small values of the perturbation in the refractive index, the bilinear transformed reflectance for inhomogeneous layers can be inverted. The normalized "ac" component of  $B(w)$  is obtained from eqs.(7) and (8) (first order):

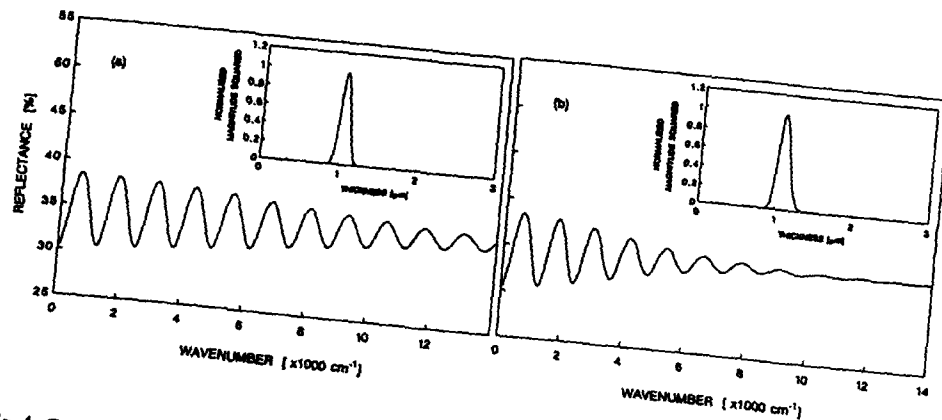


Fig. 4 Calculated optical reflectance and Fourier power spectrum of the bilinear transformed reflectance of a semiconductor sample containing a surface layer with thickness  $d_s = 1 \mu\text{m}$ ;  $n_s = 3.87$ ;  $n_b = 3.45$ .  
(a)  $\sigma = 0.05 \mu\text{m}$  (b)  $\sigma = 0.2 \mu\text{m}$

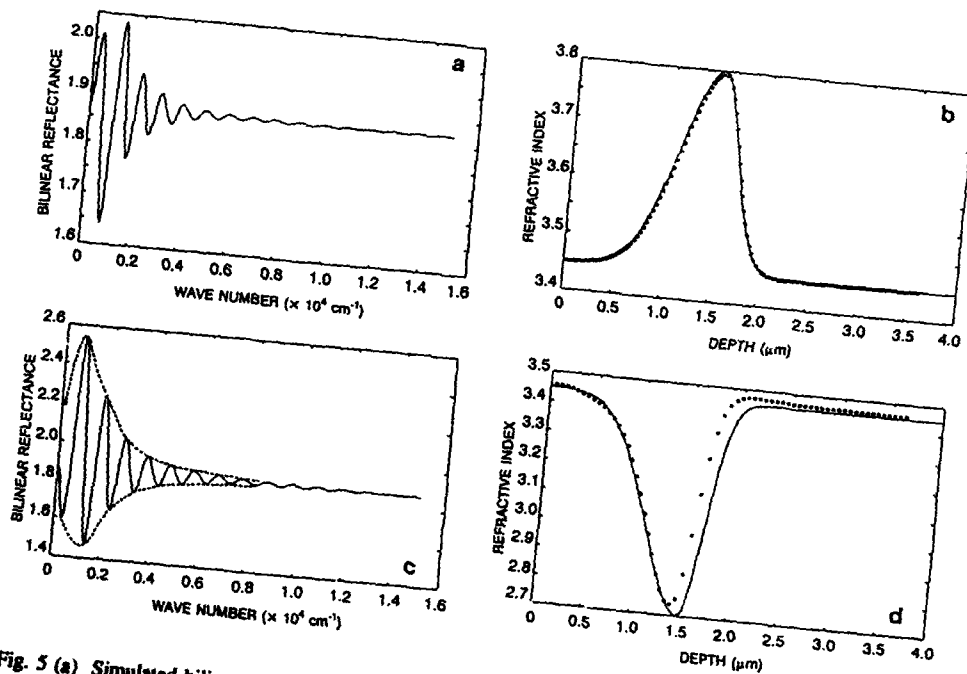


Fig. 5 (a) Simulated bilinear transformed reflectance for a double gaussian profile with  $n_s = 3.45$ ;  $n_b = 3.8$ ;  $x_p = 1.5 \mu\text{m}$ ;  $\sigma_1 = 0.4 \mu\text{m}$ ;  $\sigma_2 = 0.2 \mu\text{m}$ . (b) Comparison between the estimated profile (open circles) and the profile used in the simulation (solid line). (c) Simulated bilinear transformed reflectance for a double gaussian profile with  $n_s = 3.45$ ;  $n_b = 2.7$ ;  $x_p = 1.5 \mu\text{m}$ ;  $\sigma_1 = 0.4 \mu\text{m}$ ;  $\sigma_2 = 0.2 \mu\text{m}$ . (d) Comparison between the estimated profile (open circles) and the profile used in the simulation (solid line).

$$B_{ac}^{(1)} = \frac{(B(w) - B_0)}{B_1} = \int_0^x \frac{1}{n(x)} \frac{dn(x)}{dx} \cos \left( 4\pi w \int_0^x n(\xi) d\xi \right) dx \quad (14)$$

For an arbitrary refractive index profile  $n(x)$  for which  $|n(x) - n_1| \ll n_1$ :

$$B_{ac}^{(1)}(w) = \frac{B(w) - B_0}{B_1} = \int_0^x \frac{1}{n(x)} \frac{dn(x)}{dx} \cos(4\pi w n_1 x) dx \quad (15)$$

If it is now assumed hypothetically that the refractive index function  $n(x)$  is symmetrical with respect to the origin  $x = 0$ ,  $B_{ac}$  may be expressed as a Fourier transform:

$$B_{ac}^{(1)}(\omega) = \frac{1}{m} \mathcal{F} \left\{ \frac{dn(x)/dx}{n(x)} \right\} = \frac{1}{m} \mathcal{F} \{ d(\ln(n(x))) \} \quad (16)$$

where  $\omega = 4\pi n_1 w$  and  $m$  is a constant.

Eq.(16) is invertible, allowing one to obtain the unknown refractive index profile from the measured bilinear transformed reflectance. It follows directly from eq.(16) that:

$$n(x) = n_1 \exp \left[ m \int_0^x \mathcal{F}^{-1} \{ B_{ac}^{(1)}(\omega) \} dx \right] \quad (17)$$

If the refractive index changes are not small, higher order terms have to be considered, and eq.(15) modified accordingly [22]:

$$B_{ac}^{(2)}(w) = B_{ac}^{(1)}(w) + \frac{B_0}{B_1} \rho_2(w) \quad (18)$$

where  $\rho_2(w)$  has been defined in eq.(9).

The effect of the second order term can be eliminated from the analysis because it contributes in most cases only to a slowly varying shift in the mean value of the oscillatory part of the bilinear transformed reflectance, as can be seen in Fig. 3(a).

In order to investigate the validity of the theory, reflectance versus wavenumber data was generated for buried asymmetric gaussian refractive index profiles. The reflectance curves were obtained by sub-dividing the double gaussian profile (standard deviation  $\sigma_1$  for  $x < x_p$ , and  $\sigma_2$  for  $x > x_p$ ) into a large number of differential layers ( $>60$ ), and subsequently computing the reflectance by the matrix technique [11]. Eq.(17) was applied to the bilinear transformed data when  $|n_p - n_1|/n_1 \ll 1$ . Bilinear transformed reflectance data for profiles which did not satisfy this condition, was first processed in order to remove the second order term expressed in eqs.(9) and (18).

**Small refractive index change:** The simulated bilinear transformed reflectance for a double gaussian profile with  $n_1 = 3.45$ ;  $n_p = 3.8$ ;  $x_p = 1.5 \mu\text{m}$ ;  $\sigma_1 = 0.4 \mu\text{m}$ ;  $\sigma_2 = 0.2 \mu\text{m}$ , is presented in Fig. 5(a). Following the processing described by eqs.(15) - (17), the estimated refractive index profile shown in Fig. 5(b) was obtained. The discrepancy of 0.16% in the peak values between the estimated (open circles) and the actual profile (solid line) is caused by the simple numerical integration routine which was employed for the evaluation of the integral which occurs in eq.(17).

**Large refractive index change:** Substoichiometric oxide/nitride layers may exist in as-implanted



samples, particularly for doses below the critical dose [23]. Under the correct conditions, which depend on implant temperature, dose, and post-implant anneal, the buried layer may convert to an insulating layer with sharp interfaces. This last case had been studied in great detail by various optical techniques [e.g.5,7,24], and will not be addressed in the present work. Before the high temperature anneal, it is reasonable to expect that the implanted material will contain a mixed phase of silicon and  $\text{SiN}_x$ . This will lead to material with a graded or inhomogeneous refractive index profile which is smaller than the refractive index of silicon. The technique for inverting the bilinear transformed reflectance in order to obtain the refractive index profile, will now be illustrated for a hypothetical material containing a double gaussian profile with  $n_s = 3.45$ ;  $n_p = 2.7$ ;  $x_p = 1.5 \mu\text{m}$ ;  $\sigma_1 = 0.4 \mu\text{m}$ ;  $\sigma_2 = 0.2 \mu\text{m}$ . The bilinear transformed reflectance is shown in Fig. 5(c). Because the maximum change in refractive index is nearly 22%, the second order term is not negligible. This can be seen from the asymmetry of the envelopes defined by the maxima and minima in Fig. 5(c), respectively. After a simple digital signal processing step which involves a cubic splines interpolation of these envelopes, the second order term was computed and subtracted. Removal of the average value  $B_0$  and by normalization with respect to  $B_1$ , lead to the function  $B_e^{(1)}(w)$ . Following the same procedure as before, the estimated profile shown in Fig. 5(d) is obtained. The integration of the inverse Fourier transform in eq.(17) was executed from the surface towards the substrate. It can be seen that the estimated profile (open circles) approximates the real profile (solid line) quite well towards the surface, but there is a large discrepancy on the trailing edge. The opposite is true if the integration is carried out from the substrate towards the surface. A compromise which leads to very satisfactory results, involves integration from both sides towards the peak.

## EXAMPLES

The measurement technique will be illustrated by means of an example for each case discussed. **Heterostructure InP-InGaAs-InP:** The epitaxial structure to be discussed was obtained commercially and consisted of nominally  $0.8 \mu\text{m}$  InP /  $0.25 \mu\text{m}$  InGaAs /  $2 \mu\text{m}$  InP /  $5 \mu\text{m}$  InGaAs on an  $n^+$  InP substrate. A Hitachi UV-3400 UV-VIS spectrophotometer was used together with a  $5^\circ$  specular reflectance attachment to measure the reflectance pattern of the samples in the  $0.2$  to  $2.6 \mu\text{m}$  wavelength range.

The measured reflectance for the range  $3900 - 8600 \text{ cm}^{-1}$  is shown in Figure 6(a). There is a clear change in the nature of the interference pattern at approximately  $w = 5800 \text{ cm}^{-1}$ . This change in structure will be immediately apparent from the difference in Fourier spectra for the high and low wavenumber domains. Before Fourier transformation, the reflectance is bilinear transformed; it is compensated for dispersion by a non-linear operation on the wavenumber axis; a splines interpolation routine is applied in order to obtain equispaced wavenumber data; it is corrected for the baseline; and the mean value is subtracted. The bilinear transformed reflectance after dispersion compensation is shown in Figure 6(b), and the power spectral density which was calculated from the Fourier transform, is depicted in Figure 6(c). As was expected, four distinct peaks appear in the spectrum, and from direct measurement they are located at optical thickness  $nd$  equal to  $2.15$ ;  $4.435$ ;  $10.068$  and  $28.84 \mu\text{m}$ , respectively. A quick estimate of layer thickness may be obtained by using nominal values for the refractive indices, namely  $n_{\text{InP}} = 3.1$  [25];  $n_{\text{InGaAs}} = 3.5$  [26]. If the layer thicknesses are denoted by  $d_1$ ,  $d_2$ ,  $d_3$  and  $d_4$ , respectively, it follows that:  $d_1 = 2.15/3.1 = 0.7 \mu\text{m}$ ;  $d_2 = (4.435-2.15)/3.5 = 0.65 \mu\text{m}$ ;  $d_3 = (10.068-4.435)/3.1 = 1.82 \mu\text{m}$ ;  $d_4 = (28.84-10.068)/3.5 = 5.36 \mu\text{m}$ . Except for the second layer which is much thicker than expected, the experimentally determined layer thickness values agree to within 10% with the nominal values. Better estimates may be obtained by first calculating the actual refractive indices from the amplitudes of the spectral peaks.

**Buried gaussian profile:** A silicon-on-insulator (SOI) sample was prepared using a p-type  $76.2 \text{ mm}$  diameter silicon wafer of  $\langle 100 \rangle$  orientation,  $8.6 \pm 1.4 \Omega\text{-cm}$  resistivity (boron doped) and a thickness of  $381 \pm 20 \mu\text{m}$ . The cleaned wafer was implanted with nitrogen ( $\text{N}^+$ ) to a dose of  $1.8 \times 10^{18} \text{ cm}^{-2}$  at  $160 \text{ keV}$ . The beam current was approximately  $2 \text{ mA}$  and the implant lasted about 2 hours. The wafer temperature was kept at about  $550^\circ\text{C}$  by controlling the incident

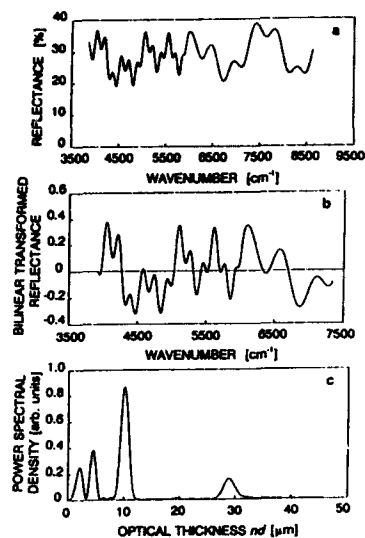


Fig. 6(a) Measured reflectance of InP-InGaAs-InP multilayer structure. (b) Bilinear transformed reflectance after dispersion compensation. (c) Power spectral density of the bilinear transformed reflectance.

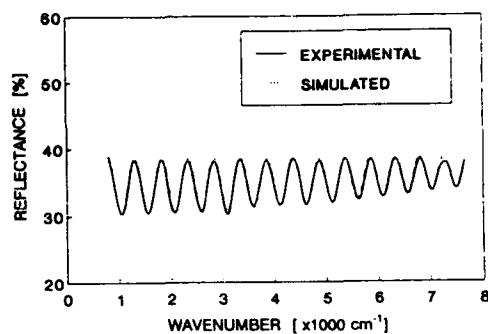


Fig. 8 Experimental [18] (solid line) and calculated (dashed line) reflectance of silicon implanted with 2.7 MeV phosphorus to a dose of  $1.74 \times 10^{16} \text{ cm}^{-2}$ .

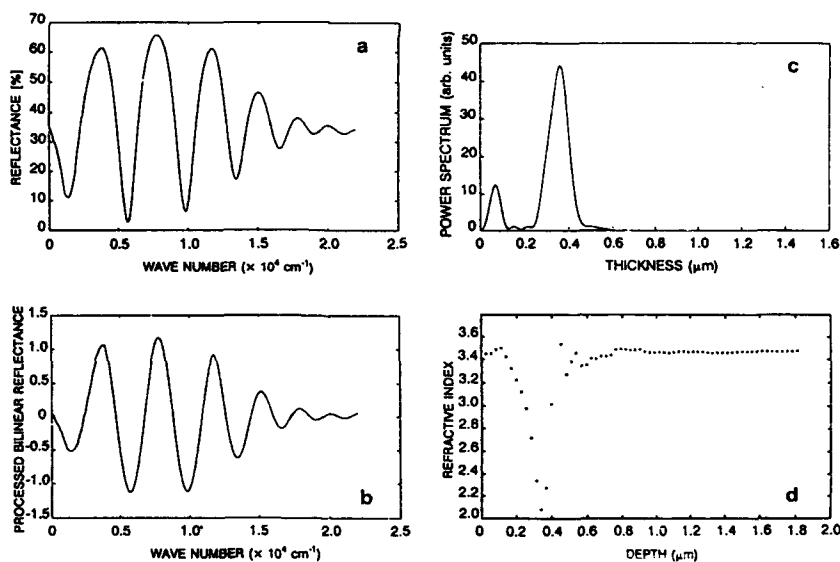


Fig. 7 (a) Measured reflectance for a silicon wafer implanted with  $1.8 \times 10^{18} \text{ cm}^{-2} \text{ N}^+$  at 160 keV (no post implant anneal). Data has been corrected for the effect of the amorphous  $\text{SiN}_x$  absorption band in the far-infrared and for dispersion at high wavenumbers. (b) Bilinear transformed reflectance after digital signal processing as described in the text. (c) Power spectral density of the bilinear transformed reflectance. (d) Estimated refractive index profile for the as-implanted silicon-on-insulator sample.

beam current. The Hitachi model 3400 UV-VIS spectrophotometer with a 5° specular reflectance attachment was used to measure optical reflectance in the 0.45  $\mu\text{m}$  to 2.6  $\mu\text{m}$  range, while a Perkin-Elmer model 1600 FTIR with a variable angle attachment set at an angle of 15° was used to characterize the sample in the 1.3  $\mu\text{m}$  to 50  $\mu\text{m}$  range of the spectrum. From the measurements in the far-infrared it was established that this sample contained a buried layer of amorphous silicon nitride[7]. The reflectance data was transformed to the wavenumber domain by inverting the wavelength values, combining the two files and applying splines interpolation to the whole data set in order to rearrange the x-values in equal wavenumber intervals. The combined data set was corrected for dispersion at high wavenumbers[15]; extrapolated to zero frequency; and the effects of the absorption band of amorphous silicon nitride removed. The final result is shown in Fig 7(a). The asymmetry in the two envelopes connecting the maxima and minima of the bilinear transformed reflectance, respectively, is evidence of a relatively large change in refractive index. Next, the reflectance was bilinear transformed (Fig. 7(b)) to remove excess frequency components [13]. This is also confirmed by the appearance of a "low frequency" peak in the power spectrum presented in Fig. 7(c). The large peak is located at an optical thickness  $nd = 1.24 \mu\text{m}$ , which, for  $n_s = 3.45$ , corresponds to a depth  $d = 0.36 \mu\text{m}$  below the surface. This agrees well with the projected range for 160 keV nitrogen in silicon, namely  $R_p = 0.367 \mu\text{m}$  [27].

**Inhomogeneous transition layer:** Experimental results of Hubler et al.[16] will be used to demonstrate the effect of a transition layer between a homogeneous layer and a substrate with different refractive index. Their research group implanted  $\langle 111 \rangle$  Si with 2.7 MeV phosphorus to a dose of  $1.74 \times 10^{16} \text{cm}^{-2}$ , forming an amorphous layer in the top part of the material with higher refractive index than the crystalline substrate and a gaussian region in between. By means of a least-squares fit they determined a thickness  $d_a = 2.52 \mu\text{m}$  for the amorphous layer, and a standard deviation  $\sigma = 0.053 \mu\text{m}$  for the transition layer. From the Fourier spectrum of the bilinear transformed reflectance we determined a value  $d_s = 2.49 \mu\text{m}$ , and from the theory presented in eqs.(12) - (13), a value  $\sigma = 0.053 \mu\text{m}$ . The measured and computed reflectance are compared in Fig. 8.

**Profiling:** The processed bilinear transformed reflectance data pertaining to the nitrogen implanted SOI sample will be analyzed according to the procedure set out before. After pre-processing, and removal of the second order term  $\rho_2(w)$  as described before, the data was scaled with  $B_1$  which depends on  $n_s$  in this sample; and the mean value  $B_0$  was subtracted. Finally, the bilinear transformed reflectance  $B_{sc}$  of Fig. 7(b) was processed according to the procedure outlined in eq.(17). The estimated refractive index profile is presented in Fig. 7(d). As is to be expected, the refractive index in the bulk and near the surface is approximately the same, while it decreases rapidly to a value of 2.06 at a distance of 0.34  $\mu\text{m}$  from the surface. Note the good correspondence between the position of the minimum in the profile, and the position of the large peak in the power spectrum presented in Fig. 7(c).

## DISCUSSION

Reflectance measurements in the visible and near-infrared parts of the optical spectrum may be used to determine layer thickness and refractive index steps in multilayer heteroepitaxial structures. Under the assumptions of small refractive index steps, low absorption, coherent reflections, and near-normal incidence, the algorithm yields an approximate cross-sectional view of the layered medium. Since the refractive index may be calculated directly from the amplitudes of the spectral peaks, the refractive index and composition (depending on the refractive index model) may be obtained. Once the refractive indices of the individual layers are known, the thickness values may be corrected in order to achieve better accuracy (< 2%).

By analyzing various regions of the reflectance pattern, for instance at low and high wavenumbers, respectively, it is also possible to determine the location of absorbing layers in the multilayer structure. This may be seen from the data for a four-layer structure consisting of InP-InGaAs-InP-InGaAs on an InP substrate.

Buried gaussian profiles and buried transition layers can be analyzed by the expressions for bilinear transformed reflectance. Under certain simplifying assumptions, simple closed-form solutions are possible. Simulated data for both cases were analyzed by the Fourier transform technique presented in the paper, and further confirmed by analysis of experimental data.

It has also been shown that reflectance measurements may be used to determine the shape of buried refractive index profiles in lossless dielectric media. This paper provided the theoretical framework required to achieve this goal. If the refractive index profile differs by a relatively small amount from the substrate refractive index, the digital signal processing is very simple. It requires only the computation of the oscillatory part of the scaled bilinear transformed reflectance, followed by a fast Fourier transform and numerical integration. This was demonstrated by using simulated reflectance data of a buried double gaussian profile. Profiles with larger refractive index peaks (or valleys), are somewhat more complicated to handle, but are not intractable. This paper presented a simple technique to remove the effects of higher order terms, illustrating it with an example. Although the double gaussian profile in this example has a valley which is 22% smaller than the substrate refractive index, the profile towards the surface was estimated quite accurately. A procedure was also outlined for achieving the same accuracy on the trailing edge of the profile.

Further evidence of the utility of the technique was provided by analyzing reflectance data obtained from nitrogen implanted silicon. In this instance the change in refractive index was roughly 40%, and the profile was located very close to the surface. Nevertheless, the results indicate correctly that a layer of silicon remains near the surface, and that the refractive index decreases rapidly towards the value  $\text{Si}_3\text{N}_4$  at a depth of 0.34  $\mu\text{m}$ . The projected range for 150 keV nitrogen ions in silicon is 0.367  $\mu\text{m}$ . [27]

#### References

1. D.K. Gaskill, J. Davis, R.S. Sillmon and M. Sydor in SPIE Proc. Modern Optical Characterization Techniques for Semiconductors and Semiconducting Devices, edited by O. Glembocki, F. Pollak and J. Song (SPIE Proc. 794, 1987).
2. G. Abstreiter, *Appl. Surf. Sci.* **50**, 73 (1991).
3. D.E. Aspnes and A.A. Studna, *Phys. Rev. B* **27**, 27 (1983).
4. S.A. Alterovitz, P.G. Snyder, K.G. Merkel, J.A. Woollam, D.C. Redulescu and L.F. Eastman, *J. Appl. Phys.* **63**, 5081 (1988).
5. P.L. Swart and B.M. Lacquet, *J. Electron. Mat.* **19**, 809 (1990).
6. P.L. Swart and B.M. Lacquet, *J. Electron. Mat.* **19**, 1383 (1990).
7. B.M. Lacquet and P.L. Swart, *J. Electron. Mat.* **20**, 921 (1991).
8. G.E. Aizenberg, P.L. Swart and B.M. Lacquet, *J. Electron. Mat.* **21**, 1033 (1992).
9. G.E. Aizenberg, P.L. Swart and B.M. Lacquet, *Appl. Surf. Sci.* **63**, 249 (1993).
10. G.E. Aizenberg, P.L. Swart and B.M. Lacquet, *J. Electron. Mat.* **22**, 143 (1993).
11. P. Yeh, Optical Waves in Layered Media (John Wiley & Sons, New York, 1988).
12. M.H. Dunn, *Appl. Opt.* **10**, 1393 (1971).
13. P.L. Swart and B.M. Lacquet, *J. Appl. Phys.* **70**, 1069 (1991).
14. S. Adachi, *J. Appl. Phys.* **58**, R1 (1985).
15. B.M. Lacquet and P.L. Swart, *J. Electron. Mat.* **20**, 379 (1991).
16. G.K. Hubler, P.R. Malmberg, C.N. Waddell, W.G. Spitzer and J.E. Fredrickson, *Rad. Eff.* **60**, 35 (1982).
17. C.N. Waddell, W.G. Spitzer, G.K. Hubler and J.E. Fredrickson, *J. Appl. Phys.* **53**, 5851 (1982).
18. G.K. Hubler, P.R. Malmberg and T.P. Smith, *J. Appl. Phys.* **50**, 7147 (1979).
19. Y. Yu, Z. Fang, C. Lin and S. Zou, *Mat. Lett.* **8**, 95 (1989).
20. G.E. Aizenberg, P.L. Swart and B.M. Lacquet, *Optics Letters* (to be published).
21. G.E. Aizenberg, P.L. Swart and B.M. Lacquet, *S.A. J. of Phys.* **10**, 131 (1993).
22. P.L. Swart and B.M. Lacquet, *S.A. J. of Phys.* **16**, 118 (1993).
23. J-P Colinge, Silicon-on-Insulator Technology: Materials to VLSI (Kluwer Academic Publishers, Boston, 1991).
24. J. Vanhellemont and H.E. Maes, *Sol. State Phen.* **6 & 7**, 525 (1989).
25. E.D. Palik, Handbook of Optical Constants of Solids (Academic Press, San Diego, 1985) p.503.
26. E.D. Palik, Handbook of Optical Constants of Solids II (Academic Press, San Diego, 1991) p.140.
27. J.F. Gibbons, W.S. Johnson and S.W. Mylroie, Projected Range Statistics (Dowden, Hutchinson and Ross, Stroudsburg, Penn., 1975).

## INFRARED AND ULTRAVIOLET ANALYSIS OF DUAL-ION IMPLANTED GaAs

BEATRYS M. LACQUET, GUSTAVO E. AIZENBERG AND PIETER L. SWART  
Sensors Sources and Signal Processing Research Group, Faculty of Engineering, Rand  
Afrikaans University, PO Box 524, Auckland Park 2006, South Africa

### ABSTRACT

Semi-insulating <100> GaAs was implanted with 170 keV H<sup>+</sup> and P<sup>+</sup> ions at room temperature using a PH<sub>3</sub> source. Fourier analysis of the bilinear transformed optical reflectance data in the infrared region of the spectrum indicated the presence of two damaged layers at different depths from the surface: (i) a deep inhomogeneous layer of low damage produced by the protons and (ii) a thin amorphized surface layer which was produced by phosphorus ions. The position and refractive index at the peak of the assumed gaussian damage profile caused by the protons, as well as the standard deviation of the profile, were estimated rapidly from the processed data. The thickness and refractive index of the surface layer were also estimated from this analysis. The presence of the amorphized surface layer was evident from the reflectance in the ultraviolet where shift and broadening of the reflectance peaks associated with the Van Hove singularities, were observed.

### INTRODUCTION

Ion-implantation is often used to selectively change the electrical properties of semiconductors, and during the processing it is not always possible to measure the electrical characteristics, especially when buried layers are formed. The process does, however, also change the optical properties of the material and therefore the use of optical techniques as a non-invasive probe is an attractive option. Techniques such as differential reflectance, spectroscopic ellipsometry, modulated optical reflectance, Raman scattering, and optical spectroscopy, have been employed in numerous situations where information regarding layer thickness, structure, composition and refractive index was required.[1-6] Most of these techniques suffer from drawbacks such as non-linear least-squares curve-fit; convergence problems, limitations in the number of layers and the thickness of individual layers, and complex and time consuming experimental procedures. It has been shown recently that the analysis of homogeneous layers in electronic materials which possess small refractive index steps between layers such as heteroepitaxial layers [7], and ion implanted semiconductors, [8,9] may readily be done by means of optical reflectometry and digital signal processing. Most of the abovementioned problems are overcome using this technique. However, in many situations the refractive index of the material changes as a function of depth. This may occur as a result of radiation damage by ion-implantation, or from the charge carrier contribution to the refractive index at long wavelengths where the carrier concentration itself is a function of the ion implantation or diffusion profile.[10-15] Optical reflectometry has been applied in the past in order to study these graded materials, but at the expense of simplicity. Since no closed-form solution existed for reflectance, it required elaborate parameter estimation procedures applied to multi-parameter models.[10-15] In this paper we will present the characterization by optical reflectometry and signal processing

techniques of a GaAs substrate implanted with both protons to form a buried damaged layer, and phosphorus which creates a damaged surface layer. A very brief outline of the theory which was used to analyze the reflectance spectra will be given, followed by the results.

## THEORY

Some processed electronic materials such as nitrogen implanted silicon or semi-insulating GaAs implanted with protons, show refractive index changes that can be approximated by a gaussian profile superimposed onto a background of constant refractive index. The refractive index profile can be described by

$$n_G(x) = n_s + (n_p - n_s) \exp\left(-\frac{(x - x_p)^2}{2\sigma^2}\right) \quad (1)$$

where  $n_s$  is the refractive index of the substrate,  $n_p$  the refractive index at the peak of the gaussian,  $x_p$  and  $\sigma$  are the physical position of the peak and the standard deviation of the gaussian, respectively. The theory was developed on the basis that this continuous gaussian refractive index profile can be divided into differential layers of infinitesimal thickness  $dx$  having a refractive index  $n(x_j)$ , and element  $j$  is found at a depth  $x_j$ . The bilinear transformed reflectance[16] at a particular wavelength  $\lambda$  is then given by[17]

$$B(\lambda) = \frac{1 + r_{01}^2}{1 - r_{01}^2} - \frac{2r_{01}}{1 - r_{01}^2} \int_0^\infty \frac{1}{n(x)} \frac{dn(x)}{dx} \cos\left[\frac{4\pi}{\lambda} \int_0^x n(\xi) d\xi\right] dx \quad (2)$$

where  $r_{01} = (1 - n_1)/(1 + n_1)$  is the reflectivity coefficient between air and the surface of the material under investigation.  $n_1$  is the refractive index at the surface. The reflectance is found by applying [18]

$$R(\lambda) = \frac{B(\lambda) - 1}{B(\lambda) + 1} \quad (3)$$

In the specific case when  $|(n_p - n_s)| \ll n_s$ , eq.(2) becomes in the wavenumber domain

$$B(w) = B_0 + Kw \exp\left(-\frac{(4\pi\sigma n_s w)^2}{2}\right) \sin(4\pi n_s x_p w) \quad (4)$$

The constant  $K$  depends on  $\sigma$ ,  $n_s$  and  $n_p$ , and  $w = 1/\lambda$ . On closer inspection, one finds that eq.(4) describes a sinusoid which is modulated by a Rayleigh function, of which the frequency  $2n_s x_p$  is proportional to the peak position  $x_p$ . The standard deviation of this gaussian distribution is found by setting the derivative of eq.(4) with respect to wavenumber equal to zero and solving for  $\sigma = (4\pi w_p n_s)^{-1}$  with  $w_p$  the wavenumber at which the peak occurs.

The phosphorus implant causes an amorphized surface layer, which is different from the damage caused by the proton implantation. This layer is considered to be a single layer

on the surface with a different refractive index than the substrate.

## SAMPLE PREPARATION AND MEASUREMENTS

Semi-insulating Cr-doped <100> GaAs was implanted with 170 keV protons and 170 keV P<sup>+</sup> to a dose of  $1.5 \times 10^{16} \text{ cm}^{-2}$ . The incident beam, sourced from PH<sub>3</sub> gas, was 7° off from the <100> axis to reduce channeling. The implant current was kept at approximately 1.5  $\mu\text{A}$ . Annealing of radiation defects during implantation was minimized by improving the thermal contact between sample and holder. In addition, the implantation was interrupted and the sample allowed to cool each time the temperature, as measured by a thermocouple at the clips holding the sample, rose to 50°C. Reflectance measurements for  $500 \text{ cm}^{-1} < \omega < 4800 \text{ cm}^{-1}$  were performed using a Fourier transform infrared spectrophotometer (Perkin Elmer 1600) with a 17° angle of incidence. For the wavenumber range  $4800 \text{ cm}^{-1} < \omega < 50000 \text{ cm}^{-1}$ , the Hitachi UV-3400 UV-VIS spectrophotometer was used with a 5° angle of incidence.

## DISCUSSION

The experimental reflectance spectrum is compared in Figure 1 with a theoretical curve calculated for unimplanted GaAs. The reflectance generally increases with wavenumber because of dispersion. The maxima at approximately  $24000 \text{ cm}^{-1}$  and  $41000 \text{ cm}^{-1}$  are associated with Van Hove singularities corresponding to the  $\Lambda_3 \rightarrow \Lambda_1$  and the  $X_3 \rightarrow X_1$  transitions, respectively.[19] In Figure 2 the data pertaining to a reduced wavenumber range ( $500 \text{ cm}^{-1}$  to  $12500 \text{ cm}^{-1}$ ) is shown. The baseline (average value) was subtracted from the reflectance curve. Two distinct oscillations are observed in this curve; a high frequency corresponding to a thick layer, and a much lower frequency component which indicates the existence of a thin layer near the surface. This data was then bilinear transformed, zero padded to 4096 data points and a fast Fourier transform executed. The resulting power density spectrum is depicted in Figure 3. It clearly shows the two expected frequency components. The peak to the right is related to the position of the peak of the damage produced by the implantation of protons. Using  $n_s = 3.34$  (at  $400 \text{ cm}^{-1}$ )[12], we measured its position to be  $1.52 \mu\text{m}$ , which agrees to within 1.3% with the depth value of  $1.54 \mu\text{m}$  which was interpolated from SIMS measurements by Wilson et al.[20] on GaAs implanted with protons at room temperature. The peak to the left of Figure 3 is indicative of a surface layer of  $0.16 \mu\text{m}$  thick. The mean range calculated from a TRIM simulation[21] for GaAs implanted with 170 keV phosphorus ion is approximately  $0.154 \mu\text{m}$ . This value agrees well with the estimated thickness of the surface layer. The refractive index  $n_{\text{surf}}$  of the surface layer was estimated to be 3.4. The estimated value was expected to be lower than the actual value, because as observed from Figure 2, it was only possible to analyze one cycle of the low frequency oscillation. Under this condition, a good thickness estimate can be expected, but not an accurate value for refractive index.

Simulations performed by means of the first order approximation indicated that the refractive index of the damaged layer produced by the implantation of protons, was lower than the refractive index of the substrate. Figure 4 is a comparison of the measured reflectance data and the reflectance curve calculated by eq.(2) and (3) using the following parameters:  $n_s = 3.34$ ;  $n_p = 3.26$ ;  $\sigma_1 = 0.092 \mu\text{m}$ ;  $\sigma_2 = 0.2$  and  $x_p = 1.56 \mu\text{m}$ . The curve fit is not good when the refractive index at the peak of the double-gaussian is assumed to

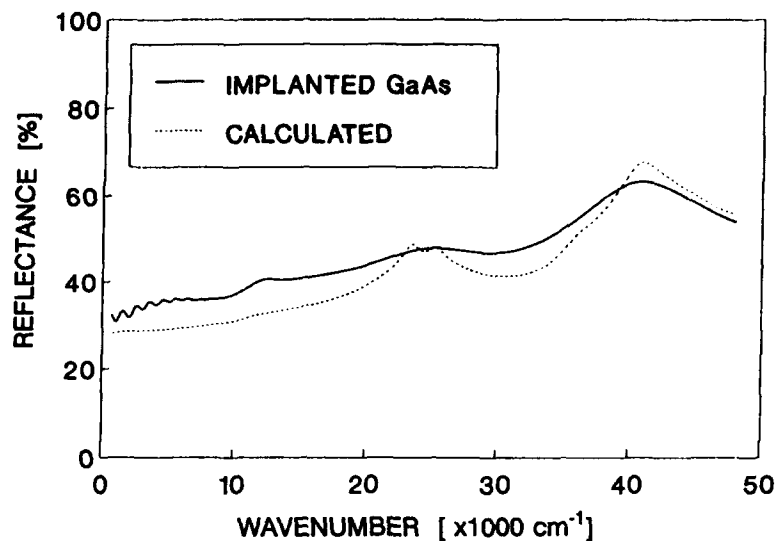


Fig. 1 Experimental reflectance of <100> semi-insulating GaAs implanted at room temperature with 170 keV protons to a dose of  $1.5 \times 10^{16} \text{ cm}^{-2}$ . Calculated reflectance for single crystalline GaAs is shown by the dashed line.

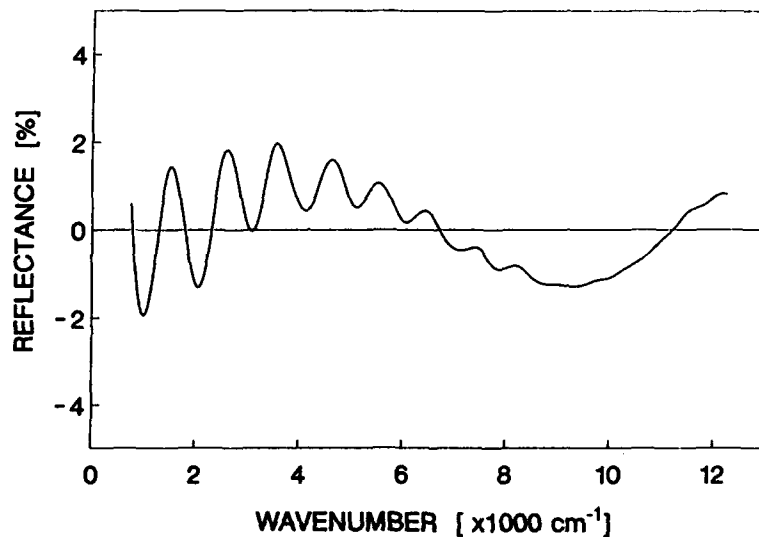


Fig. 2 Oscillatory component of the reflectance of <100> semi-insulating GaAs implanted at room temperature with 170 keV protons to a dose of  $1.5 \times 10^{16} \text{ cm}^{-2}$ . Wavenumber range:  $500 \text{ cm}^{-1}$  to  $12500 \text{ cm}^{-1}$ .



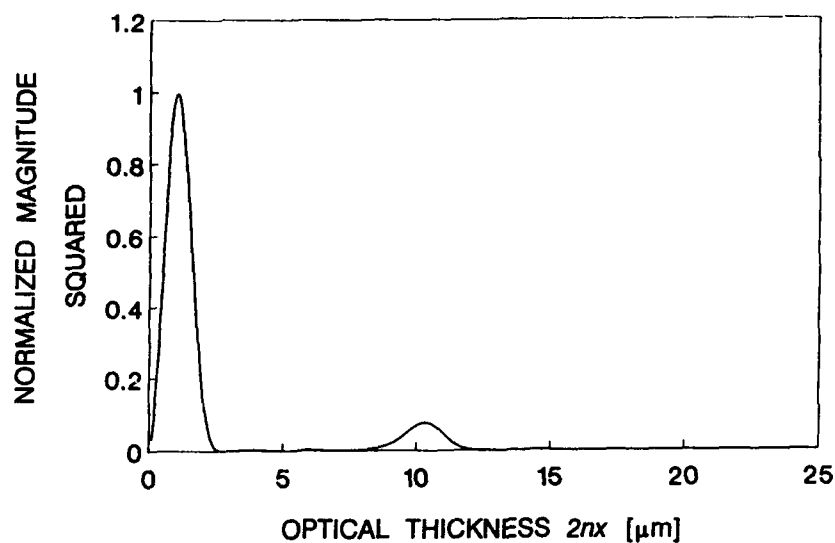


Fig. 3 Fourier spectrum of the bilinear transformed reflectance of <100> semi-insulating GaAs implanted at room temperature with 170 keV protons to a dose of  $1.5 \times 10^{16} \text{ cm}^{-2}$ .

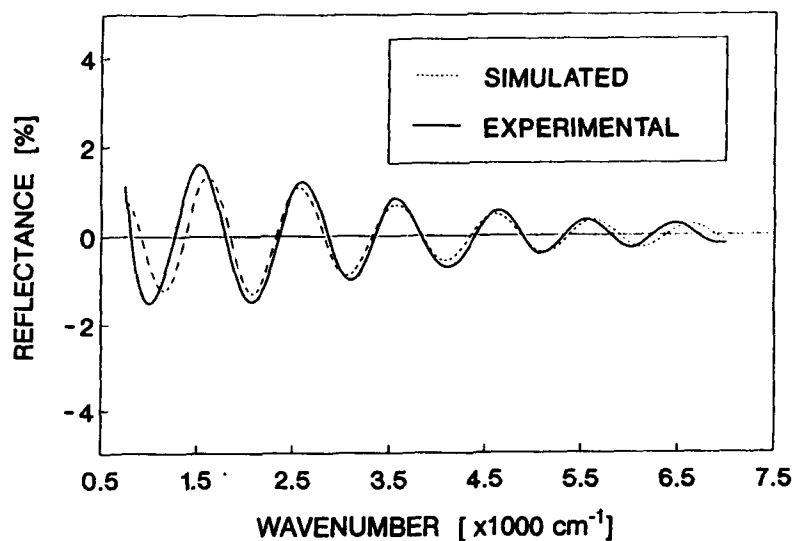


Fig. 4 Comparison between the simulated and measured oscillatory component (high pass filtered) of the reflectance of <100> semi-insulating GaAs implanted at room temperature with 170 keV protons to a dose of  $1.5 \times 10^{16} \text{ cm}^{-2}$ .

be higher than that of the substrate. Snyman and Neethling[22] studied GaAs implanted under similar conditions (energy 200 keV) and calculated standard deviations of the double-Gaussian damage profile  $\sigma_1 = 0.091 \mu\text{m}$  and  $\sigma_2 = 0.082 \mu\text{m}$ , respectively. While the value of  $\sigma_1$  is a close estimate, the large discrepancy in the value of  $\sigma_2$  is still unknown.

In Figure 1 the measured reflectance and the calculated reflectance curve of crystalline GaAs is compared. The theoretical curve was simulated by employing the refractive index and extinction coefficient values published by Palik [23]. The experimental curve shows broadening of the peaks, as well as shift of the peak positions in the ultraviolet region of the spectrum. The double peak at approximately  $24000 \text{ cm}^{-1}$  was smoothed out, while the peak at  $41000 \text{ cm}^{-1}$  moved towards lower wavenumbers at approximately  $40000 \text{ cm}^{-1}$ . The rounding of the peaks in the ultraviolet is indicative of the amorphization of the surface layer, while the shift in the peak position at  $40000 \text{ cm}^{-1}$  could be attributed to stress in the surface layer.[24] The exact nature of the stress, whether it is compressive or tensile, is not known at the moment.

### References

1. R.E. Hummel, W. Xi and D.R. Hagmann, *J. Electrochem. Soc.*, **137**, 3583 (1990).
2. J. Tatarkiewicz, *Phys. Stat. Sol.(b)*, **153**, 11 (1989).
3. M. Fried, T. Lohner, J.M.M. De Nijs, A. Van Silfhout, L.J. Hanekamp, N.Q. Khanh, Z. Laczik and J. Gyulai, *Mater. Sci. Eng.*, **B2**, 131 (1989).
4. J. Lee, C. Lee and S. Ernst, *J. Vac. Sci. Technol.* **B6**, 1533 (1988).
5. T.M. Burns, S. Chongsawangvirod, J.W. Andrwes, E.A. Irene, G. McGuire and S. Chevacharoekul, *J. Vac. Sci. Technol.* **B9**, 41 (1991).
6. S. Wurm, P. Alpern, D. Savignac and R. Kakoschke, *Appl. Phys.*, **A47**, 147 (1988).
7. P.L. Swart, B.M. Lacquet and R. Thavar, *Appl. Surf. Sci.*, **50**, 330 (1991).
8. G.E. Aizenberg, P.L. Swart and B.M. Lacquet, *Mat. Res. Soc. Symp. Proc.*, **268**, 349 (1992).
9. G.E. Aizenberg, P.L. Swart and B.M. Lacquet, *J. Electron. Mater.*, **21**, 1033 (1992).
10. G.K. Hubler, P.R. Malmberg, C.N. Waddell, W.G. Spitzer and J.E. Fredrickson, *Rad. Eff.*, **60**, 35 (1982).
11. C.N. Waddell, W.G. Spitzer, G.K. Hubler and J.E. Fredrickson, *J. Appl. Phys.*, **53**, 5851 (1992).
12. L.L. Liou, W.G. Spitzer, J.M. Zavada and H.A. Jenkinson, *J. Appl. Phys.*, **59**, 1936 (1986).
13. G.K. Hubler, P.R. Malmberg and T.P. Smith, *J. Appl. Phys.*, **50**, 7147 (1979).
14. F.R. Kessler, U. Barkow, R. Nies and N. Unzner, *Phys. Stat. Sol. (a)*, **105**, 627 (1988).
15. E. Barta and G. Lux, *J. Phys. D: Appl. Phys.*, **16**, 1543 (1983).
16. P.L. Swart and B.M. Lacquet, *J. Appl. Phys.*, **70**, 1069 (1991).
17. G.E. Aizenberg, P.L. Swart and B.M. Lacquet, *S.A. J. of Phys.*, **16**, 131 (1993).
18. P.L. Swart and B.M. Lacquet, *J. Electron. Mat.*, **19**, 1383 (1990).
19. J.C. Phillips, *Sol. Stat. Phys.*, **18**, 55 (1966).
20. R.G. Wilson, D.A. Betts, D.K. Sadana, J. M. Zavada and R.G. Hunsberger, *J. Appl. Phys.*, **57**, 5006 (1985).
21. J.F. Ziegler, J.P. Biersack and U. Littmark, The stopping and range of ions in solids (Pergamon Press Ltd, New York)
22. H.C. Snyman and J.H. Neethling, *Rad. Eff.*, **60**, 147 (1982).
23. E.D. Palik, Handbook of Optical Constants of Solids (Academic Press, Inc., Orlando, 1985).
24. B.M. Lacquet and P.L. Swart, *Mat. Res. Soc. Symp. Proc.*, **147**, 253 (1989).

## DETERMINATION OF BPSG THIN-FILM PROPERTIES USING IR REFLECTION SPECTROSCOPY OF PRODUCT WAFERS

THOMAS M. NIEMCZYK , JAMES E. FRANKE , LIZHONG ZHANG ,  
DAVID M. HAALAND , and KENNETH J. RADIGAN

\*Chemistry Department, University of New Mexico, Albuquerque, NM 87131

\*\*Sandia National Laboratories, Albuquerque, NM 87185

\*\*\*National Semiconductor, Santa Clara, CA 95052

### ABSTRACT

Three BPSG calibration sets were analyzed using infrared external reflection-absorption spectroscopy: 1) 21 films deposited on undoped silicon coated with 0.1  $\mu\text{m}$  of silicon dioxide, 2) 21 films deposited on undoped silicon, and 3) 9 films deposited on microelectronics product wafers. A multivariate partial least squares analysis of the spectral data for the first large data set showed that boron content, phosphorus content, and film thickness can be quantified with precisions of 0.10 wt%, 0.12 wt%, and 30  $\text{\AA}$ , respectively. The second large data set yielded similar results. The precisions obtained for the nine product wafer samples were 0.13 wt% B, 0.09 wt% P, and for film thickness 103  $\text{\AA}$ .

### INTRODUCTION

Borophosphosilicate glass (BPSG) thin films are widely used in the microelectronics industry as passivation layers, planarization layers, low-fusion-temperature dielectrics, etc.<sup>1</sup> Currently available analytical methods for determining boron and phosphorus content in BPSG films do not meet the demands of at-line or *in-situ* quality control process monitoring. Infrared (IR) spectroscopy satisfies many of the at-line or *in-situ* issues, but has only recently been capable of providing quantitative results using undoped and unpatterned silicon substrates. For a review on the use of quantitative IR methods for dielectric thin film analysis, see ref. [2]. A quantitative IR analysis of dielectric thin films deposited on doped and patterned silicon wafers, which are used in fabricating actual microelectronics product wafers, has not previously been reported, primarily due to the fact that doped silicon is not IR-transparent. Thus, any IR technique used for monitoring the production of BPSG thin films on actual product wafers cannot involve IR transmission. IR external reflection-absorption spectroscopy (IRRAS) is one technique that can satisfy the requirements for quality control of BPSG thin films on product wafers. In this study, we use IRRAS and partial least-squares multivariate calibration for quantitative and simultaneous determination of boron content, phosphorus content, and film thickness in BPSG thin films deposited on both undoped/unpatterned and doped/patterned silicon wafers.

### EXPERIMENTAL

Two 21-sample BPSG calibration sets were prepared on 150 mm silicon wafers using a TEOS-BPSG process at a deposition temperature of 430°C. One set was deposited on uncoated, undoped, and unpatterned silicon (monitor) wafers and the other was deposited on monitor wafers previously coated with 0.10  $\mu\text{m}$  of silicon dioxide (oxide-coated monitor wafers). The BPSG films

were then annealed at 800°C in steam for 10 minutes followed by a 900°C treatment in nitrogen for 20 minutes. BPSG film thickness in the samples deposited on monitor wafers varied between 0.6711 and 0.8218  $\mu\text{m}$ , as measured with a Nanospec film thickness analyzer. Boron ranged between 2.80-5.24 wt% while phosphorus spanned 3.17-5.25 wt%, based on quantitative wet chemical analyses (Balazs Laboratories, Sunnyvale, CA) of half-wafers from the set deposited on monitor wafers. The reported precisions of the reference methods for both B and P content were reported as  $\leq 0.1$  wt%. The precision of the film thickness measurement was reported as  $\pm 30$  Å, which was the standard deviation of five measurements taken within a 1-cm pattern centered on the wafer. The sister set of BPSG samples deposited on oxide-coated monitor wafers were assumed to possess the same values for B, P, and film thickness as described for corresponding samples in the monitor wafer set. Using the same TEOS-BPSG process described earlier, nine BPSG samples were deposited on doped and patterned silicon (product) wafers. These product wafer samples were produced with a proprietary 0.65  $\mu\text{m}$  CMOS process and then coated with BPSG thin-films having 3.0-5.2 wt% B, 3.2-5.3 wt% P, and 0.67-0.79  $\mu\text{m}$  film thickness. These nine samples each possessed a sister wafer in the monitor wafer calibration set, so their individual B, P, and film thickness parameters were presumed to be the same as the corresponding sister samples in the monitor set.

IRRAS spectra were obtained using a Nicolet 800 FTIR spectrophotometer equipped with a DTGS (deuterium triglycine sulfate) detector. Spectra were obtained by averaging 32  $4\text{ cm}^{-1}$  resolution scans. BPSG samples were held in a modified Harrick reflection accessory at 25° incidence (relative to wafer surface normal). Each sample spectrum was ratioed to a background spectrum obtained from a gold mirror to produce the appropriate reflectance ( $R/R_0$ ) spectrum. The spectral data are reported as  $-\log(R/R_0)$  versus frequency. Multivariate analysis was performed on the  $-\log(R/R_0)$  data using the particular partial least-squares (PLS) algorithm that calibrates and predicts each component property separately from the same spectral data (PLS1). The PLS1 algorithm has been described in detail elsewhere<sup>5</sup>.

## RESULTS AND DISCUSSION

Figure 1 shows the IRRAS spectra of the 21 BPSG samples deposited on oxide-coated monitor wafers. The features of these types of spectra, including absorption band assignments and optical effects, have been described<sup>3,4</sup>. Briefly, boron information is primarily observed in the B-O

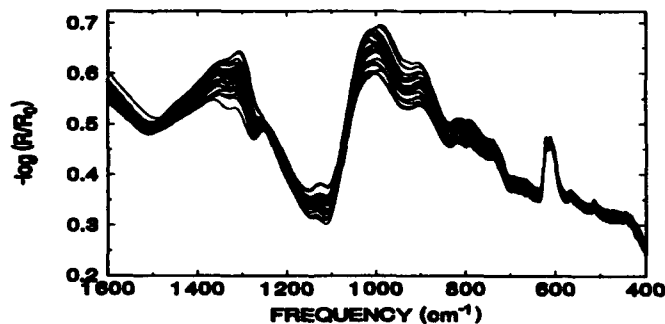


Figure 1. IRRAS spectra at 25° of 21 BPSG thin films on oxide-coated monitor wafers.

band (1300-1500  $\text{cm}^{-1}$ ) and the B-O-Si band (ca. 900  $\text{cm}^{-1}$ ), and phosphorus information is primarily observed in the P=O band (shoulder at ca. 1310  $\text{cm}^{-1}$ ) that is highly overlapped with the B-O band. Information regarding the film thickness is primarily contained in the strongly absorbing Si-O band centered at about 1100  $\text{cm}^{-1}$  in IR transmission spectra. This band appears as a pseudo first derivative feature (1000-1150  $\text{cm}^{-1}$ ) in the IRRAS spectra of Fig. 1 due to thin film optical effects. The pseudo first derivative structures present in IRRAS spectra of thin films are examples of nonlinear spectral behavior that can significantly increase the difficulty of achieving a quantitative analysis based on the spectral data. In such a situation, adequate quantitative results generally depend on the use of a multivariate calibration.

Figure 2 details the results of predicting boron content from the BPSG IRRAS spectra in Figure 1, using a PLS1 calibration model. The calibration procedure for boron consisted of taking the first derivative of the spectral data between 890 and 1600  $\text{cm}^{-1}$  and dividing the spectral intensities by the film thickness for a given sample prior to application of the PLS1 algorithm. The combined model error, bias, and experimental error are described by the standard error of prediction (cross-validated) statistic, denoted SEP(CV). The line through the 21 points in Fig. 2 represents the least-squares fit to the data. The SEP(CV) value for boron in Fig. 2 (0.10 wt%) is based on the

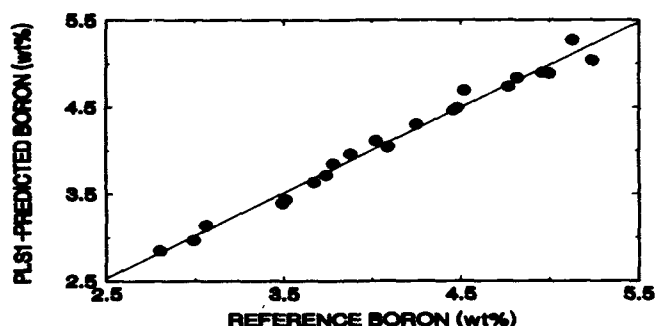


Figure 2. PLS1-prediction of boron in BPSG films from the IRRAS spectral data in Fig. 1.

difference between the cross-validated, PLS1-predicted boron values and reference-method boron values. It is germane to note that this SEP(CV) for boron is equivalent to the reported precision of the reference method for boron determination ( $\leq 0.1$  wt%). The SEP(CV) plots for phosphorus and film thickness appear similar to Fig. 2, with SEP(CV) for P of 0.12 wt% and for film thickness of 30 Å. The SEP(CV) for P is similar to the precision of the reference method ( $\leq 0.1$  wt%), and the SEP(CV) for film thickness is equivalent to the variation of film uniformity and instrument error ( $\pm 30$  Å) in a 1-cm pattern centered on the wafer. The PLS1 analysis of IRRAS spectra of BPSG films on monitor wafer samples yields similar quantitative results.

Figure 3 shows the IRRAS spectra of the nine BPSG samples deposited on product wafer samples. The spectral data in Fig. 3 exhibit features similar to those in the IRRAS spectra of Fig. 1, with two significant exceptions. The silicon phonon band at 610  $\text{cm}^{-1}$ , for example, is absent in Fig. 3. The presence or absence of this band indicates whether or not radiation reaching the detector has passed through the silicon wafer. The presence of the phonon band in Fig. 1 is an indication that

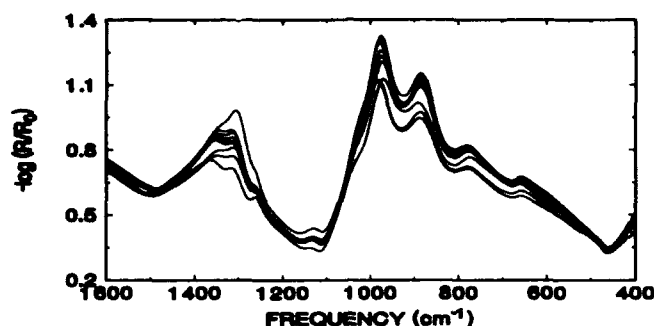
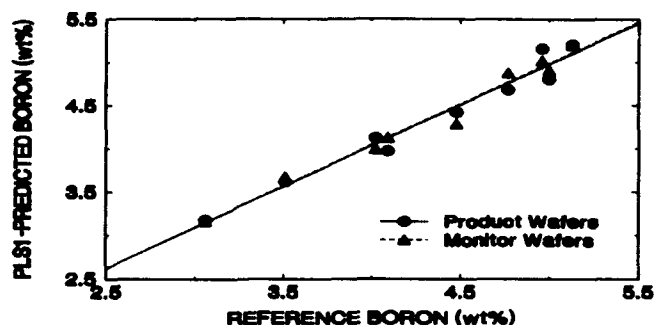


Figure 3. IRRAS spectra at 25 ° of nine BPSG thin films deposited on product wafers.

at least some fraction of the radiation reaching the detector is a result of reflection from the backside of the wafer. The absence of the feature in Fig. 3 is an indication that none of the radiation reaching the detector is a result of backside reflection. Another indication of how the different substrates affect the BPSG IRRAS spectra is shown by the approximate doubling of some reflection-absorption signals ( $-\log(R/R_0)$ ) in the product wafer spectra (Fig. 3) over the oxide-coated monitor wafer spectra (Fig. 1). This means that less IR radiation reaches the detector in some spectral regions (e.g., 800-1050 and 1250-1450  $\text{cm}^{-1}$ ) of Fig. 3 compared to Fig. 1, probably because the IR absorptivity and reflectivity differ in the two types of substrates. As a result, the major BPSG bands (at about 1370, 1320, 1000, and 900  $\text{cm}^{-1}$ ) in the IRRAS spectra of product samples appear larger than those in the IRRAS spectra of the BPSG samples on oxide-coated monitor wafers in Fig. 1. The greater magnitude of the band intensity variations may possibly be related to differences in the refractive index of the two different substrates and/or to the relative magnitudes of the incident IR wavelength (6-25  $\mu\text{m}$ ) and the pattern feature sizes (0.65  $\mu\text{m}$ ) in the product wafer samples, but these effects have not been studied. Given the favorable appearance of the IRRAS spectra of product wafers (major BPSG band intensities vary systematically with BPSG property values), a PLS1 calibration of the IRRAS BPSG product wafer spectra was performed.

For comparing the PLS1 calibration results of product and oxide-coated monitor BPSG samples, the nine samples in the oxide-coated monitor set that correspond to the nine product wafer samples were selected. PLS1 calibrations were performed on both sets of nine samples, and the results for the boron calibrations are detailed in Figure 4. For the nine oxide-coated monitor BPSG samples, the PLS1 boron calibration model used spectral frequencies between 927 and 1500  $\text{cm}^{-1}$  and preprocessed the spectral data by scaling the spectra for relative dielectric film pathlength and performing a linear baseline correction for all spectra over the 927 to 1500  $\text{cm}^{-1}$  calibration. The PLS1 boron calibration model for the nine BPSG product wafer samples used a calibration range of 455-1500  $\text{cm}^{-1}$  and linear baseline correction for spectral data preprocessing. As shown in Fig. 4, the boron SEP(CV) value for the nine oxide-coated monitor BPSG samples is 0.11 wt%, while that for the corresponding product samples is 0.13 wt%. For phosphorus determination, the nine oxide-coated monitor BPSG samples produced a SEP(CV) of 0.09 wt% and the nine product wafers yielded 0.09 wt% as well. Film thickness was predicted with a SEP(CV) of 120 Å for the oxide-coated monitor samples and 103 Å for product samples. The results for each BPSG component property using nine oxide-coated monitor BPSG samples are not statistically different than the



**Figure 4.** PLS1-prediction of boron in BPSG films from the IRRAS spectral data in Fig. 3 and nine of the spectra in Fig. 1.

results obtained using the nine product BPSG samples. Although these results have been obtained with a limited sample set, they suggest that BPSG component concentrations can be calibrated to within the precision of the reference methods for both monitor and product wafers using PLS1 multivariate calibration of BPSG IRRAS spectra.

## CONCLUSIONS

PLS1 multivariate calibration of BPSG IRRAS spectra provides a rapid (<1 min.), at-line or *in-situ*, nondestructive, and quantitative process monitor for quality control of BPSG component properties that is especially important to the microelectronics industry. Calibration precision comparable to that of the reference methods used to determine boron, phosphorus, and film thickness can be achieved using BPSG samples deposited on monitor and oxide-coated monitor wafers. Equivalent calibration precision (for B and P) or slightly worse precision (for film thickness) were obtained using a limited number of BPSG thin films deposited on product wafers. However, the calibration results using the nine corresponding BPSG films on oxide-coated monitor wafers showed the same trends in precision as the product samples, suggesting that the slightly worse precision for thickness may be related to the limited sample size. Thus, PLS1 calibration of BPSG IRRAS spectra is a very promising technique for the characterization of BPSG thin films deposited on product wafers. The availability of such a technique will greatly enhance the quality control of BPSG films used in actual microelectronics devices.

## ACKNOWLEDGMENTS

This work was performed in part at Sandia National Laboratories and was supported by the U.S. Dept. of Energy under Contract Number DE-AC04-94AL85000 and by the Semiconductor Research Corporation/SEMATECH through the University of New Mexico SEMATECH Center of Excellence.

## REFERENCES

1. W. Kern, W. A. Kurylo, and C.J. Tino, *RCA Review*, **46**, 117-152 (1985).
2. J.E. Franke, T.M. Niemczyk, and D.M. Haaland, *Spectrochimica Acta*, in press.
3. J.E. Franke, L. Zhang, T.M. Niemczyk, D.M. Haaland, and J.H. Linn, *J. Electrochem. Soc.*, **140**(5), 1425 (1993).
4. D.M. Haaland, *Anal. Chem.*, **60**, 1208 (1988).
5. D.M. Haaland and E. V. Thomas, *Anal. Chem.*, **60**, 1193 (1988).



## SPECTRAL REFLECTANCE AS AN IN SITU MONITOR FOR MOCVD

W. G. BREILAND AND K. P. KILLEEN

Sandia National Laboratories, Albuquerque, New Mexico, 87185-0601

### ABSTRACT

Near normal-incidence spectral reflectance has been used to monitor the growth of AlAs, GaAs, and AlGaAs thin films by MOCVD in real time. The method has been used in a research rotating disk CVD reactor and in a modified commercial horizontal channel reactor. Reflectance is simple, robust, and is insensitive to perturbations such as mechanical strains, wafer rotation, and imperfect windows commonly encountered in an actual MOCVD system. Data may be collected over a wide spectral range, 390 to 950 nm, in less than one second using a multichannel detector and broad-band light source. This wide bandwidth provides detailed compositional discrimination and greater thickness sensitivity than single-wavelength measurements. The technique may be used to extract wavelength-dependent optical constant data under growth temperature conditions. Examples from the growth of multi-layered structures used in the fabrication of Vertical Cavity Surface Emitting Lasers is presented. The method shows promise as a valuable tool in process modeling, optimization, and control.

### INTRODUCTION

The increasingly stringent thin-film requirements that are dictated by the next generation of microelectronic and optoelectronic devices is placing a burden on present-day MOCVD thin-film growth technology. Currently, epitaxial film structures are grown by a complex timed recipe obtained from a tedious set of calibration runs. After each run, post-process analysis is used to determine whether the desired structure and film thickness properties have been achieved. This approach is adequate for simple structures. However, complex structures may require two to three times as many calibration runs as production runs. It is also common for a perfected recipe to unexpectedly fail when one of the many dozens of process controls changes its behavior.

To address the need for better process control, real-time, *in situ* monitoring of the thin film growth is being developed as a means by which one may reduce calibration runs, detect problems as they occur rather than after a long run, and ultimately to take an active role in directly controlling growth and materials properties.

To be truly useful in a MOCVD processing environment, an ideal *in situ* monitor must meet the following requirements: 1) It must record information at real-time acquisition rates (~ second time scales) over a full growth run that may last hours. 2) It must operate under the actual growth conditions necessary to produce device-quality films. This includes high temperatures, reduced pressures, and substrate rotation in a commercial reactor that has not necessarily been designed for *in situ* monitoring. All this must be accomplished without perturbing the materials properties of the film. 3) The method must be simple, cost effective, robust, and require infrequent calibration to be viable in a production application. 4) Finally, the ideal monitor should provide quantitative measurements of desired materials properties such as thickness and composition to enable real-time closed-loop process control, eliminating the need for calibration runs and the timed-recipe approach. The device grower may thus have direct control over the final product rather than indirect control via temperature, pressure, flow rates and a timed recipe.

In this paper we investigate the viability of normal-incidence spectral reflectance (NSR) as an *in*

situ monitor for MOCVD thin film growth. Reflectance measurements have been used for many years to monitor thin film growth in a wide variety of commercial and research applications in areas other than CVD[1]. Recently, a number of research groups have reported the use of single-wavelength laser reflectance in MOCVD applications[2-6]. Spectral reflectance has the added potential to not only provide thickness information, but it may also be used to extract important materials information such as composition via spectral features in the reflectance.

The normal incidence spectral reflectance method has the following advantages: 1) It is simple to implement because it requires only one access window. 2) The method is insensitive to the polarization of light, allowing less-than-ideal window materials to be used if necessary. 3) A tungsten lamp may be used as a broad-band light source. These lamps are extremely stable, allowing DC detection to be used. 4) New, inexpensive fiber optic CCD spectrographs are now available allowing one to obtain a complete spectrum from 350nm to 1050nm in a fraction of one second. The fiber optics simplifies access to the MOCVD chamber and mitigates optical alignment problems. 5) The method is insensitive to the exact incidence angle under near-normal conditions. This allows the method to be used with rotating substrates. 6) Calibration is straightforward because semiconductor wafers are used as substrates. The optical properties of these wafers is highly reproducible, providing a self-calibration of the absolute reflectance at the beginning of each MOCVD run.

Perhaps the most significant disadvantage of the NSR technique is the perception that it is not sensitive enough to satisfy the needs of an in situ monitor. As we will demonstrate, this perception is not necessarily valid. The signal-to-noise achievable in our NSR experiments indicate that monolayer sensitivity is indeed possible.

## EXPERIMENTS

Fig. 1 shows schematics of the arrangements used to record spectral reflectance data in a home-built rotating disk research reactor and in a commercial horizontal channel MOCVD reactor. Light from low-wattage (5-100W) tungsten lamp sources is fed through multimode fibers, imaged on the substrate, and the reflected signal is fed into a small (1/4 or 1/8 m) focal length spectrograph. Two reflectance configurations are shown. In Fig. 1a, near-normal incidence (5 degree incidence angle) reflectance is recorded with separate imaging and receiving optics. Fig 1b shows true normal incidence spectra recorded with a bifurcated fiber and a single lens acting as imaging and receiving optics.

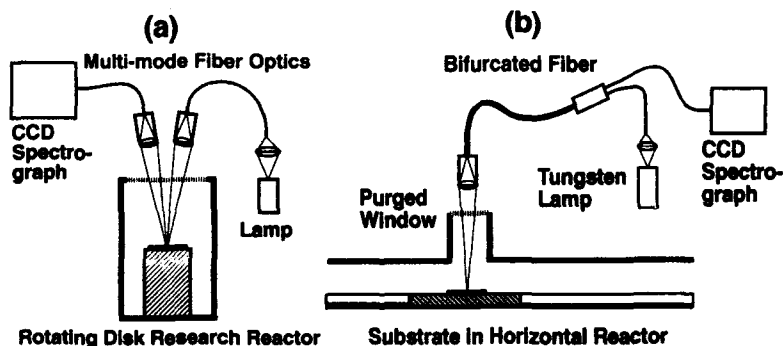


**Figure 1.** Schematic of spectral reflectance apparatus in a research (a) and in a commercial (b) MOCVD reactor.

Absolute reflectance values were obtained by measuring the room-temperature reflectance of the GaAs wafer with a Strong-type reflectometer[7]. This was then used to produce an absolute reflectance spectrum from the spectral signal off the wafer in the MOCVD reactor. Spectroscopic resolution was typically a few nanometers. Other experimental details are given in reference [8].

#### AlAs film

Fig. 2 shows the reflectance spectrum from an AlAs film deposited on GaAs at 650 C. A 1024-point spectrum was recorded every 10 sec for a total of 1500 sec. Fig. 2 shows a single-wavelength portion of this data at 450 nm. Also shown is a five-parameter fit of the data to the optical constants of the film, the optical constants of the substrate, and a film thickness parameter.

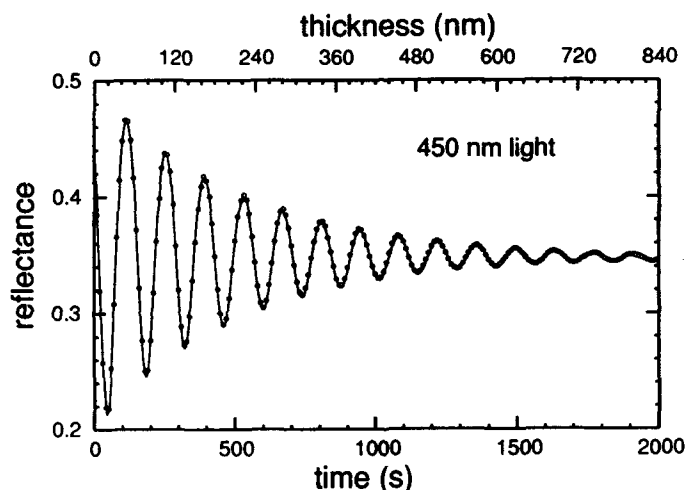


**Figure 2.** Spectral reflectance (open circles) of a growing AlAs film on GaAs at 650 C. Data shown is one wavelength (450 nm) from a total of 1024 wavelengths taken every 10 seconds during the run. The solid line is a fit to the data with a five parameter model for the optical constants of the film and substrate plus a thickness parameter. Results for this wavelength were  $N_{\text{AlAs}} = 3.8 - 0.17i$ ,  $N_{\text{GaAs}} = 4.3 - 1.7i$ ,  $\Delta d/\lambda = 9.3 \times 10^{-4}$  thickness increment over a ten-second interval

This fitting scheme was repeated for each wavelength in the spectrum. An average thickness was obtained from all wavelengths, and the optical constants were then re-fit with a fixed thickness parameter. The results of these fits are shown in Figs. 3 and 4 along with comparisons to data for high-temperature GaAs reported in reference [9]. These data compare well with the ellipsometrically determined data despite the fact that the reflectance spectra are not particularly sensitive to the substrate optical constants. Unfortunately, no spectral optical constant data for AlAs at elevated temperatures has been published. However, the values obtained at the HeNe laser wavelength agree with published results from several workers [3-5]. Note that the thickness of the film is highly over-determined when spectral reflectance data is used.

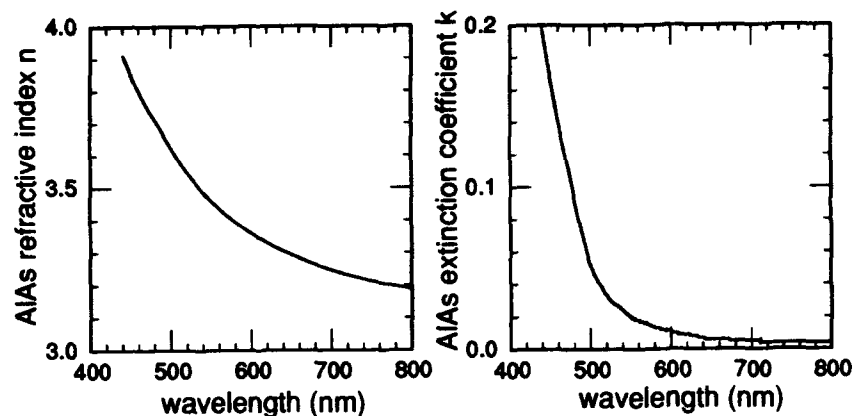


Figure 3. Optical constants of AlAs at 650 C extracted from spectral reflectance data.

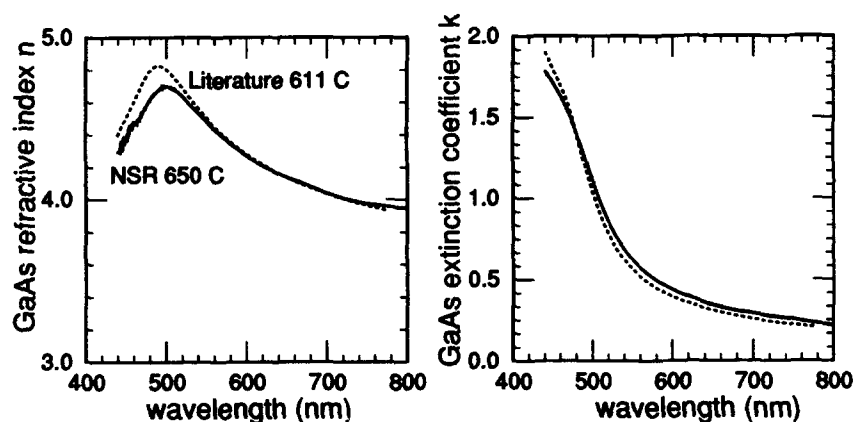
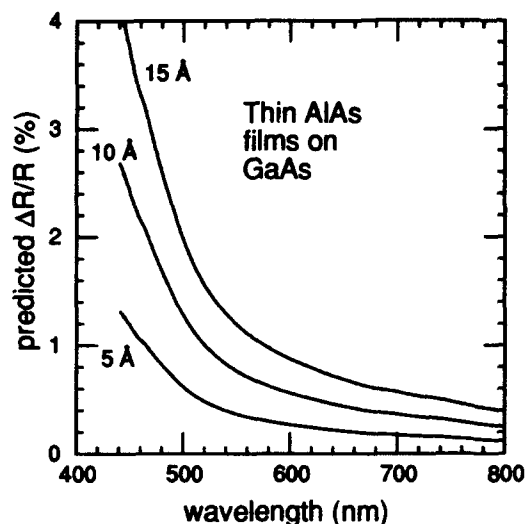


Figure 4. Optical constants of GaAs at 650 C extracted from spectral reflectance data. The constants obtained by ref. [9] at 611 C are also plotted for comparison.

#### Sensitivity of NSR

Interferometric methods such as that exploited in NSR are capable of resolving optical pathlength differences that are a small fraction of a fringe spacing; resolution is limited more by signal-to-noise than the characteristic thickness of one fringe. The sensitivity of the NSR method may be demonstrated by using the optical constant data extracted from the AlAs thin film to predict the percent change in reflectance expected for various extremely thin film thicknesses. The result of this calculation is shown in figure 5. Thickness sensitivity is highest at the blue end of the spectrum. Fig 5 predicts that monolayer sensitivity may be approached provided that signal-to-noise ratios are less than a few tenths of a percent, a value that we have achieved in some of our NSR experiments.



**Figure 5.** Predicted percent change in spectral reflectance when extremely thin layers of AlAs are deposited on GaAs. Calculations use the data from Figs. 3 and 4.

#### NSR monitoring during DBR mirror stack growth

Fig. 6 shows a grey-scale data visualization of real-time spectral reflectance during the growth of a distributed bragg reflector (DBR) mirror. The evolution of constructive interference producing a highly reflecting mirror is clearly seen in this data visualization as successive low (AlAs) and high ( $\text{Al}_{0.5}\text{Ga}_{0.5}\text{As}$ ) index quarter-wavelength layers are deposited. The data exhibit distinct spectral

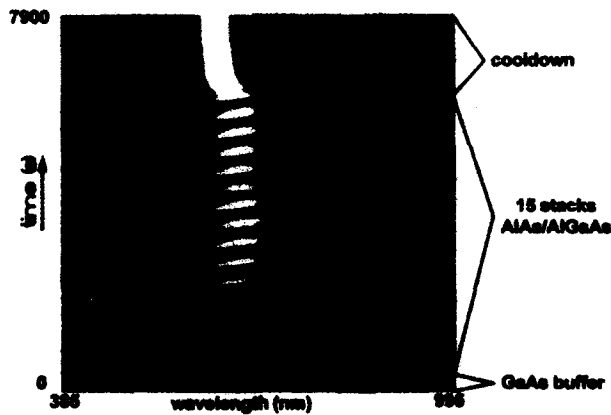


**Figure 6.** Grey scale data visualization of spectral reflectance vs time during the growth of a 15 period stack of AlAs/AlGaAs by MOCVD to form a high-reflectivity mirror at 628 nm. Grey scale intensities are proportional to reflectance: white maximum, black minimum.

patterns for different material compositions, illustrating the potential of this technique to simultaneously determine thickness and material composition during deposition. Fig. 6 also shows the effects of the temperature dependence of the optical constants. The reflectance maximum of the mirror stack shifts 34 nm to the blue as the substrate is cooled from 650 C to room temperature. This serves to point out the importance of obtaining precise optical constant data at elevated temperatures if proper active process control strategies are to be successfully implemented.

Even without active process control, NSR data have proven to be valuable "wellness" monitors that quickly detect when a particular growth run is misbehaving. This allows one to abort the run and track down the source of the problem in a shorter amount of time.

## SUMMARY AND DISCUSSION

Normal incidence spectral reflectance has been used as a real-time, in situ monitor of MOCVD growth. The data may be obtained with excellent signal-to-noise over a broad range of wavelengths using a tungsten lamp as a stable light source. High temperature optical constants may be extracted from the reflectance spectra of growing thin films. The method has the potential for monolayer sensitivity. Spectral features in the data clearly indicate that composition as well as film thickness are manifested in the reflectance. Further work needs to be done to determine whether other important information such as substrate temperature, doping levels, strain, etc. may be extracted from the spectra at growth temperatures. The method has already proved itself as a real-time "wellness" monitor during deposition. Future work will reveal whether this tool may be used to actively control the growth process to improve the quality and reproducibility of MOCVD microelectronic and optoelectronic device fabrication.

## ACKNOWLEDGEMENTS

The authors thank T. M. Kerley for critical technical assistance. This work was performed at Sandia National Laboratories and was supported by the U.S. Department of Energy under Contract No. DE-AC04-94AL8500.

## REFERENCES

1. H. A. Macleod, Thin-Film Optical Filters, 2nd ed. (Mcgraw-Hill, New York, 1989).
2. A. J. SpringThorpe and A. Majeed, *J. Vac. Sci. Technol. B* **8**, 266 (1990).
3. T. Farrell, J. V. Armstrong, and P. Kightley, *Appl. Phys. Lett.* **59**, 1203 (1991).
4. H. Sankur, W. Southwell, and R. Hall, *J. Electron. Mat.* **20**, 1099 (1991).
5. N. C. Frateschi, S. G. Hummel and P. D. Dapkus, *Electron. Lett.* **27**, 155 (1991).
6. T. Makimoto, Y. Yamauchi, N. Kobayashi, and Y. Horikoshi, *Japan. J. Appl. Phys.* **29**, L207 (1990).
7. J. Strong, Procedures in Experimental Physics, (Prentice-Hall, New York, 1938), p. 376.
8. K. P. Killeen and W. G. Breiland, *J. Electron. Mat.*, special issue, Sixth Biennial Workshop on Organometallic Vapor Phase Epitaxy, 1993 (to be published).
9. H. Yao, P. G. Snyder, and J. A. Woollam, *J. Appl. Phys.* **70**, 3261 (1991).

## REAL TIME PROCESS MONITORING WITH MULTIWAVE-LENGTH PYROMETRIC INTERFEROMETRY (PI)

F.G.BÖBEL\*, A.WOWCHAK\*\*, P.P.CHOW\*\*, J.VAN HOVE\*\*, and L.A.CHOW\*\*\*

\* Fraunhofer-Institut, Wetterkreuz 13, D-W-8520 Erlangen, Germany.

\*\* SVT Associates, 7620 Executive Drive, Eden Prairie, MN 55344

\*\*\* Dept. of Materials Science and Engineering, Stanford University, Palo Alto, CA 94305

### ABSTRACT

Pyrometry Interferometry (PI) is a powerful technique for in-situ sensing of the wafer temperature and growth rate. Evaluation of the two parameters would allow exact process control required for sophisticated device fabrication and material processing. The PI technique analyzes the interference patterns of the thermal radiation from the growing layer with a changing thickness  $d$  at growth temperature  $T$ . Since it is non-contact, applicable to all semiconductor materials and insensitive to wafer motion, the method is an ideal candidate for real time process control. We use a reflection assisted method to aid real time computation of these parameters. One could select the wavelength of interest to optimize the temperature and layer thickness resolution. We present data on MBE grown quarter wavelength stacks of GaAs and AlAs, and silicon oxidation to show PI is extremely useful for growth of surface emitting laser and for silicon processing.

### INTRODUCTION

Precise knowledge of the wafer temperature and layer thickness during thin film process is critical in the fabrication of sophisticated device structures. Optical measuring techniques have become popular because they are non-invasive and often do not require modifications of existing reactors<sup>1-3</sup>. Pyrometric Interferometry (PI) was introduced as an optical technique for simultaneous in-situ film thickness and temperature determination<sup>4,5</sup>. The basic PI makes use of the interference effects of the thermal radiation of the substrate; here the method is made more sensitive by simultaneous measurement of the reflection from an LED by the wafer surface. The thermal emission of the substrate is reflected and refracted at the interfaces of the growing layer resulting in interference effects, changing the emissivity  $\epsilon$  as a function of layer thickness  $d$ . The basic PI principle states that the measured intensity  $I(\lambda)$  should be proportional to the emissivity  $\epsilon$ , ie.,

$$I(\lambda) \propto \epsilon(\lambda, d) f_{\text{Planck}}(\lambda, T)$$

where the Planck's function  $f_{\text{Planck}}(\lambda, T) = \frac{c_1}{\lambda^5} \frac{1}{e^{\frac{c_2}{\lambda T}} - 1}$

Note that emissivity is a function of the temperature  $T$ , thickness  $d$ , and the optical constants  $n$  and  $k$ . If the function  $\epsilon(d, \lambda, n, k, T, \dots)$  is known, the measured  $I(\lambda, t)$  can then be used to evaluate  $d$  and  $T$ . One can derive an analytical expression to compute the value  $\epsilon$  as functions of the optical constants  $n_s, n_f, k_s$  and  $k_f$  of the substrate and the thin film<sup>5</sup>. However this approach would require knowing all the optical constants of the substrate and thin film whose values are not always precisely known at the growth temperature. A more straightforward way is to measure the reflection from a known light emitter at the wavelength of interest. From energy conservation considerations the reflection  $R$ , the transmission  $Tr$  and absorption  $A$  of the complete wafer sum up to unity. For nontransparent wafer  $Tr$  is zero. Therefore  $R + A = 1$ . In addition, we also know  $\epsilon = A$  from the Kirchhoff's law. We finally express  $\epsilon$  in terms of  $R$ , i.e.,  $\epsilon = 1 - R$ , and compute the emissivity from the reflection measurement. Since only the energy conservation and the Kirchhoff's Law were used, this relation holds for all temperatures and material combinations. Consequently measuring reflection  $R$  provides a convenient way of determining  $\epsilon$  which can then be used to compute the wafer temperature and thin film thickness. (We assume the film remains specularly reflective)

To evaluate the temperature we first define the reflected intensity as  $I^R$  and emitted portion as  $I^P$ . We have

$$I^R \propto R(\lambda, d), \text{ and } I^P \propto \epsilon(\lambda, d) f_{\text{Planck}}(\lambda, T).$$

To eliminate system related factors, we then normalize both  $I^R$  and  $I^P$  to the starting values  $I^R_0$  and  $I^P_0$ . One then obtains the following analytical equation for temperature  $T$ :

$$T = \frac{c_2}{\lambda} \ln \left[ 1 + \frac{e^{\frac{c_2}{\lambda T_0}} - 1}{\frac{I^P(t)}{I^P_0} \frac{(1 - R_0)}{\left(1 - R_0 \frac{I^R(t)}{I^R_0}\right)}} \right]^{-1}$$

This expression allows very fast determination of the wafer temperatures before and during the growth of thin film without any knowledge of the material constants of the thin film itself.

The thin film thickness determination relies on the interference effects of multiple reflections in the film. Using either the reflection mode or the emissivity mode the optical



thickness of the thin film can be measured. At the observed wavelength  $\lambda$ , the intensity goes through oscillations with changing thin film thickness. The oscillation period corresponds to a change in optical path of half a wavelength, i.e.,

$$\text{Period} = \lambda / (R \cdot 2 n_f)$$

Using a fast converging fitting algorithm one fits the five parameters  $n_s$ ,  $n_f$ ,  $k_s$ ,  $k_f$  and the growth rate  $R$  to the last data points.

### EXPERIMENTAL RESULTS

The basic measurement geometry is illustrated in Figure (1). The signal consists of two reflected signals from electronically modulated LED's at 650 and 950nm, and thermal emission from the sample itself at the same wavelengths. The two reflected signals are measured by detectors D1 and D2, respectively. The thermal radiation at 950 nm is measured by detector D3 in this configuration. The spot is imaged by a CCD camera for aligning the optics. Detectors D4 and D5 are used to monitor the output from the LED's such that fluctuation in the light signal can be compensated. All signals are modulated, detected by low-noise silicon detectors and digitized by a 16-bit A/D converter. The data are analyzed by a 486 personal computer.

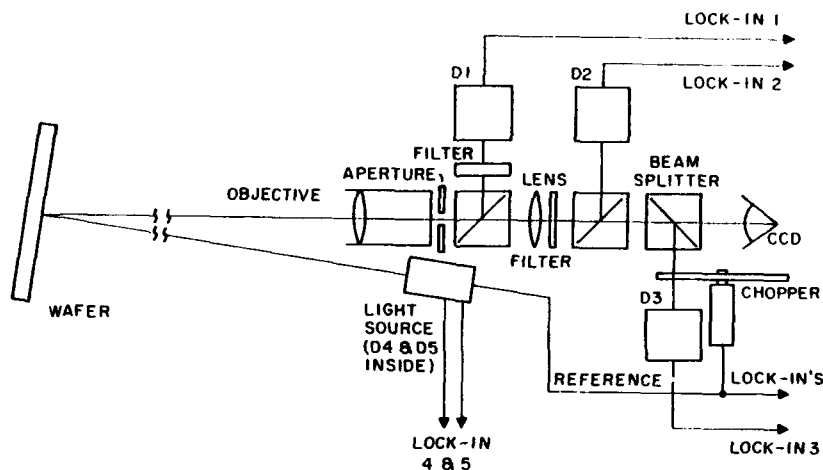


Figure (1). Measurement Configuration of the reflection assisted PI.

To demonstrate the temperature sensitivity of this technique, PI was employed during the molecular beam epitaxy (MBE) growth of GaSb on a GaAs substrate. Because of much smaller bandgap of GaSb and InAs the wafer temperature changes dramatically during their deposition<sup>6</sup>. Typically in MBE the wafer temperature is monitored by a thermocouple in contact with the wafer holder. Because this indirect thermal path and the large thermal mass of the wafer holder, the measured temperature usually has a significant lag. This is problematic when staying within a narrow temperature range is critical for high quality growth. In our experiment the temperature scale of the wafer is first determined from bandgap shift measurements<sup>1</sup> to calibrate the input power of the heater power supply. The surface temperature of the wafer is then measured by PI during growth of the GaSb layer. Thermal absorption by the smaller bandgap GaSb raises the wafer temperature significantly. In Figure (2) the measurement displays an increase of 25°C in the first 10 minutes. Such large thermal change was not detected by the thermocouple until much later because of the thermal lag. The figure shows that using the PI feedback the heater supply was dropped a total of 60° C in the next 10 minutes in order to maintain the wafer in a narrow temperature range. This demonstrates a constant growth temperature environment can be maintained by using the feedback from the PI.

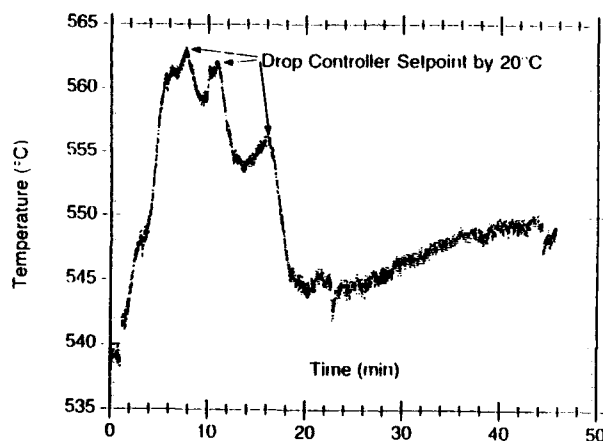


Figure (2). Temperature variation during initiation of GaSb growth on a GaAs Wafer.

Figure (3) demonstrates the high temperature resolution achievable even in a noisy thermal background. Oxidation is an important step in silicon processing that is carried out at very high temperature. The bright background in a 1000° C furnace makes other type of optical measurement difficult. When the process was started by flowing hot water vapor (water temperature: 96°C) through the furnace, the thermal signal increased abruptly. One can see a temperature rise of 1° C for the first 200 seconds or so. Note that the temperature resolution of the technique is such that furnace temperature oscillations of 0.3°C are resolved.

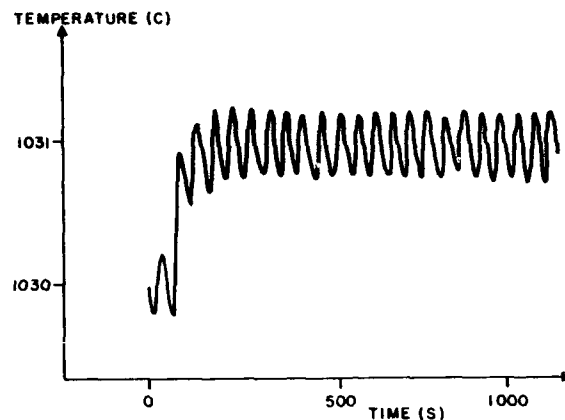


Figure (3). Minute temperature oscillations during silicon oxidation process.

Precision control of the Bragg reflectors is critical to the optical performance of surface emitting laser diodes. Using PI the operator can follow the growth of each layer very closely. The fitting routine recognizes the extremes of signal oscillation in real time. Figure (4) shows the result of the reflection oscillations of a 950 nm and a 650 nm LED during growth of quarter wave layer stacks of AlAs and GaAs. Since the quarter wavelength stack was optimized at 950 nm, the reflection signal at that wavelength was used to actuate the Ga and Al shutters. Note that the reflectivity of the layer gradually became higher and approached maximum value as the number of periods increased. The 650 nm wavelength signal is out of phase but can be used to aid computation, knowing the optical constants of the layers at the different wavelengths. From simultaneous Reflection High Energy Electron Diffraction (RHEED) intensity oscillation monitoring of AlAs, which measures thickness with atomic-layer precision, we estimated

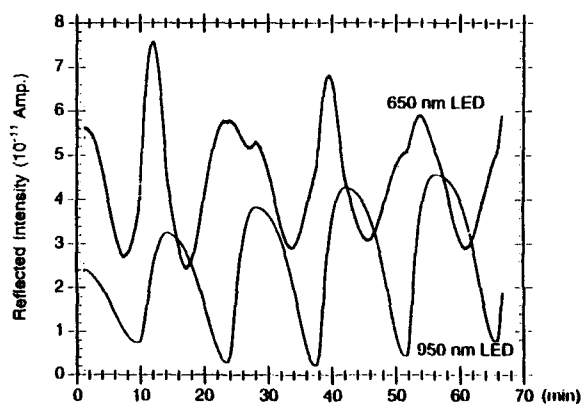


Figure (4). Reflection oscillation at 950 and 650 nm for AlAs/GaAs quarter wave stacks.

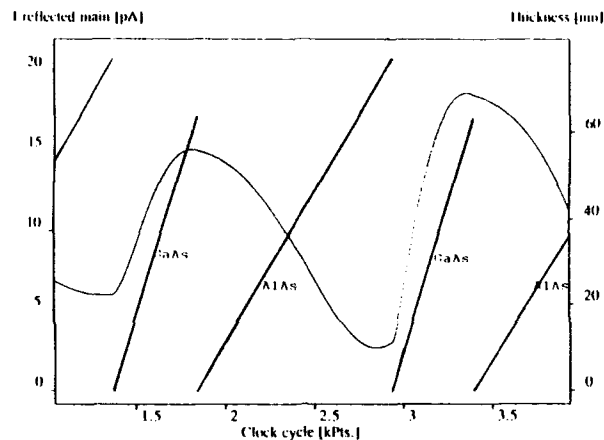


Figure (5). Real time display of thickness (straight lines) of individual layers.

that the layer thickness was measured to within 1% accuracy. Figure (5) shows that for each individual layer the layer thickness is displayed in real time on the screen. Their slopes therefore represent the growth rates of GaAs and AlAs, respectively. The constant slopes of these thickness lines are indicative of the stable growth rates during the process.

## CONCLUSION

The reflection assisted pyrometric interferometry has been shown to be a truly in-situ temperature and layer thickness technique for MBE as well as for silicon processing. The evaluation time takes less than 100 ms so it generates real time sensing feedback. We have demonstrated that temperature resolution of less than 1°C can be attained, and layer thickness measurement agreed very well with the RHEED intensity oscillation measurement.

## REFERENCES:

1. E.S. Hellman and J.S. Harris, Jr., *J. Cryst. Growth* 81, 38(1987)
2. R.J. SpringThorpe, T.P. Humphreys, A. Majeed and W.T. Moore, *Appl. Phys. Lett.* 55, 2140(1989)
3. S.R. Johnson, C. Lavoie, T. Tiedje and J.A. Mackenzie, *JVST B11*, 1007(1993)
4. F.G. Böbel, U. Bonnes, K.P. Frohmader, *Proc 11th IEEE International Electronics Manufact. Techn.(IEMT) Symposium*, Sept.(1991) San Francisco, CA, pp.1197-1201.
5. F.G. Böbel, H. Möller, *proc. 3rd IEEE Adv. Semiconductor Manufact. Conf.* Oct. (1992) Boston, MA, pp67-71. IEEE Catalog No.: 92-CH-31-3182-3.
6. B.V. Shanabrook, J.R. Waterman, J.L. Davis, R.J. Wagner, and D.S. Katzer, *JVST B11*, 994(1993).

## CHARACTERIZATION OF QUANTUM WELL STRUCTURES USING MICROSCOPE-SPECTROPHOTOMETRY

RACHEL M GEATCHES<sup>†</sup>, KAREN J REESON<sup>†</sup>, ALAN J CRIDDLE<sup>\*</sup> and ROGER P WEBB<sup>†</sup>

<sup>\*</sup>Department of Mineralogy, Natural History Museum, London, SW7 5BD, United Kingdom

<sup>†</sup>Department of Electrical and Electronic Engineering, University of Surrey, Guildford, Surrey, GU2 5XH, United Kingdom

### ABSTRACT

In this paper the application of microscope-spectrophotometry to the nondestructive characterization of a variety of multi-layer GaAs/AlGaAs structures, is described. Spectral reflectance results are used to indirectly determine variations in aluminium content, and the interdependency of aluminium content with layer thicknesses. The penetration depth of light from the visible spectrum is assessed from the correlation between spectral reflectance measurements and fitted optical models. Finally, a series of single quantum wells are investigated, and it is concluded that a significant improvement in the characterization of these materials will be achieved with an extension of the spectral measurement range into the ultra violet.

### 1 INTRODUCTION

Microscope-spectrophotometry (MSP) is a powerful tool for the nondestructive characterization of semiconducting, multi-layer structures. The technique, originally developed to characterize the optical properties of naturally occurring semiconducting materials<sup>1-4</sup> (minerals), has recently been used in its most basic form within the semiconductor industry. The technique, applied in this way, has only been capable of characterizing simple structures or has been limited to the characterization of the first few layers of multi-layer systems. A breakthrough in the characterization of multi-layer structures has been achieved by the application of theoretical optical models to the measured spectral reflectance data<sup>5</sup>. Numerical inversion techniques<sup>6</sup> are used to iteratively fit the optical model to the experimental MSP data. When optimized, the fitted data provide information about the three-dimensional structure and chemical composition of the component layers of the material investigated.

In this paper we report the findings of an MSP study of a series of GaAs/AlGaAs structures. These include a series of molecular beam epitaxy structures, in which the changes in reflectance are studied relative to variations in aluminium content and layer thickness; a multi-layer semiconductor heterostructure for light emitting diodes, to investigate the depth penetration of light from the visible spectrum; and a series of single quantum wells, with a variety of subsequent anneal and implant conditions. The experimental results and the fitted theoretical models (which enable these complex multi-layer structures to be characterized in terms of their structural and chemical composition) will be discussed. The results correlate well with other, well-established, but destructive, characterization techniques.

## 2 EXPERIMENTAL

### 2.1 Materials

Chemical and structural variations within a number of multi-layer GaAs/AlGaAs structures were measured and modelled. The samples (table I) included four samples manufactured by molecular beam epitaxy (MBE), one multi-layer, semiconductor heterostructure for light emitting diodes (LED), manufactured by organometallic chemical vapour deposition (MOCVD) and five single-quantum wells (SQW) produced using organometallic vapour phase epitaxy (MOPVE).

Table I: Layer chemical compositions and dimensions of the GaAs/AlGaAs samples.

| Molecular Beam Epitaxy samples           |  |  |  | Layer dimensions(nm) |
|--|--|--|--|----------------------|
| MBE 1                                    | MBE 2                                    | MBE 3                                    | MBE 4  |                      |
| GaAs surface oxide                       |  |  |  | 1-2                  |
| GaAs                                     |  |  |  | 10                   |
| Al <sub>0.10</sub> Ga <sub>0.90</sub> As | Al <sub>0.20</sub> Ga <sub>0.80</sub> As | Al <sub>0.30</sub> Ga <sub>0.70</sub> As | Al <sub>0.40</sub> Ga <sub>0.60</sub> As   | 10                   |
| GaAs                                     |  |  |  | 500                  |
| Al <sub>0.10</sub> Ga <sub>0.90</sub> As | Al <sub>0.20</sub> Ga <sub>0.80</sub> As | Al <sub>0.30</sub> Ga <sub>0.70</sub> As | Al <sub>0.40</sub> Ga <sub>0.60</sub> As   | 200                  |
| GaAs substrate                           |  |  |  |                      |
| Light Emitting Diode sample              |  | Single Quantum Well samples              |  |                      |
| Layer composition                        | Layer dimensions(nm)                     | Layer composition                        | Layer dimensions(nm)   |                      |
| GaAs surface oxide                       | 1-2                                      | GaAs surface oxide                       | 1-2  |                      |
| GaAs                                     | 440                                      | GaAs cap                                 | 5  |                      |
| GaAs                                     | 100                                      | Al <sub>0.20</sub> Ga <sub>0.80</sub> As | 100  |                      |
| Al <sub>0.40</sub> Ga <sub>0.60</sub> As | 1640                                     | GaAs (QW)                                | 5  |                      |
| GaAs                                     | 100                                      | Al <sub>0.20</sub> Ga <sub>0.80</sub> As | 100  |                      |
| Al <sub>0.10</sub> Ga <sub>0.90</sub> As | 1750                                     | GaAs substrate                           |  |                      |
| GaAs                                     | 100                                      | Sample                                   | Anneal conditions  |                      |
| Al <sub>0.30</sub> Ga <sub>0.70</sub> As | 500                                      | SQW 1                                    | 800°C for 180s   |                      |
| GaAs                                     | 100                                      | SQW 2                                    | 900°C for 180s   |                      |
| Al <sub>0.20</sub> Ga <sub>0.80</sub> As | 8000                                     | SQW 3                                    | 1000°C for 180s  |                      |
| GaAs                                     | 100                                      | SQW 4                                    | Implanted with 75keV<br>10 <sup>14</sup> O <sup>16+</sup> cm <sup>-2</sup><br>800°C for 180s                   |                      |
| Al <sub>0.60</sub> Ga <sub>0.40</sub> As | 1000                                     |  |  |                      |
| GaAs                                     | 100                                      | SQW 5                                    | Implanted with 75keV<br>10 <sup>14</sup> O <sup>16+</sup> cm <sup>-2</sup> 700°C for<br>30s and 900°C for 180s |                      |
| GaAs substrate                           |  |  |  |                      |

## 2.2 Reflectance measurement and optical fitting procedures

Microscope-spectrophotometry (MSP) has been described in detail by a number of authors<sup>1-5,7</sup>, however, a brief description of its application to the non-destructive characterization of semiconducting materials will be given here. In this study, we used the Zeiss MPM03 microscope-spectrophotometer in the Department of Mineralogy of the Natural History Museum, London. Spectral reflectance measurements were made in plane (or linearly) polarized light from 400 to 700nm. All measurements were made relative to a pre-calibrated reflectance standard (WTiC or SiC), and the measured reflectance calculated by:

$$R_{\text{specimen}} = R_{\text{standard}} * \frac{P_{\text{specimen}}}{P_{\text{standard}}} \quad (1)$$

where,  $R$  is the reflectance and  $P$  is the photoelectric response of the specimen/standard at a given wavelength. Modulated light from a stabilized tungsten-halogen source was reflected onto the surface of the material by a 45° plane-glass reflector. The effective numerical aperture of the x4 objective was adjusted with an illuminator aperture diaphragm to give a maximum cone angle of 1-2° and measurement of the levelled material was made semi-automatically by step-scanning in 10nm steps with a motorized continuous line-interference filter (bandwidth 12nm). Having measured the reflectance of the specimen, optical models were applied and fitted to the experimental data to obtain structural and chemical information. The methods employed, which are described in greater detail elsewhere<sup>5</sup>, involve the construction of an optical model from the optical constants and layer thicknesses of the component layers of the material. This model may be iteratively fitted and optimized to the experimental data by varying the layer thicknesses and the optical constants appropriate for the component layers. Optimization is achieved by using numerical inversion techniques<sup>6</sup>, and the optimum fit is indicated by a simple root-difference-squared comparison between the optimized optical model and the experimental data (expressed as a percentage-deviation).

The optical constants required for GaAs and  $\text{Al}_x\text{Ga}_{1-x}\text{As}$  were obtained from the literature<sup>9,11</sup>. The compositions of the  $\text{Al}_x\text{Ga}_{1-x}\text{As}$  materials available were not precisely the same as those required, but were within at most  $\pm 5\%$ . The compositions used were as follows:  $x=0.10$ :  $\text{Al}_{0.099}\text{Ga}_{0.901}\text{As}$ ;  $x=0.20$ :  $\text{Al}_{0.198}\text{Ga}_{0.802}\text{As}$ ;  $x=0.30$ :  $\text{Al}_{0.315}\text{Ga}_{0.685}\text{As}$ ;  $x=0.40$ :  $\text{Al}_{0.419}\text{Ga}_{0.581}\text{As}$ ; and  $x=0.60$ :  $\text{Al}_{0.596}\text{Ga}_{0.410}\text{As}$ . The materials always have a thin oxide layer on their surface, the exact nature of which is unclear, but which can vary from  $\text{Ga}_2\text{O}_3$  to  $\text{As}_2\text{O}_3$ . Four GaAs oxide models obtained from the literature<sup>12</sup> were applied to the optical models for the GaAs/ $\text{Al}_x\text{Ga}_{1-x}\text{As}$  samples.

## 3 RESULTS/DISCUSSION

### 3.1 MBE samples

Reflectance spectra for the four MBE samples were modelled using the optical fitting procedure outlined in section 2.2. The four oxide models were then applied to the overall optical model one by one. Each of them provided a good theoretical fit to the experimental data. We cannot conclude from this, therefore which oxide is the most suitable model for these MBE materials. Figure 1 shows the best-fit results.

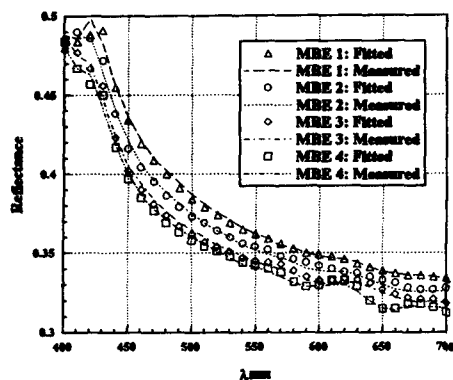


Figure 1: Fitted and measured reflectance for MBE samples.

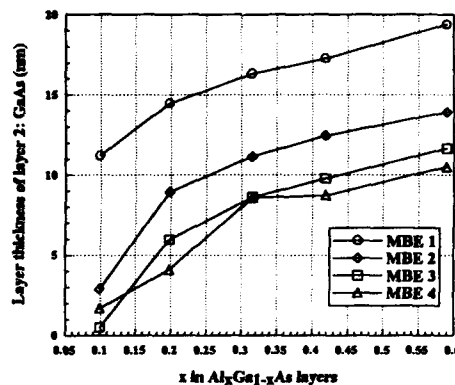


Figure 2: Variations of thickness for layer 2 (GaAs) relative to  $x$ .

The proportion of aluminium was then varied for each of the four samples. The strongest correlations between aluminium content and layer thickness were found for layers 2 (GaAs) and 3 (AlGaAs). The thin GaAs oxide layer contribution is minimal, as are the contributions from layers 4 (GaAs) and 5 (AlGaAs) as they are buried and, consequently, have diminishing contributions due to absorption. Figures 2 and 3 show the results of varying  $x$  on the layer thickness of layers 2 and 3 for each of the MBE samples. From these figures it can be seen that, increasing  $x$

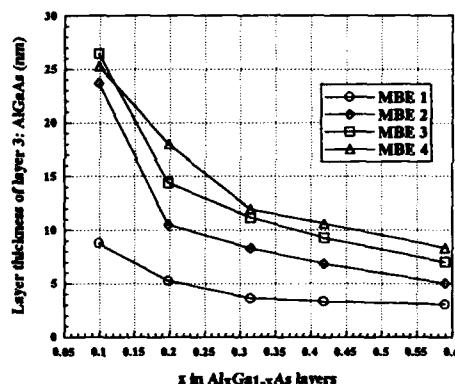


Figure 3: Variations of thickness for layer 3 (AlGaAs) relative to  $x$ .

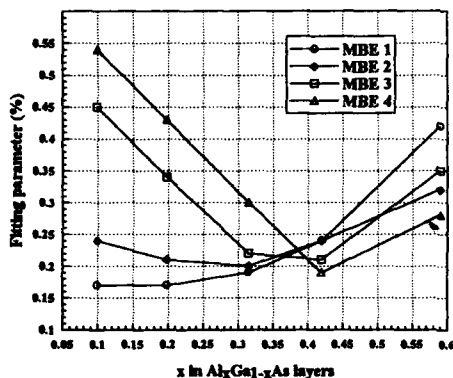


Figure 4: Variations in percentage-deviation relative to  $x$ .

results in a decrease in the thickness of layer 3 ( $\text{Al}_x\text{Ga}_{1-x}\text{As}$ ) and a corresponding increase in layer 2 (GaAs). Figure 4 shows the variation in the percentage-deviation for the best-fit solutions relative to  $x$ . From this we can predict the best-fit parameters, i.e., a minimum percentage-deviation from figure 4 will indicate an optimum value for  $x$ , and correlating this with figures 2 and 3, an estimate of the corresponding layer dimensions can be found. The predicted layer thicknesses



for layers 2 and 3 (table II) correlate extremely well with those measured destructively by SIMS (table I). However, in every case, the predicted value of  $x$  is higher than the growth conditions indicated. Having said that, the SIMS results are in accord with the MSP values.

Table II: Predicted values for layer thicknesses and  $x$

| MBE Samples                                     | 1    | 2    | 3    | 4    |
|---|------|------|------|------|
| $x$ (in $\text{Al}_x\text{Ga}_{1-x}\text{As}$ ) | 0.15 | 0.28 | 0.38 | 0.46 |
| Thickness of layer 2 (GaAs) in nm               | 13.0 | 10.5 | 9.5  | 9.0  |
| Thickness of layer 3 (AlGaAs) in nm             | 7.0  | 9.0  | 10.0 | 10.0 |

### 3.2 LED sample

The LED structure investigated was a complex multilayer material consisting of 13 layers. The structure was initially modelled using the full compliment of layers as given in table I. Simpler models were then applied, omitting the deeper layers, until the model was too simple and no longer provided a good-fit. This procedure provided equally good fits for the full 13-layer model and a simplified 4-layer model, which implies that light from the visible spectrum does not significantly penetrate more than 2500nm into the GaAs/ $\text{Al}_x\text{Ga}_{1-x}\text{As}$  structure. These results are summarized in figure 5 and the fitted layer dimensions for the 4-layer model given in table III. It is seen that the fitted results correlate extremely well with the measured reflectance and the layer thicknesses measured destructively using TEM.

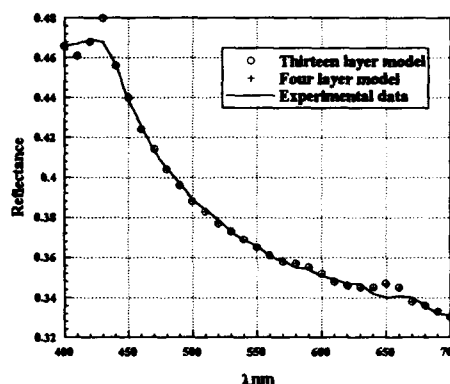


Figure 5: Fitted and measured reflectance for LED sample

Table III: Fitted layer dimensions for the first four layers of the LED sample.

| Layer composition                             | Layer thicknesses (nm)    |             |
|---|---------------------------|-------------|
|   | Fitted (four layer model) | TEM results |
| GaAs native surface oxide                     | 3.49                      | 1-2         |
| GaAs  | 516.07                    | 440         |
| GaAs  | 113.52                    | 100         |
| $\text{Al}_{0.419}\text{Ga}_{0.581}\text{As}$ | 1665.53                   | 1640        |

### 3.3 SQW samples

Finally, the measurement and fitting procedures were applied to the SQW samples, to establish the physical nature of the GaAs quantum well. Good fits were obtained for each of the five samples (figure 6), however, no significant differences or trends were observable between the samples. Light penetration, aluminium concentration and surface oxide considerations were taken into account (as applied in sections 3.1 and 3.2), however, no significant conclusions could be drawn. Using the best-fit model parameters, we then simulated the expected reflectance interference patterns for an extended wavelength range from 230 to 820nm. It can be seen from figure 7 that significantly more information may be elucidated from an extended wavelength range reflectance spectrum. This is in agreement with other studies which show that higher doses of oxygen are required for appreciable interface mixing.

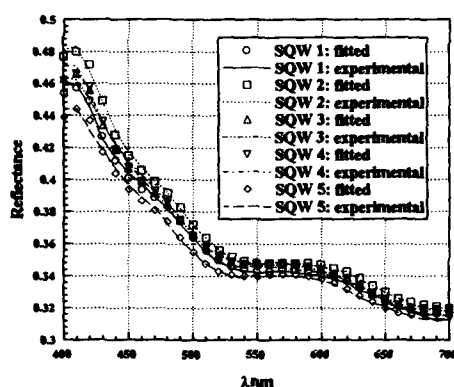


Figure 6: Fitted and measured reflectance spectra for SQW samples

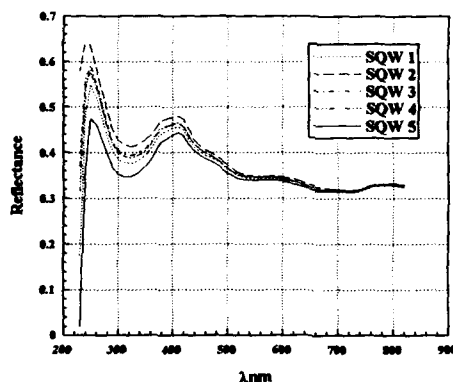


Figure 7: Simulated extended wavelength reflectance spectra for SQW samples

## 4 CONCLUSIONS

This study has shown: 1) how chemical and structural information for GaAs/AlGaAs structures is derived from spectral reflectance measurements; 2) how, in MBE structures, layer thicknesses and their compositions are characterized; and 3) that, in a 13-layer MQW, light from the visible spectrum penetrates to a depth of about 2500nm. Optical models were also developed for a series of SQWs, these were extrapolated by simulation to shorter and longer wavelengths. It is concluded that the accuracy and completeness of optical characterization will be significantly improved by extending spectral reflectance measurements into the UV.

### Acknowledgements

We would like to thank GEC-Marconi, Bernard Weiss and Padraig Hughes (University of Surrey) for supplying the samples. Particular thanks go to Pete Pearson (GEC-Marconi) for useful discussions. The work undertaken in this paper was supported by the UK Science and Engineering Research Council (grant reference GR/H14366).

## References

1. A.J. Criddle, in Advanced Microscopic Studies of Ore Minerals, edited by J.L. Jambor and D.J. Vaughan (MAC/COM short courses 17, 1990), p. 1.
2. A.J. Criddle, in Advanced Microscopic Studies of Ore Minerals, edited by J.L. Jambor and D.J. Vaughan (MAC/COM short courses 17, 1990), p. 135.
3. K.J. Reeson, PhD thesis, CNAA, 1987.
4. A.J. Criddle and C.J. Stanley, Quantitative Data File for Ore Minerals, 3rd ed. (Chapman and Hall, 1993).
5. R.M. Geatches, K.J. Reeson, A.J. Criddle, R.P. Webb, P.J. Pearson, P.L.F. Hemment, and A. Nejim, *Mats. Sci. & Eng.*, in press (1993).
6. M.S. Caceci and W.P. Cacheris, *BYTE*, 1984, 340-362.
7. H. Piller, Microscope Photometry, (Springer Verlag, Berlin, Heidelberg, 1977).
8. R.M. Azzam and N.M. Bashara, Ellipsometry and Polarized Light, (North Holland, Amsterdam, 1977).
9. D.E. Aspnes, *EMIS Datareview*, RN=15437, 1989, pp. 157-160.
10. D.E. Aspnes, S.M. Kelso, R.A. Logan and R. Bhat, *J. Appl. Phys.* **60** (2), 754 (1986).
11. S. Adachi, *EMIS Datareview*, RN=16094, 1989, pp. 513-528.
12. D.E. Aspnes, G.P. Schwartz, G.J. Gualtieri, A.A. Studna, and B. Schwartz, *J. Electrochem. Soc: Solid State Sci. & Technol.* **128** (3), 590 (1981).

## LIGHT SCATTERING MEASUREMENTS OF SURFACE ROUGHNESS IN MOLECULAR BEAM EPITAXY GROWTH OF GaAs

C. Lavoie, M. K. Nissen, S. Eisebitt, S. R. Johnson, J. A. Mackenzie, T. Tiedje\*  
Department of Physics, \*Also Department of Electrical Engineering,  
University of British Columbia, Vancouver, BC, V6T 1Z1

### ABSTRACT

In-situ measurements of diffuse light scattering at  $\lambda = 457$  nm are reported from the surface of GaAs films during growth by molecular beam epitaxy. Three different scattering angles are measured simultaneously corresponding to spatial frequencies in the surface roughness of  $q = 0.9$ , 12, and  $17 \mu\text{m}^{-1}$ . During growth the initial surface roughness caused by the oxide desorption decreases at high spatial frequencies and increases at low spatial frequency. The low spatial frequency roughness corresponding to scattering vectors parallel to [110] increases more rapidly during growth than for scattering parallel to  $[1\bar{1}0]$ .

### INTRODUCTION

Recent theoretical [1] and experimental work [2] has shown that the surface of single crystal epitaxial films is in general not atomically flat during growth but rather has a tendency to become progressively rougher due to the interplay between the random nature of the deposition process and the effects of surface diffusion of the deposited atoms. The lengthscale and amplitude of the surface roughness is variable depending on crystal orientation, growth rate and temperature. Ex-situ scanning tunneling microscopy measurements on quenched GaAs surfaces show surface roughness with lateral lengthscales in the 0.1 to  $1 \mu\text{m}$  range [2] that is easily accessible in light scattering experiments. In this paper we report in-situ diffuse light scattering measurements on GaAs surfaces during molecular beam epitaxy (MBE) growth. Light scattering has a number of important advantages as a probe of surface morphology. It is highly sensitive to the surface structure and can detect changes in the surface composition and structure at the submonolayer level [3]. It is also amenable to real time measurements during growth, something that is not yet possible with scanning tunneling microscopy. Compared with electron diffraction, light scattering is more sensitive to low spatial frequency surface structures.

### EXPERIMENT

The GaAs films were grown in a VG V80H molecular beam epitaxy system on (001) on-axis oriented ( $\pm 0.5^\circ$ ) polished semi-insulating GaAs substrates. The light scattering measurements were carried out with 5 mW at 457 nm from an  $\text{Ar}^+$  laser. The incident laser light is brought into the MBE through an effusion cell port at an angle  $\theta_i = 25^\circ$  relative to the surface normal, and the scattered light is detected simultaneously in three geometries through two other effusion cell ports and a shutter port as indicated schematically in the inset in Fig. 1. The three detectors labelled A, B, and C in Fig. 1 are located at the scattering angles listed in Table I, where  $\theta_s$  is measured from the surface normal and  $\phi_s$  is the azimuthal angle measured from the plane of incidence. From the scattering angles, one can calculate the corresponding scattering vectors  $q$  in the plane of the semiconductor surface and these magnitudes are listed in Table I. The detector at A which is near the specular beam, is sensitive to low spatial frequencies in the surface morphology and the detectors at B and C are far from the specular beam and accordingly are sensitive to high spatial frequencies [4]. All optical ports are equipped with gold coated mirrors in UHV to prevent window coating due to direct line of sight exposure of the window to the hot substrate [5].

Table I. Scattering angles and corresponding scattering vectors.  $\theta_i = 25^\circ$

| Detector | $\theta_s$ ( $^\circ$ ) | $\phi_s$ ( $^\circ$ ) | $q$ ( $\mu\text{m}^{-1}$ ) |
|----------|-------------------------|-----------------------|----------------------------|
| A        | 25.3                    | 9                     | 0.9                        |
| B        | 25                      | 90                    | 8.2                        |
| C        | 55                      | 180                   | 17.1                       |

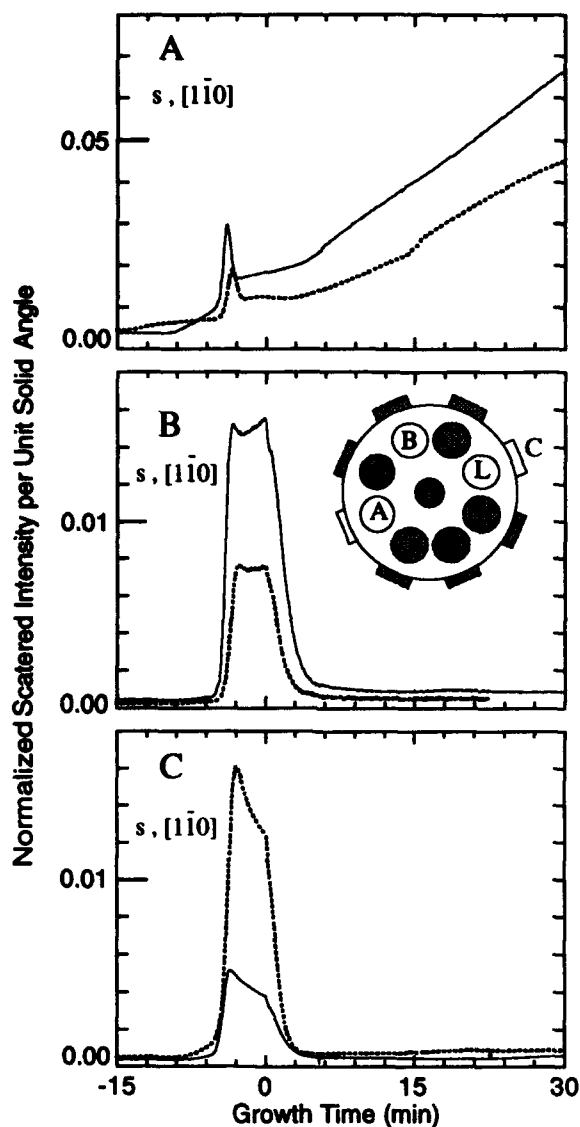


Fig. 1. Time evolution of the scattered intensity at three detectors A, B and C during oxide desorption and growth of GaAs. The light is incident along  $[1\bar{1}0]$ . For a given detection geometry A, B or C the changes in the two curves show the reproducibility. Note the very different behaviors depending on the position of the detector.

Considerable care was taken to avoid particle contamination of the substrates before they were loaded into the MBE system. The as-received two-inch diameter wafers were textured on the back with a nitric acid etch in order to improve heater coupling and enhance the performance of the optical temperature measurement system. After etching, the wafers were rinsed in de-ionized

water, blown dry with nitrogen, given a two minute UV ozone treatment to remove residual carbon and then cleaved into four pie-shaped pieces. The pieces were then mounted on In-free Mo holders and loaded into the MBE chamber. All wafer handling was carried out in a HEPA filtered laminar flow hood, inside a conventional laboratory (not a clean room). The ozone treated substrates were transferred directly into the growth chamber without a prebake in the preparation chamber, and ramped at 5 °C/min in an As<sub>2</sub> flux until the oxide is desorbed. Then the substrate heater power was fixed to give a growth temperature of 600 °C as measured by diffuse reflectance spectroscopy [6]. The substrate temperature was allowed to stabilize for 2 min then the Ga shutter was opened to start film growth. The growth rate was 1 μm/hr and the ratio of As to Ga was 3.5 as measured with a retractable ion gauge, not corrected for the differential ionization probability.

### LIGHT SCATTERING RESULTS

The light scattering signal as a function of time during the oxide desorption and subsequent film growth is shown in Fig. 1 for the three different detectors with s-polarized light incident parallel to the [110] direction in the surface. We show two independent runs (solid and dotted lines) that were nominally identical, in order to illustrate the reproducibility of the measurements from run to run. Although there are differences in the overall intensity, the shapes of the two sets of data as a function of time are very similar. The intensity differences may be due to small changes in the optical alignment of the two samples in successive runs. The Ga shutter is opened at the origin on the time axis in Fig. 1. Negative times in Fig. 1 correspond to the period during which the substrate temperature is being ramped up to the growth temperature. The abrupt increase in the scattered intensity about 5 min before the growth starts is caused by the surface roughening which takes place when the oxide desorbs. It is interesting to note that the oxide desorption shows up as a step in the scattered light intensity for large scattering angles while the oxide desorption produces a peak in the scattered intensity at low spatial frequencies. Fig. 2 shows a SEM picture of a similar oxide-desorbed surface to that shown in Fig. 1. This figure shows that the substrate is covered with small pits 100 - 1000 Å in diameter which, according to scanning tunneling microscopy measurements, are more than 100 Å deep.



Fig. 2. Field emission scanning electron microscopy picture of a GaAs surface after thermal removal of the oxide.

During film growth the large scattering angle detectors that are sensitive to high spatial frequencies show a rapid decay in intensity during growth while the small angle scattering shows a

progressive increase in scattered intensity. This result suggests that the high spatial frequency surface roughness associated with the oxide desorption pits smooths out during growth while long lengthscale roughness increases.

The scattered intensity for the large angle detectors does not always decay in a simple way during growth. See for example the small undulation near  $t = 0$  in detector B in Fig. 1. Much larger effects are sometimes observed, as shown in Fig. 3 in which the solid line in Fig. 1 B is reproduced (curve *a* in Fig. 3) together with the scattered intensity as a function of time for two similar growth experiments. (No special care was taken to align the incident beam with a crystallographic axis in the substrate for curves *b* and *c* in Fig. 3.) We speculate that the large oscillation in the scattered intensity as a function of time in curve *c* in Fig. 3 is associated with particulates or other point defects on the surface of the substrate. In this picture the roughness due to the oxide desorption, is responsible for the initial scattering intensity which decreases rapidly during growth, while the scattering intensity associated with the point defects is amplified as material accumulates around them. The point defects then account for the peak in the scattering intensity at later times. Eventually with enough deposition the point defects are covered up and the scattered intensity decreases again. Evidence in support of this interpretation is that the sample in curve *c* had an additional preparation step that may have contributed to the surface contamination, in that it was etched with HCl and rinsed with water in addition to the preparation steps described above. Also less care was taken to avoid particulate contamination with samples *b* and *c* in Fig. 3 compared with sample *a*. A similar type of behavior has been seen in silicon MBE [7]. Further experiments are needed to confirm this explanation of the time dependence of the scattering intensity in Fig. 3 and in other light scattering experiments [5,8].

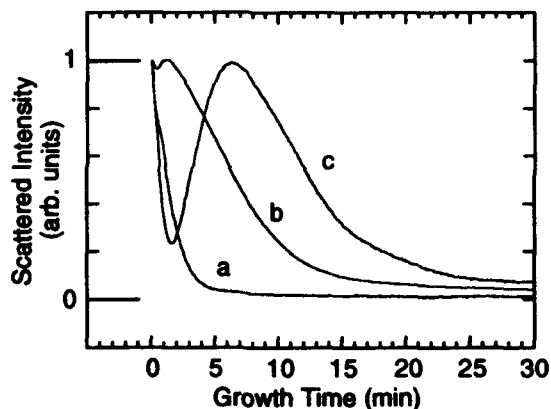


Fig. 3. Time evolution of the scattered intensity during growth of a GaAs buffer layer for three different substrate preparations. The expected order of cleanliness is *a*, *b* and *c* where *a* is the cleanest UHV loaded sample.

We now discuss the high spatial frequency light scattering parallel to  $[1\bar{1}0]$  in Fig. 1 (detector C), during the period between oxide desorption and the start of growth. This scattering decreases with the substrate exposure time to the As flux. We conclude that the substrate becomes smoother parallel to the  $[1\bar{1}0]$  direction during As exposure at 600 °C. The out of plane scattering (detector B in Fig. 1) which includes a contribution from the surface morphology in the  $[110]$  direction does not show a similar smoothing behavior. The effect of crystal orientation on the smoothing effect is shown more clearly in Fig. 4 where the scattering at detector C, which is in the plane of incidence, is shown for two different crystal orientations. As shown in Fig. 4, when the scattering vector is parallel to the  $[1\bar{1}0]$  direction the surface becomes smoother with time while the scattering is more or less constant when the scattering vector is parallel to  $[110]$ . This suggests that the surface morphology becomes anisotropic with height variations along  $[1\bar{1}0]$  decreasing in amplitude, while height variations along  $[110]$  remain unchanged.

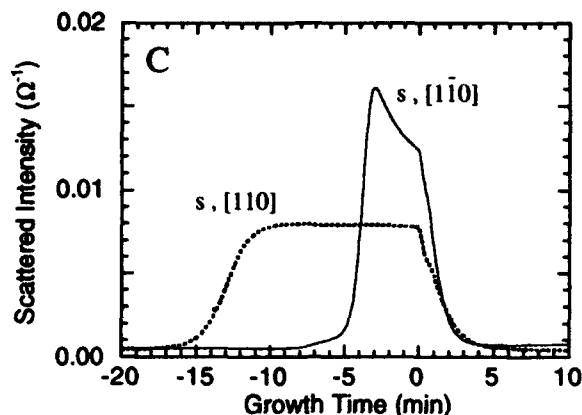


Fig. 4. Time evolution of the scattered intensity at detector C ( $q = 17.1 \mu\text{m}^{-1}$ ) of s polarized light during oxide desorption and GaAs growth when the plane of incidence is along the indicated crystallographic directions. Note the decrease in intensity after desorption and before growth when the laser is incident along  $[1\bar{1}0]$ .

An analogous crystal orientation effect is observed during growth in the low spatial frequency light scattering data shown in Fig. 5. The low spatial frequency roughness increases with time during growth; however, as seen by others [8], the scattering intensity increases with time faster when the light is incident along  $[1\bar{1}0]$  than when it is incident along  $[110]$ . Because the near specular detector A is located out of the plane of incidence as shown in Table I, the scattering vector is perpendicular to the plane of incidence for detector A. This means that the scattering with incident light along  $[1\bar{1}0]$  is actually sensitive to the surface morphology at right angles or in other words parallel to  $[110]$ . Accordingly, during growth, as well as during the As exposure, the surface becomes anisotropic with more surface roughness in the  $[110]$  direction than in  $[1\bar{1}0]$ . This effect has also been observed in scanning tunneling microscopy experiments performed ex-situ on quenched substrates [2].

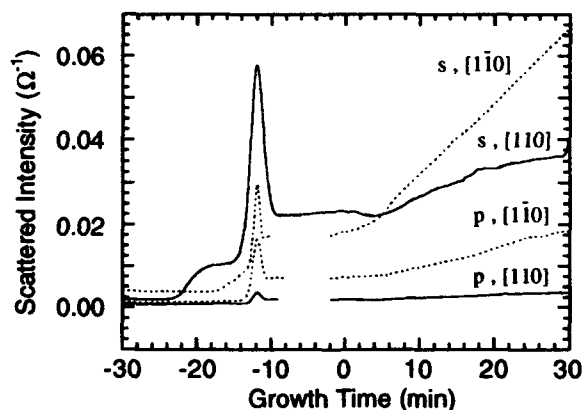


Fig. 5. Time evolution of the scattered intensity at detector A ( $q = 0.93 \mu\text{m}^{-1}$ ) of both s and p-polarized light during oxide desorption (peak) and GaAs growth when the plane of incidence is along the indicated crystallographic directions.



Fig. 5 also illustrates the effect of the polarization of the incident light on the scattered intensity. The p-polarized light shows similar temporal behavior to the s-polarized light but with lower overall intensity. Similar polarization effects were also observed for the higher spatial frequency detectors at B and C.

The observed time dependencies of the scattered light intensity suggest that the surface roughness evolves during growth towards large amplitudes at low spatial frequencies and small amplitudes at high spatial frequencies, at least when compared to the starting oxide-desorbed surface. The changes in the surface morphology are driven by the flux of deposited atoms. Various continuum models have been proposed to describe the surface height  $z(r,t)$  as a function of time  $t$  and position  $r$  on the surface, during epitaxial growth. For example in the presence of a diffusion bias caused by asymmetric barriers to diffusion across steps on the surface, to lowest order the evolution of the surface morphology with time can be described by [1],

$$dz/dt = v \nabla^2 z + f(r,t) \quad (1)$$

where  $f$  is the fluctuating deposition rate at the position  $r$ , at time  $t$ . Since the scattered light intensity at a given angle is sensitive to the surface morphology at a single spatial frequency it is natural to transform Eq. 1 to the Fourier domain,

$$d\hat{z}/dt + v q^2 \hat{z} = \hat{f}(q,t) \quad (2)$$

In the case where the roughness due to the initial conditions exceeds the roughness driven by the depositing flux of atoms the flux term can be ignored in Eq. 2 and the surface power spectral density  $\hat{z}(q,t)^2$  at spatial frequency  $q$  should decay exponentially with characteristic time  $\tau = 1/(2q^2v)$ . From the slope of the approximately exponential decay of the scattered light intensity in Fig. 1 C for example, we estimate  $\tau = 1$  min. for  $q = 17.1 \mu\text{m}^{-1}$  and conclude that  $v = 3 \times 10^{-13} \text{ cm}^2/\text{s}$  for the given growth conditions.

## SUMMARY

The intensity of light diffusely scattered from the substrate has been measured as a function of time during MBE growth of GaAs at three different scattering angles. The scattered intensity is found to depend on incident polarization, crystal orientation and the magnitude of the scattering vector. In particular the initially pitted surface resulting from the oxide desorption is found to roughen during growth, at low spatial frequencies ( $q = 0.9 \mu\text{m}^{-1}$ ), and smooth at high spatial frequencies ( $q = 8.2 \mu\text{m}^{-1}$ ).

We thank M. Plischke, M. Siegert and T. Pinnington for helpful discussions and the Natural Sciences and Engineering Research Council for support.

## REFERENCES

1. J. Villain, J. Phys. I. (France) **1**, 19 (1991).
2. M. D. Johnson, C. Orme, A. W. Hunt, J. Sudijono, L. M. Sander, and B. G. Orr, to be published.
3. J. E. Epler and H. P. Schweizer, Appl. Phys. Lett. **63**, 1228 (1993).
4. J. M. Bennett and L. Mattsson, *Introduction to Surface Roughness and Scattering*, (Optical Society of America, Washington, D. C., 1989) and references therein.
5. C. Lavoie, S. R. Johnson, J. A. Mackenzie, T. Tiedje, and T. van Buuren, J. Vac. Sci. Technol. A **10**, 930 (1992).
6. S. R. Johnson, C. Lavoie, T. Tiedje, and J. A. Mackenzie, J. Vac. Sci. Technol. B **11**, 1007 (1993).
7. D. J. Robbins, A. J. Pidduck, C. Pickering, I. M. Young and J. L. Glasper, SPIE **1012**, 25 (1988).
8. F. G. Celii, L. A. Files-Sesler, E. A. Beam III, and H.-Y. Liu, J. Vac. Sci. Technol. A **11**, 1796 (1993).
9. G. W. Smith, A. J. Pidduck, C. R. Whitehouse, J. L. Glasper, and J. Spowart, J. Crystal Growth **127**, 966 (1993).

# REAL-TIME *IN SITU* MONITORING OF DEFECT EVOLUTION AT WIDEGAP II-VI/GaAs HETEROINTERFACES DURING EPITAXIAL GROWTH

C.M. ROULEAU and R.M. PARK

University of Florida, Department of Materials Science and Engineering, Gainesville, FL 32611

## ABSTRACT

We report the real-time *in situ* observation of heterointerface dislocation formation during the growth of lattice-mismatched widgap II-VI/GaAs heterostructures. Such observations were made by employing a near-normal incidence HeNe laser probe during epitaxial growth which generated both a laser reflection interferometry (LRI) signal as well as an elastically scattered laser light (ELLS) signal. We believe that the scattered light signal is generated at the II-VI/GaAs heterointerface based on the observation of a  $\pi$  phase difference between the LRI and the ELLS signals which were monitored simultaneously. We suggest, therefore, that the observed ELLS signal is a consequence of dislocation formation at the heterointerface which occurs due to plastic deformation in lattice-mismatched systems.

## 1. INTRODUCTION

Following breakthroughs in the ZnSe p-type doping area<sup>1,2</sup> emphasis has shifted recently in the wide-bandgap II-VI semiconductor research field toward the provision of lattice-matched widgap II-VI/GaAs epitaxial structures for blue/green diode laser application.<sup>3</sup> Although the first blue/green diode lasers represented a considerable achievement,<sup>4,5</sup> the structures employed in the fabrication of these devices were not completely lattice-matched and, consequently, devices exhibited short lifetimes even at reduced temperatures.

It is generally accepted that perfect lattice-matching between widgap II-VI epitaxial materials and GaAs substrates will be a primary requirement with regard to the development of long-lived (at room temperature) ZnSe-based blue/green diode lasers. At present, however, time consuming *ex situ* characterization techniques such as high resolution x-ray diffraction and cross-sectional transmission electron microscopy are applied to determining the extent of lattice-matching in widgap II-VI/GaAs heterostructures.

In this paper, we show that dislocation evolution occurring at a slightly lattice-mismatched II-VI/GaAs heterointerface can, in fact, be monitored *in situ* using an optical probing technique. Such analysis, in addition to obviating the need to perform *ex situ* structural characterization, permits the real-time monitoring of dislocation evolution during epitaxial growth which can lead to a more fundamental understanding of the plastic deformation process itself.

Real-time *in situ* monitoring techniques, in general, represent very powerful capabilities with regard to process diagnosis and control. For example, with respect to molecular beam epitaxy (MBE), reflection high energy electron diffraction (RHEED) is employed on a routine basis to determine surface reconstruction and to assess the quality of substrate surfaces and

subsequent epilayers. Recently, however, optical techniques have become increasingly popular due to their noninvasive nature and their ability to provide information on properties other than crystal structure. Ellipsometry, for instance, has far reaching capabilities that include real-time, *in situ* monitoring and control of alloy composition, growth rate, and substrate temperature during MBE deposition.<sup>6-8</sup> Also, real-time, *in situ* monitoring of the free-carrier concentration in doped ZnSe films by quantitative cathodoluminescence analysis has been reported.<sup>9</sup> In addition, Lavoie *et al.*<sup>10</sup> and Rouleau and Park<sup>11</sup> have reported real-time, *in situ* monitoring of the GaAs oxide desorption process prior to epitaxial growth by measuring the intensity of laser light scattering at the GaAs surface, Rouleau and Park<sup>11</sup> having shown a low temperature H atom treatment to be superior by such measure to conventional *in situ* thermal cleaning of GaAs. Also along these lines, Pidduck *et al.*<sup>12,13</sup> have performed similar elastic laser light scattering measurements during Si MBE and have concluded that changes in the surface morphology occurring during layer processing can conveniently be monitored and characterized by such means.

The purpose of the present paper is to report our efforts to develop an *in situ* monitoring technique that can be applied during epitaxial growth which is capable of monitoring the evolution of dislocations occurring at mismatched widegap II-VI/GaAs heterointerfaces (as opposed to surfaces).

## II. EXPERIMENTAL

The experiments were carried out in a custom designed MBE system equipped with conventional effusion cells for Zn, Se and Te and a RHEED system for assessing substrate surface quality and subsequent epilayer quality. In addition to these conventional components, for this work the MBE chamber was also configured with a laser probe apparatus as illustrated in Fig. 1.

The apparatus consisted of a 1mW HeNe laser ( $\lambda=632.8\text{nm}$ ) mounted outside the MBE growth chamber, the laser beam being directed through a viewport towards the substrate which was mounted on a heated Mo substrate holder. The detector/amplifier stage of the apparatus consisted of a CCD camera and a video monitor. The camera was mounted outside the system on its own viewport, its optical axis lying  $10^\circ$  away from the optical axis of the incident laser beam, the laser beam being a near-normal incidence. The camera was focused on the substrate surface and the visible spot arising from elastically scattered laser light (ELLS) due to defect evolution was displayed on the video monitor. The intensity of the scattered laser light was quantified by attaching a Si photodiode to the monitor's CRT over the image of the spot and the output voltage from its respective bias network was recorded as a function of time.

The specularly reflected beam was utilized in this experiment to monitor film thickness by employing laser reflection interferometry (LRI)<sup>9</sup> which involves characterization of the Fabry-Perot intensity oscillations exhibited by the signal. It should be noted that the intensities of both the scattered laser light and the specularly reflected laser light were recorded simultaneously so that signal phasing could be compared.

Due to the unorthodox nature of the detection system employed in quantifying the intensity of elastically scattered laser light, it was important to characterize the transfer function of the CCD camera-based detection system and the apparatus illustrated schematically in Fig. 2 was employed to perform this task. A tungsten lamp, lens, diffuser and laser line filter combination was used to simulate a 632.8nm input signal whose intensity could be varied over

a wide dynamic range. To quantify the intensity of light entering the camera system from the simulated source, a beam splitter was placed in front of the camera lens to direct a portion of the input light towards a photodiode. The output voltage from the bias network associated with this photodiode was then proportional to the light intensity directed into the camera system. The system transfer function was deduced by comparing the output voltage from the other bias network with the input voltage, both intensities being recorded simultaneously on an XY recorder as indicated in the figure.

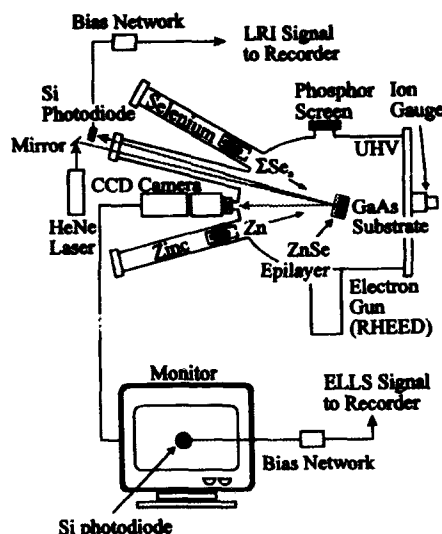


Figure 1 Schematic diagram of the experimental setup used to record elastically scattered laser light (ELLS) and specularly reflected laser light during the molecular beam epitaxial growth of widegap II-VI/GaAs heterostructures.

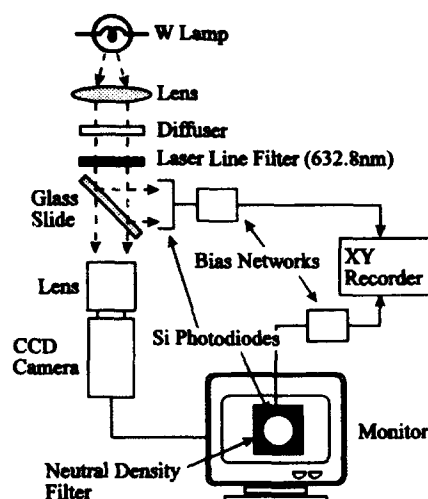


Figure 2 Schematic diagram of the apparatus used to characterize the camera-based detection system used to detect elastically scattered laser light.

### III. RESULTS

#### CCD camera-based detection system characterization

As illustrated in Fig. 3, the detection system exhibited a threshold beyond which a linear regime was observed. As the input intensity increased, the system responded in an increasingly nonlinear fashion as indicated in the figure. This was most likely due to the automatic gain control circuitry in both the CCD camera and the monitor. For further increases in input intensity, the system response was clamped, presumably in response to the saturation of the CCD array. Using this information, attempts were made throughout the experiments to keep the detection system in a regime where clamping did not occur. The system was, however, allowed

to operate in the linear/nonlinear regimes so that a reasonable degree of dynamic range could be achieved.

### Widegap II-VI/GaAs heteroepitaxy

As illustrated in Fig. 4, laser light scattering was not detectable (by the system) upon ZnSe growth initiation until approximately 280nm of material had been deposited whereupon increasingly intense scattering was detected with increasing film thickness having an oscillatory form as shown in the figure. It should be noted that in order not to observe scattering upon growth initiation, it is imperative that the GaAs surface be specular following oxide removal.<sup>11</sup>

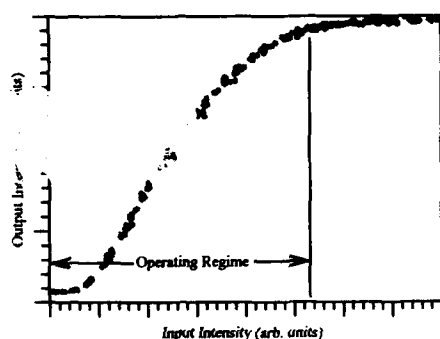


Figure 3 Camera-based detection system transfer function recorded at 632.8nm.

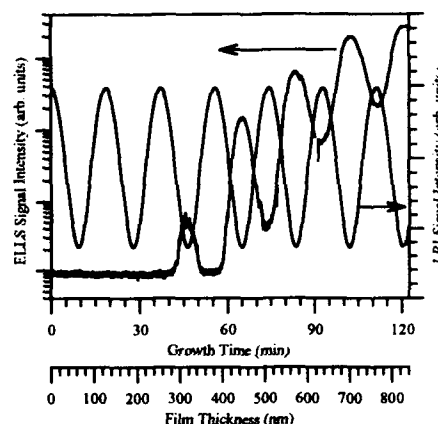


Figure 4 Intensity of scattering occurring near the heterointerface as a function of ZnSe epitaxial deposition time and layer thickness. Also included is a laser reflection interferogram.

The growth was terminated near  $0.84\mu\text{m}$  to avoid saturating the detection system. The most striking feature of Fig. 4 is the  $\pi$  phase difference between the ELLS signal and the LRI signal which, using ray tracing, can be explained by placing an emitter at the heterointerface and considering intense scattering at the heterointerface as opposed to the free surface. To explain further, we have developed the qualitative model illustrated in Fig. 5.

As indicated in Fig. 5, the laser beam impinges on the sample at near-normal incidence and a portion of the beam is transmitted into the epilayer and proceeds towards the heterointerface. We consider that in addition to specular reflection off the heterointerface, a small portion of the beam is scattered into other (nonspecular) angles due to the presence of dislocations which occur in response to attainment of the critical thickness. For simplicity, we consider only that angle which points in the direction of our detector as indicated in the figure. The scattered beam traverses the epilayer and in addition to transmission through the free surface, a portion of the beam is redirected back towards the heterointerface by reflection off the free surface. Since the index step from epilayer to vacuum is negative, no phase shift is introduced upon reflection. The reflected portion of the beam again traverses the epilayer, reflects off the

heterointerface, and then makes a final pass through the epilayer to emerge on the vacuum side of the free surface. At this point, a  $\pi + 2\delta$  phase shift has been introduced,  $\pi$  resulting from prior reflection off the heterointerface and  $2\delta$  resulting from traversing the epilayer twice. The phase difference,  $\Delta_{\text{ELLS}}$  between the newly emergent beam and the original portion of the scattered beam is then  $2\delta + \pi$  which is necessarily a function of the wavelength of the laser,  $\lambda$ , the refractive index of the epilayer,  $n$ , the thickness of the epilayer,  $z$ , and the angle of transmittance within the epilayer,  $\theta$ . In a similar manner, it can be easily shown that  $\Delta_{\text{LRI}} \approx 2\delta$  since  $\theta_{\text{LRI}} \approx \theta_{\text{ELLS}}$  due to the small angles involved. Finally,  $\Delta_{\text{ELLS}} - \Delta_{\text{LRI}} = \pi$  and hence the  $\pi$  phase difference between the ELLS signal and the LRI signal as observed in Fig. 4. It is interesting to compare our results with those of Olson and Kibbler<sup>14</sup> who employed a similar technique to monitor scattering from GaP during MOCVD of GaP/Si. The GaP/Si system is very similar to the ZnSe/GaAs system with respect to lattice mismatch (0.36%) and refractive index steps (@ 632.8nm) so it's reasonable to assume that under similar conditions, similar results may be achieved. Comparing sets of data, it is obvious that their data resembles our LRI data (see Fig. 4) which we would contend places the source of their scattering outside the epilayer or more appropriately, at the free surface. They do indeed attribute their ELLS signal to surface scattering and it is quite trivial using our arguments above to show the lack of a  $\pi$  phase difference between a ELLS signal and a LRI signal for such a case. Consequently, our results clearly differ from previously published results that have concerned surface scattering, in our case the  $\pi$  phase shift discussed above indicates heterointerface rather than surface scattering. We believe that the amplitude of the modulation and the "DC component" of our ELLS signal are dependent on the optical properties of the heterointerface as well as its morphological properties, these characteristics being controlled by the multiplication and propagation of dislocations near the heterointerface while the film is growing.

Our laser probe technique was also applied during the MBE growth of ZnTe/GaAs epilayers and the scattering data recorded from this system is compared and contrasted to that observed from the ZnSe/GaAs system in Fig. 6.

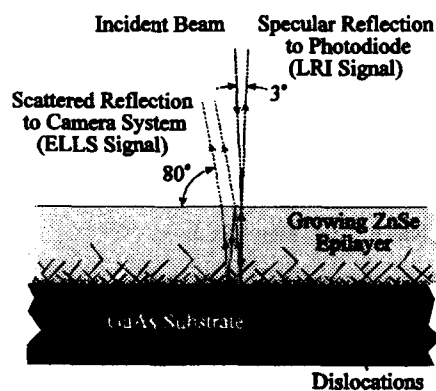


Figure 5 A ray model illustrating the employment of a HeNe laser beam to probe the ZnSe/GaAs heterointerface during epitaxial deposition. Dislocation evolution upon attainment of the critical thickness gives rise to a scattered signal which was detected and quantified using the apparatus in Fig. 1.

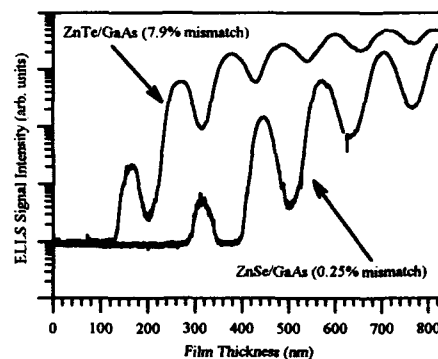


Figure 6 Elastically scattered laser light data recorded in real-time during the deposition of ZnSe/GaAs and ZnTe/GaAs heterostructures. The lattice-mismatches indicated correspond to room temperature lattice-mismatches.

As can be seen from the figure, scattering is detected earlier (in terms of layer thickness) from the ZnTe/GaAs heterointerface as opposed to the ZnSe/GaAs heterointerface. Furthermore, the rate of change of scattering (with respect to layer thickness) is greater in the case of ZnTe/GaAs. Both of these observations seem to be highly correlated with the degree of lattice-mismatch as indicated in the figure.

#### IV. CONCLUSIONS

We conclude that the *in situ* optical probe described here is capable of detecting the onset of plastic deformation in lattice-mismatched heteroepitaxial systems, such as ZnSe/GaAs, in real-time during epitaxial deposition. Furthermore, the technique by its real-time nature is appropriate for dislocation evolution monitoring. Finally, we conclude that should perfectly lattice-matched structures be grown, the laser light scattering reported here would not be observed which could have important consequences for the provision of lattice-matched structures for widegap II-VI/GaAs diode lasers.

#### ACKNOWLEDGEMENTS

The research has been financially supported by the National Science Foundation (Grant No. DMR-9116880) and by the Advanced Research Projects Agency (University Research Initiative Grant No. N-00014-92-J-1895).

#### REFERENCES

1. R.M. Park, M.B. Troffer, C.M. Rouleau, J.M. DePuydt and M.A. Haase, Appl. Phys. Lett. **57**, 2127 (1990).
2. K. Ohkawa, T. Karasawa and T. Mitsuyu, Jpn. J. Appl. Phys. **30**, L152 (1991).
3. H. Okuyama, T. Miyajima, Y. Morinaga, F. Hiei, M. Ozawa, and K. Akimoto, Electron. Lett. **28**, 1798 (1992).
4. M.A. Haase, J. Qui, J.M. DePuydt, and H. Cheng, Appl. Phys. Lett. **59**, 1272 (1991).
5. H. Jeon, J. Ding, W. Patterson, A.V. Nurmikko, W. Xie, D.C. Grillo, M. Kobayashi, and R.L. Gunshor, Appl. Phys. Lett. **59**, 3619 (1991).
6. R.H. Hartley, M.A. Folkard, D. Carr, P.J. Orders, D. Rees, I.K. Varga, V. Kumar, G. Shen, T.A. Steele, H. Buskes, and J.B. Lee, J. Vac. Sci. Technol. B **10**, 1410 (1992).

7. G.N. Maracas, J.L. Edwards, K. Shiralagi, K.Y. Choi, R. Droopad, B. Johs, and J.A. Woolam, *J. Vac. Sci. Technol. A* **10**, 1832 (1992).
8. W.E. Quinn, D.E. Aspnes, M.J.S.P. Brasil, M.A.A. Pudensi, S.A. Schwarz, M.C. Tamargo, S. Gregory, and R.E. Nahory, *J. Vac. Sci. Technol. B* **10**, 759 (1992).
9. C.M. Rouleau and R.M. Park, *Appl. Phys. Lett.* **60**, 2723 (1992).
10. C. Lavoie, S.R. Johnson, J.A. Mackenzie, T. Tiedje, and T. van Buuren, *J. Vac. Sci. Technol. A* **10**, 930 (1992).
11. C.M. Rouleau and R.M. Park, *J. Appl. Phys.* **73**, 4610 (1993).
12. A.J. Pidduck, D.J. Robbins, A.G. Cullis, D.B. Gasson, and J.L. Glasper, *J. Electrochem. Soc.* **136**, 3083 (1989).
13. A.J. Pidduck, D.J. Robbins, D.B. Gasson, C. Pickering, and J.L. Glasper, *J. Electrochem. Soc.* **136**, 3088 (1989).
14. J.M. Olson and A. Kibbler, *J. Cryst. Growth*, **77**, 182 (1986).



## THE UTILITY OF LASER LIGHT SCATTERING IN ASSESSING THE MIXABILITY OF REAGENTS FOR CHEMICAL VAPOR DEPOSITION

BIN NI\*, GENE P. RECK\* AND JAMES W. PROSCIA\*\*

\*Department of Chemistry, Wayne State University, Detroit, MI 48202

\*\*Ford Motor Company, Glass Division, Dearborn, MI 48120

### ABSTRACT

The premixability of reagents used in chemical vapor deposition reactors is important to insure that gas feed lines and nozzles do not become clogged with particulates during operation. Even if reactants are to be kept separate until introduced into a reaction chamber, it is desirable to limit the number of particles formed. A reactor which utilizes laser light scattering to monitor particulate formation when gaseous reagents are mixed is described. The reaction of tin (IV) chloride with water is commonly used to produce tin oxide films by chemical vapor deposition. It was found by the light scattering experiment that at temperatures above about 110 °C the number of particulates formed is greatly reduced. Therefore, it would be most desirable that these reagents be mixed above this temperature when depositing tin oxide from this reaction. The reaction of titanium tetrachloride with various amine was also investigated by this method. This reaction has been demonstrated to produce titanium nitride above 450 °C. For each case, it was observed that there was a temperature above which the number of particulates was significantly reduced. This temperature was always below the optimal temperature for producing titanium nitride films.

### INTRODUCTION

In most CVD processes particle contamination can be a major contributor to poor film quality. The particles can be from contamination of source chemicals, carrier gases, the reactor or from gas phase chemical reactions. Light scattering, particularly of laser light, is an easy means to detect and monitor these particles since in the appropriate limit the scattering is directly proportional to the particle density. Earliest studies in fact used the eye as the detector(1). Subsequent work has been more complicated(2-5). In this paper we report on the use of laser light scattering to monitor the relationship between particle formation due to chemical reaction and the temperature. The goal of this work is to determine the temperature above which gases maybe mixed without particle formation or if they do form they immediately vaporize. Knowledge of these temperatures can be used to determine temperatures for preheating of the gas streams. Although other reactions have been studied, we limit our discussion here to the reaction between  $TiCl_4$  and a variety of amines to form films of TiN at temperatures above 450°C(6). We report results using three different techniques in two different reactors which were specially constructed to provide optical access to the region where the gases mix and above the film formation region. From the results of such measurements it is quite easy find a temperature range for film formation where particle formation is not a problem.

### EXPERIMENTAL

Reactor 1 is constructed of stainless steel with provision for optical windows which allow optical access to region of particle formation. The windows are so designed that a positive pressure of nitrogen keeps the windows free of particulates. The reactor is approximately xx by xx with sidearms of length yy. The main section of the reactor is contained in furnace whose temperature maybe controlled. The reactor is pictured in Figure 1. The injector and gas flow direction are in the downward direction.

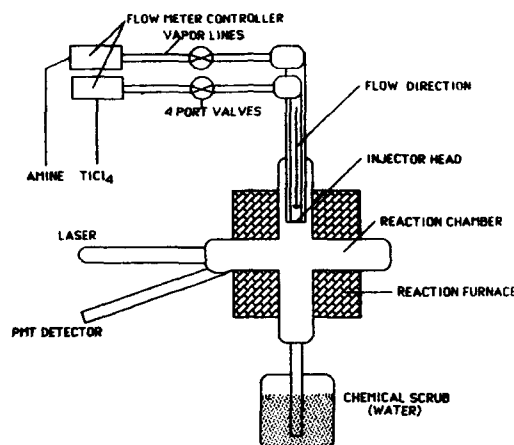


Figure 1 Schematic of reactor 1.

The light source was an unfocused 1mw He-Ne laser with a beam diameter of 16 mm at the reaction region. The scattered light was monitored through the second arm which was at an angle of  $120^\circ$  with respect to the entrance arm. A photo multiplier with output to a strip chart recorder with time constant of .1 s recorded the signal. A cut-off filter was used to assure that only the scattered light and not the infra-red from the oven was recorded. Two kinds of measurements were made on the scattered light. Measurements of type 1 (height) were the average intensity of the scattered light as read from the strip chart as a function of oven temperature. It was observed that when the signal was from scattered light from the oven (not just high signal levels) that the noise level increased with intensity of scattered light. Presumably this is due to an increase in turbulence. Measurements of type 2 (width) were of the magnitude of the noise level.

A third approach was also used. In this case another stainless steel reactor was constructed similar the first but with only four arms and the gas injector perpendicular to the plane of the arms. The gas flow was still downward. An excimer laser ( Lambda Physik, EMG xxx XeCl, 308 nm, 200 m, 22 ns pulse ) was used as the light source. The beam size at the reaction region was 1.3 x 3 cm. The spectrum of the scattered light was detected with a 1/4 m Jarrell-Ash monochromator with 1200 groves/mm grating and an intensified diode array detector (Tracor Northern TN-6500 system with an array of 1024 diodes). The advantages of this third approach are that only the scattered light at the appropriate wavelength is monitored and the increased laser power allowed us to perform experiments at 1/25 th the flow rate.

In all the experiments, the background scattered light was determined by turning the flow of each of the reagents on and off. In fact, in order to avoid problems of particle build up in the lines and nozzle much of the time while the oven temperature was changing no reagents were flowing. At higher temperatures this results in an apparent decrease in scattered light when the flows are started. This is most likely due to a lack of temperature equilibrium caused by the fact that these reactions are endothermic so that the reaction region cools while the background from the furnace remains the same.

## RESULTS

Initial experiments were done on the well studied reaction of  $\text{SnCl}_4$  and  $\text{H}_2\text{O}$  using only the height of the scattered intensity as a monitor of the extent of particle formation. This result is shown in Figure 2

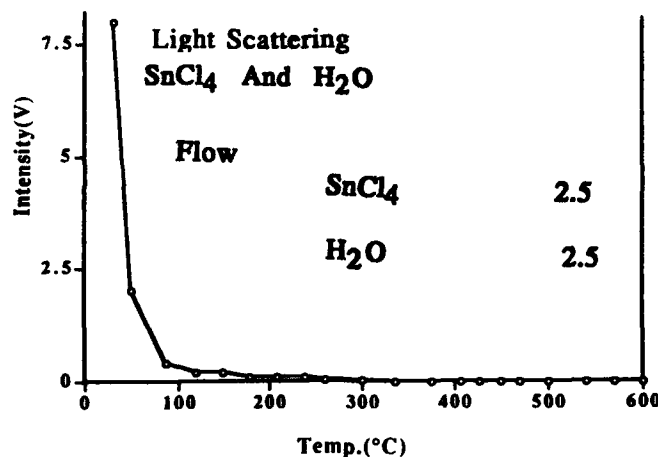


Figure 2. Scattered intensity vs temperature for SnCl<sub>4</sub> and H<sub>2</sub>O

Experiments were also performed with TiCl<sub>4</sub> and a wide variety of amines under conditions that we have previously used to produce films with good adhesion, color and low carbon and chloride content. The results for three amines (others were also done) from reactor 1 are shown in Figures 3, 4, 5.

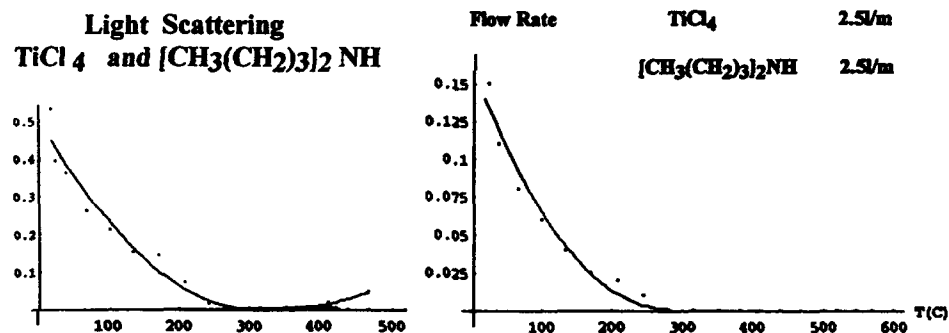


Figure 3. Height measurement is on the left and the width measurement is on the right.

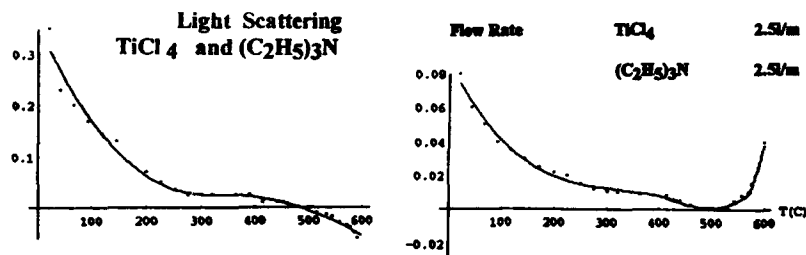


Figure 4. Height measurement is on the left and the width measurement is on the right.



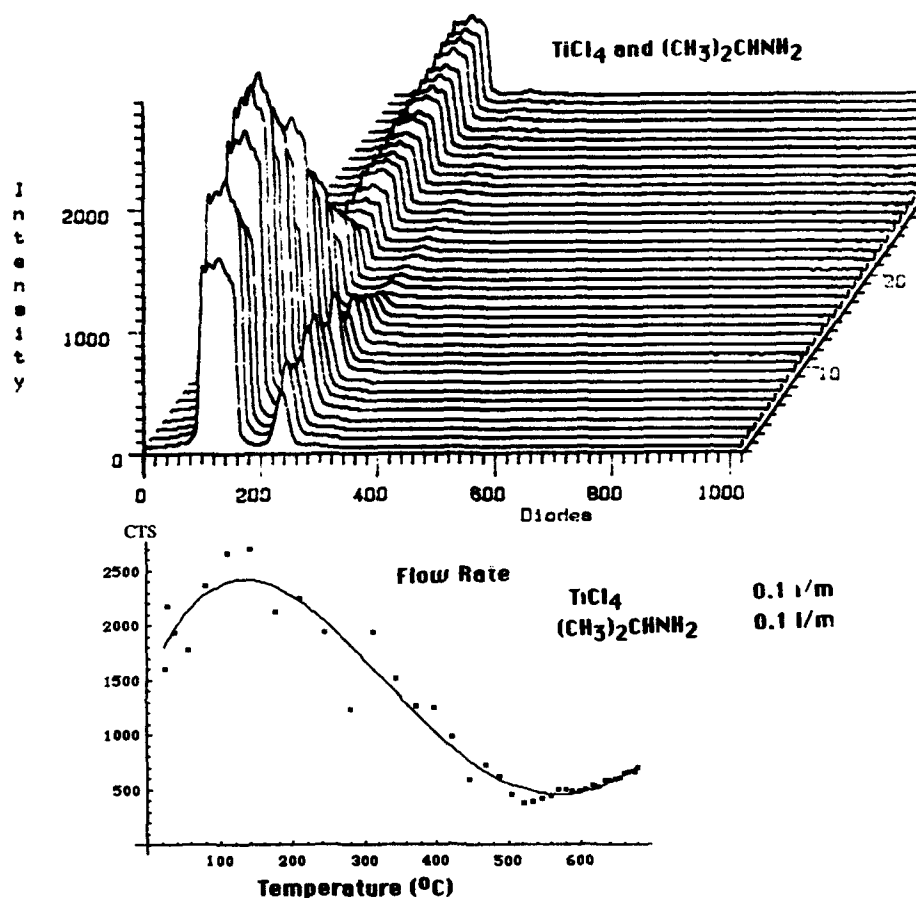


Figure 6. Top: Spectrum of scattered light as a function of temperature. Bottom: Plot of peak height vs. temperature for the top spectrum.

temperature at which particles are no longer detected for all the amines we studied. If the mechanism for particle formation were similar and involved similar intermediates, one expects a similarity in the temperatures. At the higher temperatures, the onset of particle formation is also comparable for all the amines, therefore we expect that particle formation could come from the same process independent of the amine used.

When the results of the He-Ne laser and excimer laser are compared the similarities are not as apparent. In the excimer experiments the flow rates are so much lower that we are actually measuring a much lower level of particle formation hence see particles at much higher temperatures.

## CONCLUSIONS

The results of laser light scattering measurements in the reaction of  $TiCl_4$  and amines using three different methods are similar. The experiments are easily done so that any of the methods described here may be used to effectively monitor particle formation and determine a range of temperatures where particle formation is not a problem.

## REFERENCES

1. F. C. Eversteijn, Phillips Res. Rep., 26, 134 (1971).
2. C. H. J. Van den Brekel and J. M. Bollen, J. Cryst. Growth, 54, 310 (1981).
3. W. G. Breiland and P. Ho, in *Proceedings of the Ninth International Conference on Chemical Vapor Deposition*, ed. McD. Robinson, C. H. J. van den Breckel, G. W. Cullen, J. M. Blocher, Jr. and P. Rai-Choudhury, (The Electrochemical Society, Inc., Pennington, NJ, 1984), pp. 44-59.
4. S. R. Kurtz and R. G. Gordon, Thin Solid Films 140, 277 (1986).
5. W. G. Breiland and P. Ho in *Chemical Vapor Deposition, Principles and Applications*, ed. M. L. Hitchman and K. F. Jensen, (Academic Press, New York, NY, 1993), pp. 91-158.
6. J. W. Proscia, K. B. Williams and G. P. Reck, Abstract of Papers, Fourth Chemical Congress of North America, New York, NY, (American Chemical Society: Washington, DC; 1991); INOR 309.
7. C. H. Winter, T. S. Lewkebandara, P. H. Sheridan and J. W. Proscia, Mat. Res. Soc. Symp. Proc. 282, 293 (1993).
8. C. H. Winter, P. H. Sheridan, T. S. Lewkebandara, M. J. Heeg and J. W. Proscia, J. Am. Chem. Soc. 114, 1095 (1992).

---

PART III

---

**Photorefectance and  
Photoluminescence Spectroscopies**

## **CONTACTLESS ELECTROMODULATION CHARACTERIZATION OF COMPOUND SEMICONDUCTOR SURFACES AND DEVICE STRUCTURES**

J.M. WOODALL; School of Electrical Engineering, Purdue University, West Lafayette,  
IN 47907-1285 USA

### **ABSTRACT**

This paper will review the use of contactless electromodulation methods, such as photorefectance (PR) and contactless electroreflectance (CER), to characterize the electronic properties of compound semiconductor surfaces exposed to different growth and post-growth conditions. Also the characterization of properties critical to device performance can be evaluated. For example, using PR and CER it has been found that there is a lower density of surface hole traps than electron traps in certain as-grown MBE (001) GaAs samples and that this condition persists even after air exposure. This behaviour is in contrast to other samples, including both bulk and MBE grown (001) surfaces in which the Fermi level is pinned mid-gap for both *n*- and *p*-type structures. We also have observed that Ar<sup>+</sup> bombardment under UHV conditions results in Fermi level pinning close to the conduction band edge and that thermal annealing restores mid-gap pinning. Finally, using PR we are able to characterize the electric fields and associated doping levels in the emitter and collector regions of heterojunction bipolar transistor structures (fabricated from III-V materials), thus demonstrating the ability to perform in-process evaluation of important device parameters.

### **INTRODUCTION**

The fabrication of modern-day electronic, optical and opto-electronic devices involves a number of complicated procedures, ranging not only from the actual epitaxial growth of thin layers but also to pattern definition and transfer. In a functional device the physical properties of each layer should be optimal. Thus, not only are the epitaxial growth steps crucial, but further processing steps also must be monitored. Therefore, it becomes important to have available as many noninvasive techniques as possible to probe the various processing steps and to relate these to actual device parameters and performance. Ideally, one would like to perform the characterization procedure at room temperature on entire wafers, possibly even before the structure is removed from the processing chamber.

In the past decade there have been considerable advances in semiconductor device fabrication due not only to thin film growth but also to various processing procedures. Developmental efforts are driving device design toward more compact structures, a trend which places ever increasing demands on materials/processing/device parameters and hence evaluation procedures in order to upgrade performance and yield.

Optical probes are ideal for the noninvasive monitoring/control of processing procedures. For applied work, an optical characterization technique should be as simple, inexpensive, compact, rapid and informative as possible. Other valuable aspects are the ability to perform measurements in a contactless manner at (or even above) room



temperature on wafer-sized samples. Because of its simplicity and proven ability, modulation spectroscopy [1,2] (particularly contactless modes) is now a major tool for the study and characterization of bulk/thin film semiconductors in addition to semiconductor microstructures (quantum wells, superlattices, etc.) and interfaces (heterojunctions, semiconductor/vacuum, semiconductor/metal). This optical method is also useful for the evaluation of process-induced damage [1-4] and actual device parameters [1,5].

A particularly useful form of modulation spectroscopy is electromodulation [electric field modulated reflectivity] since it is sensitive to surface/interface electric fields and can be performed in contactless modes [photorefectance (PR) or contactless electroreflectance (CER)] that require no special mounting of the sample [1,2]. Therefore, these modes can be employed on wafer-sized material without altering the sample. The sensitivity of EM methods to surface/interface electric fields has proven to be one of its most important properties for materials/device characterization. For sufficiently high built-in electric fields the EM spectrum can display an oscillatory behavior above the band gap called Franz-Keldysh oscillations (FKOs), which can be readily employed to monitor these fields at surfaces/interfaces, including actual device structures [1,2,5].

## BACKGROUND

Under the influence of an electric field  $F$  in the  $z$ -direction the energy bands are tilted by an amount  $eFz$ . An electron attempting to tunnel from the valence band into the conduction band sees a triangular barrier. Resonances appear whenever an integral number of de Broglie wavelengths fit into the triangular well formed by the electric field. The de Broglie wavelength is equal to  $h/p$ , where  $h$  is Planck's constant and  $p$  is the momentum of the electron (hole). It can be shown that the energy of the  $n^{\text{th}}$  resonance,  $E_n$ , is proportional to  $F^{2/3}$ . Thus the period of these resonances, or FKOs, are a direct measure of the built-in electric field. In transport theory this tunnelling phenomenon through a triangular barrier is called Fowler-Nordheim tunnelling. Thus FKOs are the optical analog of Fowler-Nordheim tunneling in transport.

The exact form of  $\Delta R/R$  with broadening is quite complicated. Aspnes has written a relatively simple expression [1,6]:

$$\begin{aligned} \Delta R/R &\propto \exp[-2(E-E_g)^{1/2}\Gamma/(\hbar\Theta)^{3/2}] \\ &\times \cos[(4/3)(E-E_g)^{3/2}/(\hbar\Theta)^{3/2} + \chi][E^2(E-E_g)]^{-1} \end{aligned} \quad (1a)$$

where  $E$  is the photon energy,  $E_g$  is the energy gap,  $\Gamma$  is the broadening parameter,  $\chi$  is an arbitrary phase factor and the electrooptic energy  $\hbar\Theta$  is given by:

$$(\hbar\Theta)^3 = q^2\hbar^2 F^2 / 2\mu_{\parallel} \quad (1b)$$

In Eq.(1b)  $\mu_{\parallel}$  is the reduced interband effective mass in the direction of the electric field.

From Eq.(1a) the position of the  $n^{\text{th}}$  extrema in the FKOs is given by:

$$n\pi = (4/3)[(E_n - E_g)/\hbar\Theta]^{3/2} + \chi \quad (1c)$$

where  $E_n$  is the photon energy of the  $n^{\text{th}}$  extrema. A plot of  $(4\pi/3)(E_n - E_g)^{3/2}$  vs. the index number  $n$  will yield a straight line with slope  $(\hbar\Theta)^{3/2}$ . Therefore, the electric field (F) can be obtained directly from the period of the FKO's if  $\mu_1$  is known.

The period of the FKO's is determined by the dominant field in the structure [1]. There are two limiting cases to be considered. If modulation is from flatband, i.e., no dc field then the field is clearly the ac modulating field,  $F_{ac}$ . However, a more interesting situation occurs when there exists a large dc electric field,  $F_{dc}$ , in the material and a small modulating field is applied, i.e.,  $F_{ac} \ll F_{dc}$ . In this case the period of the FKO's are given by  $F_{dc}$  and not  $F_{ac}$  [1].

The treatment of FKO's discussed above has assumed a uniform electric field. However, in many situations, such as the space-charge region (SCR) of a doped material this is not the case. It has been clearly demonstrated that for small modulation the FKO's are a measure of the maximum field in the structure [1].

## GaAs SURFACES

After many decades of intense study, the origin of the surface states GaAs is still not understood [7]. Furthermore, except for isoelectronic heterojunctions, e.g. GaAlAs/GaAs, there is no viable technology for making either MOS or MIS-like structures with low interface state densities. In the case of GaAs it is not clear there is still an interest in MOSFET devices, since modeling results show no performance improvement over Si for sub-micron gate length structures [8]. However, there is still an interest in the passivation of GaAs surfaces and the control of the electronic properties of metal/GaAs interfaces, e.g. ohmic and Schottky contacts; and, thus, an interest in understanding the electronic properties of various kinds of GaAs surfaces and interfaces.

In particular, it is desirable to have a characterization tool which could follow the evolution of the surface properties as a GaAs substrate moves from its starting properties through epitaxial growth and on through various processing stages to the finished device. Modulation spectroscopy is such a universal tool, since it is a low intensity optical probe which can operate in almost any environment, including UHV, MOCVD, air, etc.

It has long been recognized that the FKO's observed in EM had great potential for gaining information about surface/interface electric fields due to Fermi level pinning. However, in principle this has proven to be difficult [1]. Generally, one observes only a few FKO from the space-charge region of a doped semiconductor. At low doping concentrations, where  $\Gamma$  is small, the electric field may not be sufficiently large to observe FKO's. Increasing the impurity concentration to enhance the built-in field also generally makes  $\Gamma$  larger, probably due to ionized impurity scattering. As a consequence the FKO's get damped out [see Eq.(1a)] and the lineshape becomes third-derivative. Thus, FKO's are generally seen only in a limited doping range [1].

To overcome this problem a number of groups are making effective use of the FKO's detected in PR or CER from special structures which contain a large, uniform electric field to study Fermi level pinning on (a)  $n$ - and  $p$ -type GaAs (001) surfaces

[1,3,9-12] including studies of the effects of process-induced damage [3,4] and metallization [12] and (b) low temperature grown GaAs [13] and InGaAs [7] with excess As. Some of these investigations have been performed *in-situ* in an UHV chamber [3,12].

These structures are made by fabricating an undoped layer of thickness  $L$  ( $\sim 1000\text{\AA}$ ) on a buried doped  $n^+(p^+)$  buffer on a doped  $n^+(p^+)$  (001) substrate. Such configurations have been designated  $UN^+(UP^+)$ , respectively (or  $SIN^+$  and  $SIP^+$  in [9]). In the  $n^+(p^+)$  buffer/substrate the Fermi level occurs near the conduction (valence) band edge. At the surface/interface the Fermi level is pinned at some value. Therefore, there exists in the undoped region a large, almost constant electric field,  $F$ . From the large number of observed FKO's it is possible to accurately determine the built-in field and hence the built-in potential (barrier height). In such configurations the barrier height,  $V_B$ , can be related to the electric field,  $F$ , (deduced from the FKO) by [12]:

$$V_B = FL + (kT/q) + SCC \quad (2b)$$

where the second and third terms are the Debye length and space-charge layer corrections, respectively.

Because of the photovoltaic effect in these structures the measured barrier height ( $V_B$ ) is the Fermi level ( $V_F$ ) minus the photovoltage ( $V_p$ ), i.e., [12]

$$V_B(T) = V_F(T) - V_p(T) \quad (2a)$$

Plotted in Fig. 1 are the values of  $V_B(T)$  as a function of temperature for GaAs  $UN^+/UP^+$  structures in air [12]. Note that  $V_B$  saturates at about 425K for the low light levels used in this experiment and that below room temperature  $V_p(T)$  is an appreciable factor.

The results of Fig. 1 have been explained on the basis of current-transport theory assuming that the Fermi level is pinned at some value  $V_F$ , and that there is only one pinning level. In this case  $V_p(T)$  can be expressed as [12]:

$$V_p(T) = (\eta kT/q) \ln \{ [J_{pc}/rJ_0(T)] + 1 \} \quad (3a)$$

where  $\eta$  is an ideality factor,  $J_{pc}$  and  $J_0(T)$  are the photo-induced and saturation (dark) current densities, respectively. The parameter  $r$  in Eq.(3a) was introduced as a geometry factor in order to take into account the fact that only a fraction of the surface has states available for the saturation (dark) current.

Therefore,  $V_B$  is given by [12]:

$$V_B(T) = V_F - (\eta kT/q) \ln \{ [J_{pc}/rJ_0(T)] + 1 \} \quad (3b)$$

with

$$J_{pc} = qP_m \gamma (1 - R_0) / \hbar \omega \quad (3c)$$

and

$$J_0(T) = [A'' \cdot T^2 / (1 + BT^{3/2})] \exp(-qV_F/kT) \quad (3d)$$

where  $P_m$  is the light intensity,  $\gamma$  is the quantum efficiency ( $=1$ ),  $R_0$  is the reflectivity of the light at the semiconductor surface ( $=0.34$ ) and  $\hbar\omega$  is the photon energy of the light,  $A''$  is the modified Richardson constant (which is proportional to the effective mass of the carrier) and  $B$  is a constant defined in [12].

From Eqs.(3), at sufficiently high temperatures,  $V_F(T)$  becomes negligible because of the factor  $\exp[-qV_F/kT]$  and hence  $V_B$  approaches  $V_F$ . Shown by the dotted and dashed lines in Fig. 1 are least-square fits of Eqs.(3) to the experimental values of

$V_B(T)$  of the  $UN^+$  and  $UP^+$  structures, respectively. The fitting parameters were  $V_F$ ,  $\eta$  and the geometry factor  $r$ . The most sensitive parameter is  $r$  since  $V_F$  can be deduced from the high temperature data, as discussed above, and  $\eta$  is obtained from the intercept as  $T \rightarrow 0$ . This analysis yields  $V_F = 0.77 \pm 0.02V / 0.75 \pm 0.02V$ ,  $\eta = 0.93 \pm 0.05 / 0.87 \pm 0.05$  and  $r = 0.02 \pm 0.01 / 0.001 \pm 0.0006$  for the  $UN^+ / UP^+$  samples, respectively. The Fermi level pinning values add up to the band gap of GaAs, in agreement with the complementarity of the  $UN^+ / UP^+$  structures. The ideality factors are  $\approx 1$ , indicating high quality diodes.

The difference in  $r$  is not readily apparent from Fig. 1 since the curves for the  $UN^+ / UP^+$  samples are almost identical. However, it must be borne in mind that  $A''$  in  $J_0(T)$  [ see Eq.(3d)] is proportional to the effective mass, and that this ratio is  $\approx 0.2$  for electrons and heavy-holes in GaAs. This accounts for the difference in  $r$  between the two types of samples. In order to demonstrate the necessity of including the geometry factor  $r$ , displayed in Fig. 1 by the dot-dashed line is a least-squares fit of Eqs.(3) to the  $UN^+$  sample with  $r = 1$ . As can be seen the agreement between the fit and experiment is not very good. It is interesting to note that with increasing  $r$  the barrier height,  $V_B(T)$ , saturates at lower temperatures for a given  $V_F$ .

Recently Yan et al [11,14] have found additional evidence for the reduced surface state density in  $p$ -type GaAs surfaces from both *ex-situ* (in air) and *in-situ* (UHV in a MBE system) studies of  $UP^+$  structures. These results are consistent with the findings of Pashley et al [15] using *in-situ* scanning tunneling microscopy (STM). Displayed in Fig. 2 is  $V_B(T)$ , in air, for an  $UP^+$  sample using CER (no pump beam) in order to minimize any photovoltage effects. Representative error bars are shown. The overall temperature

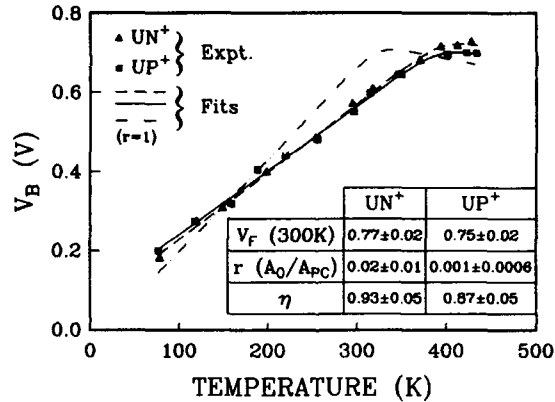


Fig. 1 measured barrier height,  $V_B(T)$ , for  $UN^+$  (triangles) and  $UP^+$  (squares) samples as a function of temperature.

behaviour cannot be explained on the basis of only one pinning level, as was done in Fig. 1. Above about 250K this curve is similar to Fig. 1. The barrier height  $V_B(T)$  increases monotonically with temperature and then saturates at about 450K. A major difference is that the saturation value of  $V_B(T)$  is only about 0.5V, instead of 0.75V for the UP<sup>+</sup> sample in Fig. 1. Thus, this pinning level, which we designate as  $V_2$ , is at least 200meV below midgap. Another important observation is that  $V_B(T)$  for the sample of Fig. 2 saturates at about the same temperature ( $\approx 425$ -450K) as the corresponding material in Fig. 1. Based on Eqs.(3) the  $r$  factor for  $V_2$  for this sample is about an order of magnitude lower than that of the prior UP<sup>+</sup> material.

Another significant difference between Figs. 1 and 2 is the low temperature behavior. For the latter sample there is a plateau of about 0.20-0.25V between 100K-250K and then  $V_B(T)$  turns over and approaches zero. The presence of this plateau indicates that there is another pinning level at about 0.2-0.25V.

We have used a modified solar cell equation for  $V_p(T)$  in order to take into account two "pinning levels" [14,16]:

$$V_p(T) = (kT/q) \ln \left\{ \frac{P_m(1-R_0)/\hbar\omega}{[A \cdot T^2 / (1 + BT^{3/2})] \sum_{i=1}^2 r_i (1-F_i) \exp(-qV_i/\eta_i kT)} + 1 \right\} \quad (4)$$

where  $\eta_i$  is the ideality factor of the  $i^{\text{th}}$  level. The factor  $(1-F_i)$  takes into account that when a certain level, particularly  $i=1$ , is full it no longer contributes to  $V_p$ . The important fitting parameters are  $\eta_i$ ,  $r_i$  and  $V_i$ , the positions of the two "pinning" levels.

However, there is another boundary condition. There must be the right amount of charge on the surface of our "parallel plate capacitor" UP<sup>+</sup> (or UN<sup>+</sup>) structure to produce the measured field, i.e.,  $V_B$ . This charge/area also determines the Fermi level,  $V_F$ . Thus we also have the following relations:

$$V_B(T) = Q(T)/C, \quad Q(T) = qN_0 \sum_{i=1}^2 r_i F_i(T), \quad C \approx \epsilon \kappa_0 / L, \quad (5a)$$

where  $\epsilon (= 12)$  is the dielectric constant of GaAs,  $\kappa_0$  is the permittivity of free space and  $L$  is the thickness of the undoped layer,  $N_0$  is the density of atoms on the surface

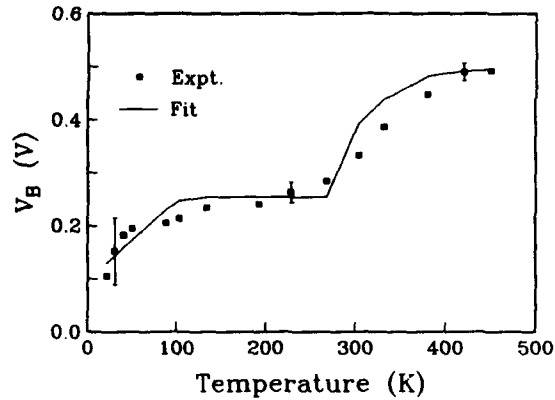


Fig. 2 Measured barrier height,  $V_B(T)$ , of an UP<sup>+</sup> sample as a function of temperature.

$$F_i(T) = \int_{-\infty}^{\infty} \{ \exp[(E' - V_i)^2 / 2\sigma_i^2] / (2\pi)^{1/2} \sigma_i \} \{ \exp[(E' - V_i) / kT] + 1 \}^{-1} dE' \quad (5b)$$

$L$  is the thickness of the undoped layer,  $N_0$  is the density of atoms on the surface ( $6.3 \times 10^{14} \text{ cm}^{-2}$ ),  $n_i$  is the number of charges that can be put on each site  $r_i$  and  $\sigma_i = 10 \text{ meV}$  for both levels.

Therefore, we have the additional constraint that:

$$V_B(T) = (qN_0L/\epsilon\epsilon_0) \sum_{i=1}^2 n_i r_i F_i(T) \quad (6)$$

Shown by the solid line in Fig. 2 is a least-squares fit of the data to Eqs. (4) and (6). The obtained values of the relevant parameters are  $\eta_1 = 1.75$ ,  $V_1 = 0.25 \text{ V}$ ,  $r_1 = 4 \times 10^{-4}$ ,  $n_1 = 1$ ,  $\eta_2 = 0.88$ ,  $V_2 = 0.5 \text{ V}$ ,  $r_2 = 4 \times 10^{-4}$  and  $n_2 = 1$ . Thus there are two pinning levels at 0.25 V and 0.5 V above the valence band. The  $r$  factors for both these levels are about two(one) orders of magnitude lower than the  $n(p)$ -type material of Fig. 1.

Yan et al [11,14] also have examined an as-grown  $\text{UP}^+$  GaAs (001) structure at 300K using PR *in-situ* in a MBE chamber before removal to air. In this case also a reduced surface state density is observed. They find  $V_B(300) \approx 0.36 \text{ V}$ , in good agreement with the data of Fig. 2 but considerable lower than the  $\text{UP}^+$  sample in Fig. 1. After the deposition of a few monolayers of As it is found that  $V_B(300)$  increases to about 0.6 V, similar to Fig. 1.

There are at least two possible reasons which could account for the lower surface-state densities observed for  $\text{UP}^+$  structures compared with  $\text{UN}^+$  structures. One explanation may be related to a recent STM result by Pashley et al [15] to characterize the electronic properties of MBE grown GaAs (001) surfaces with  $(2 \times 4)/c(2 \times 8)$  reconstructions. For  $n$ -type samples the surface forms the exact density of acceptor-like kink sites needed to pin the surface Fermi level mid-gap by compensating the donors forming the space charge region, i.e. the kink-site density increases with increasing  $n$  doping. This suggests that the MBE growth of  $n$ -type GaAs will inherently result in surface Fermi level pinning. This is consistent with our modulation experiments on  $\text{UN}^+$  structures, i.e. they always exhibit pinning. For  $p$ -type samples the kinks do not form donor sites, hence there is no driving force to form kinks since they will not assist mid-gap pinning for high doping levels. Hence, the as-grown highly doped  $p$ -type samples showed a surface Fermi level near the valance band edge, i.e. not mid-gap Fermi level pinning. This behavior could account for the observations of the present study since our samples also had (001) surfaces grown by MBE. However, this can only be part of the explanation, since the Pashley et al [15] results were obtained in UHV on pristine surfaces while our surfaces had been air exposed. Therefore, in addition to the above argument we must account for the stability in air of our low surface-state density  $\text{UP}^+$  structures.

We suggest that this stability is due to photoelectrochemical properties of  $p$ -type surface of GaAs. It is well known that many  $n$ -type compound semiconductor surfaces

including GaP surfaces, are unstable against greater than band gap energy photon illumination in aqueous solutions while *p*-type GaAs [17] and GaP [18] surfaces are stable under these conditions. The obvious photoelectrochemical difference between *n*- and *p*-type surfaces is the minority carrier type which under illumination crosses the semiconductor/electrolyte interface. It is well known that the resulting surface chemistries for *n*-type surfaces tend to be a mixture of anionic and cationic oxides and elemental anion. The minority hole current results in either photo-etching or photo-oxidation, depending on the pH of the solution. It is reasonable to conclude from the stability of *p*-type photochemical electrodes that the electron minority carrier current into the solution results in surface passivation. If so, this would account for the air stability of our *u-p* structures. We plan to confirm this in future studies by STM characterization of these surfaces.

One of the important findings of this study was the qualitative change in the nature of the surface defects as the concentration of the defects was reduced by improved MBE growth of UP<sup>+</sup> structures over those reported in the past [3,12]. Previously we had found mid-gap pinning for both air exposed and metallized UN<sup>+</sup> and UP<sup>+</sup> structures, i.e.,  $|E_{\text{band edge}} - E_{\text{F-surface}}| \sim 0.75 \text{ eV}$  [12]. This pinning has been correlated with the presence of elemental arsenic which exists at equilibrium at the interface of GaAs and its native oxide, i.e. Ga<sub>2</sub>O<sub>3</sub> and As<sub>2</sub>O<sub>3</sub>. There is some controversy as to the fundamental relation of the As with the pinning energy or pinning states. It could be argued either that the presence of As would correlate to surface native defects [19] in the GaAs which would pin the Fermi level at their respective defect levels; or the presence of As would pin the Fermi level via its work function. The As work function would fix the Fermi level at exactly mid gap whereas the native defects would be expected to pin near mid gap at slightly different energies, separated by about 0.2 eV, depending on the conductivity type, nearer the conduction band edge for *n*-type and nearer the valence band for *p*-type. However, for "pinning" to occur requires a sufficient density of states of the pinning sites, about 10<sup>13</sup> cm<sup>-2</sup>, for previous mid-gap pinned structures.

It is interesting to note that in the study of UP<sup>+</sup> samples the 0.7 eV pinning site has been greatly reduced. What is uncovered then are two new pinning levels at 0.5 and 0.25 eV above the valence band whose density is about 2.5×10<sup>11</sup> cm<sup>-2</sup>. This density is sufficient to measure in our experiment but is insufficient to firmly pin the Fermi level, i.e. dominate Schottky barrier formation at metal/GaAs interfaces. We conclude therefore that these new levels are most likely related to surface native defects and, while present at small concentration, are not a factor in the mid-gap pinning at metal/GaAs interfaces. Rather these results add support to the model which suggests that mid-gap pinning at metal/GaAs interfaces is directly correlated with As acting via its work function.

#### EFFECTS OF Ar<sup>+</sup> SPUTTERING AND ANNEALING

Shown in Fig. 3 are the effects of Ar<sup>+</sup> sputtering, thermal annealing and air exposure on V<sub>B</sub> at 300K for both UN<sup>+</sup>[V<sub>B</sub>(*n*)] and UP<sup>+</sup>[V<sub>B</sub>(*p*)] GaAs (001) configurations [3]. The sputtering/thermal annealing studies were carried out *in-situ* in an UHV chamber. Also displayed is the sum V<sub>B</sub>(*n*)+V<sub>B</sub>(*p*) and E<sub>g</sub>, the band gap of GaAs (1.42 eV). Initially, on the undamaged surfaces the barrier heights V<sub>B</sub>(*n*) ≈ V<sub>B</sub>(*p*) are at about

midgap. The quantity  $V_B(n) + V_B(p)$  is only about 0.15 eV below  $E_g$ . This small difference is probably due to the photovoltage effect,  $V_p$ .

With increased sputtering time  $V_B(n)$  decreases while  $V_B(p)$  increases although the sum  $V_B(n) + V_B(p)$  remains approximately constant. After 40 minutes of sputtering no PR signal could be obtained from the  $UN^+$  sample which indicates that the built-in field and hence  $V_B$  ( $< 0.1$  V) was too small to observe. Therefore,  $V_B(p)$  has a value approximately that of  $V_B(n) + V_B(p)$  for the previous conditions. These observations indicate that the major movement in  $V_B$  is due to changes in  $V_F$ , not to differences in  $V_p$ . After 40 min of sputtering  $V_F$  had been moved from midgap to near the conduction band edge for both materials.

Thermal annealing at 350°C for 30 min in UHV reversed the movement of  $V_B$  and hence  $V_F$ . The parameter  $V_B(n)$  went back to its original midgap value while  $V_B(p)$  decreased but did not return to its original value. About 3 days after the samples were removed from the UHV environment  $V_B(p)$  went back to approximately its original midgap value while  $V_B(n)$  remained unchanged, the final position being characteristic of GaAs with native oxides.

It is important to note that if only  $n$ -type material had been investigated the interpretation of the changes in  $V_B(n)$  would have been ambiguous, e.g., was the decrease due to the unpinning of the surface or pinning at a position closer to the conduction band.

## HETEROJUNCTION BIPOLAR TRANSISTOR STRUCTURES

Photoreflectance has been used to characterize the built-in fields and associated doping levels as well as alloy composition in GaAlAs/GaAs [20-22], InGaAs/InP [23], InGaP/GaAs [24], InAlAs/InGaAs [25] and InGaAs/GaAs [26] heterojunction bipolar transistor structures (HBTs). The PR characterization of GaAs/GaAlAs HBTs is of particular significance since certain features in the spectra of samples before fabrication have been correlated with actual device performance after fabrication. No other non-destructive means of experimentally determining the electric fields in HBT structures is currently available. Thus PR has been shown to be an effective contactless and non-destructive means of screening wafers before they are made into actual devices. The work of [20,21] was actually performed on wafer-sized samples.

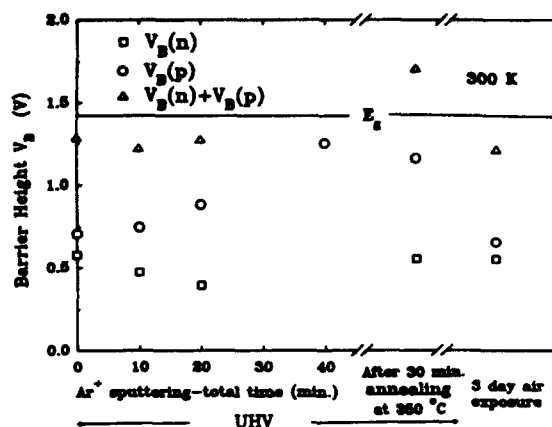


Fig. 3 Measured barrier height,  $V_B(T)$ , of  $UN^+$  (squares) and  $UP^+$  (circles) as a function of  $Ar^+$  sputtering time, thermal annealing and air exposure.



These HBT structures, fabricated by MBE or OMCVD, exhibited FKOs associated with the built-in electric fields in the  $n$ -GaAs collector region and the wide gap  $\text{Ga}_{1-x}\text{Al}_x\text{As}$  emitter portion. These measurements have made it possible to evaluate the built-in fields as well as the Al composition. The values of these fields are in good agreement with those deduced from computer generated models of the device structure. The most significant aspect of these studies was the correlation of the fields from the GaAlAs FKOs and the dc current gains in fabricated HBTs [20,21].

Photoreflectance at 300K also has been used to study an  $\text{InP}/\text{In}_{1-x}\text{Ga}_x\text{As}$  HBT structure with a carbon-doped base grown by gas source MBE (GSMBE) [23]. From the FKOs associated with both the InGaAs and InP signals it was possible to determine  $F_{dc}$  in the  $n$ -InGaAs collector (30 kV/cm) and  $n$ -InP emitter (100 kV/cm) regions. These field values were compared with numerical simulations based upon the intended structure. The PR data indicated a significantly lower donor concentration in both the collector and emitter regions. These PR results were subsequently confirmed by (destructive) capacitance-voltage (C-V) and secondary ion mass spectroscopy (SIMS) determinations of the  $n$ -doping levels.

The HBT structure used in the experiment was fabricated on a (001) semi-insulating InP:Fe substrate. The sample consisted of a  $n^+(1 \times 10^{19} \text{ cm}^{-3})$  4000Å InGaAs subcollector, a  $n^-(2 \times 10^{16} \text{ cm}^{-3})$  4000Å InGaAs collector, a  $p^+(5 \times 10^{19} \text{ cm}^{-3})$  nominal concentration of carbon atoms 600Å InGaAs base, a  $n(5 \times 10^{17} \text{ cm}^{-3})$  800Å InP emitter, a  $n(2 \times 10^{18} \text{ cm}^{-3})$  500Å InP emitter and a  $n^+(1 \times 10^{19} \text{ cm}^{-3})$  300Å InGaAs cap layer. The  $n$ - and  $p$ -dopants were Si and C, respectively.

Displayed in Fig. 4 is the PR trace of the sample at 300K. The feature around 0.75 eV corresponds to the band gap of InGaAs while the structure around 1.35 eV is related to the InP. Both features exhibit well pronounced FKOs. From a plot of  $(4/3\pi)(E_n - E_g)^{3/2}$  as a function of index  $n$  it was possible to evaluate  $\hbar\theta$  (and hence  $F_{dc}$ ) as well as  $E_g$ . The obtained values of the band gaps for the InGaAs (0.737 eV) and InP (1.35 eV) are indicated by arrows at the bottom of Fig. 7. This value of the gap for the InGaAs is in good agreement with that for InGaAs/InP and confirms the lattice-matched nature of the system.

It was found that  $F_{dc}$  in the InGaAs collector and InP emitter regions are  $(30 \pm 2)$  kV/cm and  $(100 \pm 5)$  kV/cm, respectively. The authors also have performed a numerical calculation of the potential distribution for the HBT structure with the doping profile

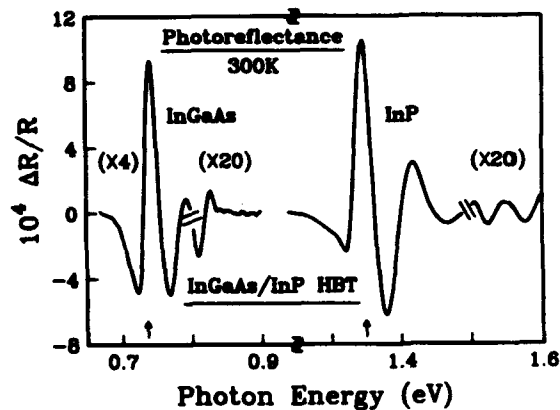


Fig. 4 Photoreflectance spectrum of an InGaAs/InP HBT structure at 300K.

shown in Fig. 4. This procedure yielded 63 kV/cm and 385 kV/cm for the peak fields in the InGaAs collector and InP emitter sections, respectively. These values are considerably larger than those deduced from the PR data, suggesting that donor concentrations in the structure fell short of their target values. The calculation and data can be brought into agreement by assuming  $n=4.5 \times 10^{15} \text{ cm}^{-3}$  and  $3.5 \times 10^{16} \text{ cm}^{-3}$  in the collector and emitter #1 sections, respectively, as indicated by the numbers in parentheses.

In order to verify these results, C-V and SIMS measurements of the doping profiles were performed. Both studies revealed Si-doping levels that were substantially lower than indicated by the growth conditions and in better agreement with the PR results. These differences were attributed to a defective heating filament in the Si source which was confirmed by visual inspection through the GSMBE viewport after material growth.

## SUMMARY

This paper has reviewed the use of contactless EM methods, such as PR and CER, as diagnostic tools for a number of semiconductor processing procedures including characterization of (a) the electronic properties of compound semiconductor surfaces exposed to different growth and post-growth conditions (b) the properties critical to device performance. For example, using PR and CER it has been found that there is a lower density of surface hole traps than electron traps in certain as-grown MBE (001) GaAs samples and that this condition persists even after air exposure. This behaviour is in contrast to other samples, including both bulk and MBE grown (001) surfaces in which the Fermi level is pinned mid-gap for both *n*- and *p*-type structures. We also have observed that  $\text{Ar}^+$  bombardment under UHV conditions results in Fermi level pinning close to the conduction band edge and that thermal annealing restores mid-gap pinning. Finally, using PR we are able to evaluate the electric fields and associated doping levels in the emitter and collector regions of heterojunction bipolar transistor structures (fabricated from III-V materials), thus demonstrating the ability to perform in-process evaluation of important device parameters.

## REFERENCES

1. F.H. Pollak and H. Shen, Materials Science and Engineering R:Reports, **R10** (1993) 275.
2. O. J. Glembocki and B. V. Shanabrook, Semiconductors and Semimetals, Vol. 67, ed. D.G. Seiler and C.L. Littler (Academic, New York, 1992) p. 222.
3. X. Yin, H-M. Chen, F. H. Pollak, Y. Cao, P. A. Montano, P. D. Kirchner, G. D. Pettit and J. M. Woodall, J. Vac. Sci. Technol., **B9**, 2114 (1991).
4. O. J. Glembocki, J.A. Dagata, E.S. Snow and D.S. Katzer, Appl. Surf. Sci., **63**, 143 (1993).
5. F.H. Pollak, H. Qiang, D. Yan, Y. Yin, and V.Y. Boccio, Photonics Spectra Magazine, Vol. 27, Issue 8, August 1993, p. 78.
6. D.E. Aspnes, Phys. Rev., **B10**, 4228 (1974).

7. J.M. Woodall, P.D. Kirchner, J.L. Freeouf, D.T. McInturff, M.R. Melloch and F.H. Pollak, *Phil. Trans. R. Soc. Lond.* **344**, 521 (1993).
8. M. V. Fischetti and S. E. Laux, *IEEE Trans. Electron Devices* **38**, 650 (1991).
9. H. Shen, M. Dutta, L. Fotiadis, P. G. Newman, R. P. Moerkirk, W. H. Chang and R. N. Sacks, *Appl. Phys. Lett.*, **57**, 2118 (1990).
10. X. Yin, H.-M. Chen, F. H. Pollak, Y. Chan, P. A. Montano, P. D. Kirchner, G. D. Pettit and J. M. Woodall, *Appl. Phys. Lett.*, **58**, 260 (1991).
11. F.H. Pollak, *J. Vac. Sci. Technol.*, **B11**, 1710 (1993).
12. X. Yin, H.-M. Chen, F. H. Pollak, Y. Cao, P. A. Montano, P. D. Kirchner, G. D. Pettit and J. M. Woodall, *J. Vac. Sci. Technol.*, **A10**, 131 (1992).
13. A. C. Warren, J. M. Woodall, P. D. Kirchner, X. Yin, F. Pollak, M. R. Melloch, N. Otsuka, and K. Mahalingam, *Phys. Rev.*, **B46**, 4617 (1992); H. Shen, F. C. Rong, R. Lux, J. Pamulapati, M. Dutta, M. Taysing-Lara, E. H. Poindexter, L. Calderon, and Y. Lu, *Appl. Phys. Lett.*, **61**, 1585 (1992); D. C. Look, D. C., J. E. Hoelscher, J. T. Grant, C. E. Stutz, K. R. Evans, and M. Numan, *Mat. Res. Soc. Symp. Proc.*, **241**, 87 (1991).
14. D. Yan, E. Look, X. Yin, F.H. Pollak, G.D. Pettit and J.M. Woodall, submitted to *Appl. Phys. Lett.*
15. M.D. Pashley, K.W. Haberern, R.M. Feenstra and P.D. Kirchner, *Phys. Rev.* **B48**, 4612 (1993).
16. H. Tsubomura and H. Kobayashi, *Critical Reviews in Solid State and Materials Science*, **18**, 261 (1993).
17. F.W. Ostermayer and P.A. Kohl, *Appl. Phys. Lett.*, **39**, 76 (1981).
18. M. Tomkiewicz and J.M. Woodall, *J. Electrochem. Soc.* **124**, 1436 (1977).
19. W. E. Spicer, I. Lindau, T. Skeath and C.Y. Su, *J. Vac. Sci. Technol.* **17**, 1019 (1980).
20. X. Yin, F. H. Pollak, L. Pawlowicz, T. J. O'Neill and M. Hafizi, *Appl. Phys. Lett.* **56**, 1278 (1990).
21. X. Yin, F. H. Pollak, L. Pawlowicz, T. J. O'Neill and M. Hafizi, *Proc. Soc. Photo-Optical Instrum. Engineers* (SPIE, Bellingham, 1990) **1286**, 404 (1990).
22. N. Bottka, D. K. Gaskill, P. D. Wright, R. W. Kaliski and D. A. Williams, *J. Cryst. Growth* **107**, 893 (1991).
23. D. Yan, F.H. Pollak, V.T. Boccio, C.L. Lin, P.D. Kirchner, J. M. Woodall, R.C. Gee and P.M. Asbeck, *Appl. Phys. Lett.* **61**, 2066 (1992).
24. L.W. Yang, P.A. Martin, J.S. Mazurowski, J.M. Ballingall, Y. Yin, D. Yan, F.H. Pollak, W. West, D.B. Davito and P.D. Kirchner, presented at the 1993 Electronic Materials Conference, Santa Barbara, June 1993 and submitted to *J. Electron. Mat.*
25. K.T. Hsu, Y.H. Chen, K.L. Chen, H.P. Chen, H.H. Lin and G.J. Jan, submitted to *Appl. Phys. Lett.*
26. A. Badakhshan, C. Durbin, A. Giordona, R. Glosser, S. A. Lambert and J. Liu, *Nanostructure Physics and Fabrication*, eds. M. A. Reed and W. P. Kirk (Academic, New York, 1989) pp. 485-493.

## PHOTOREFLECTANCE CHARACTERIZATION OF ETCH-INDUCED DAMAGE IN DRY ETCHED GaAs

O.J. GLEBOCKI\*, J.A. TUCHMAN\*, K.K. KO\*\*, S.W. PANG\*\*, A. GIORDANA\* AND C.E. STUTZ\*\*\*

\*Naval Research Laboratory, Code 6864, Washington, DC 20375

\*\*The University of Michigan, Electrical Engineering Department, Ann Arbor, MI 48109

\*\*\*Wright Patterson Laboratories, Dayton, OH

### ABSTRACT

Photoreflectance has been used to characterize the etch-induced damage in GaAs processed in an Ar/Cl<sub>2</sub> plasma generated by an electron-cyclotron resonance (ECR) source. We show that the damage is localized to the surface and that it is most influenced by the RF power, with little effect from the microwave power. The Fermi-level is observed to be unchanged in n-GaAs and remains near midgap, while for p-GaAs, the Fermi level shifts from near the valence band to midgap. Etch-induced anisite defects are proposed as a possible source of the damage.

### INTRODUCTION

The decreased dimensions and increased complexity of semiconductor device structures has produced a need for better control over materials growth and processing. While fine control in epitaxial growth has existed for many years, etching of semiconductors can potentially cause defect formation. For most applications, the epitaxial growth of materials involves layer by layer processes, in which chemical reactions can occur between a substrate and a gas or molecular beam. Because the energies of the gases or molecular beams are thermal, the growth process produces pristine material. In dry etching, anisotropic material removal is almost always desired. This is accomplished by the balance between the chemical component and the physical sputtering component during etching. Typically chemical etching is isotropic and thus limits the lateral dimensions. Anisotropy is attained through the use of energetic and directional ions. A side benefit that is often attained from the combination of a reactive gas with an ion beam is an enhancement of etch rates beyond those of the chemical or sputtering processes. Because of this, etching techniques such as reactive ion etching (RIE), chemically assisted ion beam etching (CAIBE) and plasma etching with an electron cyclotron resonance (ECR) source have replaced liquid etching in many areas of device fabrication.

Since most dry etching processes involve energetic ions, they produce an undesirable side effect in the form of etch induced electronic damage. In semiconductors, damage levels as low as 1 part in 10<sup>6</sup> can render a device inoperable. Because of this, it is desirable to use low energy ions. In CAIBE and RIE, ion energies are typically well above 100 eV. Lowering ion energies to reduce damage, however, also reduces the etch rate, which is undesirable. With an ECR source ion energies below 50 eV are possible. In addition, ion fluxes and energies can be controlled separately and it is possible to have high etch rates with low ion energies. Therefore, an ECR source offers possibilities for control of etch damage without significant loss of throughput.

In this work, we have studied changes in the electronic properties of GaAs, induced by etching with a  $\text{Cl}_2/\text{Ar}$  plasma generated by an ECR source. The contactless optical spectroscopy of photoreflectance (PR) was used as a probe of subsurface etch damage and of the Fermi-level pinning position at the surfaces of etched GaAs. In order to accomplish this, we have used specially grown MBE GaAs samples that were optimized for surface electric field studies. These samples are undoped GaAs grown on  $n^+$ - or  $p^+$ -GaAs. This configuration forms a capacitor with the undoped GaAs forming the dielectric while the doped substrate and the charge in surface states form the capacitor plates. In this way, by knowing the layer thickness, we can have a sensitive monitor of the surface potential. Our studies show that in unetched samples the surface Fermi level pinning position for electrons is different from that of holes. This result is expected from previous work. Etching is shown to dramatically change the Fermi-level position for holes, from near the valence band to near mid-gap while for electrons little effect is observed. These results suggest that defects are responsible for changes in the Fermi-level pinning position. The most important parameter that influences damage is shown to be RF power, while little effect is observed from changes in the microwave power. We also show that little subsurface damage is observed in the photoreflectance measurements.

## EXPERIMENTAL DETAILS

In order to probe the electrical properties of the etched surface, we used specifically designed, undoped epitaxial GaAs layers that have constant built-in electric fields and low lifetime broadening for optical transitions. These conditions lead to many Franz-Keldysh oscillations in the photoreflectance spectrum thereby allowing us to accurately determine the built-in field.[1] Similar types of structures were recently employed by Yin et al.[2,3] and Glembocki et al.[4] for use in studies of GaAs surfaces and their modification by sputtering or chemically assisted ion beam etching. These structures consist of a 1500 Å thick undoped GaAs layer grown on either an  $n^+$  or  $p^+$  buffer layer and henceforth will be referred to as UN or UP, depending on the type of doping in the buffer layer. The sample configuration is similar to a capacitor with the undoped region serving as the dielectric. For example, in the case of UN samples, the Fermi-level pins at mid-gap at the surface, while in the heavily doped region the Fermi level is in the conduction band. Such a configuration produces a constant electric field ( $\sim 50$  kV/cm) in the undoped layer.

The photoreflectance apparatus used in this study is similar to those previously described in the literature.[5] The probe light consisted of a monochromatic beam created by passing white light from a 100 W quartz halogen lamp through a SPEX 1/4 m monochromator. The PR pump beam was either a 0.25 mW green (5430 Å) or 1 mW red (6328 Å) HeNe laser mechanically chopped at 400 Hz. The monochromatic, reflected light was detected with a Si photodiode and analyzed by a lock-in amplifier. The pump laser power density was approximately  $50 \times 10^{-6}$  W/cm<sup>2</sup>, while probe beam had a power density of  $1 \times 10^{-6}$  W/cm<sup>2</sup>. The sample temperature was varied in the range of 77 K to 500 K through the use of a Janis liquid He dewar and resistive heating as appropriate.

The samples used in this study were etched in a plasma generated by an ECR source on top of a RF-powered electrode. The ECR source used is a multipolar plasma disk source surrounded by twelve permanent magnets, and is driven at 2.45 GHz. The ECR cavity is tunable with a sliding short and a microwave input probe. The ion energy can be independently controlled by the 13.56 MHz RF power supply. The distance between the sample stage and the ECR source

is adjustable between 7 and 27 cm. In this study,  $\text{Cl}_2$  gas was introduced into the etch chamber through a gas ring situated 1 cm below the wafer stage, while Ar gas was introduced radially through the base of the ECR source.

The samples to be etched were introduced into the etch chamber through a load-lock. Before transferring the samples into the etch chamber, the load-lock was pumped to a base pressure of  $2 \times 10^{-5}$  Torr by a turbomolecular pump. The etch chamber is pumped by a 1500 l/s turbomolecular pump backed by a roots blower package. Before etching was started, the chamber was pumped to a base pressure of  $5 \times 10^{-6}$  Torr.

Two aspects of etching with an ECR source were probed in this study: the effects of ion flux and ion energy. In studying the effects of ion flux on surface damage, the samples were etched at different microwave powers, but with a fixed self-induced dc bias,  $|V_{dc}|$ , of 100 V. A  $\text{Cl}_2/\text{Ar}$  chemistry of 20%  $\text{Cl}_2$  at 0.5 mTorr and a 12 cm source to sample distance was used in etching these samples. In order to maintain a constant  $|V_{dc}|$  the RF power was increased from 31-47 W as the microwave power was increased from 0-500 W. In all cases, the etch depth was kept constant at  $\sim 350$  Å. The effects of ion energy on surface damage were investigated by changing the RF power. The sample to source distance was 15 cm and the  $\text{Cl}_2/\text{Ar}$  mixture contained 30%  $\text{Cl}_2$  at a pressure of 0.6 mTorr and a microwave power of 50 W. Increases in RF power from 20-300 W resulted in increases in  $|V_{dc}|$  from 77-484 V.

Both the UN and UP samples were etched simultaneously for each condition and all sample sizes were approximately  $1 \text{ cm}^2$ . In order to ascertain the effects of etching on the samples, PR spectra were taken before and after the etch on each of the samples. In the control samples, we found variations in surface electric fields of less than 5% for both types of samples, UN and UP.

## THEORETICAL CONSIDERATIONS

Photoreflectance spectroscopy measures the built-in electric field in a semiconductor in the following way: a constant applied electric field modifies the band edge of a semiconductor in a manner predictable by Franz-Keldysh theory. For the case of Lorentzian broadening and ignoring excitonic effects, the PR line shape is represented by Airy functions, which, for photon energies greater than the band gap can be asymptotically written as:[6]

$$\frac{\Delta R}{R} \sim C V_p \cos \left[ \frac{4}{3} \left( \frac{E - E_g}{\hbar \theta} \right)^{3/2} + \phi \right] \exp \left[ - \frac{\Gamma (E - E_g)^{1/2}}{(\hbar \theta)^{3/2}} \right] \quad (1)$$

where  $C$  is a constant,  $V_p$  is the modulation (AC) voltage in the region of the electric field,  $E$  is the photon energy,  $E_g$  is the energy gap,  $\Gamma$  is lifetime broadening and  $\hbar \theta$  is the electro-optic energy. In photoreflectance, the modulation voltage,  $V_p$  is just the photovoltage induced by the pump laser. The quantity,  $\hbar \theta$  is related to the electric field,  $F$ , and the reduced interband effective mass along the direction of the electric field,  $\mu_{||}$  [ $= (\mu_e^{-1} + \mu_h^{-1})^{-1}$ ], through  $\hbar \theta = (e^2 F^2 \hbar^2 / 2 \mu_{||})^{1/3}$ . It is important to note that Eq. (1) is valid only if  $E - E_g \gg \hbar \theta$ . It is clear that Eq. (1) exhibits a periodic behavior and that the built-in electric field can be determined from the period of the FKO's using the following relationship:

$$n\pi = \frac{4}{3} \left[ \frac{(E_n - E_g)}{A_0} \right]^2 + \phi. \quad (2)$$

where  $E_n$  is the energy of the  $n$ th maxima.

Although Eq. (2) can be used to determine the field, care must be taken in photoreflectance of UN/UP structures. Yin et al. [1,2] have shown that in these structures, the photovoltage can be significant and give the following expression for the true barrier height, including the photovoltaic effect:

$$V_b = V_F(T) - \frac{\eta kT}{q} \ln \left[ \frac{A_{pc} J_{pc}}{A_0 J_0(T)} + 1 \right] + V_d \quad (3)$$

where  $V_F(T)$  is the temperature dependent Fermi level,  $\eta$  is the quantum efficiency parameter,  $J_{pc}$  is the photocurrent density and  $J_0$  is the saturation current. In Eq. (3),  $A_0$  is the area containing surface states, while  $A_{pc}$  is the illuminated area. The term,  $V_d$  is a correction due to band filling and depletion layer effects. In Eq. (3),  $J_0(T)$  is the saturation current and is given by:

$$J_0(T) = \frac{A^* T^2}{(1 + BT^{3/2})} \exp \left( \frac{-qV_F(T)}{kT} \right) \quad (4)$$

where for n-GaAs,  $A^* = 8.0 \text{ A/cm}^2 \text{ K}^2$  and  $B = 3.3 \times 10^{-4} \text{ K}^{-3/2}$  and for p-GaAs  $A^* = 54.0 \text{ A/cm}^2 \text{ K}^2$  and  $B = 4.9 \times 10^{-5} \text{ K}^{-3/2}$ .

## RESULTS

Shown in Fig. 1 are four room temperature photoreflectance spectra for an UN (1a) and an UP (1b) structure before and after etching with an ECR source. The etch conditions consisted of a  $\text{Cl}_2/\text{Ar}$  plasma excited by a microwave power of 50 W and an RF power of 300 W. This circumstance results in the most energetic ions used in the study and thus should produce the most noticeable damage.

In all of the spectra of Fig. 1., the band gap of GaAs occurs at 1.424 eV. Above the band edge there are a large number of Franz Keldysh oscillations which are a direct result of the constant electric field in the undoped layer. From the data in Fig. 1, several things are apparent. First, we note that for the unetched samples, the period of the FKO's for the UN structure is greater than the period for the UP sample, indicating that the surface field for the n-type material is larger than for the p-type. We further note that etching produces spectra with larger periods, which indicates an increase in the surface field. This increase can be a result of two effects, the

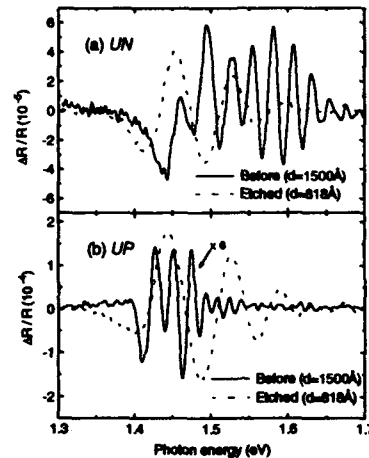


Figure 1. Photoreflectance spectra for the control (solid) and etched (dotted) (a) UN and (b) UP structures. The undoped layer thickness is  $d$ .

reduced thickness of the undoped region and possibly an increase in the surface potential. Interestingly, in the case of the etched samples, the periods of the UN and UP structures appear to be very similar. We can see this better by using the energetic positions of the maxima in Fig. 1 and fitting them to Eq. (2). Figure 2 shows a plot of the data and fits to Eq. (2) for the UN and the UP samples. Since the slope of the lines in Fig. 2 is directly related to the surface electric fields, we can easily see that the surface potential before etching was different for the UN and UP samples, but after etching it is nearly the same.

In order to obtain a better value for the surface pinning position, the photovoltaic effects must be reduced. It is clear from Eqs. (3) and (5) that the photovoltaic contribution to the barrier height saturates at high temperatures and in previous work, it was demonstrated that the saturation usually occurs near 400 K.[1,2] Under these conditions, Eq. (3) will yield the true Fermi level pinning position. Shown in Fig. 3 are the Fermi positions for the UN and UP samples as a function of the self induced bias,  $|V_{dc}|$  (RF power). This data was taken with a sample temperature of 400 K, thereby reducing the photovoltaic effect. The Fermi-level positions of the unetched samples agree well with previously reported data for (100) GaAs. We clearly see that the Fermi level position of the UN samples is hardly affected by changes in  $|V_{dc}|$  (ion energies), whereas the Fermi level position of the UP sample moves away from the valence band and stabilizes near midgap. This behavior will be discussed later in terms of the nature of the surface states in GaAs.

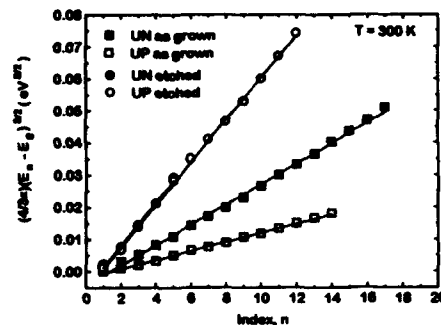


Figure 2. Fits (lines) of the energetic positions of the FK0 maxima (symbols) to Eq. (2). The slope of the straight line is related to surface electric field.

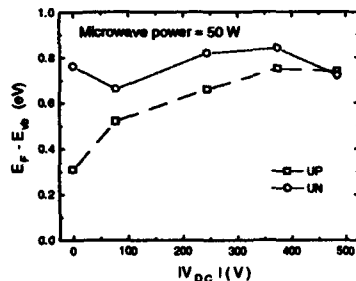


Figure 3. The Fermi level pinning position as a function of self-induced DC bias. All energies are relative to the top of the valence band (vb).

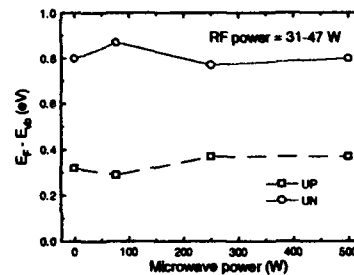


Figure 4. The Fermi level pinning position as a function of microwave power. All energies are relative to the top of the valence band (vb).

The data for variations in the Fermi level pinning position as a function of ion flux (microwave power) is shown in Fig. 4. In this case, the samples were etched with a fixed  $|V_{dc}|$  of 100 V. At this voltage, little surface damage was expected. Increasing the microwave power produces no change in UN pinning position, and a very weak if any motion of the UP pinning



position toward midgap. Clearly for low  $|V_{dc}|$ , the Fermi-level pinning is virtually independent of the ion flux. Because we have not performed the same experiment at other  $|V_{dc}|$ , it is not possible for us to generalize this result to high RF powers.

## DISCUSSION

The results of our work have both fundamental and technological implications. From a fundamental point of view, the shift of the Fermi level positions during etching of GaAs in a  $Ar/Cl_2$  plasma generated by an ECR source reflects directly on the nature of the etched surface. The important result that we have obtained is the fact that because of the etch, the Fermi-level of the UP samples shifts toward midgap, while the Fermi level of the UN materials does not shift. This eliminates certain models for the nature of the GaAs/oxide interface as modified by etching. Because  $Cl_2$  is used in the gas mixture, one might speculate that it is the cause of the shift of the Fermi-level. Studies of the adsorption of  $Cl_2$  on (110) GaAs surfaces show that due to the electronegativity of  $Cl_2$ , the Fermi level of n-GaAs is expected to shift to within 0.1-0.2 eV of the valence band.[7] Higher  $Cl_2$  coverage pinned both types at 0.55 eV above the valence band.[7] Our results show no shift at all in n-GaAs and only shifts in the UP structures, but toward midgap. This clearly is inconsistent with any  $Cl_2$  induced interface states at the GaAs/oxide interface. On the other hand, the adsorption of oxygen on (110) GaAs leads to different pinning positions in n-GaAs and p-GaAs.[8] These Fermi level positions, however, are very similar to those of the unetched surfaces.

Based on the discussion above, we believe that the etch induced surface states are not related to the presence of chemical species, such as oxygen or chlorine on the surfaces of the etched materials. Another possibility is in advanced unified defect model of Spicer et al.[9] They propose that antisite defects such as  $As_{Ga}$  and  $Ga_{As}$  will result in double donor or double acceptor type surface states. The  $Ga_{As}$  defect states lie close to the valence band and would tend to pin p-GaAs, while the  $As_{Ga}$  defect states are near midgap and would heavily pin n-GaAs. Spicer et al. argue that changes in the As/Ga ratio at the surface would shift the Fermi level toward the conduction band minimum if the ratio increased and toward the valence band maximum if it decreased. A recent PR study of  $P_2S_5$  passivation of (100) GaAs, found that the Fermi level in the UP materials shifted toward the valence band.[10] Surface studies showed that the passivation produced a monolayer thick Ga rich oxide.

Based on the previous discussion, we suggest that etching with an ECR source produces an As rich surface and that because of this, the Fermi level shifts toward midgap in the UP structures. Since in the UN materials, the Fermi level is already pinned at midgap (at the  $As_{Ga}$  defect state) further reductions in the  $Ga_{As}$  sites would have little effect. Preliminary Auger electron spectroscopy of the oxides on the control and etched samples indicates, qualitatively an increase in the As/Ga ratio in the etched samples. This is consistent with the motion of the Fermi-level toward mid-gap. Interestingly, because  $P_2S_5$  passivation has the opposite effect, it may be possible to use this procedure to reduce the etch damage.

Finally, it is important to note that the work of Pollak et al. [11] on untreated (100) GaAs surfaces also shows the existence of two surface states, in agreement with our work. The Fermi-level positions obtained by Pollak et al. were similar to those reported here. This clearly demonstrates that the electronic properties of the (100) GaAs surface can be understood in terms of the chemical nature of the GaAs/oxide interface and can be related to well known results obtained under ultra-high vacuum conditions.

## SUMMARY

In summary, we have used photoreflectance spectroscopy to characterize the etch damage in GaAs etched with an ECR source. We found that the damage was mainly localized to the surface and that the etch had little effect on the Fermi level in n-GaAs, but caused a significant shift of the p-GaAs Fermi-level toward midgap. It is suggested that the damage is caused by defects at the GaAs surface. It was also determined that RF power most influences the surface damage, with little noticeable effects from the microwave power.

## ACKNOWLEDGMENTS

We are grateful to Dr. R Kaplan for performing AUGER analysis.

## REFERENCES

1. C. Van Hoof, K. Deneffe, J. De Boeck, D.J. Arnet and G. Borghs, Appl. Phys. Lett. **54**, 608 (1989).
2. X. Yin, H.M. Chen, F.H. Pollak, Y. Cao, P.A. Montano, P.D. Kirchner, G.D. Pettit and J.M. Woodall, J. Vac. Sci. Technol. **B9**, 2114(1991)
3. X. Yin, H.M. Chen, F.H. Pollak, Y. Cao, P.A. Montano, P.D. Kirchner, G.D. Pettit and J.M. Woodall, J. Vac. Sci. Technol. **B10**, 131(1991)
4. O.J. Glembocki, J.A. Dagata, E.E. Dobisz and D.S. Katzer, Proc. Mat. Res. Soc. **236**, 217 (1992).
5. O.J. Glembocki, Proc. Soc. Photo-Optical Instrumentation Engineers, 1286, 1(1990) and references therein.
6. D.E. Aspnes, Phys. Rev. **153**, 972(1967) and R.N. Bhattacharya, H. Shen, P. Parayanthal, F.H. Pollak, T. Coutts and H. Aharoni, Phys. Rev **B37**, 4044(1988).
7. D. Troost, L. Koenders, L.-Y. Fan and W. Monch, J. Vac. Sci. Technol. **B5**, 1119(1987)
8. K. Stiles, D. Mao and A. Kahn, J. Vac. Sci. Technol. **B6**, 1170(1988)
9. W.E. Spicer, N. Newman, C.J. Spindt, Z. Liliental-Webber and E.R. Weber, J. Vac. Sci. Technol. **B8**, 2084(1990)
10. O.J. Glembocki, J.A. Dagata, A. Giordana, D.S. Katzer and C.E. Stutz, presented at the 1992 meeting of the American Vacuum Society, Chicago, IL, December, 1992; O.J. Glembocki, J.A. Dagata, E.A. Dobisz and D.S. Katzer, Proc. Mat. Res. Soc. **236** 217(1992).
11. F.H. Pollak, J. Vac. Sci. Technol., **B11**, 1710(1993).

## IN-SITU DIAGNOSTICS OF PLASMA-INDUCED DAMAGE ON GaAs BY PHOTOREFLECTANCE SPECTROSCOPY

HIDEO NAKANISHI and KAZUMI WADA

NTT LSI Laboratories

3-1 Morinosato-Wakamiya, Atsugi, Kanagawa 243-01, Japan

### ABSTRACT

Photoreflectance spectroscopy (PR) is used to make in-situ diagnostics of sub-surface damage behavior during Ar-plasma etching of n-type GaAs. The in-situ PR diagnostics first unveil anomalous damage behavior at an early stage of plasma etching: Franz-Kerdysh oscillation shows an abrupt decrease in the surface electric-field strength from 130 to 30 kV/cm within 10 sec. This indicates that acceptor-like defects with a concentration of more than  $1 \times 10^{17} \text{ cm}^{-3}$  are created at the very beginning of the plasma etching. The  $\Delta R/R$  abruptly decreased to 4% in intensity upon within 5 sec. of plasma etching and subsequently recovered. This indicates that recombination centers are quickly introduced, then further plasma etching gradually removes such centers, possibly by etching the damaged layer. Photoluminescence (PL) intensity decreases to 72% but does not show any recovery, indicating that PL is dominated by recombination centers in a deeper region. Thus, in-situ PR diagnostics is the first method to provide detailed findings on new damage behavior during Ar-plasma etching.

### Introduction

Plasma processing is an indispensable technology for making semiconductor devices. However, a problem associated with plasma processing is that plasma irradiation creates point defects in sub-surface of semiconductors, which can induce deep levels in the energy bandgap. The defects are referred to as "damage". Such damage degrades the material properties. Plasma damage has been extensively studied, however, many of the studies did not pay serious attention to the diagnostic system requirements stated in the next section. Quite recently, pioneering work has been done on surface physics and in-situ diagnostics of surface-potential change caused by Ar sputtering have been made using photoreflectance spectroscopy (PR).<sup>1)</sup>

In the present paper, we report the results of setting up a reactive ion-etching system equipped with PR to make in-situ diagnostics of plasma-induced surface and sub-surface damage in GaAs. In-situ diagnostics revealed the kinetics of introducing plasma-induced damage such as recombination centers as well as compensation centers.

### Requirements for plasma-induced damage diagnostics

We have set up an in-situ diagnostics system for plasma-etching damage, equipped with PR as shown in Fig.1.<sup>2,3)</sup> Before we describe detailed experimental results, we will discuss the requirements that a damage diagnostics system should fulfill. There are three minimum requirements:

#### 1) In-situ

Damage is easily transformed if surface is exposed to the air, since plasma-etched surfaces are highly activated. Surface metallization also generates damage which is not specifically understood. Therefore, damage diagnostics should be performed in-situ and without making physical contact with the sample.

## 2) Non-invasive

Damage can be reduced by minority-carrier injection in terms of recombination-enhanced defect reaction. So, the probing power used for damage diagnostics should be low enough to avoid influencing damage.

## 3) Surface-sensitive

Plasma-induced damage is often located in the sub-surface region. Characterization methods should be surface sensitive.

The first requirement can be met by using optical probes. Since plasma processing is usually performed at a pressure close to atmospheric pressure, an electron beam cannot be used as a probe. The second requirements means that Raman spectroscopy becomes less appropriate if highly intense laser is used. As shown in Fig. 2, high-power-laser irradiation can remove plasma-induced damage. We have also reported that even damage-induced by ion-implantation can be reduced by using high-power-laser irradiation.<sup>4)</sup> The third requirements means that photoluminescence spectroscopy (PL) is less appropriate because the presence of surface depletion layers in semiconductors makes it difficult to evaluate damage by PL, as we will show. Therefore, we concluded that PR is, at present, the best method for in-situ, non-invasive, surface-sensitive diagnostics.

## Experiment

A schematic representation of our in-situ system for diagnosing plasma-etching damage is shown in Fig. 1. PR measurements were performed as follows: The pump beam was supplied by chopping an Ar<sup>+</sup>-ion laser (514.5 nm) with a power density of the order of 1 mW/cm<sup>2</sup>. A GaAs:Si wafer ( $n = 2 \times 10^{17}$  cm<sup>-3</sup>) was placed in a plasma etching chamber. Thus, in-situ observation of damage-introduction kinetics caused by plasma irradiation could be done without exposure to air or metallization of the sample surfaces.

Plasma irradiation was performed in a parallel-plate reactor operating at 13.56 MHz at a pressure of 10 Pa at 50 W, which corresponds to a self-bias voltage of 200 V. Irradiation time was 5, 10, 30, 60 or 120 sec. The etching rate was around 1 nm/min. Prior to plasma irradiation, the sample surface was etched off by 1- $\mu$ m-thick wet etching to eliminate any existing residual damage on the surface.

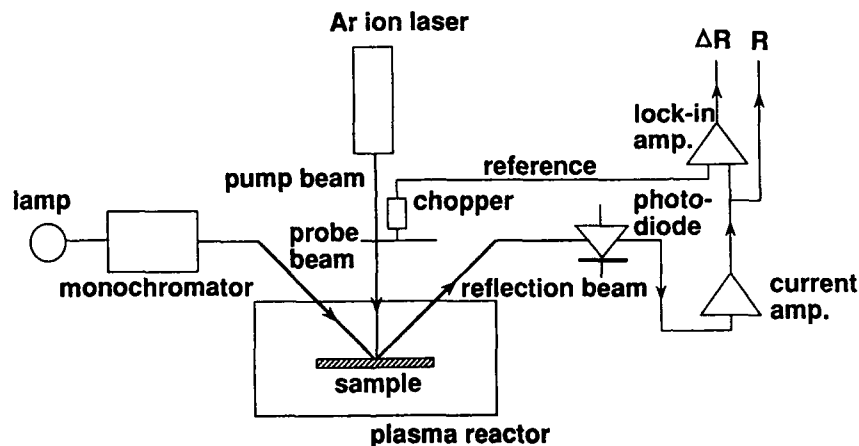


Figure 1 Schematic representation of an in-situ PR-based diagnostics system for plasma-induced damage.

In-situ damage diagnostics were performed as follows: The PR measurement was performed before plasma irradiation, then plasma was irradiated for a given time without optical illumination. After plasma irradiation, the sample was left for 30 min. to cool to room temperature since the sample temperature rose during plasma irradiation. Then we performed the PR measurements. Preliminary study was done using this system for in-situ real-time diagnostics during plasma irradiation. This will be reported in a forthcoming paper.

## Results

### Change in PR spectrum due to plasma irradiation

Figure 3 shows typical PR spectra before and after Ar plasma irradiation for 1 min. Two interesting changes can be seen. After plasma irradiation, the spacing of Franz-Kerdysh Oscillations (FKOs) became more narrow and the intensity of  $\Delta R/R$  weakened. We found that the former is due to the creation of compensation centers and the latter to the creation of recombination centers, both caused by plasma processing. These are discussed in the following section.

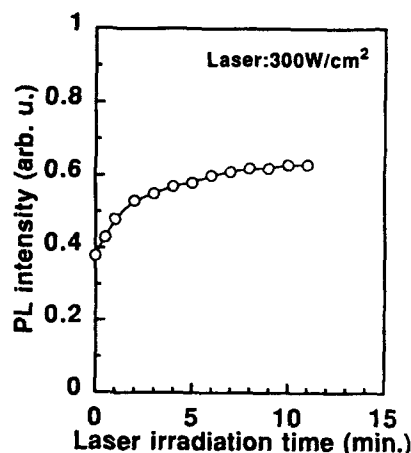


Figure 2 Reduction of plasma damage by high-intensity laser irradiation.

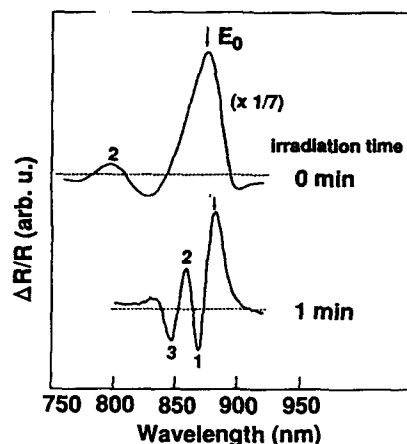


Figure 3 Franz-Kerdysh Oscillation before and after plasma irradiation

### Compensation center creation

Figure 4 shows the irradiation time dependence of the surface electric-field strength. Here, the electric-field strength  $F$  was calculated using the expression derived by Aspnes and Studna.<sup>5)</sup> The initial electric-field strength of 130 kV/cm rapidly decreased to 30 kV/cm within 10 sec. then gradually decreased to 20 kV/cm. The surface electric-field is expressed by

$$F = (2 V_s q (N_D - N_A) / \epsilon_s)^{1/2}, \quad (1)$$

where  $V_s$  is the surface potential,  $\epsilon_s$  is the dielectric constant,  $q$  is the elemental charge, and  $N_D$  and  $N_A$  are the donor and acceptor impurity concentrations, respective-

ly. In the present case,  $N_A$  is the plasma-induced compensation-center concentration. Based on Eq. (1),  $N_D - N_A$  was calculated and plotted in Fig. 4. Here, a change in  $V_S$  did not significantly affect  $N_D - N_A$ . Figure 4 shows that about  $10^{17} \text{ cm}^{-3}$  compensation centers were created within 10 sec. Charge compensation was evaluated by using the capacitance-voltage characteristics of Au Schottky diodes fabricated on the plasma-irradiated sample surfaces. These results are also shown in Fig. 4. This shows that PR is even more surface-sensitive than evaluation using Schottky-diode characteristics.

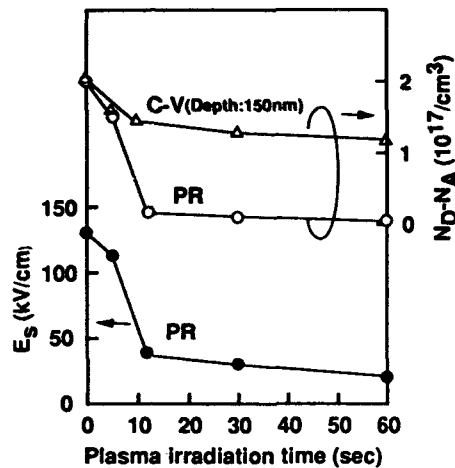


Figure 4 Reduction in surface electric field-strength by plasma irradiation.

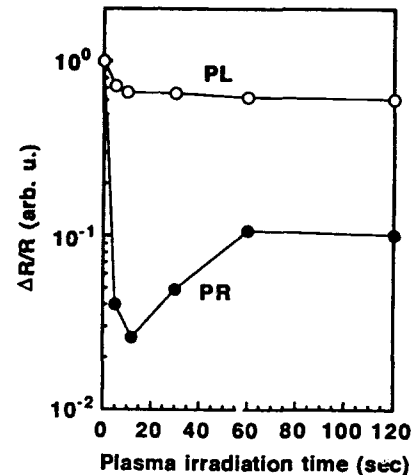


Figure 5 Reduction in  $\Delta R/R$  intensity by plasma irradiation.

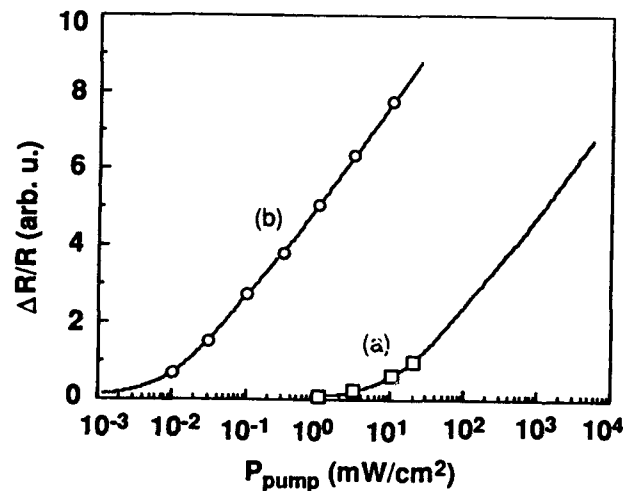


Figure 6 Dependence of  $\Delta R/R$  intensity on pumping power - Effect of recombination centers.

### Recombination center creation

Figure 5 shows the  $\Delta R/R$  intensity dependence on irradiation time. The intensity was measured by taking the peak intensity of  $E_0$  transition. The  $\Delta R/R$  intensity abruptly falls to 4 % during first 5 sec. then gradually recovered. The PL intensity decreased to 72 % and no recovery was observed. This indicates that PR is much more sensitive than PL. This is because PR only measures the region with a high electric field located close to the sample surface whereas PL measures luminescence from the flat band region located deep in the bulk. However, it is not clear what is characterized by  $\Delta R/R$  intensity.

The  $\Delta R/R$  intensity should be proportional to the potential difference  $\Delta V$  between the Fermi level and the quasi-Fermi level because of excess carriers in the sub-surface layer excited by modulated pump laser in sub-surface layer. Since steady-state excess-carrier concentration is expressed by the product of the carrier-generation rate  $G$  and the recombination lifetime  $\tau$ ,  $\Delta V$  is preliminarily shown by

$$\Delta V = k_B T / q \ln \{A (1 + G \tau)\} \quad (2)$$

$$G = B P_{\text{pump}} \quad (3)$$

$$\tau^{-1} = \tau_i^{-1} + \tau_e^{-1}, \quad (4)$$

where  $k_B$  is the Boltzmann constant,  $T$  is temperature,  $P_{\text{pump}}$  is the pumping-laser power, and  $A$  and  $B$  are constants. Here, the effects of the probe beam and reduction of photo-excited carriers by drift and diffusion are implicitly included in  $A$  and  $B$ . The expression shown above should hold in the low-field regime of a fully depleted space-charge region. Figure 6 shows the  $\Delta R/R$ -intensity dependence on the pumping power, based on Eqs. (2) and (3).

The experimental data are also shown in Fig.6. These data were obtained (a) after 10 sec. of plasma irradiation and (b) without irradiation are well explained by Eqs. (2) and (3). It is clear that plasma irradiation reduced recombination lifetime by three orders of magnitude. The detailed analysis will be reported elsewhere.

### Discussion

In-situ PR diagnostics are effective for investigating plasma-induced damage. Based on the new phenomena observed, the nature and behavior of damage are described as follows.

#### Nature of damage

Recombination centers were abruptly created within 5 sec. of plasma irradiation then gradually decrease in number with continued plasma irradiation. In contrast, compensation centers were created after 10 sec. and accumulated to make the sample semi-insulating with continued irradiation, as shown in Fig. 5. These kinetic differences suggest that recombination centers are different from compensation centers. This is also supported by our previous experiment: we studied the annealing kinetics of compensation centers and found that the diffusivity was high even at room temperature.<sup>5)</sup> In contrast, recombination centers were not fast diffusers.

#### Behavior of damage

Recombination centers and compensation centers were both rapidly created within 10 sec. of plasma irradiation. This rapid-creation mechanism is not understood well, but the creation is probably related to the initial etching stage. For example, there will normally be a thin native oxide layer on the sample surface, even if the surface is

treated with HCl to remove the layer. This may induce electrical breakdown at the very beginning of plasma irradiation. However, to fully understand what is happening during such phenomena, we should clarify what is the most fundamental cause of damage introduction. Since plasma consists of photons as well as ions, electrons and radicals, the circumstances are complicated. The first question is what is responsible for creating damage. For example, plasma luminescence intensity instantaneously increases after plasma generation. Such transience peculiar to plasma generation may influence the anomalous creation of both centers.

Second, what causes the decrease of recombination centers? Temperature elevation and removal of the sub-surface during plasma irradiation might be the motive forces. As mentioned above, compensation centers created by plasma irradiation are mobile even at room temperature but recombination centers are not. Thus, temperature elevation should enhance in-diffusion of compensation centers to the bulk, while recombination centers still stay in the very sub-surface layer. It is recently clarified that plasma luminescence enhances in-diffusion of compensation centers as well<sup>6)</sup>. Thus, etching off the sub-surface layer can reduce the number of recombination centers created by plasma irradiation but compensation centers diffuse in and accumulate. This is one explanation for the observed anomaly. Further studies are definitely needed. However, it is clear that the physics and chemistry of damage in semiconductors are among the most important areas of materials science and engineering. In-situ diagnostics will be a key issue.

### Summary

Photoreflectance spectroscopy (PR) was successfully used to make in-situ diagnostics of sub-surface damage behaviors during Ar-plasma etching of n-type GaAs. The in-situ PR diagnostics revealed the following anomalous damage behavior during an early stage of plasma etching: an abrupt decrease in the surface electric-field strength and an abrupt decrease then gradual recovery in  $\Delta R/R$  intensity. The decrease in electric field strength indicates that acceptor-like defects with a concentration of more than  $1 \times 10^{17} \text{ cm}^{-3}$  are created at the very beginning of the plasma etching. The change in  $\Delta R/R$  intensity shows recombination center creation. The  $\Delta R/R$  intensity is expressed by using recombination lifetime, which qualitatively reproduces such an abrupt decrease. The recovery of the intensity suggests that recombination centers are gradually removed, possibly due to temperature elevation or due to etching of the damaged layer. It is also shown that photoluminescence PL is not as surface-sensitive as PR, presumably because the PL process is dominated by recombination in a deeper region where damage is not severe. In-situ-PR diagnostics is the first method to provide detailed findings on new damage behavior during Ar-plasma etching.

### Acknowledgement

The authors are grateful to K. Yamada of our laboratories for helpful discussion and critical comments.

### References

1. X. Yin, H.-M. Chen, F. H. Pollak, Y. Chan, P. A. Montano, P. D. Kirchner, G. D. Pettit and J. M. Woodall, *J. Vac. Sci. Technol.*, B9, 2114, 1991.
2. H. Nakanishi and K. Wada, *Jpn. J. Appl. Phys.* 32, 6206, 1993.
3. K. Wada and H. Nakanishi, *Mater. Sci. Forum.* 143-147, 1433, 1994.
4. H. Nakanishi, M. Kanada and K. Wada, *Appl. Phys. Lett.* 61, 546, 1992.
5. D. E. Aspnes and A. A. Studna, *Phys. Rev.* B7, 4605, 1973.
6. H. Nakanishi and K. Wada, unpublished.



# PHOTOREFLECTANCE CHARACTERISATION OF REACTIVE ION ETCHED SILICON

M. Murtagh, J. T. Beechinor, P. A. F. Herbert, P. V. Kelly and G. M. Crean  
C. Jeaynes<sup>†</sup>

National Microelectronics Research Centre, Lee Maltings, Prospect Row, Cork, Ireland.

<sup>†</sup> Dept. of Electronic Engineering, University of Surrey, Guildford GU2 5XH, England.

## ABSTRACT

Reactive ion etching (RIE) of p-type 2-3  $\Omega\text{cm}$  resistivity silicon (100) was characterised using Photorefectance (PR), Rutherford Backscattering Spectrometry (RBS) and Spectroscopic Ellipsometry (SE). Isochronal (5 minutes) etching was performed at various DC etch biases (0-500V) using a  $\text{SiCl}_4$  etch chemistry. The substrate etch rate dependence on applied bias was determined using mechanical profilometry. A distinct shift in the  $\Lambda_2$ - $\Lambda_1$  Si transition and significant spectral broadening of the room temperature PR spectra was observed as a function of etch bias. Photorefectance results are correlated with RBS, SE and etch rate analysis. It is demonstrated that the PR spectra reflect a complex, competitive, plasma-surface interaction during the RIE process.

## 1. INTRODUCTION

Reactive ion etching (RIE) techniques will be applied extensively in fabrication of deep submicron Si CMOS technologies in order to achieve the highly anisotropic etch profiles required. However, due to the fine geometry processes, increasingly precise control of etch selectivity, etch rate and minimisation of etch induced lattice damage will be necessary.

Recently, several laser based characterisation techniques have been proposed for process control monitoring of dry etch induced damage. These include photothermal radiometry [1], modulated optical reflectance [2] and photorefectance [3,4]. The photorefectance probe in particular appears to be a potentially powerful diagnostic tool due to its sensitivity to interband transitions. However, very little work has been performed to-date on PR characterisation of dry etch induced damage in silicon [3] and in particular on correlation of PR with conventional analysis techniques. This is essential in order to gain acceptance of the technique within a microelectronic processing environment. In this paper, PR is applied to the characterisation of  $\text{SiCl}_4$  RIE of silicon with PR experimental data correlated to Rutherford Backscattering Spectrometry (RBS) and Spectroscopic Ellipsometry (SE) analysis.

## 2. EXPERIMENTAL

Single crystal CZ p-type (B doped) Si (100) wafers of resistivity 2-3  $\Omega\text{cm}$  were employed in this study. Isochronal (5min) reactive ion etching (RIE) was performed in an Oxford Instruments Plasmatech RIE-80S parallel plate diode chamber at DC etch biases in the range 0-500V using a  $\text{SiCl}_4$  etch chemistry. The partial pressure of  $\text{SiCl}_4$  was 7mTorr. The RIE etch rate was determined using a Tencor mechanical profilometer.

A schematic of the experimental PR arrangement is detailed in Figure 1. The light source was a 150W Xenon lamp. A double scanning monochromator arrangement was employed to probe the photon energy range from 3.0 to 3.7eV at 7meV resolution. The incident probe beam spot size was 2x1mm at 45° angle of incidence. The modulation source was a 700Hz mechanically chopped, 80mW Ar-ion laser with a 2mm<sup>2</sup> spot size. A UV enhanced Si photodiode was used to record the reflected light intensity. All measurements were performed at room temperature (RT).

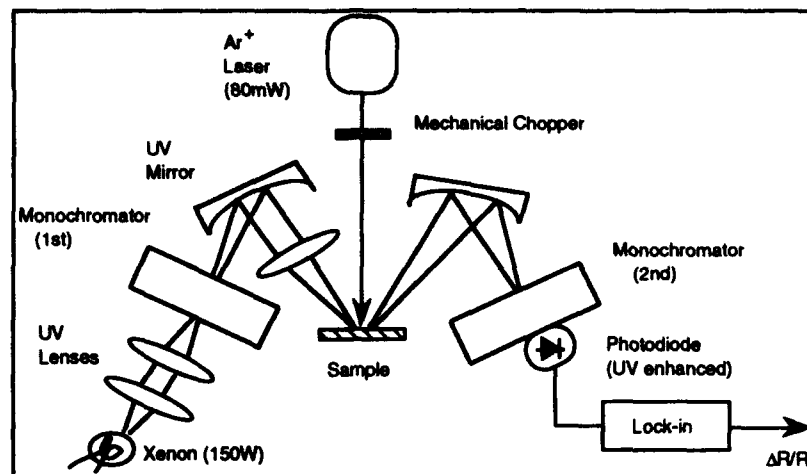


**Figure 1.** Schematic of the PR experimental arrangement.

The crystalline quality of the near surface Si substrate after RIE processing was quantified using channelling RBS. The beam spot size was 1mm in diameter. Measurements were performed using a 1.5 MeV  $^4\text{He}$  beam at a scattering angle of  $160^\circ$

Ellipsometry was performed over the energy range from 2.0eV to 4.5eV at 0.02eV intervals using a phase modulated SE at an angle of incidence of  $70^\circ$ . The lateral resolution was approximately 5x2mm.

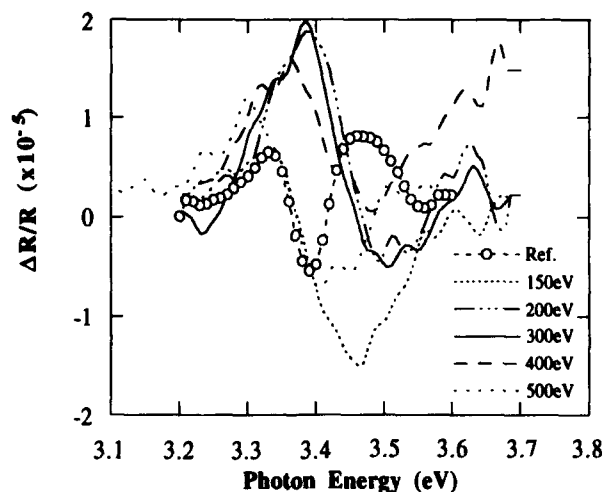


**Figure 2.** Photorefectance spectra of the  $\text{SiCl}_4$  etched Si substrates for the different isochronal etch biases (0-500V).

### 3. RESULTS AND DISCUSSION

The experimental PR spectra from the series of RIE etched Si substrates and the reference substrate are presented in Figure 2. The Si ( $E_1$ )  $\Lambda_3$ - $\Lambda_1$  transition [5] is clearly evident in each spectrum in the region of 3.3eV to 3.4eV.

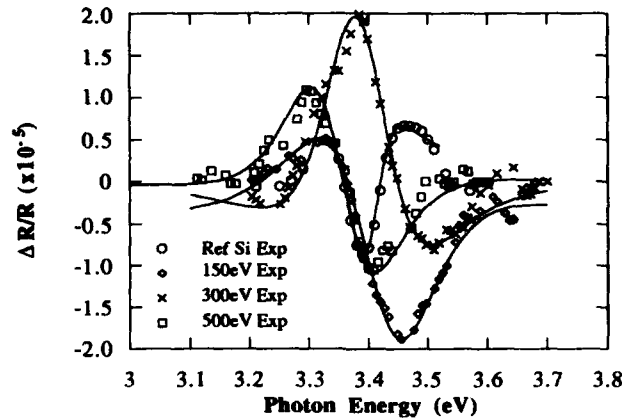


**Figure 3.** Experimental and best fit (—) calculated PR spectra for some of the  $\text{SiCl}_4$  etched samples.

As the PR lineshapes were found to be independent of the pump source intensity, the spectra were fitted using an Aspnes third-derivative-functional-form (TDFF) low field approximation of the dielectric function, corresponding to a two dimensional critical point [6]. Figure 3 presents typical experimental and best fit (—) calculated PR spectra for the RIE samples. The results are tabulated in Table I. Three distinct observations can be made; firstly that an apparent shift in the PR Si  $E_1$  transition is observed as a function of applied RIE bias, secondly that for all etched samples a significant increase in the phenomenological broadening ( $\Gamma$ ) parameter is observed over that of the unetched reference and thirdly that the 200V bias sample has the same  $E_1$  transition peak position as the reference wafer.

**Table I.** Extracted PR line shape parameters obtained from a TDFF best fit to the experimental PR spectra

| Sample               | $E_1$ Transition (eV) | Broadening ( $\Gamma$ ) (meV) | Phase ( $\theta$ ) (degree) | Strain ( $\epsilon$ ) (%) |
|----------------------|-----------------------|-------------------------------|-----------------------------|---------------------------|
| Si reference         | 3.396 ( $\pm 0.004$ ) | 70                            | 105                         | -                         |
| $\text{SiCl}_4$ 150V | 3.415 ( $\pm 0.004$ ) | 165                           | 35                          | -0.1371                   |
| $\text{SiCl}_4$ 200V | 3.396 ( $\pm 0.004$ ) | 145                           | 290                         | -                         |
| $\text{SiCl}_4$ 300V | 3.393 ( $\pm 0.004$ ) | 140                           | 295                         | 0.0217                    |
| $\text{SiCl}_4$ 400V | 3.360 ( $\pm 0.004$ ) | 170                           | 280                         | 0.2589                    |
| $\text{SiCl}_4$ 500V | 3.355 ( $\pm 0.004$ ) | 130                           | 357                         | 0.2958                    |

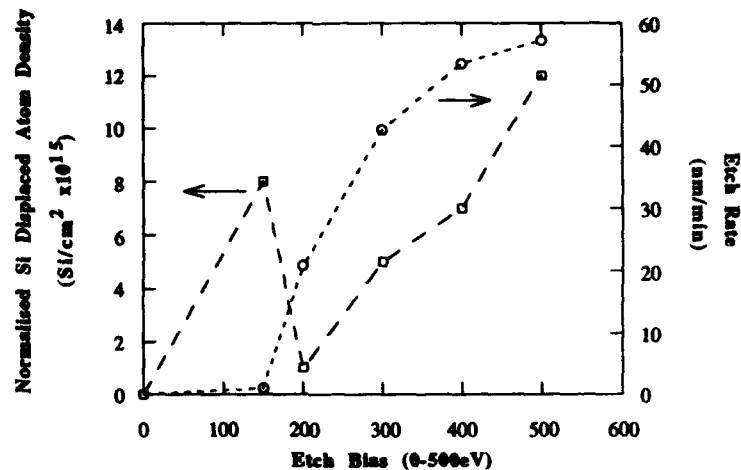


**Figure 4.** Etch rate and Si displaced atom density (normalised with respect to the unetched reference) plotted as a function of increasing sample etch bias (0-500V).

The  $\text{SiCl}_4$  chemistry RIE etch rate as a function of applied voltage bias was determined experimentally using mechanical profilometry on patterned substrates. This relationship is presented graphically in Figure 4. It is observed that no pronounced material removal occurs below 200eV.

Figure 5 presents typical RBS channelling spectra for the RIE etched samples. The surface damage layer was characterised by integrating the silicon surface yield and also integrating the chlorine surface peaks (not shown in the energy window of Figure 5) as a function of etch bias. Table II summaries the RIE induced displaced Si atom areal density (relative to the reference sample) along with the Cl atom density.

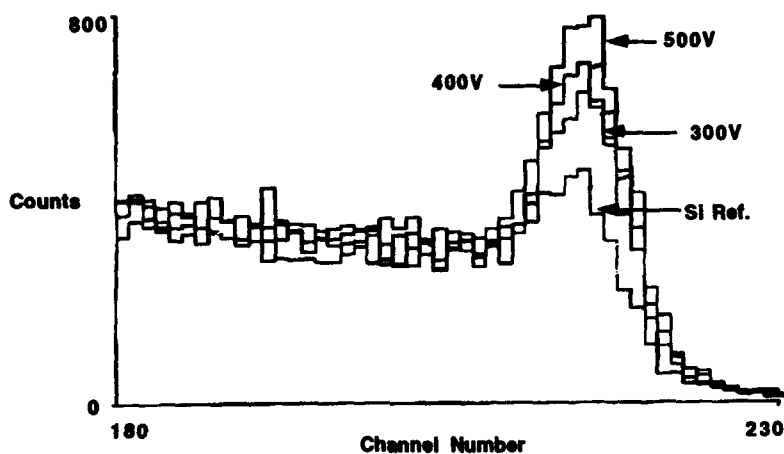


**Figure 5.** RBS channelling spectra for the ref, 300V, 400V and 500V  $\text{SiCl}_4$  RIE samples.

The RBS data in Table II shows a distinct increase in total RIE induced lattice damage as a function of increasing applied bias voltage. In addition it is noted that the 200eV sample has no detectable RIE induced crystalline disorder compared to the unetched reference. Both observations are consistent with the PR spectra and extracted lineshape parameters detailed in Table I. The increase in Cl incorporated in the surface damaged region above 200eV is in agreement with the etch rate studies performed and consistent with the increasing volatility of the chlorine as the etch energy and thus etch temperature increases [7].

**Table II. RIE induced lattice disorder as determined using RBS**

| Sample                 | Displaced Si atom density<br>( $10^{15}/\text{cm}^2$ ) | Cl atom density<br>( $10^{13}/\text{cm}^2$ ) |
|------------------------|--|--|
| Si reference           | -  | -  |
| SiCl <sub>4</sub> 150V | 8 ( $\pm 1$ )  | 12.0 ( $\pm 5$ )                             |
| SiCl <sub>4</sub> 200V | 1 ( $\pm 1$ )  | 18.0 ( $\pm 5$ )                             |
| SiCl <sub>4</sub> 300V | 5 ( $\pm 1$ )  | 21.0 ( $\pm 5$ )                             |
| SiCl <sub>4</sub> 400V | 7 ( $\pm 1$ )  | 33.0 ( $\pm 5$ )                             |
| SiCl <sub>4</sub> 500V | 12 ( $\pm 1$ )   | 45.0 ( $\pm 5$ )                             |

The increase in the broadening parameter for the etched substrates is in agreement with etch induced carrier scattering mechanisms [3]. The relative independence of this parameter with etch bias is consistent with the emergence of the chemical component of the etch above 150V, as detailed in Table II, which is insensitive to the ion extraction voltage [7].

As no splitting is observed in the RT PR silicon  $E_1$  transition (assuming band splitting to be unresolved with an energy separation below  $\Gamma/2$ ) the PR spectra were fitted using a single oscillator model. One hypothesis therefore proposed to account for the red shift detailed in the transition energy data in Table I, for the etched samples above 200V is the presence of a hydrostatically strained near surface silicon region which is assumed to originate from the hydrostatic component of a two-dimensional tensile strain  $\epsilon$ , in the plane perpendicular to the  $\langle 100 \rangle$  direction [3]. The origin of this tensile stress is perhaps due to the creation of vacancies during the etch as the red shift scales with damage layer thickness as determined from RBS analysis. Using an appropriate expression for hydrostatic strain [5], the strain ( $\epsilon$ ) was calculated for each etch bias and is presented in Table I.

The significant change in the PR spectral lineshape as illustrated by the PR phase factor  $\theta$ , for etches above 150V, is however indicative of a change in the fundamental mechanism of the generation source for the PR feature [8]. An alternative physical explanation of the apparent red shift for these samples may therefore be the existence of a RIE induced shallow trap at the Si surface. Despite the increasing presence of chlorine in the etched substrates, as the etch bias is driven above 200V, it is unlikely that the chlorine contributes to the trap states since it remains electrically and optically inactive [9]. It is more likely that the etch induced trap states are correlated with the density of displaced silicon atoms, which is similarly dependent upon the etch bias [9].

The apparent blue shift (19meV) in the  $E_1$  transition peak for the 150V etch PR spectrum is indicative of a compressively strained Si surface layer [10]. This is consistent with injection of impurities into the Si lattice and reflects a pre-steady-state etch situation where the injection of defects and their subsequent removal are not balanced. This is supported by the mechanical profilometry etch rate measurements shown in Figure 4, which show that less than 50Å of Si

material is removed. Above this applied bias it is proposed that etching of the substrate will remove the majority of such implanted impurities.

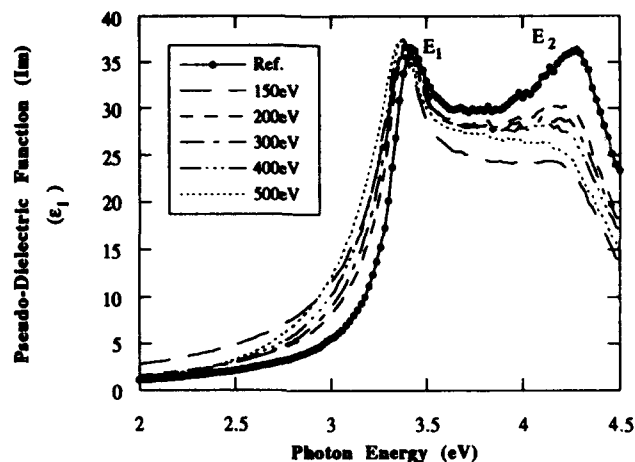


Figure 6. The imaginary part of the pseudo-dielectric function for each isochronal etch bias.

Figure 6 details the imaginary part of the experimentally determined pseudo-dielectric function for the RIE series of samples. Both the  $E_1$  and  $E_2$  Si peaks are observable at approximately 3.4 eV and 4.2 eV respectively. Two trends are evident in the SE spectra; the red shift in the  $E_1$  peak and the reduction in the  $E_2$  peak intensity, both as a function of increasing etch bias. This is indicative of increased lattice disorder [11] and the data have been fitted using a simple two layer optical damage model as illustrated in Figure 7. The results clearly show an increase in the surface damage layer thickness, modelled as an amorphous silicon layer ( $\alpha$ -Si), with etch bias above 300V. The extracted displaced silicon atom density from the SE spectra, obtained from the layer thicknesses and assuming both a  $\text{SiO}_2$  density of  $6 \times 10^{22}/\text{cm}^3$  and a Si density of  $5 \times 10^{22}/\text{cm}^3$  are in good agreement with the RBS data presented in Table II.

| Oxide               | Sample                | Damage layer thickness<br>(Å) | Oxide thickness<br>(Å) | Displaced Si atom<br>density (10 <sup>15</sup> /cm <sup>2</sup> ) |
|---------------------|-----------------------|-------------------------------|------------------------|---|
| Damage Layer (α-Si) |                       |                               |                        |   |
| Si substrate        | Si Ref.               | 0                             | 16.21                  | 0   |
|                     | SiCl <sub>4</sub> 150 | 0                             | 48.54                  | 6.5   |
|                     | SiCl <sub>4</sub> 200 | 0                             | 29.06                  | 2.6   |
|                     | SiCl <sub>4</sub> 300 | 2.96                          | 30.53                  | 4.4   |
|                     | SiCl <sub>4</sub> 400 | 8.20                          | 31.29                  | 7.1   |
|                     | SiCl <sub>4</sub> 500 | 14.40                         | 34.78                  | 10.1  |
| Model               |                       |                               |                        |   |

Figure 7. Spectroscopic ellipsometry model employed for the determination of the displaced Si atom density from the extracted damage layer and oxide layer thicknesses for each of the isochronal RIE samples (0-500eV).

#### 4. CONCLUSIONS

A series of isochronal  $\text{SiCl}_4$  RIE etched Si(100) substrates have been characterised using PR, RBS and SE, with the substrate etch rate dependence on applied bias determined by mechanical profilometry. Both SE and RBS channeling analysis detail increasing lattice disorder as a function of increasing applied etch bias.

The PR spectra reflect a complex, competitive, plasma-surface interaction RIE process. Above 200V, the etch rate is such that the predominant mechanism is removal of material. The red shift observed in the PR spectra is consistent with the generation of a near surface (100Å) tensile stress perhaps arising from the creation of vacancies during this etch process or with the generation of etch induced shallow trap states. Below 200V, other competitive plasma effects dominate, in particular the injection of impurities into the silicon lattice. This is reflected in the observed blue shift in the 150V PR spectrum.

Further work is in progress to verify the above hypothesis using both channeling RBS and low temperature photoluminescence studies.

#### ACKNOWLEDGEMENTS

This work was partially funded by the Commission of the European Communities (CEC) under the ESPRIT Research Programme within Basic Research Action No. 6878 Epioptics Applied to Semiconductor Interfaces (EASI).

#### REFERENCES

- [1] G. M. Crean, I. Little and P. A. F. Herbert, Appl. Phys. Lett., Vol. **58**, 4, (1991).
- [2] M. Murtagh, G.M. Crean, T. Flaherty and C. Jeynes, Appl. Surf. Sci., **54**, (1992).
- [3] W. Shen, M. C. Fanani, F. H. Pollak, M. Tomkiewicz, H. J. Leary and J. P. Gambino, J. Appl. Phys. **66** (4), 1785 (1989).
- [4] M. Murtagh, P.V. Kelly, P.A.F. Herbert, M. O' Connor, G. Duffy and G. M. Crean, Appl. Surf. Sci., **63**, (1993).
- [5] F. H. Pollak and G. W. Rubloff, Phys. Rev. Lett. **29**, 789 (1972).
- [6] D. E. Aspnes, Surf. Sci. **37**, 418 (1973).
- [7] T. Tadokoro, F. Koyama and K. Iga, J. Vac. Sci. Technol. **B7**, 5, (1989).
- [8] A. K. Berry, D. K. Gaskill, G. T. Stauff and N. Botika, Appl. Phys. Lett. **58** (24), (1991).
- [9] C. Harris, W. D. Sawyer, M. Konuma and J. Weber, E-MRS Conf., Strasbourg, Paper No. **B-XII.3**, (1989).
- [10] F. Herman, "The Electronic Energy Band Structure of Silicon and Germanium", Proc. IRE, **43**, 1703, (1955).
- [11] S. Lynch, M. Murtagh, G. M. Crean, P. Kelly, M. O'Connor and C. Jeynes, Thin Solid Films, **233**, (1993).

## LAYERED SEMICONDUCTOR PHOTOREFLECTANCE DIAGNOSTICS

Konstantin.O.Boltar and Valery.A.Fedirko  
Moscow State University of Technology "Stankin",  
Vadkovski per.3a, 101472, Moscow, Russia

### ABSTRACT

We have investigated IR reflectance spectra of semiconductor structures consisting of up to 5 epitaxial GaAs/GaAlAs layers on GaAs wafer, diffused and implanted profiles in Si wafers to find the semiconductor structures parameters.

### INTRODUCTION

Nondestructive characterization of semiconductor multilayer structures is an important step in the fabrication of semiconductor devices. Infrared (IR) reflectance spectrum of semiconductor surface contain information specific for each semiconductor lattice. IR reflectance spectrum also depends on the free charge carriers concentration and their mobility. IR reflectance spectrum of multilayer semiconductor structure have rather complex form due to the interference depending on the thickness of the layers. So one can extract the values of the semiconductor structure parameters from the IR reflectance spectrum.

Such a procedure is well known for a bulk semiconductor and was also applied for GaAs wafer with one <sup>1</sup> and two <sup>2</sup> epitaxial layers. Bulk semiconductor free charge carriers concentration can be easily found from the IR reflectance spectrum minimum wavenumber. The definition of multilayer semiconductor structure parameters needs more complicated computer simulation techniques.

In this work IR reflectance spectra of GaAs/AlGaAs structures consisting of up to 5 epitaxial layers on GaAs wafer, inhomogeneously doped Si wafers have been measured. Model spectra have been constructed and compared with measured ones. The fitting procedure gives the layer thickness, the free charge carriers concentration and the mole fraction of AlAs in AlGaAs in each epitaxial layer, free charge carriers concentration distribution in diffused and implanted Si wafers.

### EXPERIMENTAL

Bruker IFS-113V Fourier transform spectrometer is used for IR reflectance spectra measurements in 50-5000  $\text{cm}^{-1}$  wavenumber band. Spectral resolution is 2  $\text{cm}^{-1}$ . IR beam diameter is 5 mm, incidence angle equals 5 degrees, IR beam divergence is about 2 degrees. Evaporated gold mirror is used for reference beam calibration. The IR spectra measurement accuracy is about 1 %.

### SPECTRUM SIMULATION

We simulate IR reflectance spectrum for any layered structure using Abeles matrix method <sup>3</sup>.

The dielectric permittivity of a semiconductor  $\epsilon$  is a sum of the lattice  $\epsilon_l$  and the free charge carriers  $\epsilon_c$  fractions. For silicon the lattice dielectric permittivity may be set equal to its static value 11.7, while in the polar crystal  $\text{Al}_x\text{Ga}_{1-x}\text{As}$  it is a function of a mole fraction  $x$  and exhibits strong frequency dispersion. It is calculated in two oscillator model <sup>4,5</sup>:



$$\epsilon_L(\nu) = \epsilon_1 + \frac{\nu_{L1}^2 - \nu_{T1}^2}{\nu_{T1}^2 - \nu^2 + i\nu \Gamma_1} + \frac{\nu_{L2}^2 - \nu_{T2}^2}{\nu_{T2}^2 - \nu^2 + i\nu \Gamma_2} \quad (1)$$

were  $\nu$  is a wavenumber,  $\epsilon_1 = 10.89 - 2.73x$ ,  $\nu_{L1} = 292 - 53x + 0.15x^2 \text{ cm}^{-1}$ ,  $\nu_{T1} = 268 - 5.2x - 0.09x^2 \text{ cm}^{-1}$ ,  $\nu_{L2} = 359 + 71x - 0.27x^2 \text{ cm}^{-1}$ ,  $\nu_{T2} = 359 + 4.4x - 0.02x^2 \text{ cm}^{-1}$ ,  $\Gamma_1 = 0.03 \nu_{T1}$ ,  $\Gamma_2 = 0.06 \nu_{T2}$ . We also add imaginary part of  $\epsilon_L$  corresponding to the multiple optical phonon absorption in GaAs wafer at wavenumbers 450 and 520  $\text{cm}^{-1}$ , which was determined experimentally.

The free charge carriers fraction of the dielectric permittivity is supposed to be a function of a wavenumber, carriers concentration, effective mass and carriers collision frequency according to the Drude model<sup>4</sup>:

$$\epsilon_C(\nu) = \frac{Ne^2}{3.14m^* \nu(\nu + i\nu_c)} \quad (2)$$

$N$  being free charge carriers concentration,  $e$  - electron charge,  $m^*$  - effective charge carriers mass,  $\nu_c$  - charge carriers collision frequency. We use effective mass values  $m_e^* = 0.27m_0$ ,  $m_h^* = 0.36m_0$  for electrons and holes in Si<sup>4</sup> and  $m_e^* = (0.07 + 0.08x)m_0$ ,  $m_h^* = (0.4 + 0.6x)m_0$  for electrons and holes in AlGaAs composition<sup>5</sup>.

Charge carrier collision frequency  $\nu_c$  depends on the wavenumber and carriers concentration. We use for  $\nu_c$  the empirical formula (compare with<sup>1,4</sup>):

$$\nu_c(\nu) = f(\nu) \text{MAX}(1, 0.57 \cdot 10^{-9} \text{SQRT}(N)) \quad (3)$$

with the function  $f(\nu)$ , different for electrons and holes, found experimentally from the IR absorption spectra of the material. The influence of  $f(\nu)$  on the final results is small, so one can use very rough model for  $f(\nu)$ .

We have neglected the dependence of optical effective mass on carriers concentration and the light holes dielectric permittivity fraction in AlGaAs.

## FITTING PROCEDURE

The layer thickness  $d$ , mole fraction  $x$  of AlAs in GaAlAs and charge carrier concentration  $N$  are used as fitting parameters. Starting from some (rather intuitive) set of parameters  $d$ ,  $N$ ,  $x$  for each semiconductor layer we calculate the complex dielectric permittivity of each layer and the reflectance spectrum of multilayer structure.

Then we compare the measured and simulated IR reflectance spectra and iterate for the best agreement between them. Minimum root mean squares (RMS) difference between simulated and measured spectra is chosen as a criteria. The minimisation is performed by the combination of Newton method for each parameter and gradient descent method.

The starting set of parameters is strongly effect the computation time. It is determined from the characteristics features of a spectrum. The number of spectrum points extends from 20 to 200. The number of layers is restricted by a dramatic increase of the computation time.

The above program is realized on IFS-113V spectrometer computer using FORTRAN, so the simulated spectra can then be processed by any spectrometer peripheral. The fitting procedure takes from some minutes for one layer structure to some hours for five layers structure.

## RESULTS

### GaAs epitaxial structures

Fig.1 shows the measured IR reflectance spectrum of an epitaxial n<sup>+</sup>-n-GaAs structure (curve 1) and the simulated one (curve 2). The RMS difference equals .29%. Fig 2 shows the fitted electrons concentration profile (bar curve 1) and the C-V profiling of this structure (marker curve 2).

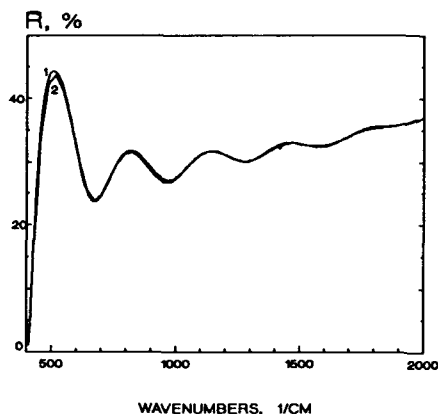


Fig.1

The results coincide within the accuracy of both methods. The IR reflectance method does not permit to measure small charge carriers concentrations (less than  $10^{16} \text{ cm}^{-3}$ ) and interlayers fine structure. However this nondestructive method gives more precise layers thickness values what is inherent to optical methods.

### AlGaAs epitaxial structures

IR reflectance spectrum for complex structure containing 4 epitaxial layers on GaAs wafer have been simulated in three bands of  $5000\text{-}2000 \text{ cm}^{-1}$ ,  $2500\text{-}400 \text{ cm}^{-1}$  and  $450\text{-}50 \text{ cm}^{-1}$ , separately.

The sample consists of a n-type GaAs wafer with  $N=5 \cdot 10^{17} \text{ cm}^{-3}$ , 18.7 microns n-type GaAs with  $N$  less then  $10^{16} \text{ cm}^{-3}$ , 1.30 microns p-type  $\text{Al}_{0.82}\text{Ga}_{0.18}\text{As}$  with  $N=4 \cdot 10^{18} \text{ cm}^{-3}$ , 0.27 microns p-type  $\text{Al}_{0.10}\text{Ga}_{0.90}\text{As}$  with  $N=4 \cdot 10^{17} \text{ cm}^{-3}$ , 0.67 microns p-type GaAs with  $N=8 \cdot 10^{18} \text{ cm}^{-3}$ .

The measured (curves 1) and simulated (curves 2) IR reflectance spectra for the above bands are shown in Fig. 3-5 respectively. The first band spectrum gives information only about the widths  $d$  and the AlAs mole fractions  $x$  for two cap AlGaAs layers. Supposing these values known we have found the other layers widths  $d$  and the free carriers concentrations  $N$  from the second band. The third band is used for more accurate definition of the whole parameter set.

The RMS differences between simulated and measured spectra equal 1.02%, 0.71% 5.5% respectively. The fitted mole fractions  $x$  differ less then 2% from those measured by ESCA method. All fitted parameters are in a good agreement with the delivery specification. Some additional discrepancy between the simulated and measured spectra in  $450\text{-}50 \text{ cm}^{-1}$  band may be due to roughness of the free charge carrier collision frequency  $\nu_c$  evaluation.

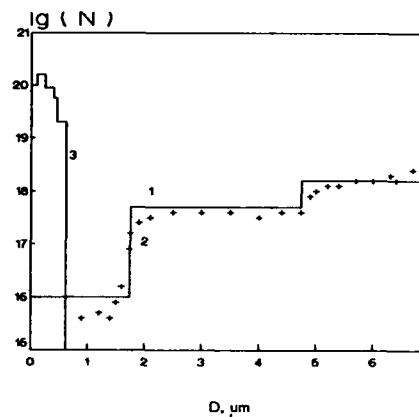


Fig.2

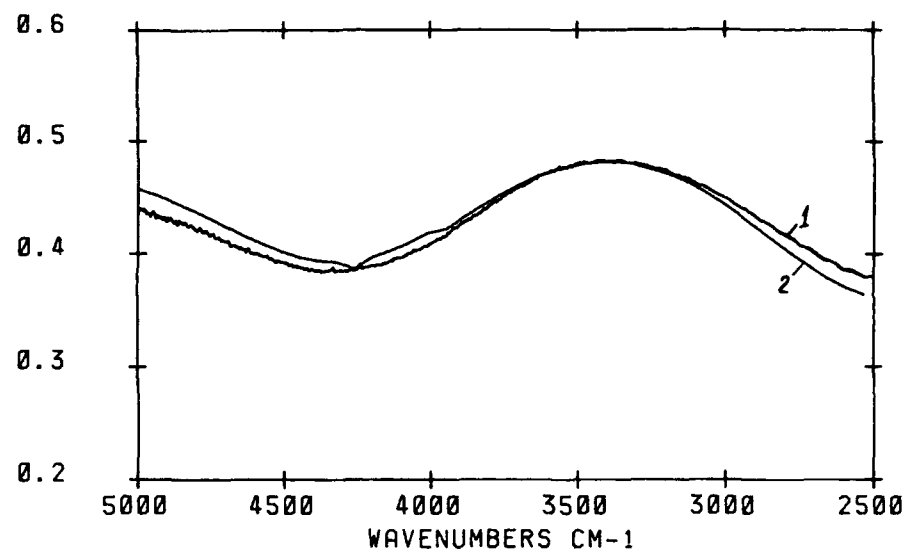


Fig. 3

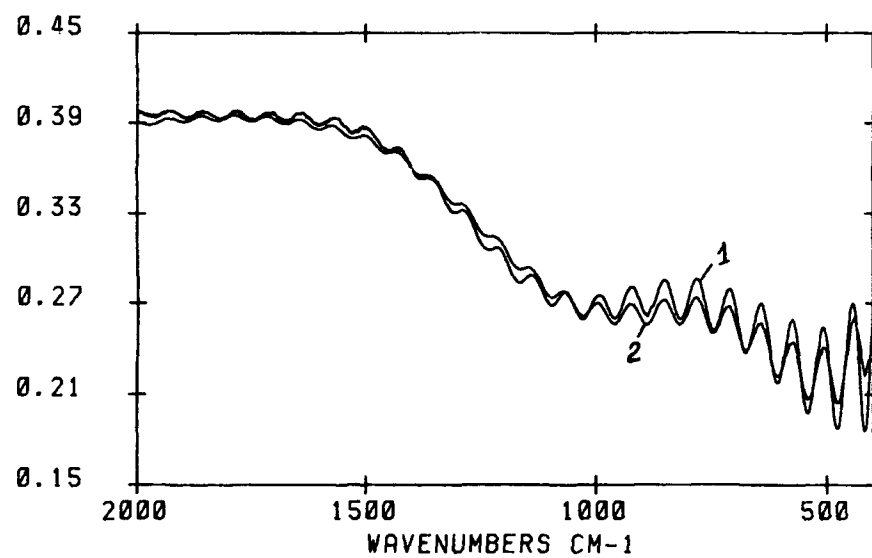


Fig. 4

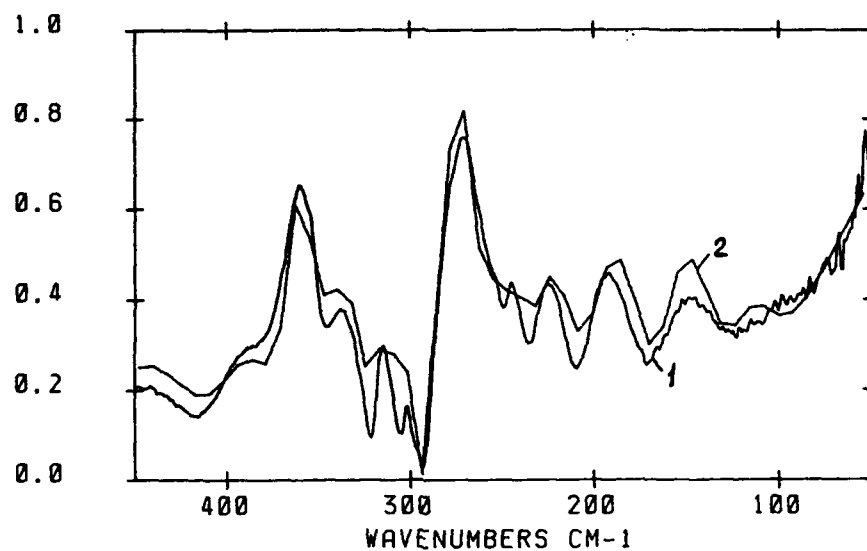


Fig. 5

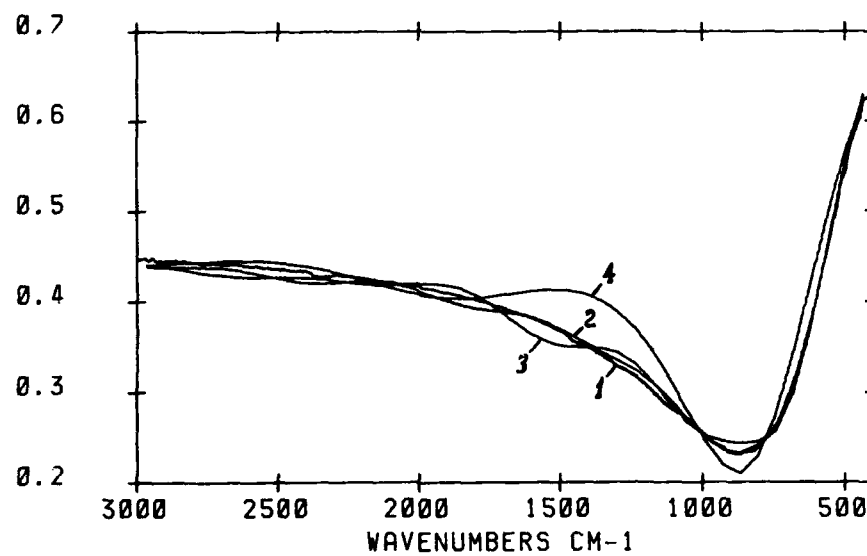


Fig. 6

### Diffused Si profile

When analyzing the continuous profile of a diffused or implanted silicon wafer we have approximated it by a number of layers with uniform free charge carriers concentration.

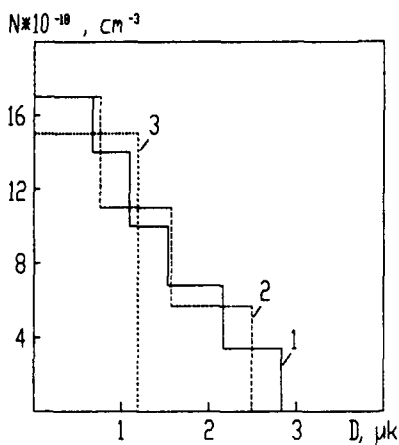


Fig. 7

IR reflectance spectrum of a diffused n<sup>+</sup>-n Si wafer (curve 1) and the simulated ones for 5 uniform layers (curve 2), 3 uniform layers (curve 3), and 1 layer (curve 4) are shown in Fig 6. The free electron concentration approximation step functions for 5 (curve 1), 3 (curve 2), 1 (curve 3) layers approximations are shown in Fig 7.

The RMS differences between simulated and measured spectra equal 0.6%, 0.9%, 2.56% respectively. Further increase of the number of approximating layers is restricted by the inaccuracy of IR reflectance spectra measurements.

The calculated surface resistance value 21.1 Ohm for 5 layers approximation is in a good agreement with the value 17.5 Ohm measured for this structure by the 4 probe method.

### Implanted Si profiles

The simulated step profile for implanted p<sup>+</sup>-p Si structure is shown in the Fig. 2 (curve 3). The RMS between simulated and measured spectra equals 0.21%, calculated surface resistance value 23.9 Ohm, the measured one 22 Ohm. We draw ones attention to the fact that the simulation procedure gives the maximum free charge carriers concentration at some distance from the surface which is a characteristic feature of any implanted structure.

### CONCLUSION

IR reflectance spectroscopy may be used as an effective instrument for noninvasive diagnostics of multilayer semiconductor structures.

### REFERENCES

1. N.A.Denisova, T.A.Kruse, A.B.Rezvov, D.I.Tetelbom, *Mikroelektronika*, 13 (4), 269, (1984).
2. P.Grosse, *Trends in analytical chemistry*, 8 (6), 222 (1989).
3. M.Born, E.Wolf, *Principles of optics*, (Pergamon Press, Oxford, 1968)
4. K.Seeger, *Semiconductor physics*, (Springer-Verlag, Wien - New-York, 1973).
5. S.Adachi, *J. Appl. Phys.*, 58 (3), R1, (1985).

## Optical Characterization of InGaAs/InP Quantum Wires and Dots

S.Q. Gu, E. Reuter, Q. Xu, H. Chang, R. Panepucci, I. Adesida, S.G. Bishop  
Center for Compound Semiconductor Microelectronics, Materials Research Laboratory, and  
Beckman Institute, University of Illinois at Urbana-Champaign, Urbana, Illinois 61801  
C. Caneau and R. Bhat  
Bell Communications Research, Red Bank, New Jersey, 07701

### ABSTRACT

High resolution electron beam lithography and reactive ion etching in methane-hydrogen ( $\text{CH}_4/\text{H}_2$ ) plasmas have been used to fabricate InGaAs/InP open quantum well wires (QWW) with widths ranging from 200 to 40 nm and quantum dots (QD) with diameters ranging from 600 to 100 nm. Low temperature photoluminescence (PL) spectra were investigated in these nanostructures as a function of excitation intensity, wire width, and dot diameter. The peak emission of the dry-etched 40 nm wires is shifted to higher energies by about 2 meV as compared to 100 nm wires. This "open wire" result is consistent with results reported for buried InGaAs/InP wires of the same width. The blue-shift of the PL peak reaches 10 meV in QDs as their diameters decrease to 100 nm. The magnitude of the observed blue shift in the QDs is larger than the blue-shift predicted on the basis of quantum confinement for the same size dots.

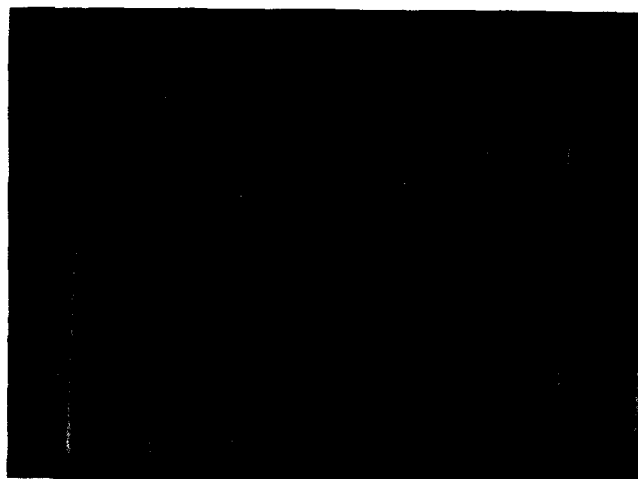
### INTRODUCTION

Non-equilibrium epitaxial growth techniques allow the fabrication of layered semiconductor heterostructures with bandgap profiles tailored on a monolayer scale to produce two-dimensional (2D) structures such as quantum wells and superlattices. The combination of 2D growth with nanometer-scale lateral patterning techniques enables the fabrication of lower dimensional mesoscopic structures such as quantum wires (1D)<sup>1</sup> and quantum dots (zero-dimensional). Quantum wires and dots have been fabricated from layered semiconductor quantum well heterostructures by a variety of techniques<sup>2-7</sup> in the past decade. In most cases, the quantum well structure is patterned by high resolution optical or e-beam lithography followed by dry or wet etching, impurity induced disordering, or selective epitaxy. The optical and electrical properties of such structures are often dominated by the effects of process-induced defects on the lateral surfaces or interfaces (sidewall effects). For example, the photoluminescence (PL) efficiency in dry-etched open wires and dots diminishes significantly with decreasing lateral dimension<sup>2</sup>, making it difficult to observe the spectral manifestations of lateral confinement (e.g. blue-shifts) expected in these nanostructures. Furthermore, for those cases in which blue-shifts of the PL peak energy position have been reported in etched wires and dots, the observed blueshifts can be much larger than the values expected from theoretical calculations of lateral confinement based on the physical width of the etched wire structures<sup>2,8,9</sup>.

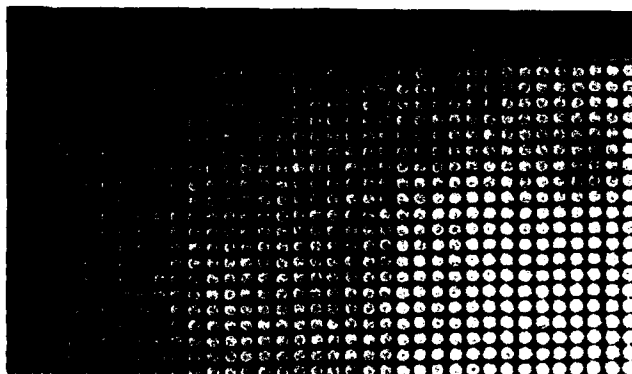
In the present work, the interaction between the effects of lateral confinement and the effects of process-induced defects have been investigated in InGaAs/InP nanostructures. High resolution electron beam lithography and reactive ion etching (RIE) in methane-hydrogen plasmas ( $\text{CH}_4/\text{H}_2$ ) have been used to fabricate InGaAs/InP open quantum well wires (QWW) with widths ranging from 200 to 40 nm and quantum dots (QD) with diameters ranging from 600 to 100 nm. The peak energy, efficiency and lineshape of the PL in these dry-etched quantum wires and dots have been investigated as functions of wire width, dot diameter and excitation laser power. The results show a blue-shift of PL peak energies and a rapid drop in PL intensity in QWWs with decreasing wire width below 100 nm. The magnitude of the observed blue shift is consistent with the results reported for buried InGaAs/InP wires of the same width. In the QDs with diameter less than ~100 nm, the PL intensity decreases dramatically and the PL peak energies exhibit a blue-shift with a magnitude much larger than the value predicted by theory for these dot sizes.

## DESCRIPTION OF EXPERIMENT

The fabrication procedure for the nanostructures investigated in the present work is identical to that described in our previously reported studies of InGaAs/InP QWWs<sup>10</sup>. Wires and dots were fabricated from a lattice-matched InGaAs/InP single quantum well heterostructure grown by metal-organic vapor phase epitaxy (MOVPE). The QW structure consisted of a 200 nm InP buffer layer grown on a semi-insulating InP substrate, followed by a 5 nm InGaAs quantum well layer and a 20 nm InP barrier (cap) layer. Samples were first coated by plasma-enhanced chemical vapor deposition (PECVD) with a 40 nm layer of SiO<sub>2</sub>, and then patterned by high resolution electron beam lithography, followed by a 30 nm Ti evaporation and lift-off. The Ti mask pattern was transferred into SiO<sub>2</sub> by CHF<sub>3</sub> RIE dry etching. Finally, open quantum wires were defined by a CH<sub>4</sub>/H<sub>2</sub> RIE to a depth of 50 nm through the InP/InGaAs quantum well. The masking materials were removed by wet etching with buffered hydrofluoric acid (HF).



(a)



(b)

Fig. 1 (a) SEM micrograph for 60 nm-wide InGaAs/InP quantum well wires; (b) SEM micrograph for 340 nm diameter quantum dots.

Figure 1a shows a SEM micrograph of 40 nm-wide wires, which have been patterned with 600 nm periodicity and etched to a depth of 50 nm. Figure 1b shows a SEM micrograph of 340 nm diameter, which have been patterned with 400 nm periodicity and etched to a depth of 50 nm. For each QWW width or QD diameter, an array of wires or dots is patterned and etched within a  $60\text{ }\mu\text{m} \times 60\text{ }\mu\text{m}$  field. For reference, non-etched QW control mesas were also reserved on the sample. The sample was cooled to 5 K in a variable temperature liquid helium cryostat, and PL was excited by separately illuminating each field of wires or dots with 514.5 nm Ar<sup>+</sup> laser light which was mechanically chopped at 80 Hz. PL spectra were analyzed by a 1 m focal length single grating monochromator and detected with a 77 K Ge pin photodiode and a lock-in amplifier.

## RESULTS AND DISCUSSION

Our previous studies<sup>10</sup> of QWWs demonstrated that many factors which are unrelated to quantum confinement or reduced dimensionality can influence the efficiency and spectral distribution of the PL. Phenomena which will broaden the high energy portion of the PL spectra with increasing excitation intensity include band filling in k-space, the flattening of band bending at sidewall interfaces<sup>11</sup>, and recombination in the narrower segments of QWWs. In contrast, the high electron-hole plasma (EHP) densities achieved at high excitation intensity can induce a pronounced red-shift of the low-energy edge of the emission band which can be attributed to the effects of band gap renormalization associated with many body effects in dense EHPs<sup>12</sup>. Therefore, it is important to obtain PL spectra from different samples (wires or dots) at constant excitation intensity, and ideally, at the lowest possible excitation intensity in order to make meaningful comparisons of PL peak position and line shape for nanostructures of different lateral dimensions.

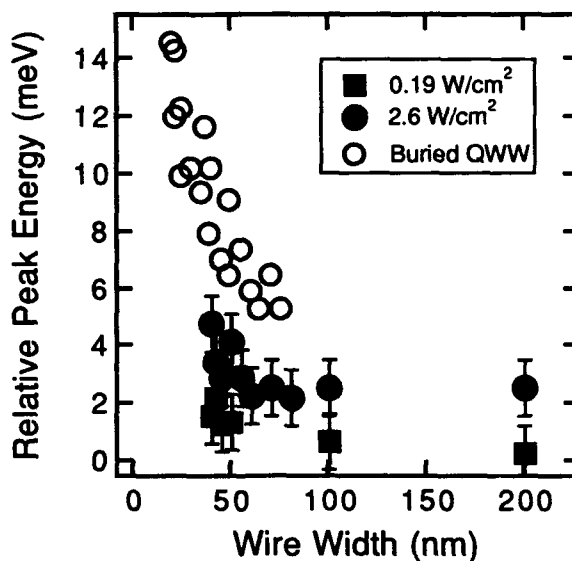


Fig. 2 The relative peak energies of PL spectra in InGaAs/InP QWWs as a function of wire width at 5 K. The solid symbols represent the present wires under two excitation intensities. The open symbols correspond to the reported data from buried wires with an arbitrary energy shift.



Figure 2 shows the peak energy in our InGaAs/InP QWWs as a function of wire width. For a factor of  $\sim 13$  increase in excitation intensity the two curves are displaced by about 2 meV in peak energy. In addition, both curves exhibit an apparent blue-shift as the wire width decreases below 100 nm, reaching a shift of approximately 2 meV for the 40 nm wires. The magnitude of this blue shift is consistent with results reported for buried InGaAs/InP wires<sup>3</sup> of the same width (shown in Fig. 2).

Figure 3 shows the peak energy in the InGaAs/InP QDs relative to the QW peak energy as a function of dot diameter. For dot diameters larger than 400 nm, no blue shift is observed in the QDs. However, the PL spectra exhibit a large blue shift with decreasing dot diameter below 240 nm, reaching a value of about 10 meV for the 100 nm diameter dots. This 10 meV blue-shift observed in the 100 nm QDs is much larger than the 3 meV blue-shift predicted theoretically on the basis of quantum confinement for this dot diameter. Similar behavior has been observed in PL studies of dry-etched open GaAs/AlGaAs and InGaAs/InP QWWs. This apparent discrepancy has been attributed by previous workers to a variety of effects including (i) strain relief of the lattice mismatch between the well and the barrier<sup>8</sup>; (ii) a change or transition in the recombination process from an extrinsic to an intrinsic transition as the wire width or dot diameter approaches the mean distance between impurities<sup>8</sup>; or (iii) an optically inactive layer near the sidewalls that reduces the effective quantum confinement size<sup>2</sup>.

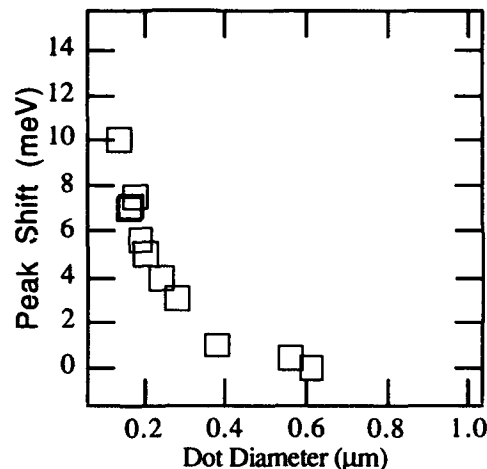


Fig. 3 The relative peak energies of PL spectra in InGaAs/InP QDs as a function of dots diameter at 5 K.

More recently Gustafsson et al<sup>9</sup> have proposed an explanation for the observation of the large blue shifts in QWWs and QDs in terms of the shifts of the PL spectra attributable to monolayer (ML) fluctuations in the QW thickness. Usually, photoexcited carriers or excitons in a QW diffuse laterally from the thinner to the thicker (lower effective band gap) portions of the QW layer before recombining radiatively. However, these workers proposed that the transfer of excitons from the thinner portions to the thicker areas within a single QW is significantly reduced or impeded by patterning the QW layer into QWW nanostructures. The PL spectrum produced by carriers constrained to recombine in thinner portions of the QW would be blue-shifted by an amount commensurate with the reduction in the QW thickness (in increments of one ML). They obtained cathodoluminescence (CL) spectra in InGaAs/InP QWWs fabricated

from QWs with thicknesses of 3, 10 and 20 MLs and found that for spectrally unresolved ML splittings the suppression of the exciton transfer in QWWs can broaden the luminescence peak and shift the peak to higher energies. This shift could be misinterpreted as a blue shift due to lateral quantum confinement. For the present QWWs, the above effect apparently does not play an important role, since the observed blue shift of the PL from the 40 nm wires is not inconsistent with theoretical predictions based on quantum confinement effects.

The proposal of Gustafsson et al should be equally valid for the case of a QW patterned into QDs. In a QW mesa or larger size QD, under low excitation intensity the photo-excited carriers within the thinner areas diffuse to the thicker portions (lowest band gap) before recombining. If the QW is patterned into small dots, some dots may lie entirely within the thinnest portion of the QW. For these dots, photo-excited carriers cannot diffuse to the thicker portion of the well before recombining. The probability that a significant number of the dots will lie entirely within the thinner portions of the QW increases with decreasing dot diameter. For the present QWs, having a thickness of ~16 MLs, a difference of 1 ML in the thickness corresponds to a peak energy splitting or shift of about 14 meV. If we assume that for the 100 nm diameter QDs, 50% of the dots occupy the thinner QW, there would be a blue shift of about 7 meV in the energy of the PL peak for these dots. This estimate is consistent with the 10 meV blue-shift of the PL observed in the 100 nm QDs. We may discuss the broadening of the PL spectra with decreasing dot size.

#### SUMMARY

Photoluminescence spectroscopy has been used to characterize InGaAs/InP QWWs and QDs fabricated by high resolution e-beam lithography and reactive ion etching. Low temperature PL spectra obtained from QWWs with widths ranging from 200 to 40 nm reveal a ~2 meV blue-shift in the spectral energy of the PL peak for the 40 nm wide QWWs. The magnitude of this shift is consistent with results reported for buried InGaAs/InP wires of the same width and with theoretical predictions based on the effects of lateral quantum confinement. The PL spectra from the QDs with diameters ranging from 600 to 100 nm exhibit a spectral blue shift which reaches a value of ~10 meV for the 100 nm diameter dots. This shift far exceeds the predictions of quantum confinement theory for dots of this diameter, and is consistent with excessively large blue shifts observed by other workers in dry-etched QWWs and QDs.

#### ACKNOWLEDGEMENTS

Partial support for this work is provided by the Office of Naval Research University Research Initiative N00014-92-J-1519, NSF Grant No. ECD 89-43166, NSF Grant No. DMR 89-20538, and JSEP Grant No. N00014-90-J-1270.

#### REFERENCES:

1. Y. Arakawa and H. Sakaki: *Appl. Phys. Lett.* **40**, 939 (1982).
2. A. Forchel, A. Menschig, B.E. Maile, H. Leier and R. Germann, *J. Vac. Sci. Technol. B*, **9**, 444 (1991).
3. M. Notomi, M. Naganuma, T. Nishida, T. Tamamura, H. Iwamura, S. Nojima, and M. Okamoto, *Appl. Phys. Lett.* **58**, 720 (1991).
4. Ch. Greus, L. Butov, F. Daiminger, A. Forchel, P.A. Knipp and T.L. Reinecke, *Phys. Rev. B* **47**, (1993).
5. K. Kash, R. Bhat, D.D. Mahoney, P.S.D. Lin, A. Scherer, J.M. Worlock, B.P. Vender Gaad, M. Koza and P. Grable, *Appl. Phys. Lett.* **55**, 413 (1987).
6. M. Tsuchiya, J.M. Gaines, R.H. Yan, R.J. Simes, P.O. Holtz, L.A. Coldren, and P.M. Petroff, *Phys. Rev. Lett.* **62**, 466 (1989).
7. J.S. Weiner, J.M. Calleja, A. Pinczuk, A. Schmeller, B.S. Dennis, A.R. Goni, L.N. Pfeiffer,

- and K.W. West, Appl. Phys. Lett. **63**, 237 (1993)
8. A. Izrael, B. Sermage, J.Y. Marzin, A. Ougazzaden, R. Azoulay, J. Etrillard, V. Thierry-Mieg, and L. Henry, Appl. Phys. Lett. **56**, 830 (1990).
  9. A. Gustafsson, X. Liu, I. Maximov, L. Samuelson, and W. Seifert, Appl. Phys. Lett. **62**, 1709 (1993).
  10. S.Q. Gu, E. Reuter, Q. Xu, H. Chang, R. Panepucci, I. Adesida, S.G. Bishop, C. Caneau and R. Bhat, to be published.
  11. F. Hirler, R. Kuchler, R. Strenz, G. Abstreiter, G. Bohm, J. Smoliner, G. Trankle and G. Weimann, Surface Science **263**, 536 (1992)
  12. V.D. Kulakovskii, E. Lach, A. Forchel and D. Grutzmacher, Phys. Rev. B **40**, 8087 (1989).

## PHOTOREFLECTANCE STUDY OF MODULATION-DOPED GaAs/GaAlAs QUANTUM DOTS FABRICATED BY REACTIVE-ION ETCHING

P.D. WANG\*, C.M. SOTOMAYOR TORRES<sup>\*,†</sup>, M.C. HOLLAND\*, H. QIANG<sup>\*\*,†</sup>, F.H. POLLAK<sup>\*\*,†</sup> and G. GUMBS<sup>\*\*\*</sup>

<sup>\*</sup>Department of Electronics and Electrical Engineering, University of Glasgow, Glasgow, G12-8QQ Scotland

<sup>†</sup> Royal Society of Edinburgh Research Fellow

<sup>\*\*</sup>Physics Dept., Brooklyn College of CUNY, Brooklyn, NY, 11210 USA

<sup>\*\*\*</sup> Physics Dept., Hunter College of CUNY, New York, NY, 10021 USA

### ABSTRACT

Using contactless photoreflectance at 300K and 77K we have investigated the intersubband transitions from two modulation-doped GaAs/GaAlAs quantum dot (QD) arrays fabricated by reactive-ion etching (RIE). The samples consisted of 8 nm decoupled GaAs/GaAlAs quantum wells with dot sizes (lateral dimensions) of 60 and 100 nm. The lineshapes of the "1C-1H" and "1C-1L" features were indicative of a screened exciton, i.e., the derivative of a broadened two-dimensional density of states (step function), due to the presence of the electron gas. On the other hand, even at 300K the "2C-2H" features exhibited a well-defined sharp excitonic lineshape, i.e., derivative of a Gaussian profile. Even at room temperature it is possible to detect the effects of the lateral quantum confinement. We have observed a 2 meV blue shift of the "2C-2H" feature of the 60 nm QD array in relation to the 100 nm QD array. At 77K we have found evidence for a "parabolic-like" in-plane confining potential on the smaller QD array. This experiment demonstrates the considerable utility of PR in studying these reduced dimensional systems.

### INTRODUCTION

There has recently been considerable activity in the field of reduced dimensional system nanostructures such as quantum wires and dots (QD) from both fundamental and applied perspective [1-6]. Considering the huge success of physics and devices based on two-dimensional (2D) semiconductor systems (i.e., quantum wells, superlattices, heterojunctions), there has been a natural trend to continue to diminish systems' dimensionality. These reduced dimensional nanostructures exhibit interesting properties involving singularities in the density-of-states and unique transport phenomena [1,2]. For quantum dots evidence has been found for a "parabolic-like" in-plane confining potential [1], as opposed to the square well potential along the growth direction. Interesting new transport phenomena such as Coulomb blockade has been demonstrated [1,7]. New optical applications include low threshold, high yield laser structures and photodetectors [3-5].

One (1D) and zero (0D)-dimensional systems can be formed in several ways. For, example, 2D structures are easily obtained in the growth direction by thin film methods such as molecular beam epitaxy (MBE) or organometallic chemical vapor deposition. Therefore, an obvious way to obtain quantum wires (1D) and dots (0D) is to pattern usual 2D heterostructures such as quantum wells with nanoscale lithographic techniques [8,9]. The dry reactive-ion etching (RIE) method has drawn much attention for larger processing depth of abrupt potential barriers, excellent control on lateral size, and ability to fabricate complicated shapes [8]. This technique

can now routinely produce nanostructures of scale about 100 nm.

The lateral confinement of QDs is expected to bring about dramatic changes in the transport properties and in addition to the optical features. If one restricts the particles to narrow lines or dots (boxes), further quantization can occur as compared with the 2D situation. In such a 0D system with cylindrical symmetry the electron (hole) energy levels will be characterized by three quantum numbers, i.e.,  $n_z C[H(L)]$ ,  $n_x C[H(L)]$  and  $n_y C[H(L)]$ . For example,  $n_z C[H(L)]$  corresponds to the conduction (C) or heavy(H)/light(L)-hole subbands along the growth (z)-direction, while the other two quantum numbers specify the in-plane quantization. If the lateral dimension is substantially larger than  $L_z$  (the confinement dimension along the z-direction), there will be (a) a ladder of small levels ( $n_x$ ,  $n_y$ ) formed within the subband ladder of well separated transitions corresponding to 2D quantization ( $n_z$ ) along the z-direction and (b) these "2D" levels will be blue-shifted. A size of about 100 nm, which is bigger than the Bohr radius in GaAs, makes it difficult to observe these effects in optical experiments, particularly interband transitions, as compared to the resolution of low temperature transport measurements.

Despite the proven value of modulation spectroscopy, particularly contactless modes such as photoreflectance (PR) in studying 2D systems [10,11] there has been very little work done on 1D or 0D nanostructures. Photoreflectance has been used to study 1D SiGe/Si quantum wires [12] and the effects of RIE on large ( $\approx 0.5 \mu\text{m}$ ) GaAs/GaAlAs QD arrays [13]. Several authors have measured the electrotransmission spectra of  $\text{CdS}_x\text{Se}_{1-x}$  nanocrystals embedded in a glass matrix [14].

In this paper we report a PR investigation at 300K and 77K of the intersubband transitions from two modulation-doped GaAs/GaAlAs QD arrays fabricated by RIE. The samples consisted of 8 nm decoupled GaAs/GaAlAs quantum wells with dot sizes (lateral dimensions) of 60 and 100 nm. The lineshapes of the "1C-1H"/"1C-1L" features were indicative of a screened exciton, i.e., the derivative of a broadened 2D density of states (step function), due to the presence of the electron gas (EG). The notation  $m_z C-n_z H(L)$  denotes a transition between the  $m_z^{\text{th}}$  conduction and  $n_z^{\text{th}}$  valence subbands of heavy (light)-hole character. Rigorously speaking the notation should include three quantum numbers for both the electrons and holes because of the effects of the lateral confinement. In this paper we use " $m_z C-n_z H(L)$ " to indicate the quasi-2D transitions.

In contrast to the "1C-1H"/"1C-1L" resonances, the "2C-2H" features exhibited a well-defined sharp excitonic lineshape, i.e., derivative of a Gaussian profile. Even at room temperature it is possible to detect the effects of the lateral quantum confinement, a 2 meV blue shift of the "2C-2H" feature of the smaller QD array in relation to the larger material. At 77K the "2C-2H" feature of the 60 nm QD array exhibits oscillatory features, i.e., the  $n_x$ ,  $n_y$  ladder. Comparison with a first-principles, many-body calculation provides evidence for a "parabolic-like" in-plane confining potential. This experiment demonstrates the considerable utility of PR in studying these reduced dimensional systems.

## EXPERIMENTAL DETAILS

The PR apparatus has been described in the literature [10,11]. The pump beam was the 6328Å line of a He-Ne laser chopped at 200 Hz. The sample used in this study was grown by MBE on a (001) semi-insulating GaAs substrate with a  $1 \mu\text{m}$  not-intentionally doped GaAs buffer. The active region was a  $0.58 \mu\text{m}$  thick multiple quantum well structure (MQW) structure which consisted of the following layers repeated 10 times: a 30 nm GaAlAs layer, a Si  $\delta$ -doping layer ( $2 \times 10^{12} \text{ cm}^{-2}$ ), 20 nm of a GaAs(0.85 nm)/AlAs(0.85 nm) superlattice structure, and a 8 nm GaAs quantum well (QW) region. There was a 17 nm GaAs cap on top of the entire

structure. Shubinikov-de Haas measurements indicated that the EG density in the GaAs QWs corresponded to a "two-dimensional" concentration of  $8.5 \times 10^{11} \text{ cm}^{-2}$ . The adoption of the asymmetric barrier growth pattern was to compensate the different properties of MBE grown GaAs/AlAs and AlAs/GaAs interfaces, and was shown to produce more symmetric well potential profile [8]. The dots were fabricated by RIE using  $\text{SiCl}_4$  [8]. The dot arrays formed a square lattice pattern, with the separation between neighbouring dots being 4 times the individual dot diameter. The samples reported in this work include 60 nm and 100 nm QD arrays. They were fabricated with a single mask on the same mesa, each measuring 1 mm by 4 mm separated by a 1 mm gap.

## EXPERIMENTAL RESULTS

Displayed in Fig. 1 are the PR spectra of the two QD arrays at 300K. The structure around 1.42 eV is from the direct gap,  $E_0$ , of the GaAs buffer/substrate while the peak at around 1.8 eV is  $E_0$  from the GaAlAs portion of the sample, which makes it possible to evaluate an Al composition of 27%.

The signal around 1.5 eV is quite unusual for modulation spectroscopy from a QW system. Such traces generally exhibit sharp, derivative-like features (i.e., positive and negative lobes) associated with excitons, even at 300K. In addition, these reported lineshapes are symmetric [10,11].

The 1.5 eV traces of Fig. 1 lie on only one side of the baseline. The signal around 1.5 eV corresponds to the screened " $1C-1H$ "/" $1C-1L$ " excitonic transitions. The screening is due to the presence of the EG. We have recently observed similar signals in PR associated with the 2D EG in GaAlAs/InGaAs/GaAs modulation-doped QWs [10,15]. Such lineshapes were accounted for on the basis of the first-derivative of a broadened step-like 2D density of states (due to the screening of the exciton) times a Fermi level filling factor [10,15].

Near 1.6 eV there is a sharp derivative-like feature originating from the " $2C-2H$ " transitions in the QWs. The energy position can be obtained accurately from a lineshape fit. The sharpness of these " $2C-2H$ " features is an indication (a) of the high quality of the QD arrays and (b) the absence of screening by the EG. The fact that we do not observe any "symmetry-forbidden" transitions (e.g.,  $m_c \neq n_c$ ) is indicative of the symmetric nature of the band profile.

We have made a detailed comparison the 1.6 eV features at 300K in the two QD arrays, as shown by the solid (100 nm QDs) and dashed (60 nm QDs) lines in Fig. 2. Note that there is a blue-shift of the smaller dot size in relation to the other sample. The obtained energy positions from the lineshape fits (dotted lines) are denoted by arrows at bottom of the figure. A 2 meV blue shift of this feature is observed. This shift is obvious in Fig. 2 even without any lineshape fit, owing to the very narrow excitonic nature of the " $2C-2H$ " features. This observed blue-shift is evidence for the lateral quantum confinement effects on the smaller dot size sample,

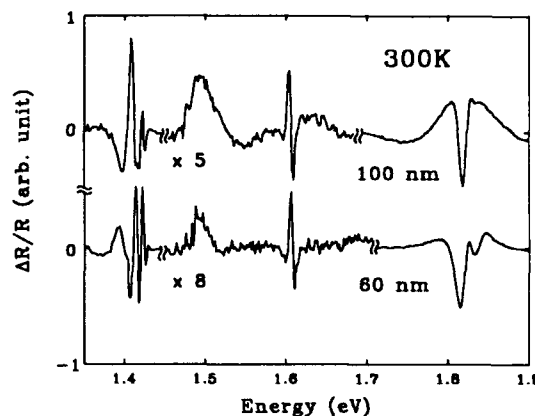


Fig. 1 Room temperature PR spectra of the 100 nm and 60 nm GaAs/GaAlAs QD arrays.

as will be discussed below.

Shown in Fig. 3 is the experimental PR trace of the 60 nm QD structure at 77K. The whole spectrum has been blue shifted in relation to the data of Fig. 1 due to the temperature dependence of the band structure of the constitute materials. Notice the enhancement of the series of features around 1.7 eV. We have found them to be reproducible. One possible explanation of these oscillatory features in this nanostructure might be Franz-Keldysh oscillation effects. If this were the case a plot of extrema index number  $l$  should be linear in  $(E_l - E_{2C-2H})^{3/2}$ , where  $E_l$  is the energy of the  $l^{th}$  extrema [10,11]. However, we find a linear relationship with  $(E_l - E_{2C-2H})$ , as shown in Fig. 4. As discussed below we interpret this observation in terms of the "parabolic-like" in-plane confining potential, as opposed to the square well potential along the growth direction. The "1C-1H"/"1C-1L" feature does not exhibit such oscillations because of the screening effects of the EG which occupies the 1C level.

## DISCUSSION

In Fig. 2, we show clearly that there is a blue shift of the lowest "2C-2H" feature of the 60 nm sample with respect to the 100 nm QD array. This is due to the lateral size confinement. We can make a rough estimation of this effect. For a 2D box with infinite barriers (we shall see below that this is not rigorously correct), the energy difference ( $\Delta E$ ) of the 0D "ground state" (i.e.,  $n_x = n_y = 1$ ) of the quasi-2D "2C-2H" feature between two QDs of different lateral sizes,  $a_1$  and  $a_2$ , is:

$$\Delta E \approx (\hbar^2 \pi^2 / \mu) [(1/a_1)^2 - (1/a_2)^2]$$

where  $\mu$  is the in-plane reduced interband effective mass.

Using,  $\mu=0.074$  (in units of free electron mass) of GaAs,  $a_1 =$

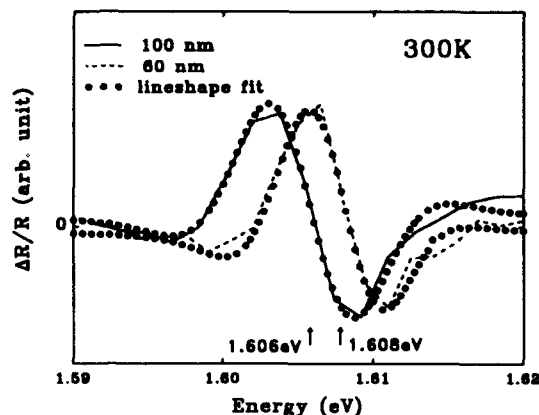


Fig. 2 Experimental PR spectra at 300K in the region of "2C-2H" for the 100 nm (solid line) and 60 nm (dashed line) QD arrays. The dotted curves are lineshape fits.

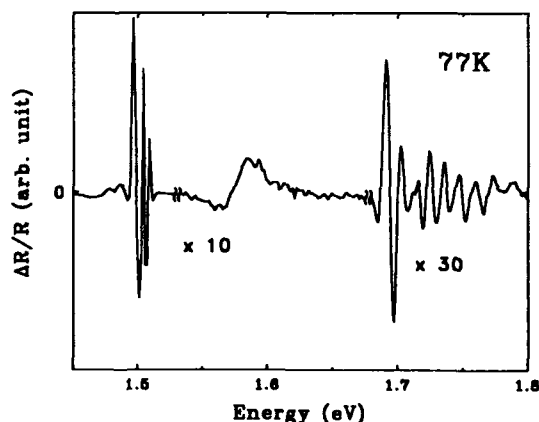


Fig. 3 PR spectrum of the 60 nm QD array at 77K.

60 nm, and  $a_2 = 100$  nm, we can deduce a value  $\Delta E \approx 1.8$  meV, which is in excellent agreement with the experimental data. The room temperature observation of this 2 meV energy shift is a consequence of the derivative nature of PR and the high quality of the small dimension QD arrays.

As discussed earlier, further evidence for the effects of lateral confinement are the oscillatory structures above "2C-2H" in the 77K data of the 60 nm dot array. These are the manifestations of the in-plane quantization. The fact that the extrema index scale linearly with energy is strongly suggestive of a "parabolic-like" in-plane potential, which produces evenly spaced, harmonic oscillator ladders in the  $m_z^{\text{th}}(n_z^{\text{th}})$  conduction (valence) levels [1].

In order to confirm this interpretation we have performed a first-principles, many-body calculation of the absorption coefficient and its derivative (with respect to photon energy) for an array of quantum dots having the characteristics of the 60 nm array sample. The theory which we have done for the interband absorption characterization of quantum dots includes the depolarization shift due to electron-electron interaction, impurity scattering, and the effect due to interface imperfection.

Harmonic potentials have been used to simulate lateral confinement of quantum dots. We have derived a self-consistent field theory for the infrared absorption of polarized or unpolarized incident light in this system. Many of the observed features of the oscillatory portion of the PR spectrum of Fig. 3 are reproduced in our theory. The features in the absorption spectrum are significantly amplified. The thermal broadening of the peaks sensitively depends on the electron density and the temperature. Based on the known temperature in the experiment, it gives us a convenient way of determining the number of electrons in each dot by fitting the thermally-broadened lineshape. Excellent agreement has been found between the results of the theory and the oscillatory features above "2C-2H" in Fig. 3. The details of this work will be the subject of a future publication.

## SUMMARY

This investigation has shown the considerable utility of PR, which is not only contactless but requires no special mounting of the sample, as a valuable tool in studying nanostructure systems such as QDs. Since the lateral dimensions of current lithographic technology produce confinements which result in meV band edge shifts, a high resolution optical technique, such as PR, is essential in order to study the phenomenon associated with lateral confinement. Even at 300K we have been able to evaluate the blue-shift due to the lateral confinement. In addition, the derivative-like nature of PR also has revealed oscillatory features at 77K which can be accounted for on the basis of a "parabolic-like" in-plane potential. Good agreement has been

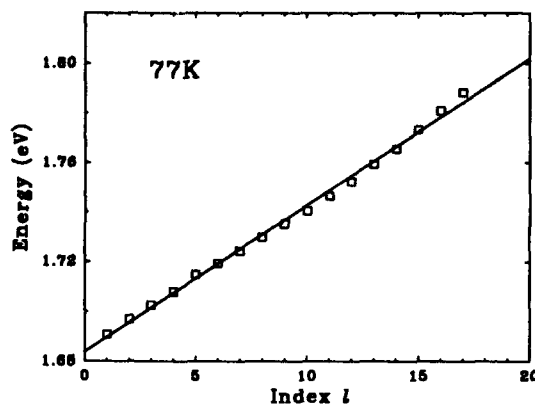


Fig. 4 The energies of the oscillatory features above "2C-2H" at 77K as a function of extrema index number  $l$ .



found between experiment and a first-principles, many-body theoretical calculation of the effects of this in-plane potential.

#### ACKNOWLEDGEMENTS

The authors HQ and FHP acknowledge the support of NSF grant #DMR-9120363, the Olympus Corporation, PSC/CUNY grant #664239 and NATO travel grant 5-2-05/RG-920115. The authors PDW, CMST and MCH received support from the UK Science and Engineering Research Council grant #GR/H44714. They also acknowledge the NATO travel grant. The work of GG was supported in part by PSC/CUNY grant #662505. We wish to thank Dr. E. Skuras for the electrical characterization of the samples.

#### REFERENCES

1. D. Heitmann and J.P. Kotthaus, Physics Today, Vol.46, No. 6, p.56, June 1993; D. Heitmann, T. Demel, P. Grambow, M. Kohl and K. Ploog, Proc. 20<sup>th</sup> Int. Conf. Physics of Semiconductors, Thessaloniki, 1990, ed. E.M. Anastassakis and J.D. Joannopoulos (World Scientific, Singapore, 1990) p. 13.
2. C. Weisbuch and B. Vintner, Quantum Semiconductor Structures: Fundamentals and Applications (Academic, New York, 1991).
3. E. Kapon, D.M. Huang and R. Bhat, Phys. Rev. Lett. **63**, 430 (1989).
4. H. Benisty, C.M. Sotomayor Torres and C. Weisbuch, Phys. Rev. **B42**, 8947 (1991).
5. H. Benisty, in Phonons in Semiconductor Nanostructures, eds J-P. LeBurton, J. Pascual and C.M. Sotomayor Torres (Kluwer, Dordrecht, 1993) p. 447.
6. P.D. Wang and C.M. Sotomayor Torres, J. Appl. Phys. **74**, 5047 (1993).
7. M.A. Kastner, Physics Today, Vol. 46, No. 1, p. 24, Jan. 1993.
8. C.M. Sotomayor Torres, A.P. Smart, M.A. Foad and C.D.W. Wilkinson, Festkörperprobleme/Advances in Solid State Physics, Vol. 32, ed. U. Rössler (Vieweg, Braunschweig/Weisbaden, 1992) p. 265.
9. R. Cheung, S. Thoms, M. Watt, M.A. Foad, C.M. Sotomayor Torres, C.D.W. Wilkinson, U.J. Cox, R.A. Cowley, C. Dunscombe and R. H. Williams, Semicond. Sci. Technol. **7**, 1189 (1992).
10. F. H. Pollak and H. Shen, Materials Science and Engineering R: Reports **R10**, 375(1993).
11. O. J. Glembocki and B. V. Shanabrook, Semiconductors and Semimetals, Vol. 67, ed. D.G. Seiler and C.L. Littler (Academic, New York, 1992) p. 222.
12. Y-S. Tang, C.D.W. Wilkinson, C.M. Sotomayor Torres, D.W. Smith, T.E. Whall and E.H.C. Parker, Superlattices and Microstructures **12**, 535 (1992); also, Solid State Comm. **85**, 199 (1993).
13. H. Qiang, F. H. Pollak, Y. Tang, P.D. Wang, and C.M. Sotomayor Torres, submitted to Appl. Phys. Lett.
14. G. Mei, S. Carpenter, L.E. Felton and P.D. Persans, J. Opt. Soc. Am. **B9**, 1394(1992); P.D. Persans, M. Silvestri, G. Mei, E. Lu, H. Yuselici and J. Schroeder, Brazilian J. Phys. **23**, 144 (1993); F. Hache, D. Ricard and C. Flytzanis, Appl. Phys. Lett. **55**, 1504 (1989).
15. Y. Yin, H. Qiang, F.H. Pollak, D.C. Streit and M. Wojtowicz, Appl. Phys. Lett. **61**, 1579(1992); Y. Yin, H. Qiang, D.Yan, F.H. Pollak and T.F. Noble, Semicon. Sci. Technol. **8**, 1599(1993).

## **Raman and Photoluminescence Characterization of FIB Patterned AlGaAs/GaAs Multiple Quantum Wells**

Ahn Goo Choo, Xuelong. Cao, Spirit Tlali, and Howard E. Jackson  
*Department of Physics, University of Cincinnati, OH 45221-0011*

and  
Peter Chen, Andrew J. Steckl, and Joseph T. Boyd  
*Department of Electrical and Computer Engineering, University of Cincinnati,  
OH 45221-0030*

### **Abstract**

Raman and photoluminescence (PL) spectra have been used to characterize  $\text{Al}_{0.3}\text{Ga}_{0.7}\text{As}/\text{GaAs}$  multiple quantum well (MQW) structures that have been patterned by focused ion beam (FIB) implantation followed by rapid thermal annealing (RTA). Microprobe Raman scattering is used to identify the appropriate RTA and FIB implantation conditions that provide for removal of implantation-induced damage and for compositional intermixing. FIB patterned wire-like structures are characterized by spatially resolved PL spectra.

### **Introduction**

Selective intermixing of MQWs is of particular interest for fabrication of such structures as channel waveguides, index-modulation gratings and index-guided diode lasers, and for the study of low dimensionality effects in quantum well wires and quantum dots. FIB implantation and RTA are very useful techniques for obtaining these structures using the direct-writing capability of FIB.<sup>1,2</sup> The basic idea is that the bandgap and thus the refractive index is modified upon intermixing. Spatially resolved Raman and PL spectra were found to be simple and nondestructive methods to characterize these structures. Microprobe Raman employs an optical microscope to illuminate the sample and collect the scattered light. Therefore its spatial resolution is limited by the optics to 0.8  $\mu\text{m}$  at room temperature. The spatial resolution for PL at low temperature is measured to be 1.3  $\mu\text{m}$ . Raman and PL spectra obtained with a spatial scanning capability is used to study patterned wire-like structures. Raman scattering is used to characterize implantation-induced damage as well as the Al concentration change after intermixing. PL spectroscopy is used to characterize the change in subband energy and impurity levels formed by implanted ions. We use spatially resolved Raman and PL spectra to characterize FIB implantation-induced damage and local compositional intermixing in patterned wire-like structures.

## Experiment

The sample used in this work were  $\text{Al}_{0.3}\text{Ga}_{0.7}\text{As}/\text{GaAs}$  MQWs consisting of 29 periods of the same well and barrier width of 3.5 nm, sandwiched between a 50 nm  $\text{Al}_{0.3}\text{Ga}_{0.7}\text{As}$  cap and a 30 nm single quantum well (SQW) on a 1  $\mu\text{m}$   $\text{Al}_{0.3}\text{Ga}_{0.7}\text{As}$  buffer layer grown on (100) GaAs substrate. The patterned structure is shown in Fig. 1. For FIB implantation of the sample we used a  $\text{Ga}^+$  ion beam of 120 keV energy with a dose of  $1 \times 10^{14} \text{ cm}^{-2}$ . The RTA condition was 950°C for 10 sec. The width of the implanted regions was 3  $\mu\text{m}$ , and the spacing between them was 1  $\mu\text{m}$ .

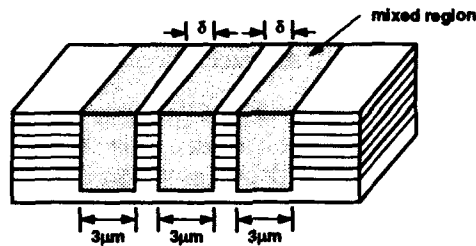


Fig. 1. Schematic of FIB patterned MQW structure.

Spatially resolved Raman and PL spectra were used to characterize the patterned wire-like structures. The 514.5 nm line of  $\text{Ar}^+$  laser is used to excite the sample, and the 0.1  $\mu\text{m}$  spatial scanning capability of an inchworm stage was employed.

## Results and Discussion

The Raman spectrum of an as-grown sample is shown in Fig. 2(a). The two peaks observed at  $280 \text{ cm}^{-1}$  and  $292 \text{ cm}^{-1}$  are the GaAs-like longitudinal optical (LO) phonons from the cap and the  $\text{AlGaAs}$  barrier layers of MQW region, and GaAs LO phonon from the GaAs well layers of MQW region, respectively. The peak at  $378 \text{ cm}^{-1}$  is the  $\text{AlAs}$ -like peak from the cap and the barrier layers. The peak positions depend on the Al concentration.<sup>3</sup> By monitoring the peak position after each process, the change in Al concentration can be obtained. Two small peaks seen on the left sides of the peaks are transverse optical (TO) phonon modes which are not allowed by the selection rule in the backscattering geometry of (001) zinc-blende-type structure, but are present because of some disorder. Following RTA only (Fig. 2(b)), the GaAs peak shifts down by  $1.1 \text{ cm}^{-1}$  which corresponds to a small amount of interdiffusion. The broad Raman peaks from the implanted sample, as shown in Fig. 2(c), resemble a phonon density of states due to heavy disorder. Subsequent RTA removes implantation-induced damage as shown

in Fig. 2(d). The  $292\text{ cm}^{-1}$  peak moved to  $285.4\text{ cm}^{-1}$ , corresponding to complete compositional intermixing. These measurements provide direct evidence that selective intermixing induced by FIB implantation and subsequent RTA has been achieved.

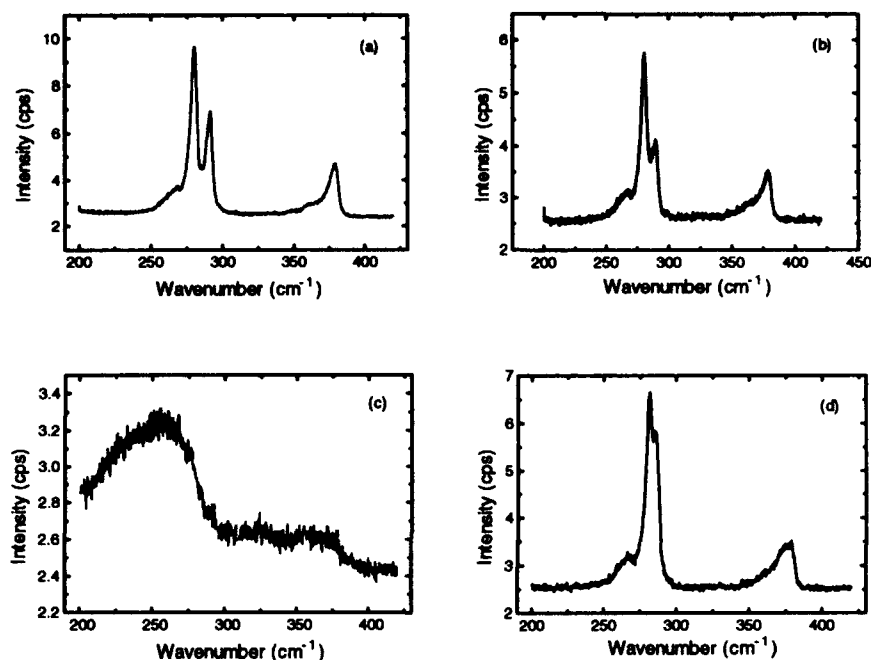


Fig. 2. Raman spectra from an  $\text{Al}_{0.3}\text{Ga}_{0.7}\text{As}/\text{GaAs}$  MQWs. (a) as-grown, (b) after RTA, (c) after FIB implantation, and (d) after FIB implantation and subsequent RTA.

Consider intermixing in a single quantum well in which the well of smaller gap energy is sandwiched by the barriers of larger gap energy. After partial intermixing a step function profile of band structure has changed to an error function band structure. Therefore, the interband transition energy increases due to two effects, an increase in the Al concentration within the well and a decrease in the effective well width. As mentioned above, the change in the Al concentration can be directly obtained by monitoring the Raman peaks. The change in energy of the subband transition is measured by the shift of the PL peak position. Therefore, the combination of Raman and PL spectra can be used to characterize the whole process of intermixing, including the effective well width, in single quantum wells and MQWs.

Spatially-resolved low temperature PL spectroscopy was used to characterize FIB patterned wire-like structures. The peak position in the PL spectra corresponds to the subband transition energy between an electron and a heavy hole. An example is shown in Fig. 3 where two peaks are observed, one from the MQW region and another from a single quantum well after the sample had undergone RTA. The MQW peak position is shifted just a few meV

compared to the as-grown sample. After implantation, no PL signals were measured in any wire-like structure due to implantation-induced heavy disorder as shown in Fig. 2(c). Following RTA, both the MQW and SQW peaks are recovered. Two peaks appear (instead of one) from the MQW region of the 1  $\mu\text{m}$  wire-like structure as shown in Fig. 4(c). This spectrum was obtained from the center of an implanted stripe. When the excitation spot was moved to the position between the implanted stripes, the lower energy peak grew relative to the higher energy peak (Fig. 4(b)), indicating that these excitons are in an unmixed region..

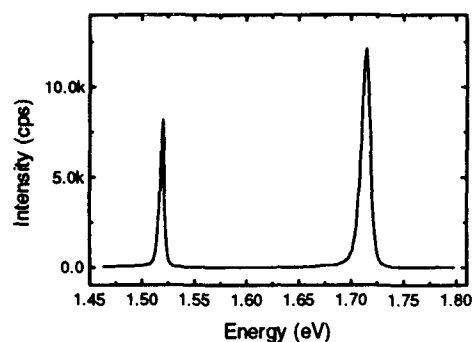


Fig. 3. PL spectrum (4.2 K) of an as-grown sample after RTA: the peak at higher energy is from MQW region and the one at lower energy is from a single quantum well.

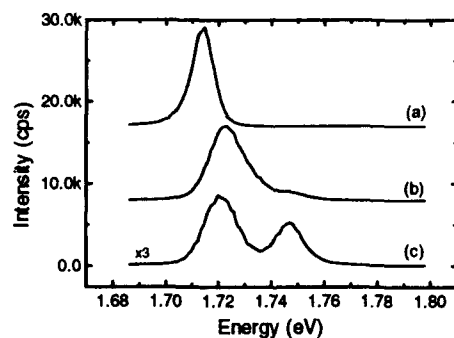


Fig. 4. PL spectra of MQWs (a) after RTA, and obtained (b) between the implanted stripes and (c) from the implanted stripe after FIB implantation and subsequent RTA.

To confirm further the locations of these peaks the excitation spot was scanned across the implanted stripes at a fixed energy. As shown in Fig. 5, The periodic structure obtained by spatial scanning at an energy of 1.748 eV has the opposite phase to that obtained at an energy of 1.723 eV, suggesting that the peak position at higher energy corresponds to the transition

energy in compositionally intermixed regions by FIB implantation and subsequent RTA, and the peak at lower energy corresponds to the exciton recombination energy between the implanted strips. Thus PL measurements with a spatial scanning capability can provide information on selective compositional intermixing of patterned wire-like structures.

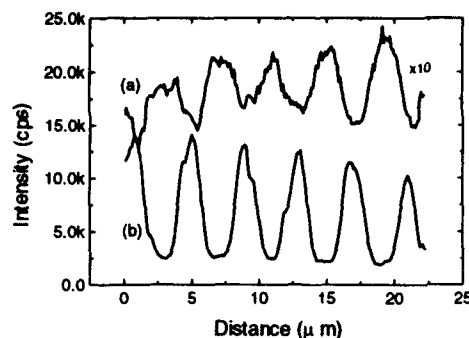


Fig. 5. The spatial scan of PL (a) at the energies of 1.748 eV and 1.723 eV.

We have also used spatially and temporally resolved photoluminescence measurement techniques to study exciton lifetimes and the in-plane transport of excitons.<sup>45</sup> The sample is excited by 5 picosecond laser pulses. In this case the positions of both the excitation spot and the sample are fixed. The spectrometer position was fixed at the energy corresponding to the exciton recombination energy between the implanted regions. The collected image is projected through scanning optics onto the spectrometer slit in order to obtain spatially resolved PL intensity. A three axis plot obtained at relatively high laser power is shown in Fig. 6. This plot suggests that the FIB patterned MQW has periodic compositional intermixing across the implanted stripes, indicating a kind of lateral confinement.

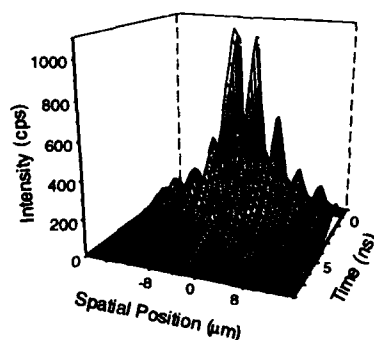


Fig. 5. Spatially and temporally resolved PL from patterned wire-like structures.

### Summary

Spatially resolved Raman and PL spectra has been used to characterize wire-like structures fabricated by using FIB implantation and subsequent RTA to produce compositional intermixing. Raman scattering is used to observe FIB implantation-induced damage and the change in Al concentration and to determine the suitable conditions for forming the patterned wire-like structures. PL measurements show the periodic modulation of the energy bands in the lateral direction suggesting exciton confinement is provided by these FIB compositionally mixed structures.

### Acknowledgements

We gratefully acknowledge the support of the National Science Foundation (ECS 9113244) and the Materials Directorate, Wright Laboratory, Wright-Patterson Air Force Base.

### References

1. M. Kumar, V. Gupta, G. N. Debrabander, P. Chen, J. T. Boyd, A. J. Steckl, A. G. Choo, H. E. Jackson, R. D. Burnham, and S. C. Smith, IEEE Photonics Tech. Lett. **4**, 435 (1993).
2. M. C. Wu, M. M. Boenke, S. Wang, W. M. Clark, E. H. Stevens, and M. W. Utlaut, Appl. Phys. Lett. **53**, 265 (1988).
3. S. Adachi, J. Appl. Phys. **58**, R1 (1985).
4. X. L. Cao, A. G. Choo, L. M. Smith, H. E. Jackson, P. Chen, and A. J. Steckl, this conference.
5. G. D. Gilliland, D. J. Wolford, G. A. Northrop, M. S. Petrovic, T. F. Kuech, and J. A. Bradley, J. Vac. Sci. Tech. B **10**, 1959 (1992).

## INFLUENCE OF GROWTH CONDITIONS ON THE MODULATION MECHANISM OF PHOTOREFLECTANCE SPECTRA OF SINGLE InGaAs/InAlAs QUANTUM WELLS

Y. BALTAGI\*, C. BRU\*, T. BENYATTOU\*, M. A. GARCIA-PEREZ\*, G. GUILLOT\*,  
M. GENDRY\*\*, J. L. LECLERCQ\*\*, V. DROUOT\*\* AND G. HOLLINGER\*\*

\* Laboratoire de Physique de la Matière (URA CNRS 358) - INSA de Lyon - 69621 Villeurbanne  
Cedex, France.

\*\* LEAME (URA CNRS 848) - Ecole Centrale de Lyon, 69131 Ecully Cedex, France.

### ABSTRACT

Using Photoreflectance (PR) measurements, we have investigated In<sub>0.53</sub>Ga<sub>0.47</sub>As single quantum wells (SQW) with In<sub>0.52</sub>Al<sub>0.48</sub>As barriers grown by MBE on InP substrates. Unusual lineshapes of PR spectra are observed for the fundamental transition in some of the SQW. This phenomenon is shown to be independent on the widths of both the SQW (5nm or 10nm) and the surface barrier layer (between 65nm and 300nm). PR spectra are recorded at different temperatures and in different samples, as well as with a secondary pump laser beam. From these measurements, it is concluded that interface defects exist in the SQW grown at 525°C without growth interruption. Such defects are clearly evidenced in room temperature PR experiments and confirmed by PL measurements.

### INTRODUCTION

The InGaAs/InAlAs system lattice-matched to InP has attracted great interest [1-3] because of its promising applications in microelectronics and optoelectronics. However the growth conditions (growth temperature, growth interruption at the quantum well interface) of the InAlAs layer remain the key point for a good layer quality as well as for low interface roughness in such InP based quantum devices. Low temperature photoluminescence studies are generally used to assess the quality of layers. In this paper we have performed extensive PR studies of InGaAs/InAlAs single quantum wells (SQW) at room temperature as well as at low temperature and shown that this technique is very powerful to get information about the quality of the layers and on the different scattering mechanisms which interfere on carrier transport.

### EXPERIMENTAL

Our experimental setup is conventional, with a 12mW HeNe laser as the pump beam and a 150W Quartz Tungsten Halogen lamp as the probe beam. The pump laser beam is chopped at 310Hz and the probe light beam is dispersed through a 0.64m Jobin-Yvon monochromator. A second continuous laser beam (Argon laser) can be superimposed for the purpose of double beam experiments. The signal is detected by a Si or Ge photodiode. For low temperature measurements, we use a variable temperature Helium gas cryostat. The sensitivity of our experimental setup is about 10<sup>-6</sup>.

The SQW were grown by Molecular Beam Epitaxy (MBE) on [100] InP substrates. Each of them consists of a In<sub>0.53</sub>Ga<sub>0.47</sub>As SQW embedded in In<sub>0.52</sub>Al<sub>0.48</sub>As barrier material lattice-matched to InP. A 400nm thick In<sub>0.52</sub>Al<sub>0.48</sub>As buffer layer was grown at 525°C. The growth temperature of the remaining layers was then either 450°C or 525°C and the top barrier InAlAs material thickness was either 65nm or 300nm as reported in table I. The samples were not intentionally doped. The top InAlAs layer of sample S3 was chemically etched from 300nm down to 65nm in order to obtain sample S3\* which only differs from sample S1 by the growth temperature. In S3, the growth was interrupted during 5 seconds at each SQW interface in order to improve the interface quality.

The alloy composition and quality were checked by low temperature Photoluminescence (PL) experiments. For each sample, PL spectra exhibit two peaks corresponding to the InAlAs layers. One peak lies at 1.517eV from the near band edge recombination, which confirms the nominal Indium composition (0.52) of the InAlAs layer. The second peak lies at a lower energy (1.478 eV) and corresponds most probably to a shallow acceptor level in the gap. The ratio of the



near band edge peak intensity over the intensity of the acceptor peak is much greater in the structures grown at 525°C and indicates that InAlAs quality is better in samples S1 and S2 than in S3.

At 5K, the SQW fundamental transition  $E_1H_1$  peak lies at 0.941eV in sample S1 and at 0.973eV in S3. The theoretical value (0.956eV) is obtained from the resolution of Schrödinger equation in a square well. As the nominal indium composition of the barrier material was checked by PL measurements, the discrepancy between  $E_1H_1$  in S1 and in S3 is most likely attributed to a strong variation in the well width which influences the energy of the fundamental level in a 5nm SQW : a 10% variation of the well width around 5nm leads to a 30meV shift of  $E_1H_1$ . A Stark effect due to the surface electric field could as well be considered for sample S1 which is red-shifted (15meV) with respect to the theoretical value, but could not explain the blue-shifted transition in S3. PR experiments will provide us a useful tool for the internal electric field determination in the next section.

Furthermore, the full width at half maximum (FWHM) of  $E_1H_1$  in S3 (8meV) is lower than the value measured in S1 (11meV) in spite of a better InAlAs material quality in S1. This is probably linked to the growth interruption performed in S3, which improves the interface quality. These PL results will be compared with the PR results in the next section.

|     | nominal<br>InGaAs<br>well<br>width (nm) | InAlAs top<br>barrier<br>width (nm) | T <sub>g</sub><br>(°C) | Growth<br>interruption |
|-----|---|-------------------------------------|------------------------|------------------------|
| S1  | 5                                       | 65                                  | 525                    | 0s                     |
| S2  | 10                                      | 65                                  | 525                    | 0s                     |
| S3  | 5                                       | 300                                 | 450                    | 5s                     |
| S3* | 5                                       | 65                                  | 450                    | 5s                     |

Table I: Growth parameters of the samples

## RESULTS

### PR spectra of SQW

The typical PR spectra of samples S1, S2 and S3, recorded at room temperature, are reported in solid lines in figure 1 together with the theoretical fits in dashed lines. The theoretical expressions used for the fit of the experimental data will be further discussed in the next section. The spectral range of figure 1 corresponds to the fundamental transition  $E_1H_1$  in the quantum well. Another weak transition is observed at high energy and is attributed to a transition  $E_1L_1$  with the first quantized light hole subband rather than to  $E_1H_2$ , which would lie at about the same energy. Indeed, the oscillator strength of the transition  $E_1L_1$  is much more intense than that of  $E_1H_2$  which is parity forbidden.

|     | T = 300K       |                         |                |                         | T = 5K         |                         |
|-----|----------------|-------------------------|----------------|-------------------------|----------------|-------------------------|
|     | $E_1H_1$<br>eV | $\Gamma(E_1H_1)$<br>meV | $E_1L_1$<br>eV | $\Gamma(E_1L_1)$<br>meV | $E_1H_1$<br>eV | $\Gamma(E_1H_1)$<br>meV |
| S1  | 0.868          | 7.3                     | 0.925          | 12.7                    | 0.940          | 4                       |
| S2  | 0.773          | 6                       | 0.798          | 17                      |                |                         |
| S3  | 0.901          | 7.3                     |                |                         | 0.975          | 4.3                     |
| S3* | 0.908          | 8.2                     |                |                         |                |                         |

Table II: Energy and broadening parameters of optical transitions from the PR spectra of the SQW in different samples.

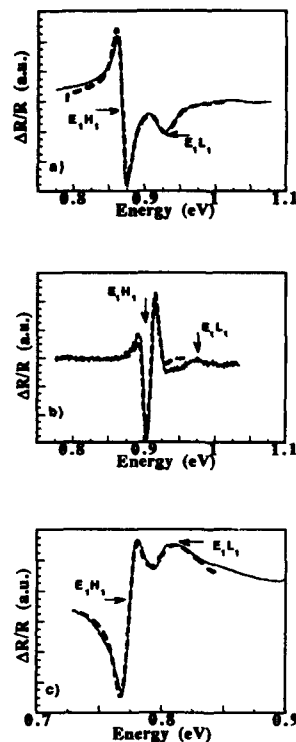


**Figure 1:** PR spectra at 300K of S1 (a), S3 (b), and S2 (c). Solid lines : experiments, dashed lines : theoretical fit using intensity modulation for a and c, and broadening parameter modulation for b.

In samples S1 and S2, this high energy transition is well defined and its amplitude is about 1/3 of that of  $E_1H_1$  as is expected from theory. This is not the case in sample S3 where the  $E_1L_1$  transition has a very low amplitude (only 1/10 of that of  $E_1H_1$ ). The energy transitions and broadening parameters of the different transitions obtained by the theoretical fits are reported in table II for measurements performed at room temperature and also at 5K.

The  $E_1H_1$  energy values at 5K are in good agreement with the PL measurements. A shift of the transitions is observed when the temperature is raised as it is normally expected. The broadening parameters  $\Gamma$  of  $E_1H_1$  are similar in the various samples at room temperature as well as at low temperature. At 5K the  $\Gamma$  value is mainly sensitive to the alloy disorder and interface roughness whereas the higher value at 300K is due to the increasing influence of phonon scattering when temperature is raised.  $E_1L_1$  is broader in S2 than in S1 : this means that the lifetime of light holes is shorter in S2 than in S1. The theoretical resolution of Schrödinger equation in a finite square well shows that the first light hole subband  $L_1$  lies at the same energy as the second heavy hole subband  $H_2$  in a 10nm SQW : there is a strong coupling between the two hole levels and therefore holes are most probably on  $H_2$  level than on  $L_1$  due to the higher density of states. In a 5nm SQW (S1), the coupling between  $L_1$  and  $H_2$  is less efficient because there is an energy gap between the two levels. This is the reason for the very broad  $E_1L_1$  transition in S2.

Finally, the lineshapes of spectra S1 and S2 are very different from that of spectrum S3 as is evidenced in figure 1. It will be addressed in the discussion section.

#### InAlAs PR spectrum

In figure 2 are plotted the 300K PR spectra of S1 and S3 in the spectral range corresponding to the energy gap of InAlAs. Both spectra exhibit about 3 Franz Keldysh oscillations (FKO) above the energy gap of InAlAs (1.45eV), from which we can measure the internal electric field in this layer [8]. The internal electric field is due to the Fermi level pinning at the surface states, which creates a space charge layer under the surface of the sample. Figure 3 is a plot of  $(4\pi/3) \cdot (E_n - E_g)^{3/2}$  versus the maximum number  $n$ . From this plot, a value of 30kV/cm is deduced for the electric field in the InAlAs layer in sample S1, and 50kV/cm in sample S3. These electric field values are very similar : no drastic difference is evidenced between these two samples, contrary to the lineshapes of the SQW response in figure 1.

## **DISCUSSION**

### Lineshape analysis

The theoretical fit used in figure 1 is the first derivative functional form of the unperturbed dielectric function  $\epsilon$  of the confined structure. It was proven to be the most suitable fit for confined

systems [4,5]. At room temperature, the unperturbed dielectric function has most likely a Gaussian form, due to inhomogeneous broadening such as phonon scattering. At low temperature the Gaussian lineshape is still valid in our samples due to alloy or/and interface broadening.

The theoretical PR lineshape is obtained from a linear combination of the first derivative of the real  $\epsilon_1$  and imaginary  $\epsilon_2$  parts of the complex dielectric function with respect to the modulating physical parameter [6]. In PR experiments on SQW, as the internal electric field is modulated by the incident laser beam, three physical parameters of optical transitions can be affected: either the energy level through the Stark effect, or the broadening parameter by a modulation of the lifetime of electrons on the quantized levels or even the intensity of the optical transition due to the modulation of the overlap of the wavefunctions associated to electrons and holes. The relative contribution of the real and imaginary parts in the spectra depends upon the Seraphin coefficients and involve the influence of interference effects as well [7].

It is worth noting that the lineshape of PR features, in particular in a SQW, varies considerably with the main modulation mechanism involved: particularly when the intensity modulation mechanism is preponderant, the lineshape is much broader than when the main modulation mechanism is an energy or broadening parameter modulation. The latter two modulation mechanisms are leading to same lineshapes for a Lorentzian absorption profile, and to similar lineshapes for a Gaussian absorption profile [5-7].

In figure 1, we can see that the lineshapes are much broader for samples S1 and S2 than for sample S3. We attribute this fact to a difference in the modulation mechanism in samples S1 and S2 as compared to sample S3: indeed, the best fits to the spectra of S1 and S2 are obtained considering the modulation of the intensity as the main mechanism whereas the best fit to the spectrum of S3 is obtained using a derivative with respect to the broadening parameter. Furthermore, to rule out any possible influence of interference on the spectrum of S1, the same PR experiments were performed with sample S3\* which has the same geometrical parameters than S1 and only differs by the growth conditions of the structure. The difference between the spectra of S3 and S3\* is only a phase modification due to interference effects. No modification of the modulation mechanism can be evidenced in S3\*: the broadening parameter modulation mechanism remains the most relevant. Therefore, the narrow barrier layer thickness is not responsible for the special lineshape observed in the PR spectra of figure 1a and 1c.

An intensity modulation mechanism is generally observed in the case of transitions which involve spatially separated electrons and holes: for instance transitions in double coupled quantum wells [6] or even in the case of forbidden transitions [7]. In figure 1, the main PR features observed for samples S1 and S2 are at an energy position corresponding to  $E_1H_1$  and do not correspond to any forbidden transition. As the wavefunctions of electrons and holes in a 5nm SQW are covering the whole well width, it is rather surprising to get an intensity modulation mechanism in such narrow wells.

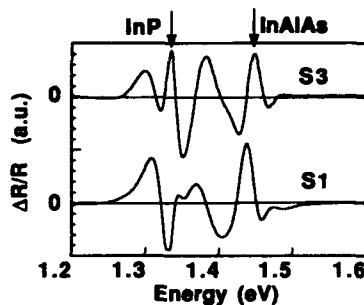


Figure 2: PR spectra of samples S1 and S3 showing the FKO of InAlAs barrier at 300K.

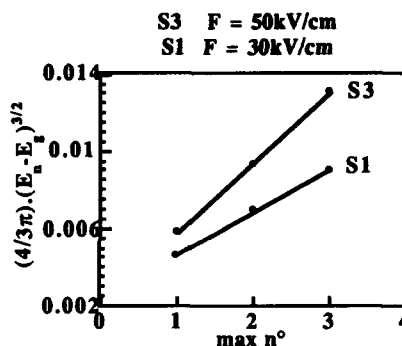


Figure 3: Plot of  $(4/3\pi)(E_n - E_g)^{3/2}$  versus maximum number  $n$ . The slope of each line is the electro-optic energy.

The low value of the electric field, as derived from FKO in figure 2, is not sufficient to spatially separate electrons and holes in a 5nm SQW. Furthermore, as its intensity is of the same order of magnitude in S1 and S3, it would have similar effects in both samples and this is not the case. So the internal electric field alone cannot by itself explain an intensity modulation mechanism in S1.

The difference between structures S1 and S3 lies only in the growth conditions : growth temperature, and growth interruption at the interfaces. So the special lineshapes observed in the PR spectrum of S1 is necessarily linked to the interface or material quality. Since the InAlAs layer quality was proven to be better in S1 than in S3 from PL experiments, we assume that there are some defects at the well interface in S1 which enhance the wavefunctions of electrons and holes near the interface. However, any effect of growth conditions on interface quality is supposed to be symmetrically distributed. The asymmetry is due to the existence of the internal electric field, which drives each carrier (electron and hole) at a different side of the SQW. The spatial separation of the wavefunctions is ensured by the combined effects of interface defect and internal electric field.

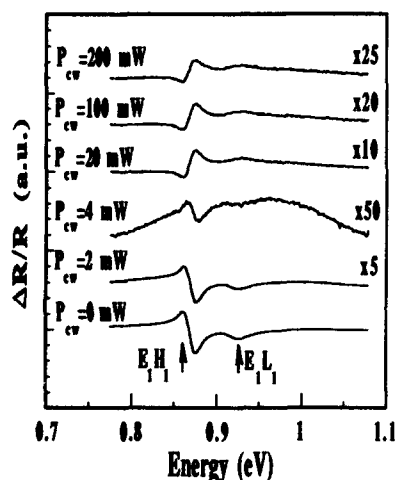


Figure 4: Spectra of sample S1 for different continuous laser beam power.

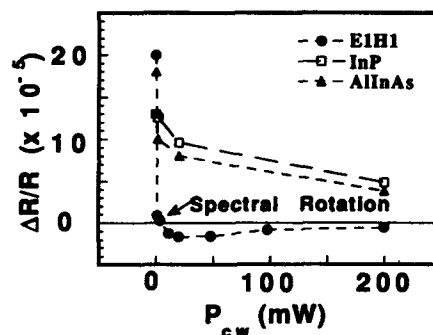


Figure 5: Evolution of the various PR transitions versus  $P_{cw}$  (continuous laser beam power)

#### Study as a function of a secondary continuous light beam

In order to further investigate this phenomenon of intensity modulation mechanism in sample S1, we have performed a double beam experiment with a continuous wave Argon laser beam superimposed on the HeNe modulation laser beam. This is supposed to optically reduce the internal electric field by reducing the band bending. Figure 4 shows the PR spectra obtained for different continuous laser beam powers ( $P_{cw}$  ranging from 0 to 200mW on a 1mm diameter spot on the sample). A drastic decrease of the intensity of the SQW transition is recorded for a value of  $P_{cw}$  equal to 4 mW. The transition intensity increases again as  $P_{cw}$  is further increased, but with a 180° rotation as compared with the signal at lower  $P_{cw}$ . This rotation is not related to any interference effects since it does not appear neither on the InP transition, nor in that of InAlAs. In figure 5, the evolution of the various transition intensities is plotted versus  $P_{cw}$ . It is worth noting that the InAlAs transition intensity is also drastically reduced for  $P_{cw}$  lower than 4mW : this is a proof for a strong reduction of the surface electric field before the phase rotation occurs.

Such a phase rotation has already been observed by several authors in electroreflectance (ER) spectra of bulk material [9] : they assigned the phase change of their ER feature to the flat band condition in the structure (internal electric field = 0). The reason for the phase change in ER is associated with the nature of band bending. For n type semiconductors in which the bands are

bent upward, the surface field when applying the modulation increases or decreases. The same thing will be seen for p type material, but due to the opposite band bending the signal will be in opposite phase. Thus in electroreflectance the flat band is evidenced by observing the spectral rotation. Our experimental results cannot be explained this way, because PR only drives material conduction band towards flatband [7] and it is surprising to observe an increase of PR intensity after flat band conditions are obtained.

One possible explanation could be that, once the bands are nearly flat, there is a modification of the modulation mechanism : from the situation of intensity modulation at low  $P_{cw}$  we come back to the more usual energy or broadening parameter modulation. Indeed, an observation of the spectra of figure 4 shows that, for  $P_{cw}$  higher than 4mW, the tail of the PR transition at low energy (which is the sign for an intensity modulation mechanism) is much reduced as compared to the spectrum recorded without continuous laser beam. Therefore, we can consider that there is a change in the modulation mechanism under the effect of a continuous laser beam. The efficiency of the latter modulation mechanism appears to be much lower.

This double beam PR experiment is a further support for our assumption of a spatial separation of the wavefunctions of electrons and holes under the effect of the internal electric field. When the conduction band is flattened by a secondary light source, then the spatial separation of electrons and holes no more exist and a conventional PR spectrum is recorded.

## CONCLUSION

From an extensive PR study of InGaAs SQW between InAlAs barriers lattice matched on InP substrates, we have evidenced the existence of an intensity modulation mechanism of the fundamental optical transition in a 5nm SQW. The influence of a secondary laser beam was studied.

The comparison of the PR lineshapes at room temperature between samples which only differ by their growth conditions, leads to important information about the interface quality of the structure. Indeed, the lineshape of the PR spectrum is an evidence for an intensity modulation mechanism in some of our samples, in which alloy quality was proven to be good from low temperature PL measurements. The unusual PR lineshape is then explained by the presence of some interface defect, and can only be observed if an internal electric field exists in the structure as is proven from double beam PR experiments. These results show that PR experiments can bring complementary information to low temperature PL experiments about the quality of a semiconducting structure.

The structures which were grown with 5 second growth interruption at the interface do not exhibit such unusual PR lineshapes and are therefore free from this interface defect. This is a further support to the beneficial effect of a growth interruption on the interface quality [10].

## REFERENCES

1. S.T.Davey, E.G. Scott, B. Wakefield and G.J. Davies, *Semic. Sci. Technol.* **3**, 365, (1988)
2. K.Satzke, G. Weiser and W. Stolz, *Phys. Rev.* **B43**, 2263, (1991)
3. S.Gupta, P.K. Bhattacharya, J. Pamulapati and G. Mourou, *J. Appl. Phys.* **69**, 3219, (1991)
4. B.V.Shanabrook, O.J. Glembocki, W.T. Beard, *Phys. Rev.* **B35**, 2540, (1987)
5. W.M. Theis, G.D. Sanders, C.E. Leak, K.K. Bajaj, H. Morkoç, *Phys. Rev.* **B37**, 3042, (1988)
6. Y.S.Huang, H.Qiang, F.H.Pollak, J.Lee, B.Elman, *J.Appl.Phys.* **70**, 3808, (1991)
7. F.H.Pollak, *Handbook on Semiconductors*, Ed M. Balkanski, North Holland, New York (1993).
8. R.N.Bhattacharya, H.Shen, P.Parayantal, F.H.Pollak, T.Couts, H.Aharoni, *Phys.Rev.* **B37**, 4034, (1989)
9. M.C.A.Fantini, W.M.Shen and M.Tomkiewicz, *J.Appl.Phys.* **65**, 4884, (1989)
10. T.Benyattou, M.A.Garcia Perez, Y.Baltagi, S.Monéger, A.Tabata, C.Bru, G.Guillot, M. Gendry, V.Drouot, G.Hollinger, *Proceedings of 4th ICFSI, Jülich, Germany*, (1993)

## CHARACTERIZATION OF PSEUDOMORPHIC HEMT STRUCTURES BY MODULATION SPECTROSCOPY

A. DIMOULAS\*, K. ZEKENTES\*\*, AND M. ANDROULIDAKI\*\*

\* University of Groningen, Department of Applied Physics, Nijenborgh 4, 9747 AG Groningen, The Netherlands.

\*\* Foundation for Research and Technology-Hellas (FORTH), P.O. Box 1527, Heraklion 711 10, Crete, Greece.

### ABSTRACT

Phototransmittance has been used to investigate several pseudomorphic  $\text{Al}_{0.32}\text{Ga}_{0.68}\text{As}/\text{In}_{0.15}\text{Ga}_{0.85}\text{As}/\text{GaAs}$  high electron mobility transistor structures, with different values of the electron density  $n_s$ . A lineshape analysis of the ground state transition made it possible to estimate  $n_s$  at room temperature. A signal from the Fermi-edge singularity (a many-body effect), was observed at low temperatures and the dependence of its intensity on temperature and electron density was examined.

### INTRODUCTION

High electron mobility transistors (HEMT), based on the  $\text{AlGaAs}/\text{InGaAs}/\text{GaAs}$  pseudomorphic (PM) heterostructure, have attracted considerable interest due to their performance in low-noise, high-power microwave applications, up to 94 GHz.<sup>1</sup> The development of non-destructive methods (e.g. optical) is important to measure the electron density  $n_s$  of the two-dimensional electron gas (2DEG) in PM-HEMTs. The effect of the high electron density on the optical excitations have been investigated by photoluminescence at low temperature.<sup>2</sup> Photoreflectance<sup>3</sup> applied to HEMT structures has led to controversial results regarding the observation of a signal from the degenerate 2DEG.<sup>4</sup> A conclusive evidence on the existence of a 2DEG signature has been given recently by Yin et al.<sup>5,6</sup> in the photoreflectance and electroreflectance studies of  $\text{GaAlAs}/\text{InGaAs}/\text{GaAs}$  modulation-doped quantum well structures. Dimoulas et al.<sup>7</sup> used phototransmittance (PT) to study PM-HEMTs with different electron densities and found that the first derivative of the absorption coefficient with respect to  $n_s$  gives the dominant contribution to the lineshape of the ground state optical transition. They also reported<sup>7</sup> the observation of the Fermi-edge singularity<sup>8</sup> (FES) in one sample with  $n_s = 1.4 \times 10^{12} \text{ cm}^{-2}$ .

In this paper, we show that the 2D joint density of states for band-to-band transitions in  $\text{Al}_{0.32}\text{Ga}_{0.68}\text{As}/\text{In}_{0.15}\text{Ga}_{0.85}\text{As}/\text{GaAs}$  PM-HEMTs can be probed directly by PT, as a result of the screening of excitons by the dense 2DEG. Also, by comparing the PT results with Hall data, we show that an estimation of  $n_s$  by PT at room temperature is possible. Finally, we investigate the dependence of the FES signal intensity on the electron density of the 2DEG.

### EXPERIMENT AND SPECTRA ANALYSIS

Five samples were fabricated by molecular beam epitaxy on 2 inch semi-insulating GaAs (001) substrates. The general structure from the top free surface to the substrate was: (500 Å)  $n^+$   $2.5 \times 10^{18} \text{ cm}^{-3}$  GaAs cap/ (100 Å) undoped GaAs/ (500 Å) undoped

$\text{Al}_{0.32}\text{Ga}_{0.68}\text{As}$  /  $\delta$ -doped layer/(thickness  $L_s$ ) undoped  $\text{Al}_{0.32}\text{Ga}_{0.68}\text{As}$  spacer/(130 Å) undoped  $\text{In}_{0.15}\text{Ga}_{0.85}\text{As}$  channel/(0.8  $\mu\text{m}$ ) undoped buffer/semi-insulating (001) GaAs substrate. The n-type  $\delta$ -doping was varied in the range between  $8.0 \times 10^{11}$  and  $2.5 \times 10^{12} \text{ cm}^{-2}$ , while the spacer layer  $L_s$  was grown at three values of 20, 40 and 60 Å, as seen in Table I. The values of sheet electron concentration, obtained by Hall measurements at 300 and 4.2 K after removal of the cap layer, spanned a wide range between  $6.5 \times 10^{10}$  and  $1.6 \times 10^{12} \text{ cm}^{-2}$  (See Table I). Phototransmittance measurements were performed by using a conventional experimental set-up<sup>9</sup> in which the transmittivity  $T$  of the sample was modulated by a 0.95 mW He-Ne laser. Two values of 15 and 0.75 mW/cm<sup>2</sup> of the laser intensity were used at room and low temperatures, respectively.

TABLE I. Experimental results for the electron density  $n_s$  and chemical potential  $\mu_s$  determined from the fitting of the Phototransmittance lineshapes of the 11h transition. Hall values are also listed for comparison. All data were obtained at a temperature of 295 K.  $L_s$  and  $\delta - d$  are the spacer layer thickness and the planar doping, respectively.

| Sample | $L_s$<br>(Å) | $\delta - d$<br>( $\times 10^{11} \text{ cm}^{-2}$ ) | $n_s$ ( $\times 10^{11} \text{ cm}^{-2}$ ) |                  | $\mu_s - E_1$ (meV) |                |
|--------|--------------|--|--|------------------|---------------------|----------------|
|        |              |  | Hall                                       | PT               | Hall                | PT             |
| S1     | 40           | 8.0  | 0.65( $\pm 0.04$ )                         | 0.003            | -58( $\pm 2$ )      | -205           |
| S2     | 40           | 13.0   | 5.4( $\pm 0.3$ )                           | 5.2( $\pm 0.4$ ) | +5( $\pm 2$ )       | +4( $\pm 3$ )  |
| S3     | 40           | 17.0   | 8.4( $\pm 0.5$ )                           | 9.0( $\pm 0.6$ ) | +23( $\pm 3$ )      | +26( $\pm 3$ ) |
| S4     | 60           | 25.0   | 14.0( $\pm 0.8$ )                          | 19.4             | +49( $\pm 4$ )      | +71            |
| S5     | 20           | 25.0   | 16.0( $\pm 1$ )                            | -                | +57( $\pm 5$ )      | -              |

The room temperature PT spectra of four of the PM-HEMT structures with different  $n_s$  values are shown in Fig. 1. The spectrum of an undoped  $\text{Al}_{0.32}\text{Ga}_{0.68}\text{As}/\text{In}_{0.15}\text{Ga}_{0.85}\text{As}$  heterostructure QW, used as a reference, with the same thickness (130 Å) of the InGaAs layer is also shown in Fig. 1.

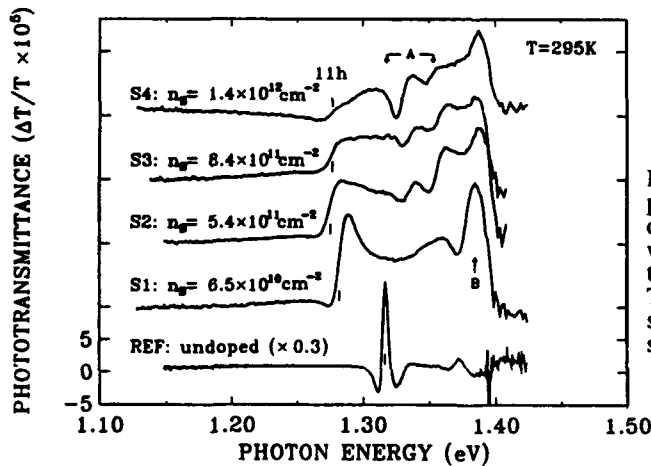


FIG. 1. Room temperature phototransmittance spectra of four HEMT structures with different values of the electron density  $n_s$ . The spectrum of an undoped structure (REF) is also shown for comparison.

In all spectra, the signal at the lowest energy is assigned to the ground state transition  $11h$ . The features at higher energies, denoted by A in Fig. 1, are associated with transitions to the second electron level  $n = 2$ . Peak B at 1.39 eV, common to all spectra of the PM-HEMT structures, is considered to be a contribution from the GaAs layers and the GaAs substrate. The  $11h$  transition in the reference sample of Fig. 1 has an excitonic character with sharp positive and negative lobes with respect to the baseline. The same transition in the doped structures, exhibits distinctly different lineshapes whose main characteristic is a unique step-like signal, more pronounced in S3. Also, it is worth noticing the lacking of negative lobes in samples S2 and S3. These unusual modulation spectroscopy lineshapes can be understood in terms of the screening of excitons by the dense 2DEG, combined with conduction-band phase space filling effects.<sup>5</sup> Since excitons are screened, band-to-band transitions with a broadened 2D joint density of states (JDOS) dominate the spectra, and produce the step-like character of the lineshape. In this sense, PT can probe directly the constant 2D JDOS in Semiconductor heterostructures. On the other hand, it is seen from Fig. 1, that the slope of the high energy portion of the  $11h$  spectrum depends sensitively on the value of  $n_s$ . The slope is negative for samples S1 and S2 but gradually turns to positive at higher densities (samples S3, S4). This is an effect of phase-space filling, which depends on the position of the electron chemical potential  $\mu_e$  relative to the  $n = 1$  electron state  $E_1$ . The same effect is also responsible for the observed decreasing behavior of the  $11h$  intensity with increasing  $n_s$ , as seen in Fig. 1. Note however, that the  $11h$  transition is resolved even if  $\mu_e$  is above the  $E_1$  level (as in the case of S2, S3 and S4). This is explained considering that the Fermi-Dirac distribution is broadened by an amount  $\sim k_B T \simeq 25$  meV, which is of the same order of magnitude as  $\mu_e - E_1$  (see Table I). Because of this, a number of conduction band states remains unoccupied, so that the absorption process is possible at room temperature.

For a quantitative analysis of the spectra, we developed a model, based on a previous work of Dimoulas et al.<sup>7</sup>:

$$\frac{\Delta T}{T} \simeq -L\Delta\alpha \simeq -L \left[ \left( \frac{\partial\alpha}{\partial n_s} \right) \Delta n_s + \left( \frac{\partial\alpha}{\partial I} \right) \Delta I + \left( \frac{\partial\alpha}{\partial \Gamma} \right) \Delta \Gamma + \left( \frac{\partial\alpha}{\partial E} \right) \Delta E \right] \quad (1)$$

Here,  $\alpha$  is the absorption coefficient and  $I$ ,  $\Gamma$ ,  $E$  are the intensity, broadening and energy parameters, respectively. By fitting the  $11h$  experimental lineshapes using this model<sup>7</sup>, it was possible to determine  $\mu_e$  (and hence  $n_s$ ) by treating it as an adjustable parameter. The results of the fitting are listed in Table I. Regarding the samples S2 ( $n_s = 5.4 \times 10^{11} \text{ cm}^{-2}$ ) and S3 ( $n_s = 8.4 \times 10^{11} \text{ cm}^{-2}$ ), the values of  $\mu_e$  and  $n_s$  obtained from PT lineshape fitting and Hall measurements agree within the experimental error. Values of  $n_s$  obtained from PT, are within 10% of those measured by Hall. In contrast, there is a large disagreement between PT and Hall data for structures S1 and S4 having the lowest and the highest  $n_s$  values, respectively. The disagreement in S1 may be explained considering that the 2DEG is not sufficiently dense to completely screen the exciton so that our model<sup>7</sup>, in which only band-to-band transitions are included, is inadequate to describe the PT lineshape. In S4, the anomalously large and broad negative lobe, is considered to be responsible for the limited success in fitting the  $11h$  transition. It can be inferred, from the preceding analysis, that it is possible to determine (with acceptable accuracy)  $n_s$  values in the range between  $5 \times 10^{11}$  and  $1 \times 10^{12} \text{ cm}^{-2}$ , by using PT spectroscopy at room temperature.

It is emphasized here, that contributions from the last three terms in eqn. (1) were found to be negligibly small, not improving the fitting results. In contrast to previous



reports in undoped<sup>9,10</sup> and modulation-doped QW heterostructures<sup>5,6</sup>, where only the terms  $(\partial\alpha/\partial\Gamma)\Delta\Gamma$ ,  $(\partial\alpha/\partial E)\Delta E$  and  $(\partial\alpha/\partial I)\Delta I$  were considered, in the present work it was found that the modulation with respect to  $n_s$  gave the dominant effect.<sup>7</sup> Taking into account the foregoing discussion the following modulation mechanism is proposed. The photoexcited electrons from the laser modulation source increase the population of the degenerate 2DEG by a small amount  $\Delta n_s$ . This produces an elementary increase  $\Delta\mu_s$  of the electron chemical potential which also affects the Fermi factor  $f_s$  and subsequently the absorption.

As a final remark on Fig. 1, it is noted that there is a significant red shift of the  $11h$  transition with increasing  $n_s$ . The latter is attributed to the combined effects of band-gap renormalization and electrostatic energy variations<sup>8</sup>.

### THE FERMİ-EDGE SINGULARITY.

The temperature dependence of the PT spectra of sample S4 ( $n_s = 1.4 \times 10^{12} \text{ cm}^{-2}$ , at 4.2K) is shown in Fig. 2 a). The  $11h$  photoluminescence (PL) spectrum of the same sample is shown in Fig. 2 b) for comparison. The assignment of the 1.348 and 1.404 eV PL peaks to the  $11h$  and  $21h$  recombinations, respectively, is well established in the literature<sup>2</sup>. Such a PL spectrum exhibiting an intense  $21h$  peak compared to the  $11h$  one, is typical of a 2DEG system having the Fermi energy  $E_f$  very close to the bottom of the second electron subband  $E_2$ .<sup>2</sup>

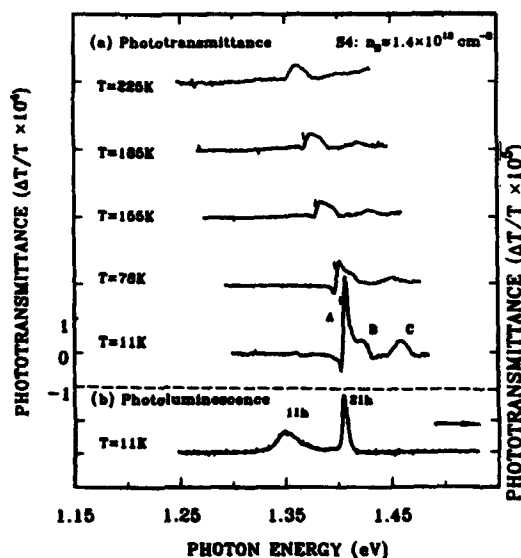


FIG. 2. a) Phototransmittance of sample S4 ( $n_s = 1.4 \times 10^{12} \text{ cm}^{-2}$ ) obtained at five different temperatures. Letter A marks the signal from the Fermi-edge singularity b) Photoluminescence of S4 obtained at 11 K.

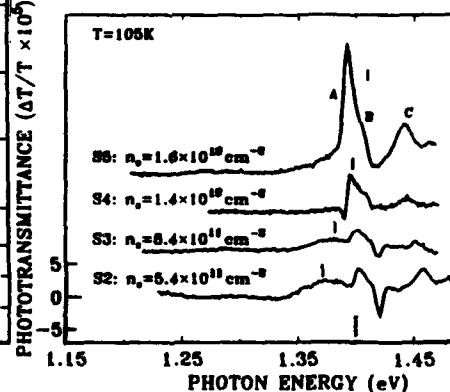


FIG. 3. Phototransmittance spectra of four of our HEMT structures with different values of electron density, obtained at 105 K. The small vertical lines indicate the position of the Fermi level. The dotted line marks the position of the bottom of the  $n = 2$  subband.

According to a simple estimation  $E_f - E_1 \simeq (\pi\hbar^2/m_e^*)n_s = 53.0$  meV, while from an inspection of the PL data of Fig. 2 b),  $E_2 - E_1 \simeq 56$  meV, implying that  $E_f$  is only 3 meV below the  $n = 2$  level. In this case the  $n = 2$  subband is populated at 11 K. In contrast to PL observations, the  $11\hbar$  transition could not be resolved in the low temperature PT spectra of Fig. 2 a) due to phase space filling which quenched absorption. In the high energy part of the spectra, peak C is associated with the  $n = 3$  electron level while a weak and broad feature, with a high energy tail denoted by B, is attributed to the  $21\hbar$  band-to-band transition<sup>5</sup>. Superimposed on B, a sharp and intense exciton-like feature A, consisting of a positive and a weaker negative lobe, dominates the 11 K PT spectrum at the  $21\hbar$  transition energy.

It is known<sup>9,10</sup> that excitons dominate the electromodulation spectra of undoped QWs at all temperatures. However, in PM-HEMTs with a high value of  $n_s$ , as in the case of S4, the appearance of an exciton-like PT signature at the  $21\hbar$  transition is not expected, since the single-electron-hole exciton is considered to be screened by the dense 2DEG. Also, the temperature sensitivity is unexpectedly large, as seen from Fig. 2 a), where the intensity of feature A decreases rapidly with increasing temperature. This is in contrast with the behaviour of peak B, the intensity of which remains constant as the temperature of the measurement changes. At 185 K, A is only weakly visible at the low energy side of the dominant peak B, while at 225 K, the former completely disappears from the PT spectrum. This behaviour, is distinctly different from the one characterizing the excitonic PT and PR spectra of undoped QWs. In the latter case<sup>9,10</sup>, the intensity decreases in a much slower rate, and the exciton remains strong and well-resolved up to room temperature. This is also confirmed by the 295 K spectrum of the reference (undoped) sample shown in Fig. 1.

Considering the difference with the well-known behaviour of the single-electron-hole exciton, it is proposed here that feature A in Fig. 2 a) originates from the modulation of a correlation-enhanced  $21\hbar$  excitonic absorption. The enhancement is due to the energy proximity of the  $n = 2$  state and the Fermi energy level<sup>2</sup>, which leads to a many-electron-hole Coulomb interaction, known as Mahan exciton. The latter manifests itself as an enhanced absorption peak near the Fermi energy<sup>8</sup> (the Fermi-edge singularity (FES)) exhibiting an increased temperature sensitivity. Indeed, as the temperature rises, the Fermi surface smears out<sup>2</sup> approximately as  $\sim k_B T$ , so that electron correlation weakens, leading to a marked decrease of the excitonic  $21\hbar$  oscillator strength enhancement. This explains, at least qualitatively, the temperature sensitivity of the modulation absorption signal A in Fig. 2 a). Similar behaviour of the  $21\hbar$  excitonic enhancement has been observed by Scolnick et al.<sup>2</sup> in photoluminescence-excitation (PLE) experiments. In that work, for a sample where  $E_f$  was  $\sim 1$  meV below the  $n = 2$  level (a situation resembling that in the present work) a decrease in the enhancement by a factor of 0.7 has been observed<sup>2</sup> from 2 to 40 K. This is to be compared with an estimated decrease of the PT signal intensity, by a factor of 0.3, from 11 to 78 K as seen from Fig. 2 a). It is worth mentioning that the  $21\hbar$  excitonic enhancement was not observed in the PR spectra of Yin et al.<sup>5</sup>, at the lowest attained temperature of 79 K, although it was clearly present in our PT spectra for the same temperature (Fig. 2 a)). This difference in observation may be explained considering that in the work of Yin et al.<sup>5</sup>  $E_f$  was a few meV above  $E_2$ , leaving the  $n = 2$  subband heavily populated. The latter has probably caused a rapid quenching of the  $21\hbar$  exciton enhancement, similar to what has been observed by Skolnick et al.<sup>3</sup>, where the  $21\hbar$  exciton could not be observed above 38 K in a sample having  $E_f - E_2 = +3.5$  meV.

The PT spectra of four of our HEMT samples, obtained at 105 K, are shown in Fig.

3. The FES signal is not resolved in samples S2 and S3 with the lowest values of electron density. This is because the Fermi energy is well below the bottom of the  $n = 2$  electron subband, leaving the latter only lightly populated. The FES feature is clearly visible in sample S4 where the Fermi level approaches  $E_2$  and its intensity is increased in S5 (the sample with the highest  $n_s$  value), since in this case the second subband becomes heavily populated. The increase of the FES signal intensity with increasing electron density further supports the assignment of this peak (peak A in Fig.2 and 3) to a many-electron-hole exciton. This behavior is in contrast with the single-electron exciton at  $11h$  transition, which, as shown in Fig. 1, is quenched in the presence of a high density 2DEG.

## CONCLUSIONS

Using modulation spectroscopy in pseudomorphic HEMT structures, we investigated the properties of the two-dimensional electron gas, such as the exciton screening and the Fermi-edge singularity. Electron density values, obtained by fitting the phototransmittance spectra at room temperature, were in good agreement with the Hall data for two of the examined structures.

## REFERENCES

1. T. Mimura, in *Very high speed IC's : Heterostructures*, Semiconductors and Semimetals, edited by T. Ikoma (Academic, New York, 1990), Vol. 30.
2. M.S. Skolnick, D.M. Whittaker, P.E. Simmonds, T.A. Fisher, M.K. Saker, J.M. Rorison, R.S. Smith, P.B. Kirby, and C.R.H. White, *Phys. Rev. B* **43**, 7354 (1991)
3. F.H. Pollak, *Superlattices and Microstructures* **10**, 333 (1991); O.J. Glemboki. *Proc. SPIE* **1286**, 2 (1990).
4. M. Sydor, A. Badakhshan, J. R. Engholm, and D.A. Dale, *Appl. Phys. Lett.* **58**, 948 (1991), and references therein.
5. Y. Yin, H. Qiang, F.H. Pollak, D.C. Streit, and M. Wojtowicz, *Appl. Phys. Lett.* **61**, 1579 (1992).
6. Y. Yin, H. Qiang, D. Yan, F.H. Pollak, and T.F. Noble, *Semicond. Sci. Technol.* **8**, 1599 (1993).
7. A. Dimoulas, K. Zekentes, M. Androulidaki, N. Kornelios, C. Michelakis, and Z. Hatzopoulos, *Appl. Phys. Lett.* **63**, 1417 (1993)
8. R. Cingolani and K. Ploog, *Adv. Phys.* **40**, 535 (1991), and references therein.
9. A. Dimoulas, J. Leng, K.P. Giapis, A. Georgakilas, C. Michelakis, and A. Christou, *Phys. Rev. B* **47**, 7198 (1993).
10. Y.S. Huang, H. Qiang, F.H. Pollak, G.D. Pettit, P.D. Kirchner, J.M. Woodall, H. Stragier, and L.B. Sorensen, *J. Appl. Phys.* **70**, 7537 (1991).

## PHOTOLUMINESCENCE CHARACTERIZATION OF InP-BASED HEMT STRUCTURES

HENRY T. HENDRIKS, STEVEN K. BRIERLEY, WILLIAM E. HOKE, AND NOREN PAN  
Raytheon Research Division, 131 Spring Street, Lexington, MA 02173

### ABSTRACT

InP-based lattice matched high electron mobility transistor (HEMT) structures have been characterized by liquid nitrogen temperature photoluminescence. A phenomenological line shape model has been utilized to fit photoluminescence spectra in order to obtain key parameters, such as the subband energies and transition amplitudes. From transition amplitude ratios and subband energies, fundamental quantum well characteristics are inferred. Changes in these parameters are linked to variations in the growth conditions of the epitaxial layer structures.

### INTRODUCTION

Lattice matched InP-based high electron mobility transistors (HEMTs) have emerged as a primary choice for an assortment of microwave applications. To obtain peak performance, the epitaxial structure and subsequent device processing steps must be optimized. Numerous techniques have been used to characterize the epitaxial structure: variable temperature Hall and Shubnikov de Haas measurements,<sup>1,2</sup> double crystal X-ray diffraction,<sup>3</sup> photoreflectance,<sup>4</sup> capacitance-voltage (CV) profiling and secondary ion mass spectroscopy (SIMS),<sup>5,6</sup> and low temperature (~4 K) photoluminescence (PL).<sup>2</sup> In this paper, we present a liquid nitrogen (77 K) temperature PL characterization technique that utilizes a phenomenological line shape model to fit the PL spectra. The parameters extracted from the fit, such as the subband energies and transition amplitude ratios, can be used to determine variations in quantum well composition and symmetry that can be related to intentional and unintentional changes in the growth conditions. This technique can provide rapid feedback with little sample preparation.

### EXPERIMENTAL DETAILS

The InP-based lattice matched HEMT structures used in this study consisted of an undoped InAlAs buffer layer, a 400 Å thick undoped InGaAs channel layer, an undoped InAlAs spacer layer, a Si delta doped layer, an InAlAs Schottky layer, and an InGaAs cap layer. The structures were grown in a VG 80H molecular beam epitaxy (MBE) machine, or in a horizontal atmospheric pressure metalorganic chemical vapor deposition (MOCVD) reactor. All were grown on Fe-doped InP substrates oriented 2° off the (100) plane. For MBE growth, conventional elemental gallium, indium, and aluminum sources were used with As<sub>4</sub> at a growth rate of 0.6 μm/hr with silicon as the dopant. The InAlAs Schottky layer and the InGaAs cap layer were doped to a carrier concentration of  $3 \times 10^{17} \text{ cm}^{-3}$ . For MOCVD growth, Trimethylindium (TMI), trimethylaluminum (TMA), trimethylarsenic (TMAs), trimethylgallium (TMG) and pure arsine were used as the source materials.<sup>6</sup> Disilane diluted in high purity hydrogen was the pulse dopant source. One of the samples did not contain a Si doping pulse, and the InAlAs Schottky and InGaAs contact layers for all three samples were undoped. A summary of the differences among the samples is given in Table I.

**Table I. Summary of Sample Differences.**

| Sample | Method | Pulsed Doped | T <sub>growth</sub> | Spacer Thickness |
|--------|--------|--------------|---------------------|------------------|
| G23032 | MBE    | yes          | T <sub>1</sub> + 60 | t <sub>s</sub>   |
| G23602 | MBE    | yes          | T <sub>1</sub>      | t <sub>s</sub>   |
| MO1237 | MOCVD  | yes          | T <sub>2</sub>      | t <sub>s</sub>   |
| MO1243 | MOCVD  | yes          | T <sub>2</sub>      | 2t <sub>s</sub>  |
| MO1233 | MOCVD  | no           | T <sub>2</sub>      | -                |

The 514.5 nm line of an Ar<sup>+</sup> laser was used to excite the samples for the PL spectra. Peak power densities were between 0.5 and 2 W/cm<sup>2</sup>. The signal was dispersed through a 1 m double monochromator with a spectral resolution of 0.7 meV, and sensed with a cooled high purity Ge detector using phase sensitive detection. All spectra were corrected for system response.

#### LINE SHAPE MODEL

The phenomenological line shape model used to fit 77 K PL spectra has been described in detail elsewhere,<sup>7</sup> and will be reviewed briefly here. It includes transitions between the first two electron subbands and the first two heavy hole subbands (Since quantum confinement shifts the light hole subbands to higher energies, they are neglected). The intensity of a direct optical transition between an electron and hole subband at a given photon energy,  $h\nu$ , depends upon the joint density of states,  $D(h\nu)$ , the respective occupation probabilities of the two subbands,  $f_e(h\nu)$  and  $f_h(h\nu)$ , and a coefficient,  $A$ , which includes the interband matrix element:

$$I(h\nu) = AD(h\nu)f_e(h\nu)f_h(h\nu). \quad (1)$$

For our 400 Å quantum wells, the joint density of states is assumed to be that of a two dimensional system represented by a broadened step function in photon energy centered on the bandgap<sup>7,8</sup>

$$D(h\nu) \propto 1/[1+\exp\{-(h\nu - E_g)/\Gamma\}], \quad (2)$$

where  $E_g$  is the energy gap separating the two subbands,  $\Gamma$  is the broadening parameter, and non-parabolicity is neglected. The occupation probability of the electron subband is given by a Fermi distribution, which as a function of photon energy can be written as<sup>7</sup>

$$f_e(h\nu) = 1/[1+\exp\{([m_h/(m_e+m_h)] h\nu + [m_e/(m_e+m_h)] E_g - E_f)/kT\}]. \quad (3)$$

At 77 K, there is insufficient thermal energy to delocalize holes, so their occupation probability is not given by a Fermi distribution. Also, the strong power densities used in this work (0.5 to 2.0 W/cm<sup>2</sup>) preclude the assumption of a Boltzmann distribution for the holes. In order to fit the PL spectra satisfactorily at 77 K, holes must be available over a considerable

wavevector (or energy) range suggesting that the holes are spatially localized, due to alloy disorder or interface roughness.<sup>9</sup> If the localized hole is assumed to have a hydrogen-like wavefunction with a characteristic radius  $a_0$ ,  $\Psi(r)=e^{-\beta r}$  (where  $\beta=1/a_0$ ), then the hole probability distribution in k-space can be written as<sup>10</sup>

$$f_h = 1/(1+E_h/E_{loc})^2, \quad (4)$$

where  $E_h=\hbar^2 k^2/2m_h$  is the hole energy (defined as positive with increasing  $k^2$ ) and  $E_{loc}=\hbar^2 \beta^2/2m_h$  is the hole localization energy. In terms of the photon energy, the hole occupation probability is<sup>7</sup>

$$f_h = \begin{cases} 1, & hv < E_g \\ 1/\{1+[m_e/(m_e+m_h)](hv-E_g)/E_{loc}\}^2, & hv \geq E_g \end{cases} \quad (5)$$

Since asymmetry of a quantum well can mix wavefunctions, the total PL intensity can be modelled as the sum of all possible direct optical transitions between the first two electron and first two heavy hole subbands,<sup>7</sup>

$$I(hv) = \sum_{ij} A_{ij} D(hv) f_{ei}(hv) f_{hj}(hv), \quad (6)$$

where  $A_{ij}$  are the numerical coefficients that include the interband matrix elements. For transitions involving the first heavy hole subband,  $E_g$  in Eqs. (2), (3), and (5) is simply the energy of the relevant electron subband. For transitions involving the second heavy hole subband in order to keep a single reference energy for multiple transitions,  $h\nu$  is replaced by  $h\nu - \Delta E_h$  and  $E_{loc}$  by  $E_{loc} - \Delta E_h$ , where  $\Delta E_h$  is the separation between the heavy hole subbands. Details are given in Ref. 7.

To evaluate Eqs. (3) and (5), the in-plane effective masses of electrons and holes must be known. Electron effective masses have been determined by interband magnetoabsorption measurements<sup>11</sup> and cyclotron resonance.<sup>12,13</sup> For doped quantum wells, the electron effective mass was taken to be 0.049,<sup>13</sup> while for the undoped structure a value of 0.041 was used.<sup>11,12</sup> In the absence of any experimental data on quantum wells, the bulk value of 0.47 was used for the heavy hole effective mass.<sup>11</sup>

## RESULTS

Figure 1 shows the 78 K PL spectrum of a typical single pulse doped lattice matched InP based HEMT (G23062) grown by MBE and the corresponding fit of the line shape model (dashed line). The agreement between the fit and the data is quite good. There is evidence in the spectra for at least two transitions denoted by a peak and a low energy shoulder. The peak corresponds to the e2-hh1 transition, and the shoulder corresponds to the e1-hh1 transition. The ratio of the numerical coefficients  $A_{21}$  and  $A_{11}$  (equivalent to the ratio of the corresponding interband matrix elements) determined from the fit is  $A_{21}/A_{11} = 6.3$ . Figure 2 shows a qualitative schematic of the asymmetric quantum well structure of the InP based HEMT. The  $A_{21}/A_{11}$  ratio is not surprising since the asymmetry of the quantum well structure shown in the

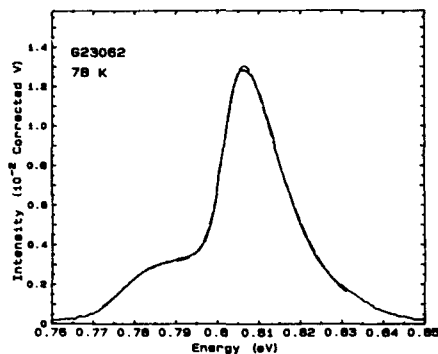


Figure 1. A 78 K photoluminescence spectrum of a single pulse doped lattice matched InP-based HEMT grown by MBE. The peak corresponds to the  $e2-hh1$  transition, and the shoulder to the  $e1-hh1$  transition. The solid curve is the experimental spectrum; the dashed line is the fit to the model.

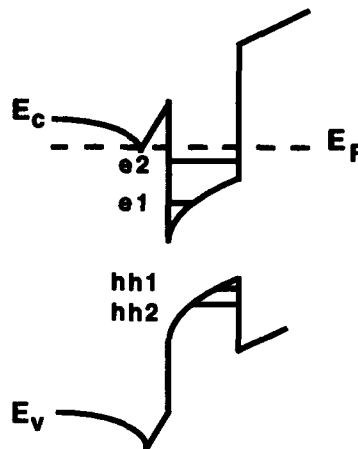


Figure 2. Qualitative schematic of an asymmetric quantum well structure from a single pulse doped lattice matched InP-based HEMT.

schematic causes a large spatial overlap between the  $e2$  and  $hh1$  wavefunctions compared to that of the  $e1$  and  $hh1$  wavefunctions. From the fit, the energies of the two lowest electron subbands (referenced to the top of the first heavy hole subband) are 0.778 and 0.802 eV. The hole localization energy is 34 meV, corresponding to a spatial localization radius of about 15 Å.

Figure 3 shows the 78 K PL spectrum and corresponding fit of a second InP-based HEMT structure, G23032, grown by MBE. The shoulder intensity of the  $e1-hh1$  transition is much stronger relative to the  $e2-hh1$  peak intensity than for sample G23062. Sample G23032 was structurally similar to G23062 except that the InGaAs cap layer was about twice as thick, and the undoped InAlAs buffer layer was about one third as thick. A comparison between the two samples for the fitted parameters:  $A_{21}/A_{11}$ ,  $E_1$ ,  $E_2$ , and  $E_2-E_1$ , is given in Table II. The table also shows the 77 K Hall carrier concentrations,  $n_{77}$ , and mobilities,  $\mu_{77}$ . The  $A_{21}/A_{11}$  ratio was significantly less for G23032 than for G23062 indicating that the quantum well from G23032 was more symmetric. Also, the  $\mu_{77}$  value was considerably greater for G23032 than for G23062 suggesting that the degree of ionized impurity scattering from the Si delta doped layer was less for G23032 than for G23062. SIMS profiles revealed that the Si delta doped layer was broadened to a much greater extent via surface segregation for G23032 than for G23062. Broadening of the Si delta-doped layer by surface segregation would reduce the degree of ionized impurity scattering at 77 K and also cause the InGaAs quantum well to be less asymmetric, since the electric field between the Si doping pulse and the edge of the well would be smaller. Sample G23032 was grown at a substrate temperature about 60 degrees hotter than sample G23062, and the higher growth temperature was believed to be responsible for the increased surface segregation. Sample G23032 showed a slightly higher  $n_{77}$  value than G23062, which may have been caused by an increased parallel conduction contribution from the delta doped Si that surface segregated into the InAlAs Schottky layer. The larger  $E_1$  value from G23032 indicated that the In mole fraction in the InGaAs quantum well was lower for G23032 than for G23062. Finally, from the SIMS profiles of the two samples, it was determined that the InGaAs quantum well was about 30-40 Å wider for G23062. However, the subband energy separation,

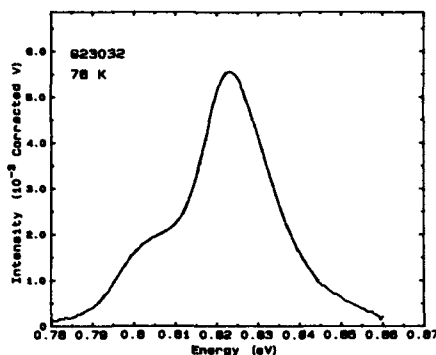


Figure 3. A 78K photoluminescence spectrum of a second lattice matched InP based HEMT, G23032, grown by MBE. Note that the intensity of the e1-hh1 transition is stronger relative to the e2-hh1 peak transition than for G23062 (Figure 1).

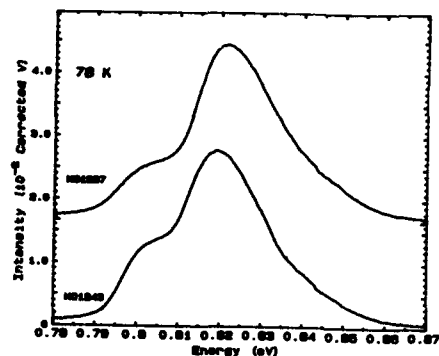


Figure 4. Two 78 K photoluminescence spectra of two single pulse doped lattice matched InP-based HEMTs, MO1237 and MO1243, grown by MOCVD. MO1243 had an InAlAs spacer thickness twice that of MO1237.

$E_2-E_1$ , was slightly greater for G23062 than for G23032 indicating that the effective width seen by the lower electron subbands is also affected by the slope of the triangular potential at the bottom of the well.

Figure 4 shows the 78K PL spectra of two MOCVD grown InP-based lattice matched single pulse doped HEMT structures, MO1237 and MO1243, and Table II shows the 78 K PL fitted parameter values and 77 K Hall results. The shoulder intensity of the e1-hh1 transition was much stronger relative to the e2-hh1 peak intensity, and subsequently the  $A_{21}/A_{11}$  ratio was significantly less for sample MO1243 than for MO1237 attesting that the quantum well from MO1243 was more symmetric. The  $E_1$  values from the two fits were almost identical indicating that the In mole fractions in the InGaAs quantum wells from the two samples were similar. The  $n_{77}$  value was considerably less and the  $\mu_{77}$  value almost double for MO1243 than for MO1237. The growth parameters from both samples were identical except that MO1243 had an InAlAs spacer thickness twice that of MO1237. A doubling of the spacer thickness would cause  $\mu_{77}$  to increase due to less ionized impurity scattering from the Si doping pulse,  $n_{77}$  to decrease due to less charge transfer from the Si delta doped layer into the InGaAs quantum well, and the quantum well shape to be more symmetric due to the reduced electric field. The comparison of the  $A_{21}/A_{11}$  ratio and the Hall measurement results confirmed the spacer thickness variation.

The InAlAs spacer thickness was the same for the two MBE samples and MO1237, yet the  $A_{21}/A_{11}$  ratio was significantly less and the  $n_{77}$  value was considerably greater for MO1237 than for the two MBE samples. This comparison indicated that the quantum well for MO1237 was more symmetric even though it contained a higher electron sheet density. These results could have been possible if the conduction and valence bands in the well near the InAlAs buffer interface were lower relative to the Fermi level for sample MO1237 than for the two MBE samples. In fact, the MOCVD buffer layers have Si concentrations in the low  $10^{16} \text{ cm}^{-3}$  range,<sup>6</sup> whereas the Si concentration in the MBE buffer layers was less than the SIMS detection limit of  $5 \times 10^{15} \text{ cm}^{-3}$ . Thus the differences in the electrically active Si concentrations between the MOCVD and MBE InAlAs buffer layers lead to different Fermi energy pinnings in the buffer layers, which causes the well from MO1237 to be more symmetric.

Finally, Table II shows the fitting parameters determined from a fit to the 78 K PL data from sample MO1233, which did not contain a Si doping pulse. The  $A_{21}/A_{11}$  ratio of 0.58 was much less and the  $E_2-E_1$  value of 11 meV was much lower for MO1233 than for the two MOCVD and two MBE samples. These values confirm the expectation that the quantum well was much more symmetric for the sample without the Si pulse than for the other four samples.



Table II. Photoluminescence and 77 K Transport Parameters.

| Sample | $A_{21}/A_{11}$ | $E_1(\text{eV})$ | $E_2(\text{eV})$ | $E_2-E_1(\text{meV})$ | $n_{77}$<br>( $\times 10^{12} \text{cm}^{-2}$ ) | $\mu_{77}$<br>( $\times 10^4 \text{cm}^2/\text{V}\cdot\text{s}$ ) |
|--------|-----------------|------------------|------------------|-----------------------|---|---|
| G23032 | 4.5             | 0.797            | 0.819            | 22                    | 3.30  | 2.92  |
| G23062 | 6.3             | 0.778            | 0.802            | 24                    | 2.94  | 2.39  |
| MO1237 | 3.5             | 0.796            | 0.816            | 19                    | 3.94  | 2.28  |
| MO1243 | 2.1             | 0.797            | 0.814            | 17                    | 3.16  | 4.28  |
| MO1233 | 0.58            | 0.807            | 0.818            | 11                    | -   | -   |

## SUMMARY

This work has shown that liquid nitrogen PL is sensitive to subtle variations in InP-based lattice matched HEMT structures. Quantitative energy and transition amplitude information have been extracted through fitting a phenomenological line shape model to the PL spectra. From the subband energies, changes in well composition were inferred. Variations of the relative intensities of the "allowed" e1-hh1 transition versus the "forbidden" e2-hh1 were related to changes in effective symmetry of the InGaAs quantum well, which was affected by InAlAs spacer thickness, the degree of surface segregation of the Si delta-doped layer, and the InAlAs buffer layer quality.

## REFERENCES

1. Y. Nakata, S. Sasa, Y. Sugiyama, T. Fujii, and S. Hiyamizu, *Jap. J. Appl. Phys.* **26**, L59 (1987).
2. Y. C. Kao, A. C. Seabaugh, H. Y. Liu, T. S. Kim, M. A. Reed, P. Saunier, B. Bayraktaroglu, and W. M. Duncan in *InP and Related Mat. for Adv. Elec. and Opt. Devices*, edited by R. Singh and L.J. Messick (SPIE Vol. 1144, 1989), pp. 30-38.
3. M. A. Tischler, B. D. Parker, P. M. Mooney, and M. S. Goorsky, *J. Elec. Mat.* **20**, 1053 (1991).
4. J. P. Estera, W. M. Duncan, Y. C. Kao, and H. Y. Liu, in *Proc. of the Fourth International Conf. on InP and Related Mat.* (IEEE, Newport, RI 1992), pp. 28-31.
5. M. A. Tischler, B. D. Parker, J. DeGelormo, T. N. Jackson, F. Cardone, and M. S. Goorsky, in *Proc. of the Third International Conf. on InP and Related Mat.* (IEEE, Cardiff, Wales 1991), pp. 602-605.
6. N. Pan, J. Elliot, J. Carter, H. Hendriks, and L. Aucoin in *Proc. International Symp. on GaAs and Related Compounds*, (Inst. Phys. Conf. Series, 1993, to be published).
7. S. K. Brierley, *J. Appl. Phys.* **74**, 2760 (1993).
8. R. Cingolani, W. Stolz, and K. Ploog, *Phys. Rev. B* **40**, 2950 (1989).
9. K. J. Nash, M. S. Skolnick, and S. J. Bass, *Semicond. Sci. Technol.* **2**, 329 (1987).
10. J. M. Rorison, *J. Phys. C* **20**, L311 (1986).
11. K. Alavi, R. L. Aggarwal, and S. H. Groves, *Phys. Rev. B* **21**, 1311 (1980).
12. R. J. Nicholas, S. J. Sessions, and J. C. Portal, *Appl. Phys. Lett.* **37**, 178 (1980).
13. R. F. Kopf, H. P. Wei, A. P. Perley, and G. Livescu, *Appl. Phys. Lett.* **60**, 2386 (1992).

## PHOTOREFLECTANCE CHARACTERIZATION OF InGaAs/GaAs SUPERLATTICES GROWN ON [111]-ORIENTED SUBSTRATES

R. G. RODRIGUES\*, K. YANG\*\*, L. J. SCHOWALTER\*\*, and J. M. BORREGO\*

Rensselaer Polytechnic Institute, Troy, NY

\*Electrical, Computer, and Systems Engineering Dep.

\*\*Physics Department

### ABSTRACT

We report the results of a photoreflectance (PR) study of InGaAs/GaAs strained-layer quantum wells and superlattices (SLs) grown by MBE on [111]B GaAs substrates. Under our measurement conditions, the PR spectra display features we can relate to the bandgaps of both materials and to optical transitions in the quantum structures. Using the photovoltaic effect to vary the surface electric field of our  $i$ - $n^+$  and  $p^+$ - $i$ - $n^+$  samples in a strictly contactless manner, we find optical transitions red-shifting with increasing intensity of illumination from a CW HeNe laser in [111]-grown structures, a well known effect which can be attributed to the strain-generated electric field (SGEF) present in these structures. We also find experimental support for the predicted effectiveness of free-carriers in screening the SGEF and thereby originating highly non-linear absorption.

### INTRODUCTION

In the past, difficulties found in the MBE growth have limited the number of experimental studies of [111]-oriented InGaAs/GaAs SLs but we are now able to grow high quality structures in this orientation<sup>1</sup>. Compound semiconductor SLs grown on [111]-oriented substrates feature a SGEF across their layers directed along the growth axis<sup>2</sup>. These structures are expected to display novel optical and transport properties as predicted by existing theory, which may have unique applications<sup>3</sup>. Photoreflectance (PR) is an established non-destructive characterization tool of semiconductor microstructures, requiring no sample preparation, and capable of accurately determining the energy location of even weak electronic transitions<sup>4,7</sup>. In this study we compare spectra from [111]B- and [100]-grown samples containing single quantum wells and superlattices. Most of these samples have  $i$ - $n^+$  or  $p^+$ - $i$ - $n^+$  diode-like structure with the thin quantum layers inserted in their intrinsic region, so that under equilibrium conditions these layers are subject to intense electric fields ( $\approx 10^5$  V/cm). These fields can easily be reduced in a contactless manner by shining a powerful laser light onto the surface of the sample. In the [111]B-grown samples, an SGEF is also present with a magnitude that can exceed that of the diode's field and pointing in the opposite direction. The SGEF is also expected to be drastically screened by free carriers<sup>8</sup>. In Fig. 1 we represent the band diagram that models these [111]B structures for the case of just one quantum well. In this particular material system, the concentration of indium in the well layer determines both the well depth and the intensity of the SGEF. Published studies of similar [111] structures include an observation of the blue shift with increasing electric field of quantum well absorption peaks and the determination of the SGEF in a contacted  $p$ - $i$ - $n$  QW at 77K using the photocurrent technique<sup>9</sup>, and the contactless measurement of the SGEF through an analysis of the Franz-Keldysh oscillations obtained about the fundamental gap of GaAs in PR tests of an  $i$ - $n^+$  QW sample<sup>10</sup>. [100] structures in the InGaAs/GaAs system have been extensively studied using PR<sup>11,12</sup>.

Table I  
MBE quantum structures in the InGaAs/GaAs system

| Ref.    | Orient. | # QWs | QW width (Å) | QW spacing (Å) | In conc. (%) | Type                             |
|---------|---------|-------|--------------|----------------|--------------|----------------------------------|
| G321    | [111]B  | 11    | 70           | 140            | 12           | undoped                          |
| G342    | [111]B  | 10    | ~60          | ~140           | 7.5          | p <sup>+</sup> -i-n <sup>+</sup> |
| G345 -a | [111]B  | 1     | ~100         | NA             | 15           | i-n <sup>+</sup>                 |
| G345 -b | [100]   | 1     | ~100         | NA             | 15 ?         | i-n <sup>+</sup>                 |
| G409 -a | [111]B  | 10    | ~70          | ~140           | ~6 ?(PR)     | p <sup>+</sup> -i-n <sup>+</sup> |
| G409 -b | [100]   | 10    | ~70          | ~140           | ~6 ?(PR)     | p <sup>+</sup> -i-n <sup>+</sup> |

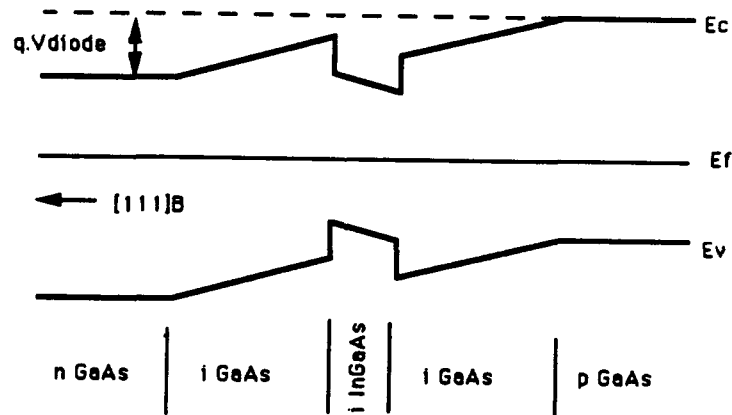


Fig. 1 - Band diagram of a [111]B-grown p-i-n InGaAs/GaAs strained-layer QW structure.

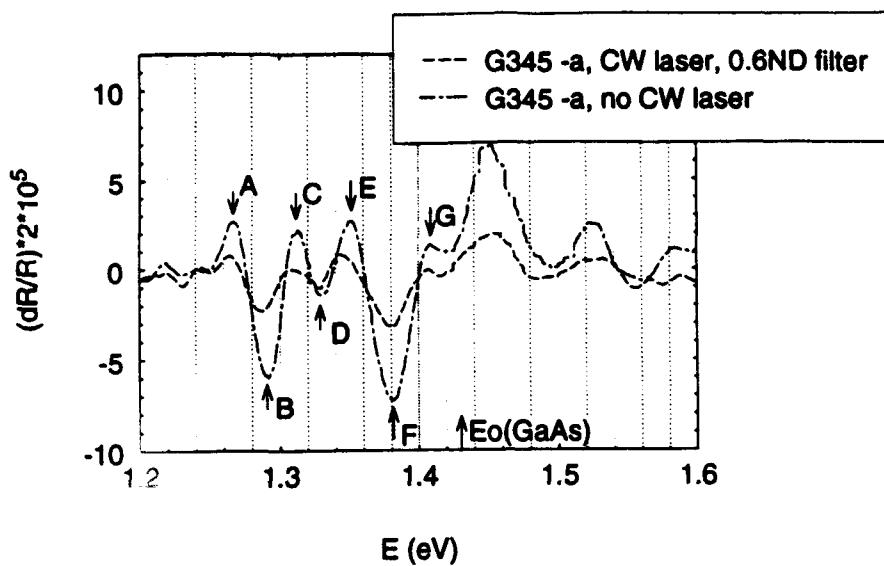


Fig. 2 - PR spectra of a [111]B-grown i-n<sup>+</sup> InGaAs/GaAs strained-layer QW structure under two different intensities of CW laser illumination.

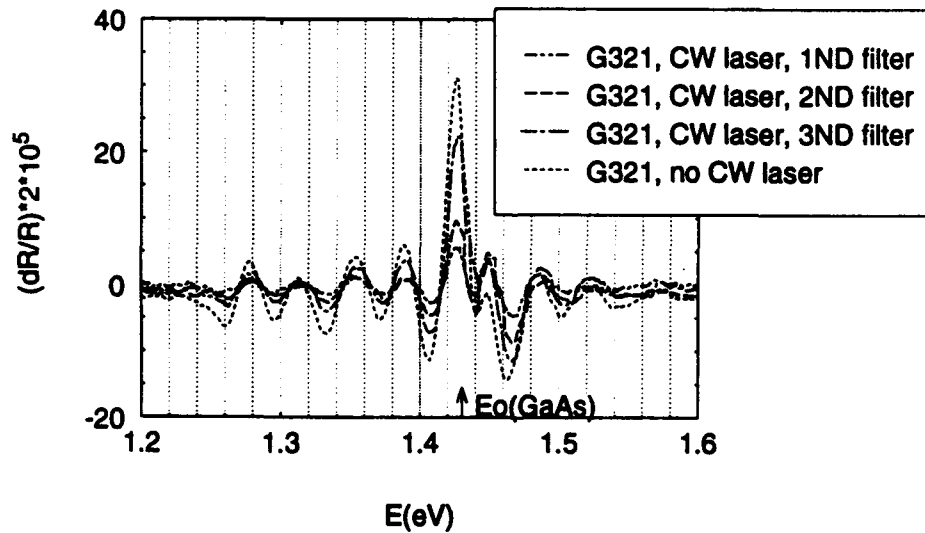


Fig. 3 - PR spectra of a [111]B-grown undoped InGaAs/GaAs strained-layer superlattice structure under different intensities of CW laser illumination.

## EXPERIMENTAL

The optimized MBE procedure used to grow on [111]B GaAs surfaces has been described elsewhere<sup>1</sup>. The main rules are to grow on GaAs substrates tilted 3° towards the  $\langle 211 \rangle$  direction, to grow at the low-temperature end of the  $\sqrt{19} \times \sqrt{19}$  surface reconstruction region (about 540°C), and under an As/Ga flux ratio of 10. A total of 11 samples grown on [111]B and on [100] substrates were inspected using PR. The structures of the relevant samples for this study are presented in Table I. Our photoreflectance setup employs a Schoeffel GH252 high intensity grating monochromator with a focal length of 0.25 meter, illuminated by a 350W quartz-tungsten-halogen lamp. Its output beam is the probe beam for PR and is focused onto a spot of approximately 6mm $\times$ 1mm. The whole area of this spot is modulated by the chopped light of a 1mW HeNe laser, carried by an optical fiber. This modulating beam is defocused on the sample and has a total power of 14 $\mu$ W over an area of about .25cm<sup>2</sup>. These two beams are powerful enough to produce some undesirable screening of the surface fields on the samples but prohibitive noise levels prevented their further attenuation. The detector is a silicon photodiode, preceded by a glass filter that rejects the scattered laser light of 632.8nm. The signal from the detector is input to a PAR preamplifier and the output of this is fed both to a DC voltmeter and to a PAR model 124 lock-in amplifier. These two instruments feed their output to the A/D board of a PC which also reads the wavelength information from the monochromator. A second HeNe laser, this one not chopped (CW), is available to shine approximately an additional 35mW/cm<sup>2</sup> light onto the probe beam spot. Together with a collection of neutral density filters, this laser can be used to screen the surface field of a sample and in this way obtain PR spectra under different electric field intensities (three-beam PR) without need for electrical contacts.

## RESULTS OF MEASUREMENTS AND DISCUSSION

Fig. 2 represents two out of a collection of PR spectra obtained from a [111]B i-n<sup>+</sup> single QW sample (G345 -a). The only difference between the conditions under which these spectra were obtained was the intensity of the CW laser beam. In the range of beam intensity that we were able to scan, spectral features A through G, corresponding to confined transitions in the quantum well, consistently shift to the red as the CW laser intensity increases, i.e., as the diode electric field decreases. This effect could be expected<sup>9</sup> and provides evidence for the presence of SGEF in the quantum well layer. The energy position of the lowest lying of these features further confirm that indium was incorporated to within the desired concentration during growth. In analogous spectra of one other sample grown simultaneously with this one but on a [100] substrate (G345 -b) our method revealed blue shifts with increasing CW laser beam intensity as expected in a QW without SGEF. Other authors<sup>10</sup> have reported finding Franz-Keldysh oscillations but no quantum well spectral features in similar samples. Fig. 3 represents a collection of PR spectra obtained from a [111]B all intrinsic material superlattice sample (G321). The most intense feature is at the bandgap energy of GaAs. We do not find any energy shift of the features as we shine a CW laser light onto the sample. Fig. 4 represents a collection of PR spectra obtained from a [111]B p<sup>+</sup>-i-n<sup>+</sup> superlattice sample (G342). The only difference between the conditions under which these spectra were obtained was again the intensity of the CW laser beam. In features A through H we observe a shift to the red as the CW laser beam intensity increases. In features A through D as the beam intensity keeps increasing we observe a blue-shift after the initial red shift. For a [100] p<sup>+</sup>-i-n<sup>+</sup> superlattice sample (G409 -b) we

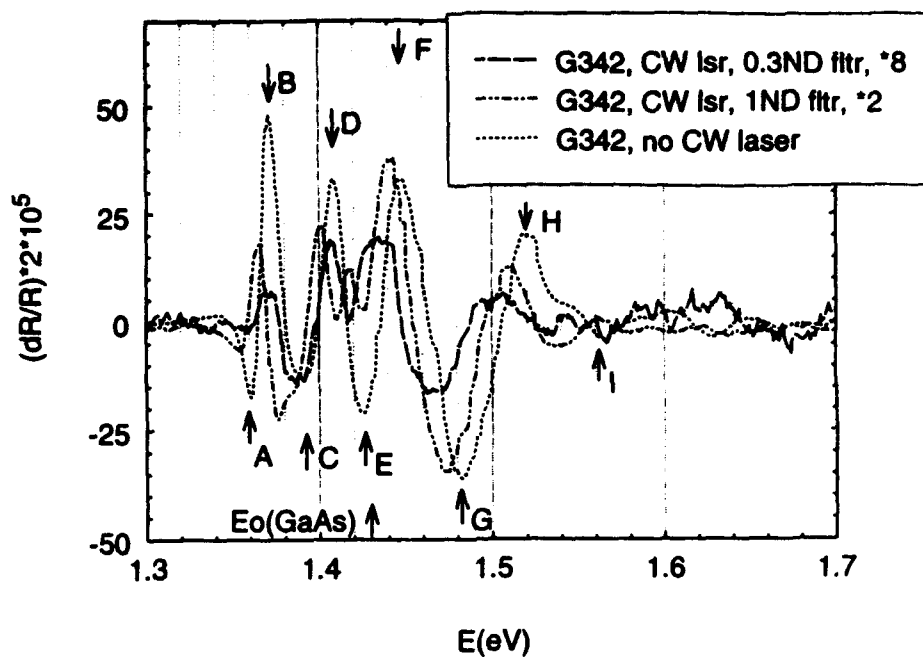


Fig. 4 - PR spectra of a [111]B-grown p<sup>+</sup>-i-n<sup>+</sup> InGaAs/GaAs strained-layer superlattice structure under different intensities of CW laser illumination.

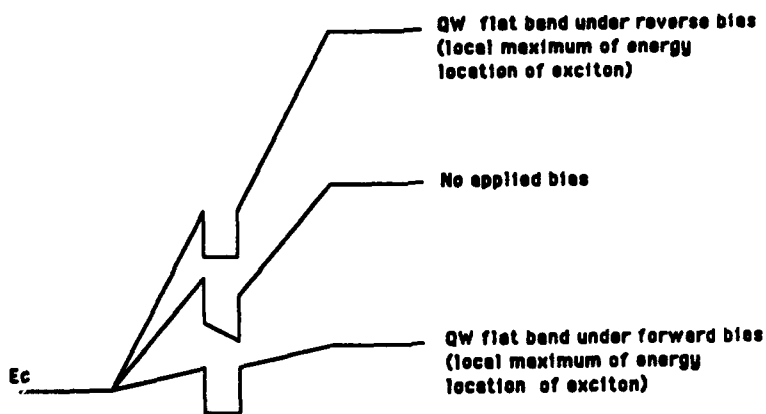


Fig. 5 - Proposed band diagram of a [111]B-grown p-i-n InGaAs/GaAs strained-layer QW structure under bias.

obtained exclusively blue-shifts with increasing CW laser beam intensity. A red-shift with decreasing electric field of a superlattice transition can be due to broadening of superlattice minibands<sup>13,14,15</sup>. In the present case the high intensity of the diode field, the sharpness and high intensity of the observed peaks, the fact that in the [100] superlattice only blue shifts with increasing CW laser beam intensity could be found, and the observation of similar red-shifts with increasing CW laser beam intensity in the [111]B single QW sample lead us to propose that in our p<sup>+</sup>-i-n<sup>+</sup> superlattices a near-complete localization occurs ( $qFD \gg \Delta$ , where F is the electric field, D is the superlattice period and  $\Delta$  is the width of a miniband). If this is the case the QWs form a so-called Stark ladder and the red-shifts observed can be interpreted in terms of single QW levels. Previous work<sup>9</sup> has demonstrated that reverse biasing the p<sup>+</sup>-i-n<sup>+</sup> diode it is possible to reach a situation in which the field of the diode perfectly cancels the SGEF and the quantum well reaches a flat-band situation. At this point the exciton energy position reaches a local maximum as a function of reverse bias intensity. Our experimental results now show that a local minimum of the exciton energy position as a function of forward bias exists in our sample. This suggests that another way to reach the flat-band situation for the quantum well is to engineer the sample in such a way that under forward bias the free carriers present screen the SGEF faster than they do the diode field (Fig. 5). At this flat-band point the energy location of the exciton will reach another local maximum. Between the forward bias local maximum and the reverse bias local maximum a local minimum such as the one we detected must exist. In some of our diode-like samples we tried fitting the features above the bandgap of GaAs to an expression valid in the intermediate field regime of electroreflectance in bulk materials<sup>16</sup>, a case in which it is possible to observe Franz-Keldysh oscillations. This modelling was found inadequate, leading us to believe that these features are affected by transitions involving unconfined levels.

#### ACKNOWLEDGEMENTS:

One of the authors (R.Rodrigues) acknowledges support from Programa CIENCIA, JNICT, Portugal, and is thankful to Prof. F. H. Pollak and to Dr. E. Mendez for very enlightening conversations on PR and on electric fields in quantum semiconductor structures.

#### REFERENCES:

- <sup>1</sup> K. Yang and L. J. Schowalter, J. Vac. Sci. Technol. B **11**, 779 (1993).
- <sup>2</sup> D. L. Smith, Solid State Comm., **57**, 919 (1986).
- <sup>3</sup> B. K. Laurich, K. Elcess, C.G. Fonstad, J.G. Berry, C. Mailhot, and D.L. Smith, Phys. Rev. Lett. **62**, 649 (1989).
- <sup>4</sup> M. Cardona, *Modulation Spectroscopy*, (Academic Press, New York, 1969).
- <sup>5</sup> D. E. Aspnes, in *Handbook on Semiconductors*, edited by T.S. Moss (North-Holland, New York, 1990), Vol. 2, p. 109.
- <sup>6</sup> O. J. Glembocki and B. V. Shanabrook, in *Semiconductors and Semimetals*, edited by R. K. Willardson, A. C. Beer and E. R. Weber, Vol. 36, edited by D. G. Seiler and C. L. Littler (Academic Press, Boston, 1992), p. 221.
- <sup>7</sup> F. H. Pollak and H. Shen, Mat. Sci. Eng. R **10**, 275 (1993).
- <sup>8</sup> C. Mailhot and D. L. Smith, Phys. Rev. B, **35**, 1242 (1987).

- <sup>9</sup> E. A. Caridi, T. Y. Chang, K. W. Goossen, and L. F. Eastman, Appl. Phys. Lett. **56**, 659 (1990).
- <sup>10</sup> H. Shen, M. Dutta, W. Chang, R. Moekirk, D. M. Kim, K. W. Chung, P. P. Ruden, M. I. Nathan, and M. A. Stroscio, Appl. Phys. Lett. **60**, 2400 (1992).
- <sup>11</sup> A. Ksendzov, H. Shen, F. H. Pollak, and D. P. Bour, SPIE, Vol. 1283, 241 (1990).
- <sup>12</sup> S. C. Shen, W. Shan, X. M. Fang, Z. Hang, and F. H. Pollak, SPIE, Vol. 1286, 221 (1990).
- <sup>13</sup> C. Weisbuch and B. Winter, *Quantum Semiconductor Structures*, p. 93, (Academic Press, Boston, 1991).
- <sup>14</sup> E. E. Mendez, F. Agullo-Rueda and J.M. Hong, Appl. Phys. Lett. **60**, 2624 (1988).
- <sup>15</sup> M. M. Dignam and J. E. Sipe, Phys. Rev. Lett. **64**, 1797 (1990).
- <sup>16</sup> D. E. Aspnes, Phys. Rev. B **10**, 4228 (1974).



## PHOTOREFLECTANCE CHARACTERIZATION OF InGaAs LATTICE MATCHED TO InP

V. BELLANI\*, M. AMIOTTI\*, M. GEDDO\*, G. GUIZZETTI\* AND G. LANDGREN\*\*

\* Università di Pavia, Dipartimento di Fisica "A. Volta", Via Bassi 6, I-27100 Pavia, Italy

\*\* Royal Institute of Technology, Semiconductor Laboratory, Electrum 229, S-16440 Kista, Sweden

### ABSTRACT

We measured photoreflectance (PR) spectra at different temperatures between 80 and 300 K, and optical absorption (OA) at 3 K on MOVPE grown  $\text{In}_{1-x}\text{Ga}_x\text{As}$  nearly lattice-matched to InP. x-ray diffraction measurements gave a lattice mismatch  $\Delta a/a_0 = -0.9 \cdot 10^{-3}$  between ternary alloy and InP, corresponding to  $x = 0.485$ . We obtained the energy gap dependence on T from PR spectra. The blue shift of the gap was accounted for in terms of compositional difference with respect to the perfectly lattice matched alloy ( $x = 0.472$ ), and elastic strain; moreover PR and OA showed evidence of the valence bands splitting at  $k = 0$  due to interfacial strain, in fine agreement with theory.

### INTRODUCTION

There is a great interest in  $\text{In}_{1-x}\text{Ga}_x\text{As}$  ternary alloy for the promising applications in optoelectronic and high-speed electronic devices:  $\text{In}_{1-x}\text{Ga}_x\text{As-InP}$  heterostructure lasers emit in 1.3-1.7  $\mu\text{m}$  spectral region which is around the maximal transmission window of the quartz optical fibers. Usually III-V alloys are grown on standard substrates, including InP. Therefore the interfacial lattice matching condition should be carefully controlled to obtain good quality structures. In fact a lattice mismatch between  $\text{In}_{1-x}\text{Ga}_x\text{As}$  and InP can produce undesirable effects, like misfits and dislocation or strain that influence the device's performances.

It is difficult to grow  $\text{In}_{1-x}\text{Ga}_x\text{As}$  perfectly matched to InP, with corresponding  $x = 0.472$ . Thus  $x$  is usually obtained unintentionally far from desired values even by about 1%. This leads to a small mismatch ( $\Delta a/a_0 \leq 10^{-3}$ ) in the heterostructure, but it is sufficient to change the material's optical properties.

Biaxial strain produces two effects on the band structure of  $\text{In}_{1-x}\text{Ga}_x\text{As}$ : i) it shifts the band gap at higher or lower energies depending on the sign of the strain; ii) it removes the degeneracy between the heavy and light holes in the valence band at  $k = 0$ . Generally the band gap value is obtained by photoluminescence measurements only indirectly [1]. Photoluminescence study can explore the effect i), but doesn't permit observation of the phenomenon ii) [1]. Instead PR can determine the band gap with higher precision. Moreover OA and PR at low temperatures permit direct observation of the gap splitting, as reported by Zielinski et al. [2], also in nearly lattice matched  $\text{In}_{1-x}\text{Ga}_x\text{As-InP}$  heterostructure.

## EXPERIMENTAL

In<sub>1-x</sub>Ga<sub>x</sub>As layers 0.6  $\mu\text{m}$  thick were grown epitaxially on *n*-doped InP substrate by low pressure Metal Organic Vapour Phase Epitaxy. The growth temperature was 650 °C. Growth rate calibrations were performed to obtain perfect lattice matched layers.

High resolution x-ray diffraction profiles (HRXRD) were obtained using CuK $\alpha_1$  ( $\lambda = 1.54051 \text{ \AA}$ ) radiation and four crystal (Ge, 220) monochromator at room temperature. They yielded the value of the tetragonal deformation of In<sub>1-x</sub>Ga<sub>x</sub>As epilayer in the direction normal to the interface, i.e. the mismatch  $\Delta a^\perp/a_0 = (a^\perp - a_0)/a_0$ , where  $a^\perp$  is the In<sub>1-x</sub>Ga<sub>x</sub>As lattice parameter perpendicular to the interface and  $a_0$  is the InP lattice parameter.

PR measurements were performed at near normal incidence with an apparatus having a HeNe laser as a pump source ( $\lambda = 6328 \text{ \AA}$  and power 5 mW) and a 100 W halogen lamp as a probe source. The laser beam was mechanically chopped at a frequency of 220 Hz. The samples were mounted on a cold finger of a microminiature Joule-Thomson refrigerator coupled with a programmable temperature controller performing measurements in the 80-300 K temperature range.

OA spectra were measured on samples immersed in liquid helium ( $T = 3 \text{ K}$ ). The detection apparatus consisted of a 1402 Spex double grating spectrometer and a liquid nitrogen cooled Ge detector of North Coast Corp. The light source was a 100 W halogen lamp, mechanically chopped at a frequency of 85 Hz. The signal was analysed with a lock-in system.

## RESULTS AND DISCUSSION

In Fig. 1 we report the PR spectra of the heterostructure at different temperatures. The lineshapes display typical Franz-Keldysh oscillations (FKO) which strongly resemble that observed originally by electroreflectance in GaAs [3] and in In<sub>1-x</sub>Ga<sub>x</sub>As [4,5] for an intermediate electric field regime. The signal  $\Delta R/R$  is of the order of  $10^{-4}$ . According to FKO theory [6], the energy position of the extrema in the PR spectra may be approximated by

$$E_n = E_0 + \hbar\Omega X_n \quad (1)$$

where  $\hbar\Omega = (\hbar^2 e^2 F_s^2 / 8\mu)^{1/3}$ ,  $X_n = [3\pi(n-1/2)/2]^{2/3}$  for a 3D critical point; ( $n = 1, 2, \dots$ ) is the extreme index;  $F_s$  is the built-in surface electric field, and  $\mu$  is the reduced effective mass in the field direction. From eq. (1) a precise value of the energy gap  $E_0$  at each temperature can be determined plotting  $E_n$  versus  $X_n$ . For all temperatures the plots show remarkable linearity, confirming the identification of the spectral features as FKO. Moreover PR spectra exhibit a splitted double band-gap feature as observed by other authors [4] in a sample with a lattice mismatch  $\Delta a/a_0$  greater than our by a factor of two. We note that the intensity of the signal increases as the temperature decreases and the period of oscillation strongly decreases implying that, according to eq. (1), also  $F_s$  decreases.

We see that at nearly 200 K the main negative peak (centred at 0.77 eV at 210 K) splits in two substructures which become more resolved by decreasing  $T$ , and which superimposes itself on the FKO behaviour of  $\Delta R/R$ . We will explain later that this behaviour is related to the strain at the interface between In<sub>x</sub>Ga<sub>1-x</sub>As and InP. Now we note that the energy separation between the two split-peaks

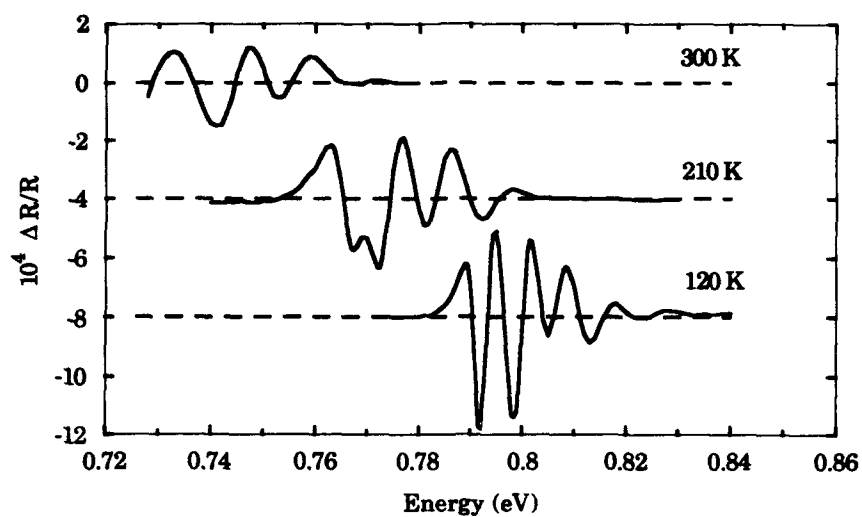


Fig. 1. Photoreflectance spectra of  $\text{In}_{0.515}\text{Ga}_{0.485}\text{As}$  on InP, at different temperatures.

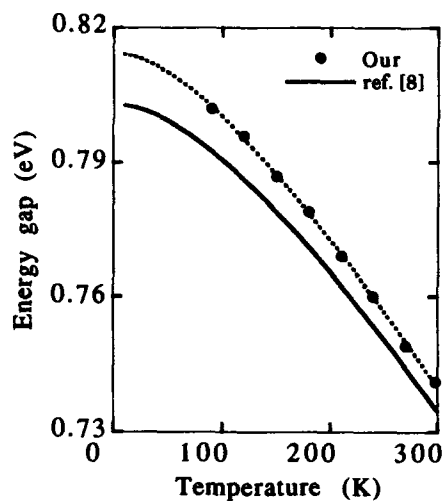


Fig. 2. Energy gap versus temperature of  $\text{In}_{0.515}\text{Ga}_{0.485}\text{As}$  on InP.

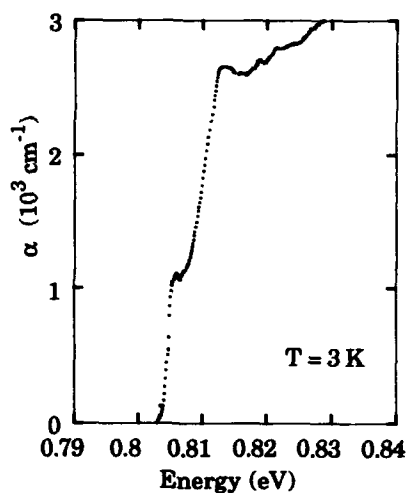


Fig. 3. Low temperature absorption of the  $\text{In}_{0.515}\text{Ga}_{0.485}\text{As}$  on InP.

remains the same ( $\sim 7$  meV) at all temperatures while the energy separation of any two peaks immediately following the band-gap region decreases as the temperature (and  $F_s$ ) is lowered. This is consistent with the predicted behaviour of the FKO's period vs.  $F_s$ . Moreover the overall spectrum shows a blue-shift due to the increase of the  $\text{In}_x\text{Ga}_{1-x}\text{As}$  gap, lowering the temperature.

Fig. 2 shows the experimental values (dots) of the gap  $E_0$  versus  $T$ . We fit the experimental points with the Varshni formula [7]

$$E_0(T) - E_0(0) = \frac{-\alpha T^2}{(T + \beta)} \quad (2)$$

where  $\alpha = 4 \cdot 10^{-4}$  eV  $\text{K}^{-1}$ ,  $\beta = 182$  K,  $E_0(0) = 0.814$  eV are the fit parameters. The fit is the upper line in the figure, where, for comparison, we draw the Varshni gap behaviour, taking recent reliable values  $\alpha = 4 \cdot 10^{-4}$  eV  $\text{K}^{-1}$ ,  $\beta = 226$  K and  $E_0(0) = 0.803$  eV from ref. [8]. We see that our curve (upper) is 7 meV higher at room temperature and 10 meV at 80 K.

In Fig. 3 the low temperature ( $T = 3$  K) OA spectrum is reported, showing two excitonic peaks, at 0.806 eV and at 0.813 eV respectively, on the absorption edge. At higher energies the absorption decreases a little, corresponding to the energy gap  $E_0 = 0.816$  eV of the material. We attribute the two peaks to the splitted valence band with ( $J = 3/2, m_J = \pm 3/2$ ) and ( $J = 3/2, m_J = \pm 1/2$ ) [1]. The split value from OA and PR spectra is the same, and is  $\sim 7$  meV.

When the lattice mismatch between the epilayer  $\text{In}_{1-x}\text{Ga}_x\text{As}$  and the InP substrate is small ( $\Delta a/a_0 \leq 10^{-3}$ ) and the thickness  $d \leq 1$   $\mu\text{m}$ , the layer lattice has only a tetragonal deformation.  $\Delta a$  is the difference between the natural unstrained lattice parameter of the  $\text{In}_{1-x}\text{Ga}_x\text{As}$  ( $a$ ) and InP ( $a_0$ ).  $\Delta a/a_0$  is related to the measured mismatch  $\Delta a^\perp/a_0 = 1.8 \cdot 10^{-3}$  of the epilayer in the direction normal to the surface by the relation [1]

$$\frac{\Delta a}{a_0} = \frac{C_{11}}{C_{11} + 2C_{12}} \left( \frac{\Delta a^\perp}{a_0} \right) \quad (3)$$

where  $C_{ij}$  is the elastic stiffness of the  $\text{In}_{1-x}\text{Ga}_x\text{As}$  layer. Taking  $C_{11} = 1.016$  ( $10^{12}$  dyn/cm $^2$ ),  $C_{12} = 0.509$  ( $10^{12}$  dyn/cm $^2$ ) from ref. [9], using the Vegard law we obtained  $\Delta a/a_0 = -0.9 \cdot 10^{-3}$ . This value of  $\Delta a/a_0$  corresponds to  $x = 0.485$  to be compared to  $x = 0.472$  of the perfectly matched alloy.

Both strain and difference in  $x$  influence the band gap  $E_0$ . The difference  $(\delta E_0)_c$ , due to the compositional contribution, between energy gap values for  $\text{In}_{1-x}\text{Ga}_x\text{As}$  and  $\text{In}_{1-x-\Delta x}\text{Ga}_{x+\Delta x}\text{As}$  is valuated to be [10]

$$(\delta E_0)_c = 0.505 \Delta x + 1.11 x \Delta x \quad (\text{eV}) \quad (4)$$

In our case  $\Delta x = 0.485 - 0.472 = 0.013$  so  $(\delta E_0)_c = 13$  meV, i.e. the gap increases.

As regards the strain contribution to  $E_0$ , the calculated energy gaps between the conduction and splitted valence bands at  $k = 0$ , to the first order in the strain, are [11]

$$E_{\pm} = \left[ -2a \frac{C_{11} - C_{12}}{C_{11}} \pm b \frac{C_{11} + 2C_{12}}{C_{11}} \right] \epsilon \quad (5)$$

where  $E_{+}$  refers to the  $m_J = \pm 3/2$  band and  $E_{-}$  to the  $m_J = \pm 1/2$  band;  $\epsilon = -\Delta a/a_0$ ;  $a$  is the hydrostatic deformation potential and  $b$  is the shear deformation potential appropriate to strain of tetragonal symmetry; we used  $a = -7.88$  eV,  $b = -1.75$  eV, from ref. [9].

The gap energy values calculated by the analysis of the FKO and the OA spectra are mainly determined by the  $m_J = 3/2$  band [2]. So the shift  $(\delta E_0)_s$  is relative to  $E_{+}$  of eq. (5). For our sample  $(\delta E_0)_s = -5$  meV at room temperature. In conclusion, the sum of the compositional and of the strain contribution to the gap shift is  $\delta E_0 = (\delta E_0)_c + (\delta E_0)_s = 8$  meV, in agreement with our experimental results, compared with those of ref. 8 (Fig. 2).

The valence band splitting, from eq. (5), results equal to 6.3 meV by the following:

$$\Delta E = E_{+} - E_{-} = -2b \frac{C_{11} + 2C_{12}}{C_{12}} \epsilon = 7.01 \epsilon \quad (6)$$

so we attribute the two peaks in PR and AO spectra at low temperatures to the + and - states splitted by the strain field. The agreement between the experimental ( $\sim 6.3$  meV) and calculated value (6.3 meV) of the splitting leads to conclusion that we have coherent growth.

Let's consider how the strain varies with temperature  $T$  [12]. We assume the thermal expansion coefficients  $\alpha_{th}(\text{InP}) = 4.56 \cdot 10^{-6} \text{ } ^\circ\text{C}^{-1}$  and for the  $\text{In}_{1-x}\text{Ga}_x\text{As}$  alloy a weighted media of the values  $\alpha_{th}(\text{GaAs}) = 6.63 \cdot 10^{-6} \text{ } ^\circ\text{C}^{-1}$  and  $\alpha_{th}(\text{InAs}) = 5.16 \cdot 10^{-6} \text{ } ^\circ\text{C}^{-1}$  (from ref. [10]). Thus the absolute lattice mismatch is  $\Delta a = 5.3 \cdot 10^{-3} \text{ \AA}$  at room temperature and  $\Delta a = 6.7 \cdot 10^{-3} \text{ \AA}$  at 100 K that leads to a reduction of the splitting  $\Delta E$  of  $\sim 1.4$  meV. Since our experimental resolution is 1 meV, the distance between the two split peaks in PR spectra appears independent of  $T$ .

## CONCLUSIONS

In conclusion we have shown that PR measurements can precisely determine the gap  $E_0$  of thin  $\text{In}_{1-x}\text{Ga}_x\text{As}$  epilayers nearly matched to InP substrate ( $\Delta a/a_0 \leq 10^{-3}$ ). The dependence of  $E_0$  on temperature  $T$  is in good agreement with the Varshni relation.  $E_0$  results blue-shifted by  $\delta E_0 = 7$  meV at 300 K and 10 meV at 80 K with respect to the  $\text{In}_{1-x}\text{Ga}_x\text{As}$  perfectly matched to InP ( $x = 0.472$ ). Theoretically this shift is due to two contributions;  $(\delta E_0)_c = 13$  meV (compositional effect) and  $(\delta E_0)_s = -5$  meV (strain effect), so that  $\delta E_0 = 8$  meV agrees well with the experimental results.

Moreover PR and OA at low temperatures resolved the valence band splitting due to the biaxial strain, even in samples nominally matched to substrate ( $\Delta a/a_0 \leq 10^{-3}$ ). Experimental splitting energy ( $\sim 7$  meV at all temperatures) is about the same as that calculated (6.3 meV), so we can conclude that the lattice mismatch is elastically adapted (coherent growth).

## ACKNOWLEDGEMENTS

We thank MASPEC-CNR Institute, Parma, for x ray measurements. Thanks are also due to D. Maghini for technical assistance. This work has been partially supported by GNSM-CNR Project "GaAsNet".

## REFERENCES

- 1 H. Asai and K. Oe, J. Appl. Phys. **54**, 2052 (1983).
- 2 E. Zielinski, H. Schweizer, K. Streubel, H. Eisele and G. Weimann, J. Appl. Phys. **59**, 2196 (1986).
- 3 D.E. Aspnes and A.A. Studna, Phys. Rev. Lett. **7**, 4605 (1973).
- 4 A. Dimoulas, P. Tzanetakis, Z. Hatzopoulos, A. Georgakilas, O.J. Glembocki and A. Cristou in The Physics of Semiconductors, ed. by E.M. Anastassakis and J.D. Joannopoulos (World Scientific, Singapore, 1990) pp.1069-1073.
- 5 J.P. Estrera, W.M. Duncan, Y.C. Kao, H.Y. Liu and A. Beam, J. Electr. Mat. **20**, 983 (1991).
- 6 M. Sydor, J. Angelo, J.J. Wilson, W.C. Mitchel and M.Y. Yen, Phys. Rev. B **40**, 8473 (1989).
- 7 Y.P. Varshni, Physica **34**, 149 (1967).
- 8 D.K. Gaskill, N. Bottka, L. Aina and M. Mattingly, Appl. Phys. Lett. **56**, 1269 (1990).
- 9 C.P. Kuo, S.K. Vong, R.M. Kohen and G.B. Stringfellow, J. Appl. Phys. **57**, 5428 (1985).
- 10 S. Adachi, J. Appl. Phys. **53**, 8775 (1982).
- 11 F.H. Pollack and M. Cardona, Phys. Rev. **172**, 816 (1986).
- 12 Z.C. Feng, A.A. Allermann, P.A. Barnes and S. Perkowitz, Appl. Phys. Lett. **60**, 1848 (1992).

---

**PART IV**

---

**Infrared and Raman Spectroscopies**

ROOM TEMPERATURE MEASUREMENT OF PHOTOLUMINESCENCE SPECTRA OF SEMICONDUCTORS  
USING AN FT-RAMAN SPECTROPHOTOMETER

J. D. WEBB,<sup>\*</sup> D. J. DUNLAVY,<sup>\*</sup> T. CISZEK,<sup>\*</sup> R. K. AHRENKIEL,<sup>\*</sup> M. W. WANLASS,<sup>\*</sup>  
R. NOUFI,<sup>\*</sup> AND S. M. VERNON<sup>\*\*</sup>

<sup>\*</sup>National Renewable Energy Laboratory (NREL), Golden, CO 80401

<sup>\*\*</sup>Spire Corporation, Bedford, MA 01730

ABSTRACT

This paper demonstrates the utility of a Fourier transform (FT) Raman spectrophotometer in obtaining the room-temperature photoluminescence (PL) spectra of semiconductors used in photovoltaic and electro-optical devices. Sample types analyzed by FT-PL spectroscopy included bulk silicon and films of copper indium diselenide (CuInSe<sub>2</sub>), gallium indium arsenide (GaInAs), indium phosphide arsenide, (InPAs), and gallium arsenide-germanium alloy (GaAsGe) on various substrates. The FTIR-PL technique exhibits advantages in speed, sensitivity, and freedom from stray light over conventional dispersive methods, and can be used in some cases to characterize complete semiconductor devices as well as component materials at room temperature. Recent innovations that improve the spectral range of the technique and eliminate instrumental spectral artifacts are described.

Introduction

Photoluminescence (PL) spectroscopy has provided a useful tool for measuring properties of semiconductor materials used in photovoltaic (PV), electronic, and optical devices. For example, near-infrared (NIR) PL spectroscopy has been used to detect light- or heat-induced defects ("dangling bonds") in hydrogenated amorphous silicon (Si),<sup>1</sup> to identify shallow donor and acceptor impurities<sup>2</sup> and dislocation defects<sup>3</sup> in crystalline Si, and to predict the efficiency of PV devices produced from copper indium diselenide (CuInSe<sub>2</sub>, or CIS) thin films.<sup>4</sup> Also, NIR-PL spectroscopy has been used to identify acceptor impurities in gallium arsenide (GaAs).<sup>5</sup> Time-resolved photoluminescence (TPL) NIR spectroscopy with nano-second time resolution has been used to measure recombination velocities at Al<sub>0.3</sub>Ga<sub>0.7</sub>As/Al<sub>0.3</sub>Ga<sub>0.7</sub>As interfaces<sup>6</sup> and to optimize the design of high-efficiency aluminum gallium arsenide (AlGaAs)-passivated GaAs solar cells.<sup>7</sup> Although some of this work has been done at room temperature, detection of PL at wavelengths longer than 1  $\mu\text{m}$  (the cutoff wavelength for Si and photomultiplier detectors) using dispersive spectrophotometers has typically required cooling samples to cryogenic temperatures in order to obtain adequate signal-to-noise ratios.<sup>1-5</sup>

Fourier transform infrared (FTIR) spectroscopy offers substantial improvements in signal-to-noise ratios over dispersive spectroscopy through Jacquinot's throughput advantage.<sup>8</sup> Room-temperature PL measurements, with FTIR detection that exploits this advantage, have been reported on materials that emit PL in the near-infrared, including indium gallium arsenide (InGaAs)<sup>9</sup> and the high-T<sub>c</sub> superconductor barium bismuthate (BaBiO<sub>3</sub>).<sup>10</sup> In the latter work, a commercial FT-Raman accessory, with a neodymium-yttrium aluminum garnet (Nd-YAG) laser operating at 1.064  $\mu\text{m}$  as the excitation source, was used with an FTIR spectrophotometer to measure the PL spectra of the superconductor. However, the literature, including the comprehensive 1990 review of FT-Raman spectroscopy by B. Schrader,<sup>11</sup> does not reference the use of FT-Raman spectrophotometers or



accessories to measure the room-temperature PL spectra of semiconductor materials, many of which emit PL at characteristic wavelengths in the near-infrared. We have reported what we believe are the first such measurements.<sup>12</sup> In this work, we describe more fully the utility of an FT-Raman spectrophotometer in the measurement of the PL spectra of semiconductor materials and devices at room temperature.

### Experimental

Silicon, CIS, GaInAs, and InPAs samples were made at NREL in the following manner. The 0.5-mm thick, polished Si sample was cut from a large-grain polycrystalline, low-carbon and oxygen rod purified by multiple float-zoning (FZ). The CIS samples were deposited by vacuum co-evaporation of the elements as approximately 3- $\mu$ m thick films on molybdenum/glass substrates. Additionally, the CIS samples were coated with approximately 70-nm thick cadmium sulfide (CdS) films to form a p-n junction. The CdS films were in turn coated with approximately 0.6- $\mu$ m thick, conductive zinc oxide (ZnO) films to give a functional PV device. The GaInAs samples are single crystal films, approximately 4- $\mu$ m thick, and were grown on crystalline indium phosphide (InP) substrates. The undoped GaInAs films were grown by metalorganic vapor-phase epitaxy at atmospheric pressure (APMOVPE) and are highly uniform in thickness and composition, but are lattice-matched to the InP substrates only for the Ga<sub>0.4</sub>In<sub>0.6</sub>As composition. The InPAs samples were also grown using APMOVPE, and consist of a surface layer several microns thick of uniform elemental composition, but doped to give a p/n junction. Underneath the doped surface layer is a linearly graded InPAs layer several microns thick with phosphorus content decreasing to zero at the surface of the crystalline InAs substrates. Using metalorganic chemical vapor deposition (MOCVD), GaAsGe alloy layers 3- $\mu$ m thick were epitaxially grown on GaAs substrates at Spire Corporation.

FTIR-PL measurements were performed at room temperature using a Nicolet System 910 FT-Raman spectrophotometer with a calcium fluoride beamsplitter and a Nicolet FT-Raman microscope. The FT-Raman spectrophotometer contains a diode-pumped 1.5-W Nd-YAG laser with continuous emission at 1.064  $\mu$ m, a white-light source for spectral instrument correction, keyboard-controlled laser power, a laser power meter, a keyboard-controlled sample-focusing stage, gold-coated reflective transfer optics, refractive sampling optics, dual Rayleigh line holographic notch filters, and LN<sub>2</sub>-cooled germanium (Ge) and indium antimonide (InSb) detectors. The refractive sampling optics are approximately f1 type, allowing a high collection efficiency for emitted radiation. The detectors, beamsplitter, and filter limit the spectral response of the system to wavelengths between 1.08 and 2.70  $\mu$ m (1.15 to 0.46 eV).

The laser beam was focused to within a spot 50  $\mu$ m in diameter on the samples. Although total laser power incident on the CIS samples was reduced to 2.0 mW, the minimum obtainable with the diode-pumped laser, for these samples it was necessary to mask the Ge detector with a metal/fused-silica neutral-density (ND) filter (Melles-Griot ND-2) to prevent saturation of the detector. It was not necessary to mask the Ge detector for the micro-FT-PL analyses of Si, for which 150 mW of laser power was used. The GaInAs and InPAs samples were analyzed using laser power settings between 17 and 350 mW, and the GaAsGe samples were analyzed at laser power settings between 0.35 and 1.0 W. Excitation power dependence of the PL peak energies was less than 0.01 eV within these ranges. The InSb detector was used without filtering to analyze the GaInAs, InPAs, and GaAsGe samples.

Photoluminescence spectra were obtained by signal-averaging 100 interferometer scans collected in 4 min at a resolution of  $4\text{ cm}^{-1}$ , or approximately  $0.7\text{ nm}$ . To reduce the intensity of instrumental spectral artifacts, especially those contributed by spectral transmittance variations in the Rayleigh line filters, the PL spectra were divided by the emissivity spectrum (obtained by scattering from potassium bromide powder) of a white-light source. A tungsten filament reference lamp (color temp. =  $1925\text{ K}$ ) was used with the Ge detector, and a quartz-halogen reference lamp (color temp. =  $2300\text{ K}$ ) was used with the less sensitive InSb detector. This procedure produced photometrically accurate PL spectra in radiance units.

### Results and Discussion

The room-temperature, micro-FT-PL spectra of two areas approximately  $4\text{ }\mu\text{m}$  in diameter on the surface of polycrystalline Si are shown in Fig. 1. One spectrum is taken near the center of a crystal and the other at a grain boundary. In previous work,<sup>12</sup> we established that the broad, featureless peaks centered at  $8818\text{ cm}^{-1}$  in Fig. 1 result from the  $1.094\text{ eV}$  indirect PL of Si. The sharp peak at  $1127\text{ nm}$  superimposed on the PL bands in Fig. 1 is attributable to the first-order scattering at a Raman shift of  $519\text{ cm}^{-1}$  by the silicon Raman phonon.<sup>1</sup>

The primary PL peak in the near-band-gap region results from recombination of intrinsic excitons.<sup>3</sup> This broad peak is resolved at cryogenic temperatures into several distinct peaks that have been associated with dislocation defects related to strain, impurities, or grain boundaries in the Si.<sup>3,13</sup> Although digital subtraction of the curves in Fig. 1 revealed no differences in their shapes or peak positions, the intensity of the FT-PL signal is much less in the area over the grain boundary than the area in the center of the crystal. The sample was well polished, so that the intensity difference was probably not caused by increased scattering at the grain boundary. It is therefore likely that micro-FT-PL, in conjunction with a motorized microscope stage, could be used for automated defect mapping of polished Si samples. Tajima<sup>14</sup> reported room-temperature, NIR PL mapping of deep defects in Si and GaAs wafers using  $647\text{ nm}$  excitation and dispersive detection; however, the spatial resolution of his system ( $0.1\text{ mm}$ ) is much less than that of the FT-PL (FT-Raman) microscope ( $4\text{ }\mu\text{m}$ ).

Figures 2 and 3 show the FT-PL spectra of two CIS PV devices having PV conversion efficiencies of  $11.4\%$  and  $8.7\%$  for terrestrial solar radiation, respectively. These spectra were resolved into Gaussian/Lorentzian components using Nicolet FOCAS Fourier self-deconvolution software. We believe these and spectra shown in our earlier work<sup>12</sup> to be the first room-temperature PL spectra reported for CIS devices or films, although room-temperature PL spectra have been obtained for CIS single crystals.<sup>15</sup> The PL spectra of the CIS absorber were collected through the ZnO and CdS overlayers of the device, which are transparent to the  $1.064\text{-}\mu\text{m}$  excitation radiation and to the emitted PL radiation. The high-efficiency device can be fit by three curves (Fig. 2), while the low-efficiency device required an additional curve in the low-energy region (Fig. 3). The high-efficiency device has a stronger PL component at  $8700\text{ cm}^{-1}$  ( $1.078\text{ eV}$ ) than the low-efficiency device. FT-PL spectra of these and other devices made by the same process and having efficiencies between  $11.4\%$  and  $8.7\%$  show a linear relationship between the maximum energy of their total fitted FT-PL spectra and device efficiency. We are currently examining CIS devices made by other processes to determine if this relationship, which is probably related to higher open-circuit voltages in the more efficient devices, can be generalized.

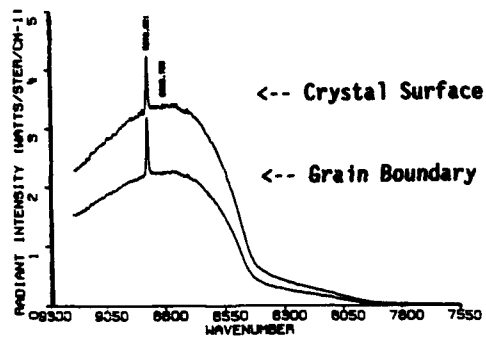


Figure 1. Micro-FT-PL spectra of polycrystalline silicon  
0.15 W excitation at  $1.064 \mu\text{m}$

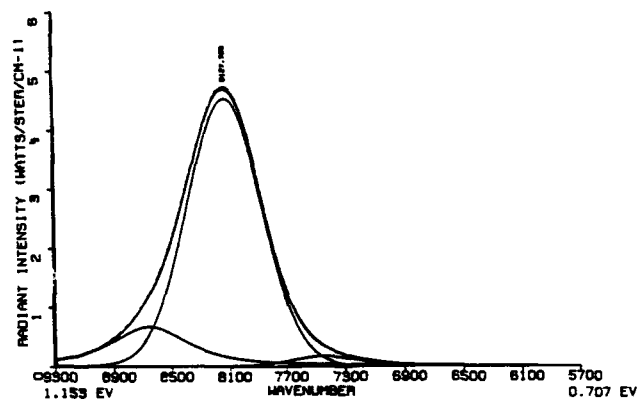


Figure 2. FT-PL spectrum of 11.4% efficient CIS device  
2.0 mW excitation at  $1.064 \mu\text{m}$   
Maximum of fitted total curve = 1.008 eV

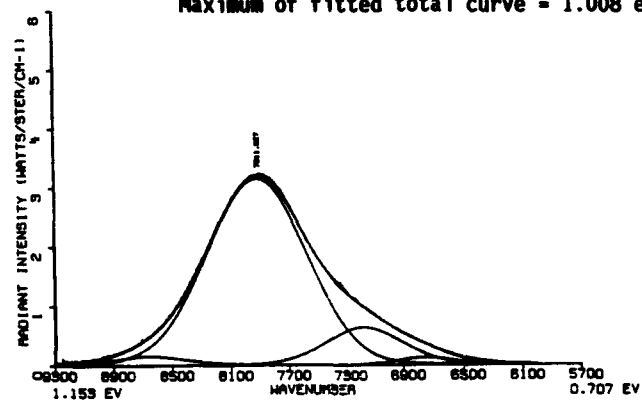


Figure 3. FT-PL spectrum of 8.7% efficient CIS device  
2.0 mW excitation at  $1.064 \mu\text{m}$   
Maximum of fitted total curve = 0.981 eV

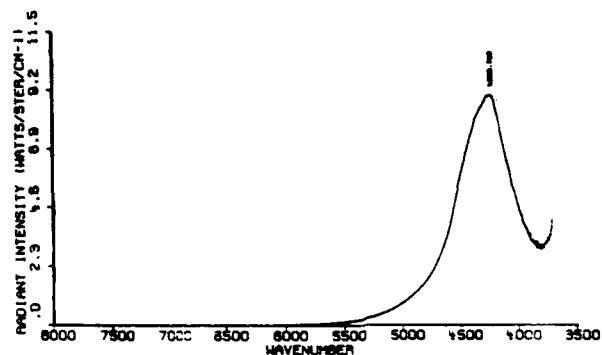


Figure 4. FT-PL spectrum of InPAs film ( $X = 0.19$ )  
0.35 W excitation at  $1.064 \mu\text{m}$

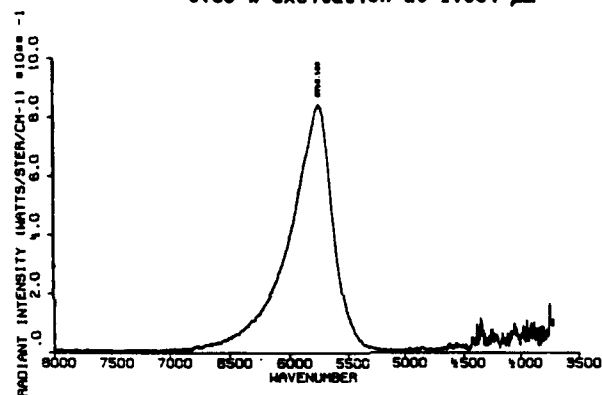


Figure 5. FT-PL spectrum of GaInAs film ( $X = 0.399$ )  
35 mW excitation at  $1.064 \mu\text{m}$

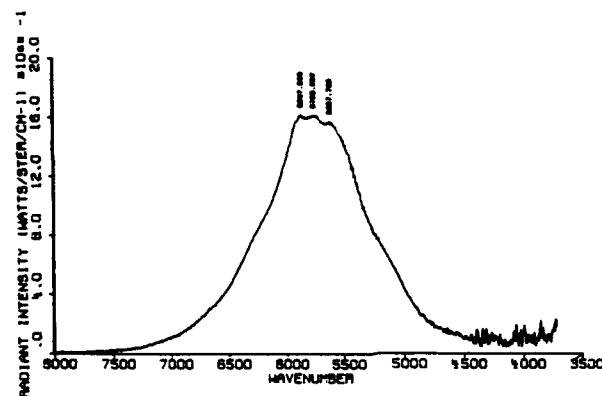


Figure 6. FT-PL spectrum of GaAsGe film ( $X = 0.40$ )  
0.90 W excitation at  $1.064 \mu\text{m}$

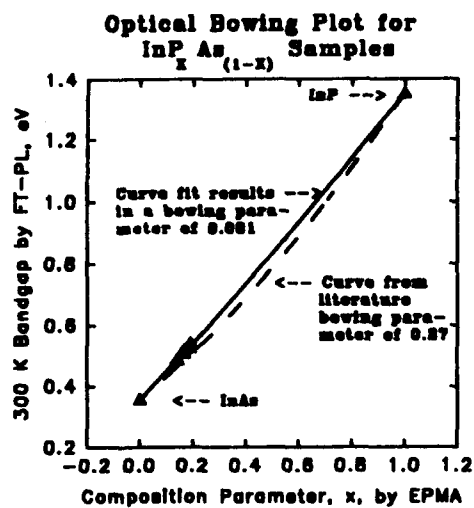


Figure 7.

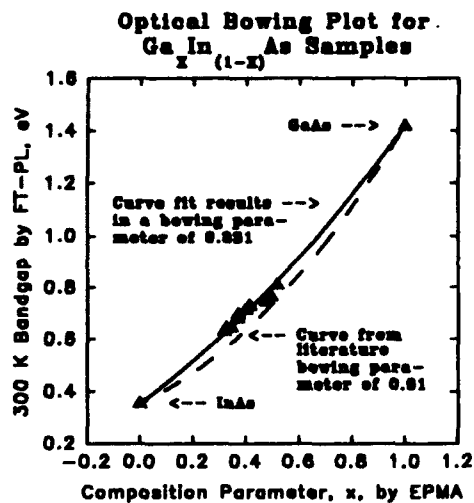


Figure 8.

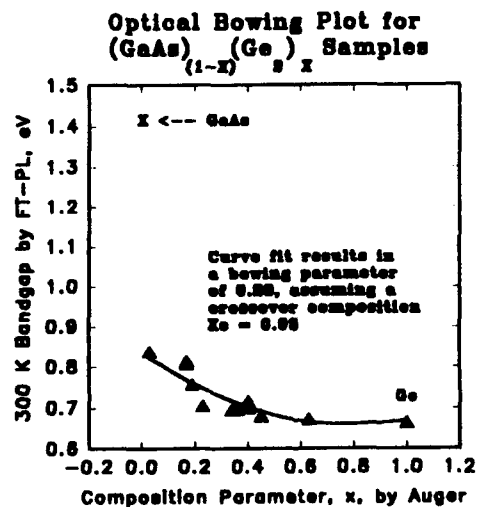


Figure 9.

Figures 4, 5, and 6 are the room-temperature FT-PL spectra of epitaxially-grown films of  $\text{InPAs}_{(1-x)}$ ,  $\text{GaIn}_{(1-x)}\text{As}$ , and  $(\text{GaAs})_{(1-x)}(\text{Ge}_2)$ , on InAs, InP, and GaAs substrates, respectively. The limited energy range and optical artifacts that we reported during earlier measurements<sup>12</sup> of these materials have been solved by the InSb detector and holographic notch filters available in the Nicolet 910 and 950 dedicated FT-Raman spectrophotometers, and the spectra are clean and low in noise. Figures 7, 8, and 9 are optical bowing plots developed from the FT-PL peak energies measured for a range of these materials having different compositions (x). Figures 7 and 8 show that the FT-PL peak energies are consistently 0.03 to 0.05 eV higher than the literature values<sup>13</sup> expected for InPAs and GaInAs films having the compositions shown. This may be because of doping in the InPAs films, and strain in the lattice-mismatched GaInAs films. FT-PL peak energies of GaInAs films showing visible striations were about 0.01 eV higher than those of smooth films. The PL peak energies for GaAsGe films shown in Fig. 9 correspond closely to less precise values<sup>17</sup> obtained by optical absorbance.

We conclude that FT-PL spectroscopy performed using a commercial FT-Raman spectrophotometer can be a useful tool for characterization of semiconductors that exhibit PL in the near-infrared, although a more thorough exploration of the relationships between the FT-PL spectra and the physical properties of the samples are needed, and an InAs rather than an InSb detector would allow lower excitation energies to be used to excite PL between 0.74 eV and 0.46 eV. The technique offers the advantages of speed, sensitivity, and freedom from stray light over conventional dispersive PL spectroscopy at the same resolution, in part because of the well-known design improvements of FTIR spectroscopy over earlier dispersive methods.<sup>8</sup> Also, the location of the excitation wavelength of the FT-Raman spectrophotometer close to the band gaps of many semiconductor materials, e.g., those used in diode lasers, maximizes the power efficiency of PL processes in these materials.<sup>18</sup> Furthermore, the FT-Raman spectrophotometer was designed to measure Raman emission, which occurs with maximum quantum yields of  $10^4$ .<sup>19</sup> Therefore, an FT-Raman instrument has more than adequate sensitivity to measure PL, which can occur with quantum yields approaching unity.<sup>18</sup>

#### Acknowledgements

The first author would like to thank Fred Walder of Nicolet Corporation for allowing him to use the Nicolet 910 FT-Raman spectrophotometer at the corporate laboratories in Madison, WI to make the FT-PL measurements. We also thank Chris Petty of Nicolet for his invaluable contributions to the measurements. NREL is operated by Midwest Research Institute for the U.S. Department of Energy under contract No. DE-AC02-83CH10093.

#### References

1. S. Q. Gu, D. Chen, J. M. Viner, M. E. Raikh, and P. C. Taylor, AIP Conference Proc. **268**, R. Noufi (Ed.), (American Institute of Physics, New York, 1992), pp. 363-368.
2. F. J. Purcell and R. Kaminski, Proc. SPIE vol. 822 (The International Society for Optical Engineering, Bellingham, WA, 1987), pp. 188-197.
3. A. Perez-Rodriguez, A. Cornet, J. R. Morante, J. Jimenez, P. L. F. Hemment, and K. P. Homewood, J. Appl. Phys. **70**, (3), 1678 (1991).

4. A. Yamada, M. Tanda, S. Manaka, H. Sano, M. Konagai, and K. Takahashi, Proc. 11th European Photovoltaic Solar Energy Conference (Commission of the European Communities, Montreux, Switzerland, 1992), in press.
5. J. Wagner, Physica Scripta, Vol. T29, J. Friedal, J. P. Laheurte, and J. P. Romagnan, eds., (European Physical Society, Sweden, 1989), pp. 167-171.
6. M. L. Timmons, T. S. Colpitts, R. Venkatasubramanian, B. M. Keyes, D. J. Dunlavy, and R. K. Ahrenkiel, Appl. Phys. Lett. 40 (19), 1850 (1990).
7. R. K. Ahrenkiel, D. J. Dunlavy, B. M. Keyes, S. M. Vernon, S. P. Tobin, and T. M. Dixon, Proc. 21st IEEE Photovoltaic Specialists Conference (Institute of Electrical and Electronic Engineers, New York, NY, 1990), pp. 432-436.
8. P. R. Griffiths and J. A. De Haseth, Fourier Transform Infrared Spectroscopy (John Wiley & Sons, New York, NY, 1986).
9. J. P. Estrera, W. M. Duncan, Y. C. Kao, H. Y. Liu, P. D. Stevens, E. A. Beam III, and T. M. Dixon, Proc. SPIE vol. 1678 (The International Society for Optical Engineering, Bellingham, WA, 1992), pp. 120-130.
10. G. Ruani, A. J. Pal, R. Zamboni, and C. Taliani, Electronic Properties of High-T<sub>c</sub> Superconductors and Related Compounds (Springer-Verlag, Berlin, Germany, 1990), pp. 331-335.
11. B. Schrader, "Possibilities and Limitations of FT-Raman Spectroscopy," in Practical Fourier Transform Infrared Spectroscopy, D. B. Chase and J. F. Rabolt, Eds. (Academic Press, New York, 1990), Chap. 4.
12. J. D. Webb, D. J. Dunlavy, T. Cizek, R. K. Ahrenkiel, M. W. Wanlass, R. Noufi, and S. M. Vernon, Appl. Spectrosc. 47 (11), 1814 (1993).
13. Gerald L. Auth, U.S. patent no. Re. 32,821 (3 January 1989).
14. M. Tajima, J. Crystal Growth 103, 1 (1990).
15. F. Abou-Elfotouh, D. J. Dunlavy, D. Cahen, R. Noufi, L. L. Kazmerski, and K. J. Bachmann, Prog. Crystal Growth 10, 365 (1984).
16. R. Blachnik, P. J. Dean, and O. Madelung, in Landolt-Bornstein Numerical Data and Fundamental Relationships in Science and Technology, Vol. 17, edited by K. H. Hellwege, (Springer-Verlag, Berlin, 1982), chapter 2.16.
17. R. J. Baird, J. Appl. Phys. 69 (1), 226 (1991).
18. J. Pankove, Optical Processes in Semiconductors (Dover Publications, Inc., New York, 1975), pp. 249-252.
19. D. A. Skoog and D. M. West, Principles of Instrumental Analysis, 2nd ed. (Saunders College, Philadelphia, PA, 1980), p. 263.

## FIBER OPTICS-BASED FOURIER TRANSFORM INFRARED SPECTROSCOPY FOR *IN-SITU* CONCENTRATION MONITORING IN OMCVD

SATERIA SALIM\*, K.F. JENSEN\* AND R.D. DRIVER\*\*

\*Department of Chemical Engineering, Massachusetts Institute of Technology, Cambridge, MA 02139

\*\*Galileo Electro-Optics Corporation, Sturbridge, MA 01566

### ABSTRACT

Fiber-based Fourier transform infrared spectroscopy for remote *in-situ* monitoring of organometallic delivery in organometallic chemical vapor deposition (OMCVD) is presented. The measurement is based on infrared absorbance of the organometallic reagent in a short single pass gas cell placed in the gas delivery line of an OMCVD system. The performance of the set-up is demonstrated for monitoring concentration transients during the delivery of two common OMCVD precursors, trimethylgallium (TMG) and trimethylindium (TMI). The time to reach saturation is shown to be faster for a TMG bubbler than for a TMI bubbler. This difference in delivery behavior is interpreted through a mathematical model of the gas handling lines and the monitoring gas cell. The utility of the system in monitoring temporal variations in TMI delivery is also demonstrated. Finally, the ability of the system to detect the chemical species unintentionally present in the feed lines is illustrated with the observation of methane gas from TMG and TMI bubblers that have been dormant for a period time. The methane gas is shown to quickly disappear with repeated use of the bubblers.

### INTRODUCTION

Organometallic chemical vapor deposition (OMCVD) is a premier technique for depositing multilayer structure of III-V and II-VI compound semiconductors used in the optoelectronic industry [1,2]. Large scale production has, however, been limited by run-to-run reproducibility in film thickness and composition because of lack of monitoring of input concentrations of organometallic sources. Precursor delivery to an OMCVD reactor is usually performed by flowing a known amount of carrier gas (typically H<sub>2</sub>) into a stainless steel bubbler containing the organometallic reagents. The exact amount of the reactant supplied to the reactor is not measured, but it is estimated by assuming saturation vapor pressure inside the bubbler and furthermore, no interaction between the reagents and the interior walls of the gas handling system. Thus, in absence of any monitoring, variations in precursor delivery remain undetected.

The delivery problem is particularly crucial for trimethylindium (TMI), which is a solid under standard operating conditions. The variation in surface area during evaporation of TMI leads to uncontrolled variations in the delivery rate, which in turn results in changes in the In content in the deposited compound semiconductor. The relatively low pressure of the precursor may also necessitate the heating of the bubbler to increase the feed rate. In that case the amount of material actually reaching the reactor will be reduced by condensation on gas handling system walls if there is any cold spot in the gas handling system. The deviation leads to changes in film composition and corresponding device properties that can only be detected by post-mortem of the final device structure. Thus, the development of a sensor system for monitoring the organometallic concentration is a key element in improving control of the OMCVD process.

Current sensor technology is based on measurements of the speed of sound [3] in a binary mixture of the organometallic precursor and its carrier gas. This approach has been employed successfully in closed loop control of TMI delivery, but the system is restricted to pressures above 400 torr, and being a physical measurement, it cannot detect the presence of different chemical species. Ultraviolet-visible (UV-vis) spectroscopy has been demonstrated as a potential optical monitoring technique [4], but photolysis reactions driven by the UV light cause difficulties with deposition on windows of the monitoring cell.

Fourier transform infrared (FTIR) spectroscopy is particularly useful for monitoring the OMCVD process since it is directly probes chemical bonds, is sufficiently simple to be suitable for



manufacturing applications, and has low energy avoiding photolysis of the organometallic precursor. Recent advances in fluoride and chalcogenide infrared fibers make it possible to expand FTIR applications beyond bench-top applications to remote *in-situ* concentration monitoring. Fluoride fibers are suitable for monitoring systems with vibrational absorption bands in the 20,000-2200  $\text{cm}^{-1}$  range. With a 90% signal transmission over 5 meters, the fluoride fibers are suitable for remote sensing applications [5,6]. Chalcogenide fibers transmit light in the 3300-900  $\text{cm}^{-1}$  range, which is the primary region of interest for studying organometallic chemistry. However, remote sensing with this fiber material is limited by adsorption, leading to a 38% loss of signal over a one meter fiber length. Most organometallic compounds used in OMCVD contain alkyl groups with strong absorbance in the region around 2800-3000  $\text{cm}^{-1}$  corresponding to C-H vibrational stretching. These vibrational frequencies are within the operation ranges of both chalcogenide and the fluoride fibers.

Previous feasibility studies of measurement of trimethylgallium (TMG) and TMI concentration have shown promising results [7]. The absorbance was linearly correlated to the partial pressure in agreement with Lambert-Beer's law. The minimum detection limit for trimethylindium was 0.05 torr for 50 seconds scan time and a 12.7 cm optical path length. In this study, we demonstrated the use of the FTIR-fiber optics based technique in monitoring the delivery characteristics of TMG and TMI reagents.

## EXPERIMENTAL SYSTEM & PROCEDURE

The fiber-optics based FTIR system, supplied by Galileo Electro-Optics Corporation, is shown schematically in Figure 1. The spectrometer is a KVB Analect Diamond-20 with a resolution of 2  $\text{cm}^{-1}$  wavenumber. The system is controlled by a Dell 486-50 MHz computer. The IR emission from the interferometer is coupled into the chalcogenide and fluoride fibers through an optical fiber launcher. The optical fiber guides the infrared radiation to the sensing region, where the light is collimated into a 12 mm beam with a prealigned optical collimator module optimized for the mid-infrared. The signal throughput using both fibers are similar. The collimated beam passes through the gas cell and is focused into the return fiber with a second pre-aligned optical module. Angular adjustment on both collimators allows the optical throughput of the system to be optimized. The light is then coupled back into the fiber and directed to the detector box. A liquid cooled mercury cadmium telluride (MCT) detector is used. The detector is equipped, as well, with a computer-driven optical channel selector (OCS) that allows multiplexing among up to seven sensor points while using only one spectrometer.

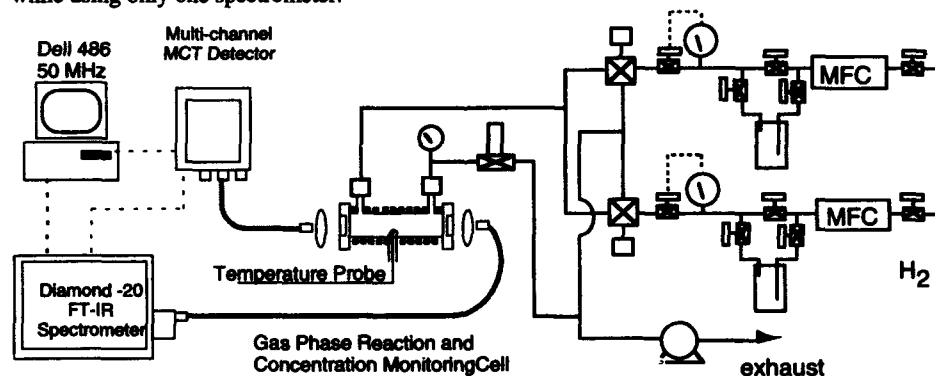


Figure 1. Schematic diagram of fiber-optics based FTIR and OMCVD reactor systems.

The experiments were performed in a Crystal Specialties OMCVD reactor system. The reactor unit was replaced by a gas-cell designed for concentration monitoring and probing gas-phase

reactions. The 12.7 cm long cell consisted of a quartz tube (2.5 cm O.D.), with quartz flanges fused to the tube ends.  $\text{CaF}_2$  windows with o-ring seals were placed at each end and sealed with stainless steel flanges. The cell could be uniformly heated to 650°C with a resistive heater. The temperature was measured by inserting a type-k thermocouple through a well into the gas-cell. Heat and mass transfer analyses showed that transport in the cell was dominated by diffusion under the conditions investigated. Consequently, temperature and concentration profiles could be assumed to be uniform across the cell and inlet effects were negligible.

Ultra-pure hydrogen (99.9995%) from Matteson was used as a carrier gas. The hydrogen flow rate was held at constant at 60 sccm. A TMI bubbler from Air Products Inc. was employed along with a TMG source from Texas Alkyl. During the experiment, the TMG bubbler was kept at -14°C and the TMI bubbler temperature was 40°C. Gas lines and the cell were heated to 40°C to minimize condensation of organometallic precursors. The gas handling and cell pressures were 600 torr and 800 torr, respectively.

The experiments were performed in the following manner. The experiments were started by opening the inlet and outlet valve of the bubbler and closing the by-pass line. The absorbance spectrum of the gas mixture was taken every minute. Once steady state concentration in the gas cell was reached, the carrier gas flow to the bubbler was cut and simultaneously the flow to the by-pass line was established. The absorbance spectra was recorded at one minute interval until the organometallic precursors were no longer detectable. Most of the measurements were done using chalcogenide fibers of two meters in total length. The transparency of the chalcogenide fibers in the infra-red finger print region, allows verification of the peaks observed in 2800-3000  $\text{cm}^{-1}$ .

## RESULTS AND DISCUSSION

Figure 2 shows absorbance spectra for TMG at different partial pressures. The magnitude of the signal at 2918  $\text{cm}^{-1}$  (symmetrical C-H stretching) was used to monitor the concentration of TMG. The corresponding calibration curve of the 2918  $\text{cm}^{-1}$  absorbance as a function of partial pressure of TMG also appears in Figure 2. The partial pressure of TMG was increased by increasing the total pressure of the cell by flowing a fixed mixture of TMG and  $\text{H}_2$ . The equilibrium partial pressure could be assumed since TMG showed no condensation effects. The linear relationship between the absorbance and partial pressure is expected from Lambert-Beer's law. The concentration of TMG is low enough that pressure broadening is not a significant effect [8]. TMI was monitored by following the peak at 2929  $\text{cm}^{-1}$  whose intensity also varied linearly with the partial pressure of the organometallic reagent [7].

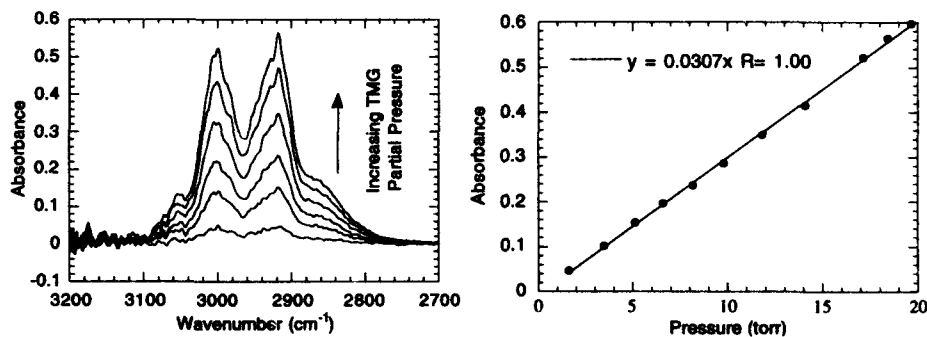


Figure 2. (Left) The absorbance of trimethylgallium at different TMG partial pressures. (Right) Absorbance of TMG at 2918  $\text{cm}^{-1}$  as a function of partial pressure.

The turn-on behavior of a TMG bubbler which has not been used for two months serves to demonstrate the ability of the FTIR technique to monitor concentration transients and detecting chemical species. Figure 3 shows the evolution of the absorption spectrum as hydrogen flow through the bubbler is initiated. A narrow sharp peak at  $3016\text{ cm}^{-1}$  attributed to methane is present at early times whereas the characteristic signature of C-H stretching vibrations in TMG dominate at later times. Deconvolution of the peak intensities shows the methane concentration reaching a maximum ~4 minutes into the transient and then decreasing exponentially (see Figure 3). The TMG signal reaches steady state after 5 minutes.

At 16 minutes, the carrier gas flow to the bubbler was closed and simultaneously the by-pass line was opened. Both the TMG and the methane peaks quickly decreased to zero. A second turn-on transient, performed 30 minutes after the first run showed a slightly faster approach to steady state (cf. Figure 3). The methane was reduced below the detection limit of the technique. A third experiment performed 30 minutes after the second run resulted in the same transient (within experimental accuracy), indicating stabilization of the bubbler behavior.

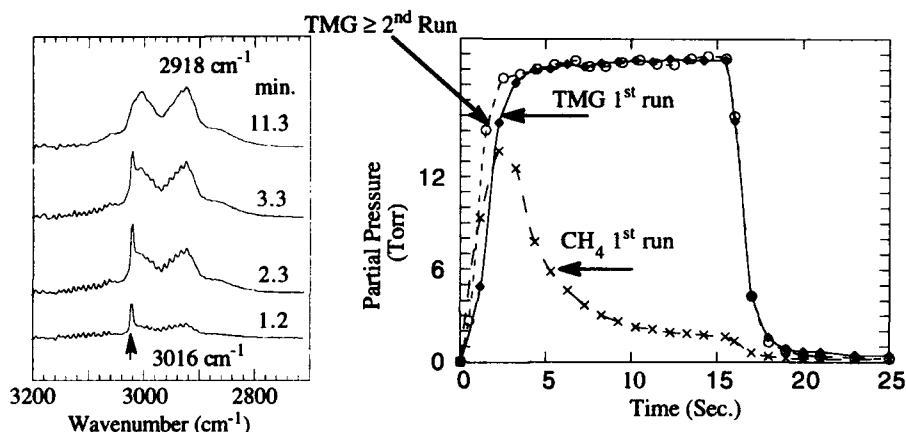


Figure 3. (Left) Evolution of absorption spectrum during start-up of a TMG bubbler. (Right) Corresponding temporal variations in  $\text{CH}_4$  and TMG.

An similar example for start-up of a TMI bubbler is shown in Figure 4. The TMI transients depend strongly on the history of the bubbler. In this case the bubbler had not been used for 2 days. The trimethylindium could be detected within one minutes after the hydrogen flow to the bubbler had been established. The first transient displays oscillations in the TMI concentrations as reported in speed of sound measurements of TMI delivery rates [9]. Subsequent runs 120 min and 150 min after the first experiments show the same behavior, indicating equilibration of the vapor pressure in the bubbler.

$\text{CH}_4$  is again observed during the start-up phase. After the third run, it is not detectable. The  $\text{CH}_4$  signal of methane is strongest when the bubbler has not been used. This behavior suggests that  $\text{CH}_4$  is most likely generated from reactions of TMI and TMG vapors with small amounts of moisture unintentionally introduced during shut-downs from previous experiments. The presence of small amounts of  $\text{CH}_4$  is not likely to effect the outcome of the film growth, since it is a stable molecule at typical deposition temperatures [10]. However, it would influence the accuracy of organometallic delivery measurement from the speed of sound in the mixture. The FTIR would have further advantage detecting the presence of oxygenated solvents left over during the synthesis of organometallic precursors.

Finally, to demonstrate the use of the method in monitoring TMI concentrations during growth runs, Figure 5 shows TMI variations over several hours. The observed variations are well known for the solid TMI precursor [3,4,9], and if unmeasured they will result in difficulties in

reproducing in contents between growth runs. The signal from IR detector could be fed-back to a carrier gas flow or bubbler temperature controller to insure constant TMI delivery.

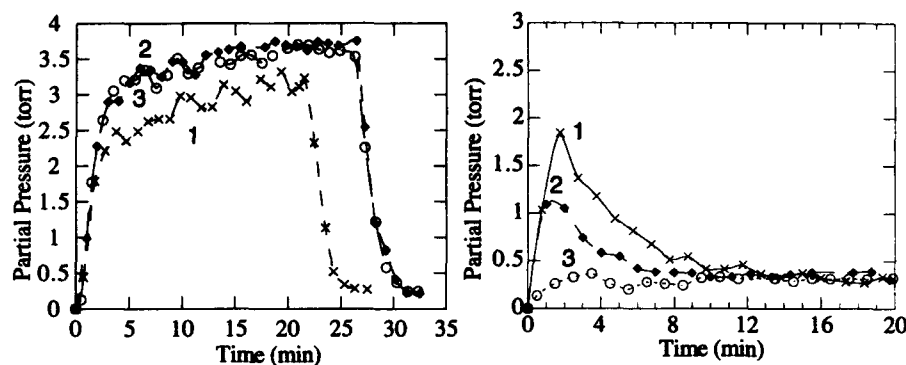


Figure 4. Transients of TMI (left) and CH<sub>4</sub> (right) during three successive usage of a TMI bubbler. Curve 1 is for a bubbler that has not been used for 2 days, curve 2 is 120 min after the first usage, curve 3 is 150 min after the first usage.

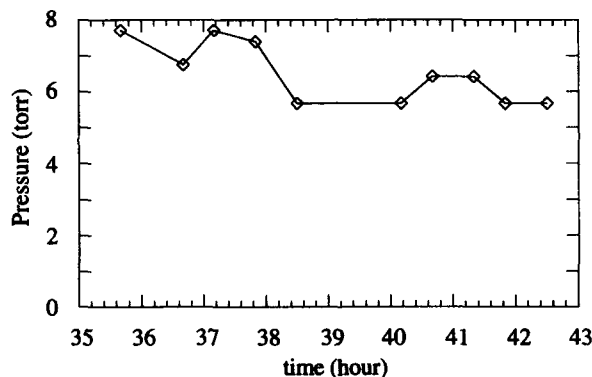


Figure 5. Temporal variation in TMI partial pressure.

In order to further characterize the response of the gas cell to transients in organometallic precursors, the process dynamics are modelled. The gas handling system behaves essentially as a plug flow reactor [11], *i.e.*, when a change in concentration is made at the run-vent valve, the time lag,  $\tau_L$ , before it shows up in the gas cell measurement is:

$$\tau_L = \frac{L}{v} \quad (1)$$

Here  $L$  is the length of the gas line between the valve and the cell and  $v$  is the gas velocity in the tube. As discussed above, the concentration and temperature fields within the cell may be considered to be well mixed. The response to a step increase in concentration of organometallic reagent from zero therefore takes the following form [11]:

$$c(t) = 0 \quad 0 \leq t < \tau_L \quad (2)$$

$$c(t) = c_0 \left\{ 1 - \exp \left[ - \left( \frac{t - \tau_L}{\tau_C} \right) \right] \right\} \quad t \geq \tau_L \quad (3)$$

Here  $c(t)$  is the precursor concentration in the gas cell as a function of time,  $t$ .  $c_0$  is the steady state concentration of the precursors, and  $\tau_C$  is the residence time of the gas cell (volume/ volumetric flow). The model for turning-off the precursor involves equivalent formulas:

$$c(t) = c_0 \quad 0 \leq t < \tau_L \quad (4)$$

$$c(t) = c_0 \exp \left[ - \left( \frac{t - \tau_L}{\tau_C} \right) \right] \quad t \geq \tau_L \quad (5)$$

Since Equations (3) and (5) have the same functional form, step-up and step-down data may be fitted to the same master response curve, say Equation (3).

Data for step-up and step-down of an equilibrated TMG bubbler (cf. >2<sup>nd</sup> run Fig. 3) fit the same functional form as shown in Figure 6 (left hand side). The model predicts the delivery line time lag ( $\tau_L$ ) and cell residence time ( $\tau_C$ ) within experimental accuracy. The good agreement between predicted and observed dynamic response implies that the delivery of TMG is not influenced by artifacts such as condensation in gas lines and on cell walls.

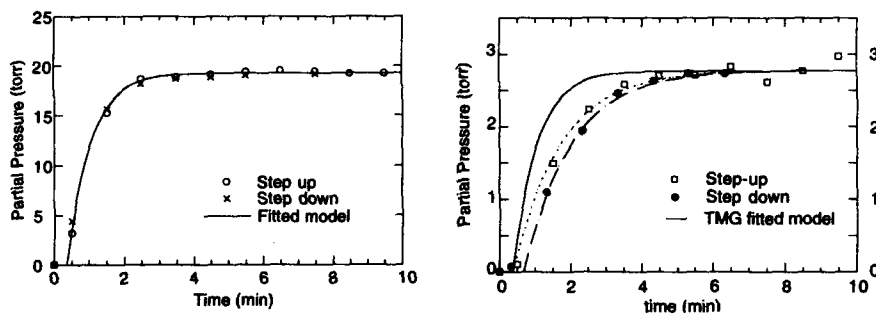


Figure 6. (Left) TMG delivery transients.  
(Right) TMI delivery transients.

In contrast to the TMG case, the TMI dynamics show difference between step-up and step-down transients (see Figure 6, right hand side). A fit of the model to data yields a residence time twice that of TMG, which represents the actual residence time of the gas cell. This behavior strongly suggests the possibility of condensation of TMI.

## CONCLUSION

Fiber optics based FTIR spectroscopy for *in-situ* monitoring of input concentrations of organometallic precursors for OMCVD has been demonstrated using TMG and TMI bubbler dynamics as case studies. As expected based on OMCVD experience, the delivery of TMG is accomplished without any artifacts whereas the solid source, TMI, displays slow transients and problems with condensation. In addition to enabling monitoring of the organometallic species, the technique also detects other species present in the feed mixture. Specifically, methane was observed in bubblers left unused for a long period of time. The presence of solvents inadvertently left over from the synthesis of the growth precursors would be detectable by the FTIR approach.

The residence time models provide a useful tool for diagnosing the possible condensation in gas delivery lines and the monitoring cell.

#### ACKNOWLEDGMENT

The authors would like to thank C.K. Lim for his technical help, M. Brubaker for the installation of the FTIR set-up, the AT&T Foundation and the National Science Foundation for providing funding for this work.

#### REFERENCES

1. T.K. Kuech and K.F. Jensen, "OMVPE of compound semiconductors", *Thin Film Processes - II*, (J. L. Vossen, W. Kern, eds.), Academic Press, San Diego, 1991, pp. 369.
2. G.B. Stringfellow, *Organometallic Vapor Phase Epitaxy*, Academic Press, San Diego, 1989.
3. J.P. Stagg, J. Christer, E.J. Thrush and J. Crawley, "Measurement and control of reagent concentration in MOCVD reactor using ultrasonics", *J. Crystal Growth*, **120**, 98 (1992).
4. G.A. Hebner, K.P. Kileen, and R.M. Biefeld, *J. Cryst. Growth*, **98**, 293 (1989).
5. a) R.D. Driver, G.M. Leskowitz and L.E. Curtiss, *SPIE 1228, Infrared Fiber Optics*, 233, (1990).  
b) M.G. Drexhage, "Glass optical fibers enter the infrared", *Laser Focus World*, **27**, 149 (1991).
6. M.G. Drexhage and C.T. Moynihan, "Infrared optical fibers", *Scientific American*, 110, September 1988.
7. S.Salim, C.K. Lim, K.F. Jensen and R.D. Driver, *Proc. SPIE*, **2069**, xxx (1994).
8. N. D. Goggeshall and E. L. Saier, *J. Appl. Phys.*, **17**, 450 (1946).
9. D.M Frigo, W.W. van Berkel, W.H.H. Maasen, G.P.M. van Miller, J.H. Wilker and A.W. Gal, *J. Cryst. Growth*, **124**, 99 (1993).
10. T.F. Kuech, G.J. Scilla and F. Cardone, *J. Cryst. Growth*, **93**, 550 (1988).
11. C.G. Hill, Jr., *An Introduction to Chemical Engineering Kinetics and Reactor Design* Wiley, New York, 1977.

# APPLICATION OF FTIR SPECTROSCOPY TO THE CHARACTERIZATION OF AS-DEPOSITED AND CHEMICAL MECHANICAL POLISHED (CMP) ELECTRON CYCLOTRON RESONANCE (ECR) PLASMA BASED $\text{SiO}_2$ FILMS

Mukesh Desai<sup>1</sup>, Ron Carpio, Rahul Jairath<sup>2</sup>, Matt Stell<sup>3</sup> and Robert Tolles  
SEMATECH, 2706 Montopolis Drive, Austin, Texas 78741

<sup>1</sup> On assignment from IBM Corporation, <sup>2</sup> On assignment from National Semiconductor Corporation,  
<sup>3</sup> On assignment from Digital Equipment Corporation

## ABSTRACT

FTIR spectroscopy has been used to characterize as-deposited and chemical mechanical polished (CMP) electron cyclotron resonance (ECR) plasma based  $\text{SiO}_x$  films. The ECR films were deposited at different  $\text{O}_2/\text{SiH}_4$  gas ratios in an attempt to vary the film stoichiometry. Transmission and reflectance-absorbance IR spectral data were combined with CMP removal rate information to characterize the  $\text{SiO}_x$  films and their polishing behavior. The asymmetric O-Si-O stretching (ASM) and Si-OH vibrational bands were found to be principal sources of information.

## INTRODUCTION

As ULSI structures have scaled to sub-micron dimensions, the relative burden of device operating speed and processing costs have been shifted from active transistors to interconnects. The increasing number of interconnects required have necessarily led to increased wiring levels. The increased topography as a result of increased wiring levels have led to stringent requirements for global planarity to meet photolithography depth-of-focus needs. Chemical mechanical polishing (CMP) has been recently used to meet these planarization requirements[1].

In a typical CMP process, the substrate to be planarized is held down against a rotating pad wetted with a polishing slurry. The polishing pad used is made of a visco-elastic syntactic foamed polyurethane material while the slurry is a aqueous alkaline solution of fine fumed silica abrasive particles[2]. Polishing is believed to occur as a result of diffusion of molecular water into the  $\text{SiO}_2$  network under stress leading to the formation and subsequent dissolution of silanol species[3]. The structural modification induced in the  $\text{SiO}_2$  glass is of particular interest from a device integrity standpoint. Indeed, damaging effects of the CMP process has been reported recently on 100 nm TEOS based films[4].

In this paper, FTIR spectroscopy has been used to characterize  $\text{SiO}_2$  films deposited using ECR plasmas at various  $\text{O}_2/\text{SiH}_4$  gas flow ratios, and the subsequent response of these films to CMP processing.

## EXPERIMENTAL PROCEDURE

The ECR plasma based  $\text{SiO}_2$  films were deposited on eight inch silicon substrates using a Lam EPIC<sup>TM</sup> ECR deposition reactor at different  $\text{O}_2/\text{SiH}_4$  gas flow ratios. Film thickness and refractive index of the films was measured using a Rudolph FE III ellipsometer. Film stoichiometry was determined using Rutherford backscattering (RBS) and FTIR spectroscopy.

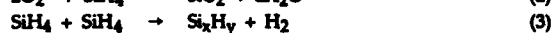
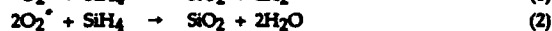
FTIR spectral measurements were performed on a Nicolet ECHO 85 system over the range of  $4000 - 400 \text{ cm}^{-1}$ . Data analysis was performed on a Nicolet 800 spectrometer. Double side polished substrates were used for all experiments requiring transmission FTIR spectra measurements. A

prime, unprocessed substrate was used as the background to ensure that the spectra obtained was solely due to the SiO<sub>2</sub> film. For experiments requiring reflectance-absorbance FTIR spectra measurements, both silicon and metal coated silicon were used as substrates. In each case, the appropriate substrate without subsequent SiO<sub>2</sub> deposition was used as the reference. The transmission measurements were made at normal incidence using the Nicolet 85. A room temperature TGS detector was employed. In the case of reflection measurements, the angle of incidence was fixed at 15°. All measurements were made at the center of the substrate and with unpolarized radiation. Both transmission and reflectance-absorbance spectra were obtained at 8 cm<sup>-1</sup> resolution by coadding 64 scans. For convenience, the reflectance-absorbance spectra are plotted in absorbance units, i.e., as  $-\log(R/R_0 \times 100)$  where R and R<sub>0</sub> are reflectivities of the sample and reference respectively.

The substrates were polished using a Westech 372 polisher using Cabot SC-112 slurry available from Rippey Corporation. SC-112 is a suspension of fumed silica dispersed in aqueous potassium hydroxide and is comprised of approximately 30 nm sized well formed, amorphous, spherical primary particles aggregated together in chains of about ten to twenty each. Since FTIR characterization of the substrates is non-destructive, it was possible to examine the each substrate at intermediate stages of polishing and, therefore, at various film thicknesses. The polishing interval in each case was 60 seconds.

#### STRUCTURE & CHEMISTRY OF ECR PLASMA DEPOSITED SiO<sub>2</sub>

The overall reactions that lead to SiO<sub>x</sub> deposition are written as [5]:



The characteristics of the SiO<sub>2</sub> film are a strong function of the O<sub>2</sub>/SiH<sub>4</sub> gas ratio. The first reaction dominates when the O<sub>2</sub> partial pressure is nearly equal to, but slightly higher than that of SiH<sub>4</sub>.

The second reaction dominates in the presence of excess O<sub>2</sub> and results in the formation of H<sub>2</sub>O. It is possible that the H<sub>2</sub>O formed during the deposition process is incorporated into the film as H<sub>2</sub>O, Si-OH or Si-H. The third reaction dominates when there is excess of silane and results in the formation of hydrogenated amorphous silicon.

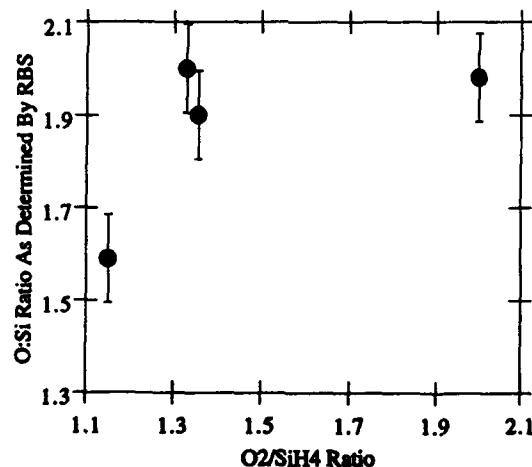


Fig. 1: Dependence of film stoichiometry on gas ratio during deposition

Figure 1 shows the stoichiometry of the deposited films as determined by RBS as a function of O<sub>2</sub>/SiH<sub>4</sub> gas ratio. The O:Si ratio in the film shows a marked rise from 1.59 at a O<sub>2</sub>/SiH<sub>4</sub> gas ratio of 1.15 to about 2.0 at a O<sub>2</sub>/SiH<sub>4</sub> gas ratio of 1.33. From then on, any increase in the O<sub>2</sub>/SiH<sub>4</sub> gas ratio



did not appear to result in any significant change in film stoichiometry. These results correlate to measurements of refractive index which were found to be at 1.54 for  $O_2/SiH_4$  gas ratios of 1.15 but decreased to 1.45 - 1.47 for  $O_2/SiH_4$  gas ratios of 1.33 or greater. This suggests a non-linear behavior in both stoichiometry and refractive index over the gas flow ratio range of 1.15 to 2.00.

Figure 2 is a stacked plot of the transmission spectra obtained for the same unpolished films while figure 3 is a stacked plot of the reflectance-absorbance spectra for the corresponding films. Transmission spectra of  $SiO_x$  deposited on Si did not match exactly with reflectance-absorbance spectra of  $SiO_x$  deposited on metallized substrates. However, as can be seen in figure 4, we found a good correlation between the two for as-deposited films. In both cases, at lower  $O_2/SiH_4$  gas ratios, the bonded Si-OH peak at about  $3650\text{ cm}^{-1}$  is hardly visible; however, at  $O_2/SiH_4$  gas ratios greater than 1.33, its presence is evident. In general, the Si-OH content of the film increases as the  $O_2/SiH_4$  gas ratio is increased from 1.33 to 2.00. The incorporation of hydrogen in the as-deposited films is evidenced through the presence of two Si-H modes at  $884\text{ cm}^{-1}$  and  $2250\text{ cm}^{-1}$ . Compared to the band at  $2250\text{ cm}^{-1}$ , the mode at  $884\text{ cm}^{-1}$  appears to be more uniformly distributed through the film.

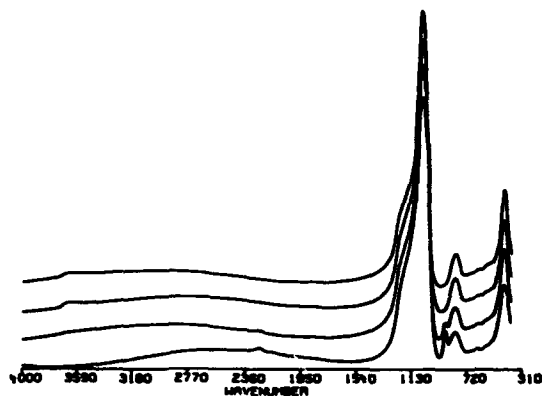


Figure 2: Transmission FTIR spectra of as-deposited ECR films at different  $O_2/SiH_4$  gas ratios: 2.00 (top), 1.357, 1.33 and 1.15 (bottom)

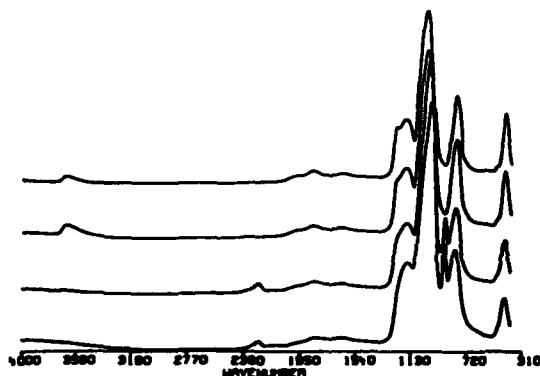


Figure 3: Reflectance-absorbance FTIR spectra of as-dep. ECR films at different  $O_2/SiH_4$  gas ratios: 2.00 (top), 1.357, 1.33 and 1.15 (bottom)

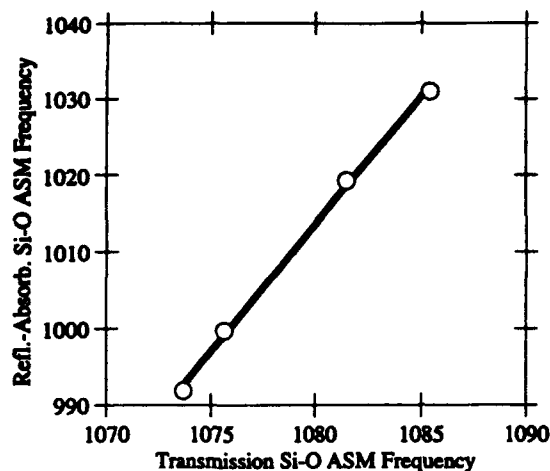


Figure 4: Correlation between reflectance-absorbance and transmission spectra of as-deposited SiO<sub>x</sub> films

These observations confirm earlier hypotheses that presence of excess O<sub>2</sub> affects the reaction mechanism in the process chamber and is manifested as the absence or presence of Si-OH groups in the deposited SiO<sub>2</sub>. Also, it is evident from both transmission and reflectance-absorbance spectra that the Si-O-Si asymmetric stretch peak position at about 1075 cm<sup>-1</sup> increases with increasing O<sub>2</sub>/SiH<sub>4</sub> gas ratio. This is, perhaps, indicative of changes in density or strain in the deposited film. Note that the bending and rocking modes at about 808 cm<sup>-1</sup> and 460 cm<sup>-1</sup> respectively are unaffected by changes in O<sub>2</sub>/SiH<sub>4</sub> gas ratio. Also, note that the reflectance-absorbance spectra actually show structure on

the high frequency shoulder of the asymmetric stretching mode. This frequency shoulder at about 1240 cm<sup>-1</sup> was found to correlate very well to oxide film thickness.

#### EFFECTS OF CMP PROCESSING

Figure 5 shows the removal rate of the SiO<sub>x</sub> films due to CMP. The removal rate was determined for discreet 60 second polishing intervals. Increasing the O<sub>2</sub> content in the reaction gas mixture leads to a significant increase in the polishing rate. Note that as the O<sub>2</sub> partial pressure in the chamber is increased, reaction 2 above is favored. Consequently, the resulting films tend to incorporate increasing amounts of H<sub>2</sub>O, Si-OH and Si-H as is shown in figures 2 and 3.

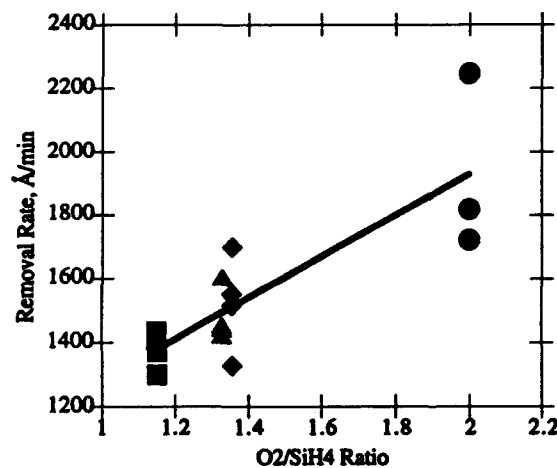


Figure 5: Dependence of CMP oxide removal rates on O<sub>2</sub>:SiH<sub>4</sub> gas flow ratio

Full-width-at-half-height (FWHH) and position of the Si-O stretching frequency are influenced by bonding environment, stoichiometry, density and porosity of the SiO<sub>x</sub> film. FWHH is known to be related to degree of perfection of the SiO<sub>x</sub> structure. We found FWHH obtained in case of transmission spectra to be linearly related to peak frequency. Figure 6 shows the variation in FWHH for the asymmetric O-Si-O stretching frequency as a function of polishing time for the different O<sub>2</sub>:SiH<sub>4</sub> ratios. FWHH is observed to be a strong function of the O<sub>2</sub>/SiH<sub>4</sub> gas ratio in

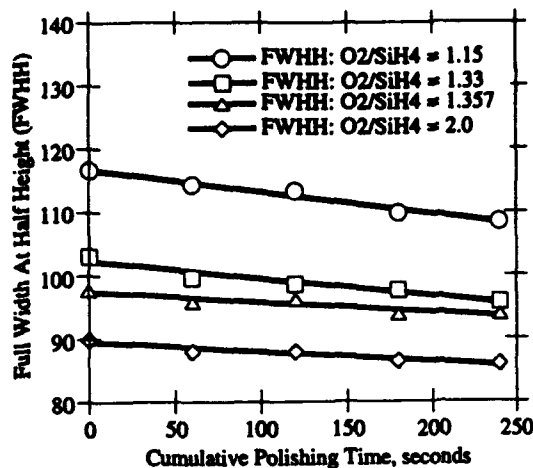


Figure 6: Variation in FWHH with polish time for different O<sub>2</sub>:SiH<sub>4</sub> gas ratios

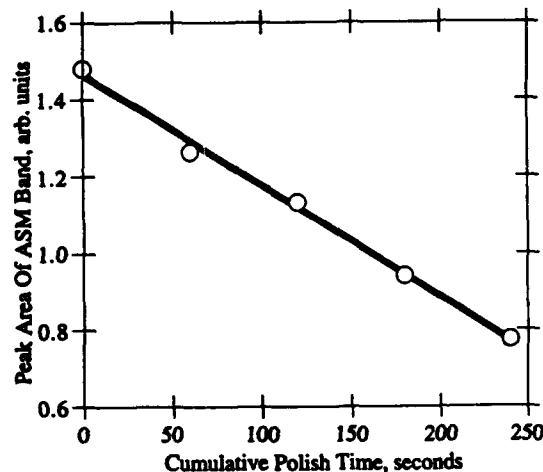


Figure 7: Variation in peak area of ASM band of trans. spectra as a function of polishing time

the case of unpolished SiO<sub>2</sub> - i.e., at polishing time equal to 0. Also, there are small changes in FWHH in each oxide group as the SiO<sub>2</sub> is polished. This suggests that the oxide film is altered microstructurally during the polishing process.

Figure 7 shows the variation in peak area of the asymmetric O-Si-O stretching mode using transmission spectral data as a function of polishing time, and therefore, film thickness. It is observed that there is an excellent correlation between peak area and polishing time.

#### CONCLUSIONS

Transmission and reflectance-absorbance FTIR spectra have been used to study and characterize as-deposited and polished oxide films deposited using ECR plasmas at different O<sub>2</sub>/SiH<sub>4</sub> gas flow ratios. Reflectance-absorbance spectra using metallized substrates appear to yield more information compared to transmission spectra. The O<sub>2</sub>/SiH<sub>4</sub> gas flow ratios during deposition was found to affect their polishing rate and amount of -OH groups present in them. Based upon these results, FTIR spectroscopy appears to be a useful, non-destructive technique to investigate CMP mechanisms.

#### ACKNOWLEDGEMENTS

The authors would like to acknowledge the help of J. Saravia and M. Davies with wafer processing and A. Harrus & D. Dennison of Lam Research Corporation with deposition of the ECR plasma SiO<sub>2</sub> films. Finally, discussions with B. Fowler of SEMATECH are greatly appreciated.

#### REFERENCES

1. B. Davari et al, IEDM Tech. Digest 1989, pg 61, IEEE, 1989
2. R. Jairath et al, Proc. Advanced Metallization for ULSI Applications (in press), 1993.

3. J.A. Trogolo & K. Rajan, Proc. Mat. Res. Soc., Vol 260, pg 869, 1992
4. S.A. Cohen et al, J. Electrochem. Soc., Vol 139, No. 12, pg 3572, 1992
5. J.A. Theil et al, J. Vac. Sci. Technol. A, Vol 8, No. 3, pg 1374, 1990

## CHARACTERIZATION OF POLYSILICON FILMS BY RAMAN SPECTROSCOPY AND TRANSMISSION ELECTRON MICROSCOPY: A COMPARATIVE STUDY\*

DAVID R. TALLANT\*\*, THOMAS J. HEADLEY\*\*, JOHN W. MEDERNACH\*\* and FRANZ GEYLING\*\*\*  
\*\*Sandia National Laboratories, Albuquerque, NM; \*\*\*SEMATECH, Austin, TX.

### ABSTRACT

Samples of chemically-vapor-deposited sub-micrometer-thick films of polysilicon were analyzed by transmission electron microscopy (TEM) in cross-section and by Raman spectroscopy with illumination at their surface. TEM and Raman spectroscopy both find varying amounts of polycrystalline and amorphous silicon in the wafers. Raman spectra obtained using blue, green and red excitation wavelengths to vary the Raman sampling depth are compared with TEM cross-sections of these films. Some films have Raman spectra with a band near  $497\text{ cm}^{-1}$ , corresponding to numerous nanometer-scale faulted regions in the TEM micrographs.

### INTRODUCTION

Polysilicon films, which have microelectronic applications, are produced by chemical-vapor-deposition (CVD). The silicon deposited in this manner ranges from fully (poly)crystalline to amorphous, depending on the conditions in the reactor. Two characterization techniques which have been successfully, but largely independently, used to characterize silicon structure are transmission electron microscopy (TEM) and Raman spectroscopy. The electron image produced by TEM (in either cross-section or "plan" view) provides visual indication of the grain size and shape of crystalline silicon domains and allows an estimate of the amount of crystalline versus amorphous structure. The spatial distribution of crystalline and amorphous regions is also apparent in TEM images. Raman spectroscopy is a light-scattering technique based on the inelastic interactions between incident photons and phonon modes in the material being illuminated. The resultant "Raman shift" of the inelastically scattered photons corresponds to the phonon frequency (energy) involved in the interaction. For single crystal silicon or polycrystalline silicon with domains of 10 nm or greater in size, the fundamental phonon mode is expressed as a narrow, symmetric Raman band occurring at a frequency shift (Raman shift) of about  $521\text{ cm}^{-1}$  from the frequency of the incident photons<sup>1</sup>. The Raman band of amorphous silicon is broad and occurs in the  $460\text{--}490\text{ cm}^{-1}$  range<sup>1</sup>. This paper presents the results of a joint TEM and Raman study of sub-micrometer-thick polysilicon films. Cross-sectional TEM images are compared to Raman spectra obtained with different effective depths of penetration by varying the frequency (wavelength) of the incident photons. Comparison of the TEM and Raman data provides insights into the structures of the polysilicon films not apparent from either set of data alone.

### EXPERIMENTAL

The polysilicon films were deposited on 150 mm diameter <100> silicon wafers on which had been grown 140 nm of field oxide. The films were deposited in a rotating disk reactor using silane or disilane as the source gas under varying conditions of temperature and flow rate.

\* This work was performed at Sandia National Laboratories, which is operated for the U.S. Department of Energy under contract number DE-AC04-94AL85000, and at the Semiconductor Equipment Technology Center (SETEC) of Sandia National Laboratories, Albuquerque, New Mexico 87185 and Livermore, California 94550 for SEMATECH under CRADA SC92-1082.

Samples were prepared in cross-section for TEM analysis. Cross-section pieces were wafered on a dicing saw, epoxied together, ground and polished to  $\approx 125 \mu\text{m}$  thickness, dimpled on the back side, ion-milled at a shallow angle to perforation and examined in a Phillips CM30 TEM at 300 kV.

Raman spectra were obtained using a triple spectrograph ( $6 \text{ cm}^{-1}$  resolution) with a charge-coupled detector (CCD). Film-side surfaces of the samples were illuminated as-received with 100mW of the 457.9 nm, 488.0 nm and 514.5 nm wavelengths from an argon-ion laser and the 647.1 nm wavelength from a krypton-ion laser. The laser beam impinged the film surface at a  $40^\circ$  angle to it and was focused to an approximately 2 mm by 0.1 mm line. All Raman spectra in this paper are presented with a vertical intensity axis and a horizontal Raman shift axis.

#### EFFECTIVE RAMAN PENETRATION DEPTH

Visible light is strongly absorbed by elemental silicon, penetrating on the order of hundreds of nanometers. Absorption coefficients vary strongly with wavelength<sup>2</sup>. An estimate of the effective depth through which Raman signals are obtained is provided by Equation (1);

$$X_d = \text{func}(\varphi)/k_\lambda [1 + \text{func}(\varphi)] (10^7 \text{ nm/cm}) \quad (1)$$

which was derived from Snell's Law of Refraction and the absorption relation for radiation,  $I = I_0 \exp(-k_\lambda x)$ .  $\text{func}(\varphi) = \cos(\sin^{-1}[\cos\varphi/n])$ , where  $\varphi$  is the angle of the laser beam propagation with respect to the film surface, and  $n$  is the index of refraction of the film at wavelength  $\lambda$ .  $I_0$  and  $I$  are the intensities of the light, respectively, at the surface and at depth  $x$  of the film, which has an absorption coefficient,  $k_\lambda (\text{cm}^{-1})$  at wavelength  $\lambda$  (same value assumed for incident and inelastically scattered photons).  $X_d$  is the depth, in nm, from which inelastically scattered light, as measured at the film's surface, is  $1/e$  the intensity of light from inelastic scatter events at the film's surface. Equation (1) takes into account attenuation of the incident laser photons by the film, the path of the laser beam in the film and attenuation of inelastically scattered photons during their propagation out of the film. Using Equation (1) with  $\varphi = 40^\circ$  and  $k_\lambda$  and  $n$  for crystalline silicon from Aspnes<sup>2</sup>, the effective penetration depths for the laser wavelengths used in this study are shown in Table 1. These penetration depths are estimates valid only for crystalline silicon. Absorption coefficients for amorphous silicon<sup>3</sup> are not as well known but appear to be at least ten times as large as for crystalline silicon, reducing penetration depths proportionately. Reflection and/or interference effects at the field oxide layer appear to prevent penetration of light past the field oxide layer.

TABLE 1  
Effective Raman Penetration Depth in Crystalline Silicon

| Wavelength, nm | $X_d$ (nm) |
|----------------|------------|
| 457.9          | 136        |
| 488.0          | 241        |
| 514.5          | 331        |
| 647.1          | 1473       |

#### RESULTS AND DISCUSSION

Figure 1 shows the TEM micrograph of a polysilicon film and the corresponding Raman spectra with excitation wavelengths as indicated. The light band at the bottom of the micrograph is the field oxide layer. Raman scatter from the field oxide was found to be of too low an intensity to contribute significantly to the Raman spectra presented in this paper, even in situations where

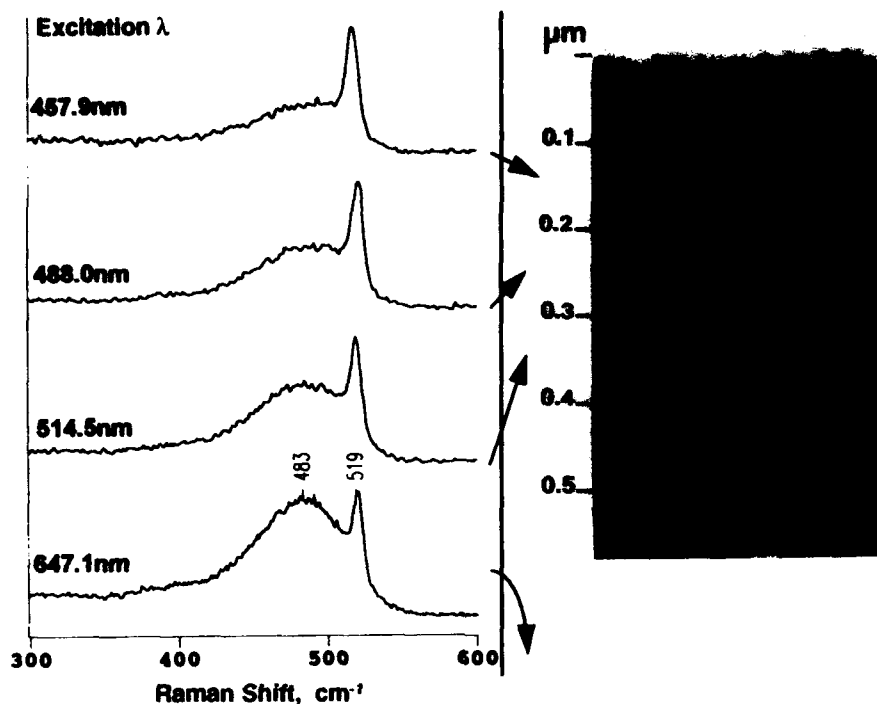


Figure 1. TEM micrograph and Raman spectra of a polysilicon film. Arrows point to the effective penetration depth of the excitation wavelength in crystalline silicon.

the excitation wavelength is expected to penetrate to the field oxide layer. Effective Raman penetration depths (estimated for crystalline silicon - Table 1) for the excitation wavelengths are also indicated in the figure. The dark/light irregular features in the micrograph are regions of crystalline silicon. The featureless, smooth areas are interpreted as regions of amorphous silicon. The micrograph suggests that regions of mixed crystalline and amorphous silicon phases underlie a crystalline surface. Below a depth of 0.4  $\mu\text{m}$ , the silicon appears to be totally amorphous. The Raman spectra change as expected for increasing penetration depth with increasing excitation wavelength. For the shorter excitation wavelengths (457.9-514.5 nm) the Raman spectra show a narrow band due to crystalline silicon ( $519\text{ cm}^{-1}$ ) and broader band of lower peak intensity due to amorphous silicon ( $483\text{ cm}^{-1}$ ), which increases slowly in relative intensity as the excitation wavelength (and penetration depth) increases. Even if the upper layers of the film were totally crystalline silicon, only the 647.1 nm excitation wavelength would be expected to penetrate below the crystalline layers to the totally amorphous region. The Raman spectrum obtained with 647.1 nm excitation shows a significantly increased relative intensity in the amorphous silicon band, corresponding to the totally amorphous silicon layer below 0.4  $\mu\text{m}$  in depth. The high absorptivity of the amorphous silicon region probably prevents significant penetration of even the 647.1 nm wavelength through the totally amorphous region to the field oxide layer.

Figure 2 shows the TEM micrograph and corresponding Raman spectra of a polysilicon film with what appears from the micrograph to be a region of largely amorphous silicon overlying silicon crystallites. With the relatively high absorptivity of amorphous silicon the actual

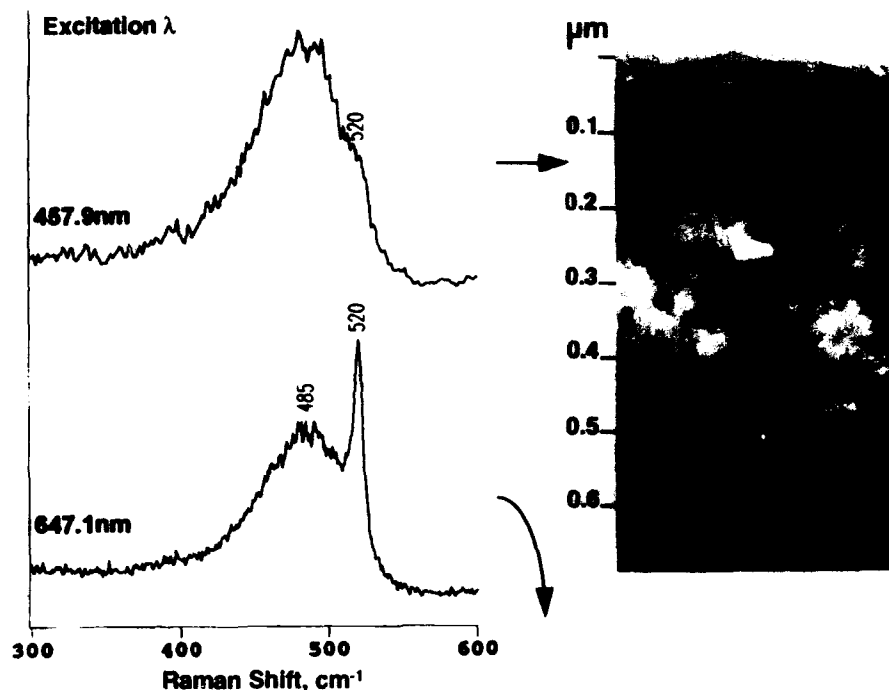


Figure 2. TEM micrograph and Raman spectra of a polysilicon film. Arrows point to the effective penetration depth of the excitation wavelength in crystalline silicon.

penetration of the excitation wavelengths may be 10% of the effective penetration depths for crystalline silicon (as indicated in Table 1 and the figure). The 457.9 nm excitation wavelength does not penetrate past the amorphous layer, so that the 457.9 nm-excited Raman spectrum shows mainly the amorphous silicon band ( $485\text{ cm}^{-1}$ ) with a hint of crystalline silicon ( $520\text{ cm}^{-1}$ ) from scattered crystallites. The 647.1 nm excitation wavelength is expected to penetrate between 0.1 and 0.2  $\mu\text{m}$  in amorphous silicon (10% of the value in Table 1) and yields a Raman band near  $520\text{ cm}^{-1}$  from the underlying silicon crystallite layer in addition to the amorphous silicon band.

Figure 3 shows the TEM micrograph of a film with an apparently crystalline but columnar silicon structure throughout its depth. The associated Raman spectra show a dominant band due to crystalline silicon ( $521\text{ cm}^{-1}$ ) plus a low-intensity band peaking near  $497\text{ cm}^{-1}$ . The band near  $497\text{ cm}^{-1}$  corresponds to neither crystalline silicon nor amorphous silicon. The constancy of the intensity ratios of the 497 and  $521\text{ cm}^{-1}$  bands for 457.9 and 647.1 nm excitation wavelengths suggests: one, that the species responsible for the  $497\text{ cm}^{-1}$  band is associated with the columnar structures and is in approximately constant concentration throughout the depth of the film; and two, that the 647.1 nm excitation does not penetrate past the field oxide layer (possibly due to reflection and/or interference effects) to the substrate silicon. If the 647.1 nm excitation significantly sampled the silicon substrate, the intensity of the crystalline silicon ( $521\text{ cm}^{-1}$ ) band should increase relative to the intensity of the  $497\text{ cm}^{-1}$  band.

An expanded image (see Figure 4) of the micrograph in Figure 3 shows numerous striations or fringes in the columnar silicon structures. These features are believed to be faults or



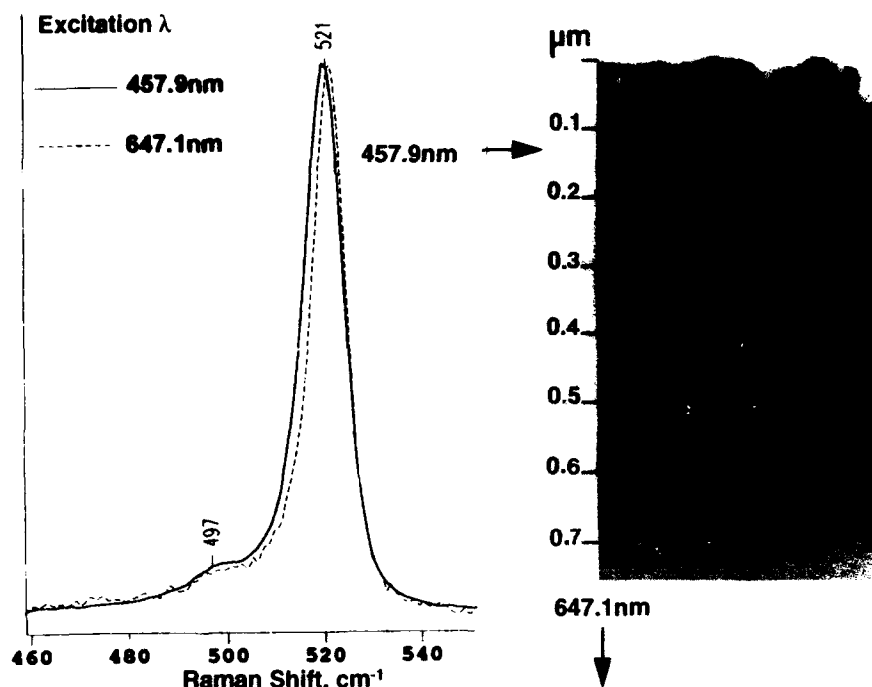


Figure 3. TEM micrograph and Raman spectra of a polysilicon film. Arrows point to the effective penetration depth of the excitation wavelength in crystalline silicon.

dislocations on the nanometer scale. A micrograph of an annealed film prepared under similar conditions (Figure 5) does not show the columnar structures and dislocations, only relatively large crystalline regions. The Raman spectrum of the annealed film (Figure 5) lacks the  $497\text{ cm}^{-1}$  band and has a significantly narrowed band due to crystalline silicon. We conclude that the Raman band near  $497\text{ cm}^{-1}$  corresponds to the faulting present in the micrographs of the as-deposited film (Figures 3-5), which we believe results in nanometer-scale silicon structures, perhaps only a few unit cells in extent. Olego and Baumgart<sup>4</sup> observed a similar Raman band at  $490\text{--}500\text{ cm}^{-1}$ , which they ascribed to surface layers of silicon that act as grain boundaries for crystalline silicon inclusions in an  $\text{SiO}_2$  matrix.

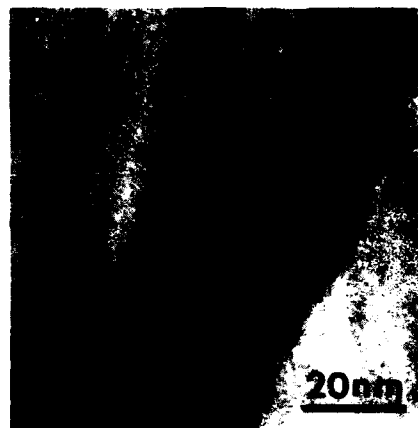


Figure 4. Expanded TEM micrograph of the columnar structures in the polysilicon film also shown in Figure 3.

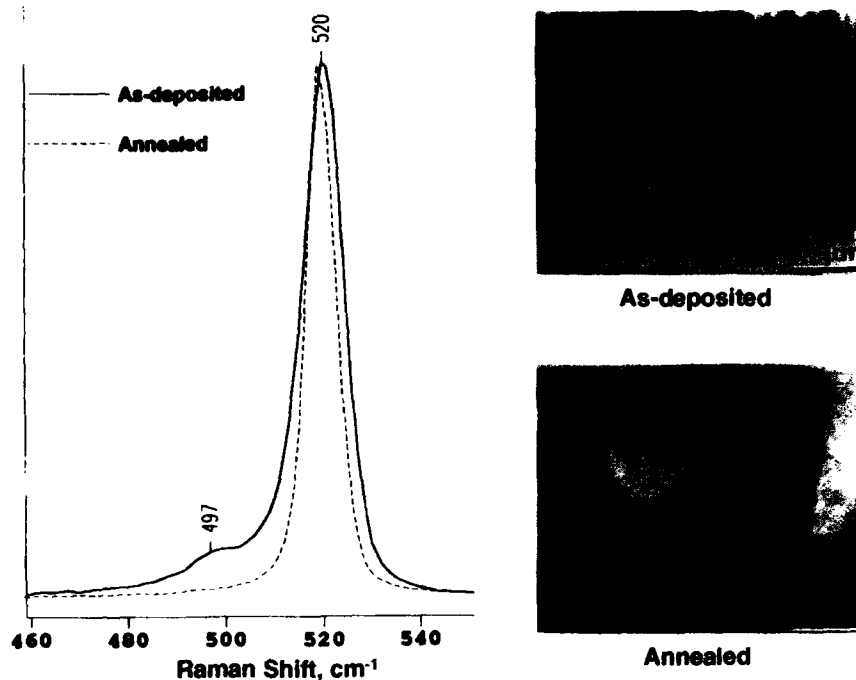


Figure 5. TEM micrographs and Raman spectra of the as-deposited polysilicon film with a columnar structure (see Figures 3 and 4) and an annealed film.

#### SUMMARY

TEM micrographs and Raman spectra of polysilicon films provide confirmatory and complementary information for the identification of crystalline and amorphous phases and their spatial distribution. Dislocations or faulting in TEM micrographs of columnar structures in polysilicon films are correlated to a specific band at  $497\text{ cm}^{-1}$  in Raman spectra and are identified as nanometer-scale silicon structures. Thus, comparison of TEM and Raman data provides insights not available from either set of data alone. More sophisticated modeling of the effective Raman penetration depth using accurate values for the absorption coefficient of amorphous as well as crystalline silicon should improve the correlation between TEM and Raman data.

#### REFERENCES

1. F. H. Pollack, *Test and Measurement World*, pp. 2-10 (May, 1985)
2. D. E. Aspnes and A. A. Studna, *Phys. Rev. B*, **27**(2), 985-1009 (1983).
3. M. A. Bosch and R. A. Lemons, *Appl. Phys. Lett.* **40**(2), 166-168 (1982).
4. D. J. Olego and H. Baumgart, *J. Appl. Phys.* **63**(8), 2669-2673 (1988).

## PHOTOLUMINESCENCE STUDY OF HYDROGEN-RELATED DEFECTS IN SILICON

A. HENRY\*, B. MONEMAR\*, J.L. LINDSTRÖM\*, Y. ZHANG\*\* AND J.W. CORBETT\*\*.

\* Department of Physics and Measurement Technology, Linköping University, S-581 83 Linköping, SWEDEN.

\*\* Department of Physics, State University of New York, Albany, NY 12222, USA

### ABSTRACT

The effect of ion-implantation followed by a rapid thermal annealing was investigated in boron-doped silicon using photoluminescence (PL) spectroscopy. The radiation induced defects giving rise to the G, W and C PL lines are completely passivated by a hydrogen plasma treatment. However this hydrogen exposure also introduces broad and deep luminescence structure as well as new sharp PL lines very near the silicon band gap. Up to twelve new lines are observed at low temperature ( $< 20\text{K}$ ). One of them exhibits a very low exciton localisation energy ( $\approx 2\text{ meV}$ ) compared to the value measured for classical shallow donors or acceptors, and is observed only at very low temperature ( $< 4\text{K}$ ). A broad deep PL band with a halfwidth of  $30\text{ meV}$  is observed at around  $925\text{ meV}$ . The excitation power dependence and the temperature dependence of the PL intensity of these sharp lines and the broad band are presented. Tentative correlations with the data currently available in the literature are presented for the understanding of the formation of the defects associated to the broad band as well as the sharp near band gap PL lines.

### INTRODUCTION

The incorporation of hydrogen into crystalline semiconductors has been a matter of intense experimental and theoretical studies [1] during the last decade, due mainly to the ability of hydrogen to passivate electrical activity of both shallow and deep level defects. Experimental techniques such as absorption spectroscopy and electrical measurements are commonly used in these studies. Although photoluminescence (PL) spectroscopy is a powerful technique for the study of defects in semiconductors, it does not yet appear to be extensively used in the case of hydrogen studies, and the list of publications on this topic is limited [2-9]. Therefore the aim of this work is to present and discuss PL data retrieved on p-type silicon samples after implantation and hydrogenation treatment. Passivation of the radiation induced defect is observed and two distinct types of recombination processes are seen after hydrogenation.

### EXPERIMENTAL PROCEDURE

#### Sample preparation.

Boron doped, (100) oriented, Czochralski grown silicon wafers have been used in this study, and they were divided into four parts which were then differently processed. The initial room-temperature resistivity of the material was  $10\ \Omega\text{cm}$ .

Ion implantations with mercury ions were performed at nominal room-temperature into a part of the polished faces of the wafers with doses in the range  $5 \times 10^{13}$  to  $5 \times 10^{14}\text{ cm}^{-2}$  at  $100\text{ keV}$ . A rapid thermal annealing (RTA) at the temperature of  $1000^\circ\text{C}$  was then carried out during  $30\text{ s}$ . This treatment is usually done in the device technology and is known to activate implanted impurities and to remove implantation damage with as little redistribution of the implanted impurities as possible. After RTA treatment, a hydrogen plasma treatment was performed on one half of the wafers during  $2\text{ hours}$  at  $200^\circ\text{C}$  in a downstream system as described in Ref.1. Subsequent conventional thermal annealing of the various samples (implanted or RTA treated or

hydrogenated) was done in a diffusion furnace in air ambient with the samples placed in a quartz tube. These annealings were performed during one hour in the temperature range of 50 to 500°C. The samples were given a 20 s dip in HF before and after each annealing. To enable a comparison and to control undesirable contamination a reference sample (starting material) was also annealed at the same time as the studied samples. An efficient radiative defect was found to be introduced in the silicon after the mercury implantation and subsequent annealing, which has recently been reported separately [10].

#### Photoluminescence spectroscopy.

PL measurements were done in the temperature range from 2K to ~100K, excited with the 514.5 nm line of an Ar<sup>+</sup> ion laser. The luminescence collected from the sample was spectrally resolved by a double grating monochromator fitted with two 600 grooves/mm gratings blazed at 1.6  $\mu\text{m}$  (SPEX 1404 0.85m). For the detection a liquid nitrogen cooled North Coast EO-817 Ge detector was used with conventional lock-in technique. The excitation power was around 10 mW/mm<sup>2</sup> on the sample with an unfocused laser spot. The spectra were not corrected for the response of our detection system. Using the 514.5 nm radiation from the Ar<sup>+</sup> ion laser as the excitation source the penetration depth of the excitation light into the silicon crystal is about 1  $\mu\text{m}$  at 2K. However the diffusion depth of the photo-generated carriers is much larger and strongly dependent on the concentration of the defects present in the crystal. However the depth of characterised material with this laser excitation will cover both the depth of implantation and of hydrogenation treatment.

#### PHOTOLUMINESCENCE RESULTS.

##### Broad band in the PL spectra

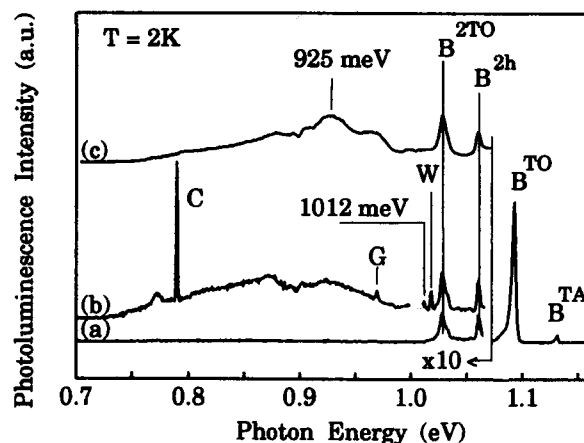


Fig.1 : PL spectra recorded at 2K on the control sample (a), after implantation with the doses of  $10^{14} \text{ cm}^{-2}$  (b), and after hydrogen treatment (c), respectively. The structure observed around 0.9 eV is due to water absorption, and the labels of the lines are explained in the text. The parts of the spectra indicated by the arrows are magnified by a factor 10 as specified on the figure.

On the part of the samples submitted to the RTA treatment alone, no changes of the PL spectrum were observed, from a comparison with the PL spectrum of the starting material (Fig.1.a). The spectra contained the phonon replica of the boron bound exciton (BE) : a very weak no-phonon (NP) transition, the transverse-acoustic (BTA), the transverse-optical transition (BTO), the two-phonon-replica transition (B<sup>2</sup>TO) and the two-hole-transition (B<sup>2</sup>h) of the boron BE [11]. However in the spectra taken from the implanted samples other BE lines are observed. They are the W, G and C lines [11], as well as a line located at 1012 meV (Fig.1.b). A typical PL spectrum observed on the samples after RTA and hydrogen treatment (with or

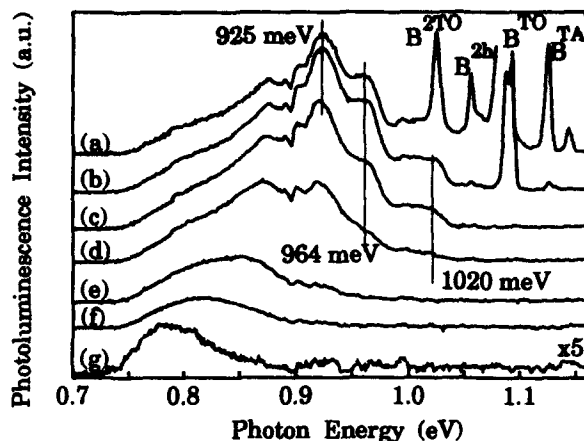


Fig.2 : PL spectra of a hydrogenated silicon sample recorded at 4K (a), 8K (b), 30K (c), 50K (d), 80K (e), 100K (f) and 140K (g), respectively.

without implantation) is shown in Fig.1.c. Together with the phonon replica of the boron BE additional broad lines or bands are observed. The dominant band is located at about 925 meV (with a rather large width of 45 meV), two broad lines as superimposed on this band are detected at about 964 meV and 1020 meV and a large background signal spreading from 0.75 to 1.00 eV completes the observed spectrum. Various sharp PL lines were also observed in the very near band gap region as will be presented in the next section.

The dependence on the laser excitation power was measured for the B<sup>2</sup>TO, W, 1012 meV lines and the broad band (925 meV). Their PL intensity was found to increase linearly with

power, until saturation is obtained at a high enough excitation power.

The two broad lines (964 and 1020 meV) are more easily observed by increasing the measurement temperature since the BE related lines then start to be rapidly thermally quenched, as shown in Fig.2 (b and c). Above 40K these broad lines (964 and 1020 meV) don't appear in the PL spectra whereas the dominant band (925 meV) shifts in position to the lower energy side and decreases in intensity. The variation of the energy position as well as the integrated PL intensity of the broad band (925 meV) are plotted in Fig.3.a and the Arrhenius plot of the temperature dependence is displayed in Fig.3.b. A thermal deactivation energy of about 45 meV is determined by the slope of the straight line fitting the high temperature data.

We have performed an isochronal annealing on the hydrogenated sample and the evolution of the broad bands is shown in Fig.4. Below 300°C of annealing no changes in intensity neither in

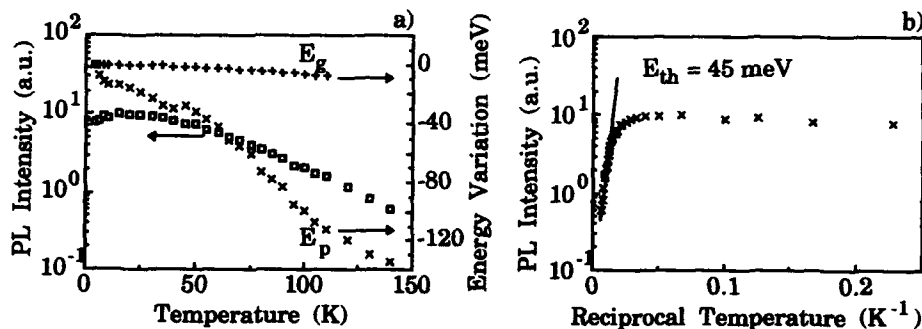


Fig.3 : (a) Variation of the energy position ( $E_p$ ) of the broad band (925 meV) and the band gap ( $E_g$ ), and PL intensity of the broad band as a function of the temperature.

(b) Temperature dependence of the broad band detected at 925 meV. The variation of the band gap is calculated using the equation :  $E_g(T) = 1170 - \frac{0.173 T^2}{T+636}$  (meV) where the temperature  $T$  is in K.

energy position are detected. After 350°C and 400°C heat treatment the broad band is shifted to higher energy and a slight decrease in intensity is observed. The broad band has completely vanished after annealing at temperature higher or equal to 450°C.

#### The near-band gap emissions.

Together with the broad band observed in the range 1.02 to 0.90 eV sharp PL lines were also observed in the very near band gap region of implanted and hydrogenated samples, as shown in Fig.5. The labels and energy positions ( $E_{pos}$ ) of these lines together with the boron related BE lines are listed in Table.I, as well as the calculated localisation energy ( $E_{loc}$ ) if these lines are considered as NP lines. Their PL intensity was found to be independent of the ion implantation dose. The dependence on the laser excitation power ( $I_{laser}$ ) of the PL intensity ( $I_{line}$ ) shows at low excitation

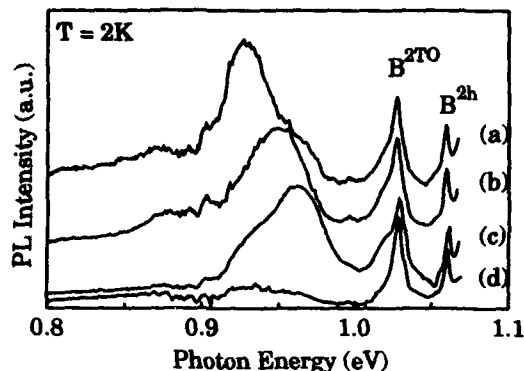


Fig.4 : PL spectra recorded at 2K before annealing (a), after annealing at 350°C (b), 400°C (c) and 450°C (d) respectively, for one hour.

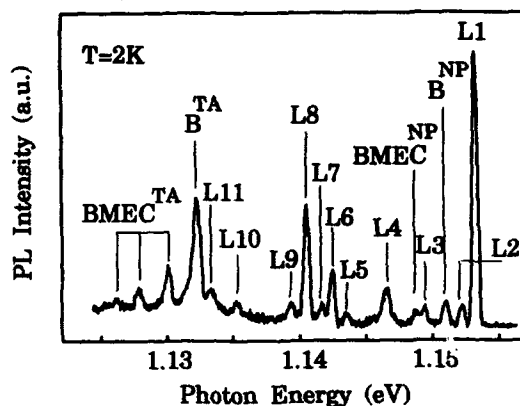


Fig.5 : High resolution PL spectrum at 2K of a silicon sample implanted, RTA and hydrogen treated. The label BMEC is used for the Bound-Multi-Exciton-Complex lines associated with the nearest BE boron line (BNP and B<sup>TA</sup>).

Table I : Label, energy position  $E_{pos}$  in meV and localisation energy  $E_{loc}$  in meV of the near band gap lines. The energy positions were measured at 2K with an accuracy of  $\pm 0.2$  meV and the localisation energies were calculated as :  $E_{loc} = E_g - E_{NP} - E_{pos}$ , where  $E_g = 1169.5$  meV is the Si gap and  $E_{NP} = 14.3$  meV is the binding energy of the FE.

power a relation as  $I_{line} = C \cdot I_{laser}^n$ , where C is a constant and n is in the range  $0.6 < n < 1$ . Fig.6.a shows PL spectra in the very near band gap region recorded at various temperatures. The PL intensity of some of these lines are plotted as a function of the temperature in Fig.6.b. As shown in the two figures, the temperature dependence of the PL

power a relation as  $I_{line} = C \cdot I_{laser}^n$ , where C is a constant and n is in the range  $0.6 < n < 1$ . Fig.6.a shows PL spectra in the very near band gap region recorded at various temperatures. The PL intensity of some of these lines are plotted as a function of the temperature in Fig.6.b. As shown in the two figures, the temperature dependence of the PL

| Label | $E_{pos}$ | $E_{loc}$ |
|-------|-----------|-----------|
| L1    | 1153.2    | 2         |
| L2    | 1152.2    | 3         |
| BNP   | 1150.8    | 4.4       |
| L3    | 1149.5    | 5.7       |
| L4    | 1146.6    | 8.6       |
| L5    | 1143.6    | 11.6      |
| L6    | 1142.5    | 12.7      |
| L7    | 1141.8    | 13.4      |
| L8    | 1140.6    | 14.6      |
| L9    | 1139.4    | 15.8      |
| L10   | 1135.3    | 19.9      |
| L11   | 1133.4    | 21.8      |
| L12   | 1068.1    | 87.1      |

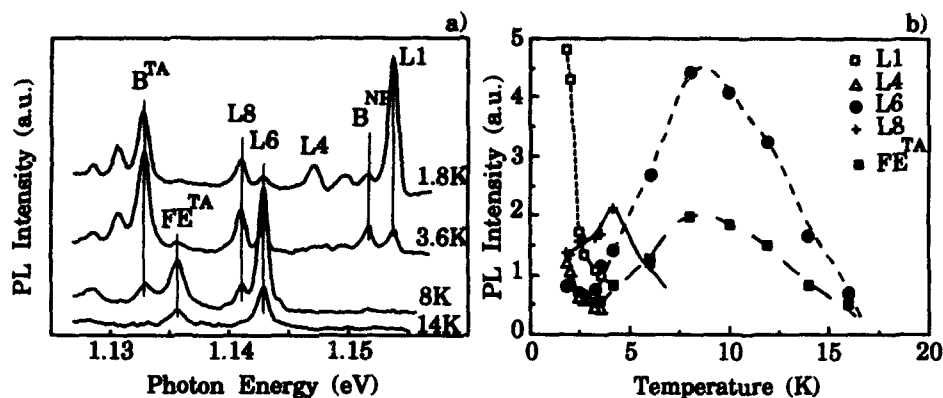


Fig.6 : (a) PL spectra after implantation, RTA and hydrogen treatment recorded at the indicated temperatures. (b) The integrated PL intensity of some of the near band gap lines as a function of the measurement temperature.

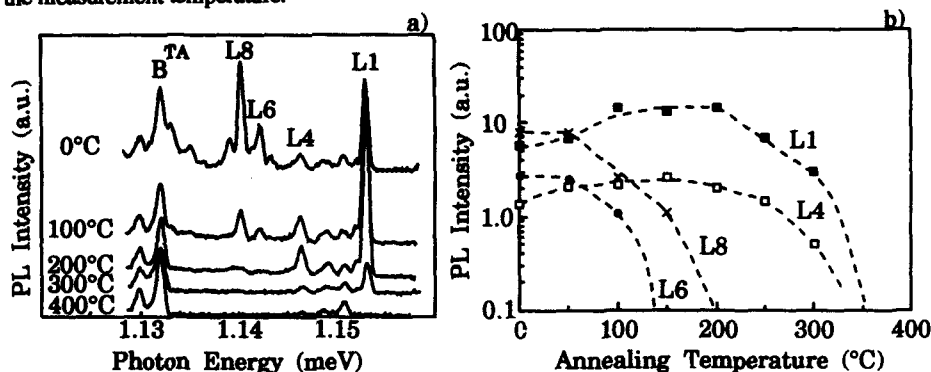


Fig.7 : (a) PL spectra at 1.8K after implantation, RTA, hydrogen treatment and subsequent annealing at the indicated temperatures. (b) The integrated PL intensity at 1.8K of some of the near band gap lines as a function of the annealing temperature.

intensity of these new near band gap lines are different. L1 and L4 decrease in intensity as the sample temperature increases, whereas L6 and L8 lines increase in intensity until a maximum is observed at around 8K and 4K respectively before being thermally quenched. No accurate determination of the thermal activation energy could be done with these data, due to a too weak PL intensity and a fast thermal quenching. In Fig.7.a PL spectra recorded before and after isochronal annealing are displayed and the PL intensity of some of the near band gap lines are plotted versus the annealing temperature in Fig.7.b. The L1 and L2 lines show a similar behaviour with an increase in intensity up to 100°C annealing, followed by an intensity decrease at about 200°C annealing. They are not observed after annealing at 400°C. The PL intensity of the L6 and L8 lines decreases faster as the annealing temperature increases and they are not detected after 150°C and 200°C annealing, respectively.

## DISCUSSION

From the PL results described above it is clearly shown that distinct recombination processes occur in our hydrogenated silicon samples and they are certainly related to different defects

involving hydrogen. The deep broad band observed at around 925 meV as well as the two broad lines observed at 1020 and 964 meV are very similar to those reported after reactive-ion-etching using various plasma conditions [2-5].

The broad PL band at 925 meV is then assumed to arise from an electron-hole recombination process around extended defects where a local modification of the crystalline potential can be considered. Both electrons and holes could be localised in potential wells due to the highly strained silicon lattice surrounding these extended defects [6]. The broad lines at 1020 and 964 meV can be associated to the NP and TO phonon replica recombinations of the same exciton bound to a complex defect which probably involves an intrinsic point defect and hydrogen. The broadening of these lines is assumed to be due to an inhomogeneous strain around this complex defect.

A series of sharp lines was previously reported in the near band gap region (from 1148 meV to 1095 meV) in samples irradiated by fast neutrons and then treated by hydrogen plasma. These lines were associated with excitonic transitions at hydrogen donor complexes [8]. Moreover sharp PL lines in the range 1147-1137 meV were also reported from samples first hydrogenated and then irradiated and annealed [9]. The centres responsible of these lines were suggested to contain as many as four hydrogen atoms. However the sharp PL lines that we observe very near to the silicon band gap are different from the Ref.7-9, and are reported here for the first time, to our knowledge.

All these lines seem to be related to different centers. We never found a correlation between them, changing the various experimental parameters such as the conditions to create these lines (implantation dose), or the PL experimental conditions as the excitation power or the temperature. By comparison with the few similar investigations from the literature cited above we believe that many parameters must be taken in to account to understand the formation of the centers giving rise to these sharp PL lines. Firstly the starting material must be considered and it is well known that with different doping (n or p-type) and growth technique (Czochralski or Float-zone) different kinds of defects can be created by irradiation or implantation. This probably explains the different lines observed in our work, as compared to Ref.7-9. The nature of the particle irradiation could also play a role regarding the nature of created defects, which could be considered as single or point defects.

We suggest that these lines are associated to the NP recombination of isoelectronic bound exciton localised at various defects which probably involve hydrogen atoms. One possible model for these defects would be that they are complex defects formed by hydrogen reacting with primary defects present after the irradiation, and which may act as a nucleation site for the formation of more extended hydrogen related defects. More detailed spectroscopic studies will be necessary to make any definite conclusions about the identity of these defects.

## REFERENCES

1. S.J. Pearton, J.W. Corbett and T.S. Shi, *Appl. Phys. A* **43**, 153 (1987).
2. N.M. Johnson, F.A. Ponce, R.A. Street and R.J. Nemanich, *Phys. Rev. B* **35**, 4166 (1987).
3. M. Singh, J. Weber, T. Zundel, M. Konuma and H. Cerva, *Mater. Sci. Forum* **38-41**, 1033 (1989).
4. I.-W. Wu, R.A. Street and J.C. Mikkelsen, Jr, *J. Appl. Phys.* **63**, 1628 (1988).
5. A. Henry, B. Monemar, J.L. Lindström, T.D. Bestwick and G.S. Oehrlein, *J. Appl. Phys.* **70**, 5597 (1991).
6. H. Weman, B. Monemar, G.S. Oehrlein and S.J. Jeng, *Phys. Rev. B* **42**, 3109 (1990).
7. V.I. Obodnikov, L.N. Safronov, and L.S. Smirnov, *Fiz. Tekh. Poluprovodn.* **10**, 1373 (1976) [*Sov. Phys. Semicond.* **10**, 814 (1976)].
8. J. Hartung and J. Weber, *Mater. Sci. Eng. B* **4**, 47 (1990).
9. A.N. Safonov and E.C. Lightowers, in *Proceedings of 17th International Conference on Defects in Semiconductors*, Gmunden, 1993.
10. A. Henry, B. Monemar, J.P. Bergman, J.L. Lindström, P.O. Holtz, Y. Zhang and J.W. Corbett, *Phys. Rev. B* **47**, 13 309 (1993).
11. G. Davies, *Rep. Phys.* **176**, 83 (1989) and references therein.



## **Raman Scattering Characterization of Ultrathin Films of $\beta$ -SiC**

Ahn Goo Choo, Spirit Tlali, and Howard E. Jackson

*Department of Physics, University of Cincinnati, OH 45221-0011*

and

J. P. Li and Andrew J. Steckl

*Department of Electrical and Computer Engineering, University of Cincinnati,  
OH 45221-0030*

### **Abstract**

Raman scattering has been used to characterize ultrathin films of  $\beta$ -SiC, ranging in thickness from 38 nm to 240 nm. These films were prepared on the surface of a  $\langle 100 \rangle$  Si substrate by a carbonization process at a temperature of 1300°C. In each case, the LO phonon near 970  $\text{cm}^{-1}$  and the TO phonon near 795  $\text{cm}^{-1}$  are observed, indicating the formation of  $\beta$ -SiC crystal. The Raman linewidths and peak positions indicate evidence of nonuniform stress and disorder. The Raman intensity of the TO phonon is nearly twice the intensity of the LO phonon measured both with and without the Si substrate, which indicates that the crystal growth was not entirely confined in the  $\langle 100 \rangle$  direction.

### **Introduction**

$\beta$ -SiC is a promising wide band gap semiconductor with potential use for high temperature, high power, and high frequency devices due to its good structural stability, high thermal conductivity, and moderate electron mobility.<sup>1</sup> High quality epitaxial layers are necessary for the fabrication of these devices. A chemical vapor deposition technique has been developed to obtain high quality  $\beta$ -SiC epitaxial layers.<sup>2,3</sup> Because SiC has a lattice mismatch of 20 % and a difference of 8% in the coefficient of thermal expansion, the SiC epitaxial layer is grown on a buffer layer, formed by carbonizing the Si surface using  $\text{C}_3\text{H}_8$  or  $\text{C}_2\text{H}_4$ . This transition layer is necessary to relieve the large lattice mismatch. Although measurements of thick growth films have been reported,<sup>4,5</sup> Raman scattering measurements from the films grown in this manner have not yet been reported. We report Raman scattering measurements to study the films of varying thickness grown in this manner.

### **Experiment**

Carbonized films on (100) Si surface were prepared by reacting (100) surface with propane ( $\text{C}_3\text{H}_8$ ) or ethylene ( $\text{C}_2\text{H}_4$ ) at a temperature of 1300°C.<sup>6</sup> The substrates for carbonization were (100) n-type Si wafers with 4-6  $\Omega\cdot\text{cm}$  resistivity. The thickness of the films varied from 38 nm

to 240 nm. The surface orientations were the same as the (100) substrate, as characterized by x-ray measurements. Table I summarizes the growth details. To view the SiC sample without the Si substrate, a window in the substrate was etched away with HF/HNO<sub>3</sub>.

Table I. Sample growth conditions.

| Sample | Thickness       | Temperature | Time   | Pressure | React Gas                             | Carrier                |
|--------|-----------------|-------------|--------|----------|---------------------------------------|------------------------|
| A      | 6 $\mu\text{m}$ | -           |        |          |                                       |                        |
| B      | 380 Å           | 1300°C      | 90 sec | 5 torr   | 70 sccm C <sub>2</sub> H <sub>4</sub> | 0.9 lpm H <sub>2</sub> |
| C      | 1400 Å          | 1300°C      | 90 sec | 5 torr   | 60 sccm C <sub>2</sub> H <sub>4</sub> | 0.9 lpm H <sub>2</sub> |
| D      | 2400 Å          | 1300°C      | 90 sec | 5 torr   | 90 sccm C <sub>2</sub> H <sub>4</sub> | 0.4 lpm H <sub>2</sub> |

Raman spectra were measured at room temperature in the backscattering geometry using the 514.5 nm line from an argon-ion laser. The penetration depth of the 514.5 nm line in  $\beta$ -SiC was about 400  $\mu\text{m}$ , obtained from the absorption coefficient of 25 cm<sup>-1</sup>.<sup>7</sup>

### Results and Discussion

Figure 1 shows the Raman spectra of the thick sample A without the Si substrate. The configurations for these measurements are (a) Z(XX+XY) $\bar{Z}$ , (b) Z(XX) $\bar{Z}$  and (c) Z(XY) $\bar{Z}$ , where Z//[100]. This polarization analysis of the Raman spectra allows the orientation of the sample to be determined. The peaks at 797.4 cm<sup>-1</sup> and 973.3 cm<sup>-1</sup> correspond to transverse (TO) and longitudinal (LO) optical phonon modes, respectively. The full width at half maximum of both peaks was 3.4 cm<sup>-1</sup>. The result is in agreement with the polarization selection rule of

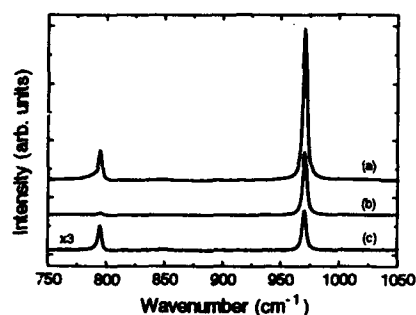


Fig. 1. Raman spectra of sample A without the Si substrate. (a) Z(XX+XY) $\bar{Z}$ , (b) Z(XX) $\bar{Z}$  and (c) Z(XY) $\bar{Z}$

zinc-blende-type (100)  $\beta$ -SiC except for the observation of a relatively large transverse optical phonon mode intensity. The polarization selection rules and the narrow Raman lines are characteristic of single crystal (100)  $\beta$ -SiC. The LO and TO phonon peaks of the free-standing film (i.e. without Si substrate) were found to shift upward by 0.86  $\text{cm}^{-1}$  and 1.22  $\text{cm}^{-1}$  respectively, compared with that of the as-grown sample. The SiC films on substrates are under biaxial stress, because the lattice constant of  $\beta$ -SiC (4.359 Å) is smaller than that of Si (5.430 Å). A removal of the substrate reduces this stress and thus shifts the phonon peaks in the manner indicated above.

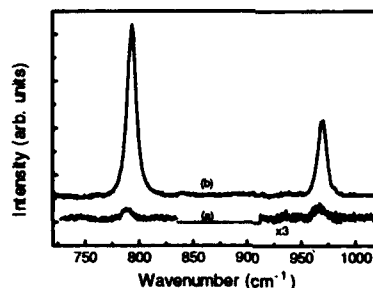


Fig. 2. The Raman spectra of sample B (a) with and (b) without the Si substrate.

The Raman spectra of sample B (a) with and (b) without the Si substrate are shown in Fig. 2. The LO and TO phonon responses are clearly seen in both cases, which suggests the film is a single crystal. An enhancement of Raman signals of the  $\beta$ -SiC free films with respect to that of the  $\beta$ -SiC films on the Si substrate is observed, and has been explained by the difference in the reflection processes at the SiC/air interface and the SiC/Si interface.<sup>5</sup> The Raman spectra of samples C and D are shown in Figs. 3 and 4, respectively, in order to analyze peak position and lineshape compared to the thick sample A. Asymmetrical broadening, a larger shift in peak position and a relative intensity switch between TO and LO phonon modes, compared to the results of sample A, are clearly observed. These are possibly explained by strain<sup>8</sup> and disorder.<sup>9</sup>

Thin films on substrates are generally under biaxial stress. The application of this stress causes polarization-dependent splittings and/or shifts which are linear in the stress: one of the doublet components becomes the LO phonon while the singlet and the other doublet component become the TO phonons. The phonon frequencies of each component are expressed by

$$\text{LO phonon:} \quad \Omega_s = \omega_{LO} + \Delta\Omega_H - \frac{1}{3}\Delta\Omega \quad (1)$$

$$\text{TO phonon:} \quad \begin{cases} \Omega_d = \omega_{TO} + \Delta\Omega_H - \frac{1}{3}\Delta\Omega \\ \Omega_s = \omega_{TO} + \Delta\Omega_H + \frac{2}{3}\Delta\Omega \end{cases} \quad (2)$$

$$\Omega_s = \omega_{TO} + \Delta\Omega_H + \frac{2}{3}\Delta\Omega \quad (3)$$

where  $\omega_{LO}$  and  $\omega_{TO}$  are the frequencies of the LO and TO phonons in the absence of stress,  $\Delta\Omega_h$  is the shift due to the hydrostatic component of the strain, and  $\Delta\Omega_s$  is the shift due to the shear

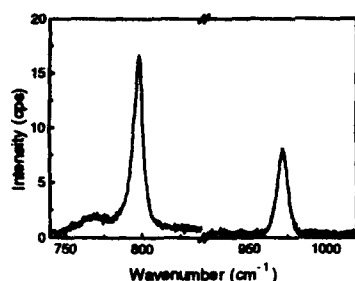


Fig. 3. The Raman spectrum of sample C without the Si substrate.

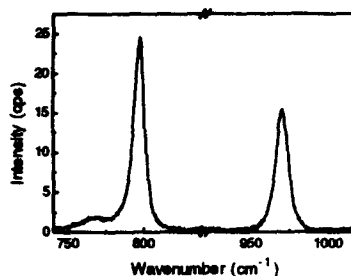


Fig. 4. The Raman spectrum of sample D without the Si substrate.

component of the strain.<sup>8</sup> The frequencies of the LO and TO phonons are expressed as a function of hydrostatic pressure:

$$\omega_{LO} = (972.7 \pm 0.3) + (4.75 \pm 0.09)p - (2.5 \pm 0.4) \times 10^{-2} p^2 \quad (4)$$

$$\omega_{TO} = (796.2 \pm 0.3) + (3.88 \pm 0.08)p - (2.2 \pm 0.4) \times 10^{-2} p^2 \quad (5)$$

where  $\omega_{LO}$  and  $\omega_{TO}$  in  $\text{cm}^{-1}$  and  $p$  in GPa.<sup>10</sup>

The asymmetrical broadening of Raman peak can be explained by disorder<sup>9</sup> expected from the layer with the structural defects.<sup>11</sup> A spatial correlation model in reference 9 can be employed to characterize disorder induced asymmetrical broadening of Raman peaks. We now combine equation (4) and (5) with the spatial correlation model to explain the Raman lineshapes observed in Figs. 2, 3 and 4. This combination of two effects approximately fits the measured Raman data. For better fit, however, one may need to consider a nonuniform distribution of stress and disorder.

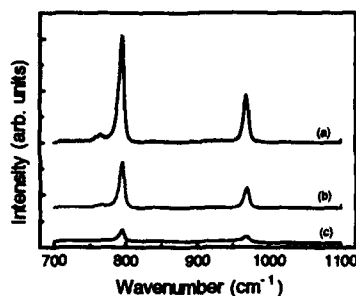


Fig. 5. Raman spectra of sample C without the Si substrate. (a)  $Z(XX+XY)\bar{Z}$ , (b)  $Z(XY)\bar{Z}$  and (c)  $Z(XX)\bar{Z}$

A polarization analysis of the Raman spectra for sample C is shown in Fig. 5 (same behavior for sample D with and without the substrate). The intensity ratio of LO phonon to TO phonon is about 0.5, independent of polarization configuration and different from that observed in Fig. 1, which may indicate that the crystal growth was not wholly confined in the  $\langle 100 \rangle$  direction.

#### Summary

Raman scattering has been used to characterize ultrathin films of  $\beta$ -SiC prepared by a carbonization process. The Raman linewidths and peak positions indicate evidence of nonuniform stress and disorder. The Raman scattered intensity from the TO phonons is nearly twice that of the LO phonons, measured both with and without the Si substrate. In all samples well-defined LO and the TO phonon modes were clearly observed, suggesting the formation of crystalline  $\beta$ -SiC.

#### References

1. G. Pensl and Reinhard Helbig, *Festkörperprobleme* **30**, 133 (1990).
2. S. Nishino, J. A. Powell, and H. A. Will Appl. Phys. Lett. **42**, 460 (1983).
3. S. Nishino, H. Suhara, H. Ono, and H. Matsunami, J. Appl. Phys. **61**, 4889 (1987).
4. H. Mukaida, H. Okumura, J. H. Lee, H. Daimon, E. Sakuma, S. Misawa, K. Endo, and S. Yoshida, J. Appl. Phys. **62**, 254 (1987).
5. Z. C. Feng, A. J. Mascarenhas, W. J. Choyke, J. A. Powell, J. Appl. Phys. **64**, 3176 (1988).
6. Andrew J. Steckl and J. P. Li, IEEE Trans. Elect. Devs. **39**, 64 (1992).
7. L. Patrick and W. J. Choyke, Phys. Rev. **186**, 775 (1969).
8. F. Cerdeira, C. J. Buchenauer, F. H. Pollak, and M. Cardona, Phys. Rev. **B 5**, 580 (1972).
9. P. Parayanthal and Fred H. Pollack, Phys. Rev. Lett. **52**, 1822 (1984).
10. D. Olego, M. Cardona, and P. Vogl, Phys. Rev. **B25**, 3878 (1982).
11. S. R. Nutt, D. J. Smith, H. J. Kim, and R. F. Davis, Appl. Phys. Lett. **50**, 203 (1987).

## CHARACTERIZATION OF $\text{Cd}_{1-x}\text{Zn}_x\text{Te}$ ALLOYS USING INFRARED REFLECTIVITY AND RAMAN SCATTERING SPECTROSCOPY

D. N. TALWAR\*, Z. C. FENG\*\*, AND P. BECLA\*\*\*

\* Department of Physics, Indiana University of Pennsylvania, Indiana, PA, 15705-1087

\*\* Department of Physics, National University of Singapore, Singapore 0511

\*\*\* Francis Bitter National Magnet Laboratory, Massachusetts Institute of Technology, Cambridge, Massachusetts 02139

### ABSTRACT

Study of impurity-induced phonon disordering in  $\text{Cd}_{1-x}\text{Zn}_x\text{Te}$  alloys is reported for a variety of samples by using far-infrared reflectivity and Raman scattering spectroscopy. Substantial differences were noted among the various published values for the optical phonon frequencies versus  $x$ . Contrary to an earlier Raman study on MBE grown  $\text{Cd}_{1-x}\text{Zn}_x\text{Te}/\text{GaAs}$  films, our results within a two-mode behavior, yield an increase of both the CdTe- and ZnTe-like transverse optical phonons with  $x$ . Unlike earlier speculations for a gap-mode in  $\text{ZnTe}:\text{Cd}$  of  $\sim 140\text{--}145\text{ cm}^{-1}$ , our Greens function theory predicts it to be at a relatively higher frequency of  $\sim 153\text{ cm}^{-1}$ .

### 1. INTRODUCTION

Considerable efforts have been made in recent years to evaluate the basic properties of mixed II-VI compounds for applications in photo-voltaic, photo-conductive and infrared (IR) detection devices. Earlier, narrow band-gap mercury-cadmium-telluride (MCT) was used as an epilayer in fabricating high performance optical devices.<sup>1,2</sup> However, this material suffers from serious drawbacks related to the poor lattice stability of its alloys. Since the epitaxial layers used in IR detector arrays depend critically upon the quality of the surface and on the substrate, a considerable interest has been stimulated to search for more stable materials for electro-optical devices. Like other ternary compounds  $\text{Cd}_{1-x}\text{Zn}_x\text{Te}$ , offers a large tunability with  $x$  for both the lattice parameter and for the band gap. It is at the value  $x = 0.04$  that  $\text{Cd}_{1-x}\text{Zn}_x\text{Te}$  is lattice matched to  $\text{Hg}_{0.78}\text{Cd}_{0.22}\text{Te}$  for the infrared detector applications. Although several studies<sup>1,2</sup> have been performed in recent years to understand the electronic properties of  $\text{Cd}_{1-x}\text{Zn}_x\text{Te}$  (e.g., band-structure, defect induced deep-electronic states, etc.) very little attention is paid for the optical examination of its dynamical behavior.<sup>3</sup>

The purpose of the present paper is to examine the unique phonon mode behavior in novel  $\text{Cd}_{1-x}\text{Zn}_x\text{Te}$  alloys by using far-infrared reflectivity, which emphasizes the transverse optical (TO) modes, and Raman scattering spectroscopy, which is superior for the longitudinal optical (LO) modes.<sup>4</sup> Comprehensive theoretical calculations are also presented for the disorder-induced phonons in  $\text{CdZnTe}$  by using a phenomenological lattice dynamical theory. Calculated results

for the compositional dependence of optical phonons will be compared with the infrared and Raman scattering data. Unlike earlier speculations<sup>5</sup> that the gap-mode in  $\text{ZnTe:Cd}$  lies near  $\sim 140\text{--}145\text{ cm}^{-1}$  our theory predicts it to be at a relatively higher  $\sim 153\text{ cm}^{-1}$  frequency. Group theoretical analysis suggests that the gap mode exhibits a triply degenerate vibrational state and it should be detected both by IR absorption and Raman scattering spectroscopy in samples with low Cd-composition.

## II. EXPERIMENTAL

### Infrared Reflectivity and Raman Scattering Spectra

The  $\text{Cd}_{1-x}\text{Zn}_x\text{Te}$  ternary alloys (with  $x$  ranging from 0.005 - 0.5) used in the present study were prepared at the Francis Bitter National Magnet Laboratory, Massachusetts Institute of Technology by reacting the 99.9999% pure elemental constituents in evacuated quartz tubes.

The  $x$  composition values were calculated from the mass densities. The far infrared (FIR) reflectivity measurements were performed by using a Fourier transform spectrometer and a Golay detector for good signal-to-noise ratios between  $\sim 50$  and  $350\text{ cm}^{-1}$ . Data were taken at near-normal incidence and at sample temperatures of 300, 80, and 20-30 K. Although the main features of the IR spectra did not change significantly between 80 and 20-30 K, small features sharpened noticeably at the lowest temperatures. In Fig. 1, we display the IR spectra for  $\text{Cd}_{1-x}\text{Zn}_x\text{Te}$  (with  $x = 1, 0.5, 0.4, 0.3, 0.2, 0.1$ , and 0.005) recorded at 300 K.

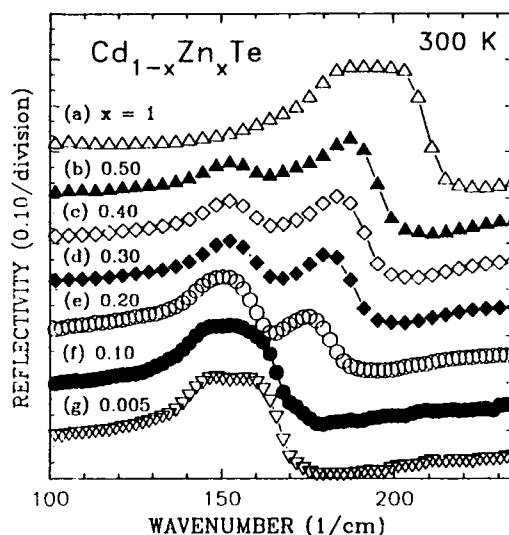


**Fig. 1** Far infrared reflectivity data for bulk  $\text{Cd}_{1-x}\text{Zn}_x\text{Te}$  with compositions  $x$  of (a) 1, (b) 0.5, (c) 0.4, (d) 0.3, (e) 0.2, (f) 0.1, and (g) 0.005 measured at 300 K.

For alloy semiconductors, the IR spectra in the long wavelength range are mainly modulated by the transverse optical phonons. A perusal of Fig. 1 clearly shows a two-mode behavior between the two end members of the alloy. A single band

between 160 and 215  $\text{cm}^{-1}$  corresponds to an IR active mode for pure ZnTe, whereas for  $x = 0.005$  a broad band of CdTe is exhibited between 120 and 175  $\text{cm}^{-1}$ .

Figure 2 displays Raman spectra recorded at 80 K for nine  $\text{Cd}_{1-x}\text{Zn}_x\text{Te}$  alloy (with  $x = 0.005 - 0.5$ , and 1.0) samples over the frequency range 100 - 440  $\text{cm}^{-1}$ . This range covers both the first- and second-order phonon features. Because of the (100) surface of our samples, only LO phonons are allowed in the Raman measurement geometry. However, a few TO modes do appear in Fig. 2. These features are attributed to the alloy disordering and/or to the slight deviation from the true back scattering geometry. For the sample with the lowest  $x = 0.005$  value (c.f. Fig. (2i)) the CdTe-like mode  $\text{LO}_1$  and the ZnTe-like mode  $\text{LO}_2$  are mixed together. The  $\text{LO}_2$  mode appears as a weak shoulder at the high energy side of the  $\text{LO}_1$ . As  $x$  increases to 0.01 the  $\text{LO}_1$  and  $\text{LO}_2$  modes are clearly resolved (c.f. Fig. (2h)) and for  $x = 0.03$ , these modes are well separated (see Fig. 2g). However, in IR measurements the two types of phonon modes for these three samples are not clearly recognizable.

For the four samples with  $x < 0.1$  the second-order LO-phonons ( $2\text{LO}_1$ ,  $\text{LO}_1 + \text{LO}_2$  and  $2\text{LO}_2$ ) also appeared between 310 and 380  $\text{cm}^{-1}$ . Their intensities were comparable to the first-order features, due to the incoming resonance at the 488 nm excitation. For samples with  $x = 0.2 - 0.5$ , the  $\text{LO}_1$  becomes weak. However, the  $\text{LO}_2$  mode still possesses a clear band shape. The second-order phonon features are almost non-observable for these samples. For pure ZnTe, the first-order Raman active LO-phonon ( $\sim 210 \text{ cm}^{-1}$ ) is in excellent agreement with the inelastic neutron scattering data.<sup>6</sup> We also observed a second-order (2LO) phonon feature near 420  $\text{cm}^{-1}$ . Results of IR and Raman scattering experiments reported in Figs. 1 and 2 for the low Zn composition have demonstrated characteristics of the lattice dynamics of  $\text{Cd}_{1-x}\text{Zn}_x\text{Te}$  in terms of being a two-mode system.

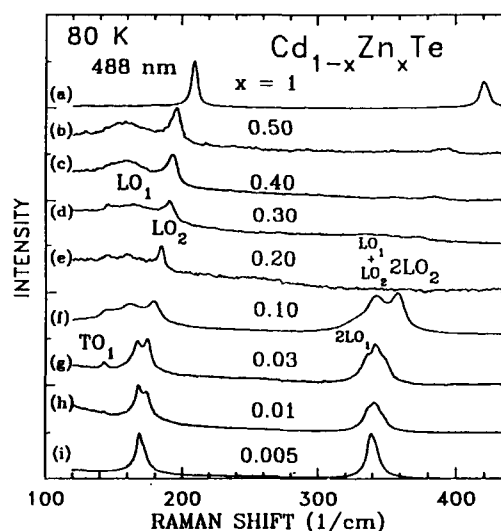


Fig. 2 Raman scattering spectra of bulk  $\text{Cd}_{1-x}\text{Zn}_x\text{Te}$  with compositions  $x$  of (a) 1, (b) 0.5, (c) 0.4, (d) 0.3, (e) 0.2, (f) 0.1, (g) 0.03, (h) 0.01, and (i) 0.005 measured at 80 K.



### III. THEORY

The dynamical properties of crystalline solids are generally considered in terms of the response of the medium to the excitation from an electromagnetic wave. The response may be elastic or inelastic and can be characterized either in terms of a dielectric function or in terms of a scattering cross section.<sup>3</sup> Here, we are concerned with the effects of defects on two typical response functions: (i) the dielectric susceptibility tensor  $\{\chi_{\alpha\beta}\}$ , and (ii) the scattering tensor  $\{i_{\alpha\gamma\beta\lambda}\}$ . In terms of these response functions the optical properties of  $\text{Cd}_{1-x}\text{Zn}_x\text{Te}$  alloys are studied using an average-t-matrix (ATM) formalism. The details of our theoretical formalism will appear elsewhere.<sup>4</sup>

The calculations of composition dependent phonon modes in  $\text{Cd}_{1-x}\text{Zn}_x\text{Te}$  were performed in two steps. In the first step, we used a bond-orbital model<sup>7</sup> and estimated the lattice distortions and there by force variation caused by Zn (Cd) defects in CdTe (ZnTe). In the second step, the frequencies of impurity vibrations were obtained by using an ATM formalism. Based on our comprehensive lattice dynamical study<sup>4</sup>, we have suggested that the two-mode pattern is typical of those ternary  $\text{A}_{1-x}\text{B}_x\text{C}$  compounds for which the optical bands of the two binary compounds (AC and BC) do not overlap and where, near the extremes of the composition range, the impurity modes of minority ions (e.g., AC : B and BC : A) lie well outside the reststrahlen peak of the host crystals. In spite of the fact that we do not start with a realistic theory of phonons for the host crystals, the disorder-activated transverse acoustic (DATA), longitudinal acoustic (DALA), and optical (DAO) structures in ternary compounds are very well described by the ATM. Comparison of these calculations for phonons in  $\text{Cd}_{1-x}\text{Zn}_x\text{Te}$  with the IR and Raman data reported in here has exhibited a two-component structure.

### IV. DISCUSSION AND CONCLUSIONS

By combining the infrared and Raman scattering methods, we have studied both the transverse and longitudinal optical phonons in a variety of bulk  $\text{Cd}_{1-x}\text{Zn}_x\text{Te}$  samples (with compositions over the range  $x = 0.005 - 0.5$ , and 1). The samples used in the present investigations were grown by the two-zone Bridgman method. Our experimental results confirm that, within a two-mode behavior, both the CdTe- and ZnTe-like TO mode frequencies increase with  $x$ , unlike any other II-VI ternary compounds with known phonon modes. The infrared spectra show signs of clustering behavior like that seen in MCT.<sup>1</sup> It is not clear to us why Olego *et al.*<sup>5</sup> have observed a constant CdTe-like TO frequency versus  $x$  for their  $\text{Cd}_{1-x}\text{Zn}_x\text{Te}$ /GaAs films. One possibility is that the stress from the lattice mismatch between film and substrate (10-14 %, depending on the  $x$  value) might have influenced the TO frequencies. The other possibility is that the TO modes are not sufficiently sharp in Raman data to give reliable frequencies.

In the ATM formalism, although the numerical simulation of the density of states for imperfect systems is complicated, it has provided a meaningful profile of the

impurity induced spectra both in the optical and in the acoustical phonon frequency region.<sup>4</sup> This profile of impurity induced features in the optical phonon region is found to be in very good agreement with the IR and Raman data. The polarization dependent Raman data in the acoustical phonon region is, however, not available for comparison with the present theoretical results. A study is now underway, using Raman scattering spectroscopy in different geometries for detailed polarization selection-rule analyses. The results of such a study will be reported elsewhere.

Based on an ATM calculation and detailed group theoretical analysis, we suggest that the gap mode in ZnTe: Cd system lies at a relatively higher frequency  $\sim 153 \text{ cm}^{-1}$  than reported in earlier studies.<sup>5</sup> This mode exhibits a triply degenerate  $F_2$  vibrational state and should be detected both by IR and Raman scattering spectroscopy in samples with low Cd composition.

**Acknowledgements:** The authors gratefully acknowledge useful discussions on the subject matter with Professor S. Perkowitz of Emory University, Atlanta, Georgia. Part of the work performed by DNT at the Wright Laboratories, Solid State Electronics Directorate, WP AFB, Ohio was supported by the National Research Council Associateship program.

#### References

1. See for example, R. Dornhaus and G. Nimitz, in *Narrow Gap Semiconductors*, edited by G. Höhler and E. A. Niekisch (Springer, Berlin 1983), pp. 119-300.
2. See for example, *Semiconductor Science and Technology* 6, 12C (1991) *Proceedings of the NATO Workshop on Narrow Gap Semiconductors*, Oslo, Norway June 25-27, 1991.
3. See for example, M. Bernasconi, in *Phonons: Theory and Experiment III*, edited by P. Brüesch (Springer, Heidelberg, 1987); D. W. Taylor, in *Optical Properties of Mixed Crystals*, edited by R. J. Elliott and I. P. Ipatova (North-Holland, 1988) p. 35.
4. D. N. Talwar, Z. C. Feng and P. Becla, *Phys. Rev. B* 15 (in press)
5. D. J. Olego, P. M. Raccach, and J. P. Faurie, *Phys. Rev. B* 33, 3819 (1986).
6. N. Vagelatos, D. Wehe and J. S. King, *J. Chem. Phys.* 60, 3613 (1974).
7. D. N. Talwar, K. S. Suh and C. S. Ting, *Phil. Mag.* B56, 593 (1987).

## OPTICAL CHARACTERIZATION OF AlInP/GaAs HETEROSTRUCTURES

F.G. JOHNSON\*, G.E. KOHNKE, AND G.W. WICKS  
The Institute of Optics, University of Rochester, Rochester, NY 14627

### ABSTRACT

A 45 period GaAs/Al<sub>0.54</sub>In<sub>0.46</sub>P superlattice was grown by molecular beam epitaxy using valved solid-sources to supply both the arsenic (As<sub>4</sub>) and the phosphorus (P<sub>2</sub>) group V fluxes. The room temperature optical transmission spectrum shows evidence of ground state excitons. Higher energy confined states are exhibited in photovoltage and photoreflectance spectra. Doublets corresponding to the m=1 through m=7 folded longitudinal-acoustic phonon modes are observed in the Raman spectrum. Analysis of these phonon doublets enables the structure of the superlattice to be determined. The interface roughness was found to be approximately 2 monolayers, and the layer thicknesses were determined to be 82 Å GaAs and 48 Å Al<sub>0.54</sub>In<sub>0.46</sub>P.

### INTRODUCTION

Group III compositional heterostructures such as Al<sub>x</sub>Ga<sub>1-x</sub>As/GaAs have been widely studied and used in a variety of device applications. Group V compositional heterostructures have attracted interest as well. Arsenide/phosphide (As/P) heterostructures have recently been used in aluminum-free semiconductor lasers [1] and high speed heterojunction bipolar transistors. [2] These As/P heterostructures have been successfully grown by metalorganic chemical vapor deposition (MOCVD) [3] and gas source molecular beam epitaxy (GSMBE) [4] using phosphine gas to supply the phosphorus flux.

It is somewhat more difficult to grow As/P heterostructures using conventional solid-source molecular beam epitaxy (MBE). There is significant leakage of both arsenic and phosphorus fluxes around the mechanical shutters which makes it difficult to abruptly switch between fluxes. This difficulty can be avoided by using two independent valved solid-sources to supply the As<sub>4</sub> and the P<sub>2</sub> fluxes. This new solid-source MBE technique allows the group V fluxes to be switched abruptly, and Ga<sub>0.5</sub>In<sub>0.5</sub>P/GaAs heterostructures have been grown with minimal group V intermixing between the layers. [5] The quality of the interfaces in these heterostructures is a critical parameter that will affect the performance of devices grown using this technique. The optical properties of an Al<sub>0.54</sub>In<sub>0.46</sub>P/GaAs superlattice are discussed in this paper and are used to determine the quality and width of the interfaces. Evidence of room temperature excitons is exhibited in the optical transmission spectrum, and confined states of higher energy are observed using photoreflectance [6] and photovoltage [7] spectroscopy techniques.

Raman spectroscopy is useful for characterizing semiconductor layers. Longitudinal-optic (LO) phonon energies can be used to determine ternary compositions. [8,9] The longitudinal-acoustic (LA) Raman spectrum is useful for analyzing the periodicity and roughness of the interfaces in a superlattice. The new periodicity of the superlattice causes the LA phonon dispersion curve to be folded into a smaller mini-Brillouin zone, resulting in the appearance of doublets in the Raman backscattering spectrum. The energies and intensities of these doublets can be related to the superlattice periodicity and the interface abruptness respectively. [10] Accurate models have been developed that determine the doublet peak intensities by considering both the acoustic and photoelastic modulations in the superlattice [11-13], but they rely on information about the complex photoelastic tensor for the superlattice layers. A simpler model exists that relates the functional form of the photoelastic modulation to the relative intensities of the LA

\*present address: Department of Electrical Engineering, Laboratory for Physical Sciences, University of Maryland, College Park, MD 20740.

phonon peaks. [10] This model has been used to characterize interfaces in GaAs/AlAs [14] and Si/Ge<sub>x</sub>Si<sub>1-x</sub> [15] superlattices and is used here to determine the interface widths and the well and barrier thicknesses present in an Al<sub>0.54</sub>In<sub>0.46</sub>P/GaAs superlattice.

## EXPERIMENTAL

A 5000 Å buffer layer of Ga<sub>0.5</sub>In<sub>0.5</sub>P was grown on a (001) GaAs substrate misoriented by 2° towards the [111]A direction. Next, a 45 period Al<sub>0.54</sub>In<sub>0.46</sub>P/GaAs superlattice was grown at 505° C by solid-source MBE using two valved solid-sources to supply the As<sub>4</sub> and P<sub>2</sub> fluxes. The growth rates and ternary composition were determined by measuring the period of the reflection high energy electron diffraction (RHEED) oscillations prior to the growth. The As<sub>4</sub> beam equivalent pressure (BEP) was  $1 \times 10^{-5}$  Torr corresponding to a Ga:As atomic flux ratio of 1:2. The P<sub>2</sub> BEP was  $2 \times 10^{-4}$  Torr corresponding to an (Al+In)/P atomic flux ratio of 1:80. The group V fluxes were switched automatically using the valved solid-sources and stepper-motor controlled needle valves. To allow for the finite pumping speed of the group V species from the growth chamber, growth interruptions of 2 sec and 6 sec were inserted at the Al<sub>0.54</sub>In<sub>0.46</sub>P on GaAs and GaAs on Al<sub>0.54</sub>In<sub>0.46</sub>P interfaces respectively.

Off-resonance Raman spectra were acquired at room temperature in the backscattering geometry using  $5 \times 10^4$  W/cm<sup>2</sup> from the 5145 Å line of an argon laser. A 1 m double spectrometer with a system resolution of 2 cm<sup>-1</sup> was used to analyze the LO and LA phonon spectra. The photoreflectance spectrum was recorded using a 4580 Å pump beam with a modulation frequency of 400 Hz and a probe beam from a tungsten light source dispersed through a prism-grating monochromator. For transmission measurements, the GaAs substrate was selectively etched (5 H<sub>2</sub>SO<sub>4</sub> : 1 H<sub>2</sub>O<sub>2</sub> : 1 H<sub>2</sub>O) leaving the buffer and superlattice layers. A beam of collimated white light was then passed through the sample and analyzed by a 1 m double spectrometer. For the photovoltage measurement, the spectrum was obtained using an electrochemical capacitance-voltage profiler.

## RESULTS AND DISCUSSION

The superlattice structure was characterized using double-crystal x-ray diffraction. Peaks are observed in the (004) symmetric rocking curve that correspond to the Ga<sub>0.5</sub>In<sub>0.5</sub>P buffer layer and the superlattice  $n = 0$  average composition and  $n = \pm 1, \pm 2, \pm 3$ , and  $\pm 4$  satellite peaks. The superlattice periodicity can be calculated from the splitting of the satellite peaks and is equal to 130 Å. The inset (lower curve) of figure 1 shows the optical transmission spectrum from the superlattice. The spectrum exhibits  $n = 1$  confined electron to heavy-hole and light-hole transitions. The appearance of absorption peaks associated with each transition provides evidence of excitons in the GaAs wells. The upper curve shown in figure 1 is the photovoltage spectrum. The features labeled by the arrows coincide with the positions of the  $n = 1, 2$ , and 3 confined electron to heavy-hole transitions. The photoreflectance spectrum shown in figure 2 has features corresponding to the  $n = 1, 2$ , and 3 electron to heavy-hole and light-hole transitions as well.

There is some residual phosphorus incorporation in the GaAs well layers due to the presence of a background pressure of phosphorus in the growth chamber. Raman spectroscopy was used to characterize the level of phosphorus incorporation in the GaAs wells. The energy of the GaAs-like LO phonon peak in the Raman spectrum was shifted from the value expected for a GaAs binary (292 cm<sup>-1</sup>) to a lower energy (289 cm<sup>-1</sup>). By comparing this peak shift to the shift seen in GaAs<sub>1-x</sub>P<sub>x</sub> calibration layers, the phosphorus incorporation was found to be  $x \approx 0.02 - 0.03$ . The well width was then determined to be approximately 82 Å by using a finite well model to fit the  $n = 1$  electron to heavy-hole transition energy seen in the transmission spectrum. The well thickness and superlattice periodicity are consistent with the thicknesses expected from the growth rates.

The Raman spectrum of the superlattice's LA phonons is shown in figure 3. Folded doublets of order  $m = \pm 1, \pm 2, \pm 3, \pm 4, -5, \pm 6$ , and  $-7$  can be seen in the spectrum along with a broad peak around 80 cm<sup>-1</sup> associated with zone edge disorder-activated transverse acoustic

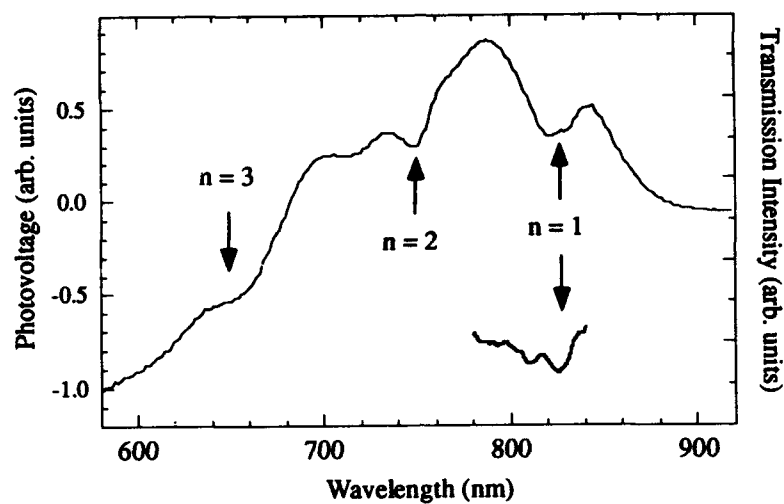


Figure 1. Photovoltage spectrum (upper curve) showing  $n = 1, 2$ , and  $3$  electron to heavy-hole transitions. Transmission spectrum (lower curve) showing  $n = 1$  electron to light and heavy-hole exciton transitions.

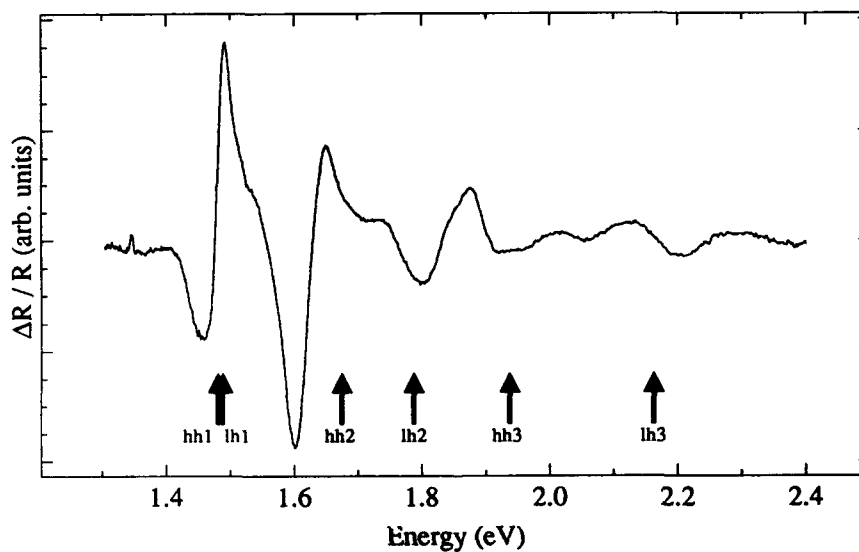


Figure 2. Photoreflectance spectrum showing features associated with the  $n = 1, 2$ , and  $3$  confined electron to light and heavy-hole transitions.

(DATA) phonons. The visibility of a large number of folded LA phonon peaks in the Raman spectrum enables an analysis of the interface roughness. Using the photoelastic model, it can be shown that the intensities of the highest order folded LA phonon doublets are sensitive to the abruptness of the interfaces and rapidly decrease with increasing interface roughness.

Using the photoelastic model [10], the intensities of the folded LA phonon peaks of order  $m$  can be related to the superlattice composition profile by

$$I_m \propto \omega_m (n_m + 1) |P_m|^2 \quad (1)$$

where  $\omega_m$  is the phonon frequency,  $n_m$  is the Bose factor, and  $P_m$  is the Fourier coefficient obtained from the transform of the photoelastic profile, which is proportional to the composition profile of the superlattice. The interface roughness present in the superlattice was determined by calculating the values of the Fourier coefficients for superlattices with graded interfaces and comparing these values to the experimental values from the  $\text{Al}_{0.54}\text{In}_{0.46}\text{P}/\text{GaAs}$  superlattice sample. The relative intensities of the folded LA phonon peaks were calculated for superlattices with interface widths of 0, 1, 2, and 4 monolayers. The calculated ratios  $I_m / I_1$  are plotted in figure 4: the top solid line is for a superlattice with abrupt interfaces, the upper dashed line is for 1 monolayer of interface roughness, the lower dashed line is for 2 monolayers of interface roughness, and the bottom solid line is for 4 monolayers of interface roughness. The experimental values of  $I_m / I_1$  are found from figure 3 using the lower energy peak of each doublet. It can be seen in figure 4 that the intensities of the higher order LA phonon peaks rapidly diminish with increasing interface roughness. By comparing the experimental data to the calculated results, we assign an interface roughness of approximately 2 monolayers to the superlattice.

The relative intensities of the lower order folded LA phonon peaks provide information on the structure of superlattice. The composition profile of the superlattice can be reconstructed from the values of the Fourier coefficients  $(P_m / P_1)^2$  found from the intensities of the 7 folded LA phonon peaks in the Raman spectrum. The period of the superlattice was already found using x-ray diffraction and is equal to 130 Å. If we assume that the composition profile of the superlattice is a symmetric function about the center of the GaAs well with a periodicity of 130 Å, the profile can be represented by a Fourier cosine series with 7 terms. The relative magnitudes of each term in the series expansion can be found using equation (1). The sign of each term was determined by choosing the series that best fit a square wave in the regions away from the interfaces. The composition profile resulting from the summation of the terms in the Fourier cosine expansion is shown in figure 5. The layer thicknesses in the reconstructed composition profile are 82 Å and 48 Å and are consistent with the well width that was found by fitting the  $n = 1$  transition energy with a finite well model. The width of the interfaces in figure 5 is approximately 2 monolayers and is consistent with the fit from figure 4.

## CONCLUSION

Solid-source MBE was used successfully to grow a  $\text{GaAs}/\text{Al}_{0.54}\text{In}_{0.46}\text{P}$  superlattice with abrupt interfaces and confined exciton states. Raman spectroscopy was particularly useful in characterizing the superlattice structure. The relative intensities of the first 7 folded LA phonon doublets were used to calculate the interface roughness (2 monolayers) and the layer thicknesses (82 Å GaAs and 48 Å  $\text{Al}_{0.54}\text{In}_{0.46}\text{P}$ ) of the superlattice.

## ACKNOWLEDGEMENTS

The authors would like to thank M.W. Koch for assistance with the MBE growths. This work was supported in part by the New York Center for Advanced Optical Technology.

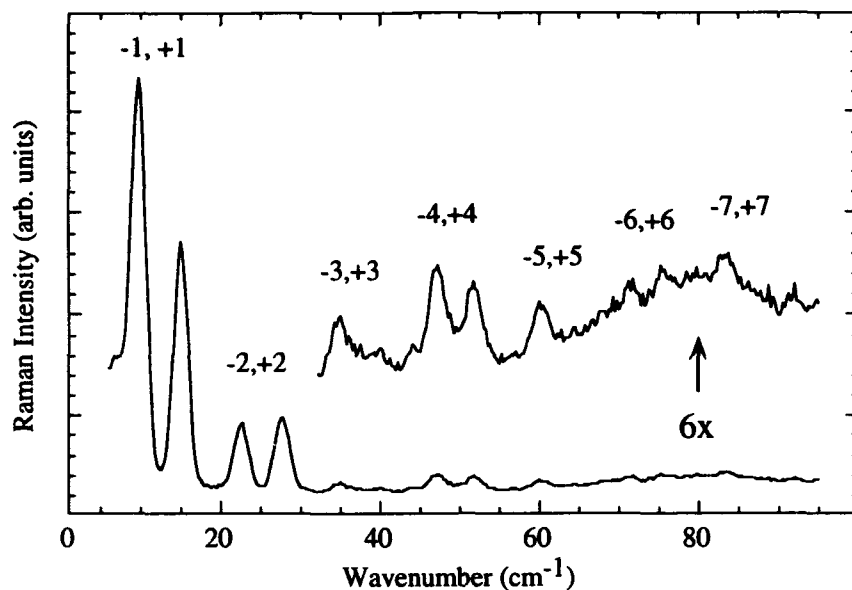


**Figure 3.** Raman backscattering spectrum (295 K) of the superlattice showing the  $m = \pm 1, \pm 2, \pm 3, \pm 4, -5, \pm 6$ , and  $-7$  folded longitudinal-acoustic phonons.

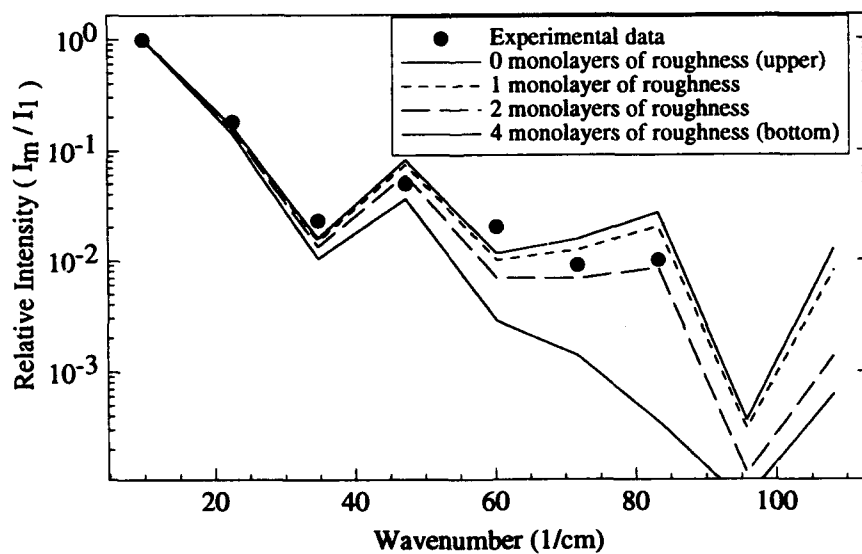


**Figure 4.** Plot of the relative intensities ( $I_m / I_1$ ) of the lower folded LA phonon peaks. Solid circles represent experimental data. The lines represent calculated intensities for superlattices with 0, 1, 2, and 4 monolayers of interface roughness.

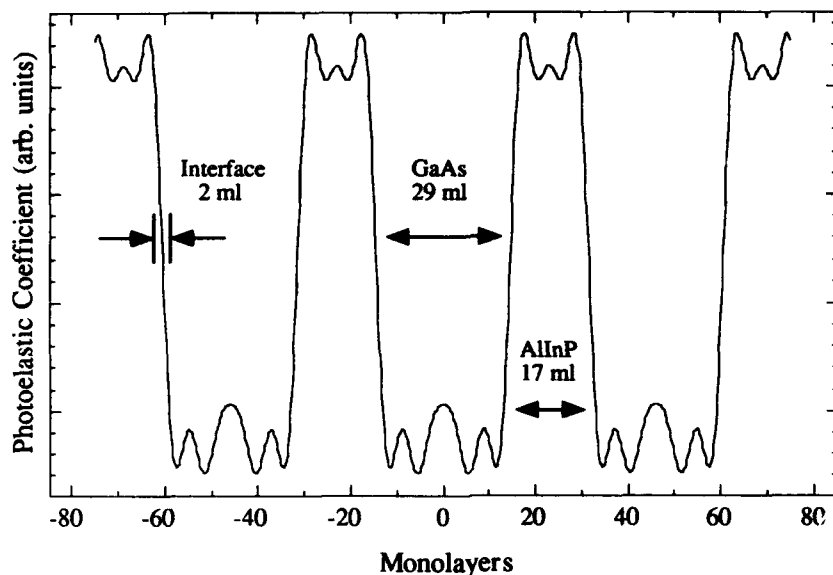


Figure 5. Cosine series representation (first 7 terms) of the superlattice using Fourier coefficients found from the LA peak intensities in the Raman spectrum.

#### REFERENCES

1. G. Zhang, J. Nappi, A. Ovtchinnikov, and H. Asonen, *Electron. Lett.* **29**, 429 (1993).
2. H. Leier, A. Marten, K.H. Bachem, W. Platschen, and P. Tasker, *Electron. Lett.* **29**, 868 (1993).
3. X. He and M. Razeghi, *Appl. Phys. Lett.* **62**, 618 (1993).
4. H.Y. Lee, M.J. Hafich, G.Y. Robinson, K. Mahalingham, and N. Otsuka, *J. Cryst. Growth* **111**, 525 (1991).
5. F.G. Johnson, G.W. Wicks, R.E. Viturro, and R. LaForce, *Mater. Res. Soc. Proc.* **281**, 49 (1993).
6. F.H. Pollak and O.J. Glembocki, *Proc. SPIE* **946**, 2 (1988).
7. P. Blood, *Semicond. Sci. Technol.* **1**, 7 (1986).
8. R. Tsu, H. Kawamura, and L. Esaki, in *Proceedings of the 11th International Conference on the Physics of Semiconductors*, edited by M. Miasek (P.W.N. Polish Scientific, Warsaw, 1972), Vol. 2, pp. 1135-1141.
9. G.W. Wicks, *Proc. SPIE* **1037**, 30 (1988).
10. C. Colvard, T.A. Gant, M.V. Klein, R. Merlin, R. Fischer, H. Morkoc, and A.C. Gossard, *Phys. Rev. B* **31**, 2080 (1985).
11. B. Jusserand, D. Paquet, F. Mollot, F. Alexandre, and G. Le Roux, *Phys. Rev. B* **35**, 2808 (1987).
12. J. He, B. Djafari-Rouhani, and J. Sapriel, *Phys. Rev. B* **37**, 4086 (1988).
13. H. Kushibe, M. Nakayama, and M. Yokota, *Phys. Rev. B* **47**, 9566 (1993).
14. B. Jusserand, F. Alexandre, D. Paquet, and G. Le Roux, *Appl. Phys. Lett.* **47**, 301 (1985).
15. D.C. Houghton, D.J. Lockwood, M.W.C. Dharma-Wardana, E.W. Fenton, J.M. Baribeau, and M.W. Denhoff, *J. Cryst. Growth* **81**, 434 (1987).



# CHARACTERIZATION OF INTERFACIAL STRUCTURE OF InGaAs/InP SHORT PERIOD SUPERLATTICES BY RAMAN SCATTERING AND HIGH RESOLUTION X-RAY DIFFRACTION

TERUO MOZUME

Central Research Laboratory, Hitachi Ltd., Kokubunji, Tokyo 185, Japan

## ABSTRACT

The x-ray diffraction (XRD) of InGaAs/InP short-period superlattices (SPSL's) grown on (001)InP substrates by gas source molecular beam epitaxy (GSMBE) and by gas source migration enhanced epitaxy (GSME) shows that the GSMBE grown SPSL is strain free, and that GSME grown SPSL's with InGa-P and In-As heterointerfaces have strain-induced zeroth-order satellite peak shift consistent with that in simulation results for the InGaAs/InP SPSL with one monolayer of InGaP and InAs inserted in each interface. Partial destruction of the long-range order is confirmed by the observation of the extra diffraction peak in GSMBE grown SPSL and by weak intensity of satellite peaks and nonuniform spacing between satellite peaks in GSME grown SPSL's. Raman scattering shows that the strain is accommodated in the interface layer in GSME grown samples. A confinement model without interface disorder fits the GaAs LO phonon very well. These results indicate that the local atomic arrangements are tailored by GSME, but that long range-order is impaired by the misfit dislocations in GSME grown SPSL's and by the exchange between As to P at the interfaces in GSMBE grown SPSL.

## INTRODUCTION

InGaAs/InP(001) heterostructures are important for microwave devices as well as for optoelectronic devices, and the performance of these devices is strongly influenced by the microscopic structure of the heterointerfaces. Atomically abrupt interfaces are more difficult to create in InGaAs/InP than in AlGaAs/GaAs<sup>1)</sup>, primarily because residual group V material is incorporated into the succeeding layer containing different group V species<sup>2)</sup>.

Several groups have recently attempted to make atomically abrupt heterointerfaces in material systems containing As and P atoms, such as InGaAs/InP and (Al)GaInP/GaAs, by molecular beam epitaxy (MBE) and its variants: gas source molecular beam epitaxy (GSMBE)<sup>3,4)</sup>, chemical beam epitaxy (CBE)<sup>5)</sup>, and organometallic vapor phase epitaxy (OMVPE)<sup>3,4)</sup>. They have tried to reduce residual group V sources and interchange between As and P at each interface by interrupting growth and using a special switching sequence for source supply. Migration enhanced epitaxy (MEE)<sup>6)</sup> is effective for making atomically controlled heterointerfaces, since structures can be grown at low temperatures and with an alternating supply of group III and group V atoms. High-quality InGaAs/InP short-period superlattices have been grown by matching the surface atomic number of group III and group V species to the surface site number at each interface<sup>4, 7-9)</sup>.

The structure near the interfaces of InGaAs/InP short-period superlattices (SPSL's) has been investigated by using synchrotron radiation to study the P-K edge and Ga-K edge X-ray absorption fine structure (XAFS), and by highly sensitive Raman scattering spectroscopy<sup>7-9)</sup>. These studies suggest the atomic configuration at the interface can be tailored by GSME.

This paper reports Raman scattering and x-ray diffraction investigations of the structure of InGaAs/InP short-period superlattices and interfaces grown by GSMBE and GSME.

## EXPERIMENTAL

Samples were grown in a GSMBE system under growth conditions reported in Ref. 8. Elemental Ga and In were used for the group-III growth species derived from effusion cells, AsH<sub>3</sub> and PH<sub>3</sub> were decomposed in a low-pressure thermal cracker cell maintained at 900 °C. To make the heterointerface abrupt, an effusion cell shutter and gas switching valves were used for switching between AsH<sub>3</sub> and PH<sub>3</sub>. In<sub>0.53</sub>Ga<sub>0.47</sub>As/InP short-period superlattices (Fig.1) were grown on (001)InP substrates by GSMBE and GSMEE. (a) is GSMBE grown ((InGaAs)<sub>2</sub>(InP)<sub>2</sub>)<sub>120</sub> structure whereas (b) and (c) are GSMEE grown ((InGaAs)<sub>2.5</sub>(InP)<sub>2.5</sub>)<sub>80</sub> structures with InGa-P and In-As interfaces. The InP growth rate and InGaAs composition were determined from reflection high energy electron diffraction (RHEED) oscillations, which have been used to optimize MEE conditions for InP, InGaAs, and InP/InGaAs SPSSL's. Substrate temperatures determined by an optical pyrometer were 500 °C for GSMBE and 410 °C for GSMEE.

X-ray diffraction measurements were performed using a powder  $\theta$ -2 $\theta$  diffractometer and a high resolution four-crystal diffractometer (Philips Materials Research Diffractometer). Rocking curves were simulated using a computer program developed by P. F. Fewster at Philips and based on the solution of the Takagi-Taupen equations of dynamical diffraction theory<sup>10</sup>.

Raman scattering was measured at room temperature and in the backscattering configuration along the (001) direction. The scattering geometries used were the  $z(x,y)z$  and  $z(x,x)z$  configurations. The triple-stage spectrograph (Dilor, model XY), consisting of a subtractive double monochromator with a focal length of 500 mm for the filter stage and a single polychromator with a focal length of 500 mm for multichannel detection, was used. Cooled-type charge-coupled devices (Photometrics, model TK512) were used for multichannel detection. A double monochromator with a focal length of 1000 mm and a usual photon counting system was also used. A He-Ne laser and an Ar<sup>+</sup> laser were used as excitation sources.

## RESULTS AND DISCUSSION

### X-ray diffraction

XRD was used to determine the structural quality of the SPSSL's and parameters such as the period and strain of the layers. The superlattice period  $\Lambda$  was averaged over the position of the satellite peaks of order  $n$  according to the equation:<sup>11)</sup>

$$\Lambda = (n_i - n_j) \lambda / 2(\sin \theta_{n_i} - \sin \theta_{n_j}), \quad (1)$$

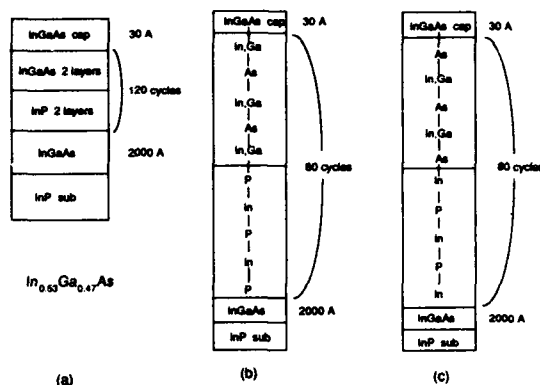


Fig. 1. Sample structures.  
(a) GSMBE grown ((InGaAs)<sub>2</sub>(InP)<sub>2</sub>)<sub>120</sub> superlattice  
(b) GSMEE grown ((InGaAs)<sub>2.5</sub>(InP)<sub>2.5</sub>)<sub>80</sub> superlattice with InGa-P interfaces  
(c) GSMEE grown ((InGaAs)<sub>2.5</sub>(InP)<sub>2.5</sub>)<sub>80</sub> superlattice with In-As interfaces

where  $n_i$  are the diffraction orders and  $\theta_{n_i}$  are the diffraction angles for  $n_i$ -order diffraction.

Figure 2(a) shows the x-ray diffraction patterns around the InP (002) diffraction for the GSMBE grown SPSL. No separation between the zeroth-order peak for the SPSL and that for the InP substrate is observed. A 12.2-Å superlattice period is inferred from the spacing between the  $\pm 1$ st satellites, and fairly in good agreement with the calculated result for the  $(\text{InGaAs})_2(\text{InP})_2$  SPSL. As seen from the simulated rocking curves for the  $(\text{InGaAs})_2(\text{InP})_2$  SPSL ( Fig. 2(b) ), the 2nd-order satellite peaks should not appear. The diffraction peak indicated by an arrow in Figure 2(a) is probably caused by the interface roughness and composition variation due to the interchange of As and P, which interchange extends over several monolayers<sup>5</sup>). Figure 3(a) shows the x-ray diffraction pattern around the InP (002) diffraction for the GSMEE grown SPSL with In-As heterointerfaces. Separation of the zeroth-order superlattice satellite peak from the InP substrate diffraction is observed and is consistent with the simulated high resolution x-ray diffraction (HRXRD) spectrum of the  $(\text{InGaAs})_2(\text{InAs})(\text{InP})_2$  structure ( Fig. 3(b) ). In the HRXRD spectrum of the GSMEE grown SPSL with InGa-P heterointerfaces, the zeroth-order satellite peak is shifted from the InP (002) peak in a manner consistent with the simulated result. As shown in Figure 3(a), the intensity of satellite peaks ( -1st to 2nd order) is weak, and the separation between each of the satellite peaks is not uniform. Because the amount of residual As and P atoms on the interface layer is reduced by optimizing the MEE sequence<sup>8</sup>), the interface roughness and composition variation due to the interchange of As and P will not occur in GSMEE grown SPSL's. And the tailored interface atomic configuration is also suggested by the P-K edge and Ga-K edge x-ray absorption fine structure analysis<sup>8,9</sup>). This nonuniformity of the satellite peak's separation ( Fig. 2(b) ) is therefore probably caused by dislocation due to the lattice mismatch strain. The superlattice period calculated from 2nd-order and -1st-order peaks using equation (1) is 14.7 Å and is in fairly good agreement with the period calculated for  $(\text{InGaAs})_2(\text{InAs})(\text{InP})_2$  despite the expected lattice mismatch. This suggests that coherently grown region is limited and long-range order is impaired by the lattice mismatch between the InAs layer and the InP and InGaAs layers.

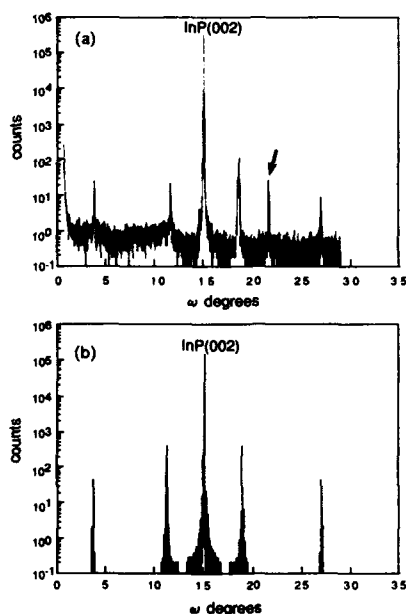


Fig. 2 (a) Experimental and (b) simulated x-ray rocking curves of  $(\text{InGaAs})_{2.0}(\text{InP})_{2.0}$  120 short-period superlattice

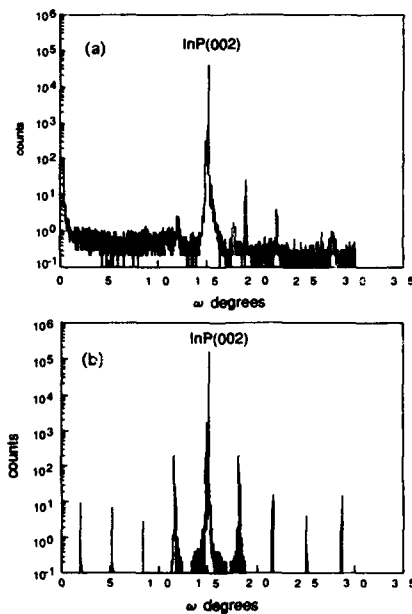


Fig. 3 (a) Experimental and (b) simulated x-ray rocking curves of  $(\text{InGaAs})_{2.5}(\text{InP})_{2.5}$  30 short-period superlattice with In-As heterointerfaces

## Raman studies

The frequencies of the main optic phonons of a superlattice can be determined both from the confinement and from the strain in the individual layers. If we use the linear chain model and assume abrupt interfaces and perfect confinement as standing waves, we can roughly describe the modes confined in the phonon potential well by the bulk energy dispersion of phonon modes corresponding to wave vectors:  $k_m = (\pi/(n+1)a) m$ ,  $m=1, \dots, n$  (2)

Here  $a$  is the lattice constant,  $n$  is the number of monolayers in a single slab, and  $m$  is the order of the confined LO phonon. Since the optical phonons in III-V compounds have negative dispersions, the confinement effect results in a red-shift of the superlattice peaks with respect to the bulk frequency. According to Ref. 13, the strain-induced shift of the longitudinal optical (LO) frequencies ( $\Delta\omega$ ) is described by:

$$\Delta\omega/\omega = (K_{11}/2)\epsilon_{zz} + (K_{12}/2)(\epsilon_{xx} + \epsilon_{yy}), \quad (3)$$

where  $K_{ij}$  are anharmonic spring constants and  $\epsilon_{xx} = \epsilon_{yy}$  and  $\epsilon_{zz}$  are the components of the strain tensor in the individual layers. The components  $\epsilon_{ii}$  are calculated using the room-temperature lattice parameters and considering that the mismatch strain is confined to each layer:

$$\epsilon_{xx} = \epsilon_{yy} = \Delta a/a \quad (4)$$

$$\epsilon_{zz} = -(2C_{12}/C_{11})\epsilon_{xx}, \quad (5)$$

where  $C_{11}$  and  $C_{12}$  are the elastic compliance constant. The parameters used are listed in Table I.

Figure 4 shows the lower-energy Raman band (200-290  $\text{cm}^{-1}$ ) measured using an  $\text{Ar}^+$  laser as the excitation source. As in Ref. 14, we assign this band to InGaAs optical vibrations. No peak shifts of the GaAs-like LO phonon line (264  $\text{cm}^{-1}$ ) is observed between samples. From the bulk dispersion of GaAs<sup>15-17</sup>) and InAs<sup>18,19</sup>), the confinement shifts of 2 and 3 monolayer GaAs slab are -5  $\text{cm}^{-1}$  and -3  $\text{cm}^{-1}$ , and those of 1, 2, and 3 monolayer InAs slab are -10  $\text{cm}^{-1}$ , -5  $\text{cm}^{-1}$  and -3  $\text{cm}^{-1}$ . In GSMBE grown SPSL, no strain is observed in the HRXRD spectrum. Therefore the observed red-shifts of GaAs-like LO phonon (-6  $\text{cm}^{-1}$ ) and InAs-like LO phonon (-2  $\text{cm}^{-1}$ ) are

Table I Parameters used to calculate Raman shifts

|   |                 | InP    | InAs   | GaAs   | GaP    |
|---|-----------------|--------|--------|--------|--------|
| lattice constant (Å)  |                 | 5.8687 | 6.0583 | 5.6533 | 5.4512 |
| anharmonic spring constant  | $K_{11}$ for LO | -1.87  | -1.753 | -2.0   | -1.48  |
|   | $K_{12}$ for LO | -2.87  | -2.323 | -2.7   | -2.51  |
|   | $K_{11}$ for TO | -2.57  | -2.053 | -2.57  | -1.50  |
|   | $K_{12}$ for TO | -2.87  | -2.623 | -2.87  | -2.10  |
| elastic compliance constant ( $\times 10^{-11}$ dyn/cm <sup>2</sup> ) | $C_{11}$        | 10.22  | 8.329  | 11.88  | 14.120 |
|   | $C_{12}$        | 5.76   | 4.526  | 5.38   | 6.253  |
|   | $C_{44}$        | 4.60   | 3.959  | 5.94   | 7.047  |

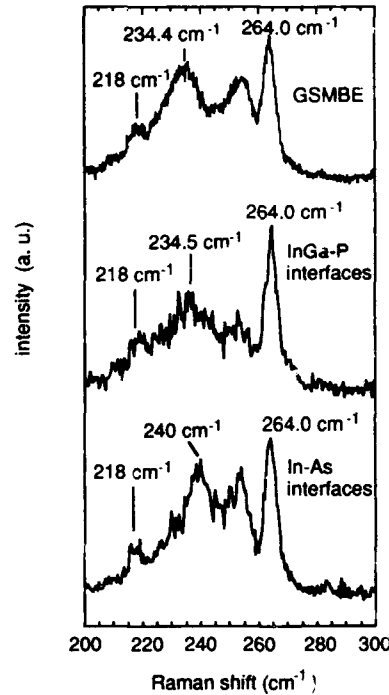


Fig. 4 Raman scattering spectra of InGaAs/InP SPSL's grown by GSMBE and GSMEE using  $\text{Ar}^+$  laser as the excitation source

attributed to confinement shifts. These results imply the interface broadening in GSMBE grown SPSL is less than one monolayer. Suppose the strain is accommodated by the interface InGaP and InAs monolayer in GSMEE grown samples, the red-shift of GaAs-like LO phonon is well explained by confinement shift. The red-shift of about  $2\text{ cm}^{-1}$  observed in InAs-like LO phonon of GSMEE grown SPSL with InGaP heterointerfaces is fairly in good agreement with the theory. The strain induced blue-shift of the interface InAs LO phonon in GSMEE grown SPSL with InAs interface is about  $10\text{ cm}^{-1}$ , and the confinement shift for InAs interface layer is  $-10\text{ cm}^{-1}$ . Therefore the total shift is zero. InAs LO phonon peak observed in InAs interface SPSL is very close to that of InAs bulk ( $238.6\text{ cm}^{-1}$ ). The peaks observed near  $218\text{ cm}^{-1}$  are probably due to InAs TO phonons. The InAs TO phonon band is flat, so the InAs confined TO phonon lines may differ a little between samples. From the polarization measurements, peaks near  $254\text{ cm}^{-1}$  observed in GSMBE grown SPSL and GSMEE grown SPSL with InAs hetero interfaces are not the TO phonons. The origin of the peaks around  $254\text{ cm}^{-1}$  observed in GSMBE SPSL and GSMEE SPSL with In-As heterointerfaces is under investigation.

Figure 5 shows the higher-energy Raman band measured using a He-Ne laser as the excitation source in the  $z(x,y)\bar{z}$  configuration at room temperature. This band is assigned to In(Ga)P vibration<sup>20</sup>. In the GSMBE grown sample and the GSMEE grown SPSL with InGa-P interfaces, strong first order GaP LO phonon lines ( $348$  and  $350\text{ cm}^{-1}$ ) and InP LO phonon line ( $336$  and  $342\text{ cm}^{-1}$ ) are observed, despite the low concentration of Ga-P bonds. This is consistent with the report of a GaP-type vibration that is as sharp and as intense as that for a InP LO mode with only  $1.5\%$  of the Ga found in InGaP<sup>20</sup>. Soni et al.<sup>21</sup> reported that in Raman spectra for indium-and-phosphorus rich quaternary InGaAsP samples, the GaP LO phonon lines are sharp and similar to the InP LO phonon lines. No clear GaP line, however, is observed in the SPSL with In-As type interfaces. Well-defined interfaces are therefore formed by GSMEE.

#### 4. SUMMARY

InGaAs/InP short-period superlattices (SPSL's) grown by gas source molecular beam epitaxy (GSMBE) and by gas source migration enhanced epitaxy (GSMEE) on (001)InP substrates were investigated by x-ray diffraction (XRD) and Raman scattering. XRD shows that the GSMBE grown SPSL is strain relaxed, whereas SPSL's with InGa-P and In-As heterointerfaces grown by GSMEE have strain-induced zeroth-order satellite peak shift. An extra diffraction peak is observed in the GSMBE grown SPSL which should not appear from the simulation. The XRD results of GSMEE grown SPSL's are consistent with the simulated results for the InGaAs/InP SPSL with one monolayer of InGaP or InAs inserted in each interface. Raman scattering shows that the strain is accommodated in the interface layer in GSMEE grown samples. A confinement

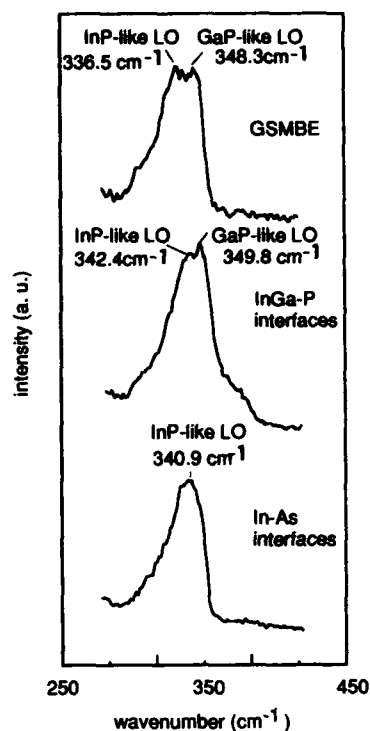


Fig. 5 Raman spectra of InGaAs/InP SPSL's grown by GSMBE and GSMEE using He-Ne laser as the excitation source

model without interface disorder fits the GaAs LO phonon very well. Clear Ga-P LO phonon peaks are seen in a GSMBE grown SPSP and in a GSMEE grown SPSP with InGa-P heterointerfaces. These results indicate that the local atomic arrangements are tailored by GSMEE, whereas the long-range order is impaired by the misfit dislocations in GSMEE grown SPSP's and by As-P exchange at the interfaces in GSMBE grown SPSP.

## ACKNOWLEDGEMENTS

I am grateful to H. Kashima, and K. Hosomi for growing SPSP's, to I. Yamaji and A. Iwahashi of Japan Philips for high-resolution X-ray diffraction measurements, to T. Ryan for valuable discussion of the XRD data, to K. Ogata and T. Tamura for x-ray diffraction measurements, to G. Araki, M. Fujishima, and S. Muramatsu for their valuable discussion on Raman analysis, and to H. Sato for her assistance.

## REFERENCES

1. T. Y. Wang, E. H. Reihlen, H. R. Jen, and G. B. Stringfellow, *J. Appl. Phys.* **66**, 5376 (1989).
2. P. J. Skevington, M. A. G. Halliwell, M. H. Lyons, S. J. Amin, M. A. Z. Rajman-Greene, and G. J. Davis, *J. Cryst. Growth* **120**, 328 (1992).
3. T. Anan, S. Sugou, K. Nishi, and T. Ichihashi, *Appl. Phys. Lett.* **63**, 1047 (1993).
4. N. Takeyasu, H. Asahi, S. J. Yu, K. Asami, T. Kaneko and S. Gonda, *J. Cryst. Growth* **111**, 502 (1991).
5. A. Antolini, P. J. Bradley, C. Cacciatore, d. campi, L. Gastaldi, F. Genova, M. Iori, C. Lambaerti, C. Papuzza, and C. Rigo, *J. Electron. Mater.* **21**, 233 (1992).
6. Y. Horikoshi, M. Kawashima, and H. Yamaguchi, *Jpn. J. Appl. Phys.* **25**, L868 (1986).
7. K. Ogata, K. Suenaga, A. Nakano, and T. Mozume, *Mat. Res. Soc. Symp. Proc.* **281**, 109 (1993).
8. T. Mozume, H. Kashima, K. Hosomi, K. Ogata, K. Suenaga, and A. Nakano, to be published in *Appl. Surf. Sci.*.
9. T. Mozume, H. Kashima, K. Hosomi, K. Ogata, K. Suenaga, and A. Nakano, to be published in *J. Cryst. Growth*.
10. P. F. Fewster and C. J. Curling, *J. Appl. Phys.* **67**, 4154 (1987).
11. P. F. Fewster, *Philips J. Res.* **41**, 268 (1986).
12. B. Jusserand, D. Paquet and A. Regreny, *Phys. Rev.* **B30**, 6245 (1984).
13. F. Cerderia, A. Pinczuck, J. C. Bean, B. Battlog, and B. A. Wilson, *Appl. Phys. Lett.* **45**, 1138 (1984).
14. T. P. Pearsall, R. Carles, and J. C. Portal, *Appl. Phys. Lett.* **42**, 436 (1983).
15. E. Molinari, S. Baroni, P. Giannozzi, and S. de Gironcoli, *Phys. Rev.* **B45**, 4280 (1992).
16. B. Samson, S. R. P. Smith, T. Dumelow, K. J. Moore, and K. Woodbridge, *Superlatt Microstr.*, **11**, 403 (1992).
17. S. Baroni, P. Giannozzi, and E. Molinari, *Phys. Rev.* **B41**, 3870 (1990).
18. R. Carles, N. Saint-Cricq, J. B. Renucci, M. A. Renucci, *Phys. Rev.* **B22** 4804 (1980).
19. H. Borchers and K. Kunc, *J. Phys.* **C11**, 4145 (1978).
20. T. Inoshita, *J. Appl. Phys.* **56**, 2056 (1984).
21. R. K. Soni, S. C. Abbi, K. P. Jain, M. Balkanski, S. Slompkes and J. L. Benchimol, *J. Appl. Phys.* **59**, 2184 (1986).

---

PART V

---

**In-Situ Diagnostics**

## IN-PROCESS DIAGNOSTIC SYSTEM FOR SEMICONDUCTOR MATERIALS USING UHV WAFER TRANSFER CHAMBER

F. Uchida, M. Matsui, H. Kakibayashi, M. Kouguchi, A. Mutoh, H. Nagano\*  
Hitachi Central Research Laboratory, Kokubunji, Tokyo 183.  
\*Hitachi Advanced Research Laboratory, Hatoyama, Saitama 350-03

### ABSTRACT

We have developed a novel stand-alone diagnostic system that can analyze a semiconductor wafer surface in each process without introducing contamination. This allows us to analyze the relationship between chemical conditions and device properties.

A UHV (Ultra High Vacuum) wafer transfer chamber is used between the measuring apparatus and the semiconductor processes. The chamber vacuum system, which consists of a battery driven ion pump and a liquid N<sub>2</sub> shroud, achieves a pressure of  $2 \times 10^{-8}$  Pa (corresponding to about 100 min. until one monolayer of contamination has been adsorbed).

Wafer transfer lines have been constructed between semiconductor vacuum processes, CVD (Chemical Vapor Deposition) and measuring instruments, ESCA (Electron Spectroscopy for Chemical Analysis) and TEM (Transmission Electron Microscope). Our results from ESCA and TEM showed measurements that carbon contamination and oxidation was suppressed.

### 1. INTRODUCTION

In the field of microelectronics manufacturing, adhesion of contamination and disturbance of crystal structure during processing are severe problems, because they cause poor device performances, that is, current-voltage characteristics. The continuing improvement of device performance demands new materials and processes. Therefore process optimization based on the precise analysis of the contamination and crystal defects can provide increased reliability in manufacturing.

In present ULSI manufacturing, however, semiconductor devices are fabricated by transferring the wafer among various types of equipment in the clean room. Therefore the wafers are subject to the atmospheric environment during transfer. Figure 1 shows the relation between the deposition time for monolayer and partial pressure of reactive impurities. At unity sticking coefficient, atmospheric conditions correspond to  $10^9$  sec per monolayer deposition of reactive impurities. So, it is difficult to separate the infinitesimal contamination and defects based on process disturbance or those based on wafer transfer. These problems can be resolved by directly connecting the process equipment and analysis equipment. However, this is not a realistic approach as it increases the need for extra analysis equipment and facilities. We have therefore developed UHV wafer transfer chambers which can be easily attached and detached from the



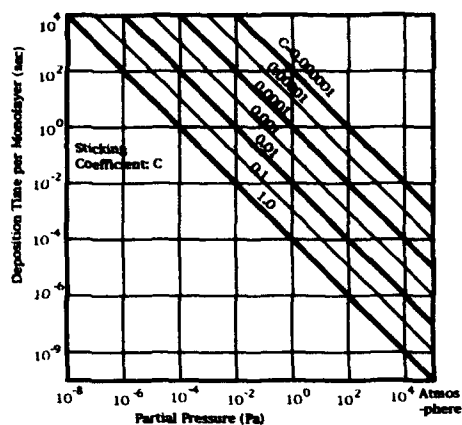


Fig. 1 Monolayer deposition time for reactive impurity.

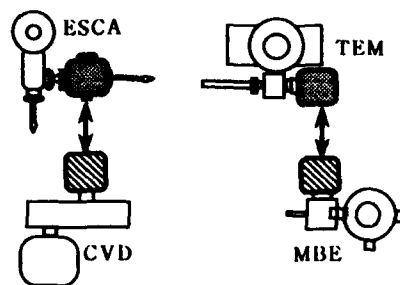


Fig. 2 Wafer transfer lines by using types of UHV transfer chamber.

various equipment and analyzing instruments. This paper describes two types of UHV transfer chamber (Fig. 2). One is for surface measurement by ESCA and the other is for crystal structure imaging by TEM.

## II. EXPERIMENTAL

### A. Wafer transfer chamber

The role of the UHV transfer chamber is to transfer the wafer from the process equipment chamber to the measuring instrument chamber without exposure to air. It therefore needs a stand-alone vacuum pumping system and an adaptive wafer handling mechanism. Figure 3 shows the structure of UHV transfer chamber. The vacuum system of the UHV transfer chamber consists of a battery driven ion pump (30 liter/sec.) and a liquid  $N_2$  shroud. The battery can drive the ion

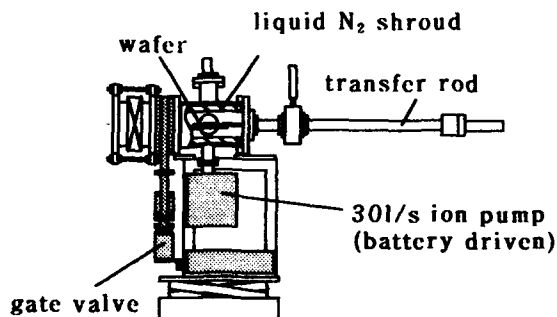


Fig.3 Structure of UHV transfer chamber

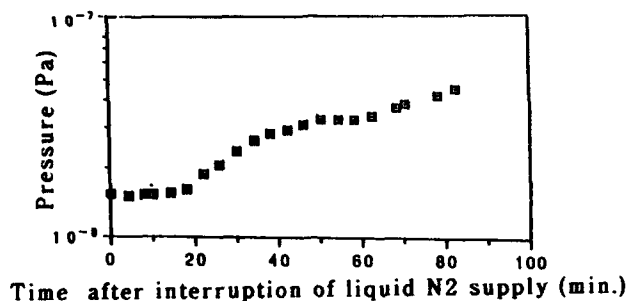


Fig. 4 Pressure characteristics of UHV transfer chamber after interruption of liquid N<sub>2</sub> supply.

pump for 36 hours. The transfer rod which permit a horizontal stroke of 1000 mm and vertical motion of 20 mm, is used for wafer handling. The UHV chamber is supported on a trolley with vertical motion of 450 mm in order to allow attachment to the equipment.

Figure 4 shows how the chamber pressure depends on time after interruption of liquid N<sub>2</sub> supply. Before interruption, a pressure of  $2 \times 10^{-8}$  Pa, which corresponds to about 100 minutes per monolayer deposition of reactive impurity (as shown in Fig. 1), is achieved with the ion pump and the liquid N<sub>2</sub>. However, when the liquid N<sub>2</sub> supply was interrupted the pressure increased gradually and reached of  $5 \times 10^{-8}$  Pa, corresponding to about 40 minutes per an atomic layer deposition of reactive impurities, after 80 minutes. This feature of the UHV transfer chamber shows that it can transfer the wafer with contamination of less than one monolayer in 40 minutes.

#### B. TEM observation system

In order to observe the atomic structure of initial stage of the semiconductor-film growth using the UHV transfer chamber, we developed a TEM sample holder which can be positioned in both the growth chamber and the TEM analyzing chamber. Figure 5 shows the sample holder for TEM observation. The holder has a carbon thin film and a local heating mechanism. The growth is performed on the carbon thin film (20- or 30-nm thick) which can be heated at growth temperature by a 0.45 mm thick ceramic heater during film growth. The TEM was HITACHI H-9000 UHV with resolution of 0.19 nm.



Fig. 5 A sample holder for TEM observation.

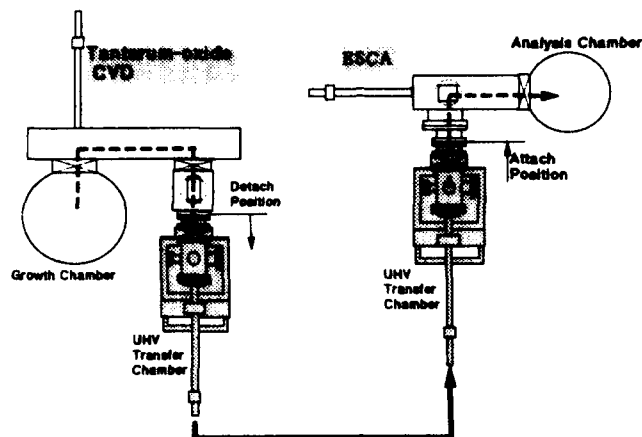


Fig. 6 Schematic Layout of UHV Wafer Transfer Line.

### III. RESULTS

#### A. Wafer transfer chamber

We used the UHV transfer chamber to measure the surface chemical contamination of CVD-grown  $\text{Ta}_2\text{O}_5$  (Tantalum oxide). Figure 6 shows the schematic layout of UHV wafer transfer system. Firstly a  $\text{Ta}_2\text{O}_5$  (about 2-nm-thick) thin layer was grown on a wafer in the CVD growth chamber and the wafer was transferred to the UHV transfer chamber. The wafer was then transferred to an ESCA load lock chamber for surface analysis. Figure 7 shows the ESCA spectrum of  $\text{Ta}_2\text{O}_5$ . Figure 8 shows the carbon spectrum using the UHV transfer chamber and a  $\text{N}_2$  gas environment cassette. The carbon spectrum of the UHV transfer chamber is about 40 % of the  $\text{N}_2$  gas cassette. This result shows that carbon contamination is reduced by using the UHV

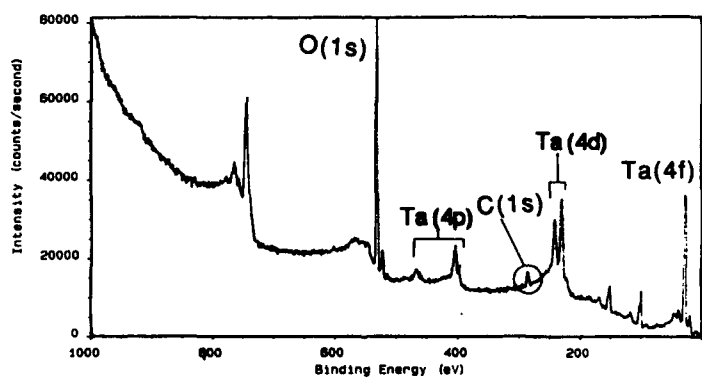


Fig. 7 ESCA spectrum of  $\text{Ta}_2\text{O}_5$

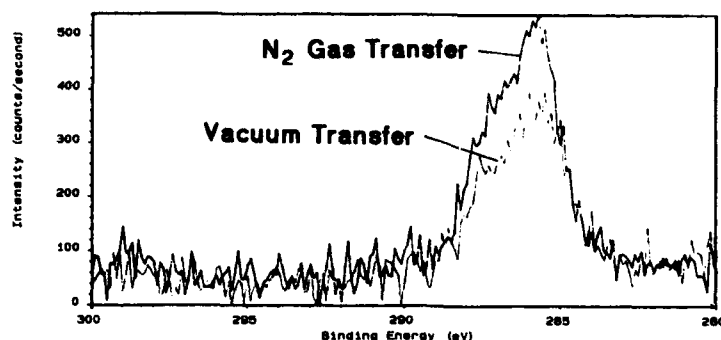


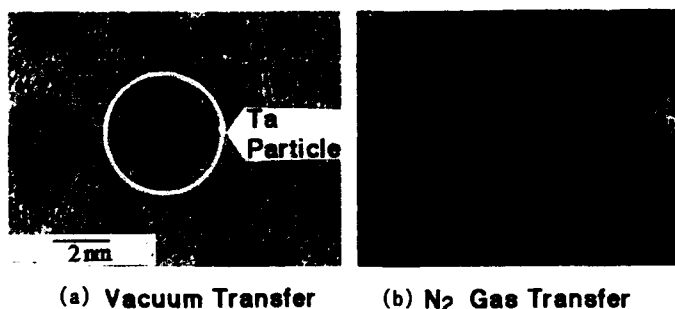
Fig. 8 Comparison of carbon spectrum between vacuum transfer and  $N_2$  gas transfer.

transfer chamber. The carbon spectrum of the UHV transfer chamber shows that there is residual carbon from the organic Ta gas remaining in the  $Ta_2O_5$  thin film.

#### B. TEM observation system

The UHV transfer chamber for the TEM observation system was used to transfer a Ta thin layer which was rapidly oxidized. The Ta thin layer was 3-nm thick and grown by MBE with a vacuum of  $3.5 \times 10^{-8}$  Pa.

Figure 9 shows high resolution TEM images of Ta thin layer samples after vacuum transfer and atmospheric transfer. In the case of vacuum transfer (Fig. 9a) 3-nm-diameter Ta lattice fringe are clearly seen in the image. Analysis of this image shows that the Ta crystal structure is mainly  $\beta$ -structure with small amount of  $\alpha$ -structure. In the case of atmospheric transfer (Fig. 9b), on the other hand, lattice fringes are not clearly seen because the Ta crystal has changed to the amorphous state because of adhesion of contamination and oxidation, particularly at the triple points of the grain boundaries.



(a) Vacuum Transfer (b)  $N_2$  Gas Transfer

Fig. 9 TEM image of 3-nm-thick Ta Thin Layer Grown by MBE.

#### IV. SUMMARY

A UHV transfer chamber was developed and used to in-process diagnostics of film growth processes. This chamber was used to transfer a wafer and a TEM specimen from the process equipment to ESCA and TEM equipment under vacuum conditions of  $2 \times 10^{-8}$  Pa without supplying external power. We obtained the following results. (1) carbon contamination was suppressed in CVD grown  $\text{Ta}_2\text{O}_5$  thin film, (2) oxidation was suppressed in MBE grown Ta.

#### ACKNOWLEDGMENTS

The authors would like to thank the following staff of Hitachi Central Research Laboratory: Dr. Yuzuru Ohji and Dr. Misuzu Hirayama for their contributions to experiments, and Dr. Ken-ichi Mizuishi and Yasuhiro Mitsui for their encouragement and support throughout this work.

#### REFERENCES

1. M. Moslehi, S. Shatas, K. Saraswat, and J. Meindel, IEEE Trans. Electron Device, vol. ED34, 6, 1407(1987).
2. B. Deal and D. Kao, Mat. Res. Soc. Symp., (1987).
3. M. Morita, T. Ohmi, E. Hasegawa, M. Kawasaki and K. Suma, Appl. Phys. Lett., 55, 6, 562(1989).
4. M. M. Moslehi, R. A. Chapman, M. Wong, A. Paranjpe, H. N. Najm, J. Kuchne, R. L. Yeeakley and C. J. Davis, IEEE Trans. ED, 39, 4 (1992).
5. G. W. Rubloff and D. T. Bordonaro, IBM J. Res. Develop., 36, 233 (1992).
6. M. Koguchi, H. Kakibayashi and R. Nakatani, Jpn. J. Appl. Phys. 32, 4814 (1993).

## DEVELOPING A METHOD FOR WIDE-CONTROL OF THE SELF-BIAS AND ITS ADOPTION TO ION-DAMAGE CONTROL

TAKEO OHTE\*, MAKOTO GOTO\*\* AND MINORU SUGAWARA\*\*\*

\*Gunma College of Technology, 580 Toriba-cho, Maebashi, Gunma 371, Japan

\*\*Gunma Polytechnic College, 918 Yamana-cho, Takasaki, Gunma 370-12, Japan

\*\*\*Gunma University, 1-5-1 Tenjin-cho, Kiryu, Gunma 376, Japan.

### ABSTRACT

We have developed a technique which enables us to reduce the self-bias voltage without introducing any substantial disturbance to the main plasma. This approach is based on decreasing the floating potential of the powered electrode by means of injecting an electron current from the electrode. Instead of employing a hot cathode, we have used an auxiliary glow discharge to supply the electron emission. The controllable range of the self-bias has been extended to almost 0 V. A theoretical explanation of the variation of the floating potential with the emission current has been carried out. Measurements of the floating voltage ( $V_f$ ) are plotted against  $\ln(1/I_{au})$ , where  $I_{au}$  is the auxiliary discharge current. A good linear relationship of  $V_f$  vs.  $\ln(1/I_{au})$  is obtained as expected from the theory, and its slope gives the electron temperature.

In order to appraise the degree of damage induced by the bombardment of ions accelerated by the sheath voltage, we have estimated the damage by measuring the dark current of a sample diode fabricated from the film. It has been observed experimentally that when the sheath voltage was depressed from -73 V to -36 V at a pressure of 0.11 Torr, the dark current of the sample diode was suppressed drastically from  $1.3 \times 10^{-10}$  A to  $5.3 \times 10^{-11}$  A.

### INTRODUCTION

The r.f. planar discharge has been used widely in plasma processing. Positive ions are accelerated across the sheath by the sheath voltage, and bombard the powered electrode. In plasma etching, the kinetic energies of the incident ions have an important role on both the etch rate and etching anisotropy, but induce damages to the surfaces of films [1]. Therefore, we need to reduce the sheath voltage independently of other plasma parameters. Chan et al. [2] have demonstrated experimentally in the low frequency region (500 kHz) that the time-averaged sheath potential varies as a function of gas pressure and r.f. voltage.

We have developed a method to suppress the self-bias by supplying supplemental electron flow from the powered electrode to the plasma through the sheath region [3]. The aims of this paper are, (1) to discuss a model which describes the mechanism of controlling the sheath voltage, (2) to confirm the reduction of film damages by suppressing the sheath voltage.

### PRINCIPLE

The principle of the method is shown schematically in Fig. 1. It is known that the electron velocity is much greater than the ion velocity in low pressure plasmas. When an electrode is isolated electrically, the floating potential must develop in front of the electrode, in such a way as to make the net current (electron current + ion current) zero.

Let us consider that an extra electron current  $I_{em}$  is emitted from the electrode and flows back to the plasma through the sheath region. Because the electron current  $I_e$  from the plasma to the sheath region is flowing against the electron emission current  $I_{em}$ , a part of the plasma current will be cancelled. Accordingly, a net electron current of  $(I_e - I_{em})$  flows from the

plasma into the sheath region. As a result, the net electron current should be cancelled with the ion current,  $(I_e - I_{em}) = I_i$ , therefore,

$$I_e = (I_i + I_{em}) \quad (1)$$

where  $I_i$  designates the plasma ion current.

Eq. (1) indicates that the electron current from the plasma should be increased by an amount  $I_{em}$  in order to achieve no net current. This causes the floating potential to be decreased.

#### MODEL

The probe theory used in this model is the classical one of the perfect plane probe [4]. In order to arrive at a tractable, yet physically realistic solution, the following assumption will be made.

- 1) The ion and electron temperatures  $T_i$  and  $T_e$  are independent of time and spatial coordinates, with  $T_i$  being equal to the neutral gas temperature.
- 2) The ion and electron densities inside the plasma volume are constant in time.
- 3) The ions enter the sheath from the presheath with the speed required by the Bohm-sheath criterion. The rate at which ions enter the sheath from the presheath is thus constant. This assumption is valid in the limit of  $t_r \ll 1/f$ , where  $t_r$  is the transit time of the ions through the sheath and  $f$  the applied frequency.
- 4) At 13.56Mhz, the regime of interest, the ions only see the average bias, but the electrons respond to the modulation.

When there exists an r.f. component of the voltage between the plasma and the powered electrode, one is effectively modulating the bias voltage, sweeping up and down along the d.c. characteristic curve. This sinusoidal modulation along the exponential electron retardation section of the characteristics yields a modified first order Bessel function result. Furthermore, once an r.f. component is present, the displacement current may also contribute to the sheath d.c. current, which is neglected in this calculation. Finally, when external electron emission from the powered electrode is present, the floating voltage  $V_f$  is modified to give,

$$V_f = \frac{kT_e}{e} \ln \left( \frac{I_{eo} I_o (eV_{rf}/kT_e)}{I_{io} + I_{em}} \right) \quad (2)$$

where  $kT_e$  designates the electron temperature,  $I_{eo}$  and  $I_{io}$  denote electron saturation current and ion saturation current, respectively, and  $e$  denotes the electron charge. Also,  $I_o$  is the first order Bessel function of variable  $(eV_{rf}/kT_e)$ , where  $V_{rf}$  is the peak amplitude of the r.f. modulation,  $I_{em}$  is the electron current supplied from the powered electrode. Under normal condition,  $I_{io}$  can be neglected in comparison with  $I_{em}$ , and so eq.(2) can be simplified to,

$$V_f \approx \frac{kT_e}{e} \ln \left( \frac{I_{eo} I_o (eV_{rf}/kT_e)}{I_{em}} \right) \quad (3)$$

Namely, the relationship between  $V_f$  and  $\ln(1/I_{em})$  must be linear and its slope gives the

## EXPERIMENTAL

The etching experiments were carried out in an r.f. discharge chamber with the electrodes as shown schematically in Fig.3. The chamber is constructed of the aluminum, with an inner diameter of 40 cm and configured with parallel plate electrodes which are made of aluminum.

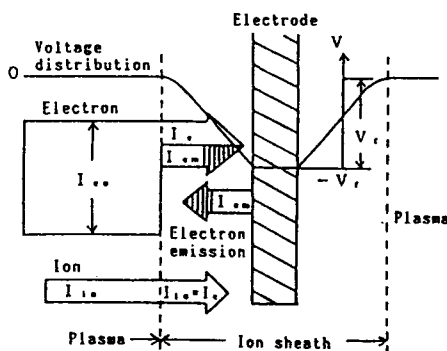


**Fig. 1 The principle of controlling the self-bias voltage.**

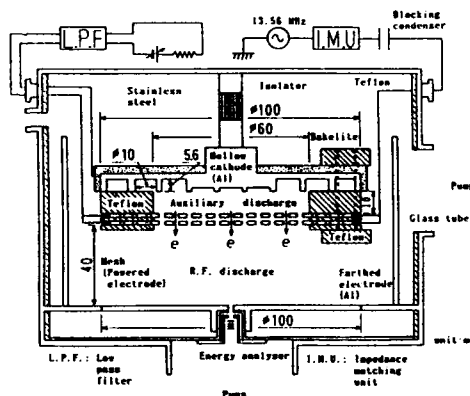


**Fig. 2 Construction of the discharge chamber and the electrodes for discussing the model.**



The r.f. power was supplied through a matching unit to the mesh-electrode. The silicon wafers are placed on the powered electrode. Etching characteristics of the amorphous silicon wafer have been taken in an etching gas of  $\text{CF}_4/\text{O}_2$  (6:1) with variable self-bias control. The damage induced in the films was evaluated by measuring the dark current of a sample diode made from the film. The measuring circuit is shown in Fig. 4, with the reverse voltage applied to the sample diode.

## RESULTS AND DISCUSSION

Typical data of  $V_f$  against  $\ln(1/I_{\text{am}})$  taken at 0.3 Torr, 20 W of r.f. power are shown in Fig. 5, where  $I_{\text{am}}$  is the d.c. auxiliary discharge current which is assumed to be proportional to  $I_{\text{em}}$ . It is clearly seen that a linear relationship of  $V_f$  vs  $\ln(1/I_{\text{am}})$  is established as expected by eq (4). In the higher current region, however, the experimental data deviate from the linear relationship, which could be explained by an increase in the electrical transparency of the mesh electrode because of a thinner sheath thickness. Also, the electron temperatures estimated from the slopes are equal to 7.7 eV for both the 2x20 mesh and the 2x100 mesh. In order to confirm this value, we have measured the electron temperature by the double probe method. In order to minimize the effect of the r.f. potential variation, we have used a floating double probe. An electron temperature of 8 eV at a pressure of 0.3 Torr and 20 W of r.f. power has been obtained. This result agrees well with values obtained above.

Using an etching gas ( $\text{CF}_4/\text{O}_2 = 6/1$ ), we have repeated the etching characteristics with the variable self-bias as shown in Fig. 6. It is shown experimentally that the etching rate is not reduced appreciably when the self-bias is reduced. In order to estimate reduction of film damage qualitatively, the dark current has been reduced from  $1.3 \times 10^{-10}$  A to  $5.3 \times 10^{-11}$  A for a reverse voltage of -1 V when the sheath voltage is varied from -73 V to -36 V as shown in Fig. 7. From these results, we estimate that the threshold of the sheath voltage for inducing damage is about -40 V.

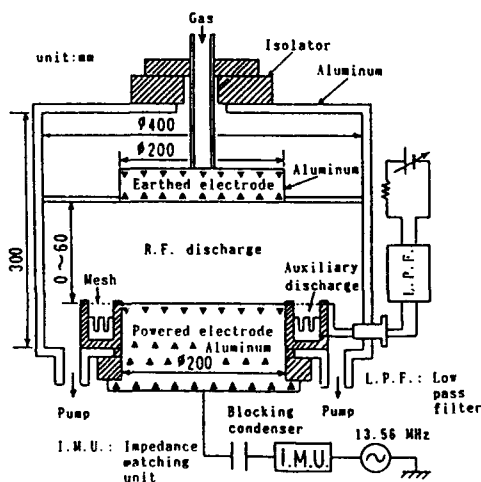


Fig. 3 Construction of the discharge chamber for etching the amorphous films.

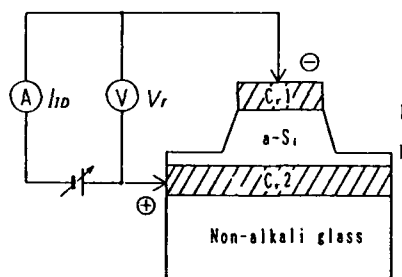


Fig. 4 A method of measuring the dark current  $I_d$  by applying the reverse voltage  $V_d$ .

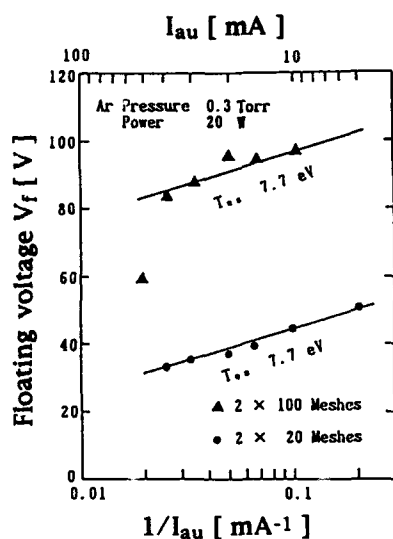


Fig. 5 Relation between  $V_f$  and  $\ln(1/I_{au})$ .

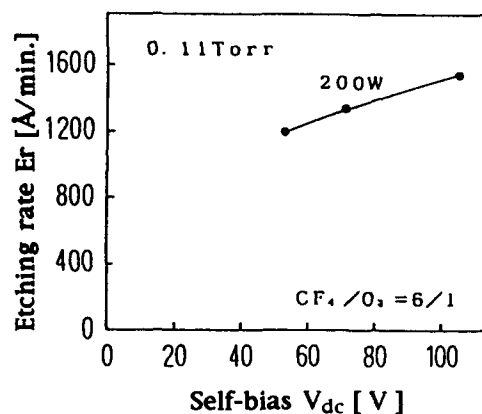


Fig. 6 Typical data of the etching rate with the self-bias.

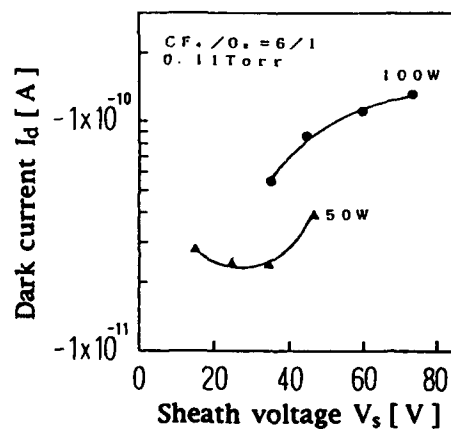


Fig. 7 Typical data of the damage with the sheath voltage.  
(Inverse voltage applied to the diode:  $-1 \text{ V}$ )

## CONCLUSIONS

- (1) The self-bias can be reduced by use of a supplemental electron flow from a powered electrode to the plasma through the sheath. A model which describes the mechanism of controlling the sheath voltage is proposed, and the results derived from this model agree with those of the experiment fairly well.
- (2) The damage induced in the films is reduced substantially by means of suppressing the sheath voltage. The threshold of the sheath voltage for inducing film damage is about -40 V.

## REFERENCES

- [1] J.W.Coburn and Eric Kay, J. Appl. Phys. 43, 4965(1972)
- [2] Chung Chan, Zhong-Jun Jin and Christopher Whitaker, J. Appl. Phys. 62, 1633(1987)
- [3] M.Sugawara, T.Ohte and T.Miyamoto, JCPIG XIX, (1989) p.400-401
- [4] A.M.Pointu, J. Appl. Phys. 60, 4113(1986)
- [5] M.Sugawara, B.Bergevin, B.Stansfield and B.C.Gregory,  
INRS Energie Rapport Interne, Number 033, 1970

## RELATING PHOTORESIST ETCH CHARACTERISTICS TO LANGMUIR PROBE MEASUREMENTS IN AN ELECTRON CYCLOTRON RESONANCE SOURCE

K. T. Sung, W. H. Juan, and S. W. Pang  
Department of Electrical Engineering and Computer Science,  
The University of Michigan, Ann Arbor, MI 48109-2122

M. Dahimene  
Wavemat Inc., Plymouth, MI 48170

### ABSTRACT

In this work, Langmuir probe measurements were used to characterize a multipolar electron cyclotron resonance (ECR) plasma source. This system has many controllable parameters including microwave power, rf power, gas, pressure, flow rate, and source distance. Both double and triple Langmuir probes were used for the plasma characterization. The results from the Langmuir probe measurements were correlated to the etch characteristics of photoresist. Ion density and photoresist etch rate were found to increase with microwave power but decrease with source distance. However, rf power does not have significant influence on ion density although the photoresist etch rate increases substantially with rf power. Ion density first increases then decreases at higher pressure. Maximum ion density occurs at lower pressure for larger distance below the ECR source. Ion density uniformity for an O<sub>2</sub> plasma is  $\pm 2\%$  across a 16 cm diameter region at 23 cm below the source. For photoresist etched at 10 cm source distance, etch rate uniformity is  $\pm 2\%$  for a 15 cm diameter wafer. The results from the Langmuir probe measurements indicate that photoresist etching is enhanced by ion density and ion energy.

### I. INTRODUCTION

As the device dimensions decrease to sub-half micrometer scale, requirements for dry etching become more stringent. These include vertical profile, smooth morphology, high etch rate, and reproducible etching. To meet these needs, different high density plasma sources have been developed. In this work, a multipolar electron cyclotron resonance (ECR) source was used to generate high density plasma. The ECR source can generate high density plasma with low ion energy at low pressure. As a result, it can potentially satisfy all the needs for dry etching.

Langmuir probe measurements are used to obtain charge particle density, plasma potential, and electron temperature [1-10]. By mapping these characteristics at different positions in the chamber, plasma uniformity is obtained. These plasma characteristics are used to optimize photoresist etching. A number of controllable inputs to the plasma system were varied, including microwave power, rf power, gas, pressure, flow rate, and distance below the ECR source. Their effects on plasma characteristics and photoresist etch rate were investigated.

### II. EXPERIMENTAL

Figure 1 shows the schematic of the ECR source on top of a rf-biased electrode with the Langmuir probe inserted through the diagnostic window on the chamber wall [11]. Plasma is generated within the quartz disk which is surrounded by 12 permanent magnets arranged in a multipolar configuration. Microwave power is input into the quartz disk through a copper probe.

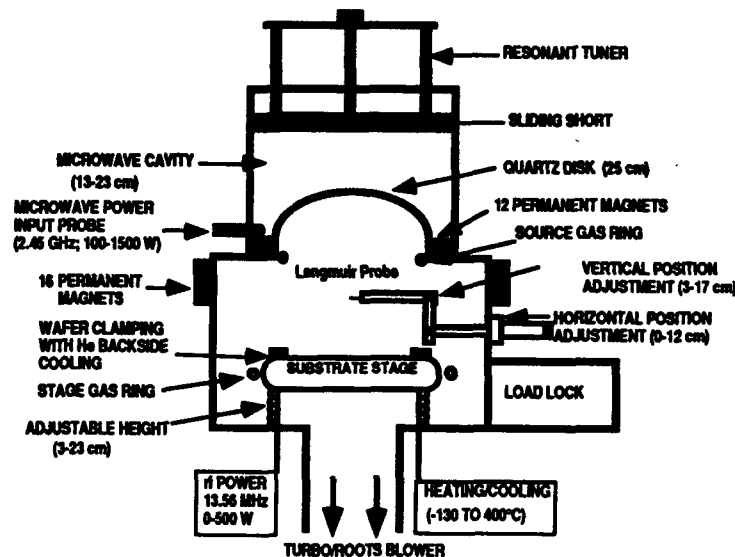


Figure 1 Schematic of the ECR source on top of a rf-powered electrode.

There are 16 additional permanent magnets extending up to 11 cm below the ECR source to reduce recombination of charged particles at the chamber wall. Samples are placed on substrate stage which is rf powered.

The Langmuir probes used in this work include double probe and triple probe. The double Langmuir probe was made of stainless steel wires which were 0.051 cm in diameter and 0.4 cm in length. The size of the probe should be small enough so that the plasma will not be disturbed. However, smaller probe size causes a larger uncertainty of the actual electron collecting area[1]. The actual electron collecting area is determined by the dark space sheath area formed around the probe which is proportional to the Debye length. The Debye length decreases as the electron density increases. As a result, the area correction factor is expected to be small for the ECR source since the plasma density is high. The data shown in this work are not corrected for this difference in collecting area. From the current-voltage (I-V) curve measured by the double Langmuir probe, the ion density is[12,13]

$$N_i = \frac{i_p}{0.6 q A_s} \sqrt{\frac{m_i}{k T_e}}$$

where  $i_p$  is the ion saturation current,  $q$  is the electron charge,  $A_s$  is the sheath area around the probe,  $m_i$  is the mass of the ion,  $k$  is the Boltzmann constant, and  $T_e$  is the electron temperature. The electron temperature is determined by the slope of the I-V curve. It is assumed that the ions in the plasma are singly and positively ionized.

The triple Langmuir probe was made of tungsten wires which had the same size as the double probe. The ion density and electron temperature can be obtained without voltage sweep. As a result, triple Langmuir probe is useful in real-time process control[14]. Both double and triple probes can be moved across the substrate stage. For double Langmuir probe, measurements were performed from 3 to 17 cm below the ECR source. For triple Langmuir probe, measurements were performed at 23 cm below the ECR source. The electron density and temperature measured by the double and triple Langmuir probes agree with one another.

For photoresist etching experiments, Shipley AZ5214 was spun on Si wafer and baked at 90°C for 40 min. The photoresist thickness was measured to be about 1.4  $\mu\text{m}$  by reflectometry.

### III. RESULTS AND DISCUSSIONS

Different gases such as Ar, O<sub>2</sub>, Cl<sub>2</sub>, and N<sub>2</sub> were excited in the plasma and their plasma properties were studied. The results were related to the photoresist etch rate to provide insight on etch mechanisms and process control[5].

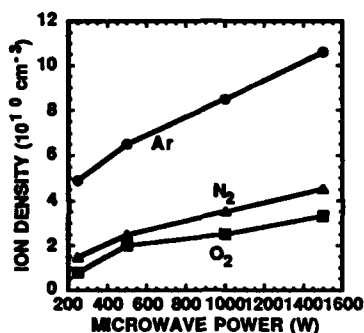


Fig. 2. Ion density dependence on microwave power for Ar, O<sub>2</sub>, and N<sub>2</sub> plasma. The gas flow rate was 10 sccm at 1 mTorr. The source distance was 10 cm.

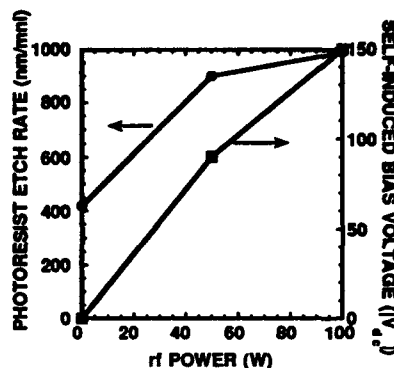


Fig. 3. Photoresist etch rate and  $|V_{dc}|$  dependence on rf power. Oxygen was flown at 10 sccm with 1000 W microwave power, 1 mTorr pressure, and 5 cm source distance.

Figure 2 shows the dependence of ion density on microwave power for Ar, N<sub>2</sub>, and O<sub>2</sub> discharges. The gas flow rate was 10 sccm with 1 mTorr pressure. The probe was located at 10 cm below the ECR source in the center of the stage. As the microwave power was increased from 250 to 1500 W, ion density increased from 7.9 to  $25.6 \times 10^{10} \text{ cm}^{-3}$  for an Ar plasma. Similar increase was observed for N<sub>2</sub> and O<sub>2</sub> discharges. The increase in ion density at higher microwave power is related to the higher ionization efficiency. More charged particles are generated at higher microwave power as long as the source gas is not completely depleted. Among the different gases investigated, Ar plasma has the highest ion density, followed by Cl<sub>2</sub>, N<sub>2</sub>, and O<sub>2</sub> discharges.

With higher ion density at higher microwave power, photoresist etch rate is expected to be enhanced[15]. As the microwave power was increased from 500 to 1500 W, the photoresist etch rate increased from 0.7 to 1.8  $\mu\text{m}/\text{min}$  while the ion density for an O<sub>2</sub> plasma only increased from  $2.8$  to  $4.1 \times 10^{10} \text{ cm}^{-3}$ . Meanwhile, the self-induced bias voltage ( $|V_{dc}|$ ) decreases with increasing microwave power. The large increase in the photoresist etch rate despite the moderate increase in the ion density and the decrease in  $|V_{dc}|$  suggests that the photoresist etch process is strongly influenced by the neutral reactive species.

Photoresist etch rate and  $|V_{dc}|$  as a function of rf power are shown in Fig. 3. Flow rate of O<sub>2</sub> was 10 sccm at 1 mTorr with 1000 W microwave power and 10 cm source distance. As the rf power was increased from 0 to 100 W, the photoresist etch rate increased substantially from 420 to 990 nm/min and  $|V_{dc}|$  increased from 0 to 150 V. However, the ion density only increased slightly from  $3.8$  to  $4.3 \times 10^{10} \text{ cm}^{-3}$ . These results indicate that at 1000 W microwave power, O<sub>2</sub> is mainly dissociated by the microwave power instead of the rf power. The substantial increase in the photoresist etch rate is due to the higher ion energy at higher rf power which can reduce the activation energy for the etch process.

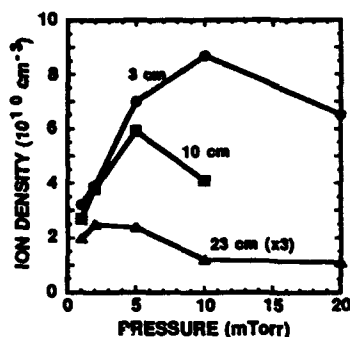


Fig. 4. Ion density dependence on pressure at different source distance. Nitrogen flow rate was 10 sccm at 1 mTorr. Microwave power was 1000 W at 3 and 10 cm; and 1500 W at 23 cm source distance.

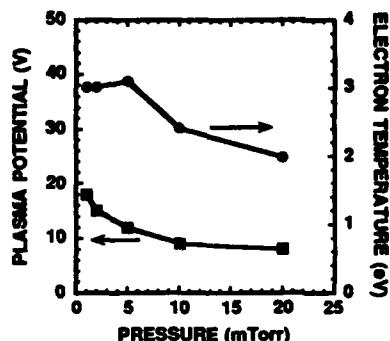


Fig. 5. Dependence of electron temperature and plasma potential on pressure. The  $O_2$  flow rate was 10 sccm with 1000 W microwave power at 3 cm below the ECR source.

The ion density for an  $N_2$  plasma was investigated as a function of pressure at three different source distances as shown in Fig. 4. The flow rate was 10 sccm at 1 mTorr. Microwave power was 1000 W at 3 and 10 cm; and 1500 W at 23 cm source distance. The ion density at 23 cm source distance was multiplied by a factor of 3 to fit in the same figure. The ion density was found to increase with pressure initially then decrease at higher pressure. However, it decreased more rapidly at longer source distance. The initial increase of ion density with pressure may be due to higher concentration of  $O_2$  available for further dissociation. At higher pressure, the mean free path is shorter and the collision probability is higher. As a result, the dissociation efficiency and hence the ion density are lower. The faster decrease of ion density at longer source distance may be related to the recombination of ions. Both the ion density and the photoresist etch rate were found to decrease almost linearly with source distance. This is attributed to the reduction in ion density and/or neutral reactive species concentration at longer source distance.

Besides ion density, electron temperature and plasma potential also affect etch characteristics. The dependence of electron temperature and plasma potential on pressure for an  $O_2$  plasma is shown in Fig. 5. The flow rate was 10 sccm at 1 mTorr with 1000 W microwave power and 3 cm source distance. The electron temperature remained about constant around 3 eV as pressure was increased from 1 to 5 mTorr. At pressure higher than 5 mTorr, electron temperature decreased with pressure and reduced to 2 eV at 20 mTorr. Meanwhile, plasma potential decreased from 18 to 8 V as the pressure was increased from 1 to 20 mTorr. Since the collision probability is higher at higher pressure, electron temperature is reduced due to collision. With lower electron energy, plasma potential is also reduced. Both the electron temperature and plasma potential can influence the dissociation efficiency, etch rate, and profile.

Figure 6 shows the relationship between the ion density and photoresist etch rate as a function of  $O_2$  flow rate. Pressure was 3 mTorr with flow rate varied from 10 to 100 sccm. For ion density measurements, the microwave power was 1500 W with 23 cm source distance. For photoresist etching of 10 cm diameter wafer, the microwave power was 1000 W with 5 cm source distance. As the flow rate was increased from 10 to 100 sccm, the ion density remained about constant around  $4 \times 10^{10} \text{ cm}^{-3}$ . However, the photoresist etch rate increased from 640 to 930 nm/min. Although the ion density does not increase with flow rate, the neutral reactive species may still increase and enhance the etch rate. Reducing the area to be etched also lower the flow rate needed to maintain a constant etch rate. The dependence of etch rate on flow rate

and etch area suggests that photoresist etching is limited by the concentrations of reactive species. For larger area to be etched, the loading effect can be significant and sufficient gas flow should be provide to enhance etch rate and improve etch uniformity.

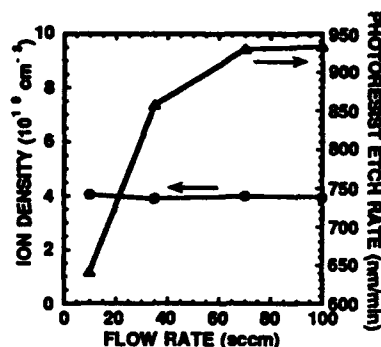


Fig. 6. Relationship between the ion density and photoresist etch rate as a function of O<sub>2</sub> flow rate. Ion density was obtained at 1500 W microwave power and 23 cm below the ECR source. Photoresist etch rate was obtained at 1000 W microwave power, 50 W rf power, and 5 cm source distance.

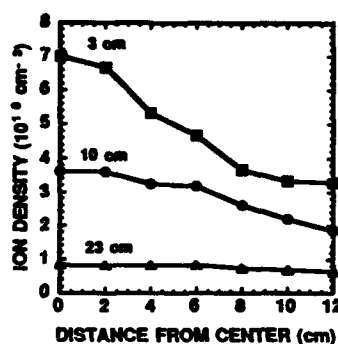


Fig. 7. Ion density uniformity of an O<sub>2</sub> plasma at different source distance. Flow rate was 10 sccm at 1 mTorr with 1000 W microwave power.

High throughput and uniform etching are required in manufacturing to lower cost and improve yield. While throughput can be increased by using large diameter wafers, it is important to maintain good etch uniformity. Figure 7 shows the ion density uniformity of an O<sub>2</sub> plasma from the center of the stage to 12 cm away from the center at different source distance. The flow rate was 10 sccm with 1 mTorr pressure. Microwave power was 1000 W at 3 and 10 cm; and 1500 W at 23 cm source distance. Ion density was found to be higher in the center and decrease towards the edge of the stage. There is a faster decrease in ion density at shorter source distance. The uniformity of ion density is  $\pm 2\%$  across the central 16 cm diameter stage at 23 cm. At longer source distance, the ions diffuse through a longer path which can minimize the ion concentration gradient and improve uniformity.

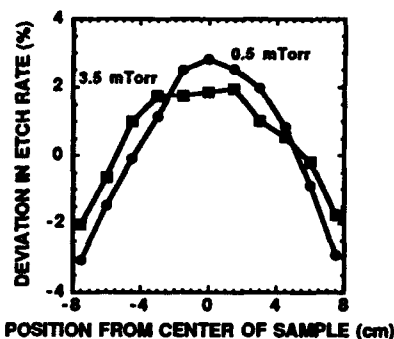


Fig. 8. Etch rate uniformity dependence on radial distance as a function of pressure. Oxygen flow was 15 sccm with 1500 W microwave power, 50 W rf power, and 10 cm source distance.

Figure 8 shows the photoresist etch rate uniformity dependence on radial distance as a function of pressure. The O<sub>2</sub> flow was 15 sccm with 1500 W microwave power, 50 W rf power, and 10 cm source distance. The etch rate uniformity across a 15 cm diameter wafer is  $\pm 2\%$  at 3.5 mTorr and  $\pm 3\%$  at 0.5 mTorr. Meanwhile, ion density uniformity at the same source distance



is  $\pm 3\%$  across the central 12 cm diameter stage. The results indicate that uniform plasma is generated by the ECR source which can provide uniform photoresist etching for 15 cm diameter wafers.

#### IV. SUMMARY

The Langmuir probe measurements have been used to characterize plasmas generated by an multipolar ECR source. Effects of the controllable input parameters, including microwave power, rf power, gas, pressure, flow rate, and source distance on the plasma properties have been studied. Ar was found to have the highest ion density, followed by  $\text{Cl}_2$ ,  $\text{N}_2$ , and  $\text{O}_2$ . Ion density and photoresist etch rate increase with microwave power and decrease with source distance. Flow rate or rf power has little influence on the ion density. However, photoresist etch rate increases with rf power and flow rate. The etch rate enhancement may be related to the higher ion energy at higher rf power and the higher neutral reactive species concentrations at higher flow rate. Ion density initially increases with pressure then decreases at higher pressure. Photoresist etch rate also follows the same trend with pressure. Uniformity of ion density was  $\pm 2\%$  across a 16 cm diameter stage for an  $\text{O}_2$  plasma at 23 cm source distance. Meanwhile, uniformity of  $\pm 2\%$  was also found for photoresist etching of 15 cm diameter wafer at 10 cm source distance. Electron temperature was 3 eV and plasma potential was 15 V at 3 mTorr which provides an optimized condition for photoresist etching of 0.1- $\mu\text{m}$ -wide, 1- $\mu\text{m}$ -deep features. The results from the Langmuir probe measurements are used to control photoresist etching by relating the etch rate to ion density and ion energy.

#### V. ACKNOWLEDGMENTS

The authors would like to thank Nichimen American Inc. for the usage of the triple Langmuir probe. This work is supported by the National Science Foundation (ECS-9111968).

#### REFERENCES

1. Electrical Probes for Plasma Diagnostics, edited by J. D. Swift and M. J. R. Schwar (American Elsevier, 1969).
2. J. Hopwood, D. K. Reinhard, and J. Asmussen, J. Vac. Sci. Technol. A8, 3103 (1990).
3. T. Oomori, M. Tuda, H. Ootera, and K. Ono, J. Vac. Sci. Technol. A9, 722 (1991).
4. O. A. Popov, J. Vac. Sci. Technol. A9, 711 (1991).
5. B. Anthony, T. Hsu, R. Qian, J. Irby, S. Banerjee, and A. Tasch, J. Electronic Materials 20, 309 (1991).
6. G. King, F. C. Sze, P. Mak, T. A. Grotjohn, and J. Asmussen, J. Vac. Sci. Technol. A10, 1265 (1992).
7. A. A. Shatas, Y. Z. Hu, and E. A. Irene, J. Vac. Sci. Technol. A10, 3119 (1992).
8. C. Charles, J. Vac. Sci. Technol. A11, 157 (1993).
9. J. Hopwood, C. R. Guarnieri, S. J. Whitehair, and J. J. Cuomo, J. Vac. Sci. Technol. A11, 152 (1993).
10. K. T. Sung, W. H. Juan, S. W. Pang, and M. Dahimene, to be published in J. Vac. Sci. Technol. A, January 1994.
11. S. W. Pang, K. T. Sung, and K. K. Ko, J. Vac. Sci. Technol. B10, 1118 (1992).
12. Plasma Diagnostics, edited by W. Lochte-Holtgreven (North Holland, 1968).
13. Plasma Diagnostics Techniques, edited by R. H. Huddleston and S. L. Leonard (Academic, New York, 1965), pp. 113-200.
14. S. L. Chen and T. Sekiguchi, J. Appl. Phys. 36, 2363 (1965).
15. K. T. Sung, W. H. Juan, S. W. Pang, and M. W. Horn, to be published in J. Electrochem. Soc. December 1993.

## **SURFACE REACTIVITY OF SILICON AND GERMANIUM IN CF<sub>4</sub> - O<sub>2</sub> REACTIVE ION ETCHING**

**CHRISTOPHE CARDINAUD, A. CAMPO, G. TURBAN**  
Laboratoire des Plasmas et des Couches Minces I.M.N. UMR 110 CNRS  
2 rue de la Houssinière 44072 NANTES Cedex 03, France

### **ABSTRACT**

Reactive ion etching of silicon and germanium in CF<sub>4</sub> - O<sub>2</sub> was investigated. Above 20% O<sub>2</sub> germanium etching is selective with respect to silicon. In agreement with the evolution of the fluorine and oxygen concentration in the plasma and of the etch products formation rate, surface analysis reveals that the growth of a SiO<sub>x</sub>F<sub>y</sub> layer slows down the silicon etching whereas the formation of GeO<sub>x</sub>F<sub>y</sub> does not inhibit germanium etching. Using a simple kinetic model, the silicon and germanium reactivity and its dependency with respect to the plasma composition are expressed in function of the experimental data. Results suggest that surface composition controls silicon etching, whereas germanium etching depends only on the fluorine flux on the surface.

### **INTRODUCTION**

Germanium is reported to be etched more rapidly than silicon in most fluorine-, chlorine-, and bromine- based plasmas<sup>1</sup> with an exception for SF<sub>6</sub> based plasmas for which the reverse has been observed<sup>2,3</sup>. In SF<sub>6</sub> - O<sub>2</sub>, as the gas mixture is enriched in O<sub>2</sub>, the silicon etch rate drops rapidly to zero because of the growth of a SiO<sub>x</sub>F<sub>y</sub> layer described as a "blocking layer". Concerning germanium a GeO<sub>x</sub>F<sub>y</sub> layer exists even at low percentages of O<sub>2</sub> but does not inhibit the etching ; through the competition between oxygen and fluorine the decrease of the etch rate is related to a change in composition of this layer<sup>3</sup>. Under the same experimental conditions CF<sub>4</sub> - O<sub>2</sub> plasmas exhibit self bias voltages more negative than in SF<sub>6</sub> - O<sub>2</sub> ; this is believed to have important implications in the surface mechanisms.

### **EXPERIMENTAL**

Experiments were performed in a diode reactor with 10 cm in diameter <100> Si and <111> Ge wafers placed onto a 15 cm in diameter aluminium powered electrode. Plasma conditions were the following : 30 sccm CF<sub>4</sub> - O<sub>2</sub> (with Ar as actinometer), 13.3 Pa, 13.56 MHz, 50 W. The self bias voltage of the sample was seen to decrease from -180 V (CF<sub>4</sub>) to -130 V (CF<sub>4</sub> - O<sub>2</sub> 50% O<sub>2</sub>) and then increased to -200 V (CF<sub>4</sub> - O<sub>2</sub> 90% O<sub>2</sub>). Atomic fluorine (F/Ar) and oxygen (O/Ar) relative concentrations, and etch products (SiF<sub>4</sub>, GeF<sub>4</sub>) formation rate were investigated by optical emission spectroscopy (OES) using F ( $\lambda = 703.9$  nm), O ( $\lambda = 777.2$  nm), Ar ( $\lambda = 750.4$  nm) emission lines, and mass spectrometry (MS) respectively. After etching, surface characterization

experiments were performed by quasi in-situ X-ray photoelectron spectroscopy (XPS), etch rates were determined by weight loss measurements.

## RESULTS AND DISCUSSION

**OES** The evolution of the fluorine concentration in the  $\text{CF}_4$ - $\text{O}_2$  plasma exhibits bell shaped curves for both silicon and germanium, very similar to the one obtained for aluminium (fig. 1). The addition of a few percent of  $\text{O}_2$  to  $\text{CF}_4$  increases the fluorine concentration, as reactions between  $\text{CF}_x$  radicals and atomic oxygen are an important source of atomic fluorine. Much lower values than those observed for aluminium show evidence of fluorine consumption : for germanium the fluorine consumption is higher than for silicon ; moreover it remains high for all  $\text{CF}_4$ - $\text{O}_2$  mixtures, whereas for silicon a strong decrease is observed for  $\text{CF}_4$ - $\text{O}_2$  ( $\% \text{O}_2 > 60$ ). The oxygen concentration starts to be significant above 10%  $\text{O}_2$ , and is significantly greater for silicon than for germanium.

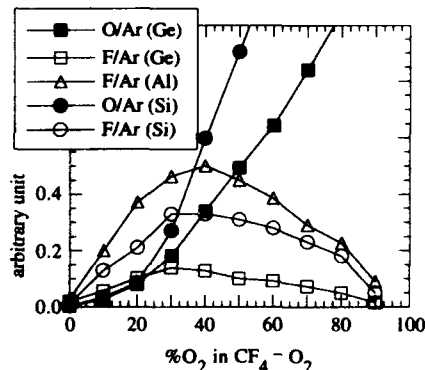


Fig. 1 : F and O concentrations in  $\text{CF}_4$ - $\text{O}_2$  for Si, Ge, and Al

**Etch rate and MS** Both silicon and germanium etch rates ( $\text{ER}(\text{Si})$  and  $\text{ER}(\text{Ge})$ ) are found to increase strongly when a few percent of  $\text{O}_2$  is added to  $\text{CF}_4$  (fig. 2). However,  $\text{ER}(\text{Si})$  starts to decrease above 10%  $\text{O}_2$  whereas  $\text{ER}(\text{Ge})$  decreases only above 30%  $\text{O}_2$ .  $\text{ER}(\text{Ge})$  is greater than  $\text{ER}(\text{Si})$  except in  $\text{CF}_4$ - $\text{O}_2$  ( $\% \text{O}_2 < 10$ ) : above 10%  $\text{O}_2$  the selectivity is in favour of germanium. A similar result has been reported for  $\text{SF}_6$ - $\text{O}_2$  etching under the same experimental conditions but

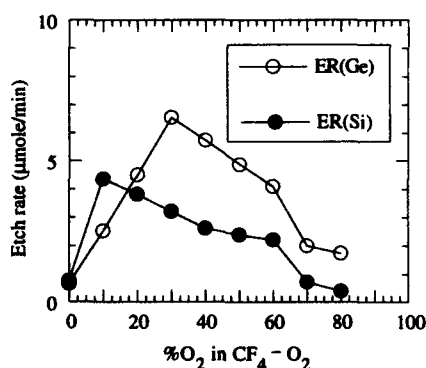


Fig. 2 : Etch rate of Si and Ge

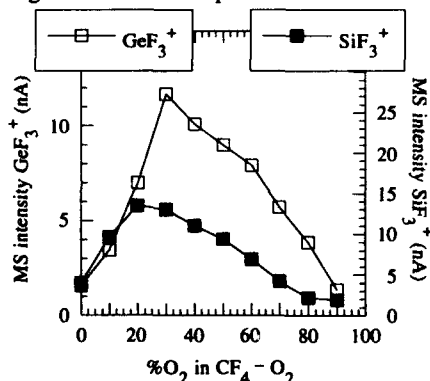


Fig. 3 : MS signals  $\text{SiF}_3^+$  and  $\text{GeF}_3^+$

then the transition occurred at 60%  $O_2^3$ . The evolution of MS signals  $SiF_3^+$  and  $GeF_3^+$  is in agreement with the etch rates (fig. 3). A careful survey of the mass spectrum up to  $m/e = 300$ , shows only traces of  $Si_2F_6$  and  $Ge_2F_6$  in  $CF_4$  etching (resulting from reactions in the gas phase), and no oxyfluoride products in  $CF_4 - O_2$ . Conclusion is that  $SiF_4$  and  $GeF_4$  are the only compounds resulting from the etching mechanism, and are not dissociated in the gas phase.

#### XPS

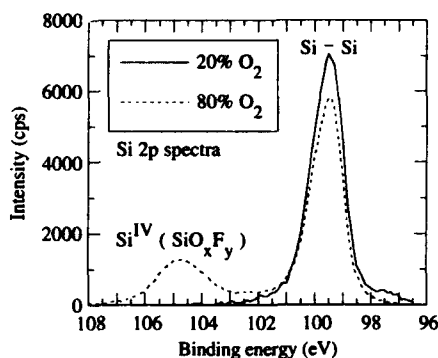


Fig. 4 : XPS spectra of Si after  $CF_4 - O_2$  RIE

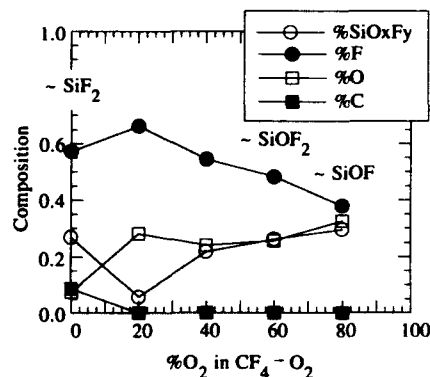


Fig. 5 : Composition of the Si superficial layer

After etching, fluorine and oxygen atoms are present on the silicon surface, carbon is observed only for  $CF_4$  etching. Up to 20%  $O_2$  the silicon surface is observed to be clean, the Si 2p spectrum shows an intense substrate contribution  $Si^0$  (fig. 4), some  $Si^I$  species due to Si - F and Si - O bonds are present. As the gas mixture is enriched in  $O_2$ , the growth of a superficial layer containing  $SiO_xF_y$  species is observed (fig. 6).

The cleanest surface is obtained for 20%  $O_2$ , corresponding to a high etch rate and a minimum thickness for the superficial layer. The calculation of this thickness is based on the ratio of the sum of the  $Si^I$  to  $Si^{IV}$  contributions over the  $Si^0$  substrate contribution.

The elemental composition of this layer changes gradually from  $SiF_2$  (0%  $O_2$ ) to  $SiOF_2$  (40-60%  $O_2$ ) and to  $SiOF$  (80%  $O_2$ ) (fig. 5). The amount of oxygen in the layer is found to be constant above 20%  $O_2$  whereas the ratio F/O drops from 2 to 1; the growth of this layer corresponds to a change in its composition, fluorine being replaced by oxygen. As shown by OES, MS and etch rate, the formation of the  $SiO_xF_y$  layer results in a slower etching rate.

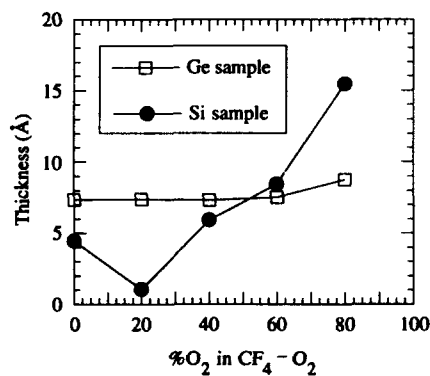


Fig. 6 : Thickness of the superficial layer

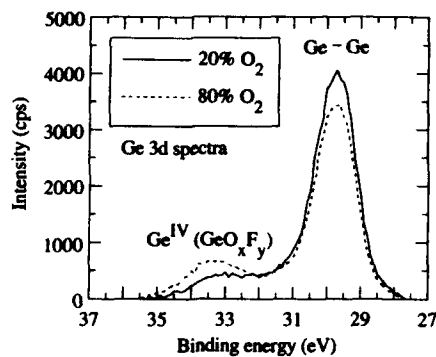


Fig. 7 : XPS spectra of Ge after  $\text{CF}_4 - \text{O}_2$  RIE

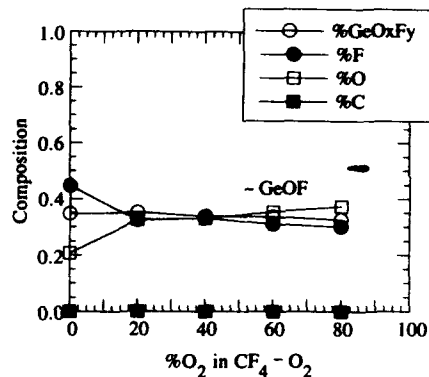


Fig. 8 : Composition of the Ge superficial layer

As soon as  $\text{O}_2$  is added to  $\text{CF}_4$ , various  $\text{GeO}_x\text{F}_y$  species corresponding to oxidation states  $\text{Ge}^{\text{I}}$  to  $\text{Ge}^{\text{IV}}$  are present on the germanium surface (fig. 7). The superficial layer remains constant in thickness (fig. 6) and composition (fig. 8), the F/O ratio being equal to 1. OES, MS and etch rate show that the presence of a  $\text{GeOF}_y$  layer does not inhibit the etching of germanium on the contrary to what is observed for silicon.

**Kinetic model** The etch product of silicon and germanium is respectively  $\text{SiF}_4$  and  $\text{GeF}_4$  and the etchant is atomic fluorine ; so let ER and MS signal be expressed as :

$$\text{ER} \propto \eta \cdot N_F \quad \text{and} \quad \text{MF}_3^+ \propto N_{\text{MF}_4} \propto \eta \cdot N_F$$

with  $\eta$  the surface reactivity,  $N_F$  and  $N_{\text{MF}_4}$  respectively the concentration of fluorine and the concentration of the etch product in the gas phase,  $M$  standing for Si or Ge.  $N_F$  is given by OES through the relation :

$$F/\text{Ar} \propto \frac{N_F}{N} \cdot \frac{N}{N_{\text{Ar}}}$$

with  $N_{\text{Ar}}$  and  $N$  respectively the concentration of argon and the total concentration in the plasma, both being kept constant. Then the ratios  $\frac{\text{ER}}{F/\text{Ar}}$  and  $\frac{\text{MF}_3^+}{F/\text{Ar}}$  are proportional to the reactivity  $\eta$ .

Indeed there is a remarkable qualitative agreement between  $\frac{\text{ER}}{F/\text{Ar}}$  and  $\frac{\text{MF}_3^+}{F/\text{Ar}}$  (fig. 9). MS and ER measurements definitely describe the same phenomenon ; this agrees with the experimental observation that  $\text{SiF}_4$  and  $\text{GeF}_4$  are the only etch product of silicon and germanium in  $\text{CF}_4 - \text{O}_2$ .

A quantitative comparison between  $\eta_{\text{Si}}$  and  $\eta_{\text{Ge}}$  can be done by using the ratio  $\frac{\text{ER}}{F/\text{Ar}}$ .

$\eta_{Ge}$  remains roughly constant, whereas  $\eta_{Si}$  decreases rapidly with addition of  $O_2$  to  $CF_4$ . The selective etching of germanium with respect to silicon is due to a greater surface reactivity. XPS results show that oxygen is present on the surface and thus competes with fluorine to occupy vacant sites on the surface. Moreover this competition changes the surface composition for silicon whereas it has no effect for germanium. Using a reasoning similar to that of Mogab<sup>4</sup>,  $\eta$  can be expressed as :

$$\eta = \frac{\eta'}{1 + C \cdot \frac{O/Ar}{F/Ar}}$$

with  $\eta'$  the intrinsic reactivity depending only on the temperature and  $C$  a constant including the ratio of the oxygen adsorption constant on the surface over the desorption constant.

Plotting ER against  $F/Ar$  gives the dependency of the etch rate on the fluorine concentration (fig. 10), in brackets are indicated the various percentages of  $O_2$  in the gas mixture. A linear relation is observed for germanium since  $\eta_{Ge}$  is constant, for silicon the loop shaped curve observed denotes a decreasing  $\eta_{Si}$  as the gas mixture gets richer in  $O_2$ . The consistency of the model can be tested by verifying that the plot of  $\frac{F/Ar}{ER}$  against  $\frac{O/Ar}{F/Ar}$  is linear (fig. 11). The model is thus valid for silicon ; concerning germanium, no dependence of  $\frac{F/Ar}{ER}$  on  $\frac{O/Ar}{F/Ar}$  is observed since  $\eta_{Ge}$  is constant.

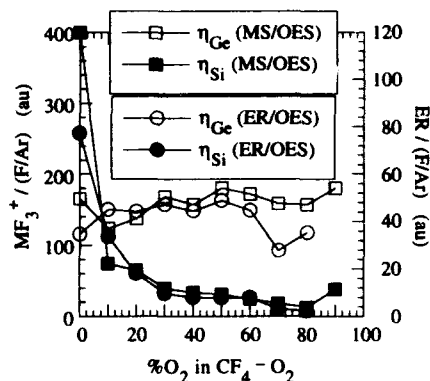


Fig. 9 : Surface reactivity (arbitrary units) of Si and Ge

expressed as  $\frac{ER}{F/Ar}$  and  $\frac{MF_3^+}{F/Ar}$

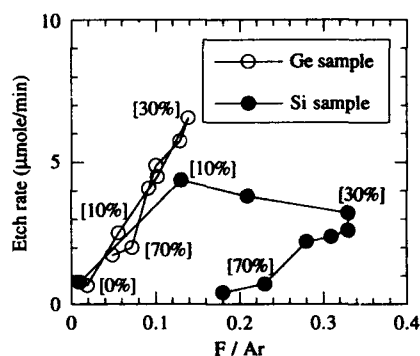


Fig. 10 : Etch rates in function of  $F/Ar$

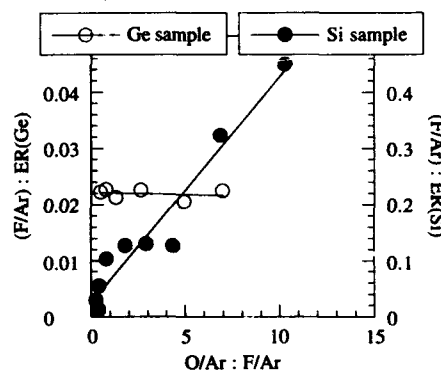


Fig. 11 :  $\frac{F/Ar}{ER}$  in function of  $\frac{O/Ar}{F/Ar}$

**Discussion** Under our experimental conditions germanium etching in  $\text{CF}_4 - \text{O}_2$  behaves in an ideal manner : the etch rate is strictly proportional to the fluorine concentration in the plasma. The main effect of the addition of oxygen to  $\text{CF}_4$  is the change of fluorine concentration in the gas. This enables to adjust the germanium etch rate by varying the gas mixture. The addition of oxygen has no or little effect on the chemical composition of the germanium surface ; there is no competition between oxygen and fluorine on the surface for this material, or, more exactly, the competition mechanism does not depend upon the oxygen concentration. This means that the oxygen desorption is faster than the adsorption. Such an ideal behaviour is not observed under the same experimental conditions in  $\text{SF}_6 - \text{O}_2$ , since then  $\eta_{\text{Ge}}$  decreases with the addition of  $\text{O}_2$ <sup>3</sup>.

We believe the ion bombardment - much more energetic in  $\text{CF}_4 - \text{O}_2$  than in  $\text{SF}_6 - \text{O}_2$  - is responsible for this major difference between the two plasmas ; in particular energetic ions could stimulate surface mechanisms of active species such as surface mobility, desorption, and diffusion through the superficial layer.

Silicon etching in  $\text{CF}_4 - \text{O}_2$  is controlled by the competition between oxygen and fluorine at the silicon surface. The adsorption of oxygen leads to the growth of a  $\text{SiO}_x\text{F}_y$  layer limiting the silicon etching. The ion bombardment which is the same for silicon and germanium appears to be ineffective to remove this blocking layer. The explanation for this different behaviour between silicon and germanium is necessarily in relation with the material itself.

Before etching, the native oxide on germanium is four times thicker than on silicon, indicating that silicon oxide is a much more efficient barrier to the diffusion of active species than germanium oxide is. During the etching the  $\text{GeO}_x\text{F}_y$  and  $\text{SiO}_x\text{F}_y$  layers are believed to have a similar behaviour to the native oxides, the  $\text{GeO}_x\text{F}_y$  layer being more permeable to the active species than the  $\text{SiO}_x\text{F}_y$  layer. The Si - O bond is stronger than the Ge - O bond and more covalent, so its removal with fluorine needs a higher activation energy. Finally the thermal conductivity of silicon is roughly twice that of germanium, so locally the surface temperature on germanium could reach higher values than on silicon, again this would enhance surface mobility, desorption, and substitution of fluorine to oxygen on the germanium surface.

## REFERENCES

1. G.S. Oehrlein, T.D. Bestwick, O.L. Jones, M.A. Jaso, J.L. Lindström, J. Electrochem. Soc. **138**, 1443 (1991).
2. G.S. Oehrlein, G.M.W. Kroesen, E. de Frésart, Y. Zhang, T.D. Bestwick, J. Vac. Sci. Technol. **A9**, 768 (1991).
3. Ch. Cardinaud, A. Campo, G. Turban, Proc. 11<sup>th</sup> Int. Symp. Plasma Chem. 903 (1993).
4. C.J. Mogab, A.C. Adams, D.L. Flamm, J. Appl. Phys. **49**, 3796 (1978).

## REAL-TIME THERMO-MECHANICAL PROPERTY EVALUATION OF THIN FILMS

JOHN A. ROGERS AND K. A. NELSON  
Massachusetts Institute of Technology, Department of Chemistry, Cambridge, MA 02139

### ABSTRACT

We describe an experimental method capable of evaluating the elastic and loss moduli and the thermal diffusivity in thin films. The versatility of the technique is demonstrated with data scans from several films of technological interest.

### INTRODUCTION

Materials development, particularly in the area of thin films, has become the driving force for advances in many technologies. In order to optimize fabrication techniques, it is important to have a flexible method to characterize these materials that has real-time nondestructive and *in situ* capabilities. Recently, we showed how to characterize unsupported and silicon-supported polyimide films with a novel technique that is noncontact, nondestructive, has real-time ( $\sim$ ms) data acquisition rates, and high ( $\sim 50 \mu\text{m}$ ) spatial resolution<sup>1,2</sup>. The method, known as Impulsive Stimulated Thermal Scattering (ISTS), involves optical excitation and detection of acoustic waveguide modes and thermal disturbances and is based on transient grating methods used in the past<sup>3,4</sup>. The information obtainable from such experiments can be used to determine the elastic and loss moduli as well as the degree of adhesion and the thermal diffusivity.

We start with a description of the technique and the experimental arrangement. We then demonstrate the versatility and capabilities of the method by displaying data collected from a wide variety of materials under various conditions. We first show the sensitivity of the technique by presenting data collected in a single laser shot from thin polyimide films. We then demonstrate the spatial resolution in a study of the tungsten coated 20 micron bevel of a razor blade and we end with a demonstration of how the method can be used to monitor film processing by following the evolution of the thermal and mechanical properties of a polyimide film in real-time as it undergoes cure.

### EXPERIMENTAL APPARATUS

The experimental arrangement used here is very similar to that described previously<sup>2</sup>. A thin film sample is irradiated with two picosecond "excitation" laser pulses derived from a Q-switched mode-locked and cavity dumped YAG laser. Optical absorption followed by rapid nonradiative relaxation leads to the sudden ("impulsive") formation of a temperature grating which images the optical interference pattern. This grating pattern is characterized by a scattering wavevector  $q$ , whose magnitude is determined by the crossing angle between the excitation pulses. Thermal expansion following this mild heating results in counterpropagating acoustic waves with wavevectors  $\pm q$  (the transient response) and a steady-state density modulation and surface corrugation which persists until thermal diffusion returns the system to equilibrium. The damped acoustic oscillations and subsequent thermal diffusion which occur following this optical excitation are observed in real-time by monitoring the time-dependent diffraction of a continuous wave probe beam derived from an argon ion laser with a fast photodiode and transient digitizing oscilloscope<sup>2</sup>.



## DEMONSTRATION OF EXPERIMENTAL SENSITIVITY AND RAPID DATA ACQUISITION TIMES

The high sensitivity of the ISTS technique results from background free detection of signal and the fact that the entire material response is monitored with every shot of the laser.

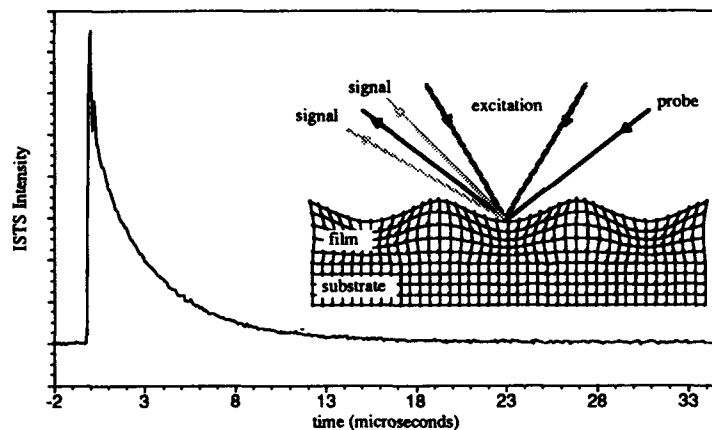
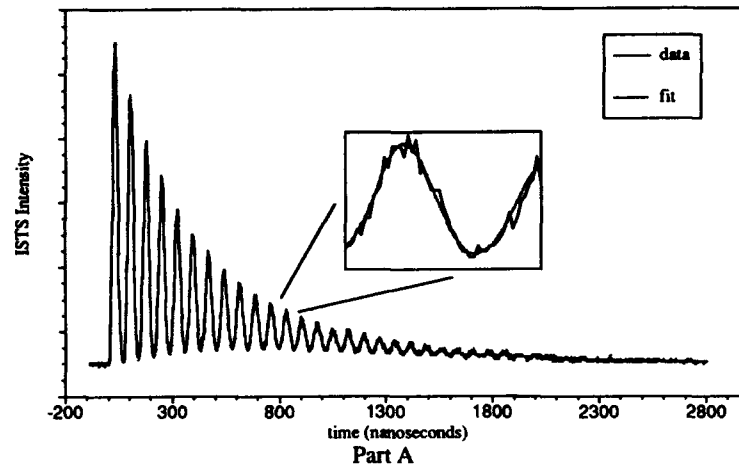


Figure 1: ISTS data from an a 3.15 micron unsupported sample of Dupont's PI2555 (BTDA/ODA/MPD). The upper trace shows acoustic oscillations and decay which leave diffraction only from the thermal grating. Decay of the thermal grating is illustrated in part B. The inset of part B gives a schematic illustration of the experiment.

These two properties enable routine data collection from a wide variety of samples in a single shot or a very few shots of the laser, resulting in millisecond to second data collection times. To demonstrate this, we show in figure 1 data collected from a 1.56 micron sample

of the polyimide BTDA/ODA/MPD. This data was collected in a single shot of the laser, resulting in a data acquisition time of approximately one millisecond. The upper trace shows acoustic oscillations and decay which occur typically on nanosecond time scales. The lower trace shows gradual decay of signal due to thermal transport both in and out of the plane of the film. Data like that shown in the upper trace enables determination of the elastic and loss moduli, and data like that shown in the lower trace enables determination of the thermal diffusivity.

#### DEMONSTRATION OF HIGH SPATIAL RESOLUTION

This technique also has high spatial resolution. This resolution is in practice limited by the wavelength of the interference grating. In particular, the spot size of the focussed excitation beams must be large enough that the excitation grating pattern is well defined (that is, there must be several interference fringes across the spot). In practice, this sets a resolution limit of tens of microns. To demonstrate this relatively high level of spatial resolution, we show in figure 2 data collected from the 20 micron bevel of a tungsten coated razor blade.

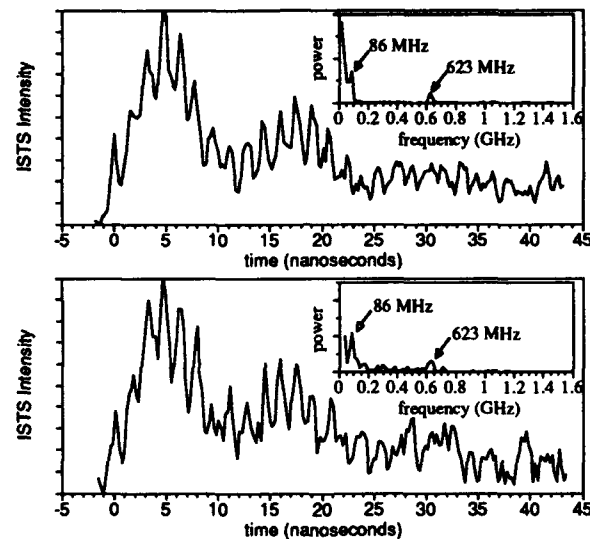
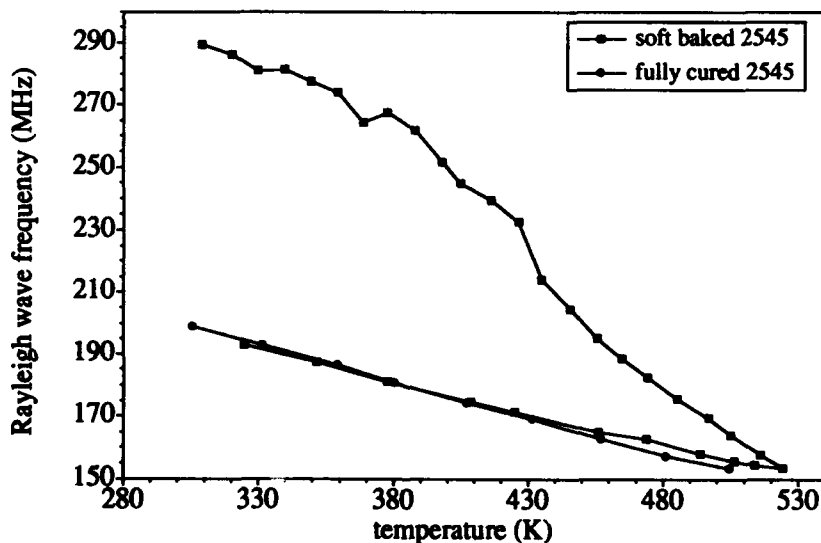


Figure 3: ISTS data collected from the 20 micron bevel of a tungsten coated stainless steel razor blade. For this set of experiments, the low optical quality of the sample necessitated the use of a pulsed probe and lock-in detection.

This figure shows data collected from two different spots on this bevel to illustrate reproducibility of the results. The oscillation frequencies that are observed in the data, and which are displayed in the insets, are determined by the mechanical properties of this tungsten coating. Properties such as these are, of course, of great interest to engineers at Gillette who wish to design high modulus coatings that will enhance wear resistance.

## DEMONSTRATION OF REAL TIME IN SITU PROCESS MONITORING

In this final section, we show how the ISTS technique can be used to follow in real-time the temporal evolution of thermal and mechanical properties during film fabrication and processing. Here we examine the process of polyimide thin film curing from the polyamic acid to the fully cured polymer. The sample consisted of a silicon supported ~6 micron film of Dupont's PMDA/ODA. Curing was carried out in vacuum, and the temperature was ramped at a rate of 2 K/min from room temperature to 525 K. After reaching 525 K, the sample was allowed to cool. During the cure, ISTS measurements were carried out every 10 K (or, equivalently, every 5 minutes). The results are given in figure 3. The data in the first frame of figure 3 show the evolution of the frequency of the Rayleigh wave (a surface acoustic wave excited by our excitation pulses which propagates at the surface of the polymer film) as a function of temperature. Initially we see an overall decrease in this frequency which can at least in part be attributed to the temperature dependence of the modulus of the polyamic acid. This is followed by a change in slope near 430 K which can be tentatively assigned to the onset of imidization. At 525 K we see that the previously uncured polyamic acid is sufficiently imidized so that the mechanical properties that we measure are the same as those in a fully cured film. Note the consistency of the temperature dependent Rayleigh frequency in the studied film and an independently cured film. (See the upper frame of figure 4). In the second frame, we show the in-plane thermal diffusivity determined from the same set of experiments. The behavior of the thermal diffusivity is consistent with that seen in the Rayleigh wave frequency. That is, we see that there is a sharp change in behavior at about 430 K, and by the time the film temperature has reached 525 K or so, the film appears to us to be fully cured. It is clear that information such as this could be quite valuable to those interested in optimization of curing conditions in these films.



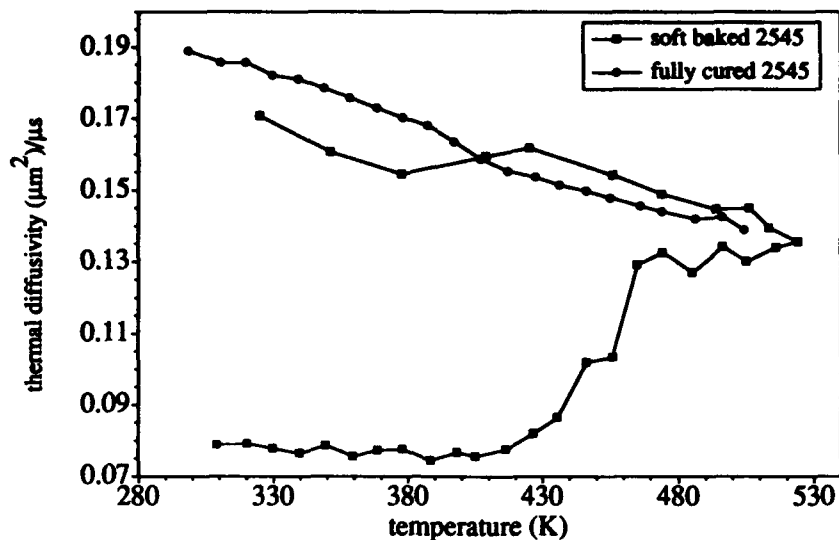


Figure 3: Rayleigh wave frequency and the in-plane thermal diffusivity in a 6 micron sample of Dupont's PI2545 (PMDA/ODA) as a function of temperature as the film undergoes cure and the polyamic acid precursor is converted to polyimide. This sort of information is valuable for process control and optimization of fabrication conditions.

#### SUMMARY AND CONCLUSIONS

We have described an experimental technique suitable for convenient characterization of film mechanical and thermal properties. We showed representative data from several samples under different conditions to illustrate the flexibility of the method.

#### ACKNOWLEDGEMENTS

We wish to thank Gillette for the razor blade sample, and Dupont, Fred Trusell, and David Volfson for the polyimide film samples. This work was partially supported by National Science Foundation Grant No. DMR-9002279 and by the Donors of the Petroleum and by the Donors of the Petroleum Research Fund, administered by the American Chemical Society. We also acknowledge support from the Electronics Packaging Program at MIT. One of the authors (J.A.R.) received support from a National Science Foundation Fellowship.

#### REFERENCE

1. A.R. Duggal, J.A. Rogers, and K.A. Nelson, *J. Appl. Phys.* 72, 2823 (1992); A.R. Duggal, J.A. Rogers, K.A. Nelson, and M. Rothschild, *Appl. Phys. Lett.* 60, 692 (1992); J.A. Rogers, S.M. Thesis, Massachusetts Institute of Technology, (1992).
2. J.A. Rogers and K.A. Nelson, accepted in *J. Appl. Phys.*
3. H.J. Eichler, P. Gunter, and D.W. Pohl, *Laser-Induced Dynamic Gratings* (Springer, Berlin, 1986).
4. K.A. Nelson and M.D. Fayer, *J. Chem. Phys.* 72, 5202 (1980); K.A. Nelson, D.R. Lutz, M.D. Fayer, and L. Madison, *Phys. Rev. B* 24 3261 (1981).

## HYDROCARBON ECR REACTIVE ION ETCHING OF III-V SEMICONDUCTORS WITH SIMS PLASMA PROBE DIAGNOSTICS

DOUGLAS L. MELVILLE, J.G. SIMMONS AND D.A. THOMPSON

McMaster University, Centre For Electrophotonic Materials and Devices, 1280 Main Street West, Hamilton, Ontario, Canada, L8S 4L7

### ABSTRACT

The advantages of *in-situ* SIMS plasma probe diagnostics are highlighted in low pressure hydrocarbon ECR reactive ion etching (RIE) of III-V materials. Three aspects of the RIE process are investigated. First, the dominant ion species in a  $\text{CH}_4/\text{H}_2/\text{Ar}$  plasma are recorded at various chamber pressures, ECR powers,  $\text{CH}_4/(\text{CH}_4+\text{H}_2)$  gas flow ratios and microwave cavity tuning. These studies have improved our understanding of the effects of these parameters on the relative concentrations of reactive precursor species in the plasma and have led to more rapid optimization of the etch system. Secondly, SIMS has been used for identification of reaction products from the III-V surface at the optimized plasma conditions. The Ar diluted mixture gives rise to significant levels of group V hydrides and organometallic compounds and the dominant group III volatile ions have been positively identified as dimethyl species. The third and final aspect reported is the application of volatile product identification to endpoint detection. In  $1\text{cm}^2$  multiple quantum well samples, layers as thin as  $50\text{\AA}$  are easily distinguishable.

### INTRODUCTION

The future development of integrated optoelectronics requires the use of suitable reactive ion etching techniques for the control of lateral dimensions and the fabrication of smooth vertical facets. Hydrocarbon based plasmas have been shown to be effective for etching many In-based III-V semiconductor alloys. However, the etch rate depends on the composition of the alloy and, in multiple quantum well (MQW) structures, this gives rise to "bumps" in the sidewalls at the more etch resistant layers<sup>1</sup>.

Further improvements in this technique will depend heavily upon a more detailed understanding of the physical and chemical mechanisms of the etch. In this work we highlight the advantages of *in-situ* SIMS plasma probe diagnostics for detailed studies of the chemistry of reactive precursor species and volatile reaction products in hydrocarbon ECR RIE of III-V compounds. The application of reaction product identification to endpoint detection is also demonstrated.

### EXPERIMENTAL DETAILS

The ECR reactive ion etch apparatus has been described in detail elsewhere<sup>2</sup>. Briefly, the system consists of a stainless steel chamber and load-lock which is evacuated with a  $1000\text{ls}^{-1}$  turbo pump. The ECR source is a Wavemat MPDR 300 (2.45 GHz) and an r.f. bias (13.56 MHz) could be applied to the stage to control the energy of impinging ions. Process gases include semiconductor grade purity  $\text{CH}_4$ ,  $\text{H}_2$  and Ar. The etch chamber was cleaned with  $\text{O}_2$  prior to every etch run to remove polymer deposits and this was followed by a 10 minute  $\text{H}_2/\text{Ar}$  clean to remove residual oxygen. Samples were masked with spin-on-glass.

Species in the plasma were analyzed with a Hidden Quadrupole Mass Spectrometer (QMS) plasma probe positioned at an angle of 17° with respect to the sample stage and with the probe tip 6cm from the sample. Differential pumping of the QMS through a 250micron diameter aperture gave operating pressures of less than 10<sup>-4</sup> Torr for RIE chamber pressures up to 20mTorr.

## EXPERIMENTAL RESULTS AND DISCUSSION

In part 1 of this section, we relate precursor ions in the plasma to etch characteristics obtained during system optimization. Part 2 investigates the volatile products in hydrocarbon etching of InP and part 3 demonstrates the application of volatile product identification to endpoint detection.

### 1. Optimization Of Etch Parameters

System optimization has been carried out by studying etch profile characteristics and mass spectra data as a function of total pressure, ECR power, gas flow ratio and microwave cavity tuning. Initially, the effect of varying the total pressure was investigated with other parameters held constant at 80W ECR power, 50W r.f. power (-200V bias) and flow rates of 2.8 sccm CH<sub>4</sub>, 18 sccm H<sub>2</sub> and 8 sccm Ar. Figure 1 shows that a clean etch profile was produced for samples etched at a total pressure of 3.5mTorr. At 10mTorr, however, micromasking occurred on the sample surface, particularly along the sidewalls. These "needle-like" features are all the same height, suggesting that they were formed at the start of the etch. The effects of increasing pressure in low pressure ECR hydrocarbon etching of InP have also been reported by Pearton *et al*<sup>3</sup>. They observed increasing polymer deposition on the surface with increasing pressure and above 30mTorr surfaces were covered with a thick polymer film. It is likely, therefore, that the features in Fig. 1 result from preferential deposition of carbon species on residue accumulations

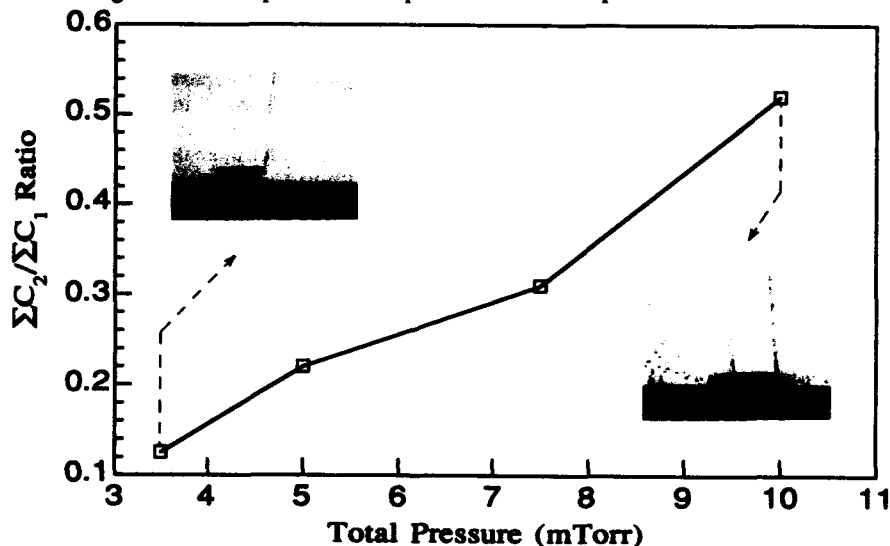


Figure 1. Etch profiles for samples prepared at 3.5mTorr and 10mTorr. Also shown is the ratio of ΣC<sub>2</sub> ions to ΣC<sub>1</sub> ions recorded in this pressure range.

left during preparation of the mask, particularly along the sidewalls.

It is interesting to consider what plasma species give rise to preferential deposition. Fig. 1 shows  $\Sigma C_2/\Sigma C_1$  ion ratio as a function of pressure, where  $C_1$  ions are  $CH^+$ ,  $CH_2^+$ ,  $CH_3^+$ ,  $CH_4^+$  and  $CH_5^+$  species and  $C_2$  ions are  $C_2H^+$ ,  $C_2H_2^+$ ,  $C_2H_3^+$ ,  $C_2H_4^+$ ,  $C_2H_5^+$  and  $C_2H_6^+$  species. As the pressure increases from 3.5 mTorr to 10 mTorr, the  $\Sigma C_2/\Sigma C_1$  ratio increases from 0.125 to 0.5. Clearly, polymer deposition is directly related to an increasing proportion of  $C_2$  ions and it is likely that these species are produced at higher pressures from gas phase polymerisation<sup>4</sup>.

The effect of varying the ECR power has been investigated for a constant pressure of 3.5 mTorr and other parameters held constant as before. In Fig. 2, the etch profiles show a dramatic increase in surface roughness as the ECR power is increased from 80W to 160W. The etch rate was also found to increase from 350 Åmin<sup>-1</sup> to 500 Åmin<sup>-1</sup> over this range. This trend may be explained from consideration of the SIMS data shown in the same figure. Positive ion mass spectra were recorded during etching and the percentage abundance of  $\Sigma H$  and  $\Sigma C_1$  ions have been plotted at each power, where H includes  $H^+$ ,  $H_2^+$  and  $H_3^+$  species. As the ECR power increases, the  $\Sigma H$  ion abundance rises dramatically and likely causes preferential removal of P from the InP surface resulting in In droplet formation. Chang *et al*<sup>5</sup> observed similar droplets during  $H_2$  RIE of InP.

Attempts have been made to remove these In droplets at 160W ECR power by increasing the proportion of methyl species in the plasma. The hope was to increase the formation of the volatile group III methyl and dimethyl species and thereby improve the surface morphology while maintaining high etch rates. Figure 3 shows the etch profiles for samples etched at 160W ECR power and  $CH_4/(CH_4+H_2)$  flow ratios ranging from 13% (as in Fig. 2) to 100%. The % ion abundance of  $\Sigma C_1$  ions and  $\Sigma H$  ions are also plotted in Fig. 3. As the flow ratio increases from 13% to 100%, the  $\Sigma H$  abundance reduces from 60% to 16% and the  $\Sigma C_1$  abundance increases from 28% to 64%. It is interesting to note that the highest  $\Sigma C_1$  % ion abundance (no  $H_2$  dilution) gave rise to the fastest the etch rates of 1200 Åmin<sup>-1</sup> and much smoother surface morphologies. These results suggest that smooth etching of InP requires balanced removal rates of In and P and that the etching is rate limited by the formation and/or removal of methyl-indium species.

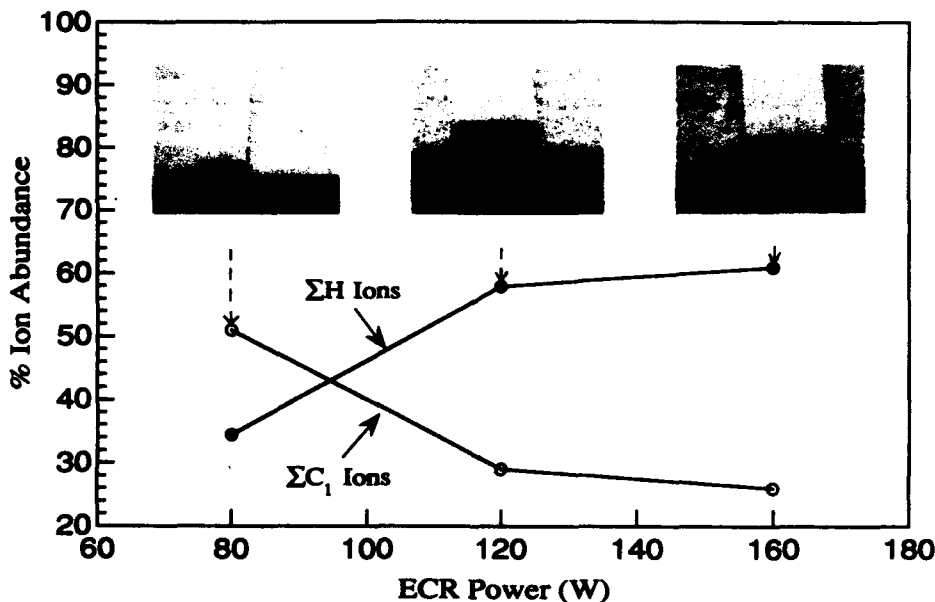


Figure2. Etch profiles for samples prepared at 80W, 120W and 160W ECR power and the corresponding % ion abundance of  $\Sigma H$  ions and  $\Sigma C_1$  ions at these powers.

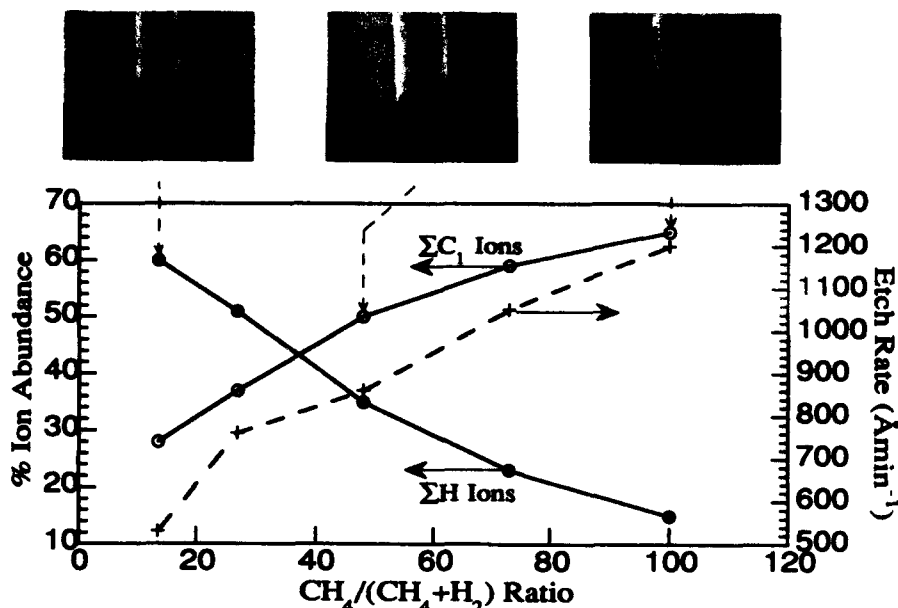


Figure 3. Etch profiles for samples prepared at  $\text{CH}_4/(\text{CH}_4+\text{H}_2)$  flow ratios ranging from 10% to 100%, 160W ECR, Ar flow rate of 8sccm and constant total flow of 28.8sccm. Also shown is the % ion abundance of  $\Sigma\text{H}$  ions and  $\Sigma\text{C}_1$  ions at these flow ratios.

Finally, InP etching has been carried out at the same system parameters as the sample prepared at 13%  $\text{CH}_4/(\text{CH}_4+\text{H}_2)$  flow ratio in Fig. 3 except that the position of the microwave tuning piston was shifted 1.5cm to a new stable resonance position. The surface morphology and the reactive ion precursor distributions were similar to the sample prepared at 27%  $\text{CH}_4/(\text{CH}_4+\text{H}_2)$  flow ratio in Fig. 3. These results show that specific microwave cavity modes produce quite different relative concentrations of ion species and, therefore, different etch characteristics. Also, SIMS studies of ion distributions have shown that, for a given r.f. bias, it may be possible to make predictions about etched surface properties based on knowledge of the relative concentrations of ion species.

## 2. Identification Of Volatile Products

The volatile products evolved during ECR hydrocarbon etching of InP have been studied in detail. Figure 4 shows mass spectra recorded from a  $\text{CH}_4/\text{H}_2/\text{Ar}$  plasma with and without InP in the chamber. The data obtained without InP in the chamber will be referred to as background. In Fig. 4a, phosphine peaks appear well above background at mass 32, 33 and 34 corresponding to  $\text{PH}^+$ ,  $\text{PH}_2^+$  and  $\text{PH}_3^+$  ions. The mass 47 and 48 peaks in Fig. 4b are attributed to the primary phosphines  $\text{HPCH}_3^+$  and  $\text{H}_2\text{PCH}_3^+$ , respectively. The signal at mass 46 is either the methyl phosphine fragment  $\text{PCH}_3^+$  or perhaps the methylene phosphine isomer  $\text{HPCH}_2^+$  and the mass 45 peak is labeled as  $\text{PCH}_2^+$ . Smaller signals (not shown) appear above background at masses 60, 61, 62 and 76 and are assigned as  $(\text{C}_2\text{H}_5)\text{P}^+$ ,  $(\text{CH}_3)_2\text{P}^+$ ,  $\text{HP}(\text{CH}_3)_2^+$  and  $\text{P}(\text{CH}_3)_3^+$ , respectively.



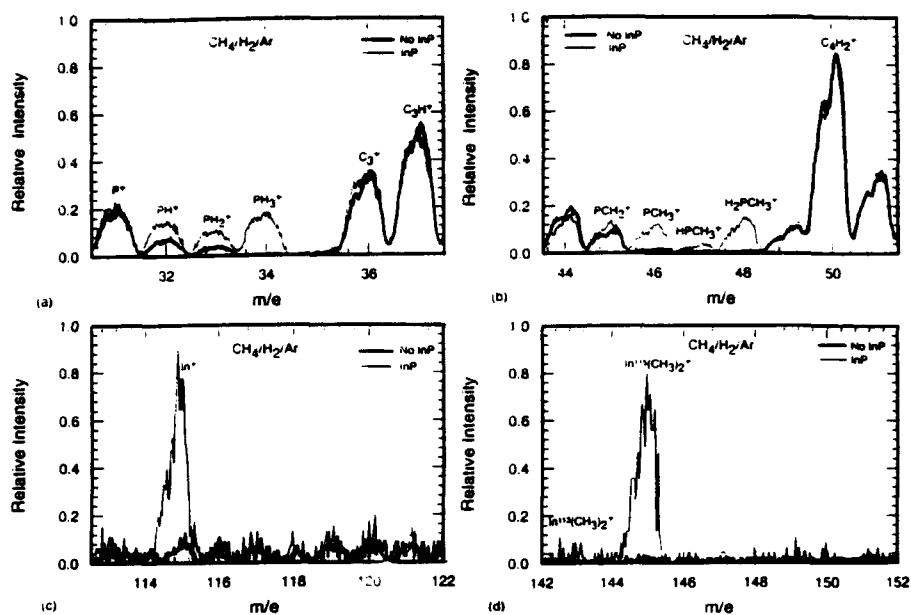


Figure 4. Detailed mass spectra profiles of a  $\text{CH}_4/\text{H}_2/\text{Ar}$  plasma with and without InP in the chamber in the mass ranges a) 31-37, b) 44-51, c) 112-122, and d) 142-152.

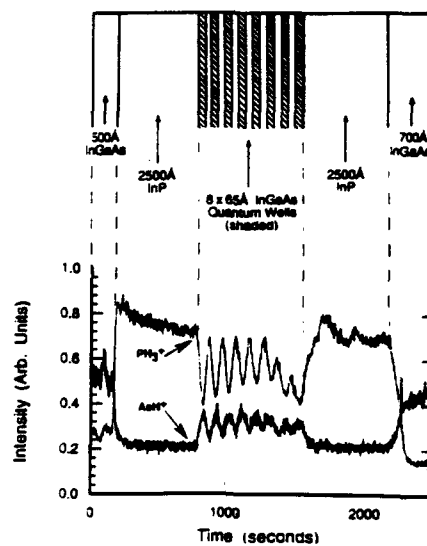


Figure 5. Depth profile of  $\text{PH}_3^+$  and  $\text{AsH}^+$  ions monitored during etching of an InP/InGaAs multiple quantum well structure.

In an attempt to identify the In reaction products, mass spectra have also been recorded in the mass range 112 to 162. The mass spectrometer sensitivity was increased to 5 times the level in Figs. 4a and 4b and the renormalised data for dominant peaks in this mass range are shown in Figs. 4c and 4d. The  $\text{In}^+$  peak is clearly visible above background at mass 115 and, more importantly, a distinct peak is observed at mass 145 attributable to  $\text{In}(\text{CH}_3)_2^+$  ions. Further peaks have been found at mass 130 and 131 (not shown), indicating the presence of  $\text{InCH}_3^+$  and  $\text{HInCH}_3^+$  species. No signal is observed for the parent trimethylindium (TMI) molecule  $\text{In}(\text{CH}_3)_3^+$  at mass 160 and this result is consistent with mass spectra data recorded by workers in the field of MOCVD<sup>6</sup> which clearly show that the main peak in the cracking pattern of TMI is  $\text{In}(\text{CH}_3)_2^+$ .

### 3. Endpoint Detection

In this section we demonstrate the application of volatile species identification to endpoint detection during etching of the InP/InGaAs multiple quantum well shown in Fig. 5. Etch parameters were 80W ECR power, 40W r.f. power (-160V), 2.2mTorr and flow rates of 2.8sccm  $\text{CH}_4$ , 18sccm  $\text{H}_2$  and 8sccm Ar. The  $\text{PH}_3^+$  and  $\text{AsH}^+$  ions were monitored during of etching and the resulting depth profiles are shown in Fig. 5. The eight 65Å InGaAs layers are easily distinguishable from peaks in the  $\text{AsH}^+$  and troughs in the  $\text{PH}_3^+$  signals.

## CONCLUSIONS

These results demonstrate the value of *in-situ* SIMS diagnostics in low pressure ECR reactive ion etching. The equipment facilitates rapid optimization of system parameters by providing detailed information about the reactive precursor chemistries in the plasma. In addition, the reaction chemistry of hydrocarbon RIE of III-V materials has been clarified and, in particular, the group III volatile product has been identified for the first time. Finally, volatile product identification has an important application in endpoint detection and quantum wells of 65Å thickness are easily resolved for sample areas of  $1\text{cm}^2$ .

## ACKNOWLEDGMENTS

We would like to thank Dr B. J. Robinson for supplying the MBE grown sample for endpoint detection. Funding was supplied by the Canadian Institute For Telecommunications Research.

## REFERENCES

1. S.M. Ojha and S.J. Clements, Proceedings of the Fifth International Conference on Indium Phosphide and Related Materials, Paris, France, p524, April 1993.
2. D.L. Melville, J.G. Simmons and D.A. Thompson, J. Vac. Sci. Technol. B, **11**, 1-8, (1993).
3. S.J. Pearton, T.A. Keel, A. Katz and F. Ren, Semicond. Sci. Technol., **8**, 1889-1896, (1993).
4. W. Zhang and Y. Catherine, Surf. Coat. Tech., **47**, 69, (1991).
5. R.P.H. Chang, C.C. Chang, and S. Darack, J. Vac. Sci. Technol., **20** (1), 45, (1982).
6. N.I. Buchan, C.A. Larsen, and G.B. Stringfellow, J. Crystal Growth, **92**, p591, (1988).

## IN-SITU MONITORING BY MASS SPECTROMETRY FOR GaAs ETCHED WITH AN ELECTRON CYCLOTRON RESONANCE SOURCE

D. J. KAHALAN AND S. W. PANG

Solid State Electronics Laboratory, Department of Electrical Engineering and Computer Science,  
The University of Michigan, Ann Arbor, MI 48109-2122

### Abstract

Quadrupole mass spectrometry (QMS) has been used as an *in-situ* diagnostic technique for GaAs etched with an electron cyclotron resonance source. Changes in the detected signal intensities for reactive species and etch products have been related to corresponding changes in the etch rate as several process parameters were varied. The detected  $^{75}\text{As}^+$  and to a lesser degree,  $^{35}\text{Cl}^+$  and  $^{70}\text{Cl}_2^+$ , were observed to follow etch rate as microwave power, rf power, source to sample distance, temperature, and pressure were varied. The self-induced dc bias ( $V_{dc}$ ) determines the etch rate dependence on etch time. The time delay before saturation of the monitored  $^{75}\text{As}^+$  signal corresponding to a constant etch rate is inversely proportional to  $|V_{dc}|$ . The addition of  $\text{N}_2/\text{O}_2$  in a 4:1 ratio to constitute 15% of the total discharge resulted in a 95% decrease in the intensity of the monitored  $^{75}\text{As}^+$  signal. The measured etch rate decreased by 75%.

### Introduction

Semiconductor devices with continuously decreasing feature sizes require precise control of etch rate, profile, and selectivity for pattern transfer. Dry etch techniques are often used to provide anisotropic etch profiles; however, etch selectivity may be low and defects may be induced due to ion bombardment. Furthermore, dry etching is found to be extremely sensitive to system conditions such as drifts in instruments or deposition on chamber walls. Therefore, a non-invasive and sensitive monitoring technique is needed to minimize run-to-run variations for dry etching to meet the demands imposed by stringent requirements for linewidth control.

Quadrupole mass spectrometry (QMS) has been used to monitor the relative concentrations of reactive species and volatile etch products during the etching of III-V materials.[1-5] We have used QMS as an *in-situ* diagnostic technique for GaAs etched with a  $\text{Cl}_2/\text{Ar}$  discharge generated by an electron cyclotron resonance (ECR) source. Etching with an ECR source provides a discharge with high ion density while maintaining low ion energy.[6-8] The concentrations of etch products and reactive species under different etch conditions have been monitored and correlated to the etch rate.

### Experimental

All etching experiments were conducted in a multipolar ECR source.[9] A sliding short and adjustable input probe allow the 2.45 GHz microwave power to be coupled into the cavity with optimal impedance matching. Resistive heating and liquid nitrogen flow allow process temperatures to be controlled over the range of -130 to 400°C. Source to sample distance can be varied with a moveable 13.56 MHz rf-powered stage while operating pressures were set by a throttled 1500 l/s turbomolecular pump. An additional magnetic confinement ring is located below the ECR source to reduce recombination of reactive species with the chamber walls. Process gases are introduced into the chamber through an adjustable gas ring located around the stage and an annular ring located at the base of the quartz dome. Base pressure for the load locked ECR source was maintained below  $5 \times 10^{-6}$  Torr.

A Spectramass Dataquad QMS mounted 66 cm downstream from the plasma chamber wall was used to monitor etch products and reactive species present within the plasma. The mass spectrometer was differentially pumped by a 80 l/s turbomolecular pump with further pressure

reduction achieved by an orifice that is 2 mm in diameter. Base pressure at the mass spectrometer sampling head was kept below  $1 \times 10^{-6}$  Torr. The ionizer electron energy used was 70 eV.

A Ni etch mask was patterned on the materials through standard optical lithography. Scanning electron microscopy was used to evaluate surface morphology while stylus profilometry was used to measure etch rates following the removal of the Ni etch mask with HCl.

## Results and Discussion

Microwave power and rf power were varied over the ranges of 0 to 1500 W and 25 to 200 W, respectively, to investigate the ability of the mass spectrometer to relate etch rate with detected signals of reactive species and etch products in the chamber. Correlation between changes in the detected signal intensities and changes in the measured etch rate were also investigated for varying source to sample distance (8 to 27 cm), temperature (25 to 350 °C), and pressure (1 to 5 mTorr). The samples were typically etched with a  $\text{Cl}_2/\text{Ar}$  discharge using a flow ratio of 4/24 sccm at 2 mTorr and 13 cm below the ECR source to provide smooth surface morphology. As illustrated in Fig. 1, as microwave power increases, the intensity of  $^{75}\text{As}^+$  signal increases corresponding to the faster observed etching of GaAs. The increased etch rate is due to the enhanced dissociation of the  $\text{Cl}_2$  gas at higher microwave power. Etch products such as  $\text{GaCl}_x$  and  $\text{AsCl}_x$  may be dissociated in the discharge by the microwave power, and to a lesser degree by the rf power before reaching the ionizer. The intensities of  $^{40}\text{Ar}^+$  was found to be independent of microwave power. Even though the concentration of  $\text{Ar}^+$  in the plasma is expected to increase with microwave power, the detected  $^{40}\text{Ar}^+$  signal intensity remained constant since the mass spectrometer was monitoring the total concentration of Ar (ions as well as neutrals) and not just Ar ions. The  $^{70}\text{Cl}_2^+$  and  $^{35}\text{Cl}^+$  signals were observed to decrease slightly as microwave power increased. An overabundance of  $\text{Cl}^+$  ions is produced by the ECR source, and therefore, changes in the  $^{70}\text{Cl}_2^+$  and  $^{35}\text{Cl}^+$  signals are less sensitive to changes in etch rate. Nonetheless, the onset of depletion of reactive species is suggested by the slight decrease in the chlorine signals as etch rate increases substantially over the large range of microwave power.

From Fig. 2, the GaAs etch rate is observed to increase from 86 to 171 nm/min as rf power was increased over the range of 25 to 250 W. The ability of the  $^{75}\text{As}^+$  signal to follow the slight increase in etch rate demonstrates the sensitivity of *in-situ* monitoring by QMS. Faster

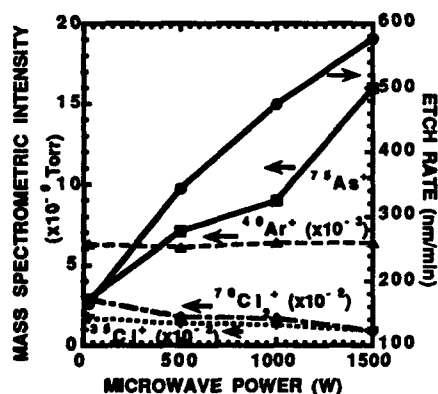


Fig. 1. Effects of microwave power on spectral intensities and etch rate. The samples were etched with 4/24 sccm  $\text{Cl}_2/\text{Ar}$  and 250 W rf power at 2 mTorr, 13 cm source distance, and 25°C.

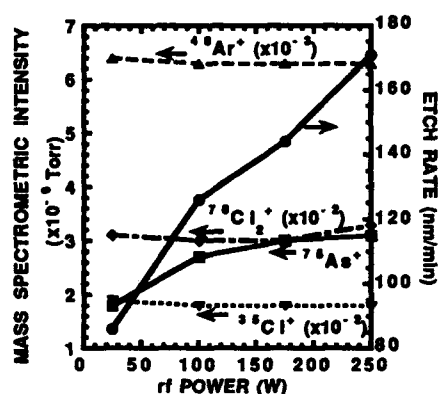


Fig. 2. Sensitivity of  $^{75}\text{As}^+$  to etch rate for increasing rf power. The etch conditions are similar to those shown in Fig. 1 with 50 W microwave power.

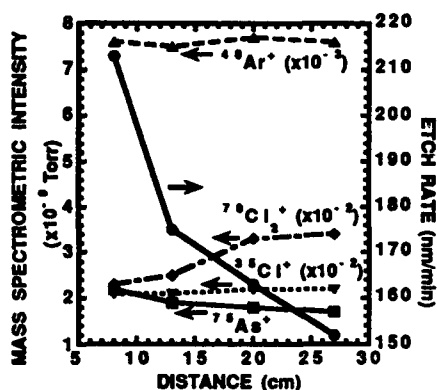


Fig. 3. Mass spectral intensities and etch rate for GaAs as a function of source to sample distance. The etch conditions are similar to those shown in Fig. 1 with 50 W microwave power.

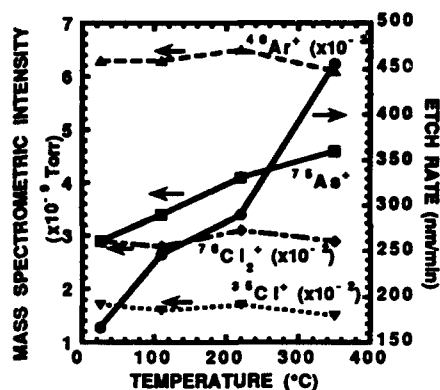


Fig. 4. Correspondence between mass spectral intensities and etch rate for increasing temperature. The samples were etched under the same conditions as shown in Fig. 1 with 50 W microwave power.

etch rates for increasing rf power indicates that ion energy enhances GaAs etching. The mass spectrometer is unaffected by substrate biasing as evidenced by the constant  $^{40}\text{Ar}^+$  signal over the range of applied rf power. The chlorine signals were nearly independent of rf power. This suggests that the increase in etch rate at higher rf power does not significantly deplete the chlorine concentration.

The differentially pumped QMS is connected to a flange on the processing chamber located 27 cm below the ECR source. The decreasing  $^{75}\text{As}^+$  signal and etch rate with source distance shown in Fig. 3 demonstrates that  $^{75}\text{As}^+$  can follow the etch rate without being affected by stage position. The self-induced bias voltages ( $|V_{dc}|$ ) increases with source distance due to the increased grounded area exposed to the plasma. It was 260 V at 8 cm and increased to 380 V at 27 cm. The fact that etch rate continues to decrease with source distance despite the increase in  $|V_{dc}|$  indicates that GaAs etching is limited by the reactive species and not by the ion energy under these etch conditions.

Higher temperatures are typically used in dry etching to promote the desorption of group III etch products. The increasing intensity of the  $^{75}\text{As}^+$  signal follows large increases in etch rate as a function of temperature as illustrated in Fig. 4. Faster etch rate is obtained at higher temperature since increased temperature is expected to increase the reactivity of chlorine species at the GaAs surface as well as promote the desorption of etch products. As temperature was increased from 25 to 350°C, the  $^{75}\text{As}^+$  signal increased from 2.9 to  $4.6 \times 10^{-9}$  Torr, corresponding to an increase in etch rate from 166 to 456 nm/min.

As shown in Fig. 5, the increasing etch rate as a function of pressure over the range of 1 to 5 mTorr is followed by a corresponding increase in the monitored  $^{75}\text{As}^+$  signal. Since the mass spectrometer is sensitive to the partial pressure of species present within the processing chamber, the  $^{75}\text{As}^+$ ,  $^{70}\text{Cl}_2^+$ , and  $^{35}\text{Cl}^+$  signals have been normalized with respect to the  $^{40}\text{Ar}^+$  signal to account for the increased concentrations resulting from increased pressure. The increased etch rate may be due to the higher concentrations of reactive species as well as the higher ion energy at higher pressure. As pressure was increased from 1 to 5 mTorr,  $|V_{dc}|$  also increased from 220 to 350 V.

Induction time, defined to be the time delay between the initiation of the plasma and the increase in the monitored  $^{75}\text{As}^+$  signal, was examined as a function of  $|V_{dc}|$ . The GaAs sample was etched at 2 mTorr with  $\text{Cl}_2/\text{Ar}$  at 4/24 sccm using 50 W of microwave power. The temporal resolution of the QMS is 1 sec. To maintain the same condition before etching, the GaAs samples were rinsed in DI water and exposed to an  $\text{O}_2$  plasma at 250 mTorr with 80 W rf

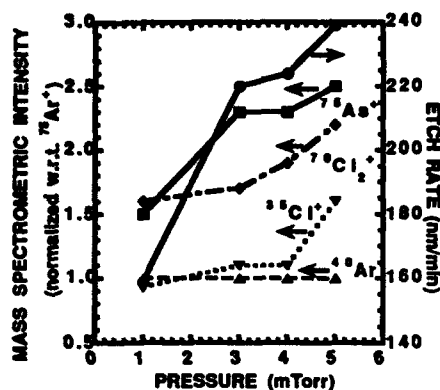


Fig. 5. Mass spectral intensity and etch rate for increasing pressure. Samples were etched with the same conditions as shown in Fig. 1 with 50 W microwave power.

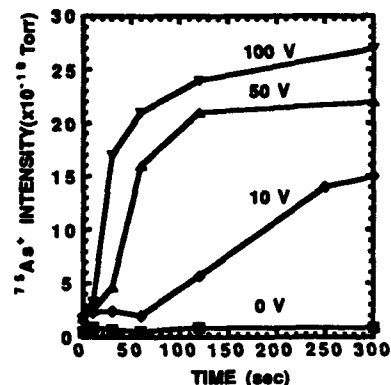


Fig. 6. Time delay for As<sup>+</sup> saturation is inversely proportional to  $|V_{dc}|$ . Samples were etched at 13 cm, 2 mTorr, and 25 °C with 50 W microwave power and  $|V_{dc}|$  ranging from 10 to 100 V.

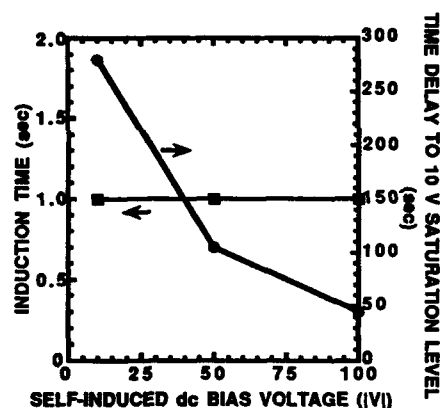


Fig. 7. Effects of  $|V_{dc}|$  on time delay in GaAs etching. Samples were etched with the same conditions as those in Fig. 6.

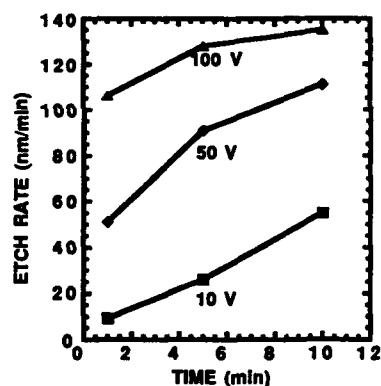


Fig. 8. Etch rate dependence on total etch time and  $|V_{dc}|$ . Samples were etched with the conditions used in Fig. 6.

power for 1 min before each run. The results from Fig. 6 show no increase in the  $^{75}\text{As}^+$  intensity at 0 V, indicating that no etching has occurred in the absence of rf power. However, with  $|V_{dc}|$  as low as 10 V, etching can still proceed without significant time delay, demonstrating the tremendous advantage of the ECR source in generating low energy ions at high density by controlling substrate bias and microwave power independently. The  $^{75}\text{As}^+$  intensity increases more abruptly for higher  $|V_{dc}|$ . These results suggest that the etching initiation is not at issue, but rather the complete removal of the surface layer such as native oxide and hydrocarbons so that the etch rate will remain constant over time. Redeposition of etch products is more significant when low energy ions are used, which also prevents constant etching over time. The results for time delay during the etching of GaAs are summarized in Fig. 7. The induction time was

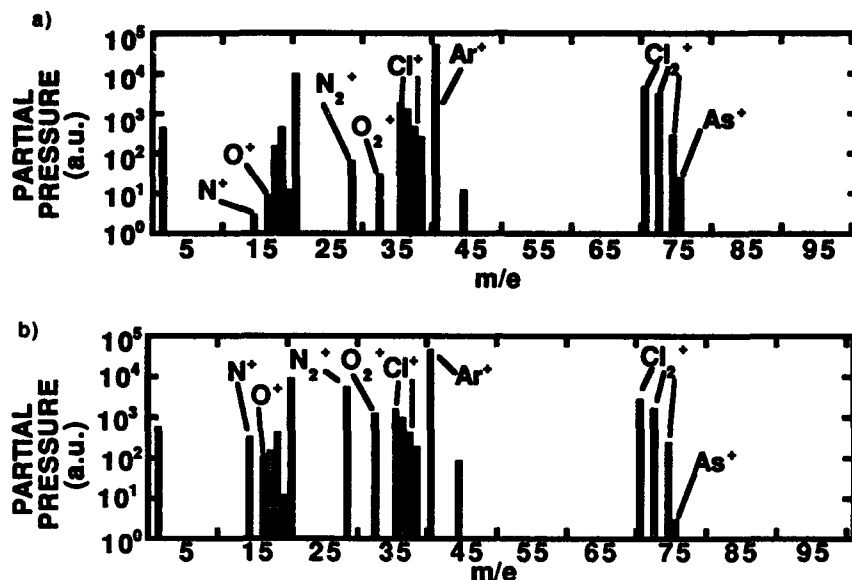


Fig. 9. Samples were etched with conditions shown in Fig. 1. Fig 9a) shows the mass spectra with no  $N_2/O_2$  addition. Fig 9b) shows the mass spectra with  $N_2/O_2$  added at 4/1 sccm.

independent of  $|V_{dc}|$ , and remained within 1 sec over the range of 10 to 100 V. However, the time delay to reach a saturated  $^{75}As^+$  signal decreased with increasing  $|V_{dc}|$ . This shows the important role of higher  $|V_{dc}|$  in obtaining a constant etch rate. In Fig. 8, the etch rate is observed to vary significantly as a function of total etch time for 10 V  $|V_{dc}|$ . The time dependent etch rate corresponds to the time delay before the  $^{75}As^+$  signal reaches saturation. At higher  $|V_{dc}|$ , the time delay is shorter to reach a constant etch rate. For samples etched at 100 V, the etch rate remained constant at 135 nm/min for etch times  $\geq 10$  min.

The effects of an air leak were simulated in real time by monitoring the spectra during GaAs etching with  $N_2$  and  $O_2$  introduced into the chamber in a 4:1 ratio. Figures 9a) and 9b) contrast the mass spectra obtained with and without  $N_2/O_2$  addition. For  $N_2/O_2$  constituting 15% of the total flow in a  $Cl_2/Ar$  plasma, the  $^{75}As^+$  signal decreased by 95% and the  $^{70}Cl_2^+$  signal decreased by 40%. The corresponding measured etch rate decreased by 75%. These results suggest that the presence of  $N_2$  and  $O_2$  in the plasma chamber promotes the formation of a nitride or oxide layer which inhibits the overall etch rate. Reactions in the gas phase between dissociated chlorine radicals and nitrogen and oxygen radicals may also deplete the concentration of reactive species available to etch the samples. These results indicate that mass spectrometry is sensitive to changes in chamber conditions such as air leaks. Therefore, the mass spectral signals can be monitored as baselines for process control.

### Summary

Quadrupole mass spectrometry has been used to monitor changes in the concentrations of etch products and reactive species due to corresponding changes in etch rate and plasma conditions. The intensity of the monitored  $^{75}As^+$  signal has been observed to follow etch rate dependence for changes in microwave power, rf power, source to sample distance, temperature, and pressure. The mass spectrometer measures the concentration of ions as well as neutral species, and is therefore not sensitive to changes in the ratio of ion to neutral density as a function of operating conditions. The self-induced dc bias determines the etch rate dependence

on etch time. With  $|V_{dc}|$  as low as 10 V, etching is initiated immediately at 10 sec, but it takes up to 4.5 min to reach a constant etch rate. *In-situ* monitoring with mass spectrometer was also used to examine the effects of a simulated air leak. The  $^{75}\text{As}^+$  signal was observed to decrease by 95% following the addition of  $\text{N}_2$  and  $\text{O}_2$  with a corresponding 75% decrease in the measured etch rate.

#### Acknowledgments

The authors would like to thank K. K. Ko and K. T. Sung for technical assistance. This work was supported by the Advanced Research Projects Agency under contract No. F33615-92-C-5922.

1. R. H. Burton, C. L. Hollien, L. Marchut, S. M. Abys, G. Smolinsky, R.A. Gottscho, *J. Appl. Phys.* **54**, 6663 (1983).
2. K. L. Seaward, N. J. Moll, and D. J. Coulman, *J. Appl. Phys.* **61**, 2358 (1987).
3. A. P. Webb, *Semicond. Sci. Technol.* **2**, 463 (1987).
4. T. R. Hayes, M. A. Dreisbach, P.M. Thomas, W. C. Dautremont-Smith, and L. A. Helmbrook, *J. Vac. Sci. Technol. B* **7**, 1130 (1989).
5. A. P. Webb, *Appl. Surf. Sci.* **63**, 70 (1993).
6. J. Hopwood, D. K. Reinhard, and J. Asumussen, *J. Vac. Sci. Technol. B* **9**, 3521 (1991).
7. S. W. Pang and K.K. Ko, *J. Vac. Sci. Technol. B* **10**, 2703 (1992).
8. S. J. Pearton and W. S. Hobson, *Semicond. Sci. Technol.* **6**, 948 (1987).
9. S. W. Pang, K. T. Sung, and K. K. Ko, *J. Vac. Sci. Technol. B* **10**, 1118 (1992).



## AlGaAs MICROELECTRONIC DEVICE PROCESSING USING AN As CAPPING LAYER

J.K. GREPSTAD,<sup>\*</sup> H. HUSBY,<sup>\*</sup> R.W. BERNSTEIN,<sup>†</sup> and B.-O. FIMLAND<sup>\*</sup>

<sup>\*</sup>Norwegian Institute of Technology, Dept. of Physical Electronics, N-7034 Trondheim, Norway

<sup>†</sup>SINTEF-SI, Dept. of Microelectronics, N-0314 Oslo, Norway

<sup>\*</sup>Present address: University of Toronto, Dept. of Electrical and Computer Engineering, Toronto, Ontario, M5S 1A4, Canada

### ABSTRACT

The case for incorporating an arsenic capping layer in compound semiconductor device processing has been investigated with x-ray photoelectron spectroscopy (XPS), low-energy electron diffraction (LEED) and scanning electron microscopy (SEM). The As cap was found to be stable upon exposure to common processing chemicals, such as acetone, photoresist, developer, and N-methyl-2-pyrrolidone, a common polyimide solvent. A clean, c(4×4)-reconstructed GaAs(001) surface was recovered after thermal desorption of the cap in ultra-high vacuum, for a sample exposed to standard (maskless) photolithography. We also report a new technique for reactive decapping at room temperature, using a beam of hydrogen radicals (H<sup>•</sup>). Pattern definition in the As cap with ~5 μm linewidth was demonstrated, using this technique. However, XPS and SEM data for the H<sup>•</sup>-etched specimens showed clear evidence of superficial gallium (sub)oxide and of As residues along the photoresist mask edges. This novel method of As cap patterning thus needs further refinement, before being useful to III-V device processing.

### INTRODUCTION

Throughout the history of semiconductor development, the close coupling between processing techniques and device improvement (and invention) has time and again been demonstrated. Modern crystal growth techniques, such as molecular beam epitaxy (MBE), have made possible the fabrication of high-speed electronic and optoelectronic devices which capitalize on the power of heterostructures.<sup>1</sup> When exposed to atmosphere or handled in compliance with standard MBE substrate preparation procedures, AlGaAs epilayers inevitably contract superficial carbon and oxygen impurities. Subsequent MBE overgrowth on such surfaces leads to free carrier depletion at the interface, despite thermal cleaning in vacuum prior to this step.<sup>2,3</sup> This carrier depletion contributes a high series resistance, which tends to impair the performance of devices. Novel techniques for interrupting the MBE growth process in order to contact or modify (buried) epilayers, while retaining a high-quality growth-interruption interface, are demanded. Such developments would strongly benefit the fabrication of present and new heterostructure devices.

*In situ* condensation of an As capping layer has been found to provide effective protection of compound semiconductor surfaces against ambient contamination for periods up to several months.<sup>4,5</sup> Moreover, this As passivation efficiently suppresses carrier depletion at interfaces of suspended MBE growth.<sup>6,7</sup> The arsenic cap is conveniently desorbed by annealing in ultra-high vacuum (UHV) environments at a substrate temperature in excess of some 350°C. Clean, reconstructed (Al)GaAs(001) surfaces may now be routinely prepared in this manner. Exploiting this cap for surface passivation purposes in microelectronic and photonic device processing demands a suitable technique for pattern definition in the condensed As layer. Regrettably,

standard photolithography does not lend itself readily to such patterning. The temperature required for thermal As desorption leads to excessive polymerization of photoresist, which renders subsequent removal virtually impossible. The problem at hand may be solved either by using a different mask material, which tolerates curing at temperatures in excess of 350°C, or by inventing a procedure for decapping at reduced temperature, without degrading the quality of the regenerated epilayer surface.

This work reports a detailed study on the durability of the As cap, when exposed to the different photolithographic processing chemicals. Moreover, the case for reactive decapping at reduced temperature, without contaminating or disrupting the recovered (Al)GaAs(001) surface, was examined. Successful patterning of the As cap was achieved by etching in a beam of hydrogen radicals at room temperature (RT), through a mask of positive photoresist on the capping surface.

## EXPERIMENTAL

Arsenic-capped  $\text{Al}_x\text{Ga}_{1-x}\text{As}(001)$  epilayers ( $0 < x < 1$ ) were grown on *n*-type GaAs substrate in a *Varian GenII Modular* MBE-system. Condensation of the protective arsenic layer was accomplished by allowing the wafer to cool in a constant flux of  $\text{As}_2$ . The thickness of the As cap typically varies from 30 nm to 3  $\mu\text{m}$ , dependent on the substrate temperature (20–50°C) at which the procedure is terminated. Further details regarding this capping and the thermal decapping can be found elsewhere.<sup>5</sup>

Four samples were cut from an As-capped wafer and exposed (~15 min) to different photolithographic processing chemicals, i.e., positive photoresist (*Shipley 1800*), developer (*Shipley MF 312*), acetone (the photoresist solvent), and NMP (N-methyl-2-pyrrolidone, a common polyimide solvent). Photosensitive polyimide which may be cured at temperatures up to 450°C, is now available and provides an alternative to photoresist for pattern definition. All treatments

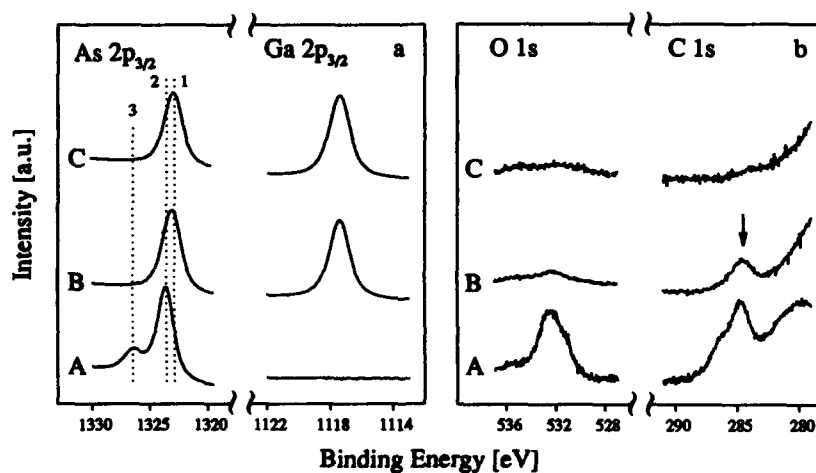


**Fig.1** Core-level photoemission spectra of As-capped GaAs(001) exposed to standard photolithography; (A) as-introduced and (B) after thermal desorption of the processed cap. Spectra (C) shows corresponding data taken on a non-processed reference sample.

were terminated with a rinse in deionized water, and the samples were left to dry in air. A fifth sample was exposed to complete (maskless) photolithography, including curing of the photoresist at 90°C for 35 min and exposure to ultraviolet (UV) for 1½ min.

Different hydrogen treatments, incl. annealing in 1 atm. H<sub>2</sub> gas and exposure to hydrogen ions (H<sub>2</sub><sup>+</sup>) and hydrogen radicals (H<sup>•</sup>), were attempted, to examine the case for reactive As desorption at reduced temperature (RT to 350°C). This processing took place in a *Fisons ESCALAB MkII* spectrometer. "Reactive" decapping at an appreciably reduced temperature was achieved with hydrogen radicals only, and took place by formation of arsenic hydrides, predominantly AsH<sub>3</sub>. The arsine desorption during H<sup>•</sup> etching was monitored with a quadrupole mass spectrometer (*Fisons SX-200*), and the radical beam source (*Oxford Applied Research MPD20A*) was turned off immediately upon observation of a distinct drop in the AsH<sub>3</sub> partial pressure, taken to indicate complete desorption of the As cap.

*In situ* x-ray photoelectron spectroscopy (XPS) and low energy electron diffraction (LEED) measurements were carried out for chemical and structural analysis of the MBE-grown epilayer surfaces, both after decapping by thermal desorption and using this novel reactive technique. The spectra shown were all recorded at near-normal emission, with Al K $\alpha$  x-rays and an analyzer pass energy of 20 eV, which yields a spectral resolution of ~1.0 eV (FWHM).

## RESULTS AND DISCUSSION

### Chemical stability upon photolithography

XPS analysis of the 4 samples exposed to photoresist, developer, acetone and NMP (N=2), respectively, suggests that the As cap remains intact after this processing. The durability of the capping is verified primarily by failure to observe any Ga core-level photoemission from these samples. The measured As 2p<sub>3/2</sub> spectra resemble closely that recorded from As capping exposed to atmosphere, only. Two spectral components may be clearly distinguished; i.e., emission from As<sup>3+</sup> of a thin superficial native oxide (As<sub>2</sub>O<sub>3</sub>) with binding energy E<sub>b</sub>=1326.4 eV, and from As<sup>0</sup> of the subsurface elemental As cap with E<sub>b</sub>=1323.5 eV.<sup>5</sup> The different chemical treatments apparently cause no dramatic enhancement of the As cap surface oxidation. Maximum As<sup>3+</sup> core-level peak intensity was recorded for the NMP-treated sample, for which the superficial oxide thickness was estimated at 10-15 Å.<sup>8</sup> The measured C 1s photoemission and spectral broadening in the As 2p<sub>3/2</sub> and O 1s data of the chemically treated samples indicate minute amounts of process-derived residual surface impurities.

Fig. 1 shows core-level photoemission spectra of the sample exposed to complete (maskless) UV lithography; (A) as-introduced in the XPS spectrometer, and (B) after thermal desorption of the processed As cap at a nominal temperature of 450°C. (Precise calibration of the sample surface temperature was not done for this study. Our thermometer measures the substrate heater temperature, which exceeds that of the sample by some 50-100 degrees). The spectra denoted (C) show corresponding data for a non-processed, thermally decapped reference sample. From the absence of Ga 2p<sub>3/2</sub> photoemission in Fig. 1a (A), we infer that the As cap remains intact after photolithographic processing. Effective decapping upon subsequent annealing is confirmed by appearance of the Ga 2p<sub>3/2</sub> spectrum (B). The As 2p<sub>3/2</sub> spectrum (B) in Fig. 1a exhibits a predominant peak at E<sub>b</sub>=1322.9 eV, shifted with respect to the As<sup>3+</sup> and As<sup>0</sup> emission of the capping surface (A). This peak is attributed to covalently bonded arsenic in GaAs.<sup>5</sup> LEED analysis of the decapped sample surface unveils a GaAs(001)-c(4×4) surface of good crystalline quality. This reconstruction is characteristic of As-terminated GaAs(001) with an ordered arrangement of chemisorbed As-As dimers.<sup>5,9</sup>

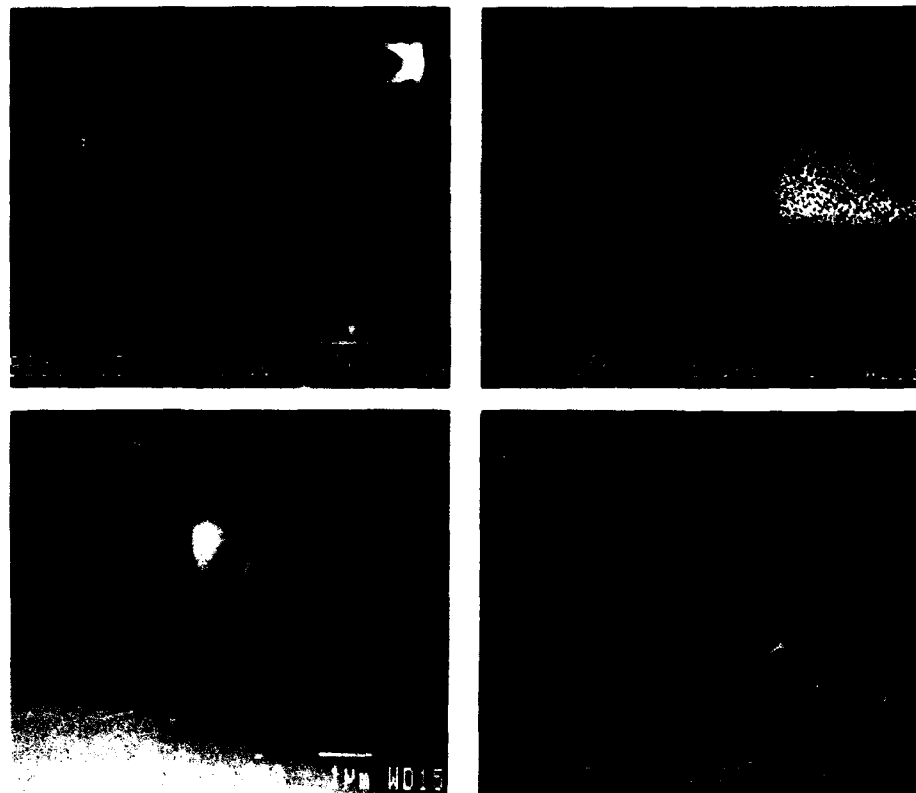


Fig.2 SEM images of a patterned As cap on AlGaAs(001) for two different test structures (a-b), and close-ups of the capping edge before (c) and after (d) removal of the photoresist mask.

The oxygen and carbon core-level spectra displayed in Fig.1b show noticeable diminution of surface impurities after decapping (B). The O 1s emission is reduced to a negligible level and compares with that recorded for a non-processed reference sample (C). The emission from residual carbon contaminants clearly exceeds that of the reference sample, however. Previous studies have established that ambient-derived contaminants desorb entirely upon thermal decapping.<sup>5</sup> The measured C 1s photoemission in (B) may thus derive from the lithographic processing. By peak intensity analysis, we find that the surface carbon impurities contribute but a minor fraction of a monolayer. This explains the GaAs(001)-c(4×4) LEED pattern observed on the thermally decapped epilayer surface.

#### Decapping and pattern definition by H<sup>+</sup> etching

Reactive desorption of the As cap at a temperature appreciably lower than that of conventional thermal desorption was achieved with hydrogen radicals, only. Fig.2 shows scanning

electron micrographs of a patterned As cap on MBE-grown AlGaAs(001), fabricated by  $H^+$  etching at ambient temperature through a  $\sim 1 \mu\text{m}$  thick mask of photoresist. Fig.2 displays two different test structures prepared in this manner (a-b), and close-ups of the capping edge before (c) and after (d) removal of the photoresist mask. Despite the presence of residual arsenic, notably along the photoresist mask edges, these micrographs demonstrate that reactive patterning of the As cap is feasible. We believe that the residual arsenic in unmasked regions (excessive in Fig.2b) can be attributed to premature termination of the  $H^+$  exposure, and that improved definition of the pattern edges may be achieved by optimization of the etching time and the capping and photoresist layer thicknesses. The highly irregular edge of both resist and capping edge in Fig.2c-d is explained by poor quality of the mask employed for UV exposure.

Fig.3 shows core-level photoemission spectra of an (unmasked) GaAs(001) sample, (A) as introduced, and (B) after decapping at RT by aggressive etching in a  $H^+$  beam for 2 mins. This etching causes complete removal of the As cap, as inferred from the measured Ga  $2p_{3/2}$  photoemission and a shift to lower binding energy of the As  $2p_{3/2}$  spectrum by 0.5 eV. Spectral broadening of the As  $2p_{3/2}$  levels, apparent in the reference spectrum (C) of Fig.1a, was not found in the data from this  $H^+$ -etched GaAs sample. Comparison of the measured peak intensities for the Ga  $2p_{3/2}$  and As  $2p_{3/2}$  core-levels with those of a thermally decapped reference sample suggests a moderate surface arsenic depletion.

The Ga  $2p_{3/2}$  spectrum (B) in Fig.3a comprises a minor component at  $E_b = 1118.2 \text{ eV}$ , i.e., shifted by 1.1 eV from the bulk GaAs core-level. The shifted Ga core-level is attributed to surface oxide. This interpretation is corroborated by the measured O 1s spectrum, which exhibits a pronounced asymmetry in Fig.3b (B), and may be suitably decomposed in two spectral components. The predominant O 1s emission is shifted from that of the native surface Ga oxide, by about 1.2 eV, and is tentatively attributed to physisorbed  $H_2O$ . We also note the presence of carbonaceous impurities on the  $H^+$ -etched epilayer surface. The superficial oxygen (incl.  $H_2O$ ) and carbon contamination presumably derives from trace amounts of gaseous impurities in the  $H_2$  gas supplied to the radical beam source. Like hydrogen, molecular impurities such as  $CO_2$  and oxygen will dissociate, and thus become far more reactive, when passing through this source. Moreover, the apparent depletion of As tends to promote oxidation of the (Al)GaAs epilayer surface. Finally, we mention that enhanced contamination in the presence of atomic hydrogen (presumably caused by exchange reactions), was previously reported for cleaved GaAs(110) and InP(110) surfaces.<sup>10</sup>

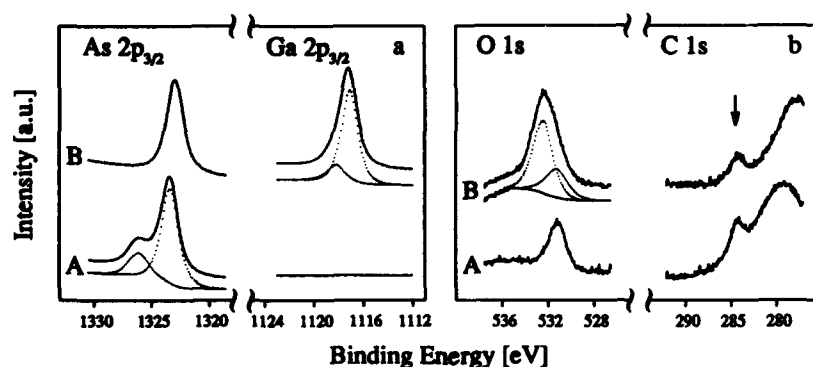


Fig.3 Core-level photoemission spectra of an As-capped GaAs(001) sample; (A) as-introduced and (B) after decapping at RT by exposure to hydrogen radicals.

LEED analysis of the  $H^+$ -etched GaAs(001) surface showed sharp  $(1 \times 1)$  diffraction spots characteristic of an ordered crystalline surface, albeit with no distinct surface reconstruction. This finding is consistent with previous data of Bringans and Bachrach,<sup>11</sup> who reported the LEED pattern of As-covered GaAs(001) to shift from  $c(4 \times 4)$  to  $(1 \times 1)$  upon exposure to atomic hydrogen. Exposure to atomic hydrogen has proven to provide effective cleaning of GaAs wafer surfaces.<sup>12,13</sup> Thus, we maintain that recovery of clean, ordered GaAs epilayers is possible, if process gas ( $H_2$ ) of sufficient purity is supplied to the radical beam source and great care is taken to secure clean UHV environments.

## CONCLUSION

In summary, this experiment shows that the As cap is durable upon exposure to the photochemicals commonly used in device fabrication. Negligible reduction of the capping thickness was found after such processing. Reactive desorption of the protective As cap was achieved by exposure to a beam of hydrogen radicals at ambient temperature. MBE-grown GaAs(001) epilayer surfaces recovered using this technique was found to be Ga-terminated, with trace amounts of superficial gallium oxide and carbon impurities. Patterning of the As cap with 5  $\mu m$  linewidth was demonstrated, by combining  $H^+$  etching with standard UV lithography.

Clearly, further process refinement is needed in order to eliminate arsenic cap residues, seen (primarily) along the patterned cap edges, and reduce the amount of surface oxygen and carbon impurities. Moreover, the influence of  $H^+$  exposure on the electrical properties of the (Al)GaAs epilayer demands attention. Implications for microelectronic device processing and suspended MBE growth on patterned epilayer structures thus remain to be ascertained.

The Norwegian Telecom Research Department (TF) and the Norwegian Research Council (NAVF) are gratefully acknowledged for financial support to this project.

## REFERENCES

1. See e.g., J.C. Bean, in *High-Speed Semiconductor Devices*, ed. S.M. Sze (John Wiley & Sons, Inc., New York, 1990), pp. 13-56
2. C.E.C. Wood and B.A. Joyce, *J. Appl. Phys.* **49**, 4853 (1978)
3. N.J. Kawai, C.E.C. Wood, and L.F. Eastman, *J. Appl. Phys.* **53**, 6208 (1982)
4. S.P. Kowalczyk, D.L. Miller, J.R. Waldrop, P.G. Newman, and R.W. Grant, *J. Vac. Sci. Technol.* **19**, 255 (1981)
5. R.W. Bernstein, A. Borg, H. Husby, B.-O. Fimland, and J.K. Grepstad, *Appl. Surf. Sci.* **56-58**, 74 (1992)
6. N.J. Kawai, T. Nagakawa, T. Kojima, K. Ohta, and M. Kawashima, *Electron. Lett.* **20**, 47 (1984)
7. D.L. Miller, R.T. Chen, K. Elliott, and S.P. Kowalczyk, *J. Appl. Phys.* **57**, 1922 (1985)
8. R.W. Bernstein and J.K. Grepstad, *Surf. Interface Anal.* **14**, 109 (1989)
9. D.K. Biegelsen, R.D. Bringans, J.E. Northrup, and L.-E. Swartz, *Phys. Rev. B* **41**, 5701 (1990)
10. F. Proix, C.A. Sébenne, M. Cherchour, O. M'hamedi, and J.P. Lacharme, *J. Appl. Phys.* **64**, 898 (1988)
11. R.D. Bringans and R.Z. Bachrach, *Solid State Commun.* **45**, 83 (1983)
12. A. Takamori, S. Sugata, K. Asakawa, E. Miyauchi, and H. Hashimoto, *Jpn. J. Appl. Phys.* **26**, L142 (1987)
13. E.J. Petit, F. Houzay, and J.M. Moison, *J. Vac. Sci. Technol. A* **10**, 2172 (1992)

## OPTICAL EMISSION END-POINT DETECTION FOR VIA HOLE ETCHING IN InP AND GaAs POWER DEVICE STRUCTURES

S. J. PEARTON, F. REN, C. R. ABERNATHY AND C. CONSTANTINE\*

AT&T Bell Laboratories, Murray Hill, NJ 07974

\*Plasma Therm IP, St. Petersburg, FL

### ABSTRACT

Narrow ( $\sim 30 \mu\text{m}$   $\phi$ ) via holes have been etched in both InP and GaAs substrates using either  $\text{Cl}_2/\text{CH}_4/\text{H}_2/\text{Ar}$  or  $\text{BCl}_3/\text{Cl}_2$  discharges, respectively. High density ( $\sim 5 \times 10^{11} \text{ cm}^{-3}$ ), low pressure (1 mTorr for  $\text{Cl}_2/\text{CH}_4/\text{H}_2/\text{Ar}$  or 15 mTorr for  $\text{BCl}_3/\text{Cl}_2$ ) conditions, combined with sidewall passivation obtained using AZ 4620 photoresist masks, produce the correct profiles for subsequent metallization to complete the via connection. Optical emission monitoring of the 417.2 nm Ga line during GaAs etching or of the 325.6 nm In line during InP etching provided a sensitive, non invasive and reliable indicator of endpoint for both types of substrates. The intensity of these lines was proportional to the microwave input power at fixed dc bias and pressure. The via holes are suitable for a range of InP and GaAs microwave power devices, including Heterojunction Bipolar Transistors and High Electron Mobility Transistors.

### INTRODUCTION

Monolithic microwave integrated circuits (MMICs) are typically fabricated with III-V materials, especially GaAs, and, more recently, InP. The active regions of these circuits require creation of through-wafer, front-to-back electrical connections.<sup>(1-7)</sup> These connections are generally created by patterning thick metal pads on the front side of the wafer, and thinning the wafer from the rear to a thickness of 75-100  $\mu\text{m}$ . The backside is then patterned with a thick photoresist or metal mask and a via hole is dry etched into the wafer, stopping at the front side metal pads. Gold is then plated into the via hole producing a low resistance, front-to-back electrical connection.

Dry etching of GaAs at rapid rates may be achieved in any chlorine-containing discharge, and various mixtures of  $\text{CCl}_2\text{F}_2$ ,  $\text{BCl}_3$ ,  $\text{SiCl}_4$  and  $\text{Cl}_2$  have been reported for via hole applications.<sup>(1-8)</sup> By contrast it is more difficult to achieve high etch rates for InP under anisotropic conditions. For smooth, shallow mesa etching applications,  $\text{CH}_4/\text{H}_2$  plasmas have proven to be extremely effective, but rates of  $\leq 500 \text{ \AA} \cdot \text{min}^{-1}$  are the maximum achievable under normal conditions.<sup>(9,10)</sup> Gas mixtures based on iodine ( $\text{I}_2$ ,  $\text{HI}$ ,  $\text{CH}_3\text{I}$ ) can provide high etch rates, but the corrosiveness and instability of these gases are disadvantages.<sup>(11,12)</sup> The major difficulty in obtaining rapid etching is the relative involatility of the In-containing etch products. This can be circumvented by using  $\text{Cl}_2/\text{CH}_4/\text{H}_2$  plasmas with the sample held at elevated temperature to enhance the volatility of the In- $\text{Cl}_x$  species.<sup>(13-15)</sup> The role of the hydrogen is to remove P as  $\text{PH}_3$  from the InP, while the  $\text{CH}_4$  provides a sidewall passivation mechanism which minimizes undercutting of the etched features. In low pressure discharges such as the Electron Cyclotron Resonance (ECR) plasmas used here, Ar is usually added to assist ignition and facilitate tuning of the forward microwave power.<sup>(16)</sup> Under optimum conditions, it

is possible to achieve InP etch rates of  $\geq 1 \mu\text{m} \cdot \text{mm}^{-1}$  using  $\text{Cl}_2/\text{CH}_4/\text{H}_2$  discharges.<sup>(17)</sup> These rates are suitable for via hole applications since practical considerations require etch times of  $\leq 100$  minutes.

Another concern during via hole etching is real-time endpoint detection. Since the effective etch rates may vary during the long plasma exposures due to heating of the wafer or the fact that etch rates may decrease as the hole deepens, because it is more difficult for the etchant gases to enter and for the etch products to exit the feature. Optical emission spectroscopy (OES) from electronically excited states of etch products is an effective, non-invasive method for monitoring dry etch processes.<sup>(18)</sup> In this paper we report on the use of OES for endpoint detection during dry etching of via holes in both GaAs and InP substrates with ECR discharges. In particular we use the 417.2 atomic emission line of Ga and the 325.6 atomic emission line of In as signatures for determining the end-point of the etching.

#### EXPERIMENTAL PROCEDURE

The GaAs and InP substrates were patterned on the front face with e-beam deposited Ti(500Å)/Pt(1000Å)/Au(4000Å). The back side of the wafers was lithographically patterned with a 15  $\mu\text{m}$  thick layer of AZ 4620 photoresist which was post-baked at 150°C to improve its etch resistance and produce slightly sloped profiles. The latter are essential for the final metallization step in completing the via.

The dry etching was carried out in a Plasma Therm Shuttlelock 720 system,<sup>(16)</sup> using either a 60  $\text{BCl}_3/15 \text{ Cl}_2$ , 15 mTorr, -150V dc, 250W (microwave) discharge for GaAs, or a 10  $\text{Cl}_2/3 \text{ CH}_4/20 \text{ H}_2/5 \text{ Ar}$ , 2 mTorr, -80V dc, 750W (microwave) discharge for InP. The sample temperatures are nominally 50°C for GaAs and 150°C for InP, with the substrates thermally bonded by high vacuum grease to the temperature controlled cathode. The total gas flow rates were 75 standard cubic centimeters per minute (sccm) for  $\text{BCl}_3/\text{Cl}_2$  and 38 sccm for  $\text{Cl}_2/\text{CH}_4/\text{H}_2/\text{Ar}$ . The plasmas were excited in an Applied Science and Technology ECR source operating at 2.45 GHz, into which the gases were introduced through electronic mass flow controllers. The sample position is separately powered at 13.56 MHz to establish the dc bias on the substrate.

Optical emission spectroscopy was performed with a Verity Instruments EP 200 DAS system operating in the range 185-900 nm. The system consists of a 0.2m scanning monochromator featuring a high efficiency ion beam etched holographic grating and a folded optics design for maximum space efficiency, and a photomultiplier tube with supporting electronics. The grating slits were 5 mm high  $\times$  100  $\mu\text{m}$  wide, corresponding to a bandpass of 0.4 nm. The scan speed was set at 100  $\text{nm} \cdot \text{min}^{-1}$  for these long runs. For endpoint monitoring, the intensity of the Ga atomic line at 417.2 nm and the In atomic line at 325.6 nm were followed as a function of the etch time.

Following completion of the dry etching, some of the vias were metallized from the rear face with a sequence of electroless and electroplating processes (1000Å Pd, 5  $\mu\text{m}$  Au, 1000Å Pd) to produce low-resistance front-to-back electrical connections. Scanning electron microscopy (SEM) was used to monitor the success of the entire process.



## RESULTS AND DISCUSSION

### (a) GaAs via holes

Representative OES spectra from the chlorine-based plasmas for etching GaAs via holes are shown in Figure 1 to illustrate our ability to detect emission lines from the etch products. At top is a  $\text{BCl}_3/\text{Cl}_2$  discharge taken with no GaAs wafers in the chamber. There is a continuum from  $\text{BCl}_x$  species and atomic lines due to chlorine transitions. Upon introducing GaAs into the chamber (center) one immediately sees strong Ga lines at 403.3 and 417.2 nm and a GaCl line at 338.3 nm. Note that these spectra were taken through a quartz window on the chamber, which cuts off emission lines below  $\sim 300$  nm. Under higher dc bias conditions where the GaAs etch rate is increased (Figure 1, bottom) these lines become more intense. Our via hole etching was performed at  $-150$  V dc and 15 mTorr, where the signal-to-noise for the 417.2 nm line was  $\sim 10:1$ .

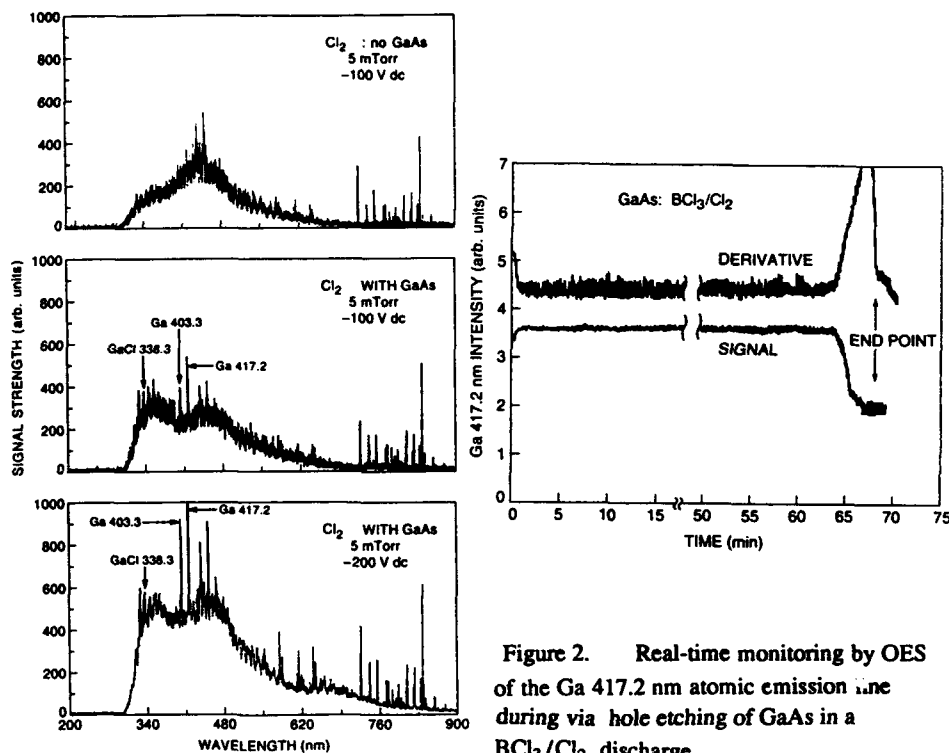


Figure 1. Emission spectra from  $\text{BCl}_3/\text{Cl}_2$  discharges (top) with no GaAs in the chamber, (center) with GaAs added or (bottom) at higher dc bias conditions where the GaAs etch rate is higher.

Figure 2. Real-time monitoring by OES of the Ga 417.2 nm atomic emission line during via hole etching of GaAs in a  $\text{BCl}_3/\text{Cl}_2$  discharge.

Figure 2 shows the OES signal and its derivative during etching of vias in a 2"  $\phi$  GaAs substrate. The test pattern contains ~250 vias over the wafer area. There is an initial slight increase in the signal intensity, possibly due to an incubation time as native oxide is removed from the surface, followed by a long period (~63 minutes) where the intensity is constant. This corresponds to the steady-state etching of the via holes. The emission intensity begins to decrease at 63 minutes and takes ~5 min to come to a new steady state. The endpoint of the etching can be seen clearly both in the signal itself and in its derivative, which is generally a more sensitive indicator. We ascribe the 5 minute transition period to the uniformity of the etching, in this case ~7% (5/68). The remnant signal after endpoint is most likely due to continued etching of the unmasked sections at the edge of the wafer and to undercutting of the existing via holes. Continued etching beyond ~68 minutes would lead to erosion by sputtering of the front-side metal, which acts as the etch-stop, and to an enlargement of the via holes.

Examples of via holes etched in thick GaAs substrates are shown in the SEM micrographs of Figure 3. Note the etching is quite anisotropic under our conditions, and is very uniform for vias of the same initial diameter. The effect of slower effective etch rates for smaller diameter vias is clearly illustrated at the bottom of Figure 3, where a 20  $\mu\text{m}$   $\phi$  via has etched 10-15% less deep than its neighboring 30  $\mu\text{m}$   $\phi$  via. As mentioned earlier, this aspect-ratio dependent etching results from the difficulty in getting gaseous etchants into, and etch products out of, smaller holes.<sup>(5)</sup>

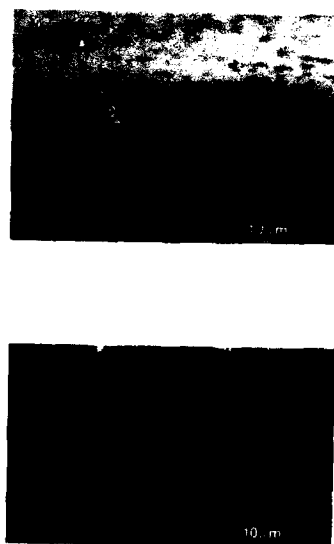


Figure 3. SEM micrographs of via holes etched into thick (500  $\mu\text{m}$ ) GaAs substrates using  $\text{BCl}_3/\text{Cl}_2$  discharges.

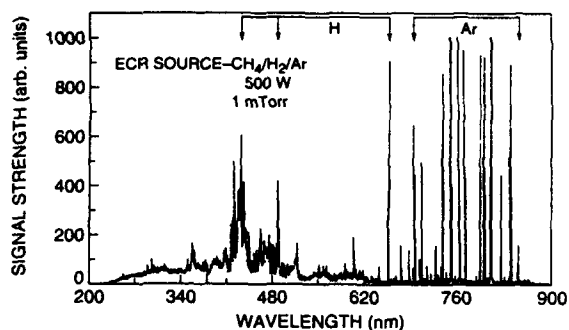


Figure 4. Emission spectrum from a  $\text{CH}_4/\text{H}_2/\text{Ar}$  discharge.

(b) *InP Via Holes*

The use of four different component gases in the mixture for etching InP produces a complex optical emission spectrum. Figure 4 shows the emission spectrum from a  $\text{CH}_4/\text{H}_2/\text{Ar}$  discharge (the  $\text{Cl}_2$  was left out in this case for clarity). The three dominant atomic hydrogen lines are present, including the major  $\text{H}_\gamma$  line at 656.2 nm, together with a molecular hydrogen continuum between 250-350 nm and CH emission at 431.4 nm.<sup>(19)</sup> The Ar produces a large number of lines between 700-800 nm. Addition of InP into the chamber produced four new emission lines at 303.9, 325.6, 410.2 and 451.1 nm, but we could not detect any P-related lines. For 2"  $\phi$  InP substrates the signal-to-noise of the 325.6 nm line was  $\sim 3:1$ , the highest of the In atomic emissions.

Figure 5 shows the time dependence of this In line during  $\text{Cl}_2/\text{CH}_4/\text{H}_2/\text{Ar}$  etching of InP via holes. In this case there is a more obvious initial increase in the signal in the first minute of etching, presumably due to the need to remove the native oxide before etching commences. The signal shows a slight increase over the entire duration of the etch, which may be due to a slow heating of the wafer under these low pressure (2 mTorr) conditions where heat transferred to the InP through ion bombardment and chemical reaction on the surface is not as easily radiated away as in the case of the GaAs etching at higher pressure (15 mTorr). The width of the transition denoting the endpoint is also slightly larger than was the case with the GaAs, which may indicate slightly poorer uniformity for this etch.

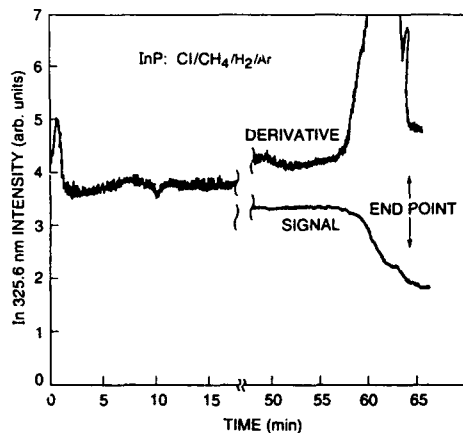


Figure 5. Real-time monitoring by OES of the In 325.6 nm atomic emission line during via hole etching of InP in a  $\text{Cl}_2/\text{CH}_4/\text{H}_2/\text{Ar}$  discharge.

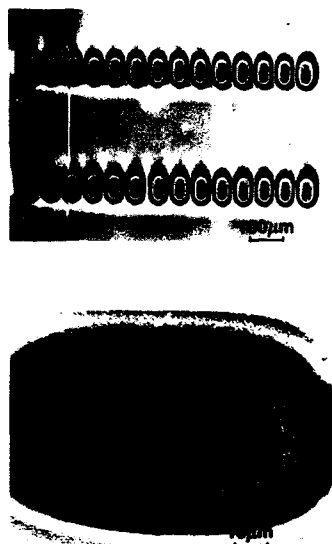


Figure 6. Completed, metallized via holes etched in an InP substrate using a  $\text{Cl}_2/\text{CH}_4/\text{H}_2$  discharge.

An array of closely-spaced metallized vias etched in an InP substrate are shown in the SEM micrographs of Figure 6, demonstrating the uniformity of the process. A close-up of one of the vias is shown in the micrograph at the bottom of the Figure. The plating of the Au around the interior of the via is uniform and conformal, producing an excellent low resistance connection. Note that this substrate was 75  $\mu\text{m}$  thick and required 63 minutes to etch, showing that averaged etch rates above  $1 \mu\text{m} \cdot \text{min}^{-1}$  are maintained with the  $\text{Cl}_2/\text{CH}_4/\text{H}_2/\text{Ar}$  chemistry even when fabricating deep holes.<sup>(20)</sup> There is a particular need for use of endpoint detection when wafers with varying areas are being processed, since the loading effect can alter effective etch rates by 30% or more.

#### SUMMARY AND CONCLUSIONS

Optical emission spectroscopy is an effective, non-invasive and accurate technique for monitoring via hole etching processes in GaAs and InP substrates. The time dependence of emission intensity of Ga or In atomic lines yields well-determined endpoints when etching small diameter (30  $\mu\text{m}$ ) vias in either type of substrate.

#### REFERENCES

1. L. G. Hipwood and P. N. Wood, *J. Vac. Sci. Technol. B* 3 395 (1985).
2. A. E. Geissberger and P. R. Clayton, *J. Vac. Sci. Technol. A* 3 863 (1985).
3. L. A. D'Asaro, A. D. Butherus, J. B. DiLorenzo, D. E. Inglesias and S. H. Wemple, *J. Phys. Conf. Ser.* 56 267 (1981).
4. E. Y. Chang, R. M. Nagarajan, C. J. Koyzak and K. P. Pande, *IEEE Trans. Semicond. Man. SM-1* 157 (1988).
5. S. Salimian, C. B. Cooper III and M. E. Day, *J. Vac. Sci. Technol. B* 5 1606 (1987).
6. S. J. Pearton, F. Ren, A. Katz, J. R. Lothian, T. R. Fullowan and B. Tseng, *J. Vac. Sci. Technol. B* 11 152 (1993).
7. T. E. Kazior, B. I. Patel and B. J. Guerin, *Proc. 13th State-of-the-art program on compound semiconductors* ed. H. Lee, O. Ueda, P. Clechet and J. M. Woodall (Electrochemical Society, Pennington, NJ 1991) Vol. 91-1, p. 299.
8. K. P. Hilton and J. Woodward, *Electron. Lett.* 21, 962 (1985).
9. U. Niggebrugge, M. Klug and G. Garus, *Inst. Phys. Conf. Ser.* 79 367 (1985).
10. S. J. Pearton, W. S. Hobson, F. A. Baiocchi, A. B. Emerson and K. S. Jones, *J. Vac. Sci. Technol. B* 8 57 (1990).
11. S. J. Pearton, U. K. Chakrabarti, A. Katz, F. Ren and T. R. Fullowan, *Appl. Phys. Lett.* 60 838 (1992).
12. D. C. Flanders, L. D. Pressman and G. Pinelli, *J. Vac. Sci. Technol. B* 8 1990 (1990).
13. C. Constantine, C. Barratt, S. J. Pearton, F. Ren and J. R. Lothian, *Appl. Phys. Lett.* 61 2899 (1992).
14. G. J. van Gurp, J. M. Jacobs, J. Binsma and L. Tiemeijer, *Jap. J. Appl. Phys.* 28 1236 (1989).
15. R. van Roijen, M. Kemp, C. Bulle-Lieuwman, L. Ijzendoorn and T. T. Thijssen, *J. Appl. Phys.* 70 3903 (1991).
16. S. J. Pearton, F. Ren, T. Fullowan, A. Katz, W. S. Hobson, U. Chakrabarti and C. R. Abernathy, *Mat. Chem. Phys.* 32 215 (1992).
17. C. Constantine, C. Barratt, S. J. Pearton, F. Ren and J. R. Lothian, *Electronics. Lett.* 28 1749 (1992).
18. P. Collet, T. Diallo and J. Caneloup, *J. Vac. Sci. Technol. B* 9 2497 (1991).
19. R. W. B. Pearse and A. G. Gaydon, *The Identification of Molecular Spectra* (Chapman and Hall, London, 1976).
20. C. Constantine, C. Barratt, S. J. Pearton, F. Ren, J. R. Lothian, W. S. Hobson, A. Katz, L. W. Yang and P. C. Chao, *Electronics Lett.* 29 984 (1993).

## REACTIVE SPUTTERING IN OXIDIZING/REDUCING ATMOSPHERES

J. D. KLEIN, A. YEN, AND S. L. CLAUSON  
EIC Laboratories, Norwood, MA 02062

### ABSTRACT

The deposition of thin films by magnetron sputtering is readily influenced by the reduction/oxidation characteristics of the plasma. Unfortunately, the redox state of the sputter plasma is often inadvertently determined by uncontrolled factors such as transient evolution of species from the target. Undesirable variations in film and target properties can be avoided by actively setting the redox conditions. This is most readily accomplished by including two competing species, one oxidizing and the other reducing, in the chamber gas mixture. Optical emission spectroscopy, an *in-situ* process monitor, was employed to observe redox interactions in nominally unreactive dc sputtering of YBCO and reactive rf sputtering of  $\text{IrO}_2$ . Optical spectroscopy of YBCO sputtering reveals that the intensity of atomic oxygen emissions decreases with  $\text{H}_2$  additions to the sputter gas blend.

### INTRODUCTION

Water vapor additions have been shown to be useful in both reactive and unreactive sputtering of electrically active oxides. Sputter deposition of *in-situ* superconducting YBCO ( $\text{YBa}_2\text{Cu}_3\text{O}_{7-x}$ ) films is susceptible to a variety of pitfalls. If the oxidation state of the target drifts with time, the target surface may change from metallic to semiconducting. Investigators have observed beneficial effects of  $\text{H}_2\text{O}$  [1] or  $\text{H}_2$  [2,3] additions in providing spatially and temporally stable sputter conditions. The generation of additional atomic oxygen has been suggested as a possible mechanism [2]. Iridium oxide thin films are employed in several electrochemical applications such as charge injection electrodes for neural stimulation and optical switching layers in electrochromic devices. The electrochemical properties of iridium oxide are quite sensitive to deposition conditions. Traditionally, a "wet" process using water additions has been employed to obtain the desired film properties [4,5]. However, the development of a "dry" process based on a  $\text{H}_2/\text{O}_2$  redox environment should enhance process stability and extend the range of available properties. Optical emission spectroscopy has been shown to be a sensitive *in-situ* process monitor for deposition of superconducting [6], ferroelectric [7,8], and electrochromic [9] thin films. Plasma emission spectroscopy was selected as a means of comparing hydrogen additions to unreactive and reactive sputter deposition of oxide thin films.

### YBCO SPUTTERING

All YBCO sputter runs were performed in a Microscience IBEX-2000 deposition chamber evacuated by a diffusion pump backed by a mechanical pump. The commercially obtained nominally stoichiometric 5.1 cm diameter YBCO target was sputtered from a narrow anode U.S. Gun II planar magnetron at a pressure of 200 mTorr. The chamber gas was set by a blend of 12 sccm Ar, 4 sccm  $\text{O}_2$ , and 0 to 4 sccm  $\text{H}_2$ . A microprocessor-controlled power supply maintained a power of 80 watts regardless of target potential. The acquisition of YBCO emission spectra was facilitated by a vacuum feed-through fiber optic cable, an Acton Research Spectra-Pro

275 spectrograph, and an EG&G Princeton Applied Research 1460/1463 diode array spectrophotometer. The collimator fitted to the collection end of the fiber optic cable allowed light collection from the entire sputter plasma.

Three species were deemed essential to the examination of the  $H_2/O_2$  redox environment. Atomic hydrogen was monitored by the 656.3 nm H I peak [10]. Atomic oxygen exhibits one readily observable peak, the 777 nm O I multiline peak. Since the sputter plasma in an  $O_2/H_2$  is in many ways a hydrogen flame, one would expect the spectral details similar to those observed in flame spectroscopy. In particular, the 306.4 nm molecular OH  $A^2\Sigma^+ - X^2\Pi$  band system [11] was evident whenever both  $O_2$  and  $H_2$  were present. Peaks associated with cation species were also observed but are not considered here.

As expected from metallurgical thermodynamics, hydrogen and oxygen were found to seek a competitive redox balance. The response of the O I 777 nm and H I 656.3 nm emission peaks to  $H_2$  flow rates is shown in Figure 1. The noted emission intensities were obtained by integrating the chosen emission peaks with respect to wavelength and normalizing according to detector exposure time. As expected, atomic hydrogen emissions increased as the  $H_2$  flow was increased. As might be expected for the simple chemical reasoning, atomic oxygen emissions decreased as the hydrogen flow rate rose. Although the sputter plasma cannot be assumed to obtain an equilibrium condition, the observed trend is that which would be predicted by metallurgical thermodynamics. That is, any increase in hydrogen content would be accompanied by a decrease in oxygen content.

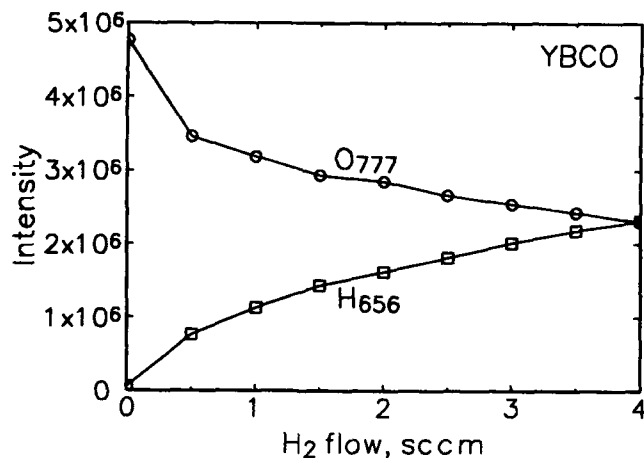


Fig. 1. The response of the O I 777 nm and H I 656.3 nm emission peaks as a function of  $H_2$  flow in YBCO dc sputtering. The indicated  $H_2$  flow was in addition to 12 sccm Ar and 4 sccm  $O_2$ .

From the hydrogen flame analogy, both hydrogen and oxygen must be considered chemically as reactants. The intent of optical emission spectroscopy is *in-situ* observation of the reaction in the sputter plasma. Reactions within the plasma are best discussed by the interplay of plasma variables. Those available here are the integrated emission intensities of H, O, and OH. Shown in Figure 2 are the intensi-

ties of the atomic O and molecular OH peaks as a function of atomic H emission intensity. As apparent from Figure 1, the O intensity drops as the H intensity rises. Moreover, the functional relationship was linear for non-zero  $H_2$  flows. On the product side of the chemical reaction, OH intensity rose as H intensity increased. The experimental data suggest two linear H-OH regimes having slightly different slopes. To the extent that optical emission indicates the reaction environment within the sputter plasma, it is obvious that the oxidation characteristics of the plasma can be precisely tailored by adjusting the hydrogen gas flow. YBCO films having zero-resistance  $T_c$ 's as high as 87 K have been deposited atop  $CeO_2$ -coated sapphire from  $Ar/H_2/O_2$  plasmas.

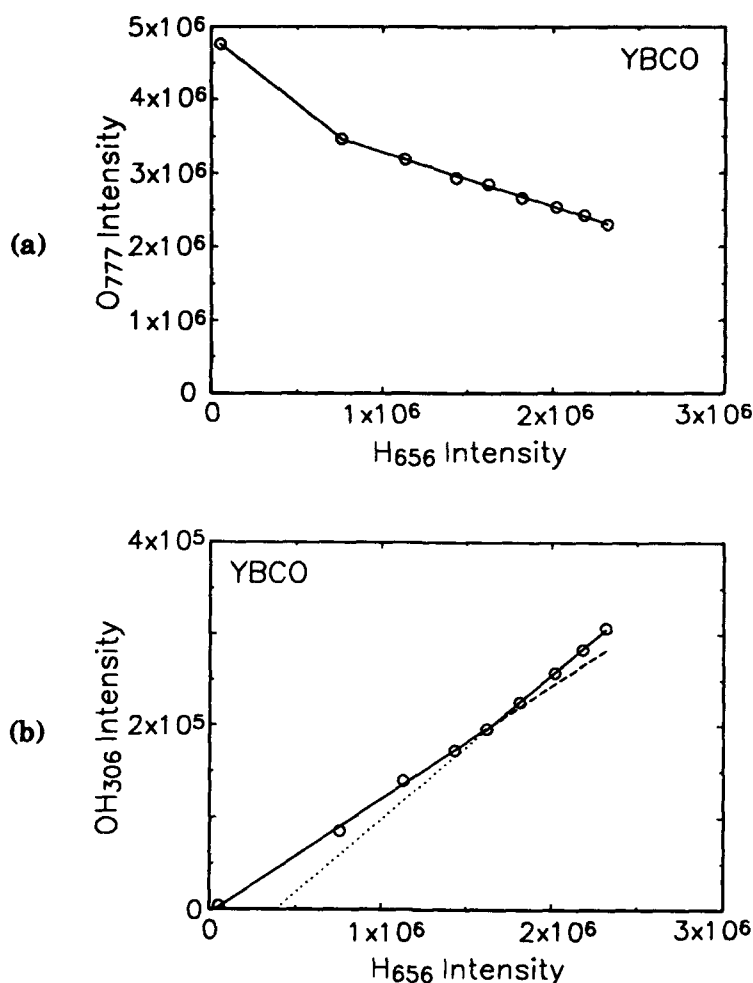


Fig. 2. YBCO dc sputter conditions shown in (a) H-O and (b) H-OH emission intensity spaces.

## IrO<sub>2</sub> SPUTTERING

Oxide film deposition from a metal target provides an interesting contrast to oxide target sputtering. Elimination of the target as an oxygen source places almost total control of plasma redox conditions in the chamber gas blend. All IrO<sub>2</sub> sputter runs were performed in a Microscience IBEX-2000 deposition chamber evacuated by a cryopump after roughing by a mechanical pump. The commercially obtained 6.35 cm diameter Ir metal target was sputtered from an Ion Tech, Ltd. planar magnetron source at a pressure of 40 mTorr. The chamber gas was fed by a blend of 15 sccm Ar, 5-11 sccm O<sub>2</sub>, and 6 to 10 sccm H<sub>2</sub>. A rf power supply applied 62.5 watts at each sputter condition. The acquisition of plasma emission spectra was facilitated by the same fiber optic cable, spectrograph, and detector setup described above. However, light collection was accomplished through an externally mounted collimator viewing the plasma through a quartz window.

One intent of the experiment was the definition of a "dry" process to supplement or replace the H<sub>2</sub>O-based deposition protocol previously employed. Toward these ends, the twelve deposition conditions shown in Figure 3 were selected to reveal the effects of H<sub>2</sub> and O<sub>2</sub> flow variations. The emission characteristics of the reactive sputter plasma are simpler and more dramatic than might be anticipated. The intensity of the atomic O peak as a function of atomic H emission intensity is shown in Figure 4a. All twelve deposition conditions fall on either of two lines in H-O emission space. The nearly vertical line defines a redox path in which O emission drops rapidly with respect to increasing H intensity. The horizontal line represents significant variations in H intensity with low O emission. The most important implication is that the redox characteristics are set by a tradeoff between H<sub>2</sub> and O<sub>2</sub> flows. Each of the three H<sub>2</sub> flows has points on both lines. The implication is that similar plasma redox characteristics can be obtained by many different flow combinations.

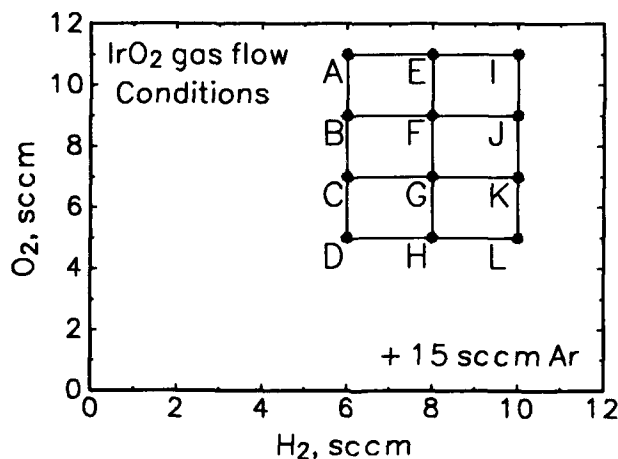


Fig. 3. The twelve Ar/H<sub>2</sub>/O<sub>2</sub> gas flow conditions used to rf sputter an Ir metal target.



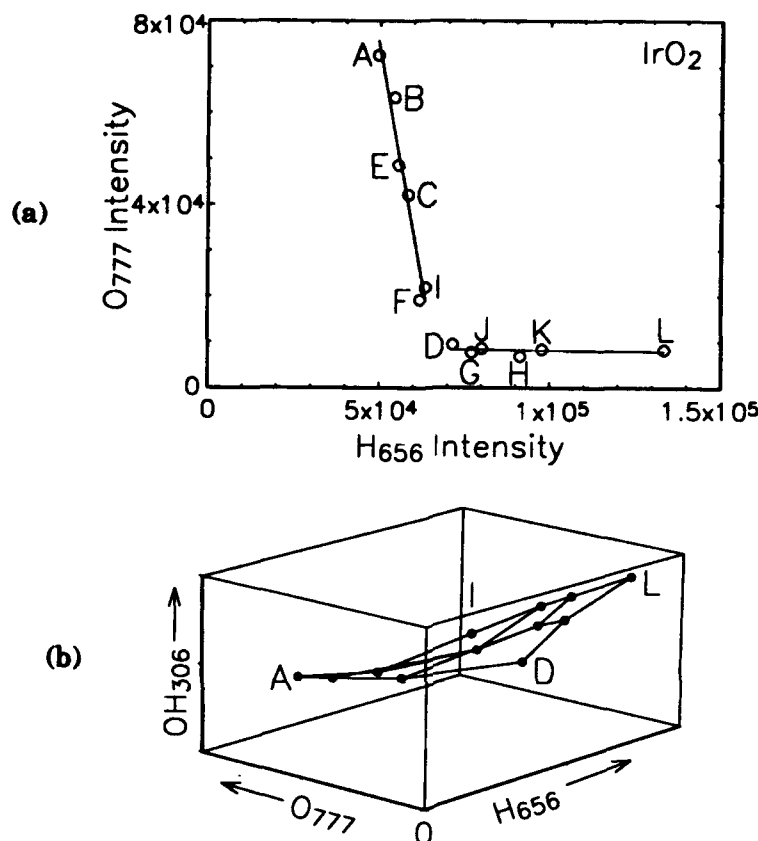


Fig. 4. Reactive IrO<sub>2</sub> sputter conditions are shown in (a) H-O and (b) H-O-OH emission intensity spaces.

A three-dimensional plot of the twelve IrO<sub>2</sub> flow conditions in H-O-OH emission space is shown in Figure 4b. For convenience, the run conditions corresponding to the corner points of the Ar/H<sub>2</sub>/O<sub>2</sub> flow matrix are noted by letters defined in Figure 3. Recalling that the H-O emission plot shown in Figure 4a is a 2-dimensional projection of H-O-OH emission space, the additional implications rendered by Figure 4b are in the area of OH emissions. As in the case of YBCO, increasing the H<sub>2</sub> flow tends to increase OH emissions. However, increasing the O<sub>2</sub> flow tends to diminish OH intensity. That is, within the run conditions considered O<sub>2</sub> and H<sub>2</sub> additions oppose each other with respect to OH emissions. However, these trends cannot be extrapolated without limit. The complete absence of O<sub>2</sub> flow would correspond to sputtering an Ir metal target in an Ar/H<sub>2</sub> environment. Under such conditions, OH emissions must be negligible.

Ar/H<sub>2</sub>/O<sub>2</sub> plasmas have been employed to deposit electrochemically active IrO<sub>2</sub> films. Electrochemical cycling of such films in sulfuric acid provided reversible modulation between 52% and 87% transmittance in the visible.

## CONCLUSION

Optical emission spectroscopy was found to be a sensitive *in-situ* monitor of the reduction/oxidation characteristics of Ar/O<sub>2</sub>/H<sub>2</sub> sputter environments. The sputter plasmas exhibited spectral characteristics similar to those encountered in hydrogen flame spectroscopy. Optical spectroscopy of YBCO dc magnetron sputtering indicated that H<sub>2</sub> additions reduced atomic oxygen emissions and increased OH emissions. Essentially linear relationships were found between O and OH emission intensity as a function of H emission intensity. Reactive rf sputtering of an Ir metal target in an Ar/O<sub>2</sub>/H<sub>2</sub> environment was performed at twelve distinct H<sub>2</sub>-O<sub>2</sub> flow combinations. Each run condition lies along one of two lines in O-H emission intensity space. In the range of Ar/O<sub>2</sub>/H<sub>2</sub> flows examined, increasing H<sub>2</sub> flow reduced atomic oxygen emissions and increased molecular OH emissions. Increasing O<sub>2</sub> flow reduced both atomic hydrogen and OH emissions.

Two significant benefits are attributed to sputtering in an H<sub>2</sub>/O<sub>2</sub> redox environment. First, the controlled presence of the two essentially competing gas species can overwhelm transient evolution of water vapor or oxygen from the target. Therefore, the H<sub>2</sub>/O<sub>2</sub> redox balance can unambiguously set the oxidation state of the sputter target surface. Second, the properties of the deposited film may depend sensitively on its oxidation state. Particularly in the case of reactive sputtering, the electronic and electrochemical properties of films can be varied through a wide range by adjusting the redox characteristics of the sputter plasma.

## REFERENCES

1. J.R. Gavaler, J. Talvacchio, T.T. Braggins, M.G. Forrester, and J. Gregg, *J. Appl. Phys.* **70**, 4383 (1991).
2. E.J. Cukauskas, L.H. Allen, G.K. Sherrill, and R.T. Holm, *Appl. Phys. Lett.* **61**, 1125 (1992).
3. J-P. Krumme, R.A.A. Hack, and I.J.M.M. Raaijmakers, *J. Appl. Phys.* **70**, 6743 (1991).
4. J.D. Klein, S.L. Clauson, and S.F. Cogan, *J. Vac. Sci. Technol. A* **7**, 3043 (1989).
5. J.D. Klein, S.L. Clauson, and S.F. Cogan, *J. Mater. Res.* **4**, 1505 (1989).
6. J.D. Klein and A. Yen, *J. Vac. Sci. Technol. A*, **9**, 2791 (1991).
7. J.D. Klein and A. Yen, *J. Appl. Phys.*, **70**, 505 (1991).
8. J.D. Klein and A. Yen in *Ferroelectrics Thin Films II*, edited by A.I. Kingon, E.R. Myers, and B. Tuttle (Mater. Res. Soc. Proc. **243**, Pittsburgh, PA 1992) pp. 167-172.
9. J.D. Klein and A. Yen in *Solid State Ionics II*, edited by G-A. Nazri, D.F. Shriver, R.A. Huggins, and M. Balkanski (Mater. Res. Soc. Proc. **210**, Pittsburgh, PA 1991) pp. 75-80.
10. *CRC Handbook of Chemistry and Physics*. 59th edition ed. by R.C. Weast (CRC Press, West Palm Beach, Florida 1978) pp. E-216-342.
11. A.G. Gaydon, *The Spectroscopy of Flames* (Chapman and Hall, London, 1974), p. 364.

## IN SITU SUBSTRATE TEMPERATURE MEASUREMENT DURING MBE BY BAND-EDGE REFLECTION SPECTROSCOPY

J. A. ROTH\*, T. J. DE LYON\* AND M. E. ADEL\*\*

\*Hughes Research Laboratories, Malibu, CA 90265

\*\*CI Systems, Ltd., Migdal Haemek, Israel

### ABSTRACT

The use of band-edge reflection spectroscopy (BRS) to determine the substrate temperature during MBE is reviewed. Data are presented for Si, GaAs, InP and CdZnTe substrates, and the use of BRS during the growth of ZnTe on Si is demonstrated. We discuss complications that arise due to optical interference in the epitaxial layers, and methods to compensate for the effects of interference are described.

### INTRODUCTION

Measurement of the actual substrate temperature during MBE is crucial for achieving epitaxial layers of the highest possible quality and with maximum control over doping profiles and layer compositions. One promising method for temperature measurement is to sense the change in the substrate bandgap by optical spectroscopic measurements sensitive to the absorption edge. Hellman and Harris [1] showed that transmission spectroscopy could be used during MBE to monitor the bandgap energy of GaAs and hence to determine the substrate temperature from the previously established relationship between bandgap and temperature [2,3]. This technique was further developed by Powell and Kirillov [4] who showed that a step-like change occurs in both transmission and reflection spectra at photon energies near the bandgap, and that the wavelength position of this step can be used to determine the temperature. Adel *et al.* [5] extended the reflection method to Si and discussed complications due to the presence of transparent dielectric films on the back side of the wafer. A variant of the reflection method which uses diffuse rather than specular reflectivity has also been demonstrated [6,7].

While all of the methods mentioned above work well for bare substrates, and therefore are appropriate for determining the substrate temperature prior to growth, the deposition of epitaxial films introduces optical interference effects which can distort the measured spectrum and complicate the extraction of temperature from the band-edge data. These effects are strongest when the films are smooth and uniform in thickness, precisely the conditions that MBE strives to achieve, and are more prevalent in reflection than in transmission spectra. In order to realize the full potential of band-edge reflection spectroscopy for substrate temperature measurement during MBE, it is desirable to characterize the effects of interference and to develop methods for correcting the errors that such effects introduce into the temperature determination.

In this paper we explore the use of band-edge reflection spectroscopy (BRS) to determine the substrate temperature under actual MBE growth conditions. We show that the reflectance technique works well for both direct-gap and indirect gap semiconductors, and is applicable over a wide range of temperatures, from 20°C to over 700°C. We illustrate the problems that arise due to interference effects in reflection measurements made from the front and back sides of the substrate, and suggest methods to compensate for such effects.

### EXPERIMENTAL

Reflectivity measurements were made using commercially available hardware and software (Model NTM1, from CI Systems, Inc., Agoura Hills, CA), with additional optical components to interface with the sample manipulator in a Vacuum Generators V80H MBE system. For BRS measurements, chopped white light from a 10W lamp is directed onto the substrate and the

specularly reflected light is collected and analyzed with a fast-scan grating monochromator and a lock-in amplifier detection system. A bifurcated fiber bundle permits the same optical system to be used both for the delivery of white light to the sample and for the routing of reflected light to the entrance aperture of the monochromator. For front-side reflectance measurements, the incident light is imaged onto the substrate wafer using a lens located just outside a normal-incidence optical viewport (i.e., the usual pyrometer port). For back-side measurements, a quartz light pipe and flexible optical fiber system are used to deliver light to the back of the wafer. With this apparatus it is also straightforward to acquire transmission data by directing the incident light onto the substrate with a lens and collecting the transmitted light with the quartz light pipe located behind the wafer. For either reflectivity or transmission measurements, a complete spectrum covering the wavelength range from 600-1800nm is acquired and the data are digitized and processed to extract a temperature at a rate of once per second.

## RESULTS

Figure 1 shows reflectivity data taken at room temperature from four common semiconductor substrates: Si, GaAs, InP and  $\text{Cd}_{0.96}\text{Zn}_{0.04}\text{Te}$ . In each case there is a large step in the reflectivity at a wavelength close to the room temperature bandgap. Even though Si has an indirect gap, its reflection step is only slightly less abrupt than those of the direct gap materials.

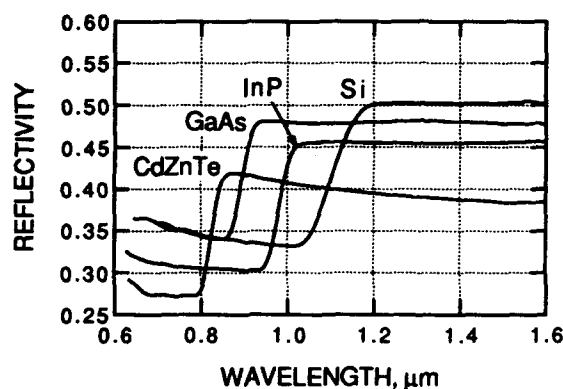


Figure 1. Room temperature reflectivity spectra from Si, GaAs, InP and  $\text{CdZnTe}$ .

The observed reflectivity step arises from the fact that for photon energies above the bandgap, where optical absorption is strong, only the first surface reflectance contributes to the overall signal. Below the absorption edge, however, some light propagates through the wafer and is reflected from the other side, and thus adds to the light reflected from the first surface. Because this second component of reflected light has traversed the substrate twice, its intensity varies exponentially with the absorption coefficient. This results in a sharp step in the net reflectivity near the semiconductor bandgap, where the absorption coefficient undergoes a large change.

The temperature dependence of the reflectivity is contained primarily in the absorption coefficient, the wavelength dependence of which tracks the decrease in the bandgap energy with increasing temperature. Figure 2 presents experimental reflectivity data taken at 20°C intervals, for GaAs and Si. It can be seen that the position of the reflection step shifts to longer wavelengths as the temperature is increased. In addition, a slight increase in the first-surface reflectance is also observed due to an increase in the real part of the index of refraction with temperature. At high temperatures, free-carrier absorption causes the magnitude of the reflectance step to decrease, and eventually to disappear altogether. With Si this occurs at about 680°C, and for GaAs the limit is over 800°C. For materials with smaller bandgaps, the onset of

free-carrier absorption occurs at lower temperatures, and this limits the utility of band-edge spectroscopy for small gap substrates such as GaSb and InAs, for example. Free-carrier absorption also makes the technique not usable for heavily-doped Si substrates, which are opaque at the band edge even at room temperature.

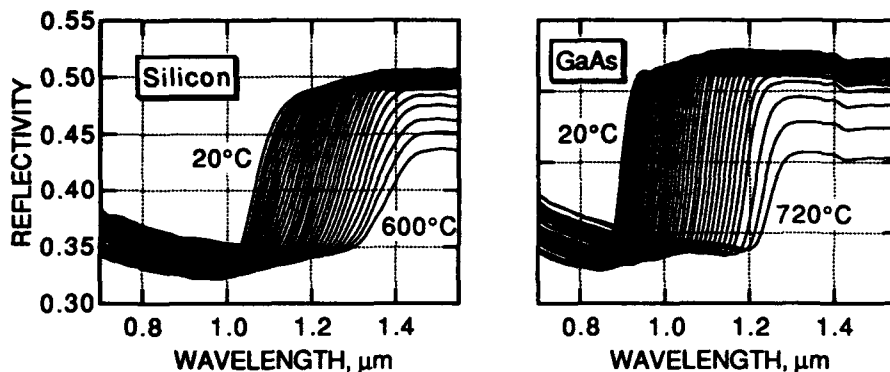


Figure 2. Reflectivity spectra for Si and GaAs, recorded at 20°C intervals.

Reflectivity spectra have been acquired as a function of temperature for bare substrates of Si, GaAs, InP, and CdZnTe. In each case, data were taken with the specimen mounted in conductive contact with a resistively heated metal block, in which was embedded a thermocouple used to measure the block temperature. Figure 3 summarizes these measurements in terms of the wavelength position of the reflectivity step versus the temperature measured by the embedded thermocouple. It can be seen from this plot that with increasing temperature the reflectance step shifts monotonically to longer wavelength, with a slope of approximately 0.4-0.5nm/°C. It is important to note that each of these curves applies to a wafer of a specific thickness, and for a given temperature the location of the reflectivity step shifts to shorter wavelengths for thinner specimens. In principle, the thickness dependence can be taken into account analytically, and if the thickness change is small, a constant temperature offset is adequate to correct for thickness variations between wafers.

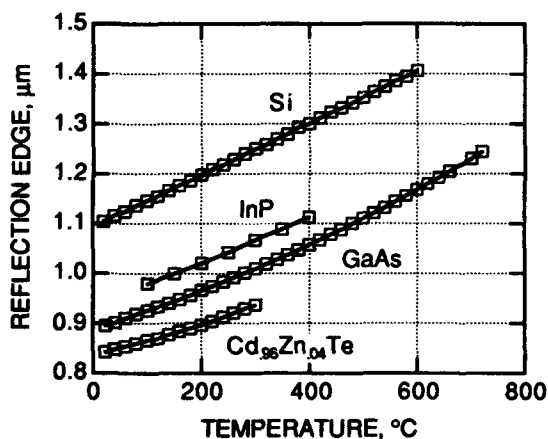


Figure 3. Temperature dependence of the reflection step wavelength for Si, InP, GaAs and CdZnTe.

Other factors, such as the alloy concentration in the case of ternary alloy substrates such as CdZnTe, and doping concentration in the case of III-V's, can also affect the temperature calibration. To account for these factors, the most reliable procedure is to accumulate separate calibration spectra for each type of substrate. If this is done, the temperature accuracy achievable on a bare substrate in the MBE chamber is approximately  $\pm 2^\circ\text{C}$ , limited primarily by the temperature accuracy of the *ex situ* calibration data. During growth the accuracy may be further degraded by interference effects, as discussed below.

The band-edge reflectance step is largest for wafers polished on both sides. However, single-polished wafers can also be used if the incident light strikes the rough (i.e., the back) surface first. Figure 4 shows reflectivity spectra for single-polished Si and GaAs, and it is clear from the figure that even though the total reflectance is reduced, the band-edge step is quite apparent, and can readily be used to determine the temperature with only a slight loss of accuracy.

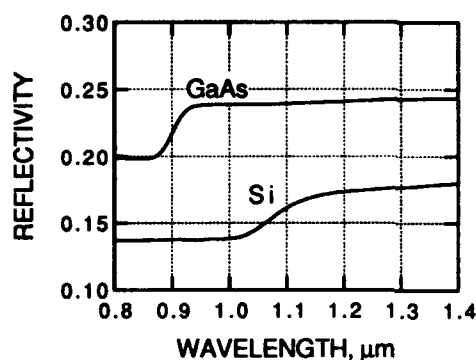


Figure 4. Reflection spectra for single-polished wafers of GaAs and Si at  $20^\circ\text{C}$ . Light incident on the rough (back) side.

Band-edge reflection spectroscopy measurements have been used to monitor the temperature of a radiantly-heated, 3-inch diameter Si wafer during a heating program similar to that typically used for *in situ* substrate cleaning and subsequent growth of ZnTe and CdTe epitaxial layers. Figure 5 compares the temperature determined by the BRS technique with the readings of a thermocouple placed in conductive contact with the substrate heater. (In these experiments, the thermocouple signal was used for closed-loop control of the heater temperature.)

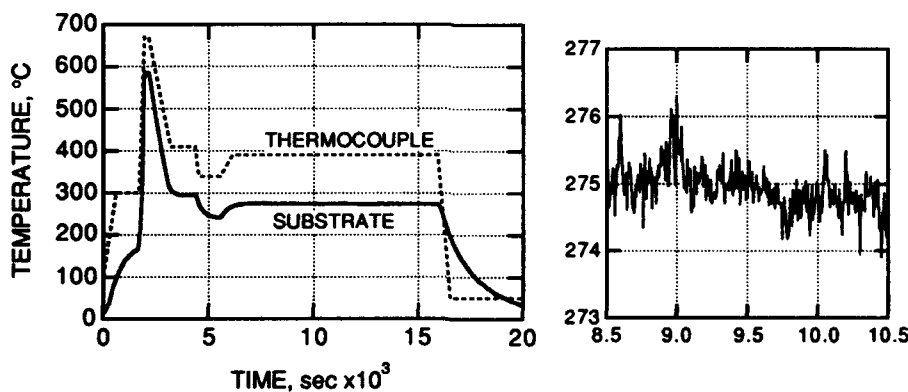


Figure 5. Temperature measurements made *in situ* on a Si wafer in the MBE chamber: a) comparison of substrate temperature determined by BRS and the indications of a thermocouple attached to the heater; b) expanded view of the segment from 8,500 to 10,500 sec.

These data show that BRS allows the true substrate temperature to be determined over a wide temperature range. Figure 5b shows an expanded view of a portion of the temperature curve to indicate the magnitude of short-term fluctuations in the substrate temperature. Excursions of less than  $\pm 1^\circ$  are observed over a time period of 2000 seconds. It can also be seen from the data that the dynamic response of the substrate wafer is quite different from that of the thermocouple, particularly at temperatures below  $300^\circ\text{C}$  where the wafer temperature takes several thousand seconds to reach steady state.

As mentioned above, the determination of substrate temperature from BRS measurements made on bare wafers is straightforward. During growth of epitaxial layers, however, optical interference effects distort the reflection spectra. These effects are most evident when reflectivity measurements are made from the front side of the wafer. Figure 6 illustrates this problem for the case of ZnTe growth on Si, where reflectivity spectra were recorded at 5 sec. intervals during the growth, corresponding to  $20\text{\AA}$  thickness increments. Interference fringes are seen on both sides of the band-edge step, and although it is not obvious in the figure, the wavelength at which the step occurs is observed to oscillate as the film thickness increases, producing an apparent oscillation in the calculated temperature. For the conditions shown, these oscillations are on the order of  $\pm 5^\circ\text{C}$ , but for thicker ZnTe layers, the excursions can reach  $\pm 20^\circ\text{C}$ .

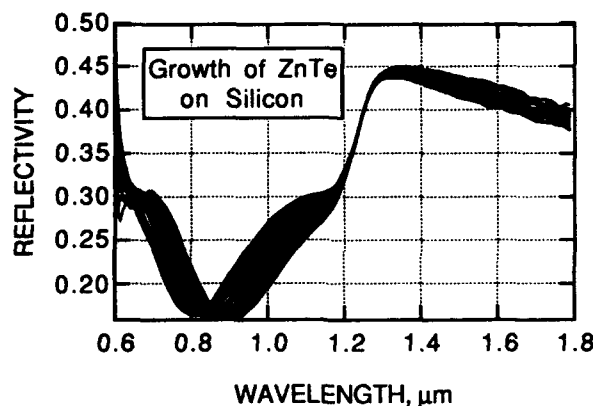


Figure 6. Reflectivity data taken during the growth of ZnTe on Si at  $175^\circ\text{C}$ . Spectra were recorded every 5 seconds, and the growth rate was  $4\text{\AA}/\text{s}$ . The ZnTe thickness is approximately  $2000\text{\AA}$  for these data.

There are several ways to correct for interference effects in order to recover the true temperature of the substrate. We have found that by applying a simple optical model, interference structure can be deconvolved from the reflectivity data in real time, and spurious temperature oscillations can be limited to less than  $\pm 5^\circ\text{C}$  for ZnTe growth on Si. A more effective approach is to make the reflectivity measurements from the back side of the substrate. In this measurement geometry interference effects are much more manageable, as can be seen from the data in Figure 7. Here we compare the back-side reflectivity spectrum of a sample containing epitaxial layers of ZnTe and CdZnTe grown on a Si substrate with the spectrum taken from the bare Si substrate prior to growth. Interference oscillations appear only on the long-wavelength side of the reflection step and their amplitude is rapidly attenuated in the vicinity of the step itself. Consequently the position of the band-edge step can be determined with good accuracy from the portion of the data where the reflectivity

just begins to rise above the first-surface value (i.e., the short-wavelength side). This procedure yields temperatures that deviate by no more than  $\pm 2^\circ\text{C}$  from those determined in the absence of the epitaxial layer.

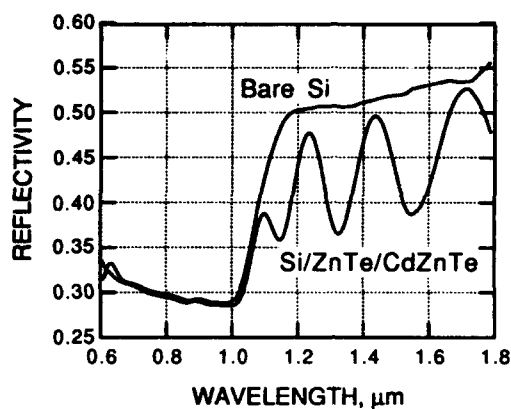


Figure 7. Back-side reflectivity spectra for a sample consisting of epitaxial layers of ZnTe and CdZnTe grown on Si by MBE, compared to the bare Si substrate. Data taken at  $20^\circ\text{C}$

#### ACKNOWLEDGMENTS

The expert technical assistance of C. A. LeBeau is gratefully acknowledged. This work was partially supported by ARPA under the auspices of Agreement MDA972-93-H-0005.

#### REFERENCES

1. E. S. Hellman and J. S. Harris, *J. Cryst. Growth* **81**, 38 (1987).
2. M. B. Panish and H. C. Casey, *J. Appl. Phys.* **40**, 163 (1969).
3. C. D. Thurmond, *J. Electrochem. Soc.* **122**, 1133 (1975).
4. R. A. Powell and D. Kirillov, MIMIC Phase III Contract No. DAAL01-89-C-0907, January 1991; D. Kirillov and R. A. Powell, U. S. Patent No. 5,118,200, June 2, 1992.
5. M. E. Adel, Y. Ish-Shalom, S. Mangan, D. Cabib and H. Gilboa, *SPIE Proc.* **1803**, 55 (1992).
6. M. K. Weilmeier, K. M. Colbow, T. Tiedje, T. Van Buuren and Li Xu, *Can. J. Phys.* **69**, 422 (1991).
7. S. R. Johnson, C. Lavoie, T. Tiedje and J. A. Mackenzie, *J. Vac. Sci. Technol.* **B11**, 1007 (1993).



## SINGLE PHOTON LASER IONIZATION AS AN IN-SITU DIAGNOSTIC FOR MBE GROWTH

APRIL L. ALSTRIN, ADINA K. KUNZ, PAUL G. STRUPP,\* AND STEPHEN R. LEONE\*\*

Joint Institute for Laboratory Astrophysics, National Institute of Standards and Technology and  
University of Colorado; Department of Chemistry and Biochemistry, University of Colorado,  
Boulder, Colorado 80309-0440

\*NRC-NIST postdoctoral fellow, present address Rocky Mountain Magnetics, Louisville,  
Colorado 80028-8188

\*\*Staff Member, Quantum Physics Division, National Institute of Standards and Technology

### ABSTRACT

Single photon laser ionization time-of-flight mass spectroscopy (SPI-TOFMS) is used to monitor the gaseous fluxes of Ga and As<sub>n</sub>, during molecular beam epitaxy of GaAs. This noninvasive and real-time probe measures densities, and hence fluxes, of multiple chemical species impinging on or scattered from a substrate during conventional MBE. With single photon ionization at 118 nm (10.5 eV, ninth harmonic of Nd:YAG laser), the photon energy is large enough to ionize the species, but insufficient to both ionize and fragment. The lack of molecular dissociation of As<sub>2</sub> and As<sub>4</sub> greatly simplifies the interpretation of mass spectra. Additionally, the geometry of the single photon ionization TOFMS permits simultaneous film growth monitoring using RHEED. Results will be presented on the probing of scattering and desorption of III-V MBE species during GaAs growth. This technique promises to be a valuable in-situ diagnostic for III-V and II-VI MBE.

### INTRODUCTION

The development of improved in-situ diagnostics for molecular beam epitaxy (MBE) is necessary for better control of the material deposition process. Through such monitoring, higher quality semiconductor devices with fewer failure rates and defects and sharper junctions will result. Laser probing of the gaseous species used in MBE allows nonintrusive and real time monitoring of the incoming and scattered chemical fluxes a few millimeters in front of the growing substrate. These in-situ diagnostics can provide feedback for continual flux adjustments, characterize and quantify the growth process, and determine the purities of the semiconductor materials used in the manufacturing process.

Only limited flux information is available with current MBE growth monitors. For example, both nude ionization gauges and quartz crystal microbalances quantify fluxes but yield no species-specific information. Although species specific, many spectroscopic techniques such as electron impact emission, hollow cathode discharge lamps for emission or absorption, and laser-induced fluorescence are not easily applied when simultaneous monitoring of multiple species is required. Reflection mass spectroscopy (REMS)<sup>1-3</sup> can be used to monitor several reflecting species, but is unable to monitor incoming fluxes. Additionally, measurements are hindered by fragmentation of molecular species in the electron impact mass spectrometer ionizer which complicates the signal interpretations. Reflection high energy electron diffraction (RHEED) monitors growth rate but does not provide information on the composition of the impinging beams. It would be valuable to have complementary, noninvasive methods to monitor multiple gaseous species quantitatively and

in real time while simultaneously monitoring film growth with techniques such as RHEED or ellipsometry.

Single photon ionization (SPI) greatly reduces molecular fragmentation compared with multiphoton ionization and electron impact ionizers. This has previously been demonstrated for large molecules such as organic polymers<sup>4</sup> and polypeptides.<sup>5</sup> The photon energy used is large enough to ionize, but not sufficient to ionize and fragment the molecule. By avoiding the dissociation of molecules such as As<sub>2</sub> and As<sub>4</sub> during MBE probing, the interpretation of mass spectra is greatly simplified. Most species relevant to III-V and II-VI MBE have ionization potentials less than the ninth harmonic (118 nm, 10.5 eV) of the Nd:YAG laser and can be detected by SPI (see Table I). The application of SPI to MBE species is a straightforward, quite general, and powerful analytical technique.

Table I. Species Ionizable at 118 nm (10.5 eV)<sup>a</sup>

| Species                           | I.P. (eV)        | Species                           | I.P. (eV) | Species                           | I.P. (eV) |
|-----------------------------------|------------------|-----------------------------------|-----------|-----------------------------------|-----------|
| Al                                | 6.0              | Cd(CH <sub>3</sub> ) <sub>2</sub> | 8.6       | Se                                | 9.8       |
| Al(CH <sub>3</sub> ) <sub>3</sub> | 9.1              | Ga                                | 6.0       | Si                                | 8.1       |
| As                                | 9.8              | Hg                                | 10.4      | Sn                                | 7.3       |
| As <sub>2</sub>                   | 9.7 <sup>b</sup> | In                                | 5.8       | Sn(CH <sub>3</sub> ) <sub>2</sub> | 8.0       |
| As <sub>4</sub>                   | 8.5 <sup>b</sup> | Mn                                | 7.4       | Te                                | 9.0       |
| AsH <sub>3</sub>                  | 10.0             | P <sub>4</sub>                    | 9.7       | Zn                                | 9.4       |
| Cd                                | 9.0              | PH <sub>3</sub>                   | 10.0      | Zn(CH <sub>3</sub> ) <sub>2</sub> | 9.0       |

<sup>a</sup> All ionization potentials from Ref. 6 except where noted.

<sup>b</sup> Ref. 7

## EXPERIMENTAL

The experimental apparatus (Fig. 1) consists of an ultrahigh vacuum chamber,<sup>8-10</sup> similar to a commercial MBE system. The chamber is equipped with low energy electron diffraction (LEED), RHEED, Auger electron spectroscopy (AES), residual gas analyzer, and Ar ion sputtering for substrate cleaning. Simultaneous MBE growth, RHEED surface analysis, and spectroscopic detection of the gas phase species approximately 1 cm in front of the substrate are possible with the chamber configuration. Mass detection is accomplished by laser single photon ionization time-of-flight mass spectroscopy (SPI-TOFMS).<sup>10</sup>

The growth of III-V materials is carried out in the home-built MBE apparatus.<sup>8</sup> The MBE source region is differentially pumped, cryoshielded, and uses two commercial oven sources to produce beams of Ga, As<sub>2</sub>, and As<sub>4</sub>. The As<sub>2</sub> source is an As<sub>4</sub> oven-cracker. The GaAs (100) substrate used in these studies is Ar<sup>+</sup> sputtered and then annealed in an As<sub>4</sub> beam to remove contamination. A GaAs buffer layer is then grown before experiments begin. RHEED shows the substrate is smooth, well ordered, and As-stable. During growth, RHEED intensity oscillations occur and are monitored with a CCD camera and photodiode system.

SPI-TOFMS is used to probe the incoming, desorbing, and/or scattering gas phase species. The ionizing laser (discussed below) passes ~1 cm in front of and parallel to the substrate which is

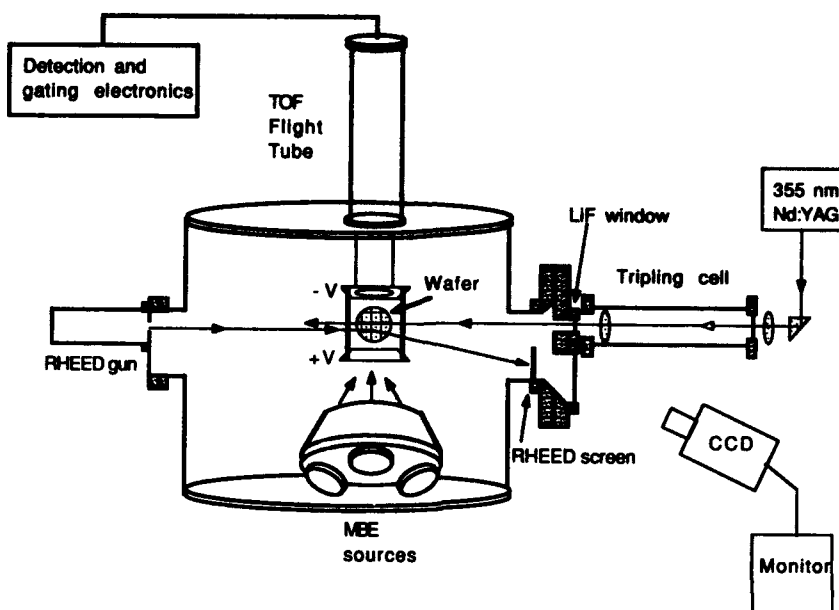


Fig. 1. Schematic of the experimental apparatus.

mounted within the Wiley-McLaren TOFMS<sup>11</sup> extraction region. Ion extraction is accomplished perpendicular to the surface normal. The generated ions travel up a 1 m flight tube and are detected by an electron multiplier. Due to its greater resistance to deterioration by arsenic, a focussed mesh multiplier is used instead of a microchannel plate. Since ion arrival times at the detector are determined by mass, time-gated signals can be selected and integrated to provide simultaneous time histories of fluxes incident or scattered from the surface.

Simultaneous access to the substrate by the molecular beams, the ionizing laser, and a RHEED electron beam is allowed with the chamber geometry. By keeping the region around the substrate near ground potential, as opposed to typical TOFMS where the extraction region is held at a high positive potential,<sup>11</sup> the RHEED electron beam interacts with the substrate surface with minimum distortion. The diffraction pattern on the phosphor screen is deflected slightly downward (approximately 2 cm in our case) when voltages are applied to the TOFMS extraction region but the pattern itself is not significantly altered. The distance that the specular beam is deflected agrees well with a calculated deflection based on electron beam energy, TOFMS extraction voltages, and chamber dimensions. A portion of the RHEED screen has been cut away to allow the introduction of the laser beam.

The 118 nm ionizing laser light is produced by focussing the 355 nm frequency tripled output of a pulsed Nd:YAG laser into a static cell of Xe and Ar.<sup>12-15</sup> Due to the refractive index differences between 118 nm and 355 nm, a LiF lens is used to diffuse the 355 nm beam and collimate the 118 nm beam which then propagates through a LiF window into the vacuum chamber and the extraction region. The 10.5 eV photons gently ionize the gaseous species ( $\text{As}_4$ ,  $\text{As}_2$ , and

Ga) with a single photon. Previous studies have shown that less than 0.4% of the  $\text{As}_4$  fragments to  $\text{As}_2^+$ , and signal levels of  $\text{As}_3^+$  are less than 0.1% (noise level) of the  $\text{As}_4^+$  signal. Neither  $\text{As}_4$  nor  $\text{As}_2$  is fragmented to  $\text{As}^+$ .<sup>10</sup> Under typical operating conditions, the Xe pressure is  $2.13 \times 10^{-3}$  Pa with  $1.86 \times 10^4$  Pa of Ar added to achieve the phase matching condition, and the 355 nm pulse energy is 15 mJ, with a 5 ns pulse duration and 10 Hz repetition rate. Values of the tripling efficiency to 118 nm in Xe are reported to be approximately  $10^{-5}$  using 20 mJ of 355 nm.<sup>15</sup>

The SPI-TOFMS technique measures species density and not flux. A velocity correction based on the mass and source temperature of each species must be applied to convert the ionization signals to fluxes. The relative sensitivities to different chemical fluxes depend on each species' ionization probability, angular distribution, and TOF collection efficiency. If relative sensitivities between species have been determined, quantitative monitoring is possible. Previous studies in our system have found the relative sensitivity factors between  $\text{As}_4$ ,  $\text{As}_2$ , and  $\text{As}$  to be 12:3:1.<sup>10,16</sup> Ga appears to have a low ionization probability at 118 nm.<sup>10,17</sup>

## RESULTS AND DISCUSSION

### Mass Spectra

The SPI-TOFMS method is used to probe the gas phase species above a GaAs wafer during growth at a surface temperature of 920 K. Figure 2 shows a mass spectrum resulting from a summation average of 1800 laser pulses. Signals corresponding to  $^{69}\text{Ga}^+$  (69 m/Z),  $^{71}\text{Ga}^+$  (71 m/Z),  $\text{As}_2^+$  (150 m/Z), and  $\text{As}_4^+$  (300 m/Z) are observed (where m is mass, Z is atomic number). The  $\text{As}_4^+$  originates from incoming and unincorporated (scattered)  $\text{As}_4$  flux. Because  $\text{As}_4$  does not

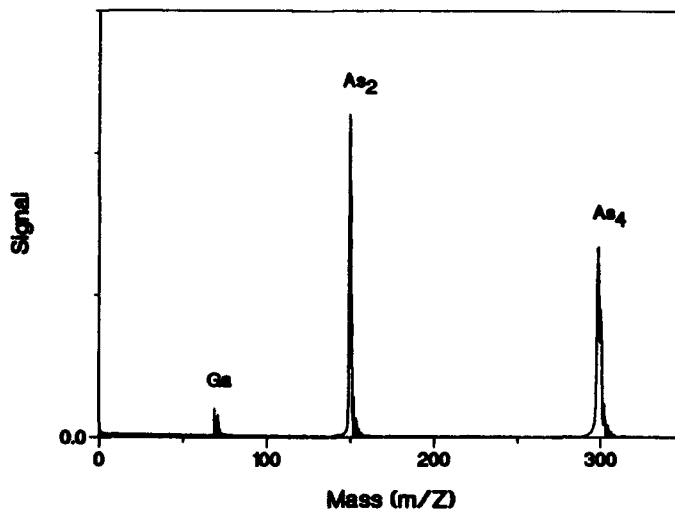


Fig. 2. Mass spectrum of gas phase species above a growing GaAs wafer at 920 K resulting from a summation of 1800 laser shots. Signals corresponding to  $^{69}\text{Ga}^+$ ,  $^{71}\text{Ga}^+$ ,  $\text{As}_2^+$ , and  $\text{As}_4^+$  are observed.

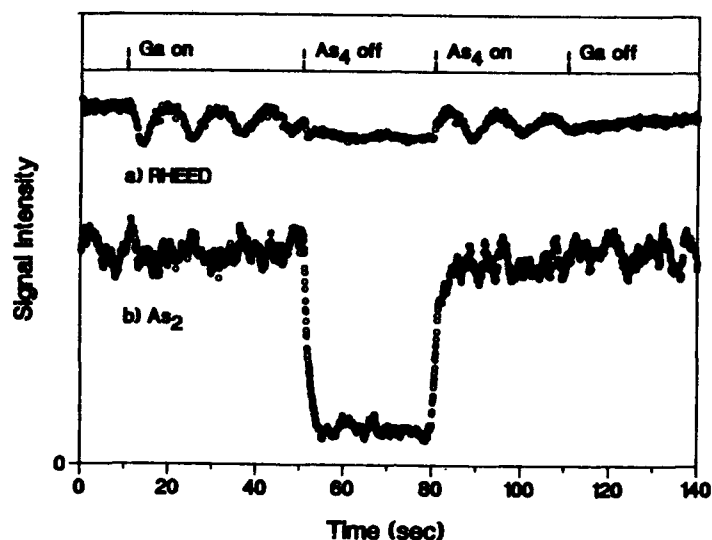


Fig. 3. An example of simultaneous monitoring with RHEED and SPI-TOFMS during GaAs growth at 800 K. (a) RHEED intensity. (b) Time behavior of the desorbing  $\text{As}_2$  flux.

fragment to  $\text{As}_2^+$  with single photon ionization at 118 nm, the entire  $\text{As}_2^+$  signal arises from  $\text{As}_2$  that is desorbed or chemically formed at the substrate.

Not only is this technique excellent for detecting scattered and desorbed species, it is well suited as a flux monitor with feedback control. By swinging the sample out of the extraction region, the incoming flux can be exclusively probed. GaAs growth depends on many parameters. The ability to monitor noninvasively the Ga flux,  $\text{As}_4$  flux, and their ratio during growth will improve process control. Previous results have also shown that SPI-TOFMS readily detects oven cross contamination.<sup>10</sup>

#### SPI-TOFMS and RHEED

Our experimental setup allows for simultaneous monitoring with RHEED and SPI-TOFMS. For the data shown in Figure 3, a GaAs substrate at 820 K was maintained under an  $\text{As}_4$  flux. After 15 sec, the Ga oven was opened and layer-by-layer growth commenced. The  $\text{As}_4$  oven was shuttered at 50 sec and reopened at 80 sec. The Ga oven was closed after 110 sec. The top trace shows the corresponding RHEED intensity changes. The behavior of the desorbing  $\text{As}_2$  flux during these times is plotted in the lower trace.

The RHEED response (Fig. 3a) is well understood by GaAs researchers. Under the  $\text{As}_4$  flux, the surface is As-stable. When the Ga flux is introduced, layer-by-layer growth at a rate determined by the Ga flux (in this case  $0.09 \text{ ML sec}^{-1}$ ) begins. Removal of the arsenic flux leads to a reconstruction change from  $2 \times 4$  As-stable through  $3 \times 1$  to the  $4 \times 2$  Ga stable. This is seen in the sudden intensity decrease and recovery at a lower intensity. Upon reintroduction of the  $\text{As}_4$  flux, the As-stable surface recovers and layer-by-layer growth begins again. After the Ga is

blocked, the growth oscillations cease.

By monitoring the ion signals measured with SPI-TOFMS, the corresponding fluctuations in species' fluxes are also obtained. The  $As_2$  is newly generated at the growing substrate and is followed by time-gated mass detection in Figure 3b. The most obvious feature is the drastic decrease in  $As_2$  desorption when  $As_4$  is not supplied to the surface. The signal decay indicates that some  $As_2$  continues to desorb after termination of the  $As_4$  flux, while the slight positive increase in time after the abrupt increase when the oven is reopened indicates that an initial uptake of arsenic occurs in the growing layer. The results indicate that it should be feasible to detect small changes in arsenic sticking coefficient by monitoring the desorbing fluxes during the layer-by-layer growth. Presently the noise in the  $As_2^+$  signal is due to pulse-to-pulse fluctuations of the laser, which will be normalized out in future experiments.

Single photon ionization time-of-flight mass spectroscopy is a promising new analytical technique for monitoring MBE growth. This nonintrusive probe is compatible with RHEED monitoring and can provide additional insight into the chemistry that occurs on and above a growing epitaxial layer. More versatile than RHEED, SPI-TOFMS can be used with rotating samples and under higher temperature growth conditions where layer-by-layer growth does not occur. SPI-TOFMS has great potential, both in practical device fabrication and in fundamental measurements of MBE growth.

Support of this research by the National Institute of Standards and Technology and by the donors of The Petroleum Research Fund, administered by the American Chemical Society, is gratefully acknowledged.

## REFERENCES

1. T. M. Brennan, J. Y. Tsao, and B. E. Hammons, *J. Vac. Sci. Technol. A* **10**, 33 (1992); *J. Cryst. Growth* **111**, 125 (1991); *Appl. Phys. Lett.* **53**, 288 (1988).
2. J. Y. Tsao, T. M. Brennan, J. F. Klem, and B. E. Hammons, *Appl. Phys. Lett.* **55**, 777 (1989).
3. F. G. Celii, Y. C. Kao, E. A. Beam, III, W. M. Duncan, and T. S. Moise, *J. Vac. Sci. Technol. B* **11**, 1018 (1993).
4. J. B. Pallix, U. Schuhle, C. H. Becker, and D. L. Huestis, *Anal. Chem.* **61**, 805 (1989).
5. C. H. Becker, L. E. Jusinski, and L. Moro, *Int. J. Mass Spectrom. Ion Proc.* **95**, R1 (1990).
6. H. M. Rosenstock, K. Draxl, B. W. Steiner, and J. T. Herron, *J. Phys. Chem. Ref. Data* **6**, Supp. 1 (1977).
7. R. K. Yoo, B. Ruscic, and J. Berkowitz, *J. Chem. Phys.* **96**, 3696 (1992).
8. R. V. Smilgys and S. R. Leone, *J. Vac. Sci. Technol. B* **8**, 1141 (1987).
9. A. L. Alstrin, R. V. Smilgys, P. G. Strupp, and S. R. Leone, *J. Chem. Phys.* **97**, 6864 (1992).
10. P. G. Strupp, A. L. Alstrin, R. V. Smilgys, and S. R. Leone, *Appl. Opt.* **32**, 842 (1993).
11. W. C. Wiley and I. H. McLaren, *Rev. Sci. Instrum.* **26**, 1150 (1955).
12. A. H. Kung, J. F. Young, and S. E. Harris, *Appl. Phys. Lett.* **22**, 301 (1973).
13. L. J. Zych and J. F. Young, *IEEE J. Quant. Electron.* **14**, 147 (1978).
14. R. Mahon, T. J. McIlrath, V. P. Myerscough, and D. W. Koopman, *IEEE J. Quant. Electron.* **15**, 444 (1979).
15. R. Hilbig and R. Wallenstein, *IEEE J. Quant. Electron.* **17**, 1566 (1981).
16. A. L. Alstrin, P. G. Strupp, and S. R. Leone, *Appl. Phys. Lett.* **63**, 815 (1993).
17. A. L. Alstrin, P. G. Strupp, L. Cook, and S. R. Leone, *SPIE* **1858**, 367 (1993).

**Real-time Monitoring and Control of Silicon Epitaxy Using  
Emission Fourier Transform Infrared Spectroscopy  
Z.H. Zhou, H. Kim\*, and Rafael Reif  
Department of Electrical Engineering and Computer Science  
\* Department of Materials Science and Engineering  
Massachusetts Institute of Technology  
Cambridge, MA 02139**

**Abstract**

Real-time epi-film thickness is measured by an Emission Fourier Transform Infrared Spectrometer (E/FT-IR). The E/FT-IR takes advantage of the heated wafer as the source of IR radiation. In our experiments, wafers were cleaned using in-situ ECR hydrogen plasma followed by film growth. The cleaning and deposition processes were monitored in real-time using the E/FT-IR technique. We have demonstrated the application of E/FT-IR for observing real-time growth rates and incubation times. Based on these real-time observations, the predeposition plasma cleaning process and the deposition process can be effectively monitored and controlled in real-time. Application of E/FT-IR in optimizing the predeposition hydrogen plasma cleaning process was demonstrated.

**Introduction**

The epitaxial film thickness is a critical parameter that must be accurately measured and controlled. For example, it is necessary to ensure that outdiffusion and autodoping during device processing do not significantly consume the epitaxial film. In addition, several bipolar transistor device parameters, such as breakdown voltage, junction capacitance, transistor gain, and high frequency performance, depend on the epi-layer thickness. There are many thin film thickness measurement techniques [1] [2]. However, they are either destructive or not applicable in the case of a silicon epi film on a silicon substrate. The commonly used technique for epi film thickness measurement is the reflectance measurement using an external IR source, and is widely used in industry [3] [4] [5]. But it is only used for *ex-situ* measurement, that is, the measurement is done outside the growth or etching chamber. And it is difficult to be adapted for *in-situ* measurement in its present form. The E/FT-IR technique, on the other hand, takes advantage of a heated wafer as the infrared source. By analyzing the IR emission, we have successfully obtained epitaxial silicon film thickness measurements on heavily doped silicon substrates [6].

**Experimental**

A Bio-Rad FTIR (model FTS-40) spectrometer equipped with a room temperature deuterated triglycine sulfate (DTGS) detector was used to collect the E/FT-IR spectra. The principles of operation for the E/FT-IR technique were reported elsewhere in detail [7]. All experiments were carried out in our multi-chamber single-wafer chemical vapor deposition (MS-CVD) reactor. A description of the reactor was reported in [8].

## Results and Discussions

### Real-time, *in situ* epitaxial process monitoring and epi-film thickness control using E/FT-IR

Although FT-IR spectroscopy using an external IR source is commonly and widely used in the semiconductor industry [9], it is only used for *ex-situ* measurements (i.e., the measurement is performed outside the process chamber) and it is difficult to adapt for *in-situ* measurements. Compared to infrared reflection absorption spectroscopy, the infrared emission spectroscopy does not need an external light source; therefore it is easier to implement, and it is relatively less sensitive to surface roughness and flatness. Moreover, it is robust against vibration, rotation and misalignment of the wafer. Thus, it is well suited for *in situ* monitoring of rotating wafers in production equipment. Consequently, emission FT-IR spectroscopy has significant potential as a real-time *in-situ* process monitor. We have demonstrated that E/FT-IR can be used for measuring epitaxial thin film thickness *in-situ* [6]. Recently, we have successfully applied the E/FT-IR technique to monitor film thickness in real-time during growth in a multi-chamber, single-wafer CVD reactor [8].

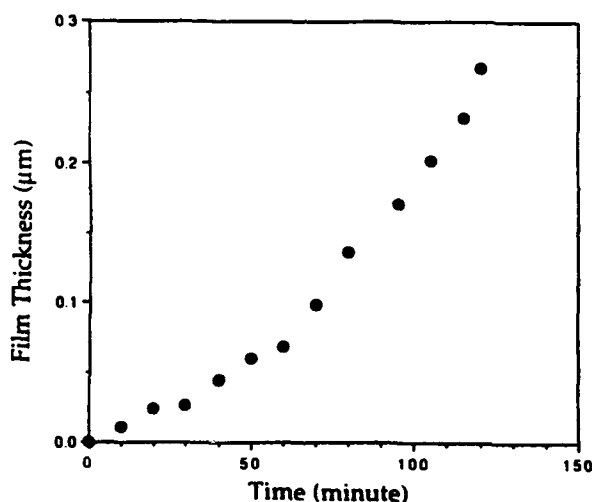


Figure 1. Real-time *in situ* film thickness monitoring during a CVD process at 650 °C.

The real-time film thickness measurement was demonstrated by depositing a film on a substrate with an existing epi-film. The E/FT-IR technique has been applied to measure film thickness *in situ* and in real-time during the deposition processes. A film was deposited on a 3 μm epi wafer (substrate is n-type doped with resistivity equal to 0.001-0.002 Ω-cm; the existing epi layer is also n-type with resistivity equal to about 0.5 Ω-cm). The growing film thickness is the total measured film thickness minus the initial epi-film thickness. Figure 1 shows the real-time film thickness measurements during a thermal CVD process at a temperature of 650 °C. The wafer is cleaned simply by dipping it in HF (10:1) solution without being rinsed before it was introduced into the CVD reactor. Deposition was carried out at a pressure of 2 mTorr by introducing 40 sccm of pure silane. The slope of the curve



gives us the growth rates, and we see that the initial growth rate is slower. Although the reasons for this change in growth rate is unknown at present, we believe it may be related to perturbations in the deposition parameters. In addition, the real-time *in situ* monitor can be used for endpoint detection and control. For example, if a  $0.27\ \mu\text{m}$  epi-layer is desired (see Fig.1), the deposition process can be terminated when the E/FT-IR gives a  $0.27\ \mu\text{m}$  epi-film thickness reading. For an even more precise endpoint control, the real-time film thickness measurements can be used to extrapolate a real-time growth rate, therefore endpoint can be predicted in real-time. The final thickness measurement was confirmed by *ex situ* FT-IR and high resolution cross-sectional transmission electron microscopy (HRXTEM) which gave measured film thicknesses of  $0.26\ \mu\text{m}$  and  $0.3\ \mu\text{m}$ , respectively. The E/FT-IR technique is particularly suited for real-time process monitoring, as it allows repeatable, fast, and accurate ( $0.01\ \mu\text{m}$  precision) measurement of film thickness. This thickness information can be fed-back in real-time to control film thickness precisely.

#### Optimization of ECR hydrogen plasma predeposition wafer cleaning

In addition to real-time *in-situ* monitor and control of epi film thickness, we have observed growth rate changes and incubation times resulting from various predeposition wafer cleaning conditions. By real-time monitoring of incubation time and growth rate, we were able to obtain qualitative information about the effectiveness of the predeposition wafer cleaning process and to assess the quality of the depositing film in real-time.

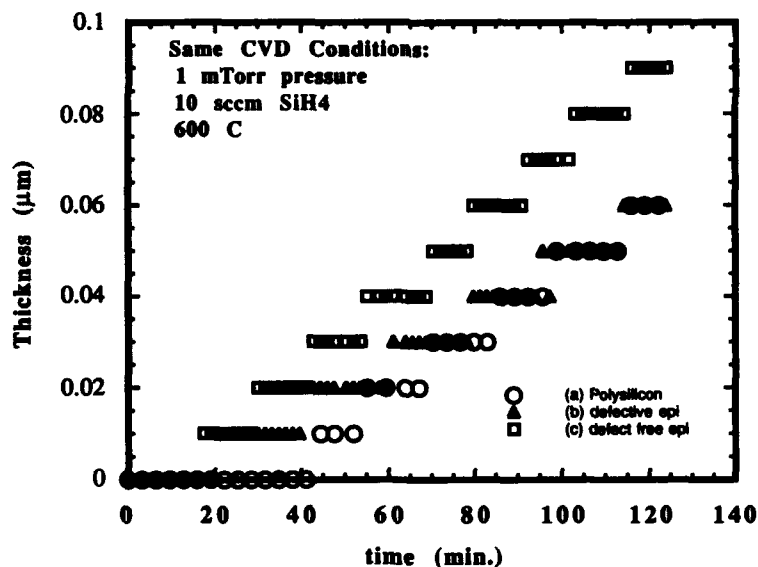


Figure 2. Real-time *in situ* monitoring of growth incubation time and growth rate during a CVD process.

Figure 2 shows the real-time thickness monitoring results of three depositions performed under the same deposition conditions (see inset in Fig.2). Data (a) (Fig.2) shows an incuba-

tion time of 30 minutes resulting from a deposition on a native oxide covered silicon surface. Subsequent cross sectional transmission electron microscopy (XTEM) confirmed that the deposited film was polycrystalline silicon. Data (b) does not show an incubation time; however, the growth rate is slower compared to that in Figure 2(c). The corresponding XTEM picture shows that the film grown with slower growth rate is a defective epi film. The XTEM picture corresponding to Data (c) shows that a defect free epi-film is deposited after ECR hydrogen plasma cleaning. However, the interface between the epi-film and substrate was clearly visible, suggesting that the process condition was not optimised. We carried out a  $L_{12}$  orthogonal design of experiments for optimising the ECR hydrogen plasma predeposition wafer cleaning process. We kept the same deposition condition after each cleaning experiment. Using the E/FT-IR, we have eliminated many unnecessary post-deposition materials characterisations (e.g. Rutherford back scattering (RBS), cross sectional transmission electron microscopy (XTEM), and secondary ion mass spectroscopy (SIMS)). When we saw an incubation time and/or slow growth rate, we knew that the cleaning process was ineffective and that the epi-film was defective, consequently we did not perform those time consuming and costly post-deposition materials characterizations. Thus, plasma cleaning process optimization time was shortened and post-deposition materials characterization cost was reduced.



Figure 3. Cross-sectional TEM picture of a defective epi-film.

In addition, we observed that a plus 10 Vdc bias applied to the wafer was important to reduce ion damage. Previously, it was shown that hydrogen plasma cleaning of silicon dioxide required ion bombardment[10]. Since the mass of hydrogen molecules is relatively small, one might expect minimum damage from hydrogen ions; however, severe damage by hydrogen ions was observed during radio frequency hydrogen plasma cleaning process [10]. We found that a plus 10 volts DC bias was required to suppress damage by ECR hydrogen plasma. Figure 3 shows a XTEM picture of a sample that was cleaned by ECR hydrogen plasma at -50 Vdc bias. Clearly, an interface layer of about 30 nm was observed. We believe this interfacial layer was the damaged surface layer prior to film growth. Moreover, the contrast

below the interface within the substrate indicates possible stress field resulting from the defective film. Moreover, the XTEM picture of a sample that was cleaned by ECR hydrogen plasma (under the same cleaning conditions) with a 0 Vdc bias showed a defect free film. However, the interface between the film and substrate of the sample was still clearly visible.

Figure 4 (a) shows the real-time thickness monitoring results of a wafer that was cleaned under an optimised cleaning condition with a plus 10 volts DC bias. The deposition condition and the optimised plasma cleaning condition are specified in Figure 4(a). The corresponding XTEM picture (Fig. 4(b)) shows that this film was defect free and the epi-substrate interface was almost invisible. This indicated that under these conditions, the ECR hydrogen plasma did not damage the wafer surface and the surface was in good condition prior to film growth.

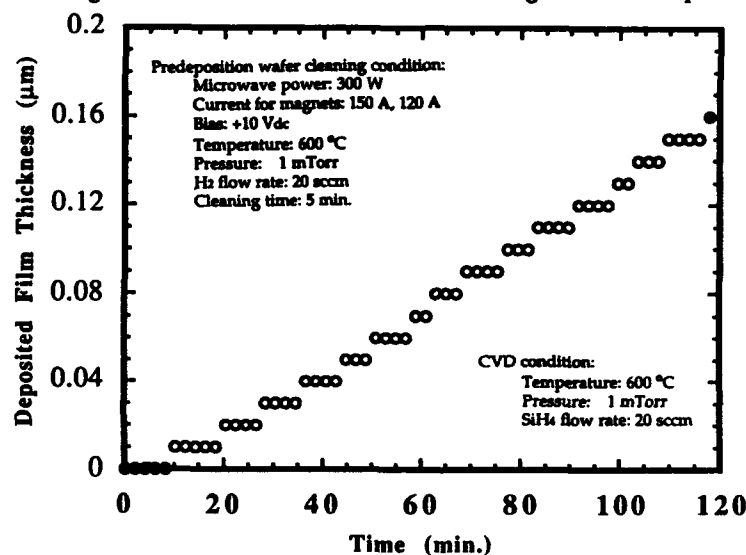


Figure 4. (a) Real-time *in situ* film thickness monitoring during a CVD process after hydrogen plasma predeposition cleaning; (b). Cross-sectional TEM picture of a defect free epi-film.

## Conclusion

We have reported an emission FTIR technique for epi-film thickness measurement. We have demonstrated that the E/FT-IR technique can be used as a noncontact, nondestructive *in-situ*, real-time film thickness monitoring tool. Moreover, an application of E/FT-IR for real-time *in situ* monitoring of epitaxial silicon film thickness is demonstrated. From the real-time thickness measurements, growth rates can be obtained in real-time and the end-point epi-film thickness can be controlled precisely. Furthermore, we have demonstrated an application of E/FT-IR for optimising the predeposition hydrogen plasma cleaning process. We have shown that by using a real-time *in situ* monitor, process optimization time can be shortened and materials characterization cost can be reduced.

## Acknowledgment

The authors are grateful to Dr. P. Langer of AT&T Bell Labs. for supplying us with epi-wafers. Zhen-Hong Zhou would like to acknowledge a Doctoral Fellowship support from AT&T Bell Laboratories since 1990. This work was completed under the support of SEMATECH contract 90-MC-503.

## References

- [1] L.I. Maissel and R. Glang, *Handbook of thin film technology*, (McGraw-Hill, New York, 1970), p. 11-29.
- [2] Y.H. Lee, Z.H. Zhou, D.A. Danner, P.M. Fryer, and J.M. Harper, *J. App. Phys.*, 68, p. 5329, (1990).
- [3] P.R. Griffiths and J.A. Haseth, *Fourier Transform Infrared Spectrometry*, (J. Wiley, New York, 1986).
- [4] K. Krishnan, P.J. Stout, in *Practical Fourier Transform Infrared Spectroscopy*, edit by J.R. Ferraro, K. Krishnan, (Academic Press, 1990), Chap.6, pp. 285.
- [5] K. Krishnan, *ASTM Spec. Tech.*, Publ. 850, pp. 358, (1984).
- [6] F. Yu, Z.H. Zhou, P. Stout, R. Reif, "In - situ Monitoring of Epitaxial Film Thickness by IEMI", *IEEE Trans. on Semicon. Manufac.* 5, 34, (1992).
- [7] Z.H. Zhou, F. Yu, I. Yang, and R. Reif, *J. of Appl. Phys.*, 73 (11), p7331-7, (1993)
- [8] Z.H. Zhou, F.Z. Yu, and R. Reif, *J. Vac. Sci. Tech.*, B.9 (2), 374, (1991).
- [9] D.L. Rehrig, "In search of precise Epi thickness measurements", *Semiconductor International*, 11, 90, (Nov. 1990).
- [10] Z.H. Zhou, E. Adyil, R.A. Gottscho, Y.J. Chabal, R. Reif, *J. Electrochem. Soc.*, 140 (11), p3316-21, (1993)

---

## PART VI

---

### **Ex-Situ Process Diagnostics**

## DEEP-LEVEL TRANSIENT SPECTROSCOPY STUDIES OF CZOCHELSKI-GROWN N-TYPE SILICON

YUTAKA TOKUDA\*, ISAO KATOH\*, MASAYUKI KATAYAMA\*\*, AND  
TADASI HATTORI\*\*

\* Department of Electronics, Aichi Institute of Technology,  
Yakusa, Toyota 470-03, Japan

\*\* Research Laboratories, Nippondenso Co. Ltd.,  
Nisshin, Aichi 470-01, Japan

### ABSTRACT

Electron traps in Czochralski-grown n-type (100) silicon with and without donor annihilation annealing have been studied by deep-level transient spectroscopy. A total of eight electron traps are observed in the concentration range  $10^{10}$ – $10^{11}$  cm<sup>-3</sup>. It is thought that these are grown-in defects during crystal growth cooling period including donor annihilation annealing. It is suggested that two electron traps labelled A2 (Ec-0.34 eV) and A3 (Ec-0.38 eV) of these traps are correlated with oxygen-related defects. It is shown that traps A2 and A3 are formed around 400 °C and disappear around 500–600 °C.

### I. INTRODUCTION

Oxygen is incorporated in Czochralski-grown (CZ) silicon during crystal growth. Oxygen normally occupies the interstitial site (Oi) and is electrically inactive. However, oxygen tends to precipitate and interact with point defects during crystal growth cooling period, since the dissolved oxygen concentration in CZ silicon is far above the solubility limit. It is possible that the resultant oxygen-related defects are electrically active. Thermal donor is one of the well-known oxygen-related defects [1],[2].

Nauka et al. [3] have observed oxygen-induced recombination centers in as-grown CZ silicon. Recently, Mishra et al. [4] have reported that oxygen-related defects act as minority carrier traps in p-type CZ silicon. On the other hand, grown-in defects in CZ silicon have been studied using positron annihilation method, which has indicated that vacancy-type defects as well as oxygen clusters are present in as-grown CZ silicon [5]. It is important to investigate grown-in defects in CZ silicon, since these may play an important role for LSI device processing through the precipitation of oxygen [6].

Deep-level transient spectroscopy (DLTS) is a powerful technique to study traps in semiconductors [7]. Grown-in defects in bulk GaAs have been extensively studied by this technique [8]. However, there are few DLTS studies on grown-in defects in CZ silicon, probably because of very small concentration of defects, although defects introduced by high temperature heat treatment have been studied by DLTS [9–11].

In this study, we apply DLTS with a bipolar rectangular weighting function to characterize grown-in defects in n-type (100) CZ silicon with and without donor annihilation annealing. Trap concentrations observed in this work are in the range  $10^{10}$  to  $10^{11}$  cm<sup>-3</sup>.

### II. EXPERIMENTAL PROCEDURE

Five, phosphorus-doped (100) n-type CZ silicon wafers (wafers A, B, C, D and E)

are used and their wafer characteristics are shown in Table I. Wafers A and B are as-grown ones without donor annihilation annealing, while wafers C, D and E receive donor annihilation annealing. Resistivity is measured using the four-point probe method. The interstitial oxygen concentrations are determined by a Shimadzu 8100M Fourier transform infrared spectrometer. The interstitial oxygen concentrations are calculated to JEIDA procedures (a conversion factor of  $3.03 \times 10^{17} \text{ cm}^{-2}$ ). The interstitial oxygen concentrations of wafers A and C are higher than those of wafers B, D and E.

Au Schottky barrier contacts are fabricated on the front surface for these wafers to make DLTS measurements. The back ohmic contacts are produced by using rubbed-on eutectic gallium-indium to avoid high temperature process. Annealing experiments in the temperature range 100 to 650 °C are carried out in flowing N<sub>2</sub> for wafers E. Annealing time is 30 min.

The DLTS method with a bipolar rectangular weighting function, which has a better signal-to-noise ratio compared to the conventional one [12],[13], is employed in this work. The capacitance is measured by using a Boonton 72B capacitance meter. DLTS measurements are made in the temperature range 80–300 K.

### III. EXPERIMENTAL RESULTS

Figure 1 shows the DLTS spectra for wafers A and B which received no donor annihilation annealing. Figure 1(a) shows the DLTS spectrum obtained from the wafer A. Four electron traps labelled A1, A2, A3 and A4 are observed. The energy levels and electron capture cross sections for these traps are presented later. Trap A1, A2, A3 and A4 concentrations are estimated to be  $3.5 \times 10^{10}$ ,  $6.2 \times 10^{10}$ ,  $1.1 \times 10^{11}$  and  $8.4 \times 10^{10} \text{ cm}^{-3}$ , respectively. Figure 1(b) shows the DLTS spectrum obtained from the wafer B. It is found that no electron traps are observed with the DLTS detection

Table I. Characteristics of n-type (100) CZ silicon wafers.

| Wafer | Resistivity<br>[ $\Omega \text{ cm}$ ] | Oxygen<br>concentration<br>[ $10^{18} \text{ cm}^{-3}$ ] | Donor<br>annihilation<br>annealing |
|-------|--|--|------------------------------------|
| A     | 5                                      | 1.4  | no                                 |
| B     | 9                                      | 1.1  | no                                 |
| C     | 40                                     | 1.4  | yes                                |
| D     | 6                                      | 1.0  | yes                                |
| E     | 30                                     | 1.0  | yes                                |

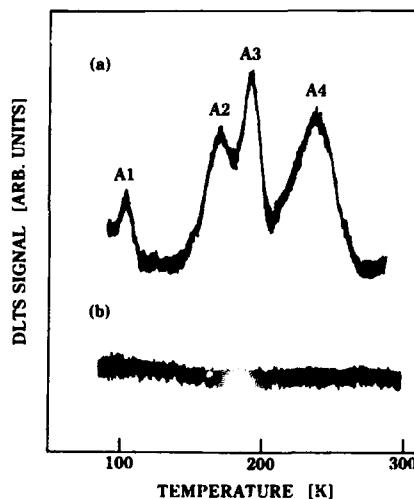


Fig. 1. DLTS spectra for the wafer A (a) and wafer B (b) (  $\tau = 19.1 \text{ ms}$  ).

limit  $\sim 10^{10} \text{ cm}^{-3}$  in the wafer B. This result seems to suggest that traps observed in the wafer A are correlated with oxygen-related defects formed during crystal growth cooling period since the interstitial oxygen concentration for the wafer A is higher than that for the wafer B.

Figure 2 shows the DLTS spectra for wafers C, D and E which received donor annihilation annealing. Traps A2 and A3 are observed in the wafer C as seen from Fig. 2(a). In addition, a trap labelled A5 is observed. Furthermore, the DLTS signals increase below 100 K with decreasing temperature, which indicates the presence of shallower electron traps. Trap A2, A3 and A5 concentrations are estimated to be  $\sim 1 \times 10^{10}$ ,  $1.8 \times 10^{10}$  and  $2.1 \times 10^{10} \text{ cm}^{-3}$ , respectively. The concentration evaluated for the trap A2 is an approximate value, since its DLTS signals are near the detection limit ( $\sim 5 \times 10^9 \text{ cm}^{-3}$ ) and because of overlapping of trap A2 and A3 DLTS signals. Figure 2(b) shows the DLTS spectrum obtained from the wafer D. No electron traps are observed in the wafer D with the lower interstitial oxygen concentration compared to the wafer C as similarly to the results for as-grown wafers without donor annihilation annealing. However, three electron traps A6, A7 and A8 are observed in the wafer E with almost the same interstitial oxygen concentration as the wafer D, as shown in Fig. 2(c). Trap A6, A7 and A8 concentrations are estimated to be  $3.1 \times 10^{10}$ ,  $2.3 \times 10^{10}$  and  $8.7 \times 10^{10} \text{ cm}^{-3}$ , respectively.

A total of eight electron traps labelled A1–A8 are observed in CZ wafers evaluated in this work. Trap concentrations are in the range  $10^{10}$  to  $10^{11} \text{ cm}^{-3}$ . The thermal emission rate results for these electron traps and the lines by a least squares fit are shown in Fig. 3. The energy levels and electron capture cross sections are listed in the

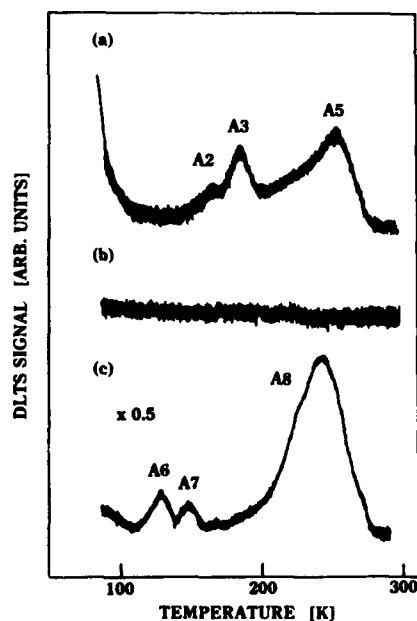


Fig. 2. DLTS spectra for the wafer C (a), the wafer D (b) and wafer E (c) ( $\tau = 19.1 \text{ ms}$ ).

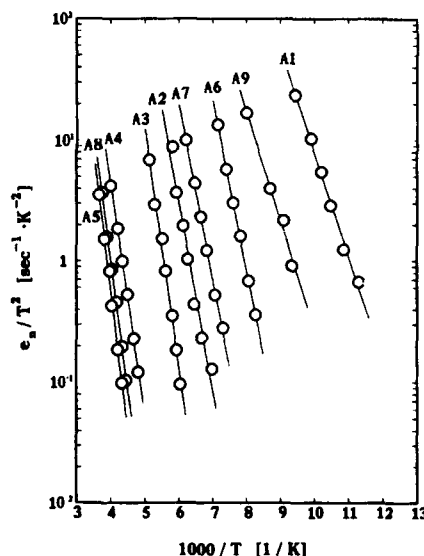
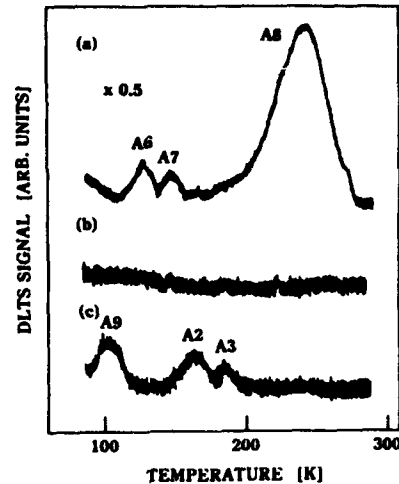


Fig. 3. Thermal emission rate data for electron traps observed in n-type (100) CZ silicon. The trap A9 is observed in the annealed wafer E at  $350^\circ \text{C}$ .



**Table II.** Energy levels and electron capture cross section of electron traps observed in n-type (100) CZ silicon. The trap A9 is observed in the annealed wafer E at 350 ° C.

| Trap | Energy level [eV] | Electron capture cross section [ $\text{cm}^2$ ] |
|------|-------------------|--|
| A1   | 0.17              | $9.0 \times 10^{-16}$                            |
| A2   | 0.34              | $2.3 \times 10^{-14}$                            |
| A3   | 0.38              | $1.5 \times 10^{-14}$                            |
| A4   | 0.38              | $6.2 \times 10^{-17}$                            |
| A5   | 0.46              | $3.5 \times 10^{-16}$                            |
| A6   | 0.28              | $4.5 \times 10^{-14}$                            |
| A7   | 0.29              | $2.7 \times 10^{-17}$                            |
| A8   | 0.43              | $1.2 \times 10^{-16}$                            |
| A9   | 0.18              | $8.8 \times 10^{-17}$                            |



**Fig. 4.** DLTS spectra for the wafer E (a), the annealed wafer E at 300 ° C (b) and the annealed wafer E at 350 ° C (c) ( $\tau = 19.1$  ms).

Table II. These values are calculated from the thermal emission rate data in Fig. 3 assuming that capture cross sections are independent of temperature.

The annealing experiments in the temperature range 100–650 ° C are carried out for the wafer E. Figure 4 shows the DLTS spectra for the wafer E annealed at 300 and 350 ° C. For comparison, the DLTS spectrum for the wafer E without annealing is shown in Fig. 4(a). Figure 4(b) shows the DLTS spectrum for the wafer E which received heat treatment at 300 ° C for 30 min. It is found that traps A6, A7 and A8 disappear by annealing at 300 ° C. Instead, three electron traps are introduced by annealing at 350 ° C as shown in Fig. 4(c). It is noted that two of three electron traps correspond to traps A2 and A3 observed in wafers A and C without annealing. The preliminary annealing experiments of the wafer B also show the growth of traps A2 and A3. However, no growth of these traps is observed for the wafer D. The emission rate data of another trap labelled A9, and its energy level and electron capture cross section are shown in Fig. 3 and Table II, respectively.

The annealing behavior of traps A2 and A3 introduced in the wafer E by heat treatment is shown in Fig. 5 together with that of traps A6, A7 and A8. Traps A6, A7 and A8 observed in the wafer E anneal out around 300 ° C. On the other hand, the trap A3 is observed in the annealing temperature range 350–400 ° C. The trap A2 shows the maximum concentration around 400 ° C and is below the detection limit around 600 ° C.

#### IV DISCUSSION AND CONCLUSIONS

A total of eight electron traps are observed in CZ wafers with and without donor annihilation annealing. Two electron traps A2 and A3 of these traps are present in the wafers with the higher interstitial oxygen concentrations irrespective of donor

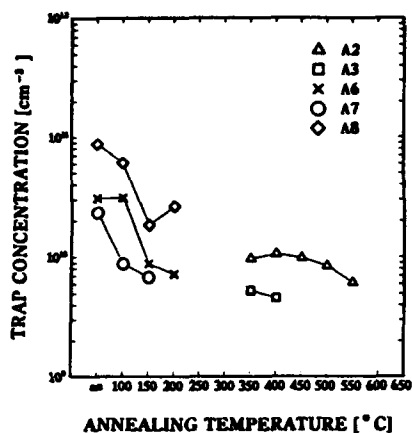


Fig. 5. Annealing behavior of traps A2, A3, A6, A7 and A8 observed in the wafer E.

annihilation annealing as seen from Fig. 1 (a) and Fig. 2 (a). Furthermore, it is found that trap A2 and A3 concentrations in the wafer C with donor annihilation annealing are approximately one order of magnitude smaller than those in the wafer A without donor annihilation annealing.

The annealing behavior of traps A2 and A3 is found from the annealing experiments for the wafer E. As seen from Fig. 5, traps A2 and A3 are formed around 400 °C and anneal out around 500–600 °C. It is thought that traps A2 and A3 are formed in the wafer A around 400 °C during crystal growth cooling period. The smaller concentrations of traps A2 and A3 in the wafer C are ascribed to the donor annihilation annealing. It is expected that the time of wafers exposed to the temperature around 400 °C during donor annihilation annealing cooling period is shorter than that during the crystal growth cooling period. This leads to the annihilation of traps A2 and A3 and the suppression of regrowth of these traps in wafers which receive the donor annihilation annealing. It is thought that the formation of traps A2 and A3 is related to the oxygen concentrations and the exposure time around 400 °C in wafers. However, no observation of the growth of traps A2 and A3 in the wafer D may suggest that another species is also related to these traps.

Nauka et al. [3] have reported the presence of oxygen-induced recombination centers in as-grown CZ silicon. They have ascribed these centers to grown-in oxygen precipitates. Recently, Mishra et al. [4] have indicated that oxygen-related defects act as electron traps in p-type CZ silicon using surface photovoltage (SPV) minority carrier diffusion length measurements. Electron traps observed by SPV measurements [4] may correspond to those observed here by DLTS, although the interstitial oxygen concentrations of CZ silicon used in SPV measurements are in the range  $5\text{--}7 \times 10^{17} \text{ cm}^{-3}$ . In the DLTS measurements, traps A2 and A3 are not observed in n-type CZ silicon with the interstitial oxygen concentrations of  $1.0\text{--}1.1 \times 10^{18} \text{ cm}^{-3}$ . However, this does not necessarily mean that these traps are absent in wafers with the lower interstitial oxygen concentrations. It is thought that trap concentrations in these wafers are below the detection limit of the DLTS measurement technique used here.

The trap A1 also may correspond to the grown-in oxygen-related defects since this trap is observed only in the as-grown wafer A with the higher interstitial oxygen concentration. It seems that the trap A1 disappears by the donor annihilation annealing, although there is the possibility that trap A1 DLTS signals are masked by the DLTS

signals resulting from shallower electron traps as shown in Fig. 2(a). Trap A4, A5 and A8 DLTS signals are observed around 240 K as seen from Figs. 1 and 2. Furthermore, these trap DLTS signals show the slightly broader shape, which suggests that these consist of several trap DLTS signals. The main trap may vary among wafers, dependent on the wafer thermal history including donor annihilation annealing. However, further investigation is necessary to discuss the origin of these traps in addition to traps A6 and A7.

#### ACKNOWLEDGMENTS

This work was supported partly by a Grant-in-Aid from the Nitto Foundation for the Promotion of Science.

#### REFERENCES

- [1] C. S. Fuller and R. A. Logan, *J. Appl. Phys.* **28**, 1546 (1958).
- [2] W. Kaiser, *Phys. Rev.* **105**, 1751 (1957).
- [3] K. Nauka, H. C. Gatos and J. Lagowski, *Appl. Phys. Lett.* **43**, 241 (1983).
- [4] K. Mishra, W. Huber and J. Lagowski in Defect Engineering in Semiconductor Growth, Processing and Device Technology, edited by S. Ashok, J. Chevallier, K. Sumino, and E. Weber (Mater. Res. Soc. Proc. **262**, Pittsburgh, PA, 1992) pp. 677-682.
- [5] S. Dannefaer and D. Kerr, *J. Appl. Phys.* **60**, 1313 (1986).
- [6] T. Y. Tan, E. E. Gardner and W. K. Tice, *Appl. Phys. Lett.* **30**, 175 (1977).
- [7] D. V. Lang, *J. Appl. Phys.* **45**, 3023 (1974).
- [8] J. C. Bourgoin, H. J. von Bardeleben and D. Stievenard, *J. Appl. Phys.* **64**, R65 (1988).
- [9] J. M. Hwang and D. K. Schroder, *J. Appl. Phys.* **59**, 2476 (1986).
- [10] Y. Tokuda, N. Kobayashi, A. Usami, Y. Inoue and M. Imura, *J. Appl. Phys.* **66**, 3651 (1989).
- [11] H. S. Kim, E. K. Kim and S-K Min, *J. Appl. Phys.* **69**, 6979 (1991).
- [12] Y. Tokuda, N. Simizu and A. Usami, *Japan. J. Appl. Phys.* **18**, 309 (1979).
- [13] Y. Tokuda, M. Hayasi and A. Usami, *J. Phys.* **D14**, 895 (1981).

## RELATIONSHIP BETWEEN MINORITY CARRIER PARAMETERS AND SOLAR CELL CHARACTERISTICS OF ELECTROMAGNETIC CAST POLYCRYSTALLINE SILICON

EIICHI SUZUKI\*, KYOJIRO KANEKO\*\*, AND TORU NUNOI\*\*\*

\*Electrotechnical Laboratory, Electron Devices Division, 1-1-4, Umezono, Tsukuba-shi, Ibaraki 305, Japan

\*\*Sumitomo Sitix Co., Research and Development Center, 1, Higashihama-cho, Amagasaki-shi, Hyogo 660, Japan

\*\*\*Sharp Co., Energy Conversion Laboratory, 282-1, Hajikami, Shingyo-cho, Kitakatsuragi-gun, Nara 639-21, Japan

### ABSTRACT

The relationship between minority carrier properties and solar cell characteristics of electromagnetic (EM) cast polycrystalline Si has experimentally been investigated. The minority carrier lifetime  $\tau$  and diffusion coefficient  $D$  were evaluated by a novel dual mercury probe method. The solar cell characteristics, e.g., a conversion efficiency  $\eta$  were measured by fabricating experimental solar cells using the corresponding wafers. The wafer showing high- $\eta$  (13.1%) has relatively high  $\tau$  (av. 8.2  $\mu$ s) with small variation of  $D$  (av. 29.6  $\text{cm}^2/\text{s}$ ). On the contrary, the low- $\eta$  (11%) wafer shows low  $\tau$  (av. 1.1  $\mu$ s), including some inferior portions with very low  $\tau$  of less than 0.5  $\mu$ s. It is also shown that  $D$  drastically deteriorates with decreasing  $\tau$  if  $\tau$  is less than around 2  $\mu$ s. To realize high efficiency polycrystalline solar cells, the wafers with high value of  $\tau$  and without considerably low- $\tau$  portions are needed.

### INTRODUCTION

For any minority carrier device such as a solar cell, the behavior of minority carriers in a semiconductor bulk as well as at the surface essentially affects its performance, e.g., energy conversion efficiency in a solar cell [1]. Among many solar cell materials, polycrystalline Si has attracted much attention because of its potentiality of low cost. Currently, electromagnetic casting of Si is expected to supply low cost and high quality polycrystalline Si wafers for solar cells [2]. Even for such polycrystalline Si, a high minority carrier lifetime  $\tau$  and a high diffusion coefficient  $D$  are required to realize low cost and high efficiency solar cells. To this aim, it is important to make clear the relationship between minority carrier parameters and solar cell characteristics experimentally. In this paper, we will describe the experimental investigation of this relationship for electromagnetic cast polycrystalline Si wafers. This will be done by comparing the experimental results of the minority carrier parameters of  $\tau$  and  $D$  measured by a novel dual mercury probe method [3]-[5] with the measurement of solar cell characteristics of fabricated experimental solar cells. We will show the good relationship between these carrier parameters and cell efficiency. We will also show the correlation between  $\tau$  and  $D$  across polycrystalline Si wafers.

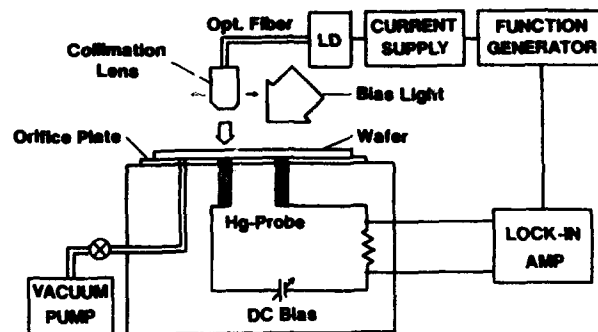


Fig.1 Measurement setup for evaluating minority carrier parameters of Si wafers by the dual mercury probe method.

## EXPERIMENTAL

We used electromagnetic cast polycrystalline silicon wafers in the experiment. The solar cell material has advantages of low contamination, high throughput, and consequent low cost potentiality, owing to the self-supporting growth technique by electromagnetic force without any crucible. The average grain size was about 1.3mm. The minority carrier parameters of  $\tau$  and  $D$  were evaluated by the dual mercury probe method as schematically shown in Fig.1. The intensity-modulated  $\text{Ga}_x\text{Al}_{1-x}\text{As}$  laser diode beam ( $\lambda = 833 \text{ nm}$ , 1-10 mW, 1-3 mm $\phi$ ) illuminates a front surface of a sample wafer just above a reverse-biased Hg-probe (0.5-2 mm $\phi$ ). A good rectifying contact was obtained even for a fairly rough surface of a polycrystalline Si wafer by a Hg-probe, associated with soft contact formation. The dual mercury probe method can also be applied to low-resistivity, p-type Si wafers. The minority carriers generated near the front surface diffuse toward the back surface accompanying with the carrier loss by recombination in the bulk and at the front surface. Only some of these minority carriers reaching the edge of the depletion layer of a reverse-biased Hg-contact are collected by the Hg-probe and are measured as a frequency-domain photocurrent (amplitude and phase shift) by a lock-in amplifier (100 kHz). The measurement was performed under DC bias light (50 mW/cm<sup>2</sup>). This method needs no special device and is almost nondestructive. We can determine the unique set of  $\tau$  and  $D$  from experimental amplitude or phase shift data as a function of frequency, by curve-fitting using a one-dimensional analytical photocurrent expression. The theoretical photocurrent was obtained by solving the diffusion and current continuity equations. It has been confirmed that the lateral diffusion effect of minority carriers is negligibly small for normal conditions. The detailed analytical procedures to obtain  $\tau$  and  $D$  from experimental data were described elsewhere [5]. This method also enables us to determine a surface recombination velocity  $s$  at any surface portion. Using wafers corresponding to the samples for which minority carrier parameters were evaluated, experimental solar cells (47mmx47mm) were fabricated by standard fabrication processes including surface texture etching for light trapping, antireflection coating, and high-low back contacts for a back surface field (BSF). The configuration and dimension of the solar cells

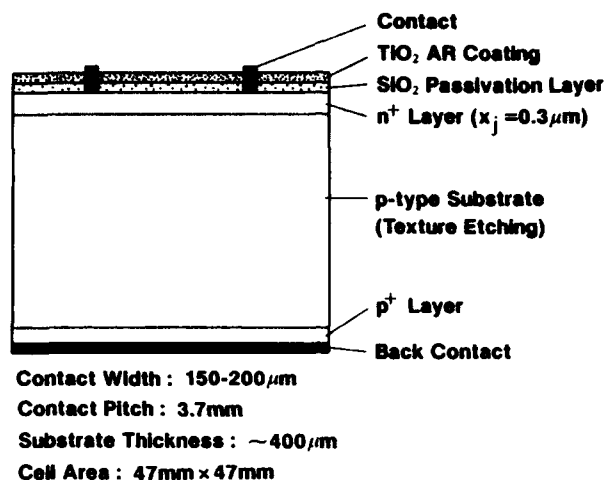


Fig.2 Configuration of experimental solar cells.

are shown in Fig.2. The solar cell characteristics, i.e., an energy conversion efficiency  $\eta$ , an open circuit voltage  $V_{oc}$ , a short circuit current  $I_{sc}$ , and a fill factor FF, were measured at AM1.5 by using a conventional solar simulator. Then we investigated the relationship between the minority carrier parameters and the solar cell characteristics.

## RESULTS AND DISCUSSION

To obtain  $\tau$  and  $D$ , curve-fitting between the frequency-dependent photocurrent and the theoretical calculation was performed automatically by a conventional personal computer based on the Newton-Raphson method. The typical result of curve-fitting is shown in Fig.3, where the phase shift data as a function of frequency are used. The amount of negative phase shift of the photocurrent increases with increasing frequency and approaches a straight line indicating a linear dependence on the square root of frequency in a high frequency region. The open circles are the measurement data and the solid line shows the theoretical curve with the  $\tau$  and  $D$  determined for this sample. It should be noted that the curve-fitting is excellent. This means that the dual mercury probe method is successful in contacting the rough surface of the chemically etched polycrystalline Si wafer used in the experiment. The accumulated solar cell characteristics at AM1.5 for each sample are listed in Table 1. The difference in  $\eta$  (11%-13%) is mainly due to  $I_{sc}$ . Figure 4 shows the map of  $\tau$  and  $D$  for three wafers corresponding to the solar cells with different  $\eta$  as shown in Table 1. The repeated data for the same wafer were obtained at different positions (2mm each). Figure 5 indicates the distribution of  $\tau$  and  $D$  as a function of position on each wafer

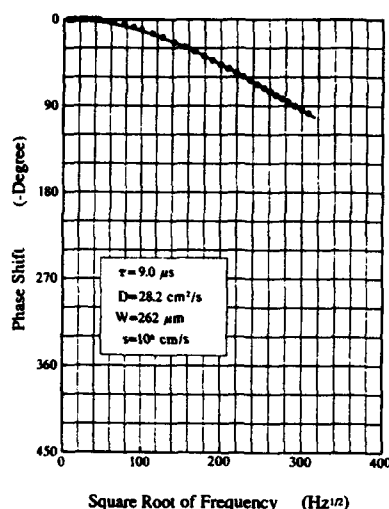


Fig.3 Typical experimental result of photocurrent phase shift vs.(frequency)<sup>1/2</sup> characteristics for the electromagnetic cast polycrystalline Si wafer. The sand-blasted front surface recombination velocity  $s$  is assumed to be  $10^6$  cm/s.

sample. We notice some remarkable characteristics from Figs.4 and 5. First, the wafer corresponding to the relatively high- $\eta$  cell indicates high average  $\tau$  of  $8.2 \mu s$  as well as high  $D$  (av.  $29.6 \text{ cm}^2/\text{s}$ ) with smaller deviation than that of  $\tau$ . The diffusion coefficient  $D$  is directly related to minority carrier mobility in the grains. It is said, therefore, that crystallinity inside grains of the electromagnetic cast polycrystalline Si showing the high- $\eta$  solar cell characteristic is good and comparable to that of singlecrystalline Si wafer, and that the higher  $\tau$  is required to realize the higher- $\eta$  polycrystalline solar cell. Secondly, the low- $\eta$  wafer shows a relatively low value of  $\tau$  (av.  $1.14 \mu s$ ) and has some portions with  $\tau$  less than  $0.5 \mu s$  and a correspondently low  $D$  as shown in Fig.4. The minority carrier lifetime  $\tau$  is mainly related to the amount of carrier recombination sites at the grain boundaries in the case of polycrystalline Si wafers. The deterioration of  $\tau$  is due to segregation of impurities, e.g., heavy metals and/or accumulation of defects, at grain boundaries. Purer starting Si material and more precise temperature control

| Sample | $\eta(\%)$ | Isc(A) | Voc(V) | FF    |
|--------|------------|--------|--------|-------|
| #80    | 13.12      | 0.782  | 0.573  | 0.732 |
| #116   | 11.76      | 0.708  | 0.574  | 0.723 |
| #95    | 10.96      | 0.674  | 0.567  | 0.717 |

Table 1 Solar cell characteristics at AM 1.5 for the different electromagnetic cast polycrystalline Si wafers.

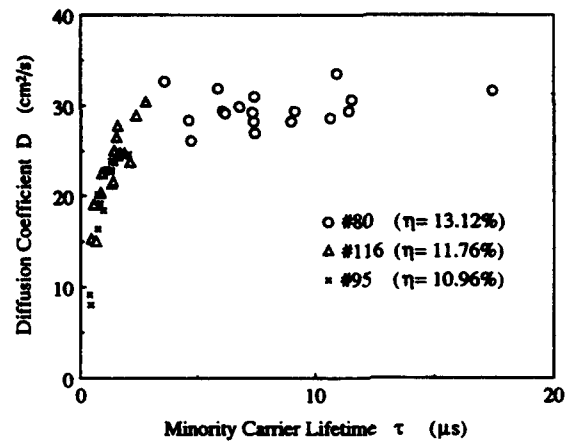


Fig.4 Minority carrier lifetime  $\tau$  versus diffusion coefficient  $D$  for the different EM cast polycrystalline Si wafers corresponding to the solar cells listed in Table 1.

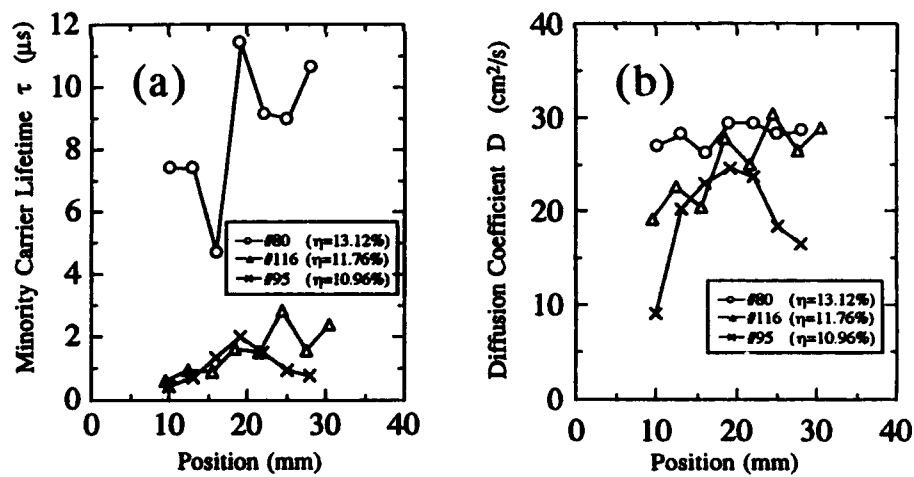


Fig.5 Spatial distribution of (a) minority carrier lifetime  $\tau$ , and (b) diffusion coefficient  $D$  for the different EM cast polycrystalline Si wafers corresponding to the solar cells listed in Table 1.



during EM casting are therefore required to realize high efficiency EM cast polycrystalline Si solar cells. Thirdly,  $D$  drastically decreases with decreasing  $\tau$  when the value of  $\tau$  is less than about  $2\mu\text{s}$  as shown in Fig.4. This suggests that when the density of impurities and/or defects at grain boundaries exceeds a certain threshold, the crystallinity degrades rapidly proportional to the concentration of the defects/impurities. From these observations, not only high average value of  $\tau$  and  $D$  is needed but also removal of regions of low  $\tau$  and  $D$  is necessary to realize high efficiency polycrystalline solar cells. In addition, minority carrier characterization by the almost nondestructive dual mercury probe method is useful for screening solar cell materials and for developing high efficiency solar cells.

## CONCLUSION

We have experimentally investigated the relationship between minority carrier parameters ( $\tau$ ,  $D$ ) and solar cell characteristics ( $\eta$ ,  $V_{oc}$ ,  $I_{sc}$ ) by using electromagnetic cast polycrystalline Si wafers. Experimental results reveal the good relationship between these carrier parameters and cell efficiency. The wafer corresponding to the high- $\eta$  cell indicates high average  $\tau$  and high average  $D$  with small deviation. The low- $\eta$  wafer includes some inferior portions with considerably low  $\tau$  and  $D$  and shows low value of both  $\tau$  and  $D$ . The minority carrier diffusion coefficient  $D$  rapidly decreases with decreasing  $\tau$  when  $\tau$  is less than around  $2\mu\text{s}$ . In contrast, in the case of  $\tau$  more than about  $2\mu\text{s}$ ,  $D$  slowly increases with increasing  $\tau$ . High efficiency polycrystalline Si solar cells require not only high average  $\tau$  and  $D$ , but also no poor quality regions where  $\tau$  and  $D$  are low.

## ACKNOWLEDGMENT

This work was supported by the New Sunshine Project, AIST, MITI, Japan.

## REFERENCES

- 1) M.A.Green, High Efficiency Silicon Solar Cells (Trans Tech Publications, Switzerland, 1987).
- 2) K.Kaneko and T.Misawa, 7th Photovoltaic Science and Engineering Conference, Nagoya, Japan, 1993.
- 3) E.Suzuki and Y.Hayashi, IEEE Trans. Electron Devices, ED-36, 1150 (1989).
- 4) E.Suzuki and Y.Hayashi, J.Electrochem.Soc., 139, 1741 (1992).
- 5) E.Suzuki and Y.Hayashi, Appl.Sur.Sci., 63, 218 (1993).

# TRAPPING OF MOLECULAR HYDROGEN IN POROUS SILICON AND AT Si/SiO<sub>2</sub> INTERFACES AND A POSSIBLE REINTERPRETATION OF THE P<sub>b</sub> CENTER

PETER STALLINGA, T. GREGORKIEWICZ, AND C.A.J. AMMERLAAN  
 Van der Waals-Zeeman Laboratorium der Universiteit van Amsterdam, Valckenierstraat 65, 1018 XE Amsterdam, The Netherlands (e-mail: pjotr@phys.uva.nl)

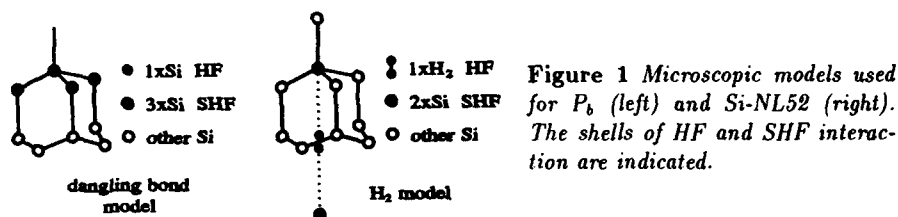
## ABSTRACT

Many recent studies of the highlighted problem of visible-range photoluminescence of porous silicon (po-Si) indicate the presence of hydrogen in this material. However, its actual role is not clear with the discussed possibilities ranging from passivation of the surface defects to some form of active participation in the photoluminescence (PL) mechanism itself. At the same time, in several magnetic resonance studies of po-Si the so-called P<sub>b</sub> center, originally identified with the <111>-directed silicon broken bond stabilized at Si/SiO<sub>2</sub> interfaces, has been reported.

Very recently the paramagnetic state of molecular hydrogen in bulk silicon has been identified. The spin-Hamiltonian parameters of the related Si-NL52 EPR spectrum appear to be identical to those of the P<sub>b</sub> center. This observation casts severe doubts on the original interpretation of the P<sub>b</sub> center while, on the other hand, offering new evidence of a prominent presence of hydrogen molecules both in po-Si and at the Si/SiO<sub>2</sub> interface. In this paper the similarities of Si-NL52 and P<sub>b</sub> centers are examined in detail, and it is argued that the centers are the same. It is concluded that many features of the P<sub>b</sub> center which could not be explained within the broken-bond model can be understood with the interstitial hydrogen molecule model.

## INTRODUCTION

With the constantly decreasing dimensions of semiconductor devices, two-dimensional structures like surfaces and interfaces become increasingly important. The active centers in such structures will have relatively more influence on the quality of the device. Therefore, it is important to be able to establish a microscopic picture of these centers.



One of the most familiar defects in Si/SiO<sub>2</sub> interfaces is the P<sub>b</sub> center, as named by Nishi [1], who first observed it. Later, its identification to a silicon dangling bond stabilized at <111> Si/SiO<sub>2</sub> interfaces was done by Poindexter [2]. The proposed structure is depicted

in Figure 1; a single (therefore paramagnetic) electron, localized mainly in a broken bond. The largest term in the spin Hamiltonian is then the Zeeman interaction  $\mathcal{H} = \mu_B B \cdot g \cdot S$ , with  $\mu_B$  the Bohr magneton,  $B$  the magnetic field,  $g$  the  $g$  tensor, and  $S$  the electron spin ( $S=1/2$ ). The wave function of the electron spin has also density outside this p-electron state of the dangling bond. Everywhere, where there is a nuclear spin the local density of the wavefunction is probed by the nucleus, because the hyperfine interaction is linearly proportional to the density at the atomic site. For the  $P_b$  model of Poindexter the largest interaction is expected with the (nearest) silicon atom to which the dangling bond is connected. In this way the observed hyperfine interaction ( $A_{\parallel} = 438$  MHz,  $A_{\perp} = 255$ ) corresponds to 6.9% of an electron in an s-state around the silicon nucleus and 53.4% in p-state [3]. Relative to the defect, the silicon atom is at a trigonal ( $C_{3v}$ ) site and this symmetry is reflected in the hyperfine interaction. A simulation of the angular dependence of the  $P_b$  spectrum is shown in Figure 2. This reveals that the center is indeed axially symmetric around  $\langle 111 \rangle$ .

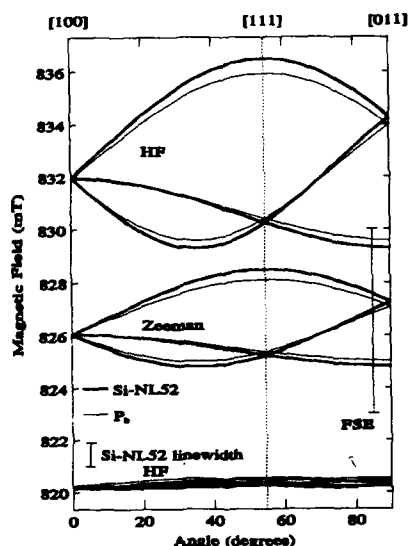


Figure 2 Simulations of the Si-NL52 (thick trace) and  $P_b$  spectra (thin trace) for a microwave frequency of 29.2 GHz. The place of the FSE scan of Figure 6 is indicated with a dashed line.

The relative intensity of the hyperfine lines, as compared to the Zeeman line, should confirm that a single silicon atom is involved in the interaction. This should be possible, because the abundances of the various isotopes of the involved atom are reflected in the fingerprint spectrum. In a crystal made of natural silicon 95.3% of the  $P_b$  centers will have a first-neighbor silicon atom without nuclear spin, resulting in a singlet spectrum, i.e., a Zeeman line. On the other hand, 4.7% of them will have a  $^{29}\text{Si}$  atom ( $I=1/2$ ) in the first interaction shell, producing a doublet spectrum, henceforth called the hyperfine (HF) lines. Therefore the fingerprint spectrum allows for a direct identification of the surroundings of the defect. In the case of the  $P_b$  center, the model predicts a (single) HF line intensity of 2.47%, i.e., a ratio of 1:40.5. The reported ratios do sometimes come close to this value, e.g.

1:67 [4]. But also ratios as high as 1:300 [5] have been observed. This cannot be understood within the broken-bond model of the  $P_b$  center.

For  $P_b$  also the next (super)hyperfine (SHF) interaction shell was resolved. In this case the intensity of the SHF lines (5% to 7.5%) indicated the presence of two or three Si atoms in the interaction shell, consistent with the model as described above (see also Fig. 1). However, the reported trigonal spectral class of the SHF interaction [4] cannot be explained with the model; the three next-nearest neighbors in the model of Figure 1 are on monoclinic I ( $C_{1h}$ ) positions.

### THE Si-NL52 SPECTRUM

A recent EPR study of high-dose-hydrogen-implanted pure silicon [6] revealed a trigonal spectrum (Si-NL52) with a spin Hamiltonian, comprised of an electronic Zeeman term and an HF interaction, i.e., similar to the Hamiltonian used to describe  $P_b$ :

$$\mathcal{H} = \mu_B B \cdot g \cdot S + S \cdot A \cdot I \quad (1)$$

The relative intensities of the HF lines of Si-NL52 depend on temperature and microwave power in a strong way. Ratios as high as 1:100 to as low as 1:3 have been observed. A microwave-power dependence of the individual components of the spectrum is depicted in Figure 3. This reveals that the changing of relative intensities cannot be due to saturation of the spectrum, since this occurs only for powers higher than -20 dBm, and the ratio is already varying for much lower powers. Following this observation, several possible causes for the anomalous variation of the ratio have been studied:

**Defect-band formation.** For high densities of the defect, the wave functions have significant overlap and the formation of a defect-band is expected [7]. The electrons in this band have an isotropic  $g$  value, close to the free-electron value of 2.0023. This is not observed for Si-NL52, where every resonance belongs to the same trigonal spectrum.

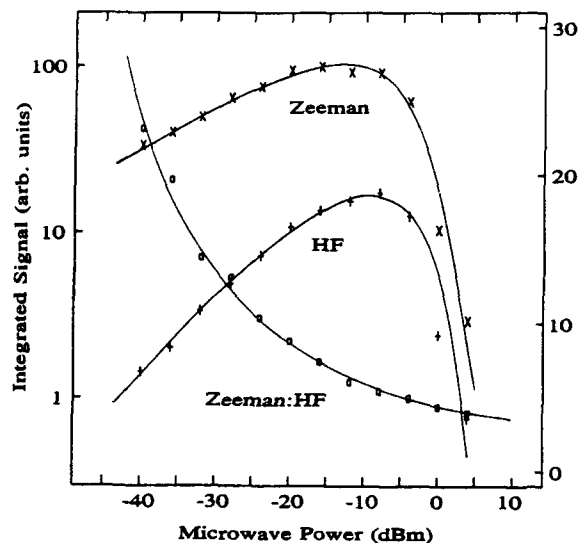
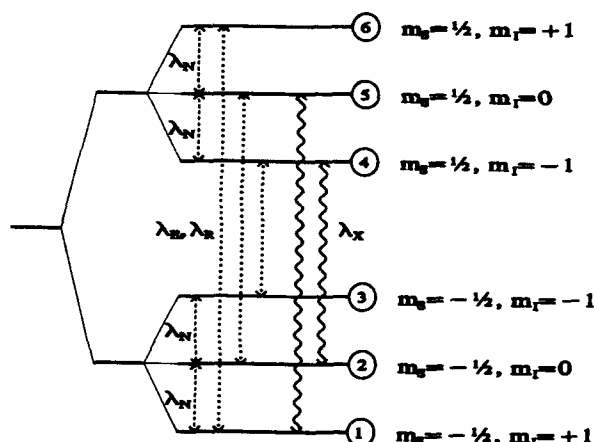


Figure 3 Microwave power dependence of the Zeeman and HF components of Si-NL52. The ratio is changing even before saturation sets in.

**Nuclear core polarization (NCP).** For  $S=1/2$  and  $I=1$ , the level diagram of Eq.1 is drawn in Figure 4. At low temperatures (4 K), the spin systems preferably are in the lowest three levels ( $m_S = -1/2$ ), with a negligible inhomogeneity in the distribution over the different nuclear states. The ratio of the occupancy of the lower levels and the higher levels is determined by the Boltzmann factor  $x = e^{\mu_B B/kT} \approx 1.3$  at  $T=4.2$  K. The most important relaxation for the electron spins is then the cross-relaxation ( $\lambda_X$ ) in which simultaneous change of the electron and nuclear spins occurs, while conserving total spin. Apart from this relaxation path also electronic ( $\lambda_E$ ) and nuclear ( $\lambda_N$ ) relaxations are to be considered, although they are of less importance. The differential equations then have the form:

$$\begin{aligned} dN_1/dt &= \lambda_N(N_2-N_1) & + \lambda_E(xN_6-N_1) & + \lambda_X(xN_5-N_1) \\ dN_2/dt &= \lambda_N(N_3-N_2) - \lambda_N(N_2-N_1) & + \lambda_E(xN_5-N_2) & + \lambda_X(xN_4-N_2) \\ dN_3/dt &= -\lambda_N(N_3-N_2) & + \lambda_E(xN_4-N_3) & \\ dN_4/dt &= \lambda_N(N_5-N_4) & - \lambda_E(xN_4-N_3) & - \lambda_X(xN_4-N_2) \\ dN_5/dt &= \lambda_N(N_6-N_5) - \lambda_N(N_5-N_4) & - \lambda_E(xN_5-N_2) & - \lambda_X(xN_5-N_1) \\ dN_6/dt &= -\lambda_N(N_6-N_5) & - \lambda_E(xN_6-N_1). & \end{aligned} \quad (2)$$



**Figure 4** Level diagram of the Hamiltonian as in equation 1. The relaxations are indicated with  $\lambda_N$ ,  $\lambda_E$  and  $\lambda_X$  for nuclear, electronic and cross-relaxations, respectively. Resonant (EPR) transitions are labeled with  $\lambda_R$ .

Without an external resonant (microwave) field, the steady-state solution of the coupled set of equations is the thermal equilibrium distribution:  $N_1=N_2=N_3 = xN/(3+3x)$  and  $N_4=N_5=N_6 = N/(3+3x)$ , with  $N$  being the total number of spin systems. When the external field is resonant, two extra terms are added. For example, the resonance  $1 \leftrightarrow 6$  gives an extra transition:

$$\begin{aligned} dN_1/dt' &= dN_1/dt + \lambda_R(N_6 - N_1) \\ dN_6/dt' &= dN_6/dt - \lambda_R(N_6 - N_1), \end{aligned} \quad (3)$$

where  $\lambda_R$  is the quasi relaxation, depending on the power of the applied microwave field. The intensity of the EPR signal is linearly proportional to the number of resonant transitions:

$$I_{\text{EPR}} \sim \lambda_R(N_6 - N_1). \quad (4)$$

As an example, the numerical solution of the equations as described above, with  $x=4$ ,  $\lambda_N=10^{-6}$ ,  $\lambda_E=10^{-4}$ ,  $\lambda_X=10^{-2}$ , and  $\lambda_R=0.1$  yields an EPR intensity ratio of 1.55:0.86:0.59. The saturation of the EPR lines distorts the normal ratio (1:1:1) in an asymmetrical way. In Figure 5a this distortion is depicted in comparison with the low-microwave-power spectrum, while Figure 5b shows the line intensities as a function of the stimulated-transition probability, which is a measure of the microwave power. Other values of the relaxation parameters  $\lambda_N$ ,  $\lambda_E$ , and  $\lambda_X$  will give different ratios, but the asymmetry always remains. This is not observed for Si-NL52, thus ruling out NCP as a possible cause for the changing of the relative intensities of the Si-NL52 components.

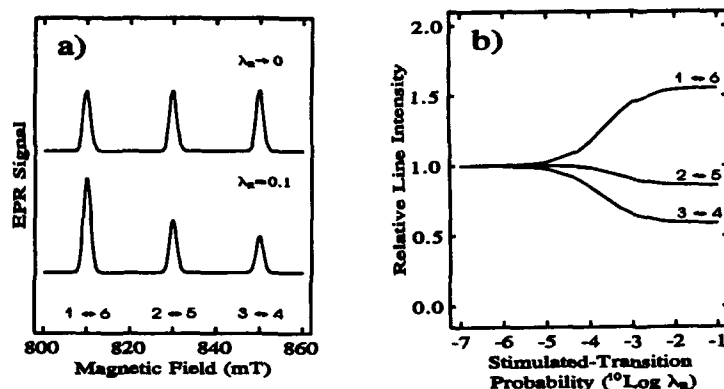


Figure 5 a) Low power spectrum (top trace) and saturated spectrum (bottom trace). The nuclear spin is polarized by the microwaves. b) Microwave-power dependence of the individual line intensities.

**Ortho and para hydrogen.** Molecular hydrogen has two forms; ortho hydrogen with parallel nuclear spins ( $I=1$ ) and para hydrogen with anti parallel spins ( $I=0$ ). Assuming Si-NL52 arises from a (charged) hydrogen molecule, the changing of relative intensities of the parts of the spectrum can be explained as an induced conversion of the ortho-hydrogen molecules, responsible for a HF triplet spectrum, to para- $H_2$ , producing a Zeeman singlet spectrum, and vice versa.

#### FIELD-SCANNED ELECTRON NUCLEAR DOUBLE RESONANCE

The method of field-scanned ENDOR (FSE) provides a way to increase the resolution of the EPR spectrum, because it distills that part of the EPR spectrum which has nuclear magnetic resonance (NMR) at a selected frequency [8]. This simplifies the complicated lineshape of the Si-NL52 spectrum, as can be seen in Figure 6. Here an FSE scan is shown in comparison with the original EPR spectrum for a direction of the magnetic field close to  $\langle 011 \rangle$ . The FSE scan shows the Zeeman line (825.0 mT), an HF line (829.6 mT) and two sets of SHF lines. The distance of the two outermost SHF lines is 1.60 mT ( $A=45$  MHz), while their intensities indicate an interaction with a shell of two silicon atoms. This is consistent with the model as depicted in the right part of Figure 1, where the first SHF shell contains two Si atoms on the extended  $\langle 111 \rangle$  H-H bond axis.

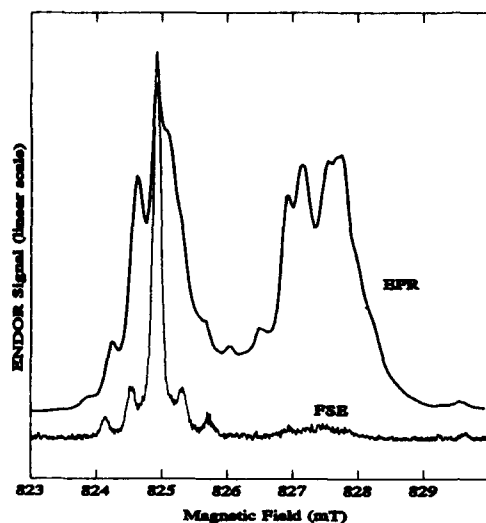


Figure 6 EPR (thick trace) and FSE (thin trace) of Si-NL52 at a magnetic field angle  $5^\circ$  from  $\langle 011 \rangle$ .

## CONCLUSIONS

The Si-NL52 and  $P_b$  spectra show remarkable similarities, because: 1) they have the same spin Hamiltonian and spin-Hamiltonian parameters, resulting in a similar angular dependence (Fig. 2), 2) show the same anomalous varying of the HF-to-Zeeman intensity ratio, and 3) have identical SHF structure. The distance of the SHF lines is equal to the distance observed for  $P_b$ , while their intensity, now measured accurately, is within the error margins as mentioned before [5]. We therefore conclude that Si-NL52 and  $P_b$  both represent basically the same defect.

On the other hand the experimental data can be better explained in the framework of the model of a paramagnetic hydrogen molecule located at an interstitial site as indicated in Figure 1. Namely, the new model can explain the varying of the HF-to-Zeeman intensity ratio, by assuming a conversion between ortho and para  $H_2$ , and it can explain the symmetry and the intensity of the SHF structure. We therefore propose the same model of interstitial  $H_2$  for  $P_b$ . Since  $P_b$  is detected at Si/SiO<sub>2</sub> interfaces and porous silicon, such a conclusion implies evidence for the presence of hydrogen at such places.

- 1) Y. Nishi, Jpn. J. Appl. Phys. **10**, 52 (1971).
- 2) E.H. Poindexter, P.J. Caplan, B.E. Deal, and R.R. Razouk, J. Appl. Phys. **52**, 879 (1981).
- 3) J.R. Morton and K.F. Preston, J. Magn. Reson. **30**, 577 (1978).
- 4) K.L. Brower, Appl. Phys. Lett. **43**, 1111 (1983).
- 5) W.E. Carlos, Appl. Phys. Lett. **50**, 1450 (1987).
- 6) P. Stallinga, T. Gregorkiewicz, C.A.J. Ammerlaan, and Yu.V. Gorelinskii, Phys. Rev. Lett. **71**, 117 (1993).
- 7) G. Feher, Phys. Rev. **114**, 1219 (1959).
- 8) T. Gregorkiewicz, H.E. Altink, and C.A.J. Ammerlaan, Acta Phys. Pol. A **80**, 161 (1991).

## STUDY OF SILICON SURFACE ROUGHNESS BY ATOMIC FORCE MICROSCOPY

ANDREW G. GILICINSKI\*, REBECCA M. RYNDERS\*, SCOTT E. BECK\*, YALE E. STRAUSSER\*\*, JAMES R. STETS\*, BRIAN S. FELKER\*, AND DAVID A. BOHLING\*

\* Air Products and Chemicals, Inc., 7201 Hamilton Blvd., Allentown, PA 18195

\*\* Digital Instruments, Inc., 520 E. Montecito Street, Santa Barbara, CA 93103

### ABSTRACT

Progress is reported in developing reliable methodology for imaging silicon surfaces with the atomic force microscope (AFM). A new form of AFM, known as tapping mode AFM, has been found to provide the best quality data for surface roughness determinations. Commercially available colloidal gold spheres have been used to fabricate tip characterization standards and are used to report tip size with roughness data. Power spectral density calculations are shown to provide a useful roughness calculation based on lateral wavelength.

### INTRODUCTION

Surface roughness measurements of silicon surfaces are critical to a number of technologies in semiconductor device manufacturing. Light scattering or interferometric methods have been used to determine roughness with sub-nanometer height precision; however, lateral resolution has been limited to the micron scale with these methods. The invention of the atomic force microscope (AFM) in 1986 [1] provided a new high resolution profilometry tool to access lateral dimensions down to the nanometer scale, with atomic resolution reported [2]. The principle of AFM involves tracing the sample topography with a sharp stylus and generating a three-dimensional topographic map of the surface, with resolution primarily limited by the diameter of the stylus tip. Quantitative measurement of surface roughness can be made with the AFM [3,4].

Ideally, the stylus applies a sufficiently low force (typically nanoNewtons) so as not to damage the sample during the imaging experiment. However, silicon surfaces have been found to be especially susceptible to damage by tip-sample interactions. Artifacts are easily generated, and methodologies for reliably obtaining accurate topographic data have not been widely reported. In addition, tip characterization standards and procedures have not been generally available, even though the tip size and shape can have a significant effect on silicon roughness measurements.

In the course of studies aimed at determining the effect of chemical vapor cleaning agents on silicon surfaces [5,6], we have developed methodology for obtaining reliable images of silicon for characterization of surface roughness. Progress in our ongoing study is reported here in three areas: obtaining accurate topographic data, characterizing the AFM tip used for imaging, and exploring new methods for calculating relevant surface roughness parameters from AFM data.



## EXPERIMENTAL

### AFM Imaging

Contact-mode AFM was done using a Digital Instruments NanoScope III AFM using "oxide sharpened" silicon nitride pyramidal tips on 0.06 N/m force constant cantilevers [7]. Imaging was done in air, and applied forces of under 30 nN were used. At applied forces above 30 nN, damage was induced on silicon surfaces. Tapping mode AFM was done in air with a Digital Instruments Multi-Mode AFM using etched single crystal silicon tips. For both types of experiments, 15  $\mu\text{m}$  scanners were used, which were calibrated with 1  $\mu\text{m}$  gold rulings [7] for lateral calibration and with 20  $\text{\AA}$  silicon oxide height standards for z-axis calibration [8].

Experiments were typically done in the following sequence. First a series of one micron square images were obtained, then a single two micron square image was taken. Often when significant tip-sample interaction had occurred in the one micron scans, a one micron "scan square" was observed in the two micron image. Other tests for damage to the surface included looking for a change in roughness (Ra or RMS) in the sequential one micron scans, and checking the roughness in sub-areas of the two micron image to see if the area within the one micron patch of repeatedly scanned surface yielded different surface roughness values than the surrounding surface that had only been scanned once. In several cases, images without any obvious damage did appear to have undergone a change that was detected by these tests, and topographic information from these data was not reliable.

### AFM Tip Characterization

Uncoated AFM tips were imaged in a JEOL 6300 field emission scanning electron microscope with an accelerating voltage of 2 kV, which allowed magnification up to 50,000x. For critical measurements, tips were analyzed before and after AFM imaging to determine whether gross damage had occurred and to estimate tip diameter. In addition, a tip characterization standard was generated using colloidal gold spheres deposited on mica with l-lysine according to a recently published method [9,10]. Standards typically consisted of a dispersion of three diameters of gold spheres of roughly 7, 14, and 21 nm diameter. To obtain roughness measurements that can be compared between samples and analysts, our imaging protocol has evolved to include AFM imaging of this tip standard after roughness analysis to provide a criteria of tip size and shape.

### Surface Roughness Calculations

Surface roughness was determined in three ways for the AFM images of silicon surfaces. Ra (average roughness, the average of absolute values of surface height variations), RMS roughness (square root of the mean of squares of distances from the mean surface level) and power spectral density were determined using algorithms in the NanoScope III software [7]. Power spectral density is a method for calculating the magnitude of roughness as a function of lateral wavelength, according to the following relation for a three-dimensional data set [11-13]:

$$\text{PSD} = W(p,q) = 1/A [\pi/2 \int dx \int dy e^{i(px+qy)} z(x,y)]^2 \quad (1)$$

where PSD is the power spectral density function in units of  $\text{length}^4$ , p and q are the lateral frequencies in inverse length units, l is the scan-length, and A is the scan area.

## RESULTS AND DISCUSSION

### AFM Imaging Methodology

Imaging of silicon surfaces with contact mode AFM was found to be extremely sensitive to the force applied in the experiment. When the applied force was over 30 nN, damage to the silicon surface was detected, either as obvious scan squares in subsequent 2 micron scans or by testing the roughness as described in the Experimental section. In all cases (over 30 sets of experiments) an applied force of under 30 nN appeared to yield artifact-free data. Humidity proved to be an important factor in imaging as well; higher humidity in the lab atmosphere appeared to correlate with increased surface damage during scanning. With sufficient care to minimizing the applied force, contact mode AFM could be successfully used to obtain surface roughness data.

Tapping mode AFM features a decrease in lateral tip-surface interactions because the tip is not in continuous contact with the surface. In this manner, chemical interactions and physical friction forces are reduced. In this work, a majority of experiments with tapping mode yielded artifact-free images. A few experiments did result in a "scanning square" as seen more commonly in contact mode AFM, so it was still necessary to check the data to confirm that the surface was not changed by the scanning.

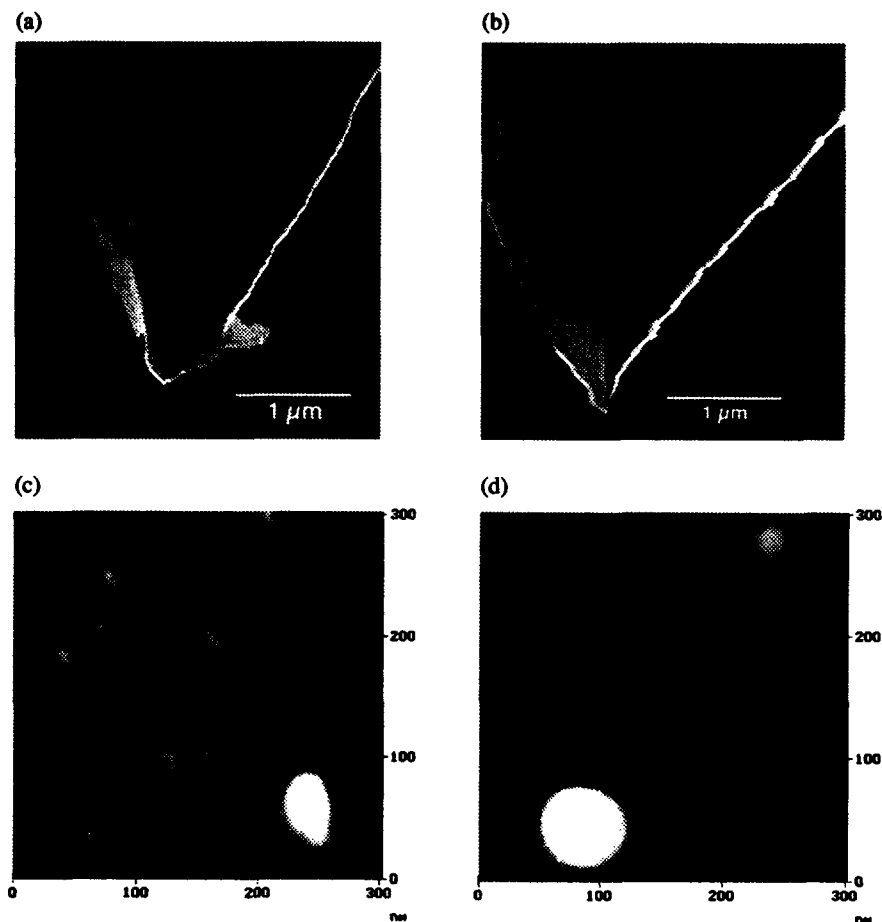
A key parameter in tapping mode is the state of the probe tip. Tapping mode tips are single crystal etched silicon probes with tip diameters under 20 nm. These tips proved fragile in use and could not typically be reused for more than several experiments without risking damage. Tip characterization after silicon imaging became a critical means of determining the validity of tapping mode data, since broken tips were found to yield seemingly artifact-free data with lower roughness than was actually present. The combination of tapping mode AFM with proper characterization of the probe tip proved to be the most effective means of obtaining reliable, reproducible images of silicon surfaces for roughness analysis.

### Characterization of AFM Probe Tips

Comparison of data is difficult if the tip size and shape are not known since a sharper probe tip will allow smaller features to be measured during an imaging experiment and roughness will be larger, other things being equal. For example, the contact mode AFM results cannot be compared to the tapping mode AFM data since contact mode uses 25-50 nm diameter silicon nitride pyramidal tips, while tapping mode uses < 20 nm diameter etched single crystal silicon probes. For this reason, contact mode results are less rough than tapping mode data for the same sample. The roughness measured in any experiment is only the minimum roughness that could be accessed with a particular probe. Tip characterization was, therefore, considered critical for reproducible roughness measurements, as well as a diagnostic that should be reported with roughness data.

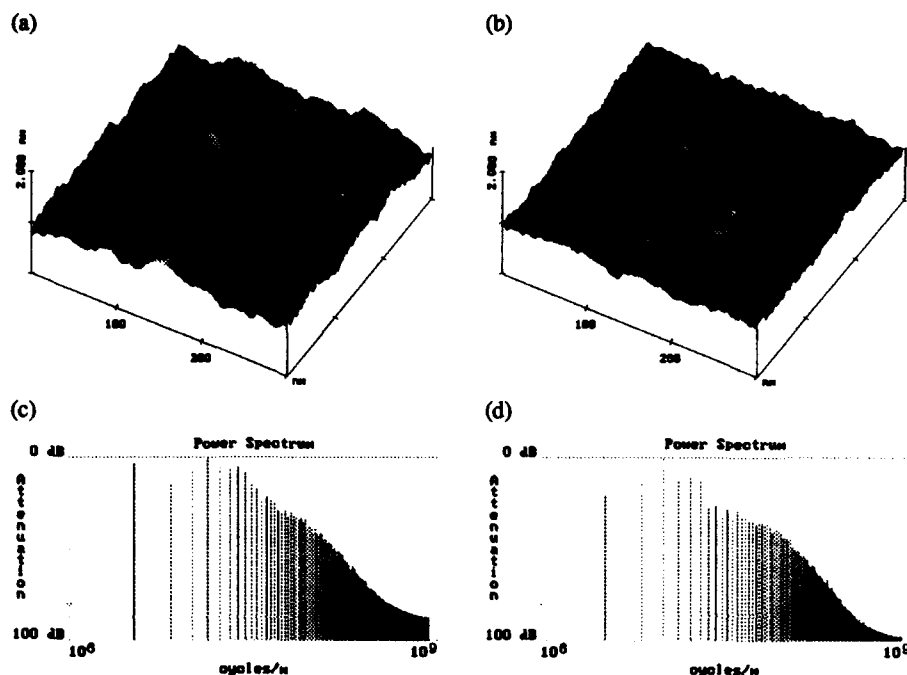
Field emission SEM proved to be valuable for obtaining a macroscopic view of the tip size and shape, and an example is shown in Figure 1. We also worked with a "tip standard" which was fabricated from commercially available colloidal gold spheres and was used to characterize tips after roughness measurements [10]. This procedure provided a stable, reusable standard.

Figure 1. Field emission SEM images of tapping mode AFM tips (etched silicon single crystal). A damaged tip with debris attached is shown in (a), while an image of a good tip is shown in (b) (slightly distorted by charging effects). Tips were also characterized by imaging colloidal gold spheres on mica; (c) is a 300 nm image generated with tip (a) which yielded triangular pictures of 6 and 15 nm gold spheres, while in image (d) tip (b) revealed uniform 21 and 6 nm spheres.



Section (profile) plots allow direct estimates of the size and shape of the AFM tip to be made. In Figure 1c, images of 14 nm diameter spheres show the diameter is over 50 nm for a damaged tip, while Figure 1d yields a calculated tip diameter of under 20 nm. The spheres are particularly useful since the heights provide their diameter directly when dispersed on mica. It should be possible to directly calculate the tip size and shape from the images, and to use these parameters to reconstruct the original topography in images obtained with each characterized tip, in an analogous manner to a published report [14].

Figure 2. Tapping mode AFM images of p-type Si(100) surfaces after (a) RCA cleaning and (b) HF cleaning. Scan areas are 300 nm, with z-axis height of 2 nm. Power spectral density analysis of the images are shown in (c) and (d), respectively.



| Si(100) sample | Ra (Å) | RMS rough. (Å) | PSD (100 nm)                       | PSD (10 nm)                       |
|----------------|--------|----------------|------------------------------------|-----------------------------------|
| RCA cleaned    | 0.71   | 0.89           | $0.74 \times 10^{-3} \text{ nm}^4$ | $2.0 \times 10^{-5} \text{ nm}^4$ |
| HF cleaned     | 0.53   | 0.65           | $1.5 \times 10^{-3} \text{ nm}^4$  | $1.2 \times 10^{-5} \text{ nm}^4$ |

#### Comparison of Wet Cleans

Data were obtained by tapping mode AFM to determine the effect of various wet cleans on a p-type silicon (100) surface. Images for RCA and HF cleaned surfaces are shown in Figure 2a-b. Qualitatively, the images suggest that the RCA clean induces more roughness on the surface, though the HF clean seems to induce a waviness with longer spacing. Ra and RMS roughness calculations show the RCA clean causes a rougher surface than HF, and power spectral density calculations appear to confirm this at a small lateral wavelength (10 nm). However, PSD reveals that at a longer wavelength of 100 nm, the roughness appears to actually be higher for the HF cleaned surface. Work is in progress to determine the error and statistical significance of this difference in PSD values. Depending on lateral wavelength of importance to a particular manufacturing process, this distinction could be critical, and illustrates the value of power spectral density analysis.

## SUMMARY AND CONCLUSIONS

We have discussed silicon surface roughness analysis by AFM, including methodology for obtaining images, AFM tip characterization, and improved calculation of surface roughness using power spectral density. Silicon surface imaging worked best with tapping mode AFM. Tip characterization by field emission SEM as well as a tip standard generated from colloidal gold spheres helped us understand the size and shape of the tip used in AFM imaging experiments. Finally, power spectral density calculations provide an improved understanding of roughness based on lateral wavelength.

## ACKNOWLEDGEMENTS

The authors wish to thank Mark George and Dr. Steven Rynders (Air Products) for helpful discussions, Dr. Howard Huff (Sematech) for illumination regarding power spectral density analysis, and Mr. Rick Giberson (Ted Pella) for helpful discussions on checking AFM tips with colloidal gold. The support of Air Products and Digital Instruments is gratefully acknowledged.

## REFERENCES

1. G. Binnig, C. F. Quate, C. Gerber, *Phys. Rev. Lett.* **56**, 930 (1986).
2. F. Ohnesorge and G. Binnig, *Science* **260**, 1451 (1993).
3. T. Ohmi, M. Miyashita, M. Itano, T. Imaoka, I. Kawanabe, *IEEE Electron Dev. Lett.*, **39** (3), 537-545 (1992).
4. I. J. Malik, S. Pirooz, L. Shive, A. J. Davenport, C. M. Vitus, *J. Electrochem. Soc.* **140** (5), L75-L77 (1993).
5. S. E. Beck, A. G. Gilicinski, B. S. Felker, J. G. Langan, M. A. George, D. A. Bohling, J. C. Ivankovits, and D. A. Roberts in Proceedings of the Third International Symposium on Cleaning Technology in Semiconductor Device Manufacturing, edited by J. Ruzyllo and R. E. Novak (Electrochemical Society Proceedings, 1993) *in press*.
6. S. E. Beck, A. G. Gilicinski, B. S. Felker, J. G. Langan, D. A. Bohling, M. A. George, J. C. Ivankovits, and R. M. Rynders in Interface Control of Electrical, Chemical, and Mechanical Properties, edited by S. P. Murarka, T. Ohmi, K. Rose, and T. Seidel (Mater. Res. Soc. Proc., Pittsburgh, PA, 1993) *in press*.
7. Digital Instruments, Inc., Santa Barbara, CA.
8. The 20 Å height standard was a generous gift from Dr. Fu-san from the laboratory of Prof. T. Ohmi at Sendai University, Japan.
9. J. Vesenska, S. Manne, R. Giberson, T. Marsh, E. Henderson, *Biophysical Journal* **65**, 992-997 (1993).
10. Ted Pella, Inc., Redding, CA.
11. J. C. Stover, Optical Scattering: Measurements and Analysis, (McGraw-Hill, New York, 1990).
12. J. M. Bennett and L. Mattsson, Introduction to Surface Roughness and Scattering (Optical Society of America, Washington, D.C., 1989).
13. M. Bullis, presented at the SEMI Microroughness Task Force, July 1993 (unpublished).
14. D. J. Keller, F. S. Franke, *Surface Science* **294** (3), 409-419 (1993).

## THE EFFECT OF POLYSILICON DEPOSITION AND DOPING PROCESSES ON DOUBLE-POLY CAPACITORS - ELECTRICAL AND AFM EVALUATION

W. M. PAULSON, L. H. BREAU, R. I. HEGDE AND P. J. TOBIN  
Motorola, 3501 Ed Bluestein Boulevard, Austin, TX 78721

### ABSTRACT

We have characterized the surface topography of silicon films from different deposition and doping process sequences using AFM and optical reflectivity. The resulting surface structures after deposition, doping, oxide growth, and oxide removal correlate with the electrical leakage currents and breakdown voltages of double polysilicon capacitors. As-deposited amorphous films had smoother surfaces than those deposited in the crystalline state. Gas-phase diffusion doping increases the surface roughness. Only the amorphous in situ doped films retained a smooth surface following oxidation, yielding low leakage capacitors with breakdown fields above 8 MV/cm. Surprisingly, implanted amorphous films exhibited the roughest interfaces, resulting in lower breakdown fields. This study has shown that AFM provides an effective, quick, non-destructive diagnostic technique for semiconductor processing.

### INTRODUCTION

The surface of polysilicon is critical for the formation of double polysilicon structures for advanced EPROM and EEPROM circuits. The yield, performance, and reliability of these circuits reflects the quality of both the thin tunnel oxides and the interpoly dielectrics. In turn, these dielectric properties depend upon the surface roughness, microstructure and dopant concentration of the polysilicon layers which are affected by the deposition temperature and pressure, the doping process, chemical cleaning, and subsequent oxidation processes [1-3]. Surface asperities in the underlying polysilicon film may increase leakage currents and cause low-field electrical breakdown. Therefore, control of the polysilicon surface topography is important for future, scaled circuits with thinner dielectrics.

The surface roughness of polysilicon films has been characterized using optical reflectivity as well as SEM and TEM analysis [2]. The development of atomic force microscopy (AFM) in recent years [4,5] has resulted in a sensitive technique to characterize surface topography. AFM can scan large areas with high vertical magnifications that yields a more direct and quantitative measurement of surface properties than other techniques. Since AFM analysis is performed at atmospheric pressure and is non-destructive, it can be implemented as a manufacturing technique to evaluate and monitor film characteristics.

In this study the surface morphology of deposited silicon films from a wide array of potential processing conditions for double polysilicon products was investigated. These films were characterized using both AFM and optical reflectivity. In addition, we have fabricated capacitors and evaluated their electrical properties to correlate with the AFM results.

### EXPERIMENTAL PROCEDURES

The 250 nm thick silicon films were deposited in a horizontal LPCVD system over a 15 nm gate oxide grown on 125 mm silicon wafers. The initially amorphous films were deposited at 550°C, while the crystalline films were deposited at 625°C. In situ doped films were produced at both temperatures using a mixture of SiH<sub>4</sub> and PH<sub>3</sub>. One set of undoped films from each temperature was subsequently doped using PH<sub>3</sub>, gas-phase diffusion. Following the diffusion process, the doped oxide formed on these wafers was removed in HF acid. A second set of undoped films was doped using As implantation at 40 KeV to a dose of  $7.0 \times 10^{15} \text{ cm}^{-2}$ . The implant was done through a 20 nm screen oxide that was deposited using CVD TEOS at 650°C

to minimize contamination. The deposition temperature was kept as low as possible to avoid significant polysilicon film grain restructuring, but 650°C was sufficient to initiate recrystallization of the amorphous silicon films. This oxide was then removed after the implant using a buffered oxide etch (BOE) with a short overetch to minimize chemical roughening of the surface.

Six different polysilicon (P1) deposition and doping combinations were produced. The conditions are summarized in Table I along with the acronyms for the sample ID's. Representative amorphous films were annealed at 900°C for 40 sec to allow film thickness and sheet resistance measurements. Following the P1 processing, the wafers were oxidized at 1000°C in a dilute Ar-O<sub>2</sub> ambient to produce 18-30 nm thick polyoxides. Wafers for AFM analysis were removed from the process at this step. Capacitor fabrication was then completed by depositing a second, polysilicon (P2) layer (at 625°C) that was highly doped using gas-phase diffusion. This process step had no effect on the capacitor characteristics. Capacitor areas were defined using photolithography and etch processes and ranged from 0.03 to 0.15 cm<sup>2</sup>. These capacitors were electrically characterized using CV's to determine the oxide thickness and IV's to measure leakage currents and breakdown fields (BF). Leakage currents are characterized by the critical field (CF) at a current density of 1.0  $\mu\text{A}/\text{cm}^2$ .

Surface topography was characterized using a scanning-probe atomic force microscope. All the scans were made in air at room temperature. Surface topography analysis utilizes a contact-mode of operation. The repulsive force was small enough ( $\approx 10^{-8}$  to  $10^{-9}$  N) to prevent damage to the surface. The data were recorded in real time with a PC and displayed as a colored image without any processing. A scanned area of 5  $\mu\text{m}$  X 5  $\mu\text{m}$  is used for comparison. AFM measures the surface roughness parameters of  $Z_r$  and RMS, where  $Z_r$  is the difference between the highest and lowest points within the given area, and RMS is the root mean square of the surface deviations.

Optical reflectance measurements were performed on the same samples that were used for AFM analysis. The reflectance measurements were performed at a wavelength of 390 nm on a spectrophotometer, which has been shown to provide good correlation to surface roughness in spite of the differences in the refractive index between films [2]. Reflectances were normalized to values from a bare silicon reference wafer.

## RESULTS

### AFM Measurements

The surface topography was characterized after four process steps. First, the initial film surface was evaluated following the deposition process. Second, the silicon films were measured after the doping step. Third, the surface parameters of the thermally grown polyoxide were determined. Fourth, the polysilicon surface was analyzed after removing the polyoxide. The oxide surface was evaluated since the polyoxide/P2 interface is critical for electron injection from the top layer, while the bottom polysilicon surface (P1/oxide) affects electron injection from the bottom surface. The RMS roughness values are summarized in Table I. It should be noted that the  $Z_r$  values exhibit the same trends as the RMS values, but with larger numerical differences. Figure 1 shows the evolving AFM images following the deposition and doping step, after the polyoxidation and after removing the polyoxide. The top row is for amorphous in situ (a-ISD), while the second row shows crystalline in situ films (p-ISD). The a-ISD films only changed slightly during these three process steps. In contrast, the p-ISD films (Fig. 1, 2nd row) were significantly rougher after the deposition with increasing surface roughness after the subsequent process steps. Note that the vertical scale of the last image in the 2nd row is double that of the other images. The 3rd and 4th rows of figure 1 show diffusion-doped polycrystalline films or ion implanted amorphous films, respectively. The diffusion-doped films exhibit significant surface topography, but little change with oxidation or oxide removal. Nearly identical surfaces were observed for the a-DD film. The amorphous films were initially smooth (Table I) and remained smooth following the implantation. However, the resulting surfaces of the implanted films (Fig. 1, 4th row) are extremely rough after oxidation and oxide removal.

Figure 2 is a plot of the RMS surface roughness for the six film combinations and the three process steps. From these results it is clear that the a-ISD films result in the lowest RMS roughness value for all process steps. In contrast, the p-ISD films exhibit the roughest surfaces following oxidation and etching, even though the as-deposited film is less rough than undoped polysilicon (Table I). The surface topography of the diffusion doped films changes less during these processes. The RMS values were nearly identical for all three surfaces for the initially polycrystalline films (p-DD). The initially amorphous film (a-DD) had a  $\approx 10$  nm RMS following the diffusion process, but became significantly smoother after the oxidation and etch steps with RMS values comparable with the p-DD sample.

Similar to the diffusion-doped case, the implanted polysilicon film (p-II) changed little with subsequent processing. It appears that in both cases the surface roughness is primarily determined by the deposition process. However, the roughness for the initially amorphous film (a-II) increased from 0.75 nm after implant to 8.66 nm after the oxidation, which was significantly greater than the p-II case. The RMS roughness for the final P1 surface (a-II) dropped to 4.9 nm, so that the P1/oxide interface is smoother than the P2/oxide interface.

Table I. Summary of the RMS surface roughness (nm) of the initial surface, after oxidation, and after removal of the oxide for the six different deposition and doping conditions.

| P1 film Condition     | ID's  | As-deposited | Doping | Oxidation | Oxide Removal |
|-----------------------|-------|--------------|--------|-----------|---------------|
| Amorphous/In situ     | a-ISD | 0.6          | n/a    | 3.0       | 1.7           |
| Crystalline/In situ   | p-ISD | 3.7          | n/a    | 10.1      | 13.5          |
| Crystalline/Implant   | p-II  | 4.5          | 5.2    | 5.8       | 5.4           |
| Crystalline/Diffusion | p-DD  |              | 5.4    | 5.7       | 5.3           |
| Amorphous/Implant     | a-II  | 0.4          | 0.8    | 8.7       | 4.9           |
| Amorphous/Diffusion   | a-DD  |              | 9.7    | 6.9       | 6.1           |

#### Optical Reflectance Measurements

Table II summarizes the data obtained from optical reflectance from the same wafers as reported in Table I. For this data the higher number represents the smoother surface. Only the data from the silicon surfaces are included since the oxide significantly changes the surface reflectivity at this wavelength. The as-deposited amorphous films yield the highest reflectivities and correlate with the low RMS values. The crystalline deposited films have lower reflectance measurements that correspond to larger AFM values. However, the reflectivity data after doping and oxide removal does not correlate with the AFM measurements. For example, the highest reflectivity is for the a-DD sample that is one of the roughest samples with an RMS roughness of 6.1 nm. There is no apparent difference in surface roughness from these optical measurements between the a-ISD, p-DD and a-II films. However, both measurements indicate rough surfaces for p-ISD films which have the lowest reflectance and the largest RMS values after the oxide removal step.

Table II. Summary of the optical reflectance measurements for surface roughness of the initial surface and after removal of the oxide for the six deposition and doping conditions.

| P1 film Condition     | ID's  | As-deposited | Doping | Oxide Removal |
|-----------------------|-------|--------------|--------|---------------|
| Amorphous/In situ     | a-ISD | 102.6        | n/a    | 96.8          |
| Crystalline/In situ   | p-ISD | 90.4         | n/a    | 90.9          |
| Crystalline/Implant   | p-II  | 93.8         | 92.0   | 94.7          |
| Crystalline/Diffusion | p-DD  |              | 94.0   | 96.4          |
| Amorphous/Implant     | a-II  | 105.7        | 93.7   | 96.0          |
| Amorphous/Diffusion   | a-DD  |              | 96.9   | 99.2          |



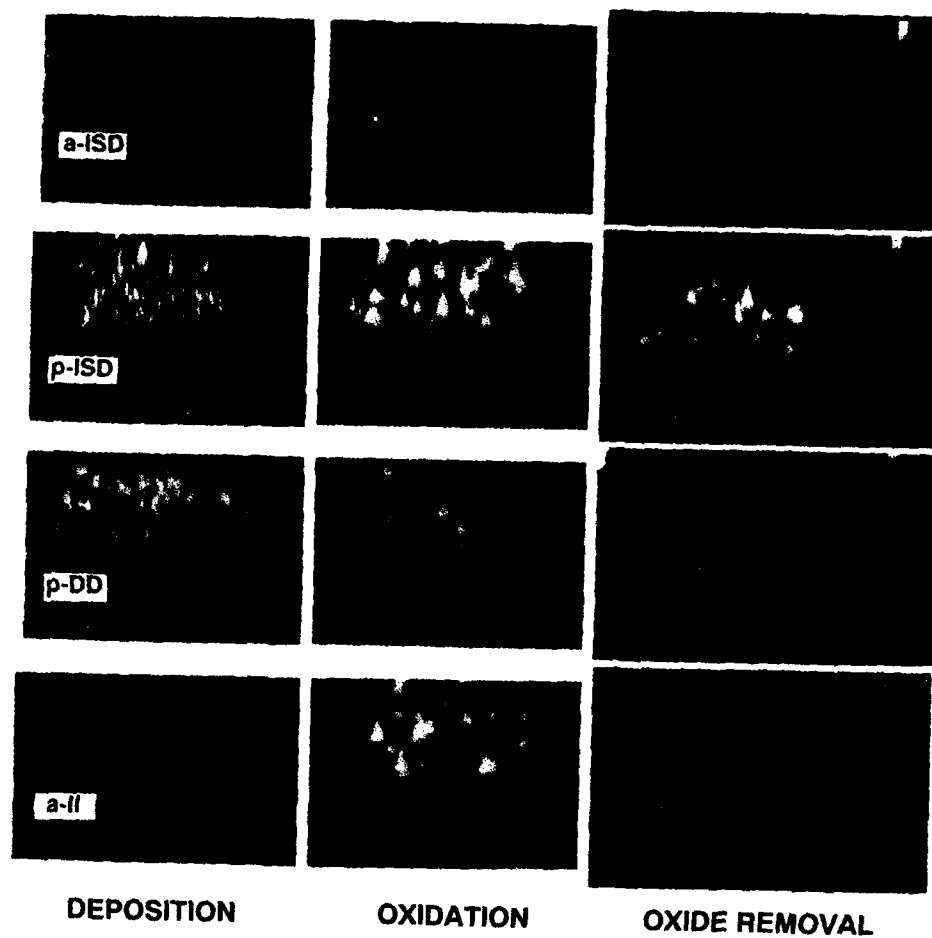


Fig. 1. AFM images of Si films for four doping conditions and three process steps .  
 1st column, after doping; 2nd column, after oxidation; 3rd column, after removing the oxides.  
 First row, a-IsD, Second row, p-IsD, third row, p-DD, fourth row, a-II. These images have the  
 same vertical scale of 50 nm except for the last image in the 2nd row with a 100 nm scale.

## Electrical Characteristics

The CF's and BF's for both +P2 and -P2 are plotted in Fig. 3 for five film combinations. These fields are asymmetric indicating different interface characteristics at the injecting electrode. The +P2 bias evaluates the properties of the bottom (P1) interface, while the -P2 bias examines the oxide/P2 interface. The first two film types are for in situ doped processes. Both the CF's and the BF's are significantly lower for films deposited in the crystalline phase (p-ISD). These lower fields correlate with increased RMS roughness values (Fig. 2) from the AFM analysis. Thus, the surface roughness correlates with the electrical parameters for these in situ doped films.

The third set of CF's and BF's (Fig. 3) is for crystalline films that were diffusion doped. Note that for these films the +P2 field is lower than the -P2 field, in contrast with the in situ doped films. The BF's are nearly identical for both polarities. The corresponding roughness values (Fig. 2) do not change during the three successive process steps.

The last set of data points in Fig. 3 is for implanted Si films (a-II and p-II). Both films have similar positive and negative CF's of about +5.0 and -6.4 MV/cm, respectively. In contrast, the BF's for the a-II are the lowest of all film types and are significantly lower than the BF's for the p-II films. The corresponding RMS surface roughness for the P1 surface (after oxide removal) is 4.9 nm for the a-II which is comparable to the 5.37 nm for the p-II films. However, these RMS values do not correlate with the positive BF's that are 30% larger for the crystalline films. For -P2 polarity the BF's are -6.4 and -9.8 for the a-II and p-II films, respectively, and correlate with oxide surface roughness values of 8.66 nm and 5.84 nm. Therefore, the BF's for electron injection from the top P2 electrode for ion implanted P1 films correlates well with the measured RMS surface roughness.

We have also compared electrical parameters and roughness measurements for different doping processes. For example, the positive CF's are similar for all films in spite of the RMS values ranging from 1.7 to 13.5 nm. Similarly, for the -P2 polarity (oxide interface) the p-DD films have a CF of 5.9 MV/cm that is significantly larger than for either of the in situ doped films. Yet, the RMS of 5.74 nm for p-DD is between the values of 3.0 and 10.1 nm for the a-ISD and p-ISD films, respectively. Furthermore, the poorest BF's are for the a-II films, but the corresponding roughnesses are comparable to other film types. Therefore, the roughness values do not correlate with the either the CF or the BF when comparing between the various doping processes.

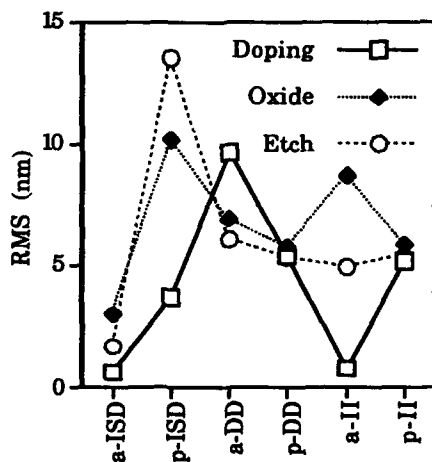


Fig. 2. RMS surface roughness versus doping process. Squares, after doping process; diamonds, after oxidation; circles, after removing the polyoxide.

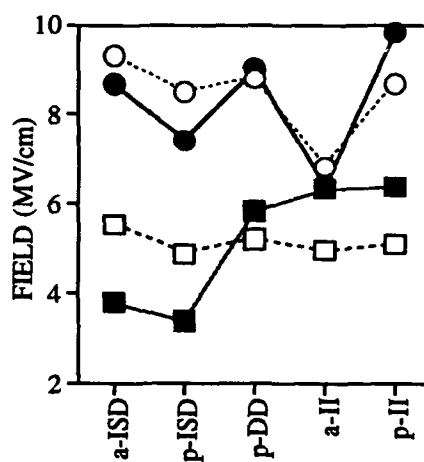


Fig. 3. Magnitude of the CF and BF for five deposition and doping processes. Squares, CF's; Circles, BF's; Open symbols, +P2; Solid symbols, -P2

## DISCUSSION

We have utilized AFM to characterize the evolving surface topography of polysilicon films following deposition, doping, oxidation and removing the oxide. The measured surface roughness correlates with the electrical properties of double-poly capacitors for certain deposition and doping conditions. Films deposited in the amorphous state are significantly smoother than crystalline deposited films. Surface roughness changes significantly with successive process steps for p-IsD and a-II films, but only slightly for a-IsD, p-DD and p-II doped layers. Both the CF's and BF's for in situ doped films correlate with the RMS roughnesses. The combination of an initially amorphous Si film plus a high-dose arsenic implant causes excessive surface roughness and degraded BF's. However, the RMS roughness values do not correlate with electrical parameters for all film types. For example, the positive CF's are similar for all films, even though the RMS roughness values range from 1.7 to 13.5 nm. Negative CF's are larger than positive CF's for diffusion and implantation doped films, while the opposite is measured for in situ doped films, in agreement with the results by Lee and Hu [6]. However, neither the RMS nor the  $Z_r$  values correlate with this polarity reversal. A more complete surface topography characterization with additional parameters such as grain size, the number and lateral dimensions of the asperities, or a power spectrum analysis may be required to find a correlation.

From these results it is clear that other parameters of polysilicon films, as well as roughness, influence the electrical properties of capacitors. These parameters include the dopant species (As or P), dopant concentration, deposition processes and microstructure [2,3,6,7]. Surface roughness is not as significant for these thin, conformal polyoxides as for thicker polyoxides (7). Therefore, the properties of the dielectric may determine the electrical characteristics.

AFM analysis is an effective technique for evaluating and monitoring surface roughness for silicon films. The analysis is performed in air so that vacuum systems are not required. Since AFM is non-destructive, it can be implemented as an inline, manufacturing technique to evaluate and monitor film characteristics. In a manufacturing mode the primary drawback of AFM is the high tip wearout and replacement frequency along with potential metallic contamination concerns. Optical reflectance measurements are quick and easy to perform, but are strongly affected by the refractive index or the optical properties of the film itself, as well as any surface oxide layers. From Table I and II it is clear that the optical measurements agree relatively well with AFM for the as-deposited films, but do not correlate with the results from the films after further processing. Furthermore, AFM provides a direct measurement of the surface roughness, whereas optical reflectivity only provides a relative value with a complicated relationship to the surface roughness of the deposited film. As a result, AFM provides significant advantages over optical reflectance in characterizing surface topography. In conclusion, we believe that the AFM technique has great potential as a process monitoring tool and will become a routine part of the semiconductor manufacturing environment.

## ACKNOWLEDGEMENTS

We appreciate the processing and measuring assistance from Le Boi La, the film depositions by Petyr Wachholz and acknowledge Bruce Doris for help with the AFM analysis. We would like to thank Thomas Mele, Fabio Pintchovski and Joe Mogab for their project support.

## REFERENCES

1. G. Queirolo, M. Brambilla and C. Mavero, MRS Symp Proc. **182**, 269 (1990).
2. M. Hendriks and C. Mavero, J. Electrochemical Soc., **136**, 1446-74 (1991).
3. S. Mori, et al., Proc. IEEE IRPS, p132 (1990).
4. D. Sarid and V. Elings, J. Vac. Sci. Technol. **B9**(2), 431 (1991).
5. H. K. Wickramasinghe, J. Vac. Sci. Technol. **A8**(1), 363 (1990).
6. J. C. Lee and C. Hu, IEEE Trans. Electron Devices **ED-35**, 1063 (1988).
7. L. Faraone and G. Harbeck, J. ECS **133**, 1410 (1986).

**DETERMINATION OF HYDROGEN IN SEMICONDUCTORS AND  
RELATED MATERIALS BY COLD NEUTRON CAPTURE  
PROMPT GAMMA-RAY ACTIVATION ANALYSIS**

**RICK L. PAUL AND RICHARD M. LINDSTROM**

Inorganic Analytical Research Division, National Institute of Standards and Technology,  
Gaithersburg, MD 20899

**ABSTRACT**

A reliable nondestructive method for measuring trace amounts of hydrogen in semiconductors and related materials has long been needed. Cold neutron capture prompt  $\gamma$ -ray activation analysis (CNP-GAA) is a nondestructive, multielement technique which has found application in the measurement of trace amounts of hydrogen. The sample is irradiated by a beam of "cold" neutrons; the presence of hydrogen is confirmed by the detection of a 2223 keV gamma-ray. The technique gives bulk analyses (the neutron and gamma radiation penetrate the sample), the hydrogen peak is free of interferences, and the results are independent of the chemical form of hydrogen present. The instrument is capable of detecting less than 10 mg/kg of hydrogen in many matrices. We have used the technique to measure hydrogen levels in a dielectric film on a silicon wafer, semiconductor grade germanium, and quartz.

**INTRODUCTION**

The presence of trace amounts of hydrogen in semiconductors and related materials can produce changes in electrical and optical properties [1]. Hydrogen has been used to electrically passivate a wide variety of defects and dopants in crystalline silicon [2-6], and at elevated concentrations, to passivate dangling bonds in amorphous silicon [7]. The presence of hydrogen in germanium crystals serves to electrically passivate some dopants [2] while activating others [8-11]. Reliable studies of the effects of hydrogen on these and other materials require techniques for accurate and nondestructive measurement of hydrogen at microgram and nanogram levels.

We have found cold neutron capture prompt gamma-ray activation analysis (CNP-GAA) to be useful for the nondestructive determination of trace amounts of hydrogen in a wide variety of materials [12-15]. We have used CNP-GAA to measure hydrogen in quartz crystals, semiconductor grade germanium, and in a dielectric film on a silicon wafer.

**TECHNIQUE**

Prompt gamma-ray activation analysis has been described in detail previously [16]. When a sample is placed in a neutron beam, nuclei of many elements in the sample absorb neutrons and are transformed to an isotope of higher mass number. Prompt gamma-rays, emitted by de-excitation of the compound nuclei are then measured using a high-resolution gamma-ray detector. Qualitative analysis is accomplished by identification of the gamma-ray energies, while comparison of gamma-ray intensities with those emitted by a standard yields quantitative analysis. The use of "cold" neutrons enhances the sensitivity compared to thermal neutrons, principally by reducing background. The analysis is both nondestructive and total, since the neutron and gamma radiation are highly penetrating and the results are independent of the chemical form of the element being measured. The hydrogen gamma-ray at 2223 keV has few known interferences.

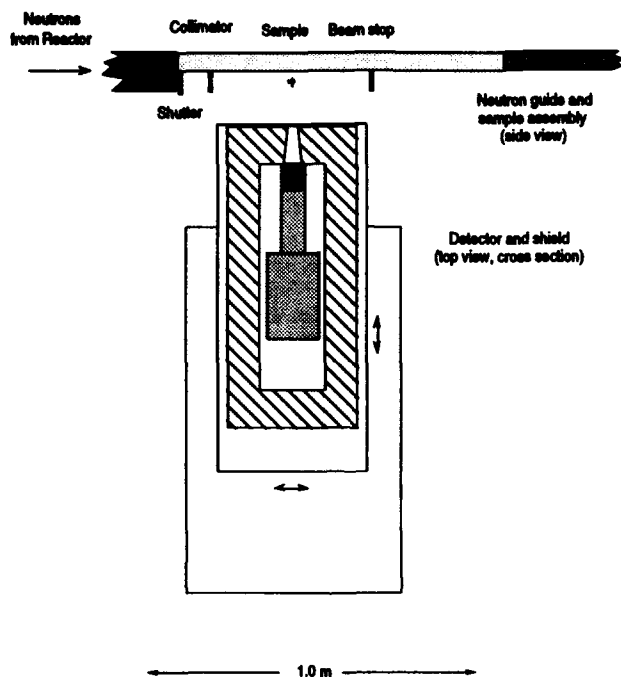


Figure 1. Scale drawing of the PGAA spectrometer. The detector and shield are shown in cross section from a top view and the guide is shown from the side, rotated about the sample position.

## APPARATUS

The instrumentation, located in the Cold Neutron Research Facility (CNRF) at NIST has been described in detail elsewhere [14,17]. Neutrons, produced by uranium fission in the core of the NIST research reactor and chilled by passage through a  $D_2O$  ice moderator at 30K, are supplied to 14 different instruments in the CNRF by a series of 8 nickel coated borosilicate guide tubes. Figure 1 shows the CNPGAA workstation located in the CNRF. The neutron beam emerges from the bottom half of neutron guide NG7 into air, and is collimated to a 20 mm diameter circle before striking the sample. Samples are normally sealed into bags of FEP Teflon<sup>1</sup> and suspended in the beam between strings of PFA Teflon. Prompt gamma-rays emitted by the sample are measured by a high

<sup>1</sup>Certain commercial equipment, instruments, or materials are identified in this paper in order to specify the experimental procedures in adequate detail. Such identification does not imply recommendation by the National Institute of Standards and Technology, nor does it imply that the materials or equipment identified are necessarily the best available for the purpose.

resolution, boral and lead-shielded germanium detector positioned perpendicular to the neutron beam. Gamma-ray spectra up to 8 MeV are taken using a 16K channel analog-digital converter connected to a multichannel pulse height analyzer. Data acquisition and reduction are performed using Canberra Nuclear Data acquisition and display software on a VAXstation 3100.

### BACKGROUND AND DETECTION LIMITS

The background in the hydrogen region (2223 keV) of a prompt gamma-ray spectrum measured for a hydrogen free material arises from three possible sources. Neutron capture by hydrogen in the atmosphere and shielding materials gives rise to  $0.06 \pm 0.01$  counts per second of gamma radiation, corresponding to 15-20  $\mu\text{g}$  of hydrogen. Interferences, gamma-rays within  $\sim 5$  keV of the hydrogen peak energy, emitted by other elements in the sample matrix represent a second possible source of background. Few interferences are known for H (Ba at 2220.0 keV, Os at 2223.3 keV and Xe at 2225.2 keV); however, current tabulations of prompt gammas are incomplete. A third possible source of background arises from Compton scattering of high energy gamma-rays. This results in decrease in signal to noise ratio by raising the continuum baseline under the hydrogen peak.

The detection limit for hydrogen in a given matrix is taken to be  $2\sigma$  of the uncertainty in the background count rate at 2223 keV. For samples which yield a relatively clean spectrum in this energy range and for which a large Compton background is not observed, the hydrogen detection limit may be taken to be essentially  $2\sigma$  of the normal background (i. e. the background with no sample in the beam), or about 5 - 10  $\mu\text{g}$ . For samples which give complex spectra with many high energy peaks, a large baseline due to Compton scattering of gamma-rays is observed. Experiments using the University of Maryland/NIST thermal neutron PGAA instrument [18] indicate that the introduction of Compton suppression improves the detection limit near 2223 keV by a factor of 1.5 - 2. A similar improvement in detection limit is expected when Compton suppression is introduced into the cold neutron instrument (see FUTURE PLANS).

### APPLICATIONS

We have determined hydrogen in quartz crystals, a dielectric film on a silicon wafer, and in crystals of semiconductor grade germanium. Although we were told to expect large amounts of hydrogen in many of these samples, the analyses have typically yielded hydrogen count rates comparable to background levels (i. e. the hydrogen count rate obtained with no sample in the beam). Nevertheless, the data may be used to establish an upper limit for the hydrogen concentration.

Five crystals of hydrothermally grown quartz (weighing from one to four grams) were analyzed for hydrogen by CNPGAA. The crystals had been grown and analyzed by infrared spectroscopy by researchers at the U. S. Army Research Laboratory in Fort Monmouth, New Jersey. Table I gives H concentrations determined by CNPGAA, along with H concentrations estimated from the IR data. Upper limits for CNPGAA analyses are expressed as  $\leq 2\sigma$ , based on sample counting statistics. Uncertainties were evaluated using guidelines given by Taylor and Kuyatt [19]. Expanded experimental uncertainties were evaluated by combining Type A uncertainties (those evaluated by statistical means) in quadrature and multiplying by a coverage factor of 2 to give a 95% confidence level. Type A uncertainties were evaluated by statistical means and originate from sample counting

Table I - H concentrations in samples of hydrothermal quartz estimated from both CNPGAA and IR data.

| Sample | mg/kg H (CNPGAA) | mg/kg H (IR) |
|--------|------------------|--------------|
| TD4    | $6 \pm 12$       | 5.4          |
| TD7C   | $\leq 5$         | 16           |
| TD7D   | $10 \pm 12$      | 12           |
| A3LZ   | $\leq 5$         | 4.9          |
| B4LZ   | $\leq 6$         | 4.6          |

Table II - Hydrogen concentrations in five samples of semiconductor grade germanium.

| Sample #     | mg H/ kg Ge | H atoms/ 100 Ge atoms |
|--------------|-------------|-----------------------|
| 1 (unetched) | $80 \pm 55$ | $0.6 \pm 0.4$         |
| 2 (unetched) | $70 \pm 50$ | $0.5 \pm 0.4$         |
| 3 (etched)   | $50 \pm 40$ | $0.4 \pm 0.3$         |
| 4 (etched)   | $60 \pm 45$ | $0.4 \pm 0.3$         |
| 5 (etched)   | $60 \pm 40$ | $0.4 \pm 0.3$         |

statistics and background subtraction (>25%), standard counting statistics (<1%), sample positioning and neutron fluence variation (~1%), and sample weighing (<1%). Type B uncertainties (those not determinable by statistical means) were negligible. Hydrogen concentrations determined for the quartz samples do not differ within statistical uncertainties from each other or (for 4 of 5 samples) from H concentrations determined by IR data.

A 1  $\mu\text{m}$ -thick layer of dielectric glass film on a silicon wafer was obtained for hydrogen analysis from Intel. Similar films had been estimated, by weight loss on heating, to contain 4-5 % by weight of  $\text{H}_2\text{O}$ . The sample was analyzed by CNPGAA, along with a blank, a bare silicon wafer of the same size and thickness of the sample substrate. Both the sample and the blank yielded hydrogen count rates within statistical uncertainty of background levels. It was determined that the dielectric film contained  $\leq 2\%$  by weight of hydrogen, or  $\leq 19\%$  by weight of  $\text{H}_2\text{O}$ , where the upper limit was estimated as  $2\sigma$  of the H count rate for the sample.

Five samples of semiconductor grade germanium, believed to contain as much as 1 atom of hydrogen per atom of germanium, were also analyzed by CNPGAA. The samples consisted of three ~ 1-gram pieces of germanium which had been etched prior to analysis, and two pieces of unetched germanium of the same approximate size. Since germanium is believed to absorb hydrogen readily upon etching, higher hydrogen concentrations were expected in the etched samples. Hydrogen concentrations determined in the samples ranged from 50 to 80 mg/kg Ge, or 0.4 to 0.6 atomic % of H (see Table II). No significant differences were observed between etched and unetched samples.

Type A errors arising from counting statistics and background subtraction yielded 15 - 20 % uncertainties in the Ge hydrogen concentrations. All other type A errors (from standard counting statistics, sample positioning and neutron fluence variation, and sample weighing) were negligible. However, due to the extremely complicated nature of the Ge spectra, peak fitting was difficult due to the inability to obtain a constant baseline. Hence the total uncertainty in sample H count rate is much larger than that evaluated from counting statistics for a single fit. A type B uncertainty of 30%, estimated by repeated fitting of hydrogen peaks using a SUM code written at NIST, was therefore added in quadrature to yield a more realistic evaluation of the total counting uncertainty. Expanded uncertainties were obtained by multiplying by a coverage factor of 2 to give a 95% confidence level.

## FUTURE PLANS

Hydrogen concentrations in many semiconductor materials analyzed have been at or below the detection limit for the technique. Further work is needed to establish whether higher levels of hydrogen may be accurately determined. Future analyses of H ion implanted quartz will help to establish a detection limit for hydrogen in this material.

Future work is also needed to determine whether elements other than Ba, Os and Xe yield gamma-ray interferences in the hydrogen region. Since prompt gamma-ray spectra for many elements (e. g. germanium) yield more peaks than are listed in current tabulations, the possibility of interferences in the hydrogen region cannot be ruled out. It may be eventually possible to correct for errors arising from hydrogen interference peaks by analyzing a blank, a sample of the material in question which is known to contain a negligible amount of hydrogen. However, the absence of hydrogen in the blank would have to be established by an independent analytical technique.

Improvements in the system are currently underway which will reduce background and improve signal to noise ratio, thus improving detection limits. Background due to Compton scattering will be suppressed by surrounding the germanium by a bismuth germanate detector. The addition of a helium-filled sample box, as well as improved gamma-ray and neutron shielding around the detector and neutron guide, will reduce background capture by hydrogen and other elements in the environment surrounding the system. Replacement of the current D<sub>2</sub>O cold source with a liquid hydrogen source will increase the neutron fluence rate by a factor of five or greater. The addition of neutron optics to focus the beam onto a smaller area (~1 mm diameter circle) may someday lead to the development of a neutron microprobe [20, 21].

## ACKNOWLEDGMENTS

We wish to thank Sam Treviño, R. Aaron Murray, Richard Deslattes, R. Gregory Downing and Intel for providing samples for analysis.

## REFERENCES

1. S. M. Myers, M. I. Baskes, H. K. Birnbaum, J. W. Corbett, G. G. DeLeo, S. K. Estreicher, E. E. Haller, P. Jena, N. M. Johnson, R. Kirchheim, S. J. Pearton, and M. J. Stavola, *Rev. Mod. Phys.* **64**, 559 (1992).
2. S. J. Pearton, J. W. Corbett, and T. -S Shi, *Appl. Phys. A* **43**, 153 (1987).
3. J. I. Pankove, D. E. Carlson, J. E. Berkeyheiser, and R. O. Wance, *Phys. Rev. Lett.* **51**, 2224 (1983).
4. J. I. Pankove, R. O. Wance, J. E. Berkeyheiser, *Appl. Phys. Lett.* **45**, 1100 (1984).
5. N. M. Johnson, C. Herring, and D. J. Chadi, *Phys. Rev. Lett.* **56**, 2224 (1986).
6. N. M. Johnson, C. Herring, and D. J. Chadi, *Phys. Rev. Lett.* **59**, 2116 (1987).
7. M. Paesler, S. C. Agarwal, and R. Zallen, Eds., Proceedings of the 13th International Conference on Amorphous and Liquid Semiconductors I: Non-Cryst. Solids, 114 (1989).



8. R. N. Hall, IEEE Trans. Nucl. Sci. NS-21, No. 1, 260 (1974).
9. R. N. Hall, Inst. Phys. Conf. Ser. 23, 190 (1975).
10. E. E. Haller, B. Joós, and L. M. Falicov, Phys. Rev. B 21, 4729 (1980).
11. B. Joós, E. E. Haller, and L. M. Falicov, Phys. Rev. B 22, 832 (1980).
12. R. L. Paul, R. M. Lindstrom, and D. H. Vincent, J. Radioanal. Nucl. Chem., in press.
13. R. M. Lindstrom, R. L. Paul, and D. H. Vincent, J. Radioanal. Nucl. Chem., in press.
14. R. L. Paul and R. M. Lindstrom, Review of Progress in Quantitative Nondestructive Evaluation Vol. 13, ed. D. O. Thompson and D. E. Chimenti, Center for NDE/Iowa State University, Ames, IA, in press.
15. D. A. Newmann, J. R. D. Copley, D. Reznik, W. A. Kamitakahara, J. J. Rush, R. L. Paul, and R. M. Lindstrom, J. Phys. Chem. Solids, in press.
16. R. M. Lindstrom, J. Res. Nat. Inst. Stand. Techn 98, 127 (1993)
17. R. M. Lindstrom, R. Zeisler, D. H. Vincent, R. R. Greenberg, C. A. Stone, E. A. Mackey, D. L. Anderson, and D. D. Clark, J. Radioanal. Nucl. Chem. 167, 121 (1993).
18. D. L. Anderson, M. P. Failey, W. H. Zoller, W. B. Walters, G. E. Gordon, R. M. Lindstrom, J. Radioanal. Chem. 63, 97 (1981).
19. B. N. Taylor and C. E. Kuyatt, "Guidelines for Evaluating and Expressing the Uncertainty of NIST Measurement Results", NIST Technical Note 1297, National Institute of Standards and Technology, U. S. Government Printing Office: Washington, DC, 1993.
20. D. F. R. Mildner, Nucl. Instrum. Methods A299, 416 (1990).
21. H. Chen, R. G. Downing, D. F. R. Mildner, W. M. Gibson, M. A. Kumakhov, I. Yu. Ponomarev, and M. V. Gubarev, Nature 357, 391 (1992).

## THE PERFORMANCE STUDY OF ION IMPLANTER BASED MEDIUM ENERGY ION SPECTROSCOPY WITH SOLID STATE DETECTOR

Z. J. RADZIMSKI\*, S. YOKOYAMA\*\*, K. ISHIBASHI\*\*\*, M. HIROSE\*\*\*

\* Analytical Instrumentation Facility, North Carolina State University, Raleigh, NC 27695, USA

\*\* Research Center for Integrated Systems, Hiroshima University, Higashi Hiroshima 724, Japan

\*\*\*Department of Electrical Engineering, Hiroshima University, Higashi Hiroshima 724, Japan

### ABSTRACT

Medium-energy ion spectroscopy using a conventional ion implanter has been developed to study the properties of semiconductor subsurface regions. The system is equipped with solid state detector and operates with He<sup>+</sup> ion energy up to 200 keV. We have tested the system performance for various applications, such as, silicon diffusion through a thin Au layer, a low dose, low energy As implantation and damage of silicon surface caused by plasma treatment.

### INTRODUCTION

Ion backscattering techniques are very powerful methods for material science. They cover a very large range of primary beam energy from keV to MeV. One of the most popular is Rutherford backscattering spectroscopy (RBS) which uses a collimated ion beam and operates usually in the energy range from 1 to 2.5 MeV [1-3]. A strong trend in semiconductor technology is to fabricate devices in a very shallow surface region. In this case a lower energy characterization techniques are more suitable since they are more sensitive to subsurface region. The technique which is very similar to RBS but operates at much lower energy is called Medium-energy ion spectroscopy (MEIS). It uses ions with energies between 50 to 200keV what is more optimal for subsurface spectroscopy applications. A cross section for angle scattering at 200keV is approximately two orders of magnitude larger than at 2 MeV while the stopping power is almost the same [4]. It has been shown that MEIS has a capability to detect the average positions of atoms in the surface layer with accuracy of 0.01 Å in crystalline materials and compositional depth profiles can be measured with a 3 to 5 Å resolution in amorphous samples [5].

The medium energy range of MEIS technique matches the ion energy utilized in many ion implanters used in microelectronics technology. This opens a broad prospective for implementation of MEIS technique for *in situ* and other surface studies using this equipment. Another important advantageous feature of MEIS technique is the simplicity of a qualitative analysis of experimental data, similarly to the RBS technique. One of the main problems for adaptation of MEIS system into an ion implanter chamber is the selection of a backscattered particle detector. The commonly used MEIS detectors such as the electrostatic toroidal analyzer [6-8] and the time of flight detector [9-10] are difficult to adapt due to their large sizes. The surface barrier detector (SBD), which is a standard detector for RBS, has relatively low energy resolution (~10 keV) in comparison with

other detectors ( $\approx 1$  keV) but can be still very attractive for many applications considering its cost and easy installation. We have developed the MEIS system equipped with solid state detector in a conventional ion implanter operating with  $\text{He}^+$  ion energy up to 200 keV [11]. The system is in operation at Hiroshima University. We have tested the system sensitivity by investigating silicon diffusion through a thin Au layer, a low dose, low energy As implantation into silicon and damage caused by Ar plasma treatment.

## EXPERIMENTAL RESULTS

One of the main disadvantage of a solid state detector when used in the medium energy range is its low energy resolution. In order to illustrate the performance of solid state detector at different primary beam energies the spectra were collected at wide range of ion energy ranging from 2 MeV to 200 keV. The spectra for 500 keV and above were obtained using a standard RBS apparatus, while 200 keV spectra were collected with ion implanter based system described in this paper. The spectra were collected for a 125 Å thick Au layer evaporated on Si(110) substrate annealed at 150°C for 10 minutes. Several interesting features can be observed on the energy distributions shown in Fig. 1. The first edge of the Si part of the spectrum corresponds to the surface layer of  $\text{SiO}_2$  formed on the Au layer from the Si diffused through the Au layer [12]. The presence of oxygen is confirmed by the peak at the energy about 33% of the primary beam energy. The second edge of the Si part of the spectrum corresponds to the Au layer / Si substrate interface. All these features can be recognized on each spectrum shown in Fig. 1 with resolution decreasing as the primary beam energy decreases. However, it is important to mention that the signal intensity increases dramatically as the beam energy is reduced what allow to collect the data at lower energy with significantly lower charge. The signal intensity dependence on the primary beam energy is shown in Fig. 2. The integrated intensity corresponding to 23 Å of Au deposited on Si substrate is shown in this figure. The data were collected at the constant charge of 1  $\mu\text{C}$  delivered to the sample. According to the theory the power factor for counts vs. energy dependence should be -2, as shown in Fig. 2, which agrees with experimental data very well considering the experimental error.

The high scattering efficiency is valuable when thin surface layers are investigated. An example of such application is the analysis of interdiffusion in the Au/Si structure. In this experiment a 23 Å thick Au layer was deposited on the Si(110) substrate and annealed at 150°C for 10 minutes. The MEIS spectra collected before and after annealing are shown in Fig. 3. After annealing a clear shift of gold peak to the lower energies is visible. The shift is caused by a thin Si surface layer which was formed after Si diffusion through the gold layer. The larger shift on the left side of Au part of the spectrum results from the diffusion of gold into Si substrate. Considering the fact that the 23 Å thick gold layer is not continuous one can not expect the appearance of an

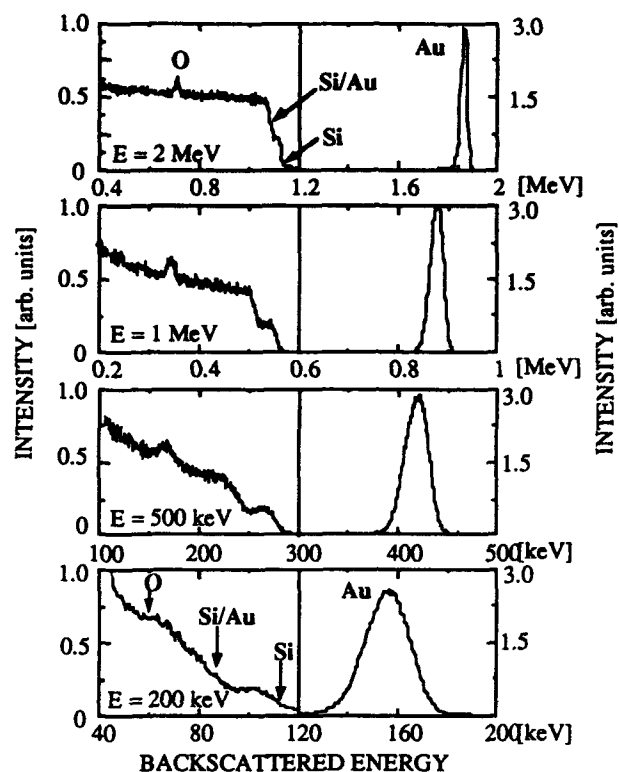


Fig. 1. The energy spectra collected at various incident energies of primary beam from a 125 Å thick gold layer deposited on Si substrate and annealed at 150°C for 10 min.

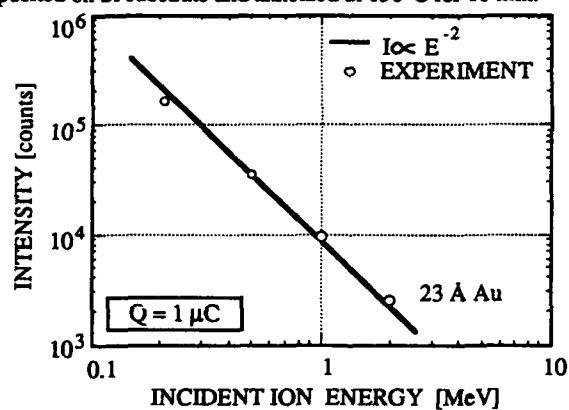


Fig. 2. The aerial intensity,  $I$ , of the Au peak as a function of incident ion energy,  $E$ , compared with the theoretical dependence  $I \propto 1/E^2$ .

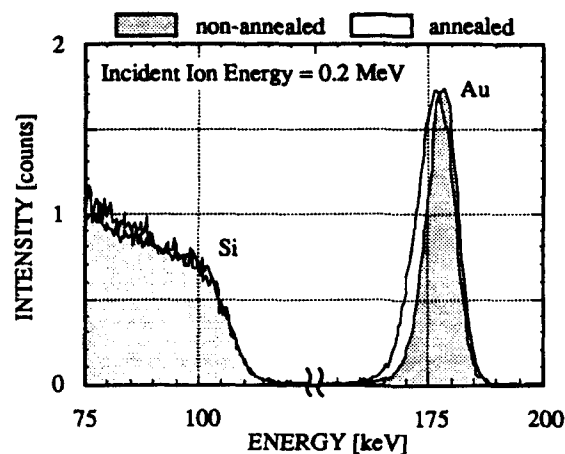


Fig. 3. The energy spectra of backscattered  $\text{He}^+$  ions obtained for a 23 Å thick Au layer evaporated on a Si(110) substrate. The spectra were measured before and after annealing at 150°C for 15 minutes.

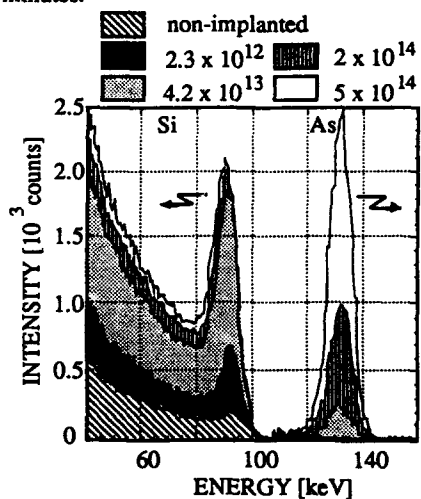


Fig. 4. The MEIS spectra of Si(110) sample before and after arsenic implantation with the various cumulative doses. The implantation was carried out at 14 keV and the MEIS spectra were taken at 175 keV in the (110)-aligned direction.

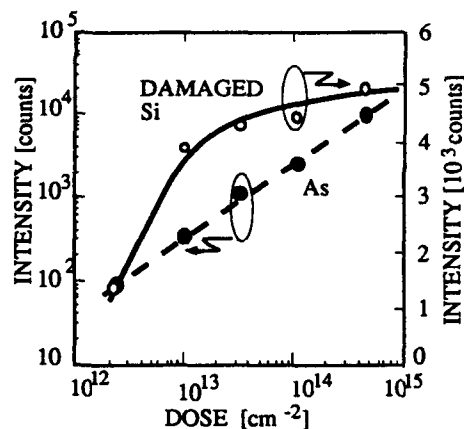


Fig. 5. Total integrated signal of As peak and that of damaged Si surface layer as a function of As cumulative dose.

extra edge in the energy distribution from a thin Si layer covering the gold islands. The area under the Au peak corresponds to the effective thickness of Au layer. By comparing the areas for non-annealed and annealed sample we estimated that the effective thickness of Au layer increased from 23 Å to 27 Å. The thickness was evaluated by comparing the spectrum with the data obtained for a standard sample.

Another example of MEIS application was to study low dose, low energy arsenic implantation into Si(110) substrate. Room temperature implantation was carried out at 14 keV with the sample tilted by 10° with respect to the ion beam. A four-step implantation was performed with cumulative doses of  $2.3 \times 10^{12}$ ,  $4.2 \times 10^{13}$ ,  $2 \times 10^{14}$  and  $5 \times 10^{14} \text{ cm}^{-2}$ . The MEIS spectra collected at 175 keV in the channeling direction for a non-implanted sample and after each implantation process are shown in Fig. 4. A very good proportionality of the As peak counts with respect to the implant dose is obtained as illustrated in Fig. 5. A clear peak at the energies 85 to 95 keV observed in Fig. 4 represents a damaged surface layer. The integrated signal corresponding to this energy interval is shown in Fig. 5 as a function of implantation dose. At the  $10^{14} \text{ cm}^{-2}$  doses the damaged signal tends to saturate which is in agreement with the critical dose for silicon amorphization [13].

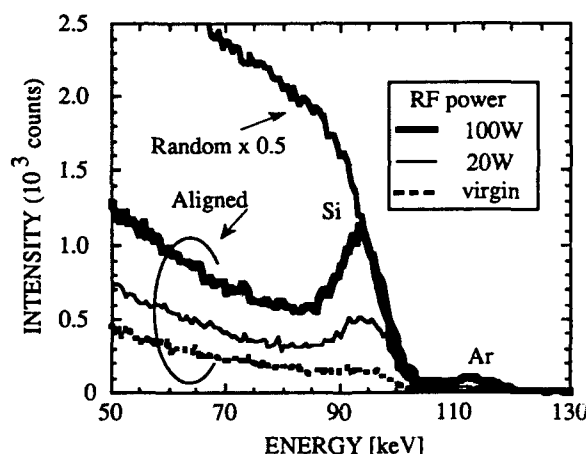


Fig. 6. MEIS spectra before and after Ar plasma treatment for different RF powers.

The last example of MEIS application described in this report illustrates the damage detection caused by short time (10 sec) Ar plasma treatment [14]. The spectra taken before and after treatment indicate relatively large damage of Si surface layer even at low RF power of 20 W. The damage increases with RF power and the depth of damage Si layer at 100 W is estimated to be  $\approx 20 \text{ nm}$ . A weak peak around 113 keV indicates the presence of Ar in the surface region.

## CONCLUSIONS

The results indicate that the implementation of MEIS in an ion implanter opens a broad prospective for *in situ* or *ex situ* surface studies in the semiconductor processing. An important observation has been made that a valuable information is provided by the system equipped with a solid state detector which has relatively poor energy resolution at the energies below 200 keV. Further improvements of detection limits and technique performance are expected with replacement of the SBD detector with a more sensitive detection system.

## REFERENCES

1. J. R. Bird and J. S. Williams, Ion Beams for Materials Analysis, (Academic Press Australia, 1989).
2. W. -K. Chu, J. W. Mayer and M. -A. Nicolet, Backscattering Spectrometry, (Academic Press, New York, 1977).
3. D. O. Boerma, Nucl. and Instr. Meth. **B50** 77 (1990).
4. J. F. Ziegler: Helium, Stopping Power and Ranges in All Elemental Matter, (Pergamon Press, New York, 1977).
5. S.M.Yalisove and W.R. Graham, J. Vac. Sci. Technol. **A6** 588 (1988).
6. Y. Kido, J. Kawamoto and Y. Miyake, Proc. 12th Symp. of ISLAT'89, Tokyo 1989, 557.
7. R. G. Smeenk, R. M. Tromp, H. H. Kersten, A. J. H. Boerboom and F. W. Saris, Nucl. Instr. and Meth. **195** 581 (1982).
8. W. R. Graham, S. M. Yalisove, E. D. Adams, T. Gustafsson, M. Copel and E. Törnqvist, Nucl. Instr. and Meth. **B16** 383 (1986).
9. M. H. Mendenhall and R. A. Weller: Nucl. Instr. and Meth. **B40/41** 1239 (1989).
10. M. H. Mendenhall and R. A. Weller: Nucl. Instr. and Meth. **B47** 193 (1990).
11. Z. J. Radzimski, S. Yokoyama, K. Ishibashi, F. Nishiyama and M. Hirose, Jpn. J. Appl. Phys. **32**, 962 (1993).
12. A. Hiraki, E. Lugujjo, M. -A. Nicolet and J. W. Mayer, Phys. Stat. Sol. (a) **7**, (1971) 401.
13. F. F. Morehead, B. L. Crowder and R. J. Title, J. Appl. Phys. **54**, 1112 (1972).
14. S. Yokoyama, Z. J. Radzimski, K. Ishibashi, S. Miyazaki and M. Hirose, Proc. of the 15th Symp. on Dry Process **73** (1993).

## LOW COHERENCE INTERFEROMETRY FOR NON-INVASIVE SEMICONDUCTOR MONITORING

CHRIS M. LAWSON\* AND ROBERT R. MICHAEL\*\*

\*Department of Physics, University of Alabama at Birmingham, Birmingham, Alabama 35294

\*\*BDM Federal Inc., 1501 BDM Way, McLean, Virginia 22102

### ABSTRACT

We report on the first use of optical low coherence reflectometry (OLCR) for Edge Defined Film-Fed Growth (EFG) silicon characterization. This OLCR sensor system has been used to measure horizontal profiles of silicon thickness and flatness to an accuracy of 1.5  $\mu\text{m}$  with the sensor head positioned 1 cm away from the silicon. The use of this noninvasive sensor for EFG silicon growth monitoring may lead to more efficient solar cell manufacturing processes.

### INTRODUCTION

Silicon sheet growth technologies[1,2] are of great interest for the development of low cost solar cell arrays, since these technologies eliminate the need for slicing silicon ingots. Edge-defined film-fed growth (EFG) has been one of the most promising of these technologies for continuous growth of silicon sheets for solar cell applications.[3,4] In order to facilitate improvements in EFG silicon sheet growth technology, it is necessary to monitor the thickness and flatness of the silicon during the growth process.

In this paper we report on the use of optical low coherence reflectometry (OLCR) to provide accurate, non-invasive measurement of the thickness and flatness of EFG grown silicon. We have recently reported on the use of such techniques to characterize sliced, Czochralski (CZ) grown silicon wafers.[5,6] The work reported in the present paper represents the first use of OLCR techniques for dimensional characterization of sheet grown solar silicon.

### EXPERIMENTS

A schematic diagram of the OLCR sensor system is shown in Figure 1. An edge-emitting light emitting diode (EELED) operating at a central wavelength of 1.55  $\mu\text{m}$  (where silicon is transparent) with a spectral width of 90 nm was used as the low coherence light source. The light from this EELED is split by an evanescent coupler into a fiber optic Michelson interferometer, consisting of a sensor leg and a reference leg. Light that exits the sensor fiber reflects off the silicon wafer, re-enters the fiber, and is combined via the evanescent coupler with light from the reference leg. Light that exits the reference leg reflects off a scanning mirror, re-enters the fiber, and combines with light from the sensing leg. The scanning mirror is used to vary the optical path length of the reference leg of the interferometer. A sinusoidal voltage is applied to a piezoelectric optical phase shifter in the reference leg to modulate the interference signal, which is detected with an InGaAs PIN photodiode detector. The photodetector output is



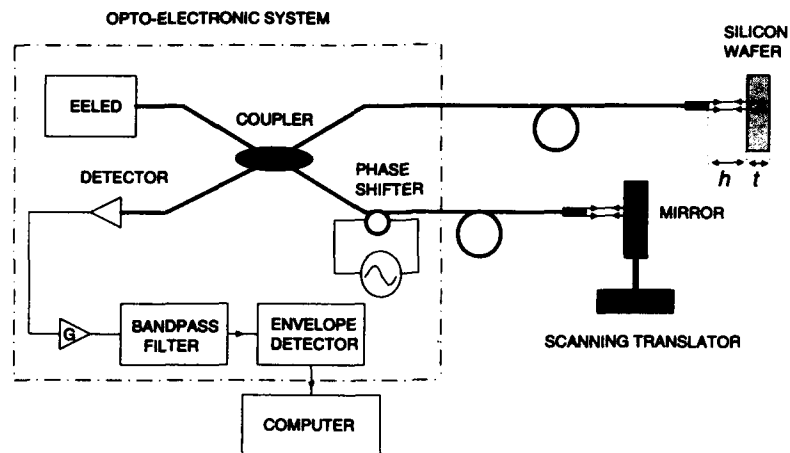


Figure 1 Optical Low Coherence Reflectometry (OLCR) Sensor System

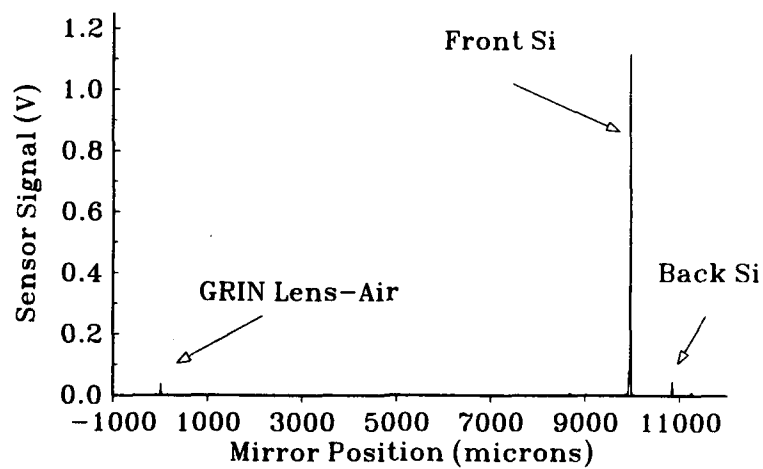


Figure 2 Typical scan of OLCR system for a EFG grown silicon wafer. Peaks are from the GRIN lens-air reflection, the reflection from the front surface of the silicon, and the back surface silicon reflection

amplified, bandpass filtered, and processed by envelope detector. The output of the envelope detector is connected to a computerized data acquisition system.

The light emitted from the fibers in both the sensor and reference legs of the interferometer is collimated with GRIN rods. This collimation process increases the amount of light that reflects back into each leg of the interferometer and enables the fiber ends to be remotely positioned (typically a few centimeters) from the reflecting surfaces of the silicon wafer and scanning mirror.

Because of the low coherence length,  $L_c$ , of the light source (about 10  $\mu\text{m}$ ), interference fringes only occur when the optical path length difference between the sensing leg and the reference leg is less than  $L_c$ . Hence, fringes are observed when the reference leg optical path length (established by the scanning mirror position) is equal to: (i) the sensing leg optical path length established by the retro-reflection from the end of the GRIN rod-air interface; (ii) the sensing leg optical path length established by retro-reflection from the front surface of the silicon; and (iii) the sensing leg optical path length established by retro-reflection from the back surface of the silicon. By monitoring the position of the scanning mirror that corresponds to these "peaks" in oscillating interference fringes, the thickness of the silicon and the sensor-silicon separation (used to determine the silicon wafer flatness), can be measured directly. The accuracy of the OLCR sensor system is established by how precisely the position of the reflection peaks can be located, which is determined by the noise modulation on the signal envelope. As discussed in detail previously,[5,6] the noise modulation on the envelope limits the position accuracy of the OLCR sensor system to approximately 1.5  $\mu\text{m}$ .

To evaluate the use of the OLCR sensor system for silicon sheet growth, an EFG silicon wafer was positioned in front of the fiber sensor head. The reference separation,  $h$ , between the fiber sensor head and the silicon wafer was set to  $1 \text{ cm} \pm 50 \mu\text{m}$  by placing the end of the GRIN rod (sensor head) against the silicon wafer and using a micrometer stage to move the silicon wafer 1 cm away from the sensor head.

Figure 2 shows the output of the signal processing electronics as a function of the scanning mirror position for a typical mirror scan. The sensor head-wafer separation distance,  $h$ , is obtained from Figure 2 by subtracting the mirror position that corresponds to the silicon front surface retro-reflection from the mirror position that corresponds to the GRIN rod-air interface retro-reflection and dividing the result by one, the refractive index of air. Similarly, the thickness of the silicon wafer,  $t$ , is obtained by subtracting the mirror position that corresponds to the silicon back surface retro-reflection from the mirror position that corresponds to the silicon front surface retro-reflection and dividing this result by 3.48 (the refractive index of silicon at 1.55  $\mu\text{m}$ ).

By horizontal translation of the OLCR sensor head, it is possible to measure horizontal profiles of the thickness and flatness of EFG silicon wafers. To perform this measurement, a micropositioner stage was used to translate the sensor head parallel to the surface of a 10 cm wide EFG silicon wafer that was cut by the supplier from a larger silicon sheet.[7] At each horizontal position, an OLCR scan similar to that shown in Figure 2 was performed. Figures 3 and 4 show the results of these measurements. The sensor-silicon separations (the difference between reflection peak locations from the front silicon surface and the collimator-air interface) are shown in Figure 3. The flatness of the wafer can be ascertained by observing the variation in the sensor-silicon separation with horizontal scan position. It can be seen from Figure 3 that the measured EFG grown silicon wafer deviates from flatness in an oscillatory way. Taking the difference between the two curves of Figure 3 and dividing through by the silicon refractive

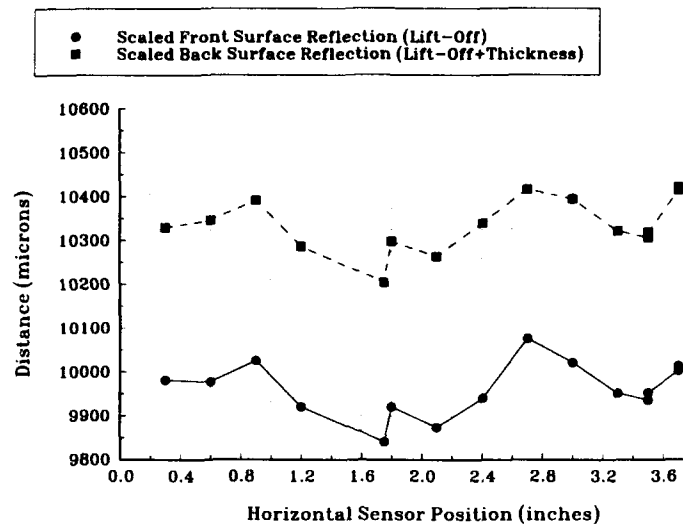


Figure 3. Front And Back Reflections vs. Horizontal Position

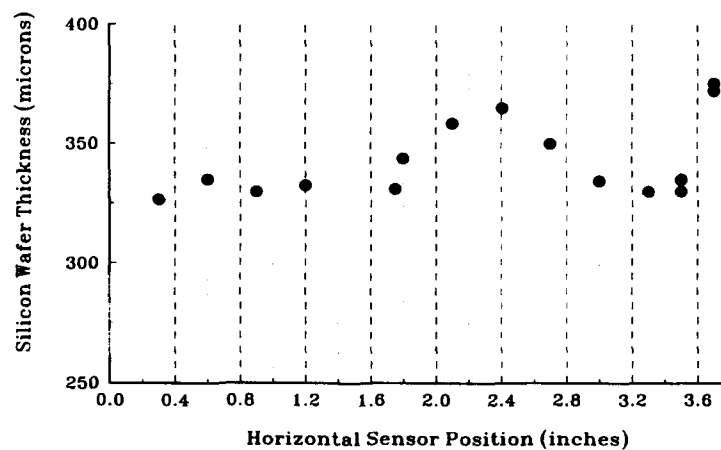


Figure 4 EFG Wafer Thickness vs. Horizontal Position

index yields the horizontal profile of the wafer thickness, shown in Figure 4. The thickness variation is seen to be about 50  $\mu\text{m}$  for this wafer.

## SUMMARY

In this paper we have reported on the first use of optic low-coherence reflectometry (OLCR) for non-invasive characterization of EFG sheet grown solar silicon. This OLCR sensor system has been used to measure horizontal profiles of silicon thickness and flatness to an accuracy of 1.5  $\mu\text{m}$  with the sensor head positioned 1 cm away from the silicon. Since wafer thickness and flatness are two important growth parameters for sheet grown silicon, the use of this noninvasive sensor for on-line silicon sheet growth monitoring may lead to more efficient solar cell manufacturing processes.

More recently, we have packaged the OLCR sensor system (the optics, signal processing electronics, and mirror scanner) into a single opto-electronic unit compatible with the environment of the crystal growth furnace. Using this packaged OLCR system, we have been able to make preliminary, quantitative, on-line measurements of EFG silicon thickness and flatness during the actual growth process. Details of these measurements will be reported elsewhere.[8]

## REFERENCES

- 1 T. Surek, Proc. Symp. on Electronic and Optical Properties of Polycrystalline or Impure Semiconductors and Novel Silicon Growth Methods, edited by K. V. Ravi and B. O'Mara (Electrochemical Society, Pennington, NJ, 1980), pp. 173-183.
2. T. Ciszek, J. Crystal Growth **66**, 655-672, (1984).
- 3 F. Wald, in: *Silicon*, edited by J. Grabmaier (Springer-Verlag, New York, 1981) pp. 147-198.
- 4 D. Harvey, J. Crystal Growth **104**, 88-92 (1990).
- 5 C.M. Lawson and R.R. Michael, "Fiber Optic Low Coherence Interferometry (FOLCI) For Non-Invasive Silicon Growth Monitoring," accepted for publication in The Journal of Crystal Growth.
- 6 C. M. Lawson and R. R. Michael, "Fiber Optic Low Coherence Michelson Interferometer For Silicon Wafer Growth Measurement," to appear in SPIE Proc. **2072** (1993).
- 7 EFG grown silicon wafer supplied by Mobil Solar Energy Corporation, Billerica, MA.
- 8 R.R. Michael, C.M. Lawson, and F. Feda, "Optical Low Coherence Reflectometry (OLCR) For Dimensional Monitoring Of Sheet Grown Silicon During The Growth Process," to be published.

## EVALUATION OF DRY ETCHING INDUCED DAMAGE OF GaInAs USING TRANSMISSION LINES AND SCHOTTKY DIODES

S. THOMAS III AND S. W. PANG

The University of Michigan, Department of Electrical Engineering and Computer Science, Ann Arbor, MI 48109-2122

### ABSTRACT

Plasma etching of GaInAs and AlInAs has been carried out in a system which consists of an electron cyclotron resonance (ECR) source and an rf-powered stage. Since the ECR source can generate a plasma with low ion energy, dry etching induced damage is expected to be minimal. In this study, Schottky diodes and transmission lines were fabricated on the etched GaInAs surface. The diode and transmission line characteristics were evaluated as a function of etch conditions. For the etching of GaInAs and AlInAs, Cl<sub>2</sub> and Ar were used as the etch gases. In addition to the ratio of the two gases, microwave power, rf power, pressure, and source distance were varied and their effects on etch rate, morphology, and surface damage were analyzed. Etch rate increased monotonically with microwave power, rf power, and Cl<sub>2</sub> percentage. Etch rate decreased with increasing distance and reached a maximum for a pressure of 1 mTorr. The etch conditions for the damage study were chosen to maintain smooth morphology. One of the most important factors influencing damage was the ion energy which can be limited by using low rf power and short source distance. Minimum damage was obtained at 1 mTorr which provides the optimal balance between high etch rate and low ion energy. Besides limiting ion energy, the addition of Cl<sub>2</sub> reduced etch-induced damage. The specific contact resistivity and sheet resistivity obtained from transmission line measurements of dry-etched n-GaInAs were lower than the wet-etched samples. Schottky diode analysis show reduction in barrier height and breakdown voltage after Ar sputtering. Addition of 10% Cl<sub>2</sub> is sufficient for full recovery of the diode characteristics.

### INTRODUCTION

Plasma etching is an attractive technique for fabricating devices with small dimensions due to the control of etch profile by directional ions. For this technique to be acceptable for high performance device fabrication, the potential etch-induced damage should be understood and limited. Different techniques have been developed to evaluate damage including electrical characteristics on simple device structures, optical analysis such as photoluminescence and photoreflectance, and surface analysis such as Rutherford backscattering and transmission electron microscopy [1-4]. In this paper, electrical characterization was used to relate the effects of etching on GaInAs/AlInAs-based heterojunction bipolar transistors. The current-voltage (I-V) and capacitance-voltage (C-V) measurements on Schottky diodes have been found to be very sensitive to surface conditions of semiconductors [5]. The barrier height, ideality factor, doping profile, and breakdown voltage can be monitored as measures of the device quality. Foad *et al.* [1] have shown that analysis of transmission lines can be used for damage assessment. Surface modification after etching can be related to the specific contact resistivity ( $\rho_c$ ) and sheet resistivity ( $R_s$ ). In addition, the damage depth can also be determined.

To minimize damage, it is important to avoid using high energy ions. The drawbacks for using low ion energy would be etch rate reduction and rougher morphology. Another approach is to remove the damage layer with a wet chemical etch, but this limits the minimum feature size and increases process complexity. Etching with an electron cyclotron resonance (ECR) source provides fast etch rates and damage free etched surfaces by generating a high density plasma with low ion energy. ECR sources have been used for the etching of GaAs, AlGaAs, and InP [6-8]. Ren *et al.* [9] have investigated surface damage of GaInAs/AlInAs etched using an ECR source and Ar gas. Etching with just the inert gas is undesirable since sputter etching tends to generate

more damage than when reactive gases are used. In this study, the effects of microwave power, rf power, pressure, distance, and  $\text{Cl}_2$  percentage on morphology, etch rate, and damage are presented.

Ohmic contacts were deposited on top of GaInAs after etching to form transmission lines without annealing. The changes in  $\rho_c$  and  $R_s$  were used as measures of device damage. It was found that  $\rho_c$  shows larger changes than  $R_s$  after etching. Schottky diodes were formed on top of GaInAs after etching. The electrical characteristics of the diodes were evaluated as a function of etch conditions.

## EXPERIMENTAL

### Plasma System

Dry etching was carried out in a chamber consisting of an ECR source and an rf-coupled stage [10]. The source and chamber are surrounded by 12 and 16 permanent magnets, respectively. This provides magnetic confinement which enhances the ionization efficiency, thereby increasing ion density. The rf power is at 13.56 MHz and can be adjusted from 0-500 W. The distance from the stage to the ECR source can be set from 5-23 cm. These controllable parameters have the largest effect on the ion energy. The gas can be introduced near the stage through a gas ring or at the source. In this study, Ar flowed through the source gas ring while  $\text{Cl}_2$  was injected at the stage.

### Material and Device Structures

Schematics of the GaInAs device structures are shown in Fig. 1. Transmission lines were formed on a 0.5  $\mu\text{m}$  thick GaInAs layer doped at  $10^{16} \text{ cm}^{-3}$  on a semi-insulating InP substrate. The Ti/Pt/Au (25/50/300 nm) ohmic contacts for the transmission lines were deposited directly on the etched surface using a standard liftoff technique. The small bandgap of GaInAs allows ohmic contacts to be formed without annealing to avoid removal of the damage. The spacing between the contact pads ranged from 2-25  $\mu\text{m}$  and the contact area was  $70 \times 70 \mu\text{m}^2$ . The transmission lines were isolated using a wet chemical etch in  $\text{H}_2\text{O}:\text{C}_6\text{H}_8\text{O}_7:\text{H}_2\text{O}_2:\text{H}_3\text{PO}_4$  (220:55:5:1). From the transmission line analysis,  $\rho_c$  and  $R_s$  can be extracted [11]. Defects induced by etching could introduce leakage currents; therefore,  $\rho_c$  is expected to be lower on the dry etched samples.

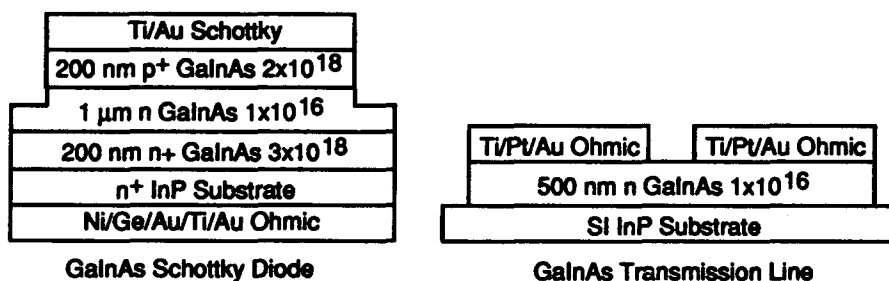


Figure 1. Device structures including Schottky diode and transmission line used for the evaluation of etch-induced damage.

Due to the low energy bandgap, Schottky diodes cannot be formed on n-type GaInAs. A surface barrier enhancement layer is needed to increase the barrier height. Therefore, a thin p<sup>+</sup>-GaInAs layer was grown on top of the n layer for barrier height enhancement [12]. The samples used for GaInAs Schottky diode measurements consist of 200 nm thick p<sup>+</sup>-GaInAs on 1  $\mu\text{m}$

thick n-GaInAs layer. The diodes were formed by depositing Ti/Au (50/300nm) on the GaInAs layer after 100 nm was etched and were 90  $\mu\text{m}$  in diameter. The variations in barrier height, ideality factor, doping profile, and breakdown voltage were evaluated after dry etching and they can be attributed to etch-induced damage.

## RESULTS AND DISCUSSION

### Etch Rate and Morphology

The etch rates for GaInAs and AlInAs were determined in order to keep a consistent etch depth for the damage study. The etch rates were found to increase monotonically with increasing microwave power, rf power, and  $\text{Cl}_2$  percentage. The etch rate decreased with increasing distance. Figure 2 shows the effects of pressure on GaInAs and AlInAs etch rates. Etch rates were maximum at 1 mTorr, probably due to the efficient coupling of the microwave power when the ECR condition was met. Using these conditions at 1 mTorr provided smooth surfaces and an etch rate of  $\sim 30$  nm/min. The etch depth was held constant at 150 nm for the transmission lines and 100 nm for the Schottky diodes. At these etch depths, defect generation should be saturated [1]. For the damage study, the ranges of the parameters used was chosen to maintain smooth morphology. These include varying the microwave power from 50-150 W, rf power from 25-200 W, source distance from 5-20 cm, pressure from 0.5-5 mTorr, and the  $\text{Cl}_2$  percentage from 0-30%.

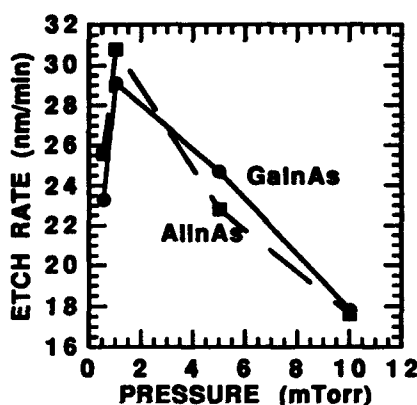


Fig. 2. Etch rates are maximum at 1 mTorr. The etch conditions were 50 W microwave and rf power, 13 cm,  $\text{Cl}_2/\text{Ar}$  at 1/9 sccm and 30  $^\circ\text{C}$ .

### Transmission Line Measurements

For the transmission line measurements, the typical etch condition was 50 W microwave power, 50 W rf power, pressure of 1 mTorr, source distance of 13 cm,  $\text{Cl}_2/\text{Ar}$  flow rate at 1/9 sccm and at 30  $^\circ\text{C}$ . The changes in the self-induced dc bias voltage ( $|V_{dc}|$ ) due to the variations in etch conditions have the strongest influence on  $\rho_c$ . The dependence of contact resistivity on rf power is shown in Fig. 3. For an rf power of 25 W ( $|V_{dc}| = 85$  V), the dry-etched sample showed similar  $\rho_c$  as the wet-etched sample. At 50 W rf power,  $|V_{dc}|$  increased to 145 V, and  $\rho_c$  was reduced by 70%. Increasing the rf power to 200 W caused  $|V_{dc}|$  to increase to 400 V. The specific contact resistivity, which was significantly lower than the wet etched sample, decreased by a factor of 20 from  $8.3\text{--}0.4 \times 10^{-5} \Omega\text{-cm}^2$ . However,  $R_s$  was found to be independent of rf power. The results suggest that  $\rho_c$  is more sensitive to surface damage than  $R_s$ .

Increasing the distance between the ECR source and the stage from 5-20 cm causes the  $|V_{dc}|$  to increase from 50-165 V. This is attributable to the increase in grounded area of the chamber exposed to the plasma. Figure 4 shows the decrease in  $\rho_c$  with increasing distance as indicated by the decrease in the y-intercept. The reduction in  $\rho_c$  may be related to the increase in ion energy and the decrease in etch rate at longer source distance.

Physical sputtering can cause significant degradation in device characteristics. By adding reactive gases in the discharge, the amount of damage can be reduced as shown in Fig. 5. The samples were etched with 50 W microwave and rf power at 1 mTorr, 13 cm below the ECR source, and at  $|V_{dc}| = 150$  V. When pure Ar sputtering was used, significant damage was

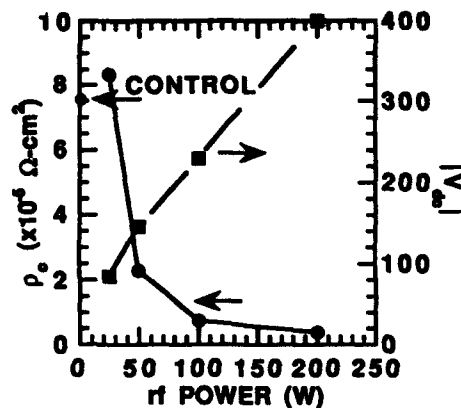


Fig. 3. Effects of rf power on specific contact resistivity of GaInAs. The samples were etched with 50 W microwave power, 1 mTorr, at 13 cm,  $\text{Cl}_2/\text{Ar}$  flow rate at 1/9 sccm, and at 30 °C.

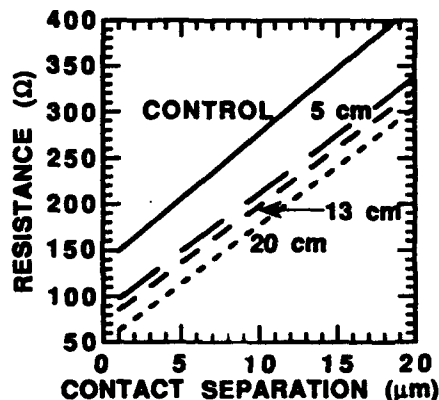


Fig. 4. Transmission line measurements showing decrease in  $\rho_c$  with increasing source distance. The samples were etched with 50 W microwave power, 50 W rf power, 1 mTorr,  $\text{Cl}_2/\text{Ar}$  flow rate at 1/9 sccm, and at 30 °C.

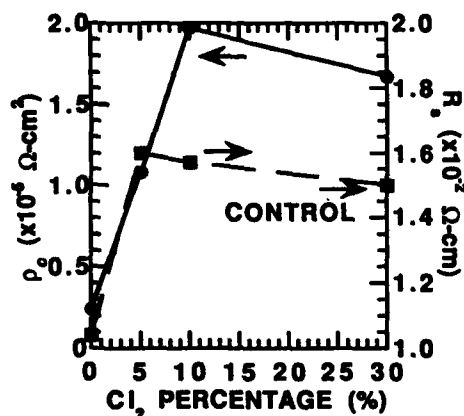


Fig. 5. Damage reduction by addition of  $\text{Cl}_2$ . Etching was carried out using 50 W of microwave and rf power, 1 mTorr, 13 cm, and 30 °C.

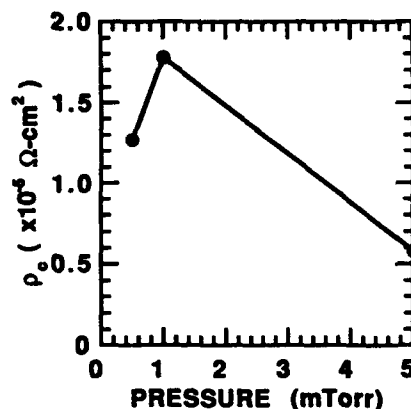


Fig. 6. Reduction in damage by optimizing pressure. The etch conditions were 50 W microwave power, 50 W rf power, 13 cm,  $\text{Cl}_2/\text{Ar}$  flow rate at 1/9 sccm, and at 30 °C.

generated. The decrease in  $\rho_c$  due to Ar sputtering at 150 V was larger than for a similar etch condition where 10%  $\text{Cl}_2$  was added but higher  $|V_{dc}|$  at 400 V was used. Addition of only 5%  $\text{Cl}_2$  to the plasma was enough to increase  $R_s$  from  $1.0\text{--}1.5 \times 10^{-2} \Omega\text{-cm}$ , which is similar to the wet etched sample. Specific contact resistivity increased when the  $\text{Cl}_2$  addition was increased to 10%; however, further addition of  $\text{Cl}_2$  did not continue to increase  $\rho_c$  and it did not fully recover



to the same level as the wet etched sample. This again shows  $\rho_c$  is more sensitive to surface damage than  $R_s$ .

Figure 6 shows that maximum  $\rho_c$  occurred at 1 mTorr where  $|V_{dc}|$  was 130 V. Increasing the pressure to 5 mTorr caused  $|V_{dc}|$  to increase to 160 V due to the decreased ion density. The etch rate also decreased as shown in Fig. 2. The increase in ion energy and the decrease in etch rate may account for the increase in surface damage at higher pressure. For pressure lower than 1 mTorr,  $|V_{dc}|$  remained at 130 V, but the etch rate decreased. The decreased  $\rho_c$  may be due to the slower damage removal at lower etch rate. For samples etched with microwave power ranging from 50-150 W, the reduction in  $\rho_c$  does not show a significant dependence on microwave power.

### Schottky Diode Analysis

Figure 7 shows the severe degradation of diode characteristics after Ar sputtering. The reverse breakdown voltage ( $V_{BR}$ ) decreases from 21-0 V when no  $Cl_2$  is added in the discharge. Likewise, the barrier height decreases from 0.62-0.35 eV. Figure 8 shows the forward I-V curves after etching with 100% Ar and 10-30%  $Cl_2$  addition. Ar sputtering results in an ohmic-like contact, whereas the samples etched with 10-30%  $Cl_2$  are very similar to the control sample. From the C-V measurements, the doping profiles after etching were the same as the control sample when 10%  $Cl_2$  was added. The reduction of etch-induced damage by the addition of reactive gas can be related to the increase in etch rate or the passivation effect by the reactive species. In general, the I-V curves of the dry-etched diodes were comparable to the control sample. This shows that the transmission line method is more sensitive to surface damage than Schottky diode measurements. With 10%  $Cl_2$  addition in the plasma,  $\rho_c$  was 25% of the control sample, while the ideality factor and barrier height were approximately the same as the control sample.

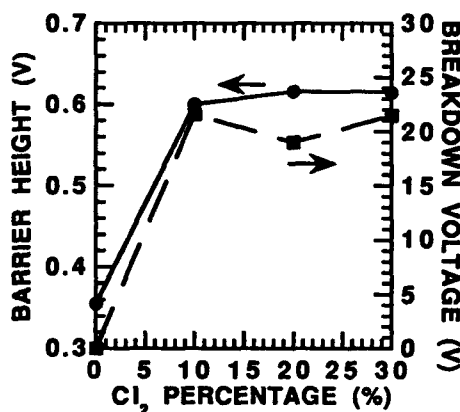


Fig. 7. Barrier height and reverse breakdown voltage increase with addition of  $Cl_2$ . The etch conditions are 50 W microwave power, 50 W rf power, 1 mTorr, 12 cm, and 30 °C.

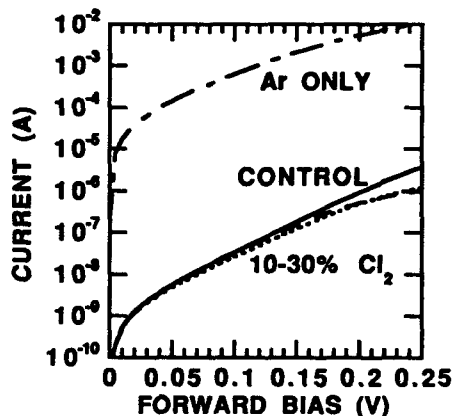


Fig. 8. Forward current for Schottky diodes after etching under same conditions as shown in Fig. 7.

## CONCLUSIONS

Surface damage is a concern for devices with vertical and lateral dimensions of sub-micrometer scale. Transmission lines and Schottky diodes were used to characterize surface damage for GaInAs-based devices. The specific contact resistivity (as measured by the transmission line method) of ohmic contacts deposited directly on the etched surface has been shown to be highly sensitive to damage effects and it tends to decrease after etching. This test structure is most suitable for characterization of damage in low bandgap materials that form ohmic contacts easily.

It has been shown that damage can be minimized by using low ion energy plasma. Using an ECR source, this was accomplished by reducing the rf-power coupled to the stage and by decreasing the stage to source distance. Additionally, the damage was reduced by using a reactive gas that increases the etch rate, thereby removing or passivating damage as it is created. Dry etch induced damage on GaInAs was found to decrease the  $\rho_c$ , barrier height, and breakdown voltage. These device parameters can be used as sensitive control signals for the development of damage-free dry etching technology.

## ACKNOWLEDGMENTS

The authors would like to acknowledge the epitaxial films grown by R. A. Metzger at Hughes Research Laboratories. This work is supported by the Advanced Research Projects Agency under Contract No. F33615-92-C5972.

## REFERENCES

1. M. A. Foad, S. Thoms, and C. D. W. Wilkinson, *J. Vac. Sci. Technol. B* **11**, 20 (1993).
2. K. L. Seaward, and N. J. Moll, *J. Vac. Sci. Technol. B* **10**, 46 (1992).
3. J. L. Benton, B. E. Weir, D. J. Eaglesham, and R. A. Gottscho, *J. Vac. Sci. Technol. B* **10**, 540 (1992).
4. L. He and W. A. Anderson, *Solid-State Electronics* **35**, 151 (1992).
5. S. W. Pang, *J. Electrochem. Soc.* **133**, 784 (1986).
6. S. J. Pearton, U. K. Chakrabarti, A. P. Perley, C. Constantine, and D. Johnson, *Semicond. Sci. Technol.* **6**, 929 (1991).
7. S. J. Pearton, U. K. Chakrabarti, W. S. Hobson, C. Constantine, and D. Johnson, *Nuclear Instruments and Methods in Physics Research B* **59/60**, 1015 (1991).
8. S. K. Noh, K. Ishibashi, Y. Aoyagi, S. Namba, and Y. Yoshizako, *J. Appl. Phys.* **67**, 2591 (1990).
9. F. Ren, T. R. Fullowan, S. J. Pearton, J. R. Lothian, R. Esagui, C. R. Abernathy, and W. S. Hobson, *J. Vac. Sci. Technol. A* **11**, 1768 (1993).
10. S. W. Pang and K. K. Ko, *J. Vac. Sci. Technol. B* **10**, 2703 (1992).
11. G. K. Reeves and H. B. Harrison, *IEEE Electron Device Letters* **EDL-3**, 111 (1982).
12. P. Kordos, M. Marso, R. Meyer, and H. Lüth, *J. Appl. Phys.* **72**, 2347 (1992).

# STUDY OF ZENER DIODES BY SEM-DVC

S.MIL'SHTEIN, D.KHARAS, S. IATROU.  
EE DEPT, UNIVERSITY OF MASSACHUSETTS LOWELL,  
MA 01854

## Abstract

A Scanning Electron Microscopy method called Dark Voltage Contrast (DVC) was applied for the first time to investigate on a microscale, the narrow depletion region of a Zener diode. Zener diodes were fabricated by the Sprague Semiconductor Corp. using conventional boron diffusion into a n-type wafer with phosphorus.

Zener diodes were chosen because of the presence of a shallow p-n junction and for the ability of Zeners to work in the breakdown regime where the dynamics of the current might influence the field distribution in the p-n junction. The samples were examined in the SEM with a beam current below 50 pA to minimize injection of electrons into the depletion region. Reverse and forward biased diodes were examined and potential distribution information was obtained, using Dark Voltage Contrast software. Doping information and C-V measurements were used to double check DVC depletion region measurements.

The main results of these studies include measurements of electrical field for three regimes of operation: forward, reverse, and breakdown, with almost ideal field distribution in some Zeners, and fluctuations in others. The field irregularities are related to the defects in the junction area. However the amount of charge build-up appears to depend on the current flow in the dynamic regime for the breakdown. The typical measurements of depletion region width were  $W_f = 14 \mu\text{m}$  when forward biased,  $W_r = 0.35 \mu\text{m}$  at 3-4 volts when reverse biased and  $W_{br} = 0.44 \mu\text{m}$  for 6 v of breakdown. This data helps to reconstruct the diffusion profile.

## Introduction

The interest in reverse bias and breakdown regimes of Zener diodes [1-3] is due to practical applications of these devices in various circuits of hybrid and integrated electronics. The  $V_{zk}$ - voltage at the Zener knee and  $V_{zo}$ -operational voltage at the linear portion of the breakdown, represent certain regimes of operation, where different physical phenomena take place in the thin depleted region of a diode. The beginning of the tunneling at  $V_{zk}$ , and avalanche increase of the breakdown current at  $V_{zo}$  were known via I-V characteristics but not observed on a microscale until now.

A recently developed [4-5] quantitative microscopic technique called Dark Voltage Contrast motivated us to use Scanning Electron Microscope (SEM- DVC) to characterize the dynamics of a Zener breakdown on a microscale. The goal of the current paper is to study

electrical field distribution in a reverse biased Zener diode and to demonstrate the correlation between the device performance and shape of the electric field inside of a Zener p-n junction.

### **Experimental Results**

The SEM-DVC technique is described in detail elsewhere [4-5] . However the principles of this method are simple. SEM images of an unbiased and reverse biased p-n junction are digitized and stored in a computer. Special software allows subtraction of the two images, resulting in a digital image of a junction, where all the electrically active elements of the image such as depleted region, charged defects and other sites of accumulated charge will show up. Electrically non active features, such as surface scratches, and contaminations that appear in both images would be subtracted out. The subtracted image is then calibrated to the bias voltages. Analyses of the calibrated image allows us to plot a one, or two dimensional distribution of the potential step in a p-n junction. From the potential distribution it is then possible to reproduce the electric field profile or distribution of charge and a doping.

Specifics of Zener operation imply a special voltage calibration method for the digital images. Simultaneous measurement of I-V characteristics with SEM -DVC observation provide the calibrating parameters. In a case, when the diode is reversed biased one can assume that the entire reverse bias creates a voltage drop only across the depleted region. However in a breakdown regime a reverse current generates a voltage drop across both the bulk of a device and the junction. Thus, using terminal bias  $V_b$  and break down part  $V_{zo}$  of current voltage characteristics, one can define  $V_{p-n}$  since  $V_{p-n} = V_b - V_{zo}$  is a voltage drop across the depleted p-n region in the breakdown regime.

Calibration of a forward biased diode presents further complication. The built-in potential of a p-n junction is defined from capacitance-voltage C-V characteristics. The first SEM image is of the diode forward biased at the voltage equal to the built-in potential, from this, an image of the unbiased diode is subtracted. The resulting digital image is calibrated to the built-in potential, giving important information about potential step and the electric field in an unbiased Zener diode. The built-in potential was measured to be  $V_{bi} = 1.3$  V, and the depleted region of an unbiased Zener diode was found to be  $W = 0.14$   $\mu m$ .

Examining the I-V characteristics of the two Zener diodes in Fig 1, one can see several differences. Zener #18 does not break as abruptly as Zener #19. This difference in performance shows up in the different shape of the potential distribution across the p-n junctions. In Fig 2, which shows the SEM-DVC measurement of potential, one can see the steep potential step in the case of Zener #19 versus a gradual rise of the potential for Zener #18. The change of Zener knee voltage  $V_{zk}$  to breakdown voltage  $V_{zo}$  could be estimated by  $\Delta V = V_{zk} - V_{zo}$ .  $\Delta V = 1.7$  V was established for Zener #19 and  $\Delta V = 2.2$  V was found for Zener #18. These results correlate with the average potential gradient,  $9.5$  V/ $\mu$ m measured for Zener #19 and  $5$  V/ $\mu$ m for Zener #18 in Fig 2. Electric field and charge profiles reconstructed from the potential distribution are plotted on Fig 3 for Zener #18 and on Fig 4 for Zener #19. In addition to a stronger field in a junction of Zener #19 ( $E = 1 \times 10^5$  v/cm) versus a weaker field in Zener #18 ( $E = 4 \times 10^4$  v/cm), the information about doping concentration was obtained. The maximum doping on the p-side was  $2.5 \times 10^{17}$  cm $^{-3}$  for Zener #18, and  $8 \times 10^{16}$  cm $^{-3}$  for Zener #19. To summarize these measurements for the two diodes.

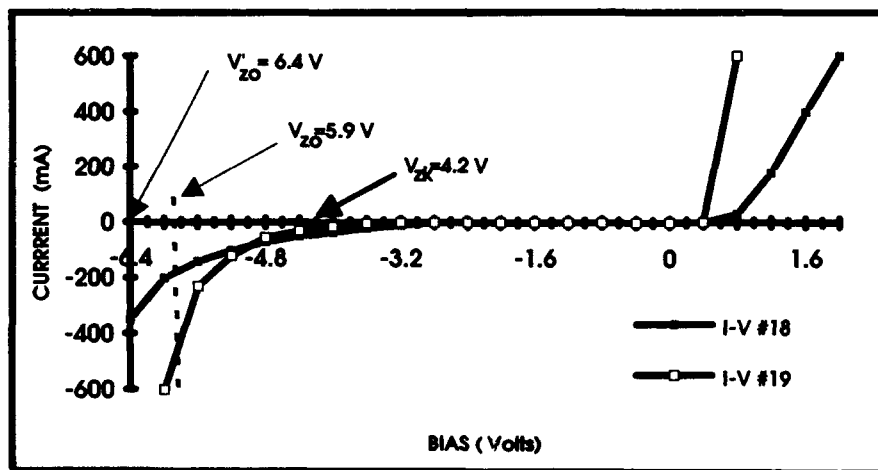


Figure 1: I-V characteristics of Zener diodes #18 and #19.

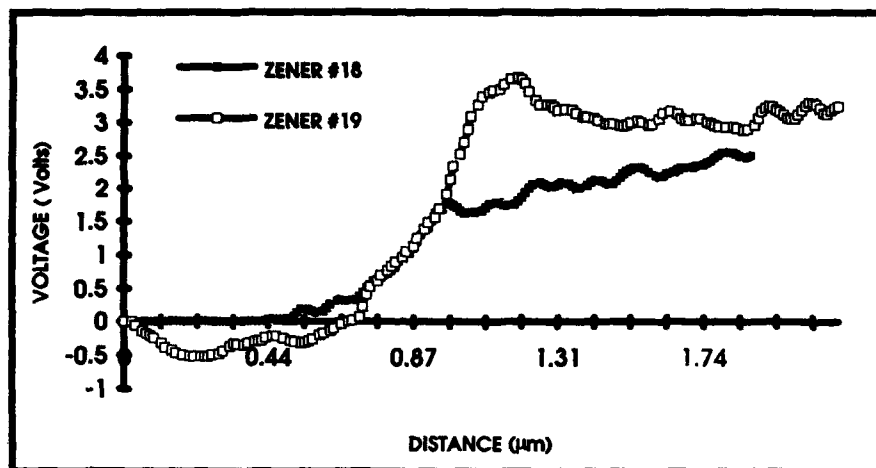


Figure 2: SEM-DVC plots of reverse biased Zener diodes #18 and #19.

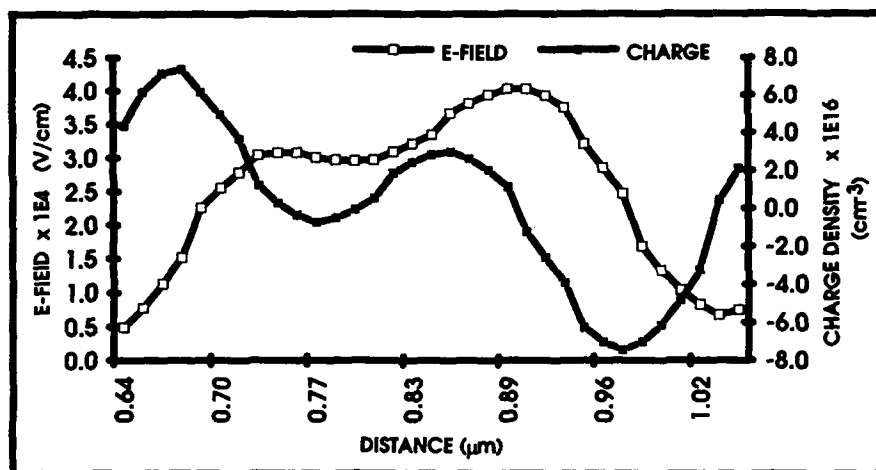


Figure 3: Electrical field and charge distribution for Zener #18

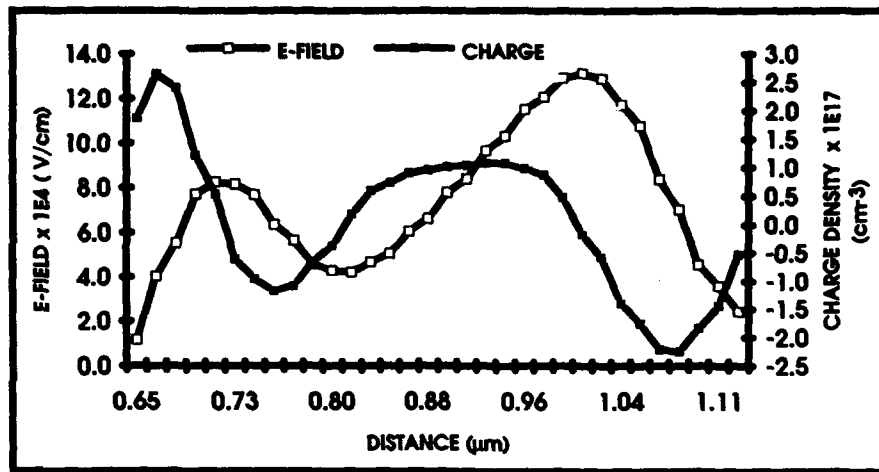


Figure 4: Electrical field and charge distribution for Zener #19.

Table I: Summary of the results.

| Parameters     | Zener 18 | Zener 19 | Units                  |
|----------------|----------|----------|------------------------|
| $N_a$          | 1.00E+19 | 1.00E+19 | $\text{cm}^{-3}$       |
| $N_d$          | 1.00E+17 | 1.00E+17 | $\text{cm}^{-3}$       |
| $\Delta V$     | 0.6      | 0.4      | V                      |
| DVC slope      | 5        | 9.5      | $\text{V}/\mu\text{m}$ |
| W              | 0.39     | 0.28     | $\mu\text{m}$          |
| E-Field        | 4.00E+04 | 9.00E+04 | $\text{V}/\text{cm}$   |
| Charge Density | 8.00E+16 | 2.50E+17 | $\text{cm}^{-3}$       |

### Conclusions

In the current study the SEM-DVC method was used to assess the performance for Zener diodes. It was demonstrated, that the potential distribution, field and doping profiles in a p-n junction could be measured on a microscale. We learned that in an abrupt Zener p-n

junction the potential and field distribution on a microscale often deviate from the linear steep slope prescribed by theory. This deviation can be explained by non-ideal impurity profiles. Although the impurity profiles are not expected to be ideal on a microscale, the best proof of it would be Secondary Ion Mass Spectroscopy (SIMS), which is not provided in this study but is in our future plans.

We performed the DVC measurements of forward and reverse biased Zener diodes. The breakdown regime seems to need more detailed analysis, because of the significant current flow through the p-n junction. This work is in our future plans.

We found a correlation between performance (I-V curves) of Zener diodes and the shape of the internal fields measured by SEM-DVC. That makes this new electron microscopy technique a good quantitative measurement of semiconductor devices fabricated on a manufacturing line or designed in R&D laboratory.

#### References

1. S.Sze, "Physics of Semiconductor Devices" (John Wiley & Sons, 1981), pp 619.
2. M. Shur, "Physics of Semiconductor Devices" (Prentice Hall, New Jersey, 1990) pp 182-194.
3. A. Sedra and K. Smith, "Microelectronic Circuits" (Sanders college Publ. Toronto, 1991). pp 144-151.
4. S.Mil'shtein, S.Iatrou, D.Kharas, R.O.Bell and D. Sandstrom, MRS, **283**, 921, (1993).
5. S.Mil'shtein, S. Iatrou, R.O.Bell and D.Sandstrom, First Hong-Kong Workshop on Semiconductors, Hong-Kong, Aug. 1992.



## CHARACTERIZATION OF CADMIUM ZINC TELLURIUM OBTAINED BY MODIFIED - BRIDGMAN TECHNIQUE

D.R. ACOSTA\* AND F. RABAGO\*\*

\*Instituto de Física, UNAM, Department of Materia Condensada, México, D.F., México.

\*\*Instituto de Física, U.A.S.L.P., Av. A. Obregón 64, 78000 San Luis Potosí, S.L.P., México.

### ABSTRACT

The growth of ternary semiconductor compounds  $Cd_{1-x}Zn_xTe$  leads to possible uses of this material like optoelectronic devices. In the present work we report the structural characterization of  $Cd_{0.98}Zn_{0.04}Te$  obtained by modified - Bridgman technique.

Structural studies were carried out using Scanning Electron Microscopy (SEM) and Conventional and High Resolution Electron Microscopy (TEM and HREM, respectively). Selected Area Electron Diffraction (SAED) was used to determine local variations in composition. Characteristics of the growth of the bulk samples were observed and structural details that might be related with the stability of ternary phase were derived.

### Introduction

The ternary compound  $Cd_{0.98}Zn_{0.04}Te$  studied in this work have promising applications in a variety of solid state devices such as solar cells [1], photodetectors [2] and light emitting diodes because its band gap is 1.53 eV. at 300K [3]. This II - VI semiconductor compound is also good for uses in medical imaging and offer more advantages in sensitivity, stability and commercial availability over other materials like mercury iodine [4]. The main purpose for us in this work is to get large, high-quality crystals for substrates, because the quality of epitaxial layers is affected by the quality of the substrate material. CdZnTe is the leading substrate for epitaxial growth of HgCdTe [5 - 7]. To get good devices requires improved control over chemical and crystallographic homogeneity of the crystals.

On the other hand, the addition of small quantities of Zn, 4% in our case, in CdTe reduces the dislocation density. The pinning of defects by the local strains is suggested as the mechanism for the improvement seen in  $Cd_{0.98}Zn_{0.04}Te$  over CdTe crystals [8].

### Experimental

The samples investigated in this work were cut from an ingot which had been grown by vertical modified - Bridgman technique under Cd vapor pressure to achieve the controlled constituent pressure above the melt [9]. Bridgman bulk-growth process is a liquid-phase growth technique [10], in which the melt is contained in a growth ampoule and is solidified by lowering the ampoule through the temperature gradient given by an appropriate furnace. The actual pressure is regulated by the coldest region of the ampoule.

Samples were grown at R. Triboulet's laboratory in the Laboratoire de Physique des Solides, C.N.R.S., Bellevue in France. Stoichiometric quantities of the purified elements were vacuum sealed in a pretreated fused silica ampoule of about 20 mm inner diameter and 10 - 15 cm long. The sealed ampoule was inserted in an eight-zone furnace controlled by a computer to examine the temperature profile.



Figure 1. SEM image of a big grain of  $Cd_{0.96}Zn_{0.04}Te$  crystal. Laminar configuration and irregular details are shown in this sample.

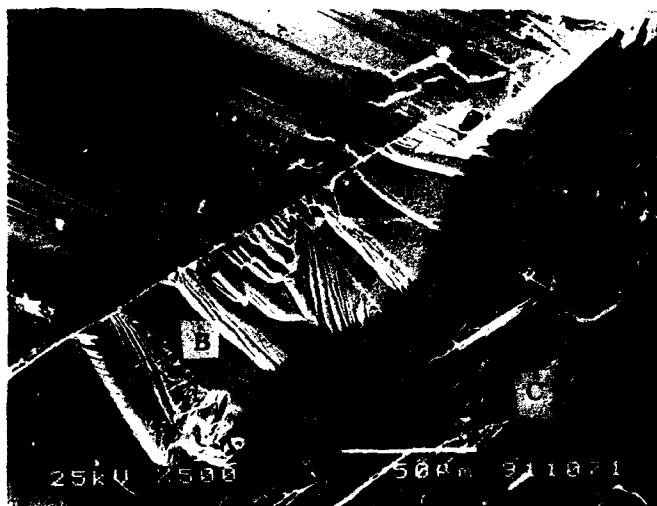


Figure 2. Three different details of a SEM image of a  $Cd_{0.96}Zn_{0.04}Te$  crystal. The region A shows a piling up of planes, B is a layered configuration region and C is a region with rugosities.

SEM observations were carried out in a JEOL 5200 microscope and TEM and HREM observations were carried out in a JEOL 4000 EX equipped with a high resolution pole ( $C_s=1.00\text{mm}$ ). For SEM studies, small pieces (around  $0.3\text{mm}$  in size) were mounted directly on the holder. For HREM observations, samples did not receive special thinning treatment: Small grains were cracked and grinded softly in an agata mortar; then the fine powder was sprayed, in each case, on 200 mesh copper grids covered with carbon perforate films. HREM images were obtained from the thin border of crystallites.

### Results

We can observe in the figure 1 a SEM image of a large grain of  $Cd_{0.96}Zn_{0.04}Te$  showing laminar configuration in one direction and a transverse phase with irregular details which resemble an amorphous state. Two different phases are thus present in our sample. Another image of SEM is shown in figure 2 where we observe three different details. That marked with an A shows a piling up of planes; the B zone shows a layered configuration and clean terraces; the C zone is similar to B but with rugosities on the surface. The TEM, shown in figure 3, comes from the point of a needle of a  $Cd_{0.96}Zn_{0.04}Te$  crystal and shows a granular configuration with changing thickness. White dots in the figure correspond to pinholes in the material. Another figure of TEM is shown in figure 4, where we see a laminate of  $CdZnTe$  where a layered configuration is visible near the rounded zone. The black spots correspond to crystallites growing in the laminates.



Figure 3. TEM photograph of the point of a needle of a  $Cd_{0.96}Zn_{0.04}Te$  crystal, granular configuration and pinholes are present in this photograph.

Figure 5 is a SAED pattern coming from a border of the sample showed in figure 3. CdZnTe phase was determined from similar pattern. Figure 6 is another SAED pattern from a similar zone to that presented in figure 4. Spots coming from faulted structures are visible.

Finally, a HREM image, figure 7, is shown where three grains are visible. An antiphase grain boundary can also be observed. Lattice defects are not visible.

#### Discussion

In summary, from SEM, TEM and HREM observations we can conclude that the ternary  $Cd_{0.96}Zn_{0.04}Te$  growth produce laminar structure with no lattice defects in the crystals. Identification of a CdZnTe phase was obtained from SAED patterns analysis. The layered configuration in specific orientations observed in SEM images seem to be connected with directional bonding among the ternary atoms in the CdTe structure, like in the Diluted Magnetic Semiconductors [11].

In comparison with similar works we can assume that good crystals of  $Cd_{0.96}Zn_{0.04}Te$  have been successfully prepared by vertical modified - Bridgman method.

This is a preliminary work in  $Cd_{0.96}Zn_{0.04}Te$  and represents an advance in the structural understanding of this bulk material growth by modified - Bridgman technique. Optical characterization like Raman, photoconductivity and photoluminescence and electrical measurements as DLTS method are in progress. The goal is to correlate the structural studies presented in this paper with other kind of characterization.



Figure 4. TEM photograph of a  $Cd_{0.96}Zn_{0.04}Te$  crystal where a layered configuration is shown.



Figure 5. Selected Area Electron Diffraction (SAED) Pattern of  $Cd_{0.96}Zn_{0.04}Te$  crystal.



Figure 6. SAED pattern of a  $Cd_{0.96}Zn_{0.04}Te$  crystal showing spots from the faulted structures.

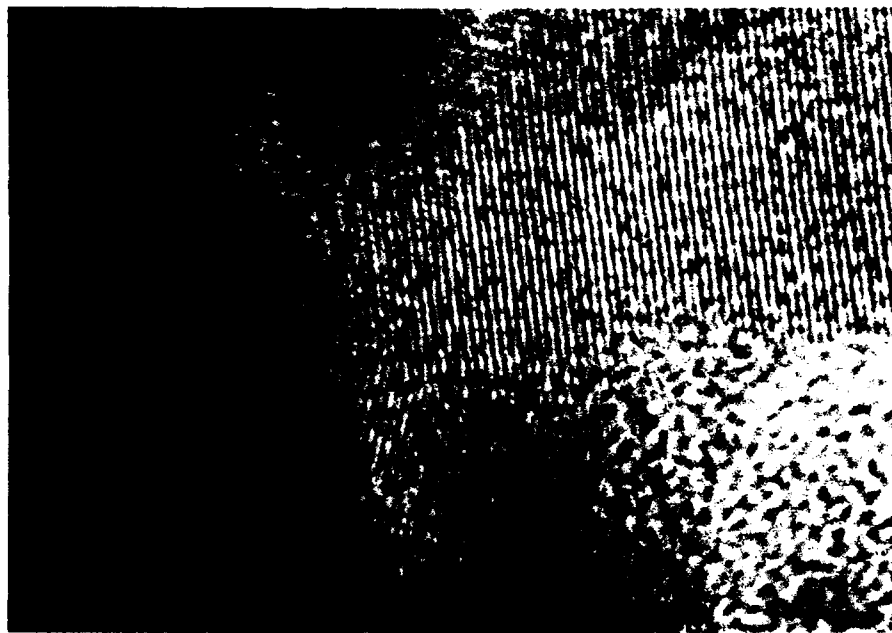


Figure 7. Three grains are observed in this HREM photograph of a  $Cd_{0.96}Zn_{0.04}Te$ , also an antiphase grain boundary can be appreciate.

### Acknowledgements

Technical assistance of M. Luis Rendón and Ma. Jacqueline Cañetas in high resolution electron microscopy and scanning electron microscopy works, respectively are here recognized. One of us (F.R.) wish to thank U.A.S.L.P. for the financial support by the contract C93-FAI-06-2.49, and the CONACyT for the partial support with the contract No. 1141-E9202.

### References

- 1.- T.L. Chu, S.S. Chu, C. Ferekides and J. Britt, J. Appl. Phys., 71, 5635, (1992).
- 2.- A.S. Dissanayake, J.Y. Lin and H.X. Jiang, Phys Rev., B48, 8145, (1993).
- 3.- D.J. Olego, J.P. Faurie, S. Sivananthan and P.M. Raccach, Appl. Phys. Lett., 47, 1172, (1985).
- 4.- F.P. Doty, J.F. Butter, J.F. Schetzina and K.A. Bowers, J. Vac. Sci. Technol. B10, 1418, (1992).
- 5.- J.J. Kennedy, P.M. Amertharaj, P.R. Boyd, S.B. Qadri, R.C. Dobbyn and G.G. Long, J. Crystal Growth, 86, 93, (1988).
- 6.- S.B. Triveli and H. Weidemeier, J. Electrochem. Soc., 134, 3199, (1987).
- 7.- L. He, C.R. Becker, R.N. Bicknell - Tassius, S. Scholl and G. Lanwehr, J. Appl. Phys., 73, 3305, (1993).
- 8.- C.G. Morgan - Pond and R. Raghavan, (Private Communication).
- 9.- S.L. Bell and S. Sen, J. Vac.Sci. Technol., A3, 112, (1985).
- 10.- A.W. Vere, *Crystal Growth*, (Plenum Press, New York, (1987), p. 69.
- 11.- D.R. Yoder, U. Desk and J.K. Furdyna, J. Appl. Phys., 58, 4056, (1985).

# **SURFACE PHOTOVOLTAGE MEASUREMENT OF MINORITY CARRIER DIFFUSION LENGTHS EXCEEDING WAFER THICKNESS: APPLICATION TO IRON MONITORING WITH PART PER QUADRILLION SENSITIVITY**

A.M. KONTKIEWICZ\*, J. LAGOWSKI\*, M. DEXTER\* AND P. EDELMAN\*\*

\*Center for Microelectronics Research, University of South Florida, Tampa, FL 33620

\*\*Semiconductor Diagnostics, Tampa, FL 33610

## **ABSTRACT**

We discuss an approach to iron concentration determination in silicon, based on wafer-scale surface photovoltage measurement of the minority carrier diffusion length in the millimeter range. The approach combines two novel aspects: it overcomes the diffusion length to wafer thickness ratio limitation of previous SPV methods, and it employs iron separation from other recombination centers using rapid photo-dissociation of iron-boron pairs. The wafer thickness limitation was eliminated by using the correct theoretical SPV wavelength dependence instead of simplified asymptotic diffusion length form adopted in all previous treatments and valid only for diffusion lengths much shorter than the wafer thickness. Photo-dissociation of Fe-B pairs and measurement of the corresponding decrease of the  $L$  value (caused by creation of iron interstitials) enables iron detection in typical silicon wafers in times of seconds with a sensitivity in the low  $10^8$  atoms/cm<sup>3</sup> range.

## **INTRODUCTION**

Iron is a critical uncontrolled contaminant in IC manufacturing and equipment. For thin gate oxides used in submicron technology, iron precipitates near the gate oxide interface can be a major cause of electrical breakdown.<sup>1,2</sup> Maintaining iron concentration below  $10^{10}$  atoms/cm<sup>3</sup> (i.e., in the part per quadrillion, ppq, range) is a requirement facing the forthcoming 0.25  $\mu$ m technology. Since interstitial Fe in Si acts as an efficient recombination center, the process-induced Fe contamination may be detected by measurement of the bulk minority carrier lifetime. In the low excess carrier excitation limit, the product of the minority carrier lifetime  $\tau$  and the diffusion constant  $D$  gives the square of the diffusion length  $L$ ,  $L^2 = D\tau$ . Thus, a diffusion length provides a measure of lifetime killing contaminants.

In the manufacturing environment, minority carrier diffusion length measurements would be most beneficial when performed in-line, on whole wafers, with minimal preparation and without contact to the wafer surface. Such wafer-scale, noncontact measurement of  $L$  can be done using the surface photovoltage (SPV) method.<sup>1,3</sup> In this method chopped monochromatic light generates excess carriers which modulate a native potential barrier on the semiconductor surface. The photon flux  $\Phi$  is small enough to assure linear SPV range where the magnitude of the SPV signal  $V$  is directly proportional to  $\Phi$  and also to the excess minority carrier density  $\Delta n_s$  beneath the surface just outside the surface space charge region. A resulting surface photovoltage is picked up by a small transparent electrode placed a fraction of a mm above the illuminated surface. A second electrode, also only capacitively coupled to the wafer, is provided by the wafer-holding chuck. The SPV signal  $V$  is measured for different light penetration depths,  $z = \alpha^{-1}$  (where  $\alpha$  is the absorption coefficient corresponding to preselected wavelengths) and  $L$  is determined from  $V(z)$ .

## **SPV MEASUREMENT OF DIFFUSION LENGTH**

The original SPV method<sup>4</sup> was based on simplified formula using the following assumption that the diffusion length is much shorter than the thickness of the measured sample (in practice  $L < T/2$ ). In the 1960s diffusion lengths in silicon were about 10  $\mu$ m and, this simplification was very well justified. The simplified formula was also used in subsequent SPV treatments.<sup>3,5</sup> In

consequence, when applied to high-purity silicon wafers of the 1990s, with  $L$  approaching 1 mm, SPV methods failed in the sense that they only yielded the longest  $L$  value of  $0.7T$  and were limited by the wafer thickness rather than the recombination centers. What has been particularly misleading to SPV users is that, in these cases, the experimental data apparently followed the dependence on  $z$  described by the simplified formula.

In the purest silicon currently available, the diffusion lengths are of the order of 1 mm and they exceed the thickness of standard wafers ( $525 \mu\text{m}$  to  $725 \mu\text{m}$ ). To overcome this problem, we have analyzed experimental data in terms of the full SPV expression as recently proposed in Ref. 6. In the low excitation limit ( $\Delta n_s \ll p_0$  where  $p_0$  is the majority carrier concentration in the bulk), the relation between the surface photovoltage,  $V$ , and the excess minority carrier concentration,  $\Delta n_s$ , can be obtained from the Poisson equation and an electrical neutrality condition. Independently,  $\Delta n_s$  can be obtained as a function of the light penetration depth,  $z$ , from a steady-state solution of the continuity equation. For long diffusion lengths, the contribution from the light reflected from the back surface will be neglected and we also assume that  $z \gg W$ . This assumption is of no consequence as long as  $z$  is small in comparison with  $T$ . Based on the treatment presented in Ref. 6, the low excitation level surface photovoltage,  $V$  may be expressed as

$$V = \text{const } \Phi_{\text{eff}} f(z), \quad (1)$$

where  $\Phi_{\text{eff}}$  is the effective flux of photons entering the semiconductor, i.e. corrected for reflectivity. The function  $f(z)$  contains the entire dependence on the light penetration depth

$$f(z) = (1 - Bz/L)/(1 - z^2/L^2), \quad (2a)$$

$$B = [(v/S_b) \sinh(T/L) + \cosh(T/L)] / [\sinh(T/L) + (v/S_b) \cosh(T/L)], \quad (2b)$$

where  $S_b$  is the back surface recombination velocity and  $v = D/L$  is the diffusion velocity. The front surface recombination velocity  $S_f$  reduces the surface photovoltage at the same ratio for all penetration depths, therefore, it is included into constant in Eqn. (1).

In the constant photon flux SPV method<sup>3,5</sup>,  $\Phi_{\text{eff}}$  remains the same for all employed wavelengths. In such a case the experimental data normalized to any  $V_0$  at a particular  $z_0$  (typically the shortest penetration depth) can be fitted to Eqn. (2) with two fitting parameters  $L$  and  $S_b$ . For short  $L$ , such that  $T \gg L$  (in practice it is sufficient if  $T \geq 2L$ )  $\sinh(T/L) = \cosh(T/L)$ , and consequently  $B = 1$ . Equation (1) becomes then

$$\Phi_{\text{eff}}/V = \text{const } (1+z/L). \quad (3)$$

This expression has been used in previous SPV methods. In the "constant magnitude SPV"<sup>4</sup>,  $\Phi_{\text{eff}}$  is measured after adjusting the photon flux to maintain the same  $V$  values for all penetration depths. In the "constant photon flux linear SPV" method<sup>3</sup>,  $\Phi_{\text{eff}}$  is constant and the inverse photovoltage  $1/V$  is analyzed versus  $z$ . In the early laboratory version of SPV<sup>7</sup>, neither  $V$  nor  $\Phi_{\text{eff}}$  were constant and, instead,  $V$  was normalized to known incident light spectrum. In all these methods, the value of  $L$  was obtained from Eqn. (3) as  $L = -z_{\text{int}}$ , where  $z_{\text{int}}$  corresponded to  $\Phi_{\text{eff}}/V = 0$ . This procedure is illustrated in Figure 1 by experimental data obtained for a high purity 2 mm thick silicon slab before and after thinning to  $490 \mu\text{m}$ . The measurements were done using a commercially available SPV system based on the constant photon flux method. Before thinning  $L = 743 \mu\text{m}$  and the condition  $T > L/2$  is satisfied. For thinned wafer  $T < L$  and Eqn. (3) should not be applicable. It is seen however that for the thinned wafer the plot  $\Phi_{\text{eff}}/V$  vs.  $z$  deviates only slightly from linearity, and only the intercept value of  $332 \mu\text{m}$  is about  $0.7T$ , i.e., significantly below the  $743 \mu\text{m}$  measured before thinning. This illustrates the misleading character of SPV analysis based on the standard short diffusion length expression.

This behavior can be readily explained using Eqns. (1) and (2). For  $z/L \ll 1$ , they lead to an approximate expression,  $\Phi_{\text{eff}}/V \sim \text{const } (1+z/L^*)$  where  $L^* \sim L/B$ . Thus, the standard SPV procedure will give the apparent diffusion lengths,  $L^*$ , which is significantly different than the real



diffusion length,  $L$ . The factor  $B$  can be notably larger than 1 for typical silicon wafers with non-oxidized surfaces for which the surface recombination,  $S_b$ , is relatively high,  $\sim 10^5$  cm/s (note that, in silicon,  $D$  is at most 33 cm<sup>2</sup>/s for minority electrons and 13 cm<sup>2</sup>/s for minority holes).

The determination of long diffusion lengths exceeding the wafer thickness must be done using the complete SPV equation (Eqn. (2a) and (2b)) with  $L$  treated as the fitting parameter. The modified SPV plot showing the quality of the fitting can be presented as:

$$V^* = V(1 - z^2/L^2)/\Phi_{\text{eff}} = \text{const}(1 - Bz/L). \quad (4)$$

In Figure 2 the same experimental SPV data as shown in Figure 1 are presented in the form of the new SPV plot. The open symbols represent the as-measured values (for clarity, they are normalized to  $V$  at  $z \rightarrow 0$ ), the filled symbols correspond to  $V(1 - z^2/L^2)$  which decreases linearly with  $z$  and intercepts the  $z$  axis at  $z_{\text{int}} = L/B$ . For thick wafers,  $B \approx 1$  and  $z_{\text{int}}$  is equal to the diffusion length. The value of  $L = 749 \mu\text{m}$  measured for 2000  $\mu\text{m}$  wafer is very similar to the one obtained with the conventional procedure. For thin slabs, the factor  $B = \coth(T/L)$  and the complete equation,  $z_{\text{int}} = L \tanh(T/L)$  has to be solved for  $L$ . The value of  $L$  obtained with this new procedure is 760  $\mu\text{m}$  which is in good agreement with the values obtained from the measurement on thick slabs. The advantage of the new procedure is apparent when this value is compared with only 332  $\mu\text{m}$  obtained from standard SPV measurements.

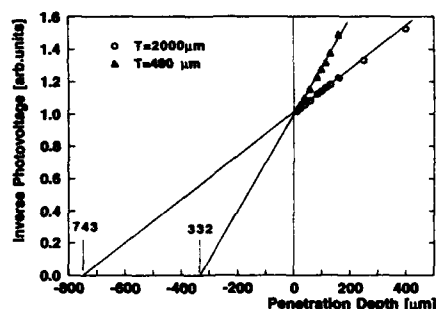


Fig. 1 Inverse surface photovoltage vs light penetration depth for a high purity silicon slab 2mm thick before and after thinning to 490  $\mu\text{m}$  (O and  $\Delta$ , respectively).

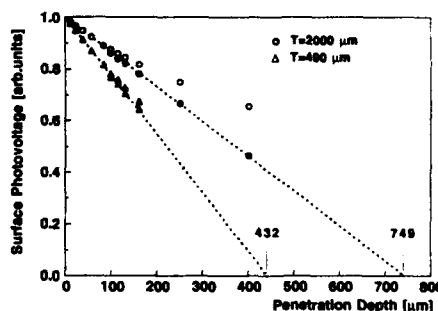


Fig. 2 SPV data for the same wafer as in Fig. 1, however, plotted according to the new procedure  $V$  vs  $z$ . Open symbols correspond to the as-measured values, filled symbols - to new SPV plot Eqn. (4).

## IRON MONITORING BY PHOTO-DISSOCIATION OF Fe-B PAIRS

Photo-dissociation of Fe-B pairs combined with SPV diffusion measurement has recently emerged as a sensitive and very fast method for determining Fe concentration.<sup>9</sup> An isolated interstitial,  $\text{Fe}_i$ , is a donor defect with an energy level 0.39 eV above the valence band and with large electron capture coefficient,  $c_i = 5.5 \times 10^{-7}$  cm<sup>3</sup>/s.<sup>10-13</sup> At room temperature,  $\text{Fe}_i$  is mobile and, in p-type silicon, it attaches to a negative boron forming an electrically neutral  $\text{Fe}_i\text{-B}_-$  pair which has an energy level 0.1 eV above the valence band.<sup>10</sup> The electron capture coefficient of the

pair,  $c_p$ , is ten times smaller than that of  $Fe_i$ , therefore, the pair dissociation results in decrease of the diffusion length. Iron concentration is determined from two measurements: when practically all of the  $Fe_i$  are paired and  $L$  is at its maximum (which is typically assured by 24 hour storage of the wafer at room temperature or by a 20 minutes anneal at 80°C), and when all pairs are dissociated and  $L$  is at its minimum. The interstitial iron concentration,  $N_{Fe}$ , can be then determined from the corresponding change of the diffusion length:

$$-\Delta(1/L^2) = D_n^{-1} c_i N_{Fe} (1 - c_p/c_i) \approx 1.5 \times 10^{-8} N_{Fe}, \quad (5)$$

where  $D_n$  is electron diffusion constant and  $L$  is in cm. Previous procedure introduced by Zoth and Bergholz<sup>10</sup> employed thermal Fe-B pair dissociation at temperatures from 200°C to 270°C followed by a quench to room temperature in order to minimize the pair reformation during cooling. The main disadvantage of this procedure is that other metal-boron pairs (e.g., Cr-B), if present, can also thermally dissociate causing ambiguity<sup>14</sup>, especially when monitoring uncontrolled contamination at very low levels such as ppq range. The ambiguity can be removed using photo-dissociation instead of thermal dissociation. The photo-dissociation appears to be a distinctive feature of Fe-B pairs<sup>14</sup> contrasting it to Cr-B pairs.

Experiments were performed on p-type Si wafers with resistivity from 1 to 20  $\Omega\text{cm}$  and corresponding boron concentration from about  $6 \times 10^{14} \text{ cm}^{-3}$  to  $1.5 \times 10^{16} \text{ cm}^{-3}$ . The wafers, obtained from commercial suppliers, were measured as-received, or after a buffered HF dip which enhances the SPV signal.<sup>3</sup> Czochralski-grown silicon, intentionally doped by adding Fe to the melt, and unintentionally contaminated wafers were used with iron concentration ranging from  $8 \times 10^8$  to  $1 \times 10^{13} \text{ cm}^{-3}$ . Diffusion length measurements were performed using the enhanced SPV procedure described above. Iron at concentration exceeding  $5 \times 10^{10} \text{ cm}^{-3}$  was confirmed by Deep Level Transient Spectroscopy (DLTS) measurement. Lower concentrations were determined by SPV using the Fe-B association kinetics as the Fe fingerprint.<sup>10</sup>

In the photo-dissociation study, the wafers were illuminated with pulses of halogen bulb light of variable duration (2-60 s) and intensity (1-20  $\text{W/cm}^2$ ). The experiment typically started with Fe-B pairing completed as evidenced by diffusion length values close to the high limit,  $L_0$ . After each series of consecutive light pulses, the diffusion length was measured, and process was continued until the lower limit,  $L_1$ , was reached. The light intensity was always high enough to assure a photo-dissociation rate much larger than thermal dissociation and association rates. Following photo-dissociation, the pair association kinetics was monitored by measuring the diffusion length versus time while the wafer was kept at a pre-selected temperature.

In Fig. 3, the concentration of Fe-B pairs, determined from diffusion length decay data using Eqn. (5) is shown as a function of the total exposure time. The upper figure corresponds to 5  $\text{W/cm}^2$  incident light with the wafers kept in air. The pair concentration decay is an exponential process characterized by the photo-dissociation time constant  $\tau_d = 13 \text{ s}$ , which is similar for both wafers in spite of the very large differences in the diffusion lengths and the Fe concentrations.

A striking reduction of  $\tau_d$  was observed upon surface passivation reducing the surface recombination [16] such as immersion in diluted HF or  $\text{SiO}_2$  coating. As shown in the lower portion of Fig. 3, for the wafers immersed in 5% HF + 95%  $\text{H}_2\text{O}$ , the  $\tau_d$  was about three times shorter in the long diffusion length wafer, as compared to that in the short diffusion length wafer. In HF+ $\text{H}_2\text{O}$ , the pair photo-dissociation was so fast that the light intensity had to be reduced to 1  $\text{W/cm}^2$  to measure the decay. Sensitivity to surface recombination proves the recombination-enhanced mechanism<sup>15</sup> in which  $1/\tau_d$  (or the dissociation rate) is determined by the concentration of excess electrons,  $\Delta n$ . Under steady state,  $\Delta n \sim \Phi/(S + D_n/L_n)$ , where  $\Phi$  is the incident photon flux,  $S$  is the surface recombination velocity and  $D_n$  and  $L_n$  are the ambipolar diffusion constant and diffusion length, respectively. For  $S \gg D_n/L_n$ ,  $\Delta n$  is low and virtually insensitive to  $L_n$ , however when  $S < D_n/L_n$ ,  $\Delta n$  increases and becomes sensitive to  $L$  consistent with Fig. 3.

The Fe-B pairing after photo-dissociation was found to be identical to that after thermal dissociation. The process was exponential with annealing time and the pairing time constant,  $\tau_p$ , was in excellent agreement with previous measurements and with the pair association treatment based on Coulomb interaction model<sup>15</sup>.

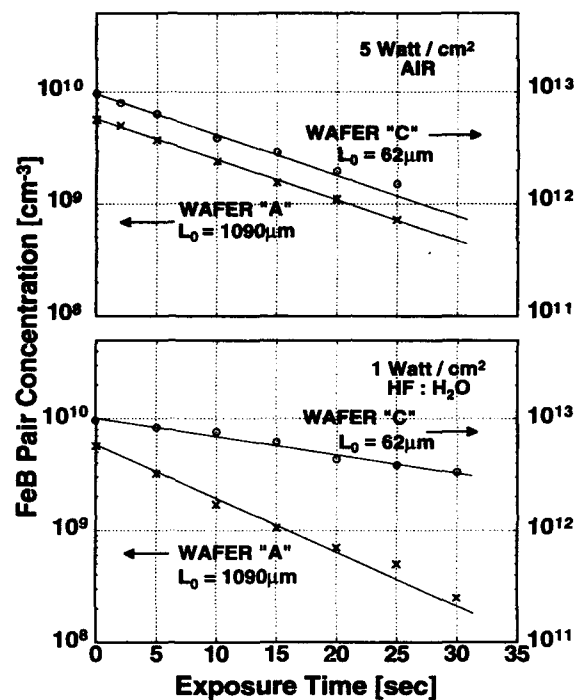


Fig. 3 An Fe-B pair concentration decay vs exposure time to white light. The "x" corresponds to wafer (A) with  $N_B = 1.8 \times 10^{15} \text{ cm}^{-3}$ ,  $L_0 = 1090 \mu\text{m}$  and  $L_1 = 848 \mu\text{m}$  while the "o" corresponds to wafer (C) with  $N_B = 1.38 \times 10^{16} \text{ cm}^{-3}$ ,  $L_0 = 62 \mu\text{m}$  and  $L_1 = 29 \mu\text{m}$ . The upper figure corresponds to illumination in air while the lower figure corresponds to illumination in diluted HF.

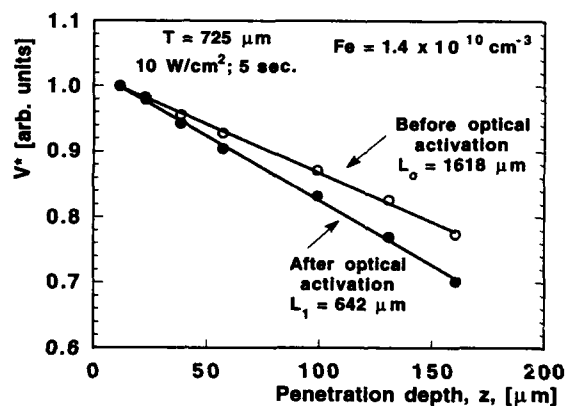


Fig. 4 SPV data for 8-inch CZ silicon wafer before and after optical activation of iron.

Optical iron activation, and a new procedure for measuring diffusion lengths exceeding the wafer thickness, have been used for determining iron concentration in state-of-the-art 8-inch diameter CZ silicon used for fabrication of 486 microprocessors. The results are shown in Figure 4. The initial diffusion length value,  $L_0 = 1618 \mu\text{m}$ , is more than twice the wafer thickness (the standard SPV method would yield an apparent value  $L^*$  of only  $550 \mu\text{m}$ ). After optical activation, this value drops to  $642 \mu\text{m}$  which gives an iron concentration of  $1.4 \times 10^{10} \text{ atoms/cm}^3$ . Based on this determination, we may conclude that iron is the major diffusion length limiting factor.

In the experiment discussed above, the diffusion length decreased by about  $1000 \mu\text{m}$ , i.e., 50 times more than the measurement uncertainty. Thus, the sensitivity for iron detection can be estimated for the low  $10^8 \text{ atoms/cm}^3$  range, i.e., in the several parts per quadrillion range.

In summary, we have shown that a new approach for measuring diffusion lengths exceeding the wafer thickness and the optical dissociation of Fe-B pairs can be combined to achieve non-contact, wafer-scale, almost instantaneous determination of iron in silicon with sensitivity in the low part per quadrillion range.

- [1] L. Jastrzebski, W. Henley, and C. Nuese, *Solid State Technol.* **35**, 27 (1992).
- [2] W. Henley, L. Jastrzebski and N. Haddad, *Proceedings of the IEEE International Reliability Physics Symposium*, March 1993, Atlanta, Georgia.
- [3] J. Lagowski, P. Edelman, M. Dexter and W. Henley, *Semicond. Sci. Technol.* **7**, A185 (1992).
- [4] A.M. Goodman, *J. Appl. Phys.* **32**, 2551 (1961).
- [5] *Annual Book of ASTM Standards*, F391-90, American Society for Testing and Materials, 1990.
- [6] J. Lagowski, A.M. Kontkiewicz, L. Jastrzebski and P. Edelman, *Appl. Phys. Lett.* **63** (1993).
- [7] A. Quilliet and M.P. Gasar, *J. Phys. Radium* **21**, 575 (1960).
- [8] See, for example, D.K. Schroeder, *Semiconductor Materials and Device Characterization* (Wiley, New York, 1990), Chap. 8, p. 373 and references therein.
- [9] J. Lagowski, P. Edelman, A.M. Kontkiewicz, O. Milic, W. Henley, M. Dexter, L. Jastrzebski and A.M. Hoff, *Appl. Phys. Lett.* **63** (1993).
- [10] G. Zoth and W. Bergholz, *J. Appl. Phys.* **67**, 6764 (1990).
- [11] K. Graff and H. Pieper, *Electrochem. Soc.* **128**, 669 (1981).
- [12] K. Wünnel and P. Wagner, *Appl. Phys. A* **27**, 207 (1982).
- [13] E.R. Weber, *Appl. Phys. A* **30**, 1 (1983).
- [14] K. Mishra, *Electrochem. Soc. Proc.* **92-2**, Extended Abstracts 426, October 1992, Toronto, Canada.
- [15] L.C. Kimmerling and J.L. Benton, *Physica B* **116**, 297 (1981).
- [16] E. Yablonovitch, D.L. Allara, C.C. Chang, T. Gmitter and T.B. Bright, *Phys. Rev. Lett.* **57**, 249 (1986).

## CHARACTERIZATION OF REACTIVE ION ETCH DAMAGE IN GaAs BY TRIPLE CRYSTAL X-RAY DIFFRACTION

VICTOR S. WANG,<sup>1</sup> RICHARD J. MATYI,<sup>2</sup> AND KAREN J. NORDHEDEN<sup>3</sup>

<sup>1</sup>Materials Science Program, University of Wisconsin, Madison, WI 53706

<sup>2</sup>Dept. of Materials Science and Engineering, University of Wisconsin, Madison, WI 53706

<sup>3</sup>GE Electronics Laboratory, Syracuse, NY 13221

### ABSTRACT

Triple crystal x-ray diffraction (TCXD) is a non-destructive structural characterization tool capable of the separation and direct observation of the dynamic (perfect crystal) and the kinematic (imperfect crystal) components of the total intensity diffracted by a crystal. Specifically, TCXD can be used to measure the magnitude of the diffuse scattering arising from defects in the crystal structure in the immediate vicinity of a reciprocal lattice point. In this study, the effects of BCl<sub>3</sub> reactive ion etching (RIE) on the near-surface region of GaAs were investigated by analyzing the changes in the diffuse scattering using both the symmetric 004 reflection as well as the highly asymmetric and more surface sensitive 113 reflection. While the results from the 004 reflections revealed little difference between the unetched and the BCl<sub>3</sub>-etched samples, maps of the diffracted intensity around the 113 reflections showed an unexpected and reproducible decrease in the extent of the diffuse scattering in the transverse direction (perpendicular to the  $\langle 113 \rangle$  direction) as the RIE bias voltage was increased. This decrease suggests that the degree of etch damage induced in the GaAs near-surface region is reduced with increasing bias voltage and ion energy. Additionally, the symmetry and orientation of the kinematic scattering was altered. Possible mechanisms for these results will be discussed.

### INTRODUCTION

An increasingly common processing technique used in compound semiconductor device and integrated circuit (IC) fabrication is reactive ion etching (RIE). Etch uniformity, material selectivity, and the ability to etch semiconductor materials anisotropically with high dimensional resolution make RIE suitable to produce the sub-micron features required in advanced microelectronic devices. While RIE combines chemical etching processes with mechanical bombardment of substrate surfaces by accelerated ions, photons, and electrons, it is primarily the mechanical processes which give rise to the greatest amount of surface and subsurface structural damage. Previous investigations have shown that RIE-induced radiation damage to GaAs surfaces results in decreased surface carrier concentrations and reduced Schottky barrier heights [1,2].

While many investigations of process-induced surface damage in GaAs have made use of electrical measurements which are quite sensitive to surface crystallographic imperfections, a structural probe is necessary to determine the mechanisms through which various processing techniques induce damage, and to correlate changes in electrical characteristics to specific structural defects. However, since fabrication techniques are specifically designed to introduce

as little damage into semiconductor surfaces as possible, the analysis of defects generated by a nominally "damage free" process would be expected to be somewhat difficult, even though such defects may significantly affect circuit performance.

### Triple Crystal X-ray Diffraction

Conventional double crystal x-ray diffraction (DCXD) has traditionally been used as a bulk materials characterization tool. However, while the total diffracted intensity measured in any x-ray diffraction experiment consists of both a dynamic (perfect crystal) and a kinematic (imperfect crystal) component, these two contributions are convoluted in DCXD, masking quantitative information that can be determined from either individual component alone. If an analyzer crystal is inserted between the sample crystal and the detector in a double crystal configuration, it is possible to create a map of the total diffracted intensity around a reciprocal lattice point by varying the angular positions of the sample and analyzer crystals near their exact Bragg conditions. This experimental technique is known as triple crystal x-ray diffraction (TCXD), and typically results in a diffracted intensity distribution in reciprocal space that is illustrated schematically in Figure 1. The characteristic pattern consists of a main "surface streak" and two "pseudo streaks" due to strong dynamical diffraction from the sample crystal, and the monochromator and analyzer crystals, respectively, as well as kinematic diffuse scattering, centered around the reciprocal lattice point. Thus, one primary benefit of TCXD is the capability of analyzing the kinematic diffuse scattering in the immediate vicinity of a reciprocal lattice point separately from the dynamically-scattered background [3].

Diffuse scattering is ideally suited for the investigation of structural defects in crystals, since the very reason diffuse scattering exists is due to the presence of defects such as vacancies, interstitials, point defect agglomerations, and dislocations, which distort lattice planes from their nominal positions. Recent high resolution x-ray diffraction work involving defects in group III-V semiconductors include studies of bulk defects in InP by Gartstein [4] and near-surface defects in MBE-grown GaAs by Bloch and co-workers [5]. We have previously reported on several high resolution x-ray diffraction studies regarding chemical-mechanical (CM) polishing-induced damage to GaAs [6], including diffuse scattering measurements by TCXD. This body of prior work involving diffuse scattering measurements on semiconductor materials suggests that TCXD is an ideal technique for monitoring the evolution of crystallographic damage in GaAs due to RIE processes.

### EXPERIMENTAL

GaAs wafers which were CM polished by the vendor and were nominally oriented  $2^\circ$  off  $\langle 001 \rangle$  about the  $\langle 110 \rangle$

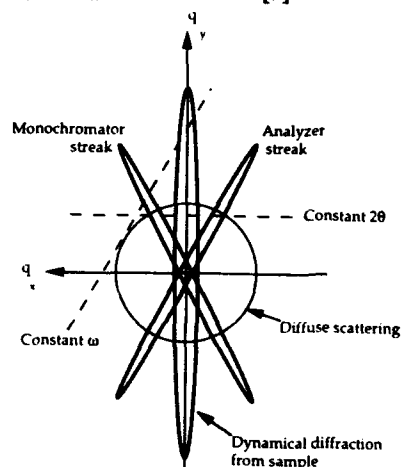


Fig. 1. Schematic TCXD intensity distribution.

axis provided the samples used in this investigation. All samples were solvent-cleaned and immersed in 1:10 HCl:H<sub>2</sub>O for oxide removal immediately prior to loading into a PlasmaTherm 2482 RIE system equipped with a 22" diameter electrode. BCl<sub>3</sub> gas was introduced at a flow rate of 14 sccm and He gas was added at 6 sccm for a resultant chamber pressure of 3.2 mTorr. The bias voltage on the electrode was varied from sample to sample in order to change the incident ion energy.

A Rigaku RU200 rotating anode generator set at 50 kV and 200 mA provided Cu K $\alpha$ <sub>1</sub> radiation, and a Bede 150 double crystal diffractometer was modified for use in TCXD [7]. Two grooved Si crystals aligned for four (220) reflections in a (-, +, +, -) configuration were used to monochromate the incident x-ray beam, and a single (220) grooved Si crystal was used as a three-bounce analyzer. As reported by Iida and Kohra [8], the use of multiple-bounce monochromator and analyzer crystals resulted in triple crystal diffraction patterns free of the dynamically-scattered pseudo streaks previously mentioned. In order to measure the total diffracted intensity around a reciprocal lattice point, TCXD scans were conducted by rocking the sample crystal while keeping the analyzer crystal in a fixed position, incrementing the analyzer crystal position, then scanning the sample crystal again with the analyzer fixed. After completing a series of scans for a given sample, real space diffractometer coordinates were converted to the reciprocal space coordinates ( $q_x, q_y$ ) using the relations of Iida and Kohra [8]. We have previously described this experimental arrangement in greater detail elsewhere [7,9].

## RESULTS

Figures 2(a) and 2(b) display the diffracted intensities measured about the 004 reciprocal lattice point for an unetched GaAs sample (#4A) which was CM polished by the vendor and a reactive ion etched GaAs sample (#4B), respectively. For the RIE-treated sample, a bias voltage of -250 V was used, and the total etch time was 15 minutes, resulting in an etch depth of approximately 1,000 Angstroms. The data shown in Figure 2 and in all subsequent triple crystal scans were contoured using the logarithm of the diffracted intensity, with each contour denoting an intensity increment of  $10^{0.25}$  counts/second. The minimum contour level was a log(intensity) of 0.25, corresponding to approximately 1.8 counts/second, which significantly exceeded the parasitic background level. While the dynamic surface streak as well as the kinematic diffuse scattering were present in both cases shown in Figure 2, no significant differences were observed in the diffuse scattering using the 004 reflections.

The symmetric 004 reflection is characterized by an x-ray photoelectric penetration depth (as calculated from kinematic theory) of 15.5  $\mu\text{m}$  for 90% absorption of Cu K $\alpha$  x-rays in GaAs. In contrast, a highly asymmetric reflection such as the 113 reflection reduces the 90% absorption depth to 1.5  $\mu\text{m}$  [10]. Figure 3 schematically compares the symmetric 004 and the asymmetric 113 diffraction geometries. Figure 4 displays the TCXD maps of

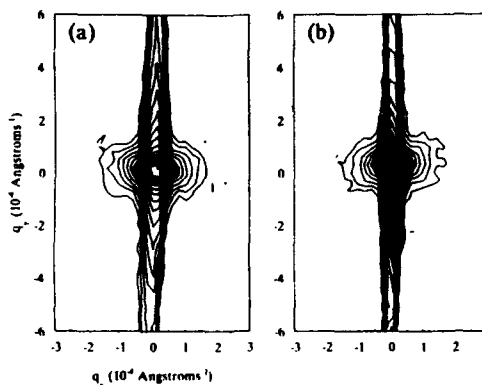


Fig. 2. 004 TCXD scans from (a) #4A (no RIE) and (b) #4B (-250 V RIE).

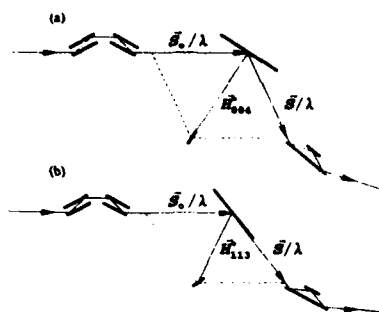


Fig. 3. TCXD geometries for (a) 004 and (b) 113 reflections.

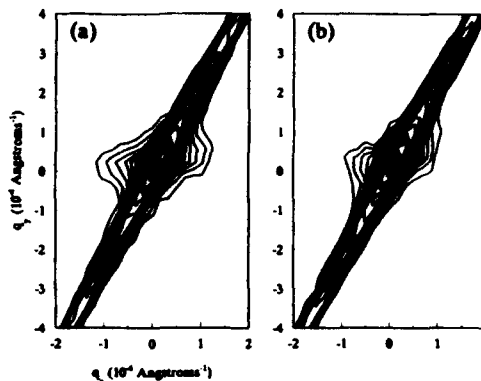


Fig. 4. 113 TCXD scans from (a) #4A (no RIE) and (b) #4B (-250 V RIE).

diffracted intensity obtained using the 113 reflection for the same two samples (#4A and #4B) analyzed above with the 004 reflection. As expected, a difference in the magnitude of diffuse scattering was observed between the unetched and the plasma-etched samples. However, quite unexpectedly, the maximum extent of the diffuse scattering in the  $q_x$  direction at the level of the minimum contour decreased from  $2.4 \times 10^{-4}$  Angstroms $^{-1}$  to  $2.0 \times 10^{-4}$  Angstroms $^{-1}$  from the CM polished sample to the RIE sample.

In order to determine if this decrease in diffuse scattering after RIE was because the concentration of defects was actually being reduced or if a damaged layer remaining from the CM polishing process was simply being etched away by RIE, another group of GaAs samples was analyzed in which all of the specimens were wet chemically-etched in a solution of 3:1:1  $H_2SO_4:H_2O_2:H_2O$  prior to plasma etching. Nearly  $2.5 \mu m$  was removed from each sample to insure that any residual structural damage resulting from CM polishing was completely eliminated. The same RIE procedures described above were used, except that total etch times were 30 minutes. Bias voltages for samples 5A and 5B were -115 V and -460 V, respectively, and sample 5C was the control sample, which was not etched by RIE. The TCXD diffracted intensity maps around the 113 reciprocal lattice point for these samples are shown in Figure 5. Again, as the bias voltage was increased, effectively increasing the energy of the ions bombarding the sample surfaces, the amount of diffuse scattering decreased, indicating a more perfect crystalline structure in the near-surface regions.

## DISCUSSION

In order to better correlate RIE process-induced damage to changes in diffuse scattering, a single parameter  $I_{excess}$  has been defined as the amount of diffracted intensity present in addition to the dynamically-scattered surface streak, where

$$I_{excess} = 4\pi \iint I_{net}(q_x, q_y) q_x dq_x dq_y. \quad (1)$$



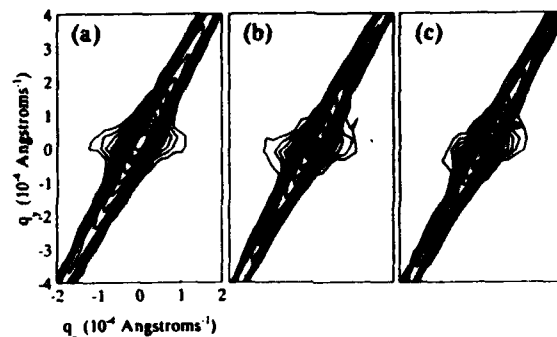


Fig. 5. TCXD scans from (a) #5C (no RIE), (b) #5A (-115 V RIE), and (c) #5B (-460 V RIE).

$I_{net}(q_x, q_y)$  is the diffracted intensity above an arbitrarily designated minimum level, which in this case was chosen to be the minimum contour level used in all of the intensity distribution maps ( $10^{0.25}$ , or  $\sim 1.8$  counts/sec). A more detailed description of  $I_{excess}$  calculations is reported elsewhere [9]. Using this procedure, an ideally perfect crystal should have an  $I_{excess}$  of zero; we have verified this by using a highly perfect Ge crystal which was grown with no detectable dislocations and was extensively etched to remove all traces of surface damage. The 113 TCXD scan for this Ge crystal is shown in Figure 6.

The results of the excess intensity calculations are listed in Table I; the integrated intensities are given in arbitrary units which have also been normalized to the excess intensity of the respective control samples. In addition to confirming that the  $BCl_3$  RIE process employed in this investigation did indeed improve the structural perfection of the GaAs samples treated ( $I_{excess}$  values for all of the RIE samples were less than those for the control samples), some further observations can be made from these results. The similarity in the absolute excess intensities of the two control samples ( $5.62 \times 10^{-3}$  for sample 4A vs.  $5.09 \times 10^{-3}$  for sample 5C) indicated that the diffuse scattering observed in sample 4A was not largely due to residual CM polish damage, but rather could more accurately be attributed to the intrinsic grown-in defect structure of bulk GaAs. Furthermore, the values of  $I_{excess}$  for samples 4B (-250 V) and 5B (-460 V) relative to the control samples were quite comparable (0.37 for 4B, 0.42 for 5B), indicating that although increasing bias voltages improved near-

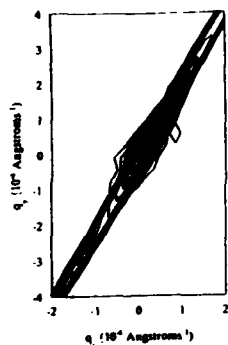


Fig. 6. 113 TCXD scan from highly perfect Ge.

Table I. Relative excess intensities.

| Sample          | Intensity from Eqn. (1) ( $10^{-3}$ arb. units) | Normalized Intensity |
|-----------------|---|----------------------|
| perfect Ge      | 0   | 0                    |
| 4A (no RIE)     | 5.62  | 1.00                 |
| 4B (-250 V RIE) | 2.10  | 0.37                 |
| 5C (no RIE)     | 5.09  | 1.00                 |
| 5A (-115 V RIE) | 4.12  | 0.81                 |
| 5B (-460 V RIE) | 2.15  | 0.42                 |

surface structure to a certain point, a threshold voltage may exist, beyond which no additional structural improvement would be observed as the bias voltage is increased.

At the higher voltages, there may be an etch rate limitation due to the deposition/re-deposition of chemical reaction products, or the chemical reactions themselves may be inhibited. As for the improvement in structure after RIE, it is conceivable that a process such as the phenomenon of ion-assisted athermal re-crystallization [11] is occurring. While it is not yet possible to rigorously assign a mechanism to the structural changes observed during RIE of GaAs, these results do suggest that further study of possible phenomena such as point defect migration and dislocation annihilation are warranted.

## CONCLUSIONS

High resolution TCXD has been very effectively used to map the diffracted intensity distributions of GaAs samples subjected to  $\text{BCl}_3$  RIE. These measurements have resulted in the definition and calculation of an excess diffuse intensity parameter which can be directly correlated to structural perfection, and, in the case of 113 reflections, is very sensitive to near-surface regions. Unexpectedly, the structural perfection of the GaAs samples actually improved after RIE. These results have led to continued x-ray analyses and complementary characterization techniques to gain a better understanding of the underlying microscopic mechanisms involved in RIE of GaAs.

## ACKNOWLEDGMENTS

We gratefully acknowledge the support of the National Science Foundation under grants ECS-8908439 and DMR-8907372. One of us (VSW) acknowledges the support of a National Defense Science and Engineering Graduate Fellowship.

## REFERENCES

1. S.W. Pang, J. Electrochem. Soc. 133, 784 (1986).
2. T. Hara, H. Suzuki, A. Suga, T. Terada, and N. Toyoda, J. Appl. Phys. 62, 4109 (1987).
3. P.F. Fewster, J. Appl. Cryst. 22, 64 (1989); *ibid.*, 24, 178 (1991).
4. E.L. Gartstein, Z. Phys. B. 88, 327 (1992).
5. R. Bloch, D. Bahr, J. Olde, L. Brugemann, and W. Press, Phys. Rev. B. 42, 5093 (1990).
6. V.S. Wang and R.J. Matyi, J. Electron. Mat. 21, 23 (1992); Mater. Res. Soc. Proc. 259, 335 (1992); J. Appl. Phys. 72, 5156 (1992).
7. R.J. Matyi, Rev. Sci. Instrum. 63, 5591 (1992).
8. A. Iida and K. Kohra, Phys. Stat. Sol. A51, 533 (1979).
9. V.S. Wang, R.J. Matyi, and K.J. Nordheden, J. Appl. Phys., in press.
10. M.A.G. Halliwell, Inst. Phys. Conf. Ser. (4th Int. Symp. on GaAs and Related Compounds) 17, 98 (1973).
11. J.E. Greene, in The Handbook of Crystal Growth, Vol. 1: Fundamentals, edited by D.T.J. Hurle (Elsevier, Amsterdam, in press); S. Nikzad and H.A. Atwater, Mater. Res. Soc. Proc. 223, 53 (1991).

## NEW ALGORITHMS FOR RAPID FULL-WAFER MAPPING BY HIGH RESOLUTION DOUBLE AXIS X-RAY DIFFRACTION,

N LOXLEY, S COCKERTON, L M COOKE,<sup>+</sup> T GRAY,<sup>+</sup> B K TANNER\*  
AND D K BOWEN\*\*

*Bede Scientific, Bowburn, Durham, DH6 5PF, U.K*

<sup>+</sup>*Bede Scientific Software Division, University of Warwick Science Park, Coventry, CV4 9EZ, U.K.;*

\**Department of Physics, Durham University, South Road, Durham, DH1 3LE, U.K.*

\*\**Department of Engineering, Warwick University, Coventry, CV4 7AL, U.K*

### ABSTRACT

We describe successful algorithms for rapid alignment of the Bragg planes normal to the incidence plane in a high resolution X-ray diffraction experiment. One is appropriate to the surface symmetric geometry and uses a technique of rotation about the specimen normal. From an experimental study of the rocking curve shape as a function of tilt, we have developed a new algorithm which uses tilting about an axis formed by the intersection of the specimen and incidence planes. This has been shown to be reliable for rapid optimization of the diffraction conditions for wafers cut up to 15° off the (001) plane and for asymmetric reflections. Additionally algorithms are outlined which permit rapid location of the maximum of the Bragg peak and deduction of the mean wafer curvature from the X-ray data

### INTRODUCTION

Double axis, or high resolution, X-ray diffraction [1] is now widely used for the non-invasive determination of the composition, thickness and perfection of epitaxial layers of compound semiconductors. Appropriate design of the X-ray optics enables the coherency of the epitaxial layer to be determined. In instruments such as the Bede QC2 diffractometers [2], capable of fast mapping over an area up to 150 mm square, and in a clean-room production environment, the orientation and alignment time overhead is of considerable importance. It is therefore crucial that efficient, effective algorithms are used to permit this task to be undertaken automatically. In high resolution X-ray diffraction, the primary task is to locate the Bragg peak by rotating the specimen crystal in the incidence plane (defined by the incident and diffracted beams). However, in order to minimize the Bragg peak width, and hence maximise the resolution, it is also important to adjust the Bragg planes to lie normal to the incidence plane. We describe efficient algorithms to achieve these adjustments together with a method of determining wafer curvature directly from a grid of rocking curves recorded point by point across the wafer. They have been extensively tested in many locations around the world.

### BRAGG PEAK LOCATION

The algorithm which we use for locating the Bragg peak is a simple binary search followed by a systematic climb up to the peak maximum. From the start position, the specimen is scanned on Axis 2, which is normal to the incidence plane, a short distance in the sense of increasing Bragg angle. The count rate in the detector is continuously monitored and if it exceeds a preset threshold, the binary search is terminated. If this does not occur, the specimen is returned to the start position and scanned twice the distance in the opposite direction. If the threshold is again not exceeded, the specimen is rotated to the end point of the initial forward scan and is then scanned an angle twice that of the previous range. Thus if the first search range is 100 units, the search sequence is: +100, -200, +400, -800, +1600, etc. This sequence is repeated until the threshold is exceeded or a scan range limit is exceeded.

Once the threshold is reached the specimen is driven in the same sense and the count rate again recorded. This sequence drives the specimen over the Bragg peak and the scan is terminated when the count rate is three standard deviations below the maximum count rate recorded. After a motion to take out backlash in stepping motor-gearbox trains, the specimen is set to the angular position at which the maximum count rate occurred.

#### ALIGNMENT OF BRAGG PLANES NORMAL TO THE PLANE OF INCIDENCE

An automated procedure for this somewhat tedious process of aligning the diffraction vectors in the first and second crystals, using a conventional tilt stage, has been given by Fewster [3]. It does fail in some circumstances and is not a rapid algorithm, having the disadvantage that the end point relies on the determination of the maximum of a relatively broad peak (at least when the incident beam is not highly divergent). A different method, based upon the rotation of the specimen about the surface normal, has been described by Tanner, Chu and Bowen [4]; this depends upon a geometrical location of the end point and should in general be more rapid for a comparable accuracy. It also lends itself to automation but it will only work for symmetrical reflections.

#### ROTARY OPTIMISATION

In the following, the first crystal is assumed to be set correctly, the specimen is mounted on Axis 2, and Rotary 2 is the axis carried on Axis 2, normal to the specimen surface. The algorithm uses the concept that the crystals' reflecting planes are parallel when the reflecting plane normal is rotated to lie in the incidence plane, and the Bragg angle has been found. The routine works on the principle that if the reflecting plane is not exactly parallel to the crystal surface, its normal will precess about the rotation axis on driving Rotary 2, and hence sweep the reflecting plane through the Bragg angle twice. The optimum position, i.e. when the reflecting plane normal is parallel to the normal of the first crystal's reflecting plane, is exactly half-way between the positions of these two reflecting positions. This is illustrated in Fig. 1 (a), which shows a 360° Rotary 2 scan of a sample with a single epilayer, indicating the positions of Rotary 2 (A,B) which will give perfect alignment of the diffracting planes. The plot is symmetrical about the ideal position, irrespective of the complexity of the rocking curve, thus giving a geometrical means of finding the ideal position without having to find any maximum positions or even having to decide which is the substrate peak.

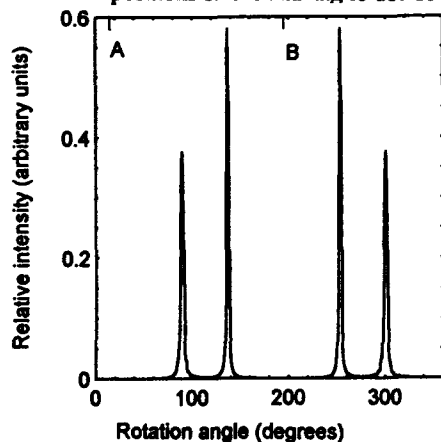


Fig 1(a) Intensity for a single epilayer on a substrate versus rotation angle

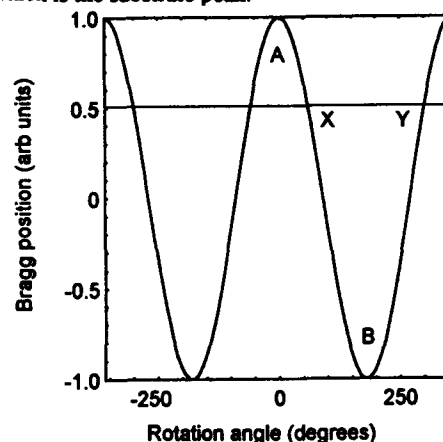


Fig 1(b) Bragg peak position vv. rotation angle

The peak is first found by a positive sense search on the Rotary 2 axis. Since wafers are usually some fractions of a degree misoriented from the nominal crystallographic plane - and sometimes deliberately offset by up to 4 degrees - this provides a rapid scan over a relatively large angle. (If this fails, a binary search is made on Axis 2.) When the Bragg position is located (Y in Fig 1(b)) on the positive sense Rotary 2 scan, this axis is searched in the opposite direction to find the 'conjugate' Bragg peak X. The correct setting of Rotary 2 is midway between these two peaks [4].

Before driving it all the way there, it is driven a short way in the previous direction and an Axis 2 search performed in order to determine the direction in which the peak shift is occurring. A final Axis 2 search should locate the peak in its optimised position. The main parameter that must be specified is the criterion for finding a peak, i.e. a count rate that is well above background but below the peak maximum. Note that if there are multiple peaks in a system, it is safest that the 'peakfound criterion' is set below the highest peak but above all the others, or the algorithm may not give reliable results. The Rotary 2 step should typically be 1 degree per 10" of rocking curve width, and the Axis 2 step about 1 or 2 times the expected rocking curve width. If these parameters are too coarse the algorithm will fail. In practice it is not difficult to find appropriate parameters for quite complex layer structures and the parameters will be unchanged for typical growth fluctuations, making the method very suitable for production control.

A simplified flowchart of the algorithm is shown in Fig 2. Not shown in the flowchart are various tests which are incorporated to cope with unusual conditions. For example if the specimen is already on a peak when the algorithm is initiated, one must move off the peak and then back again, to be quite certain which side of the peak has been found. Consistent statistical tests at three standard deviation level are applied to determine whether a threshold has been crossed, and the gating time of the detector is automatically set to determine each count with sufficient precision.

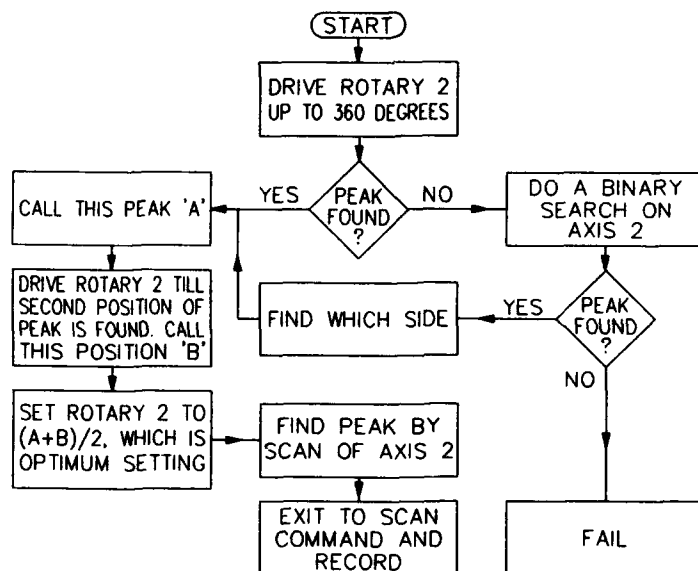


Figure 2. Rotary optimise routine

### TILT OPTIMISATION

When the Bragg planes are miscut by several degrees from the wafer surface, the rotary optimise algorithm becomes very slow, as a very small step is required on the Rotary 2 axis. Where asymmetric diffracting planes are used, the rotary optimise algorithm does not work. It then becomes essential to align the diffraction vector by rotating about the intersection of the Bragg planes with the incidence plane.

Figure 3 shows a 3D representation of variation of diffracted intensity for different positions of tilt and Axis 2 for a single layer of AlGaAs on GaAs. The data were acquired by recording a sequence of loop scans on Axis 2 of a Bede QC2a diffractometer with the tilt between reference and specimen crystals altered between each scan. We note the very sharp rise in the peak diffracted intensity as the tilt becomes small. It is also clear that the separation of the substrate and layer peaks in Axis 2 scans remains constant, independent of tilt to first order, as has been shown theoretically by Fewster [3]. The approximately parabolic shape (in the X-Y plane), clearly seen in the figure, is used by the algorithm with a step and hop peak-climbing routine to reach the apex of the intensity curve.

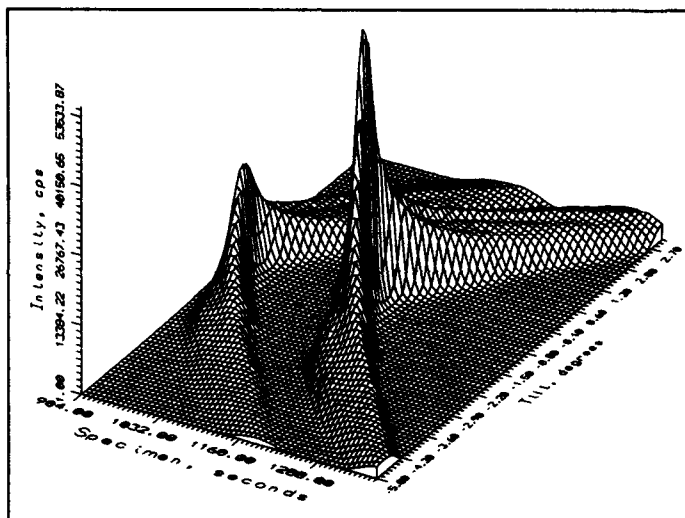


Fig. 3 Intensity for different incidence and tilt angles from a single layer of AlGaAs on GaAs.

The flowchart for the Tilt Optimise routine is shown below in Fig 4. The flowchart above gives a representation of the algorithm for the Tilt Optimise routine. The aim of the routine is to position the specimen such that the diffraction vector of the sample is parallel to the diffraction vector of the reference crystal or monochromator. A threshold level is defined by the user and then Axis 2 is moved to find a peak as described above. To determine the direction of the peak, Axis 2 is moved in negative direction until the countrate is significantly less than the threshold. We are now at point ① in the flow diagram. Axis 2 is driven in the positive direction, over the peak, until the intensity has fallen by greater than or equal to  $2\sigma$  (two standard deviations) below the maximum for this scan (point ② in Fig.4).

Since the direction of tilt is unknown, the tilt stage is moved by one step in the same direction as that in which it was last moved. If the intensity has increased, then the

direction of tilt is reversed. The peak is crossed again by adjusting the scanning axis (Axis 2) and the new peak intensity recorded and compared with the former peak intensity.

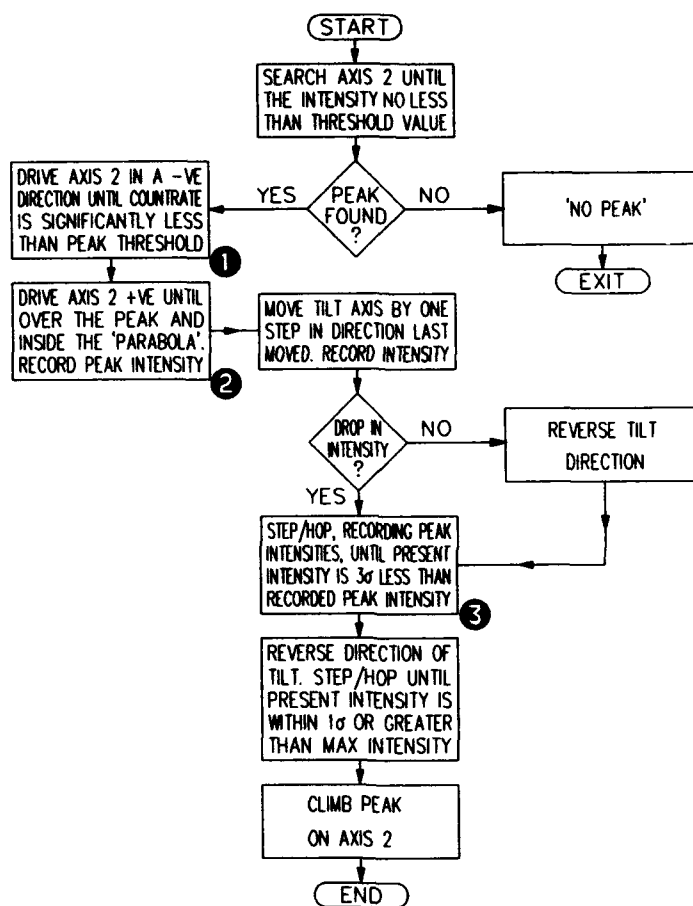


Fig. 4 The tilt optimise algorithm

The program now climbs the ridge of the parabola, adjusting Tilt in the direction set above, and moving Axis 2 across the peak repeatedly, until the intensity has risen and fallen by  $3\sigma$ . We have now moved up and over the peak and are at point ③ on the flow diagram. Figure 5 shows the step/hop section of the routine. Finally, to recover any overshoot, the tilt is reversed and the ridge is climbed in a similar way until the intensity is within  $1\sigma$  of the maximum peak intensity measured. At this point the routine finishes and the optimisation process is completed. The scanning axis (Axis 2) may also be returned to the crest of the peak, which is especially useful for centred scans, but is not essential for taking rocking curve data. We have

found this algorithm to be highly reliable and particularly useful for III-V wafers cut  $15^\circ$  off the low index surface.

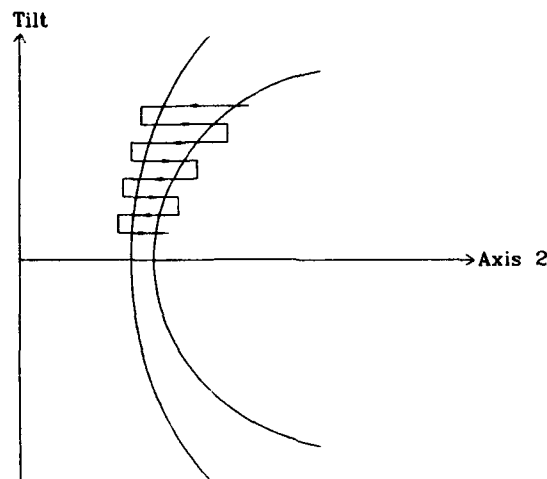


Fig 5 The step and hop sequence

#### DETERMINATION OF WAFER CURVATURE.

Wafers covered by a strained epitaxial layer adopt a bowed equilibrium shape. As a diffraction experiment measures the curvature of the Bragg planes principally normal to the incidence plane, the measured curvature is approximately cylindrical. Under this assumption, it is extremely simple to use the position of the Bragg peak from the substrate recorded as a function of position during a grid scan across the wafer to determine the radius of curvature. If the position of the Bragg peak at an arbitrary origin on the wafer is  $\theta$ , then at a distance  $s$  (measured in the incidence plane), the Bragg peak position  $\theta$  is related to the radius of curvature  $R$  by;

$$\theta = \theta_0 + (s/R)$$

If the data are taken in an  $x, y$  scan at an angle  $\alpha$  to the incidence plane,  $s = x \cos \alpha + y \sin \alpha$ . The (cylindrical) radius of curvature  $R$  in the incidence plane, is then simply derived from the data set by a linear regression.

#### CONCLUSIONS

The algorithms described have all been successfully implemented into quality control high resolution diffractometers which provide rapid area mapping of wafers up to 150 mm diameter. They provide a rapid means of optimizing the data quality without significant penalty in time or operator expertise.

#### REFERENCES

1. D. K. Bowen and B. K. Tanner, J. Crystal Growth 126 1 (1993)
2. D. K. Bowen, N. Loxley and B. K. Tanner, M.R.S. Symp. Proc. 208 119 (1991)
3. P. F. Fewster, J. Appl. Cryst. 18 334 (1985)
4. D. K. Bowen, X. Chu and B. K. Tanner, Mater. Res. Soc. Symp. Proc. 69 191 (1986)



## USE OF SYNCHROTRON WHITE BEAM X-RAY TOPOGRAPHY TO CHARACTERIZE IR DETECTOR MANUFACTURING PROCESSES

M. Dudley, Jun Wu, D. J. Larson, Jr.\*, and D. DiMarzio\*

Department of Materials Science and Engineering, State University of New York, Stony Brook, NY 11794-2275

\*Grumman Corporate Research Center, Bethpage, NY 11714

### ABSTRACT

It has been demonstrated that synchrotron white beam x-ray topography can be used to characterize IR detector materials at nearly every stage in the manufacturing cycle, including: as-grown CdZnTe single crystal boules; substrate wafers cut from different positions in the boules; thin films grown on characterized wafers; and HgCdTe focal plane array structures. Special diffraction geometries have been developed, taking advantage of the broad wavelength spectrum, large beam size, and high intensity of the synchrotron radiation source, to enable rapid and non-destructive assessment of defect densities and strain distributions after each processing step. This diagnostic method has important implications for increasing the producibility of focal plane arrays. Boule characterization can reveal defects, grain orientation, interfaces and strains, and provides guidance for optimal slicing. Wafer characterization produces multiple topographic images, providing both defect mapping and depth profiling in a single exposure. Finally, x-ray topography of HgCdTe focal plane array test articles reveals subsurface damage not observable by optical or IR microscopy. The applicability of this technique to evaluate yield, quality, and reproducibility will be discussed.

### INTRODUCTION

The low yield and high cost of II-VI based IR detectors has created a need for better non-destructive screening techniques applicable at each stage of the manufacturing process [1]. The requirements for larger focal plane size, higher integration density, and better device sensitivity can only be met by improved control of the quality of the materials used to manufacture the detectors [2]. The density of crystallographic defects, such as twins, grain and subgrain boundaries, slip bands, and dislocations, in both substrate wafers and subsequently grown films is currently quite high compared to Si. As a result, development of effective methods capable of revealing such crystallographic defects and providing insight into the relevant mechanism of generation of particular defects, leading to improvement of the perfection of the materials used for devices is very important [3].

Currently etching is the major tool used to monitor crystal quality in detector manufacturing processes [4]. Unfortunately, etching is a destructive process and can only be applied at a few stages of manufacture. The defects revealed are only those intersecting the wafer surface and their character cannot be routinely determined. In addition, etching can only be used on specific crystallographic planes and the one to one correspondence between etch pits and defects is not well established. With this in mind we have developed an improved screening methodology employing the technique of synchrotron white beam x-ray topography. We have followed almost all of the steps in the manufacturing process with rapid turnaround and have demonstrated that our technique can provide useful information essential for (1) improvement of

the quality of substrate crystals, (2) improvement of the substrate wafer slicing process, (3) monitoring epitaxial film qualities, and (4) the tracking of imperfections in the devices.

## EXPERIMENTAL TECHNIQUE

Since the substrate crystals are grown by an unseeded Bridgman technique, the orientation of the single crystal ingot is unknown and differs from crystal to crystal. The crystal quality at different positions in the ingot is also different. Due to the white nature of the synchrotron radiation source, topographic images can be obtained without pre-determination of the ingot orientation, since each set of crystallographic planes can choose its own diffraction wavelength according to the Bragg angle utilized. In addition, because of the area-filling nature of the synchrotron radiation source, which in our case is  $5 \times 0.5 \text{ cm}^2$ , large areas of ingot can be characterized in a single exposure. By setting the x-ray beam at about  $15^\circ$  with respect to the crystal growth direction, several diffraction images of the ingot surface in the circumferential direction can be obtained in a single shot. This incidence angle is chosen to ensure that sufficient x-ray penetration is obtained for most of the diffraction images so that the images are representative of the bulk quality of the ingot, instead of just the surface. By rotating the ingot 4 to 8 times around the growth direction, the whole ingot surface can be characterized in several diffraction images.

For a (111) oriented substrate wafer and subsequently grown epitaxial thin film, we set the diffraction geometry such that the incident x-ray beam is perpendicular to the  $[01\bar{1}]$  direction and makes  $81^\circ$  with respect to the  $[2\bar{1}\bar{1}]$  direction [5]. In so doing good contrast (422), (533), (220), (202), (331), (313), (551), (515),  $(55\bar{1})$ ,  $(5\bar{1}5)$ , (642), and (624) diffraction images can be recorded on a single  $8 \times 10 \text{ In}^2$  x-ray film. Each of these diffraction images has different penetration depth, strain sensitivity. They also provide extinction conditions for  $[01\bar{1}]$ ,  $[1\bar{1}0]$ , and  $[10\bar{1}]$  Burgers vectors respectively. Therefore, a single exposure can provide a vast amount of information. Experimentally, the  $(01\bar{1})$  mirror plane facilitates the orientation of the crystal with respect to the incident x-ray beam and film easy.

## RESULTS

Figure 1 shows a topograph of a CdZnTe ingot. It reveals the quality of the ingot along the longitudinal direction and the strain distribution near the surface of the ingot along this side of the ingot surface. The orientation of the crystal closest to the beginning of the growth process is not the same as the rest of the ingot. The quality of the major part of the ingot is good but it deteriorates in the region closest to the end of the growth process. However, there is a large twin in the middle part of the ingot. The twin appears curved on the topograph due to the curvature of the ingot surface. Detailed examination of the topographs reveals that there are linear and cellular structures distributed at different positions of the ingot. Figure 2 shows reflection topographs of both A and B surfaces of the same substrate wafer from vendor A. Figure 3 shows topographs of 3 (111)B oriented CdZnTe substrate wafers from vendors A, B, and C, respectively and LPE HgCdTe films subsequently grown on them by vendor D. These topographs show that defect structures such as grain boundaries, sub-grain boundaries, precipitates, and regions with localized lattice rotations, are propagated from the substrate to the film, providing exact replication into the films grown on these substrates. In addition, cross-

hatch patterns along all 3  $\langle 110 \rangle$  directions parallel to the (111) wafer surface are visible only in the films. Figure 4 shows topographs from focal plane array test articles from vendor D. In addition to the contrast from the normal device geometry and processing, one topograph shows an area of subsurface strain concentration which was not revealed by any other technique. This subsurface defect could have compromised pixel performance in this region of the test array.

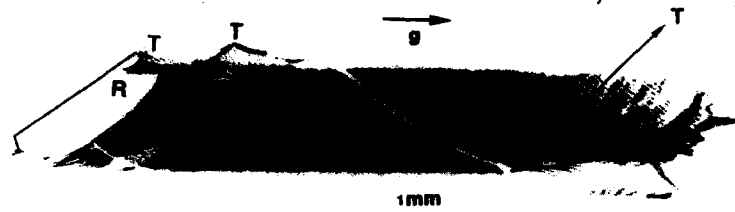


Figure 1. Synchrotron white beam x-ray topograph recorded in Bragg reflection geometry from an as grown CdZnTe ingot. "T" followed by an arrow indicates that the twin images are shifted with respect to the matrix image resulting in region with zero diffracted intensity. The arrow above "g" indicates both the crystal growth direction and the diffraction vector direction. Note also the linear contrast features, parallel to the twin boundary in the upper right of the image.

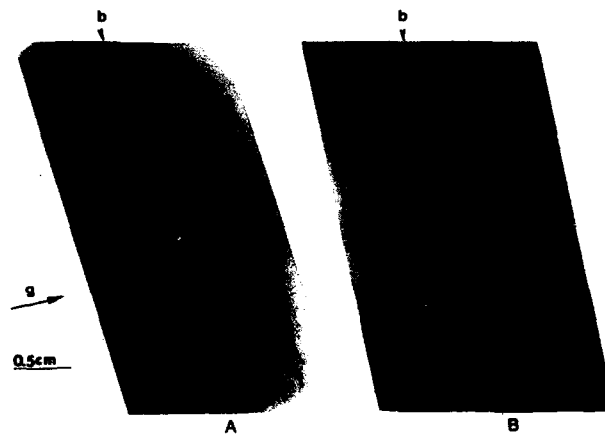


Figure 2. Synchrotron white beam x-ray topographs recorded in Bragg reflection geometry from a CdZnTe substrate wafer grown by vendor A. "b" indicates a sub-grain boundary. (a)  $g = \overline{642}$ , reflected from the A side of the wafer; (b)  $g = 642$ , reflected from the B side of the wafer.

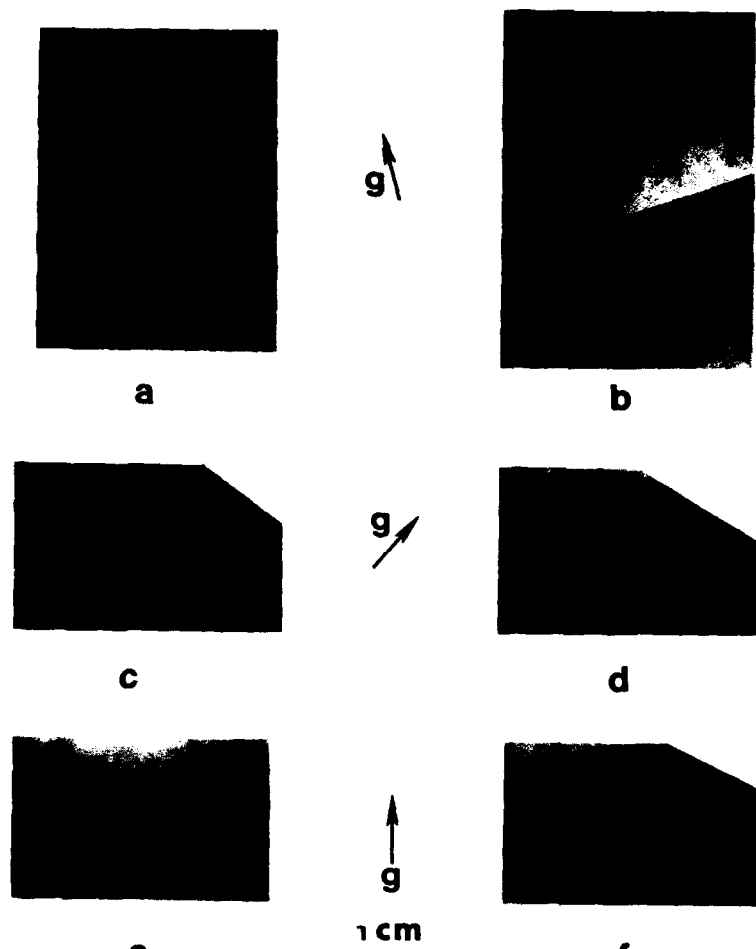


Figure 3. Synchrotron white beam x-ray topographs recorded in Bragg reflection geometry from CdZnTe substrates and from LPE HgCdTe films subsequently grown on the imaged substrates by vendor D ( $g = 422$ ). (a) Substrate A from vendor A, (b)  $16 \mu$  thick film grown on substrate A; (c) substrate B from vendor B, (d)  $19 \mu$  thick film grown on substrate B; (e) substrate C from vendor C, (f)  $19 \mu$  thick film grown on substrate C.

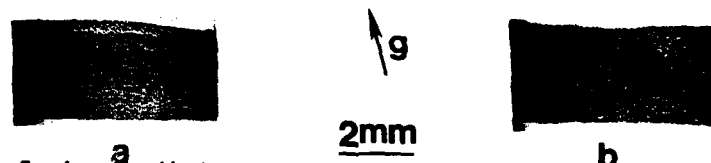


Figure 4. Synchrotron white beam x-ray topographs recorded in Bragg reflection geometry from focal plane array test articles from vendor D ( $g = 311$ ). (a) good device; (b) problem device.

## DISCUSSION

Figure 1 illustrates the information that can be revealed by imaging the whole ingot before processing using synchrotron white beam x-ray topography. The relative crystal quality from different positions of the ingot revealed by this technique can be used to determine which part of the ingot can be used for slicing wafers to be used as substrates for epitaxial film growth. The linear contrast observed can be attributed to slip bands activated by thermal stress during the cooling stage of the growth process. These linear contrast features terminate at the wavy contrast of cell boundaries as expected for sub-grain boundaries. Knowledge of the spatial distribution of defects revealed by their corresponding contrast can contribute further to the strategy of ingot slicing, enabling one to avoid densely defective regions. As a result, better quality substrate wafers can be sliced, improving yield.

Figure 2 (a) and 2 (b), respectively, were recorded from opposite sides of the same wafer. The black line contrast in Figure 2 (a) changes to white in Figure 2 (b). This reversal of contrast is caused by sub-grain boundaries rather than dislocation tangles. The wafer, however, is of high quality. It should also be noted that the sub-grain boundaries do not change their spatial distribution on progressing through the thickness of the substrate.

Comparison of the 3 topographs recorded from substrates in Figure 3 shows that each displays an unique distribution of defects. The dominant defects in the wafer from vendor A is a grain boundary crossing the whole wafer. This defect was difficult to resolve with optical or IR microscopes and so was submitted as a test of imaging sensitivity. The defect is easily detected topographically. The substrate from vendor B contains a dense distribution of highly strained regions. Prior work on CdTe identified the origin of these locally strained regions to be precipitates [6]. There is a high probability that this is also true in this CdZnTe wafer. In the topographic image recorded from the substrate of vendor C, dislocation cell structures, dislocation slip bands, and large lattice rotations are observed.

The different features presented on the topographs recorded from substrate wafers show that the crystal growth processes for each vendor are different, resulting in the generation of different defect types and distributions. This observation has the implication that by comparison of each of the growth processes, advantages may be combined so that certain types and distributions of defects can be reduced or even eliminated.

In the topographs in Figure 3 taken from the epilayer surfaces, all show the cross-hatched contrast features that are 3 fold symmetric. These features are wavy, not straight, when inspected at high magnification. Further, optical examination of the film surface shows that the features are not the result of surface terracing. However, their main trends are along the  $\langle 110 \rangle$  directions. The contrast is strong when the x-ray penetration depth for the obtained topograph is very shallow. This suggest that interfacial dislocations are not the source of the contrast. The contrast does not weaken under extinction conditions for all 3  $\langle 110 \rangle$  directions parallel to the wafer surface (111) plane. Therefore, if the contrast is caused by dislocations, the Burgers vectors of these dislocations are not parallel to the (111) wafer surface.

Figure 4 shows topographs of two  $68 \times 68$  test arrays from vendor D. The linear contrast features are revealed as a frame with vertical lines. The frame defines the extent of the array whereas the vertical lines correspond to the pixel spacing. Topographs recorded after turning the array ninety degree about its surface normal reveals the spacing in the horizontal direction. In Figure 4(a) the contrast is seen to be uniform suggesting an absence of defects. Figure 4(b) however shows a defect in the "frame" at the lower left and in the pixel area at the upper right. Optical microscopy showed that the frame defect was actually a flaw in the terraced epilayer, but

did not reveal the flaw within the pixels. IR microscopy also failed to reveal this defect, suggesting that the synchrotron white beam x-ray topography revealed a subsurface defect which was otherwise unobservable.

## CONCLUSIONS

We have demonstrated that the unique features of synchrotron white beam x-ray topography can be usefully adapted to specifically characterize IR detector manufacturing processes. The techniques developed can be used to examine whole single crystal ingots to understand the growth process and improve the yield of the substrate slicing and also the quality of the sliced substrate wafers. The technique can also be used to non-destructively reveal defect types and distributions in the substrate wafers, serving as a substrate screening or a process model validation tool. It can also be used as a quality control tool to examine epitaxial thin films. Finally it can be used to reveal flaws introduced at the device processing stages and reveal problems in focal plane array test articles otherwise unobservable.

## ACKNOWLEDGMENTS

Research supported in part by ARPA contract No. MDA972-92-C-0038 (Raymond Balcerak, COTR), and by NASA contract No. NA58.38147 (Joel Kearns, COTR). The focal plane array test articles were supplied by Loral IR Imaging Systems, Lexington, MA. Topography performed on the Synchrotron Topography Project Beamline X19C at the National Synchrotron Light Source which is supported by DOE.

## REFERENCES

1. D.G. Seiler, S. Mayo, and J.R. Lowney, *Semicond. Sci. Technol.*, **8**, 753 (1993).
2. R. Balcerak and L. Brown, *J. Vac. Sci. Technol. B*, **10**, 1353 (1992).
3. T. Tung, L.V. DeArmond, R.F. Herald, P.E. Herning, M.H. Kalisher, D.A. Olson, R.F. Risser, A.P. Stevens, and S.J. Tighe, *SPIE International Symposium on Optical Applied Science and Engineering* (1992).
4. C.K. Ard, W.J. Everson, J.L. Sepich, B.E. Dean, G.T. Neugebauer, and H.F. Schaake, *The U.S. Workshop on the Physics & Chemistry of HgCdTe & Other IR Materials* (1993).
5. D. DiMarzio, D.J. Larson, Jr., L.G. Casagrande, J. Wu, M. Dudley, and P.K. Liao, *Proceedings of the IRIS Specialty Group on Infrared Materials* (1993).
6. T. Fanning, M.B. Lee, L.G. Casagrande, D. DiMarzio, and M. Dudley, *J. Electronic Materials*, **22**, 943 (1993).

---

## PART VII

---

### **Dry Etching and Patterning**

## ULTRA-SMOOTH DRY ETCHING OF GaAs USING A HYDROGEN PLASMA PRETREATMENT

R. J. SHUL\*, KENT D. CHOQUETTE\*, A. J. HOWARD\*, D. J. RIEGER\*, C. A. DIRUBIO\*, R. S. FREUND\*\*, AND R. C. WETZEL\*\*

\*Sandia National Laboratories, MS 0603, Albuquerque, NM 87185-0603

\*\*AT&T Bell Laboratories, 6300 Mountain Avenue, Murray Hill, NJ 07974

### ABSTRACT

We have attained extremely smooth etched surfaces on GaAs using a hydrogen plasma pretreatment before etching. The resultant morphology exhibits smooth surfaces since the etching proceeds uniformly through the GaAs without micromasking effects arising from a nonuniform surface oxide. We report the effects of hydrogen plasma treatments before RIE of GaAs in two different reactors using a  $\text{SiCl}_4$  plasma. Optimization of  $\text{H}_2$  plasma pretreatments has produced improvements in RMS roughness greater than 1 order of magnitude (22.4 to 1.51 nm).

### INTRODUCTION

Typically at the start of reactive ion etching (RIE), there is an initiation period during which no GaAs etching occurs. Only after penetration of the native oxides on the surface will etching begin. Moreover, even with a short initiation period, micromasking effects due to nonuniform oxide thickness can lead to a roughening of the etched surface. Therefore, removing the native oxide before RIE should lead to greater process control and uniformity, as well as insuring a smooth etched surface necessary for epitaxial regrowth or uniform metal contacts.

Hydrogen plasmas have been previously shown to selectively remove native oxides from GaAs [1-3]. We have used a hydrogen plasma treatment before dry etching to remove the surface oxides. We discuss the effects of a hydrogen plasma pretreatment before etching with a  $\text{SiCl}_4$  plasma; the GaAs surface roughness is characterized using scanning electron microscopy and atomic force microscopy.

### EXPERIMENTAL

The GaAs wafers used in this study are two inch diameter semi-insulating substrates. The photoresist etch mask is approximately 1.4  $\mu\text{m}$  thick AZ-5214 with circular mesa features ranging in diameter from 4 to 32  $\mu\text{m}$  on 250  $\mu\text{m}$  pitch. The samples are 1  $\text{cm}^2$  to minimize loading effects. The etched surface morphology is quantified using a Digital Instruments atomic force microscope (AFM) operating in air in contact mode. The data is reported as RMS surface



roughness which represents the standard deviation of the roughness values within a  $2500 \mu\text{m}^2$  area.

RIE etches were performed at Sandia National Laboratories, Albuquerque (SNL) and AT&T Bell Laboratories, Murray Hill (AT&T) to evaluate the effect of a  $\text{H}_2$  plasma pretreatment on GaAs etching. The SNL RIE reactor is a non-load-locked 13.56 MHz rf-powered parallel plate Semi-Group RIE system. The lower electrode is 30.5 cm in diameter with an interelectrode spacing of approximately 3.8 cm. Samples were also etched at AT&T in a 13.56 MHz rf-powered parallel plate Oxford PlasmaLab RIE system with a lower electrode diameter of 16.8 cm and separation of 5.0 cm. The AT&T RIE chamber was enclosed with a glove box filled with dry  $\text{N}_2$  to reduce  $\text{H}_2\text{O}$  in the system. In both reactors samples were attached to a quartz plate, which completely covered the lower electrode, with thermal paste to ensure good thermal conduction. Immediately before loading, the samples were subjected to a 30 sec  $\text{NH}_4\text{OH}:\text{DI H}_2\text{O}$  (1:20) rinse.

Nominally matching plasma conditions between the two RIE systems did not yield similar etch results; therefore power densities were optimized for each reactor while the pressures and flow rates were held constant for both the  $\text{H}_2$  and  $\text{SiCl}_4$  plasmas. In the SNL RIE, the  $\text{H}_2$  plasmas were run at  $335 \text{ mW}/\text{cm}^2$  and the  $\text{SiCl}_4$  plasma etches were run at  $80 \text{ mW}/\text{cm}^2$ . The AT&T  $\text{H}_2$  plasma was optimized at  $320 \text{ mW}/\text{cm}^2$  and the  $\text{SiCl}_4$  plasma was run at  $160 \text{ mW}/\text{cm}^2$ . Temperature was maintained at  $0^\circ\text{C}$  and  $50^\circ\text{C}$  in the SNL reactor and  $-16^\circ\text{C}$  and  $50^\circ\text{C}$  in the AT&T reactor. All pretreatment and etch experiments were run at 20 sccm  $\text{H}_2$  flow rate at a pressure of 20 mTorr and 10 sccm  $\text{SiCl}_4$  flow rate at a pressure of 5 mTorr.

## RESULTS AND DISCUSSION

### A. Etch Rates and Profiles

The GaAs etch rates for the SNL reactor are 250 nm/min at  $0^\circ\text{C}$  and 300 nm/min at  $50^\circ\text{C}$ . The higher etch rate at  $50^\circ\text{C}$  may be due to increased volatility of the etch products and improved  $\text{H}_2\text{O}$  removal from the chamber at higher temperatures. In the AT&T reactor the etch rates are 110 nm/min at  $-16^\circ\text{C}$  and 135 nm/min at  $50^\circ\text{C}$ . Comparing the SNL and AT&T etch rate data shows a much faster etch in the SNL reactor. This is surprising since the SNL reactor is run at one-half the plasma power density of the AT&T reactor and may be attributed to differences between the two reactors.

GaAs features etched in the SNL reactor are anisotropic independent of temperature and of exposure to the  $\text{H}_2$  plasma pretreatment (Figure 1a). However, GaAs etching in the AT&T reactor shows a significant widening at the base of the mesa feature at  $50^\circ\text{C}$  and no  $\text{H}_2$  pretreatment (Figure 1b). This profile may be due to reflow of resist at higher temperature and higher incident power density from the plasma since the AT&T plasma power density is a factor of 2 greater than that used in the SNL reactor. Also, since the GaAs etch rate in the AT&T reactor is almost a factor of 3 slower than that in the SNL reactor, longer exposure times are necessary to etch to similar depths and may change the resist profile. The profile appears much more anisotropic with a  $\text{H}_2$  plasma pretreatment suggesting the  $\text{H}_2$  plasma interacts with the resist to enhance the anisotropy of the GaAs etch (Figure 1c). Low temperature ( $-16^\circ\text{C}$ ) etching in the AT&T reactor is highly anisotropic independent of the  $\text{H}_2$  pretreatment (Figure 1d) presumably due to the lack of resist reflow at the lower temperature.

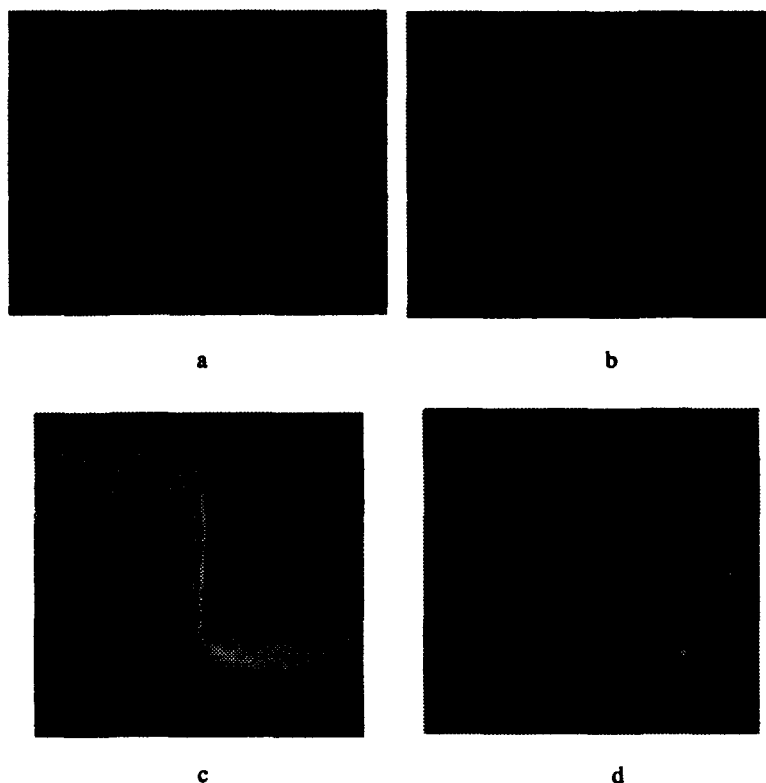


**Figure 1:** SEM micrographs of GaAs etched in SiCl<sub>4</sub> plasma (a) in the SNL reactor at 50°C without H<sub>2</sub> plasma exposure (0.75 μm deep), (b) in the AT&T reactor at 50°C without H<sub>2</sub> exposure (1.7 μm deep), (c) in the AT&T reactor at 50°C with 2 minutes of H<sub>2</sub> plasma exposure (1.1 μm deep), and (d) in the AT&T reactor at -16°C without H<sub>2</sub> exposure (1.0 μm deep).

### B. Surface Morphology

AFM images for surfaces etched in SiCl<sub>4</sub> are taken and analyzed for RMS roughness. The SNL and AT&T RMS data is shown in Figures 2 and 3, respectively. A patterned, unetched sample has an RMS roughness value of 0.628 nm. In Figure 2, the GaAs samples etched at SNL at 0°C and 50°C show a decrease in RMS roughness as the H<sub>2</sub> exposure is increased to 4 minutes; a slight increase in RMS roughness occurs as the exposure time is increased to 10 minutes. At both 0°C and 50°C, the optimum surface morphology occurs after 4 minutes of H<sub>2</sub> pretreatment. The rough etched surface observed at 0°C and 1 minute H<sub>2</sub> exposure is probably due to incomplete removal of the native oxide, which causes micromasking effects during the SiCl<sub>4</sub> plasma etch. As the H<sub>2</sub> exposure time is increased, the oxide is more uniformly removed

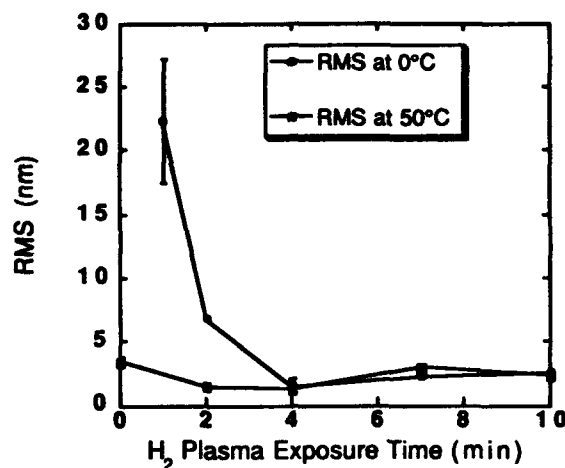


**Figure 2:** RMS roughness as a function of H<sub>2</sub> plasma exposure time for samples etched in the SNL reactor at 0°C and 50°C.

and the RMS roughness improves from 22.4 nm at 1 minute H<sub>2</sub> exposure to 1.51 nm at 4 minutes H<sub>2</sub> exposure. Without exposure to the H<sub>2</sub> plasma at 0°C, GaAs etching does not occur in a 80 mW/cm<sup>2</sup> SiCl<sub>4</sub> plasma. However, GaAs etching is achieved when the power density is increased to 160 mW/cm<sup>2</sup> with an RMS roughness of 1.34 nm. This implies that at 80 mW/cm<sup>2</sup>, the SiCl<sub>4</sub> plasma cannot penetrate the native oxide and initiate GaAs etching. At 50°C, the surface morphologies are relatively smooth regardless of the H<sub>2</sub> exposure time; however, the RMS roughness improves from 3.47 nm without H<sub>2</sub> exposure to 1.29 nm with 4 minutes H<sub>2</sub> exposure. We also note that the GaAs etches at 50°C without exposure to a H<sub>2</sub> plasma. The elevated temperatures may enhance the volatility of the etch products as well as H<sub>2</sub>O removal from the chamber, thereby uniformly removing the native oxide during the SiCl<sub>4</sub> etch.

A similar trend is observed for GaAs etching at AT&T. In Figure 3, we observe an improvement in the etched surface morphology with the addition of the H<sub>2</sub> plasma pretreatment. At both -16°C and 50°C the optimum surface morphology is observed after a 2 minute H<sub>2</sub> exposure. Low temperature etching yields very smooth GaAs surfaces independent of the H<sub>2</sub> pretreatment. The surface morphology improves slightly from 0.986 nm without H<sub>2</sub> exposure to 0.907 nm with a 2 minute exposure. Comparing the low temperature etching at SNL and AT&T, we find significant improvement of the surface morphology in the AT&T reactor at low H<sub>2</sub> plasma exposures. We believe the smoother surfaces obtained in the AT&T etches are due to the effect of the dry N<sub>2</sub> glove box which lowers the H<sub>2</sub>O concentration in the chamber and minimizes its effect on removal of the native oxide and GaAs etching. However, the surface morphologies become similar as the H<sub>2</sub> exposure is increased to 4 minutes. The roughest surface morphology in the AT&T reactor occurs without H<sub>2</sub> exposure at 50°C. The RMS roughness data is more than an order of magnitude greater than that for the low temperature AT&T etch without H<sub>2</sub> exposure. The smoother surface morphology at low temperature may be due to a lower chemical component of the etch mechanism at -16°C. Comparing the high temperature etching at SNL and AT&T, we see the AT&T RMS roughness is three times greater than the SNL roughness without H<sub>2</sub>

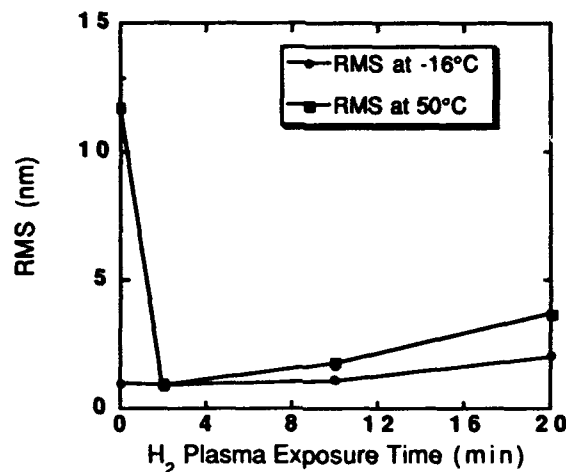


**Figure 3:** RMS roughness as a function of H<sub>2</sub> plasma exposure time for samples etched in the AT&T reactor at -16°C and 50°C.

exposure. Since the effect of the glove box is minimized at high temperatures due to lower H<sub>2</sub>O concentrations in the chamber, the higher power density in the AT&T etch may cause the rougher surfaces. Under all etch conditions studied, the surface morphology seen in the two reactors tends to converge as the H<sub>2</sub> exposure is increased.

Several trends can be deduced from this study. First, transferring processes from one reactor to another is difficult. We have observed significant variations in the etch characteristics using "identical" processes in the two reactors. Many of these variations can be attributed to the fact that the AT&T reactor incorporates a dry N<sub>2</sub> glove box which minimizes the H<sub>2</sub>O concentration in the chamber and permits more uniform removal of the native oxide and smooth GaAs etching. Additionally, differences in interelectrode spacing may effect the ion bombardment energies in the plasma and cause differences in etch characteristics. Etch variations may also be due to differences in thermal contact of the samples to the lower electrode. Second, under all conditions studied we have observed an improvement in the GaAs etched surface morphology with the addition of a H<sub>2</sub> plasma pretreatment. The surface morphologies are similar independent of reactor or temperature as the H<sub>2</sub> exposure time is optimized (2 to 4 minutes in this study). We believe that the slight increase in surface roughness with increasing H<sub>2</sub> exposure is due to an interaction between the H<sub>2</sub> and the photomask leading to micromasking effects. Also, changing the power density of the H<sub>2</sub> plasma from 335 to 165 mW/cm<sup>2</sup> has virtually no effect on the surface morphology of the GaAs etched surfaces suggesting a robust process window for the H<sub>2</sub> pretreatment.

## CONCLUSIONS

H<sub>2</sub> pretreatment for 2 to 4 minutes yields a smoother etch morphology and reproducible etch characteristics for SiCl<sub>4</sub> etching of GaAs in two different RIE reactors. Attempts to transfer processes between the two different chambers was not straightforward. However, a H<sub>2</sub> plasma

pretreatment results in improved surface morphology, as quantified with AFM, in both reactors. The H<sub>2</sub> plasma selectively removes the native oxide on GaAs before RIE, resulting in an etch morphology which exhibits significantly less surface roughness since the etching can proceed uniformly through the GaAs.

#### ACKNOWLEDGMENTS

The authors would like to thank P.L. Glarborg for her technical support and sample fabrication. This work was performed at Sandia National Laboratories supported by the U.S. Department of Energy under contract #DE-AC04-94AL85000.

#### REFERENCES

- [1] K.D. Choquette, M. Hong, R.S. Freund, J.P. Mannaerts, and R.C. Wetzel, J. Vac. Sci. Technol. **B9**, 3502 (1991).
- [2] P. Friedel and S. Gourrier, Appl. Phys. Lett. **42**, 509 (1983).
- [3] S. Sugata, S. Takamori, N. Takado, K. Asakawa, E. Miyauchi, and H. Hashimoto, J. Vac. Sci. Technol. **B6**, 1087 (1988).

## SIMULATION OF DRY ETCHING PROCESSES FOR III-V COMPOUNDS TECHNOLOGY APPLICATIONS.

K.Ketata, S.Koumetz, M.Ketata, R.Debrie; LCIA-INSA de Rouen, Place Emile Blondel,  
76131 Mont Saint Aignan, France.

### ABSTRACT

This work introduces a new dry etching simulation technique of the sputtering component of Reactive Ion Etching (R.I.E.) and presents experimental verifications for GaAs. The final objective is to correlate the etch rate to the plasma reactor parameters, which can be incorporated into a computer-simulation program.

### I. INTRODUCTION.

The actual simulators use the geometrical model of the etching when it define the etch rate, etch time, anisotropic yield to obtain the etch profil [1]. But there is important need to have the functional dependence between the etch rate and the physical conditions of R.I.E.

The etch rate of R.I.E. is frequently presented as the sum of physical and chemical components [2]. Our work is based on the same supposition.

The aim of our research is to establish the relation between the etching rate and the physical parameters which characterize the experimental conditions of R.I.E.

### II. EXPERIMENT.

The measurements were carried out on the reactor I.B.E. VEECO3 Microetch System and on the reactor R.I.E. NE110A of NEXTRAL (where the plasma is generated by application of RF power at 13.56 MHz).

### III. RESULTS AND DISCUSSION.

First, we have tried to formalise the physical component of the R.I.E. which represents the sputter etching component.

The etch rate  $R(\theta)$  could be found directly from the sputtering yield  $S(\theta)$  [3]:

$$R_i(\theta) = 9.6 \cdot 10^{25} \cdot \frac{J \cdot S(\theta)}{n} \cdot \cos \theta \quad (1)$$

where  $n$  is the atomic density of target material ( $\text{atom} / \text{cm}^3$ ),  $J$  is the current density of the ionic incident flux ( $\text{mA} / \text{cm}^2$ ),  $\theta$  is the angle of incidence ( $\theta = 0^\circ$  at normal incidence). The etch rate is given in  $\text{\AA} / \text{mn}$  always in this work.

The sputtering yield dependence on the angle of incidence is given by

$$S(\theta) = \frac{3 \cdot \alpha}{\pi^2} \cdot \frac{m_i \cdot m_a}{(m_i + m_a)^2} \cdot \frac{E}{U_0} \cdot (\cos \theta)^{-r} \quad (2)$$

according to the sputtering theory of Sigmund [4]. Here,  $\alpha$  is a factor depending on the mass ratio  $m_a / m_i$ ,  $U_0$  surface binding energy,  $m_i$  mass of ion,  $m_a$  mass of target atom,  $E$  energy of the

incident particle (ion kinetic energy),  $f$  factor depending on the mass ratio:  $f = \frac{5}{3}$  for  $10^{-1} < \frac{m_1}{m_2} < 3$  and  $f = 1$  for  $\frac{m_1}{m_2} \approx 10$  [4].

### III.1. Ion Beam Etching (I.B.E.).

Considering the apparent analogy between the physical component of R.I.E. and the I.B.E. we have started by establishing a theoretical approach using I.B.E.

The etch rate of GaAs for different angles of incidence have been measured after I.B.E. using incident argon ions of 500 eV, and current density of 0.5 mA/cm<sup>2</sup>.

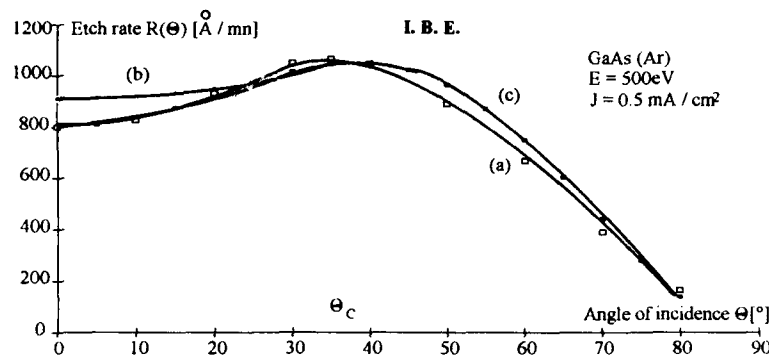


Fig. 1. Etch rate of GaAs as a function of the ion beam incidence angle  $\theta$ .

- a) Experimental curve.
- b) Theoretical curve (sputtering yield according to Sigmund).
- c) Theoretical curve (sputtering yield according to String model).

As shown in Fig. 1.a the sputtering yield increases with  $\theta$ . This increase is related to the longer path of the bombarding ions, which permits to more excited atoms to escape from the surface. For  $\theta$  greater than a critical angle  $\theta_c$  ( $\theta_c \approx 35^\circ$ ) the sputtering yield decreases as  $\theta$  increases because ion reflection increases.

The sputtering yield for the I.B.E. of GaAs by the bombarding argon ions of 500 eV and the current density of 0.5 mA/cm<sup>2</sup> according to (2) is given by:

$$S(\theta) \approx 0.8 \cdot (\cos \theta)^{-1.67} \quad (3)$$

where  $\alpha$  is equal to 0.25 according to [4],  $m_1 = 40$  a.m.u.,  $m_2 = 70$  a.m.u. and  $U_0 = 10$  eV [5].

So  $S \approx 0.8$  for the normal incidence.

The etch rate in general case according to (1) is:

$$R(\theta) \approx 2.9 \cdot 10^{25} \cdot \alpha \cdot \frac{J}{n} \cdot \frac{m_1 \cdot m_2}{(m_1 + m_2)^2} \cdot \frac{E}{U_0} \cdot (\cos \theta)^{1-f} \quad (4)$$

Where  $R(\theta) \approx 911 \cdot (\cos \theta)^{-0.67}$  (5)

in the case of the GaAs milling by the argon ions.

The curve corresponding to eq.(5) for the angles of incidence  $\theta \leq \theta_c$  is shown in Fig.1.b.

The "String Model" included in the simulator SAMPLE [6] gives for the sputtering yield the following formula:

$$S(\theta) = \frac{\Phi}{n} \cdot S_0 \cdot (A \cdot \cos \theta + B \cdot \cos^2 \theta + C \cdot \cos^4 \theta) \quad (6)$$

where  $S_0$ ,  $A$ ,  $B$  and  $C$  characterize the sputtering yield of the material to be etched,  $n$  is the atomic layer density and  $\Phi$  ion flux.

The expression (6) permits to determine the etch rate (1):

$$R(\theta) \approx 6 \cdot 10^{-14} \cdot \frac{J^2}{n^2} \cdot S_0 \cdot (A \cdot \cos^2 \theta + B \cdot \cos^3 \theta + C \cdot \cos^5 \theta) \quad (7)$$

For the case of GaAs argon milling ( $J = 0.5 \text{ mA/cm}^2$ ,  $E = 500 \text{ eV}$ ) we have:

$$R(\theta) \approx 8 \cdot 10^{-2} \cdot S_0 \cdot (A \cdot \cos^2 \theta + B \cdot \cos^3 \theta + C \cdot \cos^5 \theta) \quad (8)$$

The experimental curve (Fig.1.a) permits to evaluate  $S_0$  at about  $10^4$ .

The expression (8) gives the curve shown in Fig.1.c. We have used the values given by the etch simulateur SILVACO [7]:  $A = 6.7702$ ,  $B = -6.1548$  and  $C = 0.3846$ .

The advantage of the formula (6) for the sputtering yield is the possibility to have the approach of etch rate in the case of I.B.E. for all the angles of incidence of ion beam.

### III.2. Reactive Ion Etching.

The next step is the modeling of the physical component of the R.I.E.

To take into account only the physical component the R.I.E. of GaAs has been performed in  $\text{SF}_6$  plasma.

The etch rate for the normal incidence of the ion beam on the surface of the wafer according to (1) is:

$$R = 9.6 \cdot 10^{30} \cdot \frac{J \cdot S}{n} \quad (9)$$

(where the values of the parameters are in unity of S.I.). It is the case of the physical component of the R.I.E. where the ions are accelerated in the cathodic plasma sheath in the perpendicular direction to the surface.

The current density of the ions emitted from the plasma to the sheath could be determined from the formula of Child - Langmuir [8]:

$$J = \frac{4 \cdot \epsilon_0}{9} \cdot \left( \frac{2 \cdot e}{m_i} \right)^{0.5} \cdot \frac{V^{1.5}}{\delta^2} \quad (10)$$

where  $V$  is the voltage across sheath.  $V \approx V_{dc}$  (self-bias voltage).

The plasma sheath thickness  $\delta$  could be found from the empirical expression [9]:

$$\delta = K_0 \cdot P^{-\frac{1}{2}} \quad (11)$$



where  $K_0$  is a constant whose value is dependent on the type of the plasma.

For the  $SF_6$  plasma, the  $SF_5^+$  and  $SF_3^+$  positive ions represent about 90% of the total ion current [10], so  $K_0$  value for a mean mass of  $SF_5^+$  and  $SF_3^+$  ions ( $m_i \approx 108 \cdot 1.66 \cdot 10^{-27}$  kg) is:

$$K_0 \approx 0.04 \text{ cm} \cdot \text{Torr}^{\frac{1}{2}} = 4.6 \cdot 10^{-3} \text{ m} \cdot \text{Pa}^{\frac{1}{2}} \text{ according to [9].}$$

For example, the sheath thickness for 60 mTorr is:  $\delta \approx 0.16 \text{ cm}$ .

It is possible to find the self-bias voltage from the following empirical formula [11]:

$$V_{dc} = C \cdot e^{\frac{a \cdot P}{W}} \quad (12)$$

where  $P$  is the pressure of the gas,  $W$  RF power,  $C$  and  $a$  constants.

This formula has been verified with our curves (the error does not exceed 4%) for the self-bias voltage as a function of the pressure (Fig.2):

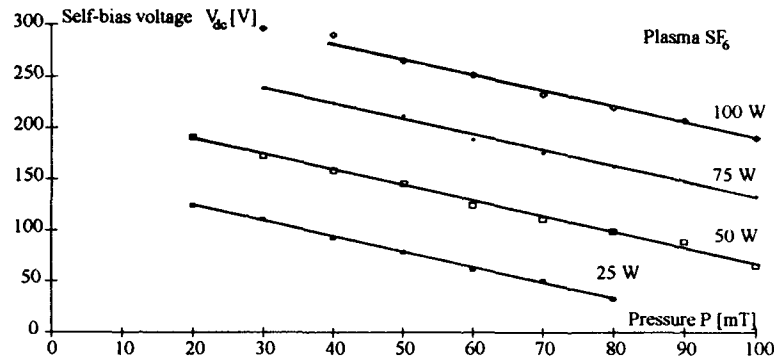


Fig.2. The self-bias voltage as a function of the pressure in the reactor for the different RF powers.

From these curves we can determine  $C$  and  $a$ . For 50W power we found  $a \approx -3.6$  and  $C \approx 213$ .

The expressions (10), (11), (12) permit to determine the ion current density in the case of the R.I.E. in  $SF_6$  plasma at 60mTorr (8 Pa) pressure and the 50W RF power:  $J \approx 0.27 \text{ mA/cm}^2$ .

The positif ions bombarding the wafer surface collect their energy in the cathodic sheath electric field:

$$E = e \cdot V \approx e \cdot V_{dc} \quad (13)$$

The sputtering yield for the normal incidence of the ion beam in the case of the GaAs R.I.E. in  $SF_6$  plasma according to (2) is:  $S \approx 0.17 \text{ atom/ion}$  with  $\alpha \approx 0.2$  [4],  $m_s \approx 70 \cdot 1.66 \cdot 10^{-27} \text{ kg}$ ,  $U_0 = 10 \cdot 1.6 \cdot 10^{-19} \text{ J}$ ,  $W = 50 \text{ W}$  and  $P = 8 \text{ Pa}$ .

The expressions (1), (2), (10), (11), (12) and (13) lead to the general formula for the sputtering component of R.I.E. rate as function of the physical parameters (in S.I. system) which characterize the etch conditions:

$$R_i \approx 1 \cdot 10^{-9} \cdot \frac{\alpha \cdot P \cdot m_i^{0.5} \cdot m_s \cdot C^{2.5} \cdot e^{\frac{2.5 \cdot a \cdot P}{W}}}{K_0 \cdot U_0 \cdot n \cdot (m_i + m_s)^2} \quad (14)$$

The etch rate as a function of the pressure for R.I.E. of the GaAs in  $\text{SF}_6$  plasma at  $W = 50\text{W}$  is then:

$$R_i \approx 52 \cdot P \cdot e^{-0.18 \cdot P} \quad (15)$$

We have:

$$R_i \approx 7 \cdot P \cdot e^{-0.024 \cdot P} \quad (16)$$

if pressure is expressed in mT.

The expression (16) gives the curve shown in Fig.3.b:

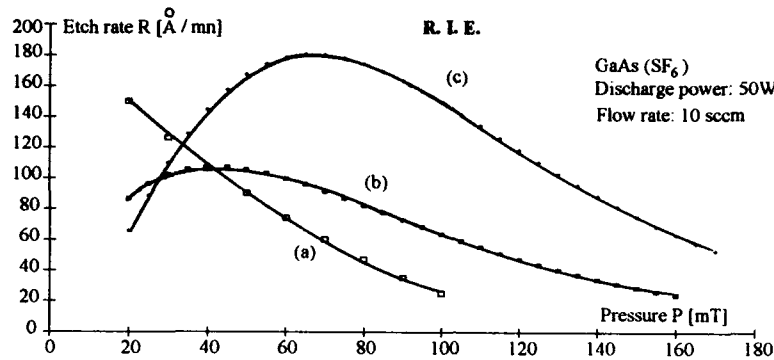


Fig.3. Etch rate of the GaAs in  $\text{SF}_6$  plasma at 50W power and 10sccm flow rate.

- a) Experimental curve.
- b) Theoretical curve (sputtering yield according to Sigmund).
- c) Theoretical curve (sputtering yield according to String model).

At a given power input, when the pressure decreases, the ionisation yield decreases so the impedance of plasma increases. Thus the applied potential raises and the self-bias voltage increases (Fig.2). But the self-bias voltage accelerates the ions in plasma sheath so etch rate raises. The sputtering yield for the normal incidence of the ion beam according to eq.(6) is:

$$S = 10^5 \cdot \frac{J}{e \cdot n} \cdot S_0 \quad (17)$$

The expressions (9), (10), (11), (12) and (17) give the general formula for the physical component of R.I.E. rate:

$$R_i \approx 3 \cdot 10^{17} \cdot \frac{C^3 \cdot P^2 \cdot e^{\frac{3 \cdot a \cdot P}{W}}}{n^2 \cdot K_0^4 \cdot m_i} \quad (18)$$

In the case of the etching of GaAs in  $\text{SF}_6$  plasma at 50W power the etch rate is:

$$R_i \approx 0.3 \cdot P^2 \cdot e^{-0.03 \cdot P} \quad (19)$$

where the pressure is expressed in mT.

The expression (19) gives the curve shown in Fig.3.c. The etch rate decreases when the pressure decreases from the certain threshold for the theoretical curves. The same drop has been observed

experimentally for a pressures below 10 mTorr [12] which may be due to a reduction in etchant concentration. We did not observe this drop because of the instable plasma below 20 mTorr (Fig. 3.a.). The difference between the theoretical and experimental curves is certainly due to effects not taken into account in our approach (for example, flow rate, temperature, distance between the electrodes, etching surface etc.).

#### IV. CONCLUSIONS.

The theoretical approach of the physical component of the Reactive Ion Etching could help us to evaluate the etch rate as a function of the gas pressure, discharge power, plasma ion mass, material atom mass (their concentration and surface binding energy) and of the mass ratio  $m_e / m_i$ . We hope to obtain the expression for the chemical etch rate also despite complexity of the chemical reactions at the time of the etching and, consequently, to find the complete theoretical approach of the Reactive Ion Etching.

#### Acknowledgments.

The authors wish to thank C.Dubon-Chevallier, N.Bouadma, P.Launay and J.Etrillard from CNET labs. Bagneux for providing some experimental results and helpful discussion.

#### References.

- [1] A.Gerodolle, J.Pelletier and al. Simulation of plasma processes with two-dimensional program TITAN. Le Vide, Les Couches Minces. Supplément N° 256. Mars-Avril 1991.
- [2] J.P. McVittie and al. SPEEDIE: A profile simulator for etching and deposition. 12<sup>th</sup> Symposium on Dry Processing in Tokyo, Japan 1990.
- [3] S.Somekh. Introduction to ion and plasma etching. J. Vac. Sci. Technol., Vol.13, No.5, Sept./Oct. 1976.
- [4] P.Sigmund. Theory of sputtering. I.Sputtering yield of amorfous and polycrystalline targets. Physical Review, Vol.184, No.2, 10 august 1969.
- [5] B.Jackman, G.C.Tyrrell. Ion/neutral beam assisted etching of semiconductors. 8th IPAT Europe Brussel. May 1991.
- [6] W.G.Oldham, A.R.Neureuther, C.Sung, J.L.Reynolds and S.N.Nandgaonkar. A general simulator for VLSI lithography and etching processes: PartII - Application to deposition and etching. IEEE Transaction on Electron Devices, Vol. ED-27, No.8, August 1980.
- [7] Silvaco international. User's manual. May 1992.
- [8] A.M.Pointu. Physique des décharges. Réactivité dans les plasmas. Ecole d'été. Edition de physique 1984.
- [9] N.Mutsukura, K.Kobayashi and Y.Machi. Plasma sheath thickness in radio-frequency discharges. J. Appl. Phys. 68(6), 15 september 1990.
- [10] Ph.Briaud. Gravure ionique réactive des couches minces de tungstène et de tantale dans un plasma RF de SF<sub>6</sub>. Thèse de doctorat. Université de Nantes 1988.
- [11] D.Bollinger, S.Lida, O.Matsumoto. Reactive ion etching: Its basis and future. Part II. Solid State Technology. June 1984.
- [12] J.Z.Li, I.Adesida and E.D.Wolf. Evidence of crystallographic etching in (100) GaAs using SiCl<sub>4</sub> reactive ion etching. J. Vac. Sci. Technol. B3(1), Jan/Feb 1985.

## REACTIVE ION ETCHING OF GaN THIN FILMS

Michael Manfra<sup>1</sup>, Stuart Berkowitz<sup>1</sup>, Richard Molnar<sup>2</sup>, Anna Clark<sup>1</sup>, T.D. Moustakas<sup>2</sup> and W.J. Skocpol<sup>1</sup>

<sup>1</sup>Department of Physics, Boston University, Boston Ma 02215

<sup>2</sup>Department of Engineering, Boston University, Boston Ma 02215

### ABSTRACT

Reactive ion etching of GaN grown by electron-cyclotron-resonance, microwave plasma-assisted molecular beam epitaxy on (0001) sapphire substrates was investigated. A variety of reactive and inert gases such as  $\text{CCl}_2\text{F}_2$ ,  $\text{SF}_6$ ,  $\text{CF}_4$ ,  $\text{H}_2/\text{CH}_4$  mixtures,  $\text{CF}_3\text{Br}$ ,  $\text{CF}_3\text{Br}/\text{Argon}$  mixtures and Ar were investigated. From these studies we conclude that of the halogen radicals investigated, Cl and Br etch GaN more effectively than F. The etching rate was found to increase with decreasing pressure at a constant cathode voltage, a result attributed to larger mean free path of the reactive species.

### INTRODUCTION

The family of refractory nitrides (InN, GaN, AlN), their solid solutions and heterojunctions are one of the most promising families of electronic materials. All three binary compounds are direct bandgap semiconductors with energy gaps covering the region from 1.95eV (InN) and 3.4eV (GaN) to 6.28eV (AlN). These materials should find applications in optical devices (LED's lasers, detectors) operating in the green-blue-UV parts of the electromagnetic spectrum. Due to their unique physical properties, the materials are also expected to find applications in high temperature, high power, and high frequency electronic devices. However, the fabrication of such devices requires the development of a number of device processing techniques, including reactive ion etching.

There are limited reports in the literature regarding etching of GaN [1-4]. Pankove [1] reported that GaN dissolves in hot alkali solutions at very slow rates, and thus, wet etching is not practical for this strongly bonded material. Foresi [2] reported the reactive ion etching of GaN grown on the R-plane of sapphire using  $\text{CCl}_2\text{F}_2$ , and Adesida [3] reported the etching of GaN using  $\text{SiCl}_4$ . Pearton [4] investigated ECR microwave discharges for the etching of GaN, InN and AlN.

In this paper we report on reactive ion etching studies of GaN grown on (0001) sapphire substrates using a variety of reactive and inert gases. The effect of plasma parameters on etch rate, morphology and selectivity were investigated.

## EXPERIMENTAL METHODS

The GaN films were grown onto (0001) sapphire substrates by the method of electron-cyclotron-resonance microwave plasma-assisted molecular beam epitaxy (ECR-MBE) using a two temperature step growth process [5,6]. In this method a GaN buffer is grown first at low temperature (500°C) and the rest of the film is grown at higher temperatures. This process was shown [5,6] to lead to high lateral growth rate resulting in a layer by layer growth. The films have the wurtzite structure with the c-axis perpendicular to the substrate. Although the films were not intentionally doped they were found to be n-type with carrier concentrations in the order of  $10^{18}\text{cm}^{-3}$ , due presumably to nitrogen vacancies.

The ion etching of the GaN films was carried out in a parallel plate reactor supplied with 13.5 MHz RF power. Various patterns were formed on the top of the GaN films with AZ 1350 J photoresist. Various reactive and inert gases were employed. The depth of the profile of the etches was determined by a profilometer or by directly measuring the thickness by a cross-sectional SEM image. The quality of the etch morphology was also assessed by SEM imaging.

## EXPERIMENTAL RESULTS AND DISCUSSION

First the etching rate from different reactive and inert gases was investigated. To compare the results the etching was carried out at the same gas pressure (11mT) and the same cathode voltage (600V). The results are listed in Table I.

Table I. Etching rates of GaN (11mT and 600V cathode voltage.)

| Gas                                    | Etching Rate (Å/min) |
|--|----------------------|
| $\text{CCl}_2\text{F}_2$               | 185                  |
| $\text{CF}_3\text{Br}$                 | 150                  |
| $\text{CF}_3\text{Br}/\text{Ar}$ (3:1) | 200                  |
| $\text{CF}_4$                          | 120                  |
| $\text{SF}_6$                          | 100                  |
| $\text{H}_2/\text{CH}_4$ (2:1)         | 30                   |
| Ar                                     | 65                   |

From these results it is apparent that F is a less efficient etchant of GaN than the other halogen radicals Cl and Br. Etching by hydrogen radicals and physical sputtering are even less efficient processes. Nevertheless, the mixture of a certain percentage of Ar in  $\text{CF}_3\text{Br}$  improves the etching rate of the reactive gas.

The effect of gas pressure on the etching rate of GaN was investigated by using  $\text{CF}_3\text{Br}/\text{Ar}$  (3:1) and a constant cathode voltage of 600V. The results are shown in Figure 1.

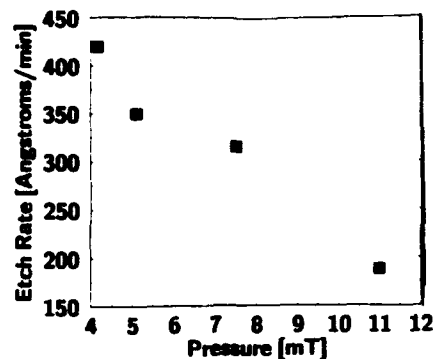


Fig. 1 Etch rate of GaN vs. the pressure of  $\text{CF}_3\text{Br}/\text{Ar}$  (3:1) at a constant cathode bias of 600V.

The higher etching rate at lower pressures suggests that the limiting step in the etching process is the mean free path of the halogen radicals. A typical etching profile obtained at 11mT of  $\text{CF}_3\text{Br}/\text{Ar}$  (3:1) and 600V of cathode voltage is shown in Figure 2.

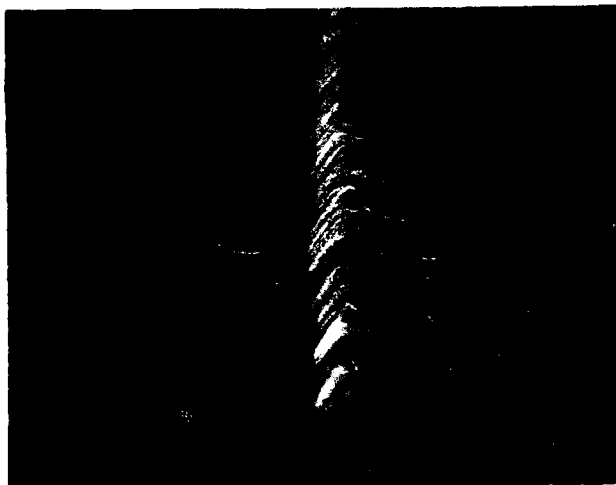


Fig. 2 A typical etch profile of GaN using  $\text{CF}_3\text{Br}/\text{Ar}$  (3:1) made under conditions described in the text.

We observed that the pyramidal features in the etching pattern are not present when etching was carried out at 5mT. By measuring the thickness of the photoresist prior to and after etching the selectivity at 5mT was found to be greater than 3:1 GaN to photoresist.

## CONCLUSIONS

We report on reactive ion etching of GaN grown onto (0001) sapphire. Various reactive and inert gases were employed from which it was found that Cl and Br etch GaN more effectively than F. The effects of plasma parameters on etch rate and surface morphology were investigated using a CF<sub>3</sub>Br/Ar mixture in a 3:1 ratio. Etch rate and surface morphology were found to improve at lower plasma pressure, resulting in an etch rate in excess of 400 Å/min at 4.2 mT.

## ACKNOWLEDGEMENTS

This work was supported by the Office of Naval Research (grant no. N00014-92-J 1436).

## REFERENCES

1. J.I. Pankove, *Electrochem. Soc. Vol 119*, 1110 (1972)
2. J. Foresi, M.S. Thesis (Boston University, 1991)
3. I. Adesida, A. Mahajan, E. Andideh, M. Asif Khan, D.T. Olsen and J.N. Kuzna *Appl. Phys. Lett.* **63**, 2777 (1993)
4. S.J. Pearton, C.P. Abernathy, F. Ren, J.R. Lothian, P.W. Wisk, A. Katz, and C. Constantine, *Semicond. Sci. Technol.* Vol **8** pg 310 (1993)
5. T.D. Moustakas, T. Lei and R. Molnar, *Physica B* 185 pg 36-49 (1993)
6. T.D. Moustakas and R. Molnar *Mat. Res. Soc. Symp. Proc.* Vol **281** (1993)

## Effects of halogen-containing gas plasma and rapid thermal anneal treatment on the reactive ion etched silicon

Kwang-Ho Kwon, Bo-Woo Kim, Hyung-Ho Park, Jin-Yeong Kang and Gun-Yung Yeom\*

Semiconductor Technology Division, ETRI, P. O. Box 8, Daeduk Science Town, Taejeon, 305-606, Korea, \* Dept. of Materials Engineering, Sungkyunkwan University, Suwon, Korea

### ABSTRACT

The effects of  $\text{SF}_6$  and  $\text{NF}_3$  gas plasma treatments, and successive rapid thermal anneal (RTA) treatment for the recovery of modified silicon surface due to  $\text{CHF}_3/\text{C}_2\text{F}_6$  plasma have been investigated using X-ray photoelectron spectroscopy (XPS) and secondary ion mass spectrometry (SIMS).

XPS analyses have revealed that  $\text{NF}_3$  and  $\text{SF}_6$  plasma treatments are effective for the removal of residue layer. SIMS results show that penetrated impurities in the contaminated silicon substrate reduce through the additional RTA treatment. The effects of  $\text{NF}_3$ ,  $\text{SF}_6$  plasmas, and additional RTA treatments for the recovery of reactive ion etched silicon surface has been also studied by measuring the electrical performance of the silicon devices.

### INTRODUCTION

Reactive ion etching (RIE) of silicon dioxide on silicon using fluorocarbon plasma is widely applied to the production of very large scale integrated (VLSI) devices. But RIE is known to induce the chemical and physical modifications on the exposed materials. The modifications include structural damage such as displaced substrate atoms, penetration of plasma constituents, and deposition of involatile materials. These modifications are inevitable in RIE and the modified surface will degrade the performance of devices fabricated on that surface [1-3]. Surface modifications have increasingly critical issues in the semiconductor industry, as the critical feature size of integrated circuit shrinks down under submicron values. Therefore, the effects of various fluorocarbon plasmas on the silicon surface and the removal of undesirable side effects have been studied in recent years [4,5]. In this study, recovery of contaminated silicon surface has been examined using  $\text{SF}_6$  and  $\text{NF}_3$  plasmas, and ex-situ RTA treatments. And electrical properties such as  $p^+$ -metal contact resistance and PtSi/n-type Schottky barrier height have been given.

### EXPERIMENTAL

The substrate used in this study was B-doped, Si(100) wafers of 0.85-1.15 ohm-cm in resistivity. The typical RIE process and the preparation of the samples used in this study was described elsewhere [6].  $\text{NF}_3$  and  $\text{SF}_6$  plasma treatments were carried out after RIE using Applied Materials Precision 5000 system. These plasma treatments were carried out with the conditions of 10 mTorr, 50 watts, and 20 sccm for 10 seconds. After the plasma treatments, the samples were successively immersed in  $\text{H}_2\text{SO}_4/\text{H}_2\text{O}_2$  (4/1) and in 1/100 HF as an additional wet cleaning. RTA treatments were carried out to analyze the effect of RTA treatment on the reactive ion etched silicon. The process condition was 700 °C, 1



minute with nitrogen atmosphere. The XPS analyses were performed with a V.G. Scientific ESCALAB 200R spectrometer using Mg  $K\alpha$  (1253.6 eV) operating at 250 W radiation. Narrow scan spectra of all regions of interest were recorded with 20 eV pass energy. The SIMS results were obtained using oxygen ion as sputtering sources. For revolution of the electrical properties through post etch treatments, Kelvin test pattern was prepared. Contact resistances of p-metal were measured at the current of 2 mA. PtSi/n-type Si Schottky barrier diodes were also made to measure the change of barrier height after various post etch treatment. The silicon wafers having 3 - 6 ohm-cm in resistivity were used to make Schottky diodes. After the Pt deposition on the silicon, the sample was sintered at  $N_2/H_2$  ambient for platinum silicide formation. The sintering was carried out at 460 °C for 30 minute.

## RESULTS AND DISCUSSION

$CHF_3/C_2F_6$  plasma exposure during RIE process introduces silicon surface modification such as several nm thick residue layer of fluorocarbon polymer on the silicon and contaminated silicon layer with carbon and fluorine[6]. Figure 1 represents the change of atomic percent after various post etch treatments. This figure shows that relative C and F atomic percents of residue layer decrease with  $SF_6$  or  $NF_3$  plasma exposure and successive wet clean while Si atomic percent dramatically increases. The increase of Si atomic percent means that the thickness of residue layer decreases. After RTA and wet clean, the fluorine decreased to the detectable amount by XPS even though the carbon remains almost same. The decrease of fluorine after the RTA and wet clean seems to be from the evaporation of fluorine due to the thermal decomposition of fluorocarbon during the RTA treatment. The changes of C 1s

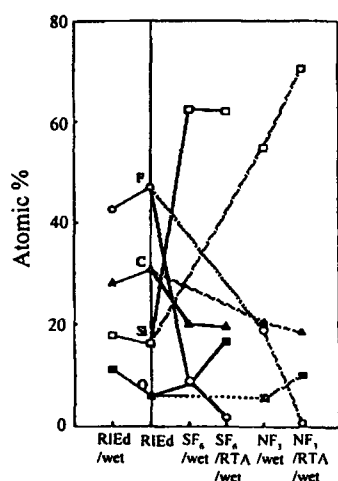


Fig. 1 The change of atomic percent on the RIEd silicon surface after various post etch treatments

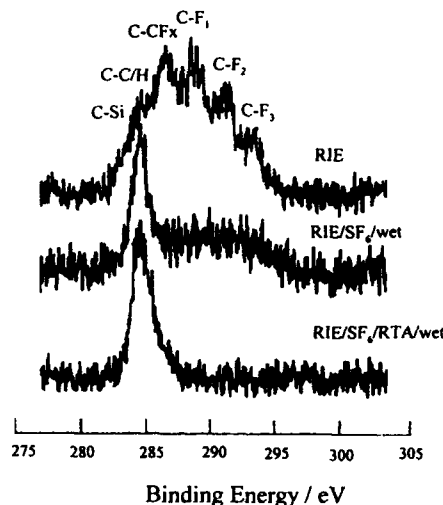


Fig. 2 The changes of C 1s spectra after post etch treatments using SF6 plasma

spectra after RIE,  $\text{SF}_6$  plasma/wet clean, and  $\text{SF}_6$  plasma/RTA/wet clean are shown in figure 2, respectively. From the figure, the decrease of  $\text{C-CFx}(x<3)$  and  $\text{C-Fy}(y=1, 2, 3)$  bonds along with the increase of  $\text{C-C/H}$  bond can be seen after the  $\text{SF}_6$  plasma/wet clean treatment.  $\text{C-CFx}(x<3)$  and  $\text{C-Fy}(y=1, 2, 3)$  bonds are easily removed with the  $\text{SF}_6$  plasma treatment even though small amount of them still remain on the surface. But the amount of  $\text{C-C/H}$  bond increases after  $\text{SF}_6$  plasma exposure. This means that through the decomposition of fluorocarbon residue layer, carbon remains on the silicon surface and fluorine evaporates. With the successive RTA and wet cleaning treatments, as shown in figure 2, the remaining  $\text{C-CFx}$  and  $\text{C-Fy}$  bonds after  $\text{SF}_6$  plasma treatment decrease further down to negligible amount. Also, no F 1s peak was found after RTA and wet clean. Therefore,  $\text{SF}_6$  plasma treatment followed by RTA treatment is an effective method to remove the residue layer on reactive ion etched silicon. Figure 3 shows the photoelectron spectra of C 1s obtained after  $\text{NF}_3$  plasma treatment. As a comparison, the C 1s peaks after reactive ion etching and the  $\text{SF}_6$  plasma treatment are shown together. As shown in the figure, no  $\text{C-CFx}$  and  $\text{C-Fy}$  bonds exist with  $\text{NF}_3$  treated sample while small amount of  $\text{C-CFx}$  and  $\text{C-Fy}$  bonds still remains on the silicon surface with  $\text{SF}_6$  plasma treated sample. This indicates that the  $\text{NF}_3$  plasma treatment can be more effective than  $\text{SF}_6$  plasma treatment for the removal of residue layer. Figure 4 represents photoelectron spectra of F 1s peaks obtained after RIE,  $\text{NF}_3$ /wet clean treatment, and  $\text{NF}_3$ /RTA/wet cleaning treatment, respectively. After  $\text{NF}_3$  treatment, all of the constituents for the fluorine bonds such as F-Si, F-O, and F-C are reduced while relative contributions of F-Si and F-O bonds to fluorine peak increase. Also FWHM(full width half maximum) of F-C bond increases. This means that F-C bonds are loosened through the above treatments. These loose F-C bonds are appeared to be easily removed by the successive RTA and wet cleaning treatments as shown in figure 2. With  $\text{SF}_6$  plasma treated sample, F-C and F-O bonds are mainly detected, and the increase of FWHM for F-C bond is also observed. These bonds can be also easily removed by successive RTA treatment at  $700^\circ\text{C}$ . Figure 5 shows that the fluorine depth profiles using SIMS for RTA treated samples at  $700^\circ\text{C}$  after  $\text{SF}_6$  and  $\text{NF}_3$  plasma exposure. Compared to the

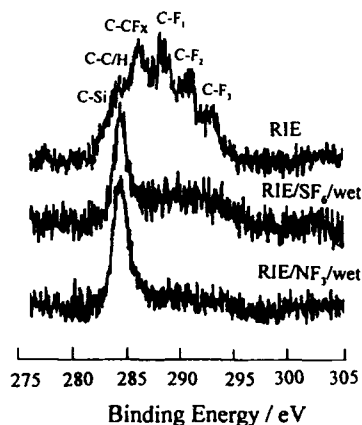


Fig. 3 The comparison of C 1s spectra after wet clean of  $\text{SF}_6$  and  $\text{NF}_3$  plasma treatments

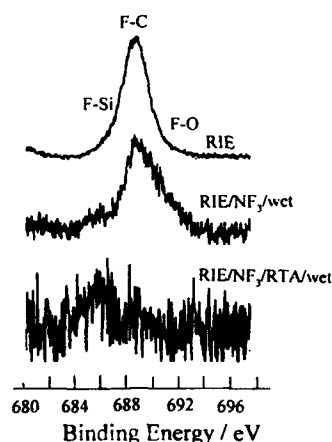


Fig. 4 The changes of F 1s spectra after post etch treatments using  $\text{NF}_3$  plasma

reactive ion etched sample, fluorine secondary ion counts after  $\text{SF}_6$  or  $\text{NF}_3$  plasmas/wet clean decrease. These seem to be due to etching of contaminated silicon. With additional RTA/wet clean after  $\text{SF}_6$  or  $\text{NF}_3$  plasma exposure, fluorine also decreases. It can be explained by the out-diffusion of fluorine. And carbon also shows the same phenomenon. From this it can be said that low temperature RTA treatments for removal of impurities in silicon is possible. Figure 6 represents the reverse leakage current densities ( $\text{A}/\text{cm}^2$ )(a) and barrier heights (eV)(b) of PtSi/n-type Si Schottky barrier diodes. The barrier height was calculated from the reverse leakage current by assuming the thermionic emission model for current transport[7]. This figure shows that the reverse leakage current is decreased and the barrier height is increased with post etch treatments. Barrier height of RIEd sample is lower than that of control sample, that is, 0.84 eV. The difference of barrier heights between RIEd and control samples is about 0.15 eV. The decrease of barrier height indicates the increase of surface energy state generated by disruption of crystal lattice at the interface between PtSi and n-type silicon[8]. The etch rates of n<sup>+</sup> polysilicon with  $\text{SF}_6$  and  $\text{NF}_3$  plasma exposure are 105 nm/minute and 120 nm/minute, respectively. These indicate that during the plasma treatments silicon was etched less than about 15 nm. Therefore the increase of barrier height and the decrease of reverse leakage current with the  $\text{SF}_6$  or  $\text{NF}_3$  plasma exposure may be induced from the removal of the contaminated silicon layer. But, the barrier heights after  $\text{NF}_3$  or  $\text{SF}_6$  plasma/wet treatments were 0.718 - 0.727 eV. This means that the contaminated silicon layer is still remained. And the barrier heights of silicon with successive RTA/wet treated samples increase to 0.761 - 0.771 eV. This may be due to the recovery of modified Si surface after successive RTA treatment. As a result, RTA treatment is effective to recovery of modified silicon surface. Figure 7 shows the contact resistance ( $R_c$ ) measured on the Kelvin pattern after various post etch treatments. It is found that the  $R_c$  changes with post etch treatments, such as  $\text{SF}_6$  plasma/wet clean and  $\text{SF}_6$

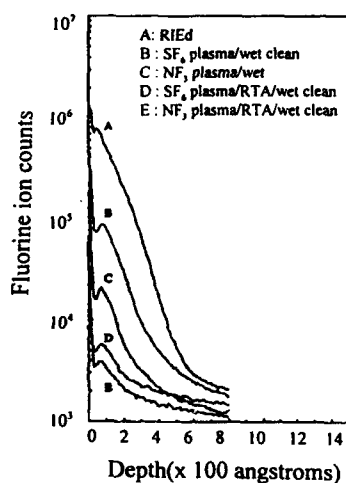


Fig. 5 Fluorine depth profile changes after various post etch treatments

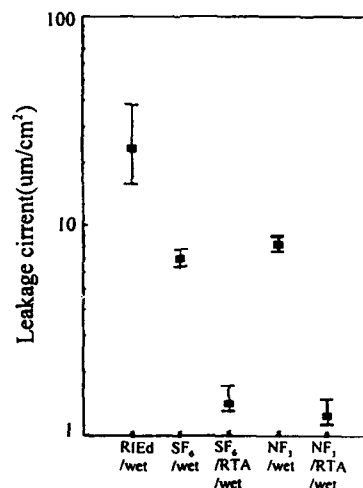


Fig. 6 The changes of contact resistance after various post etch treatments

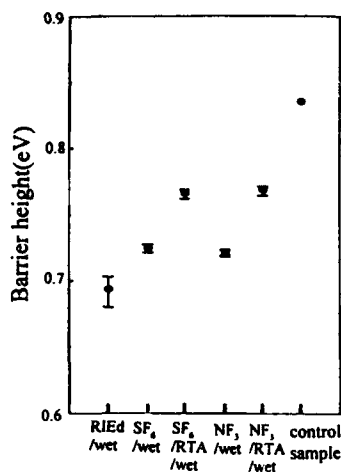


Fig. 7 The changes of barrier height after various post etch treatments

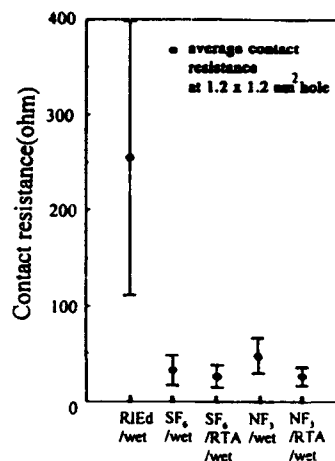


Fig. 8 The changes of leakage current after various post etch treatments

plasma/RTA/wet clean. These electrical characteristics were measured for contact having a hole size of  $1.2 \times 1.2 \mu\text{m}^2$ . Prior to this work, the thickness and composition change of residue layer with the size of open area were checked with a scanning Auger microscopy. The thickness and composition change of residue layer were not detected even though contact hole size was reduced to  $1 \times 1 \mu\text{m}^2$  in size from  $100 \times 100 \mu\text{m}^2$ . These results mean that the appearance of residue layer in the  $1.2 \times 1.2 \mu\text{m}^2$  contact hole seem to be similar to that extracted from ESCA analyses for the residue layer in wide area. Rc of the samples with NF<sub>3</sub> or SF<sub>6</sub> plasma treatment followed by wet cleaning is abruptly decreased compared to that of photoresist stripped sample using wet process. These decreases of Rc can be explained by the effective removal of residue layer on the silicon with SF<sub>6</sub> or NF<sub>3</sub> plasma exposure. Average Rc of SF<sub>6</sub> plasma treated sample is a little lower than that of NF<sub>3</sub> plasma exposed sample. Meanwhile it was found that the distribution of Rc in the NF<sub>3</sub> treated sample was wider than that of SF<sub>6</sub> plasma treated sample. Rc decreases with RTA/wet clean treatment after NF<sub>3</sub> or SF<sub>6</sub> plasma exposure. Rc of NF<sub>3</sub> plasma treated sample is similar to that of SF<sub>6</sub> treated sample after the following RTA/wet clean treatment. Compared to figure 6, decrease of Rc with RTA treatment may result from the recovery of modified silicon surface.

## CONCLUSIONS

Using XPS analysis, it is confirmed that SF<sub>6</sub> or NF<sub>3</sub> plasma treatment after RIE induces the decrease of carbon and fluorine contents and increase of silicon content on etched Si surface. This means that SF<sub>6</sub> or NF<sub>3</sub> plasma treatment is effective to remove the residue layer on the reactive ion etched silicon. During the RTA/wet treatment after SF<sub>6</sub> or NF<sub>3</sub> plasma treatment, fluorine in residue layer evaporates due to the thermal decomposition but carbon remains on silicon surface. This induces the formation of C-C/H. Therefore, after RTA/wet clean treatment, fluorine is not detected on the silicon surface. SIMS results show that penetrated impurities in the contaminated silicon substrate reduce through the additional RTA treatment. It

can be explained by the out-diffusion of fluorine. And  $R_c$  of  $1.2 \times 1.2 \text{ } \mu\text{m}^2$  contact hole decreases and barrier height of PtSi/n-type Si schottky diode increases after the RTA/wet clean treatment. The decrease of  $R_c$  and increase of barrier height with RTA treatment may be resulted from the removal of the residue layer on the silicon and the recovery of contaminated silicon layer. These results indicate that RTA after  $\text{SF}_6$  or  $\text{NF}_3$  plasma exposure is an effective method to recover of reactive ion etched silicon.

#### REFERENCES

1. A. S. Yapsir, G. Fortune-Wiltshire, J. P. Gambino, R. H. Kastle, and C. C. Parks, J. Vac. Sci. Technol., A8, 2939 (1990)
2. S. J. Fonash, Solid State Technology, 29, 201 (1985)
3. J. M. Heddleson, M. W. Horn, and S. J. Fonash, J. Vac. Technol., B6, 280 (1988)
4. J. P. Gambino, G. S. Oehrlein, M. D. Monkowski, J. F. Shepard, and C. C. Parks, J. Electrochem. Soc., vol. 137, 976 (1990)
5. G. S. Oehrlein, G. J. Scilla, and S. J. Jeng, Appl. Phys. Lett., 52(11), 907 (1988)
6. H.-H. Park and K.-H. Kwon, et al., presented at the 1993 MRS Spring Meeting, San Francisco, CA, 1993 (in press)
7. S. M. Sze, *Semiconductor Devices Physics and Technology* (John Wiley & Sons, New York, 1985), p. 167
8. Edwards S. Yang, *Fundamentals of Semiconductor Devices* (McGraw-Hill Book Co., New York, 1978), p. 128

## REACTIVE-ION-ETCHING OF 100nm LINEWIDTH TUNGSTEN FEATURES USING $\text{SF}_6/\text{H}_2$ AND A Cr-LIFTOFF MASK

LORETTA M. SHIREY<sup>1</sup>, KELLY W. FOSTER<sup>2</sup>, WILLIAM CHU<sup>1</sup> (ONT POSTDOCTORAL FELLOW), JOHN KOSAKOWSKI<sup>3</sup>, KEE WOO RHEE<sup>3</sup>, CHARLES EDDY, JR.<sup>4</sup>, DOEWON PARK<sup>1</sup>, I. PETER ISAACSON<sup>1</sup>, DANIEL MCCARTHY<sup>1</sup>, CHRISTIE R. K. MARRIAN<sup>1</sup>, MARTIN C. PECKERAR<sup>5</sup> AND ELIZABETH A. DOBISZ<sup>5</sup>

<sup>1</sup>Naval Research Laboratory, Nanoelectronics Processing Facility, Code 6804, 4555 Overlook Ave. SW, Washington, DC 20375

<sup>2</sup>Applied Research Corporation, 8201 Corporate Drive, Suite 1120, Landover, MD 20785

<sup>3</sup>SFA, Inc., 1401 McCormick Drive, Landover, MD 20785

<sup>4</sup>Naval Research Laboratory, Code 6675, 4555 Overlook Ave. SW, Washington, DC 20375

<sup>5</sup>Naval Research Laboratory, Code 6860, 4555 Overlook Ave. SW, Washington, DC 20375

### ABSTRACT

Reactive ion etching of features down to 100 nm in linewidth in tungsten has been studied using an  $\text{SF}_6$  based chemistry. The studies were carried out in a PlasmaTherm 500 etcher operated at low pressure (2 mTorr) and power (100 mWatts/cm<sup>2</sup>). Key processing parameters have been identified to achieve the resolution and aspect ratio required for high contrast x-ray masks. The critical parameters include sample temperature, gas dilution and end point detection. However, even with all of these parameters optimized, additional sidewall passivation is required to obtain the necessary 6.5:1 aspect ratio. A novel method of achieving such passivation based on an intermittent etching process is described.

### INTRODUCTION

Tungsten etching is of interest for a number of applications including the subtractive patterning of absorbers on x-ray lithography masks. To achieve a high resolution, high contrast x-ray mask for synchrotron x-ray lithography, high aspect ratios are required in thick (300-700 nm) W absorbers for 100 nm feature sizes. As a result, anisotropy and undercutting are the key process factors which must be controlled. The important processing parameters for W etching have been studied and optimized. These include sample temperature, gas mixture, etch time and sidewall passivation.

### EXPERIMENTAL

#### Patterning

Samples consist of silicon wafers with a 650 nm thick layer of low-stress W film grown over a 20 nm thick Cr film etch-stop layer [1]. For sub-micron features, the wafers are spin coated with poly-methyl-methacrylate (PMMA), a positive e-beam resist, and patterned in a JEOL JBX5DII e-beam writer at 50 keV [2]. The e-beam patterns written in PMMA consist of arrays of dots or lines with sizes ranging from 5  $\mu\text{m}$  down to a minimum width of 100 nm. After development of the PMMA, 65 nm of Cr is deposited onto the sample in an e-beam evaporator, and the etch mask pattern is defined by lift-off in acetone.

#### Etching

A PlasmaTherm 500 reactive-ion-etching (RIE) system is used for dry etching of the tungsten layer with etch chemistry based on  $\text{SF}_6$ . A parameter space study was done varying the

substrate temperature, the total power to the sample, the SF<sub>6</sub> flow rate, combinations of gases (H<sub>2</sub>, CHF<sub>3</sub>, O<sub>2</sub>, He, or N<sub>2</sub> added to the SF<sub>6</sub>), etching termination time and continuity of run.

During etching the substrate is backside-cooled, using a recirculating chiller capable of maintaining a sample temperature between 30° and -25°C. Samples are warmed to room temperature before venting the system. The vacuum base pressure is  $\sim 5 \times 10^{-6}$  Torr, and the system is operated at 2 mTorr during the etching process. The 2 mTorr pressure is the minimum pressure that can sustain a plasma discharge in this system. It is a lower pressure than that used for standard RIE etching and was expected to give higher anisotropy [3]. Total power density is maintained at 100 mW/cm<sup>2</sup> during the etching process, resulting in a sample bias of  $\sim 85$  V (not independently controllable in this RIE system).

#### Characterization And Evaluation Methods

A HeNe ( $\lambda = 633$  nm) laser monitors changes in the surface reflectivity of the sample surface and aids in determining the point at which the W is completely etched away and the Cr etch stop layer has been reached [4]. In addition to the laser monitoring system, several other tests are used to evaluate the extent of the etching. A Tencor Alpha-Step Profilometer is used to measure the depth of the step in the etched features (this includes the thickness of the Cr etch mask layer on top), and a Leica 360 FESEM is used to assess whether the W is completely removed. The W residue has a grasslike appearance, whereas the Cr etch stop layer is easily distinguished because of its smooth, flat surface.

The samples are viewed at a  $\sim 90^\circ$  tilt in the SEM to measure the features and examine the shape of the etched edges in cross-section. Percent undercutting is determined from the SEM by comparing the width of the etched tungsten feature with the width of the Cr mask feature.

#### **RESULTS**

SF<sub>6</sub> is an effective and moderately fast etching gas for W. The etch rate in this system with 5 sccm SF<sub>6</sub> is  $>1000 \text{ \AA}/\text{min}$ . SF<sub>6</sub> selectivity of W over Si (and many w-ray mask membrane materials) and e-beam resists, however, is poor. Furthermore, the W etching is not anisotropic, resulting in severe undercutting even at the 2 mTorr operating pressure. The addition of the Cr etch-stop layer between the W and the Si substrate eliminated the problem of selectivity over Si. Cr is not etched at all with the SF<sub>6</sub>, which is also the reason Cr is used as the etch mask instead of an e-beam resist. The anisotropy of the process is greatly improved by cooling the substrate to low temperatures ( $< -20^\circ\text{C}$ ) while etching [5]. The effect of sample temperature on undercutting is shown by comparing fig. 1a. and fig. 1d. Clearly the lowest temperature decreases the amount of undercutting and improves the anisotropy.

To further reduce the degree of undercutting, other gases were added to the SF<sub>6</sub> and the etched features were evaluated. The most effective combination is a 4:1 mixture of SF<sub>6</sub>:H<sub>2</sub>. The effect of adding H<sub>2</sub> to the SF<sub>6</sub> is shown by comparison of fig. 1b (SF<sub>6</sub>, no H<sub>2</sub>) to fig. 1d (20% H<sub>2</sub> in SF<sub>6</sub>). The sidewall undercutting was further reduced by accurate endpoint detection. With laser monitoring, the etch stop point can be controlled. Figs. 1c & 1d show a comparison of features after overetching (1c) and etch termination at the Cr etch stop layer (1d). This is shown graphically in fig. 2.

Using the above optimized process, 250 nm linewidth features can be etched with only a moderate amount of undercutting (28% dimension loss). However, the undercutting can be almost eliminated by etching intermittently in 5 minute etch intervals. Between intervals the sample is warmed to room temperature and the system is vented. Fig. 3 compares the results of intermittent and non-intermittent etching. With an intermittent etching process, 100 nm linewidth features with a 6.5:1 aspect ratio and straight, vertical sidewalls can be reproducibly etched into W (Fig. 4).

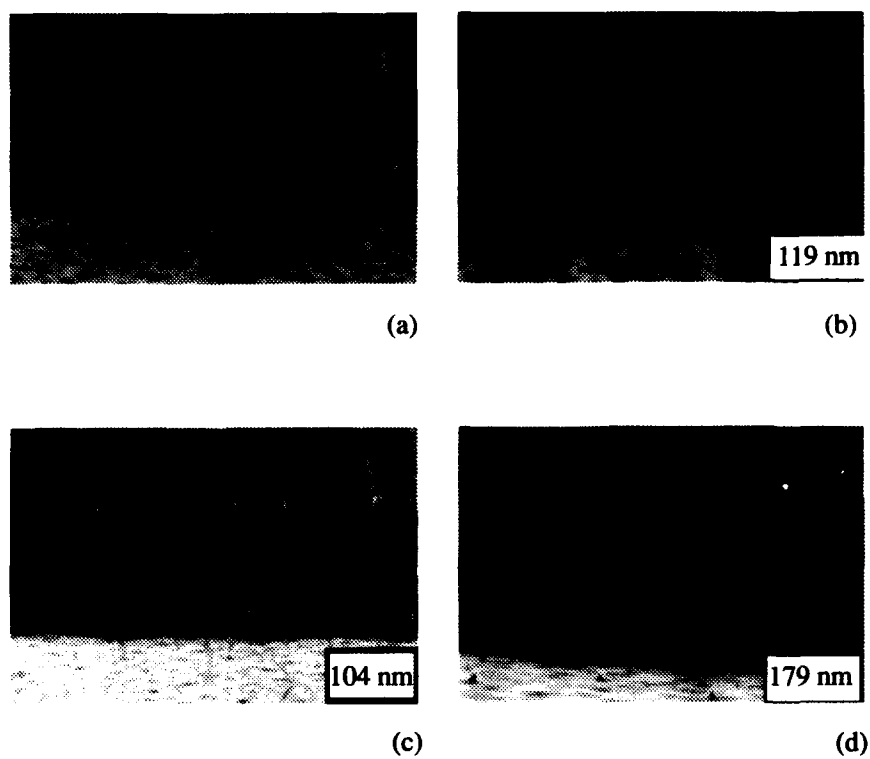


Fig. 1 SEM micrographs show 250 nm patterned lines etched in W, using  $\text{SF}_6 + \text{H}_2$  and sample temperature -20 to -25°C (except as noted): a) 15° Sample temperature b)  $\text{SF}_6$  with no  $\text{H}_2$  added c) etched beyond termination point d) laser terminated.



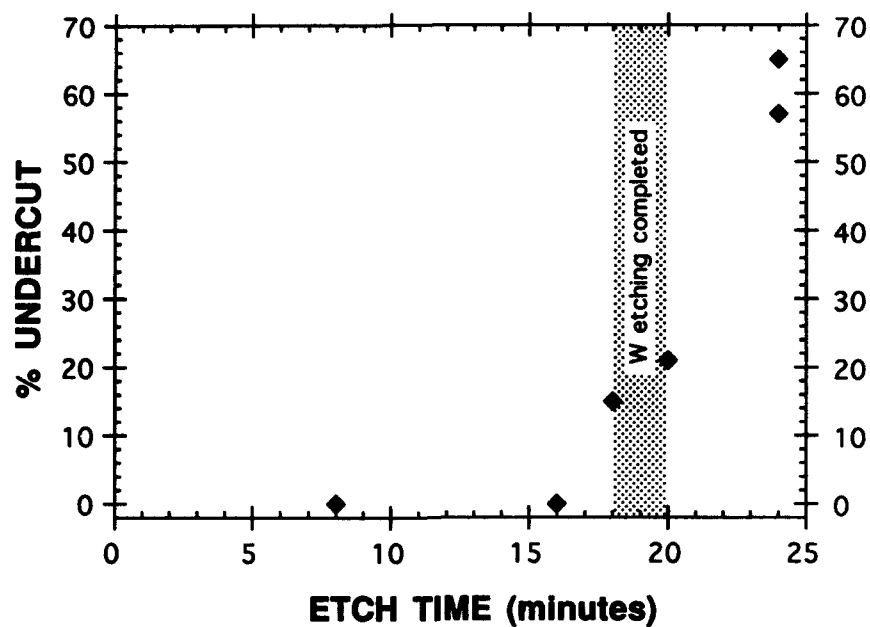


Fig. 2 Graph of etch time vs. % undercut during W etching using the described optimal conditions. Note the increase in undercutting at the point the Cr etch stop layer is exposed.

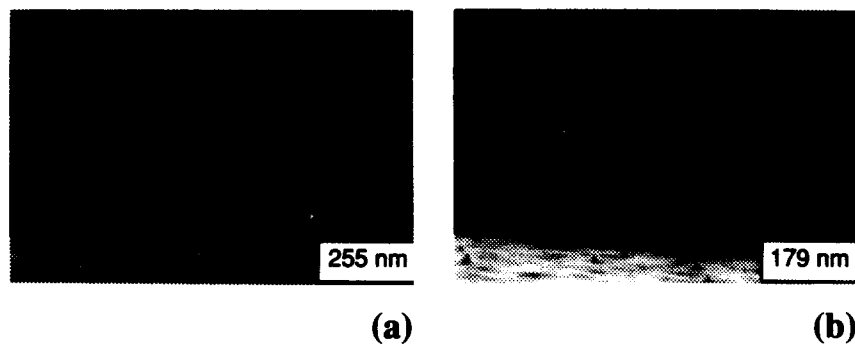
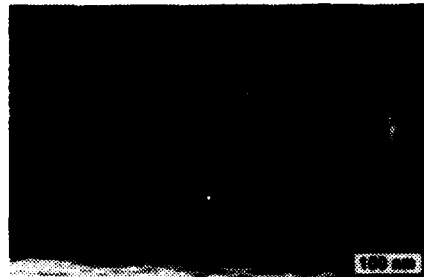


Fig. 3 SEM micrograph demonstrating a) intermittent vs. b) non-intermittent W etching

Fig. 4 SEM micrograph showing 100 nm lines etched in W using optimal etching conditions.



## DISCUSSION

The critical parameters for etching straight sidewalls in W are low substrate temperature, gas mixture to  $\text{SF}_6$ , endpoint detection and intermittent etching. The reduced undercutting achieved by low substrate temperatures confirms the work reported by C. Jurgensen, et. al. [5]. The addition of  $\text{H}_2$  is very important to reduce the undercutting. Similar results were not obtained by adding  $\text{CHF}_3$  or He to the  $\text{SF}_6$ . It appears that the  $\text{H}_2$  either passivates the sidewalls or combines with fluorine radicals in the etching gas.

Experimental results show that profile undercut predominantly occurs after the W has been etched away and the Cr etch-stop layer reached. Based upon these experimental observations we have developed a phenomenological model which explains the undercutting effect. The model assumes that ions are incident normal to the substrate (consistent with the low pressure and power: 2 mTorr and  $100 \text{ mW/cm}^2$ , respectively) and that these ions can be re-emitted from the substrate. As the etching progresses and the W is consumed, eventually the Cr etch-stop layer is reached. Since the F ions do not etch the Cr, there exists a large concentration of F ions at the Cr interface. This concentration gradient causes a re-emission of these F ions from the surface. Computer simulations of this re-emission effect assume a  $\cos^2\theta$  angular

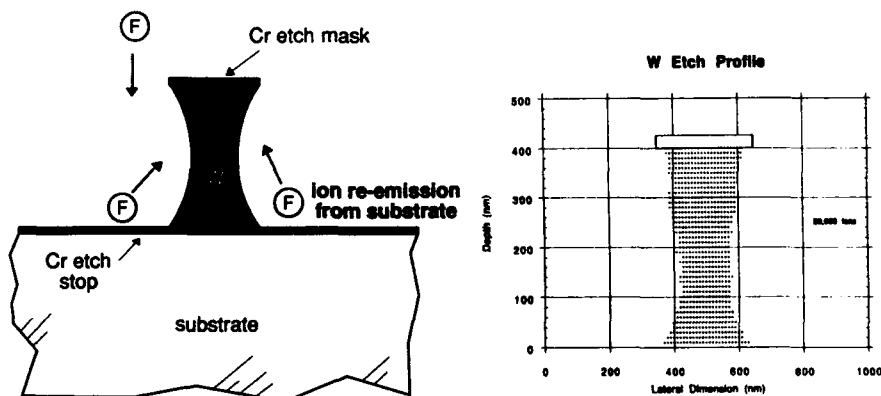


Fig. 5 Schematic diagram (left) of computer model which explains the effect of endpoint termination on the undercutting. Computer simulated cross-section profile (right) of feature etched 33% beyond time endpoint was reached.

distribution for the re-emitted ions and an exponentially decaying (from the Cr surface) density function. The output of the computer modeling, as shown in Fig. 5, agrees qualitatively with the etch profile evolution that has been observed experimentally.

The best sidewall profile was obtained by intermittently exposing the sample to air. Similar results could not be obtained by intermittently exposing the sample to O<sub>2</sub> or N<sub>2</sub>. It is likely that water vapor plays an important role in the sidewall passivation.

## CONCLUSION

It has been shown that 100 nm linewidths can be anisotropically etched 650 nm deep in W, with small amount of lateral undercutting in the W feature sidewalls. The anisotropy is optimized by a combination of cooling the sample to -25°C, diluting the SF<sub>6</sub> gas with H<sub>2</sub> (4:1) and intermittent etching. None of the above elements of this technique, when used alone, was sufficient to achieve 100 nm linewidths with straight sidewalls and no dimension loss. A passivation method in which the sample was intermittently exposed to air was demonstrated here. Cr is an effective etch mask and etch stop layer because of the selectivity of SF<sub>6</sub> for W. Even with the Cr etch stop layer, however, it is critical to terminate the etching at the endpoint. This is necessary to prevent the increased W sidewall etching occurring near the W/Cr interface resulting from re-emission of F radical ions from the Cr surface. A model was developed to explain the process. A simple laser reflectometry technique has been demonstrated to be effective for the endpoint detection necessary for accurate termination.

## ACKNOWLEDGMENTS

This work was supported by ARPA under the Advanced Lithography Program.

## REFERENCES

1. Y.C. Ku, L.-P. Ng, R. Carpenter, K. Lu, H.I. Smith, L.E. Haas and I. Plotnik, *J. Vac. Sci. Technol. B*, 9(6), 3297 (1991).
2. K.W. Rhee, A.C. Ting, L.M. Shirey, K.W. Foster, J.M. Andrews, M.C. Peckerar and Y.C. Ku, *J. Vac. Sci. Technol. B*, 9(6), 3292 (1991).
3. L. Peters, *Semiconductor International*, May, 66 (1992).
4. W. Chu, K.W. Foster, L.M. Shirey, K.W. Rhee, J. Kosakowski, P. Isaacson, D. McCarthy, C.R. Eddy, Jr., E.A. Dobisz, C.R.K. Marrian and M.C. Peckerar, (submitted to *Appl. Phys. Lett.*)
5. C.W. Jurgensen, R.R. Kola, A.E. Novembre, W.W. Tai, J. Frackowiak, L.E. Trimble and G.K. Celler, *J. Vac. Sci. Technol. B*, 9(6), 3280 (1991).

## A NEW ENVIRONMENTALLY STABLE POSITIVE TONE CHEMICALLY AMPLIFIED RESIST SYSTEM - KRS

WU-SONG HUANG\*, RANEE KWONG\*, AHMAD KATNANI\*, MAHMOUD KHOJASTEH\* and KIM Y. LEE\*\*

\* IBM Microelectronics Division, Hopewell Junction, New York 12533

\*\* IBM SRDC, T.J. Watson Research Center, Yorktown Heights, New York 10598

### ABSTRACT

It is known that one of the main shortcomings of chemically amplified resist systems is their sensitivity to airborne base contaminants. The contaminants cause unpredictable linewidth variations deeming the resist incompatible with manufacturing. Besides other issues, this drawback has greatly contributed to the slow introduction of DUV into manufacturing and discouraged most semiconductor manufactures from including DUV in their strategic plans. In this paper, we present a new positive tone chemically amplified photoresist system which is resilient to airborne base contaminants and it shows stable linewidth for more than 24 hours delay between exposure and development. This resist has high sensitivity (17-18 mJ/cm<sup>2</sup>), high contrast (7), high resolution (0.35  $\mu$ m with  $\lambda$  = 248 nm and NA = 0.37) and large process latitude in deep-UV lithography. This resist also exhibits high resolution (0.1  $\mu$ m in 0.35  $\mu$ m thick resist) in E-beam lithography at a sensitivity of about 10 uC/cm<sup>2</sup>. Both lithographic systems (deep-UV and E-beam) yield nearly vertical profiles in the resist images.

### INTRODUCTION

The fabrication of microelectronic devices has been advanced to submicron lithography. Thousands of devices are manufactured with several millions of transistors integrated within a single chip. This would not have happened without the advancement in the microlithography area. Right now, with the availability of high NA I-line tools, 0.4 micron resist image can be constantly produced with relatively large process latitude. However, the ultimate resolution limit is mainly governed by the wavelength of the exposure light. Therefore, DUV (248 nm) exposure systems should be capable of printing smaller dimension (less than 0.35 $\mu$ m) as compared to I-line (365 nm) system. Despite this simple fact, most manufacturers in the semiconductor industry are still reluctant to adopt Deep-UV system due to many reasons, among them the lack of market availability of environmentally stable resist. The environmental stability problem is not significant for the conventional diazonaphthoquinone resist systems. It manifests itself for chemical amplified resist systems<sup>1</sup>. The "chemical amplification" mechanism involves an acid generation during exposure and a thermal catalytical reaction during post exposure bake. Several of these type of resist systems based on tert-butoxycarbonyl (t-BOC) protection on phenol functionality have been reported.<sup>1-3</sup> Besides t-BOC system, the acetal groups and t-butyl carboxylic ester groups were also investigated in the chemically amplified positive tone resist systems.<sup>4-8</sup> The advantages of chemically amplified resist systems are high sensitivity, high contrast and high resolution. Most of these resist systems also have large development latitude, i.e. the development time can be changed from 100% to 300% beyond end point without significant change in the linewidth (LW) of the resist image. However, this type of resist system suffers from dramatic linewidth variation mainly caused by airborne base contaminants.<sup>9</sup> Actually, many other factors besides airborne base contaminants affect linewidth control, e.g. acid diffusivity, acid volatility and strong acid induced crosslinking etc. To solve this problem, many approaches have been adopted or suggested, e.g. applying a protective top layer, installing an air filtration system or using a photoacid generator which generates weaker acid. These approaches only reduce the effect and do not solve the fundamental problem. In this paper we present a resist system, referred to as KRS, based on totally new approach. We designed a system which has extremely high reaction rate. Therefore, the chemical amplification occurs right after exposure at room temperature

eliminating the need for post exposure bake (PEB) and the effects of associated delays. Since the protecting group is acid labile at room temperature, the effect of the resist sensitivity to air born base contaminants is significantly minimized. This resist system has demonstrated good lithographic performance in E-beam and deep-UV exposures.

## RESIST COMPOSITION

KRS resist uses polyhydroxystyrene (PHS) as base resin. This makes the resist compatible with deep-UV requirements: low absorption at 248 nm wavelength and high T<sub>g</sub> & etch resistant to O<sub>3</sub>. The dissolution inhibition of KRS resist is achieved by attaching an acid labile group to the phenol functional site. This protecting group is extremely acid labile thus giving the resist a tremendous advantage over other chemically amplified resists with regard to PEB and environmental stabilities. In most of the reported literatures, onium salts appear to show some negative tone behavior in the photoprocess.<sup>10,11</sup> Onium salts are commonly categorized as ionic acid generators which include diaryl iodonium salts, triarylsulfonium salts and the like. For various reason, most of the current efforts in deep-UV positive tone system are shifting to nonionic photoacid generators. One common observation is that the environmental stability of the resist is improved by using these nonionic acid generators, especially those that generate weaker sulfonic acids. However, the choice of photoacid generator appears to have insignificant or no effect on the lithographic performance of KRS resist. In addition, the environmental stability of KRS resist is independent of the acid generator used. The formulation used in this study contains triphenylsulfonium triflate acid generator and propylene glycol monomethyl ether acetate solvent.

## PROCESS CONDITIONS

The resist sensitivity and linewidth of most chemically amplified resist systems are very sensitive to PAB and PEB temperature. Therefore, precise temperature control of the hot plate is of utmost importance for a stable and reproducible process. As mentioned earlier, KRS resist system exhibits a large bake latitude rendering the need for high precision hot plates as unnecessary. In addition, KRS exhibits a large develop time latitude. Overall, these attributes of KRS do not put required stringent conditions on the process line. The process conditions for DUV and E-beam applications are listed in Table I.

## RESULTS AND DISCUSSION

The chemical amplification process usually involves the breaking of a chemical bond, mainly C-O-C linkage to regenerate either phenol or carboxylic acid. The detached species are usually volatile liquids or gases. When these materials escape from the exposed area, it causes film shrinkage. If the film shrinkage is too large, a complicate adverse situation may occur, e.g. difficulty in linewidth control and stress related mechanical failures. Pure t-BOC system has film shrinkage around 30% and the commercially available CAMP-6 system has film shrinkage around 15-20%. The film shrinkage of the exposed area of KRS is around 7 to 10% depending on the amount of protecting group incorporated in the resist system. In E-beam process, the shrinkage is even less due to higher PAB. Therefore, we do not believe the amount of film shrinkage here will cause any foreseeable problems in the manufacture process.

Table I. Process description for Deep-UV and E-beam exposure systems.

|            | DUV                                       | E-beam  |
|------------|---|---|
| Priming    | HMDS                                      | HMDS  |
| Underlayer | ARC if required                           | —   |
| PAB        | 100°C/2 min.                              | 110°C/3 min.                                  |
| Exposure   | Canon 0.37 NA<br>17-20 mJ/cm <sup>2</sup> | EL-3 E-beam 50 keV<br>9-12 uC/cm <sup>2</sup> |
| PEB        | not required                              | —   |
| Develop    | 0.14 N for 80 s                           | 0.14 N for 60 s                               |

## Deep-UV Lithography

To prove the resilience to airborne base contaminants, KRS was treated side by side with T-BOC system with 1-methyl-2-pyrrolidinone (NMP) vapor exposure before Deep-UV radiation and then each resist was processed with its own typical procedure. While T-BOC system failed to resolve images after 45 second of NMP exposure, KRS maintained the same linewidth even after 255 second of NMP exposure.

The linewidth is also remarkably stable against delays between exposure and develop. KRS can maintain  $\pm 10\%$  linewidth after 18 hours delay, see Figure 1. Even when PEB is introduced the linewidth was found to exhibit the same stability, i.e. no change in linewidth even after more than 24 hours delay. This is ten times better than a good t-BOC system, which usually can stand one to two hours PEB delay depending on the environmental condition.

Figure 2 depicts a plot of normalized film thickness as a function of delivered dose, showing a contrast of around 7. The contrast is due to actual change in dissolution rate of bulk material upon exposure and not to the formations of surface skin as commonly observed for the diazonaphthoquinone system. As shown in Figure 3, the end point detection measurement on the unexposed resist exhibits a much faster dissolution rate on the surface than the bulk material. A plot of the dissolution rate vs. depth of the film is shown in Figure 4.

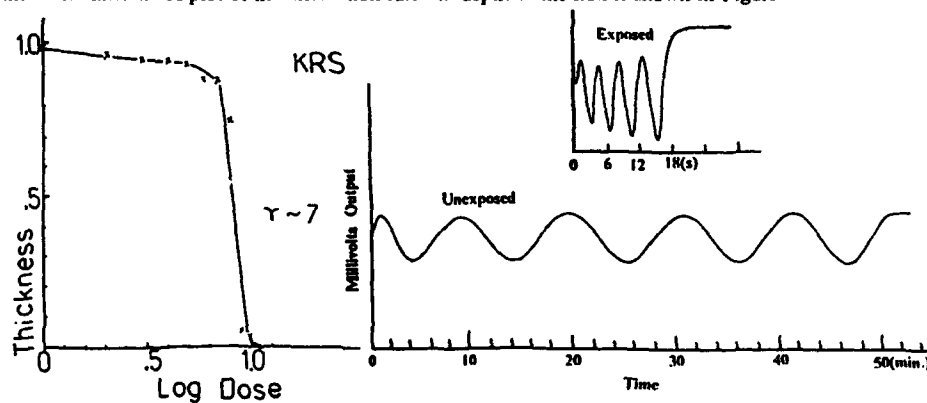


Figure 2. A contrast curve for KRS resist. Figure 3. Output of the laser end-point detection system for KRS resist.

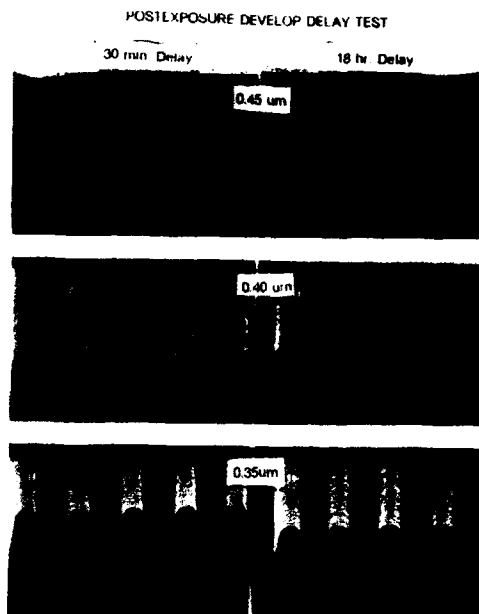


Figure 1. Scanning electron micrographs of KRS resist images for 30 minute and 18 hour delays between exposure and development

The lithographic performance of KRS, resembles that of T-BOC type resist. It has dose latitude greater than 28% for 0.4  $\mu\text{m}$  images using 0.37 NA Canon(TM) excimer laser stepper. The focus latitude is about 1.8 to 2.4  $\mu\text{m}$  at this image size. The resolution of KRS (0.35  $\mu\text{m}$ ) is better than or comparable to T-BOC system, with a K factor of 0.52. The relationship between resist image and mask dimension is linear down to 0.35  $\mu\text{m}$ . The size of the 0.35  $\mu\text{m}$  is slightly off due to the limitation of the 0.37 NA tool. The dose latitude for 0.35  $\mu\text{m}$  is between 15 and 20%, which is slightly lower than the required  $\pm 10\%$  dose latitude. The sensitivity of the resist is around 18 mJ. It swings between 14 mJ and 22 mJ depending on the resist thickness.

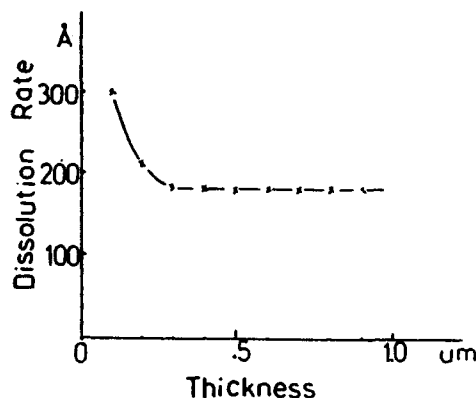


Figure 4. A plot of dissolution rate vs. film depth (distance from surface), derived from Figure 3.

#### E-beam Lithography

Most of DUV resist systems can be extended to E-beam applications. KRS has been exposed with E-beam radiation at different accelerating voltages. KRS resist system combines the advantage of chemically amplified and conventional resist. As mentioned earlier, it exhibits high contrast and sensitivity and at the same time can be processed without PEB. Figure 5 shows a plot of LW vs. dose obtained from exposures with EL-3 E-beam system at 50 KeV. KRS exhibits a large dose latitude which is required for E-beam exposures to accommodate errors resulting from proximity correction.

Although the resist sensitivity can be tuned, the sensitivity of current formulation is in the range of 8-12  $\mu\text{C}/\text{cm}^2$ . High resolution imaging has been demonstrated repeatedly<sup>12</sup>. Resolution down to 0.1  $\mu\text{m}$  has been demonstrated in 0.3  $\mu\text{m}$  thick film as shown in Figure 6.

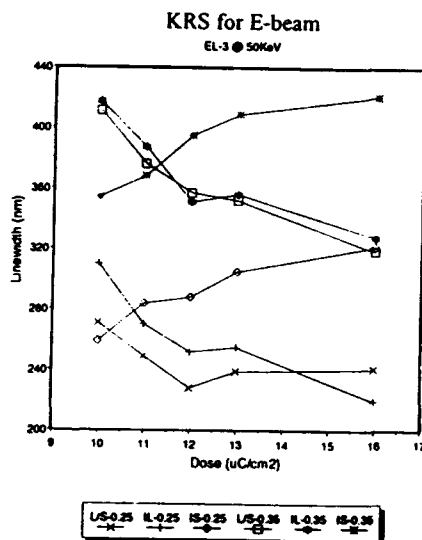


Figure 5. Exposure latitude of different features imaged in KRS with EL-3 E-beam system at 50 KeV.

#### Other Lithographic System

Although KRS has been mainly formulated for DUV and E-beam, it demonstrated reasonable lithographic performance when exposed to other sources of radiations. Sensitivity to I-line exposures has been achieved by incorporating an I-line sensitive photoacid generator. Preliminary lithographic results are very promising and demonstrate the potential applicability of KRS to I-line systems.

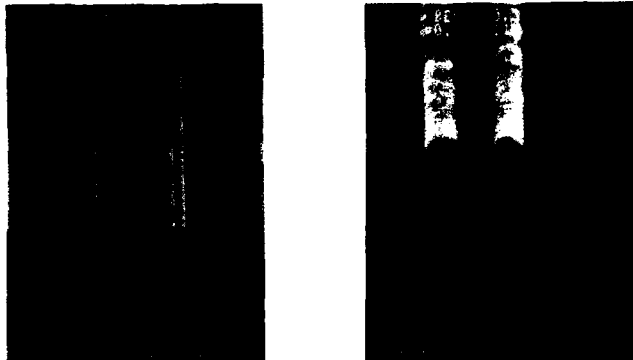


Figure 6. Scanning electron micrographs of 0.1  $\mu\text{m}$  feature printed in KRS using E-beam at 50 KeV.

The DUV formulation was found to be sensitive to X-ray radiation from a compact synchrotron radiation ring source. Initial evaluations performed at the IBM facility demonstrated that KRS exhibits high contrast and requires a dose about  $100\text{mJ}/\text{cm}^2$  upon X-ray exposures. Finally, KRS is expected to be sensitive to ion beam radiation, however no work has been done in this area.

Nevertheless, further work would be required to optimize the performance of the resist for the above lithographic systems.

#### CONCLUSION

We have presented a new resist system based on a novel approach to address the inherent problem with commercial DUV resists. The resist exhibits sensitivity to different type of radiation, among them DUV, E-beam and X-ray. High resolution imaging with large process latitudes have been demonstrated with KRS resist in DUV and E-beam lithography.

#### ACKNOWLEDGEMENTS

The authors would like to thank Gary Spinillo, Rob wood, P. Jaganathan, R. Sooriyakamuran, J. Fahey, W. Brunsvold, Wayne Moreau and Karen Petrillo for their invaluable discussions and technical support.

#### REFERENCE

1. J.M.J. Frechet, H. Ito, C.G. Willson, Microcircuit Eng. 260, (1982); C.G. Willson, H. Ito, J.M.J. Frechet, *ibid.* 261 (1982); H. Ito, C.G. Willson, Polym. Eng. Sci. 23, 1012 (1983).
2. R.G. Tarascon, E. Reichmanis, F.M. Houlihan, A. Shugard, L.F. Thompson, polym. Eng. Soc. 29, 850 (1989).
3. S.R. Turner, K.D. Ahn, C.G. Willson in Polymer for High Technology, ACS Symposium Series, No. 346, M.J. Bowden, S.R. Turner, Eds., 200 (1987).
4. G.H. Smith, S. Paul, J.A. Bonham, US Patent 3,779,778 (1973).



5. Y. Jiang and D. Bassett, *Proc. Amer. Chem. Soc. Polym. mater. Sci. Eng.*, 66, 41 (1992).
6. N. Hayashi, S.M.A. Hesp, T. Ueno, M. Toriumi, T. Iwayanagi, and S. Nonogaki, *Proc. Amer. Chem. Soc. Polym. mater. Sci. Eng.*, 61, 417 (1989).
7. H. Ito, C.G. Willson, J.M.J. Frechet, *Proc. SPIE*, 24,771 (1987).
8. H. Ito and M. Ueda, *Macromolecules*, 21, 1703 (1988).
9. S.A. MacDonald, W.D. Hinsberg, H.R. Wendt, N.J. Clecak, C.G. Willson and C.D. Snyder, *Chem. Mater.*, 5, 348, 1993.
10. L. Schlegel, t. Ueno, H. Shiraishi, N. Hayashi and T. Iwayanagi, *Microelectr. Eng.* 13, 33 (1991).
11. E. Reichmanis, F.M. Houlihan, O. Nalamasu and T.X. Neenan, *Chem. Mater.* 3, 394 (1991).
12. K.Y. Lee and W.S. Huang, *J. Vac. Sci. Technol. B*, in press.

## Author Index

- Abernathy, C.R., 341  
 Acosta, D.R., 433  
 Adel, M.E., 353  
 Adesida, I., 181  
 Ahrenkiel, R.K., 233  
 Aizenberg, Gustavo E., 87  
 Alstrin, April L., 359  
 Amioti, M., 225  
 Ammerlaan, C.A.J., 385  
 An, Ilsin, 33  
 Androulidaki, M., 205  
 Asinovsky, L.M., 47  
 Aspnes, D.E., 3
- Bachmann, K.J., 27  
 Baltagi, Y., 199  
 Bao, X.J., 65  
 Barrett, J., 39  
 Beck, Scott E., 391  
 Becla, P., 273  
 Beechinor, J.T., 59, 167  
 Bellani, V., 225  
 Benyattou, T., 199  
 Berkowitz, Stuart, 477  
 Bernstein, R.W., 335  
 Bhat, R., 181  
 Bishop, S.G., 181  
 Böbel, F.G., 105  
 Bohling, David A., 391  
 Boltar, Konstantin O., 175  
 Borrego, J.M., 217  
 Bowen, D.K., 451  
 Boyd, Joseph T., 193  
 Breaux, L.H., 397  
 Breiland, W.G., 99  
 Brierley, Steven K., 211  
 Bru, C., 199
- Campo, A., 311  
 Caneau, C., 181  
 Cao, Xuelong, 193  
 Cardinaud, Christophe, 311  
 Carpio, Ron, 249  
 Chang, H., 181  
 Chen, Peter, 193  
 Choo, Ahn Goo, 193, 267  
 Choquette, Kent D., 465  
 Chow, L.A., 105  
 Chow, P.P., 105  
 Chu, William, 487  
 Ciszek, T., 233  
 Clark, Anna, 477  
 Clauson, S.L., 347  
 Cockerton, S., 451  
 Collins, R.W., 33  
 Constantine, C., 341  
 Cooke, L.M., 451  
 Corbett, J.W., 261  
 Crean, G.M., 39, 59, 167
- Criddle, Alan J., 111
- Dahimene, M., 305  
 de Lyon, T.J., 353  
 Debrie, R., 471  
 Desai, Mukesh, 249  
 Dexter, M., 439  
 Dietz, N., 27  
 DiMarzio, D., 457  
 Dimoulas, A., 205  
 DiRubio, C.A., 465  
 Dobisz, Elizabeth A., 487  
 Driver, R.D., 241  
 Drouot, V., 199  
 Dudley, M., 457  
 Dunlavy, D.J., 233
- Eddy, Jr., Charles, 487  
 Edelman, P., 439  
 Eisebitt, S., 119
- Fedirko, Valery A., 175  
 Felker, Brian S., 391  
 Feng, Z.C., 273  
 Finland, B.-O., 335  
 Foster, Kelly W., 487  
 Franke, James E., 93  
 Freund, R.S., 465
- Garcia-Perez, M.A., 199  
 Geatches, Rachel M., 111  
 Geddo, M., 225  
 Gendry, M., 199  
 Geyling, Franz, 255  
 Gilicinski, Andrew G., 391  
 Giordana, A., 153  
 Glembocki, O.J., 153  
 Goto, Makoto, 299  
 Gray, T., 451  
 Greef, R., 53  
 Gregorkiewicz, T., 385  
 Grepstad, J.K., 335  
 Gu, S.Q., 181  
 Guillot, G., 199  
 Guizzetti, G., 225  
 Gumbs, G., 187
- Haaland, David M., 93  
 Hale, Jeffrey, 15  
 Hattori, Tadasi, 373  
 Headley, Thomas J., 255  
 Hegde, R.I., 397  
 Hendriks, Henry T., 211  
 Henry, A., 261  
 Herbert, P.A.F., 167  
 Heyd, A.R., 33  
 Hirose, M., 409  
 Hoke, William E., 211  
 Holland, M.C., 187

- Hollinger, G., 199  
 Hope, D.A.O., 53  
 Howard, A.J., 465  
 Huang, Wu-Song, 493  
 Husby, H., 335  
  
 Iatrou, S., 427  
 Isaacson, I. Peter, 487  
 Ishibashi, I., 409  
 Iwanczyk, J.S., 65  
  
 Jackson, Howard E., 193, 267  
 Jairath, Rahul, 249  
 James, R.B., 65  
 Jensen, K.F., 241  
 Jaynes, C., 167  
 Johnson, F.G., 279  
 Johnson, S.R., 119  
 Johs, Blaine, 15  
 Juan, W.H., 305  
  
 Kahaian, D.J., 329  
 Kakibayashi, H., 293  
 Kaneko, Kyojiro, 379  
 Kang, Jin-Yeong, 481  
 Katayama, Masayuki, 373  
 Katmani, Ahmad, 493  
 Katoh, Isao, 373  
 Kelly, P.V., 59, 167  
 Ketata, K., 471  
 Ketata, M., 471  
 Kharas, D., 427  
 Khojasteh, Mahoud, 493  
 Killeen, K.P., 99  
 Kim, Bo-Woo, 481  
 Kim, H., 365  
 Klein, J.D., 347  
 Ko, K.K., 153  
 Kohnke, G.E., 279  
 Kontkiewicz, A.M., 439  
 Kosakowski, John, 487  
 Kouguchi, M., 293  
 Koumetz, S., 471  
 Kunz, Adina K., 359  
 Kwon, Kwang-Ho, 481  
 Kwong, Rancee, 493  
  
 Lacquet, Beatrys M., 87  
 Lagowski, J., 439  
 Landgren, G., 225  
 Larson, Jr., D.J., 457  
 Lavoie, C., 119  
 Lawson, Chris M., 415  
 Leclercq, J.L., 199  
 Lee, Kim Y., 493  
 Leone, Stephen R., 359  
 Leong, W.H., 53  
 Li, J.P., 267  
 Lindström, J.L., 261  
 Lindstrom, Richard M., 403  
 Loxley, N., 451  
 Lucovsky, G., 27  
 Lynch, S., 39  
  
 Mackenzie, J.A., 119  
 Manfra, Michael, 477  
 Marrian, Christie R.K., 487  
 Matsui, M., 293  
 Matyi, Richard J., 445  
 McCarthy, Daniel, 487  
 McGahan, William A., 15  
 Medernach, John W., 255  
 Melville, Douglas L., 323  
 Michael, Robert R., 415  
 Mil'shtein, S., 427  
 Molnar, Richard, 477  
 Monemar, B., 261  
 Moustakas, T.D., 477  
 Mozume, Teruo, 285  
 Murtagh, M., 167  
 Mutoh, A., 293  
  
 Nagano, H., 293  
 Nakanishi, Hideo, 161  
 Natarajan, M., 65  
 Nelson, K.A., 317  
 Nguyen, Hien V., 33  
 Ni, Bin, 133  
 Niemczyk, Thomas M., 93  
 Nissen, M.K., 119  
 Nordheden, Karen J., 445  
 Noufi, R., 233  
 Nunoi, Toru, 379  
  
 Ohte, Takeo, 299  
  
 Pan, Noren, 211  
 Panepucci, R., 181  
 Pang, S.W., 153, 305, 329, 421  
 Park, Doewon, 487  
 Park, Hyung-Ho, 481  
 Park, R.M., 125  
 Patt, B.E., 65  
 Paul, Rick L., 403  
 Paulson, W.M., 397  
 Pearton, S.J., 341  
 Peckerar, Martin C., 487  
 Pickering, C., 53  
 Pollak, F.H., 187  
 Proscia, James W., 133  
  
 Qiang, H., 187  
  
 Rabago, F., 433  
 Radigan, Kenneth J., 93  
 Radzinski, Z.J., 409  
 Reck, Gene P., 133  
 Reeson, Karen J., 111  
 Reif, Rafael, 365  
 Ren, F., 341  
 Reuter, E., 181  
 Rhee, Kee Woo, 487  
 Rieger, D.J., 465  
 Robbins, D.J., 53  
 Rodrigues, R.G., 217  
 Rogers, John A., 317  
 Roth, J.A., 353

Rouleau, C.M., 125  
Rynders, Rebecca M., 391

Salim, Sateria, 241  
Schlesinger, T.E., 65  
Schowalter, L.J., 217  
Sherlock, M., 39  
Shirey, Loretta M., 487  
Shul, R.J., 465  
Simmons, J.G., 323  
Skocpol, W.J., 477  
Snyder, Paul G., 15  
Sotomayor Torres, C.M., 187  
Spinelli, L., 39  
Stallinga, Peter, 385  
Steckl, Andrew J., 193, 267  
Stell, Matt, 249  
Stephens, D.J., 27  
Stell, Matt, 249  
Stets, James R., 391  
Strausser, Yale E., 391  
Strupp, Paul G., 359  
Stutz, C.E., 153  
Sugawara, Minoru, 299  
Sung, K.T., 305  
Suzuki, Eiichi, 379  
Swart, Pieter L., 75, 87

Tallant, David R., 255  
Talwar, D.N., 273  
Tanner, B.K., 451  
Thomas III, S., 421  
Thompson, D.A., 323  
Tiedje, T., 119  
Tlali, Spirit, 193, 267  
Tobin, P.J., 397  
Tokuda, Yutaka, 373

Tolles, Robert, 249  
Tuchman, J.A., 153  
Turban, G., 311

Uchida, F., 293

van den Berg, L., 65  
Van Hove, J., 105  
Van Scyoc, J.M., 65  
Vernon, S.M., 233

Wada, Kazumi, 161  
Wang, P.D., 187  
Wang, Victor S., 445  
Wanlass, M.W., 233  
Webb, J.D., 233  
Webb, Roger P., 111  
Wetzel, R.C., 465  
Wicks, G.W., 279  
Woodall, J.M., 141  
Woollam, John A., 15  
Wowchak, A., 105  
Wu, Jun, 457

Xu, Q., 181

Yang, K., 217  
Yao, Huade Walter, 15, 65  
Yen, A., 347  
Yeom, Gun-Yung, 481  
Yokoyama, S., 409

Zekentes, K., 205  
Zhang, Lizhong, 93  
Zhang, Y., 261  
Zhou, Z.H., 365

## Subject Index

- AlAs/GaAs superlattices, 15
- algorithms, 451
- AlInP/GaAs, 279
- amines, 133
- amorphous silicon, 33
- annealing, 373
- Ar
  - plasma, 161
  - sputtering, 141
- Ar/Cl<sub>2</sub> plasma, 153
- As
  - capping layer, 335
  - implantation, 409
- aspect ratio, 487
- atomic
  - force microscope, 391, 397
  - tapping mode, 391
  - layer epitaxy, 3
- auxiliary glow discharge, 299
- $\beta$ -SiC, 267
- bilinear transform, 75, 87
- borophosphosilicate glass, 93
- breakdown fields, 397
- Brewster angle reflectance differential spectroscopy (BARDS), 27
- capacitors, 397
- carbonization process, 267
- CdZnTe, 273, 433, 457
- CF<sub>4</sub>-O<sub>2</sub> plasmas, 311
- charge build-up, 427
- chemical
  - mechanical polishing, 249
  - vapor deposition, 33, 133
- chemically amplified resist, 493
- CHF<sub>3</sub>/C<sub>2</sub>F<sub>6</sub> plasma, 481
- closed-loop feed back, 3
- cold neutron capture, 403
- concentration gradients, 241
- contactless electromodulation, 141
- contamination, 293
- conversion efficiency, 379
- copper indium diselenide, 233
- Czochralski growth, 373
- damage, 421
  - etch induced, 153
  - in silicon, 409
  - plasma induced, 161
- dark
  - current, 299
  - voltage contrast, 427
- deep
  - level transient spectroscopy (DLTS), 373
  - UV, 493
- defects, 427
- device processing, 335
- disorder, 267
- donor annihilation, 373
- double axis x-ray diffraction, 451
- dry etching, 471
- e-beam, 493
- electron cyclotron resonance (ECR)
  - assisted MBE, 477
  - etching, 153, 305, 323, 329
  - plasmas, 249
- elastic and loss moduli, 317
- electric field, 427
- electrical performance, 481
- electron
  - spectroscopy for chemical analysis (ESCA), 293
  - traps, 373
- ellipsometry, see spectroscopic ellipsometry
- end point detection, 323, 341
- epioptics, 3
- epitaxial growth, 3
- EPR, 385
- etch
  - products, 329
  - rate, 471
- ex-situ, 15
- far-infrared reflectivity, 273
- Fermi-edge singularity, 205
- Fermi-level, 153
- fiber-based, 241
- floating potential, 299
- focal plane array, 457
- focused ion beam implantation, 193
- Fourier
  - spectral analysis, 75, 87
  - transform
    - infrared spectroscopy, 241, 249
    - Raman spectroscopy, 233
- full wafer mapping, 451
- GaAs, 119, 161, 329, 341, 359, 445, 465
  - surfaces, 141
- GaAs/AlGaAs, 175, 187
  - multilayer structures, 111
- GaNAs, 233, 421
- gamma ray activation analysis, 403
- GaN, 477
- gap-mode, 273
- gas source
  - migration enhanced epitaxy (GSMEE), 285
  - molecular beam epitaxy (GSMBE), 285
- germanium, 311
- Green's function theory, 273
- growth rate, 105
- HEMT, 211
- heteroepitaxial multilayer structures, 75
- heterointerface dislocations, 125
- heterojunction bipolar transistors, 141, 341

- HF, 59
- HgCdTe, 457
- HgI, 65
- high
  - electron mobility transistors, 341
  - resolution x-ray diffraction, 451
- hydrogen, 261, 385, 403
  - plasma, 465
  - radicals, 335
- II-VI/GaAs heterostructures, 125
- III-V compounds, 471
- implantation, 175
- infrared reflectance, 175
- InGaAs, 199
- InGaAs/GaAs, 205, 217
- InGaAs/InP, 181, 225, 285
- InP, 211, 341
- in-situ
  - diagnostics, 15, 53, 359
  - monitoring, 99, 241, 329
  - process monitor, 347
  - sensing, 105
- interface
  - defects, 199
  - roughness, 279
- ion
  - backscattering techniques, 409
  - beam etching, 471
  - damage, 299
  - density, 305
  - energy, 421
  - implantation, 87, 261
  - implanter, 409
- IR reflection spectroscopy, 93
- IrO<sub>2</sub>, 347
- iron(-)
  - boron pairs, 439
  - concentration determination, 439
  - interstitials, 439
- kinetic ellipsometry, 3
- Langmuir probe, 305
- laser
  - ionization, 359
  - light scattering, 3, 133
- lateral
  - confinement, 181
  - quantum confinement, 187
- lattice matched, 225
- lifetime, 379
- light scattering, 53, 119
- lithography, 493
- magnetron sputtering, 347
- many body effects, 205
- medium-energy ion spectroscopy, 409
- mercury probe, 379
- microscope spectrophotometry, 111
- minimal data, virtual interface, 3
- minority carrier, 379
- MOCVD, 3, 279, 241
  - modified Bridgman technique, 433
  - modulation doped quantum dots, 187
  - molecular beam epitaxy, 119, 279, 359
  - multiple quantum well structures, 53, 193, 211
- nitride films, 47
- nondestructive characterization, 111, 317
- OMCVD, see MOCVD
- optical
  - constant data, 99
  - emission spectroscopy, 341, 347
  - low coherence reflectometry, 415
  - reflectance spectroscopy, 75, 87
- [111] oriented, 217
- O<sub>2</sub>/SiH<sub>4</sub> gas flows, 249
- oxide films, 47
- oxygen related defects, 373
- parabolic potential, 187
- partial least squares, 93
- pattern definition, 335
- P<sub>b</sub> center, 385
- photo-dissociation, 439
- photoluminescence, 65, 181, 193, 211, 233, 261
- photorefectance, 141, 153, 161, 167, 175, 187, 199, 217, 225
  - line shapes, 199
- photoresist, 15
- phototransmission, 205
- polycrystalline
  - silicon, 379
  - multilayers, 47
- polyimide, 317
- polysilicon, 255, 397
- power spectral density, 391
- process
  - control, 99
  - monitoring, 65
- pyrometry interferometry, 105
- quadrupole mass spectrometer, 329
- quantum
  - dots, 181
  - wires, 181
- radiation detectors, 65
- Raman scattering, 193, 255, 267, 273, 279, 285
- rapid
  - optimization, 451
  - thermal annealing, 193
- reactive
  - decapping, 335
  - ion etching, 167, 187, 311, 323, 445, 471, 477, 487
- real time, 33, 99, 317
  - characterization, 27
  - monitoring, 3
- reflectance, 33, 105
  - anisotropy spectrometry, 59
  - difference spectroscopy, 3
  - spectral, 99, 111
- reflectivity, 397

- refractive index, 75, 87
- Rutherford backscattering spectrometry, 167
- scanning electron microscopy, 427, 433
- scattered laser light, 125
- Schottky diodes, 421
- selected area electron diffraction, 433
- self-bias, 299
- SF<sub>6</sub> and NF<sub>3</sub> gas plasma, 481
- SF<sub>6</sub>:H<sub>2</sub>, 487
- sheet resistance, 75
- Si(110), 59
- silicon, 33, 105, 167, 175, 233, 261, 311, 373, 385, 415, 439, 481
  - diffusion, 391
  - surfaces, 59, 391
- SIMS, 481
  - plasma probe diagnostics, 323
- simulation, 471
- single quantum well, 111, 199
- Si-NL52, 385
- SiO<sub>2</sub>/Si<sub>3</sub>N<sub>4</sub>/SiO<sub>2</sub>/Si, 27
- Si/Si<sub>1-x</sub>Ge<sub>x</sub>, 53
- smooth etch, 465
- solar cell, 379, 415
- specific contact resistivity, 421
- spectroreflectometry, 3
- spectroscopic ellipsometry, 3, 15, 33, 47, 53, 59, 65, 167
- sputter yield, 471
- strain(-), 225
  - generated electric fields, 217
- stress, 267
- superlattices, 217, 279, 285
- surface
  - differential reflectance, 3
  - emitting laser, 105
  - photoabsorption, 3
  - photovoltage, 439
  - reactivity, 311
  - roughness, 119, 391, 397
  - synchrotron, 457
- ternary semiconductor compounds, 433
- thermal diffusivity, 317
- thickness, 75, 87
- thin films, 27, 33, 317
  - etching, 477
- time-of-flight mass spectroscopy, 359
- TiN, 133
- topography, 397
- transmission
  - electron microscopy, 255, 293
  - lines, 421
- transparent films, 15
- triple crystal x-ray diffraction, 445
- tungsten, 487
- two dimensional electron gas, 205
- uniformity, 305
- variable angle spectroscopic ellipsometry (VASE), 15
- via holes, 341
- volatile reaction products, 323
- wafer temperature, 105
- XPS, 481
- x-ray
  - diffraction, 285
  - topography, 457
- YBCO, 347
- Zener diodes, 427
- ZnSe, 125